

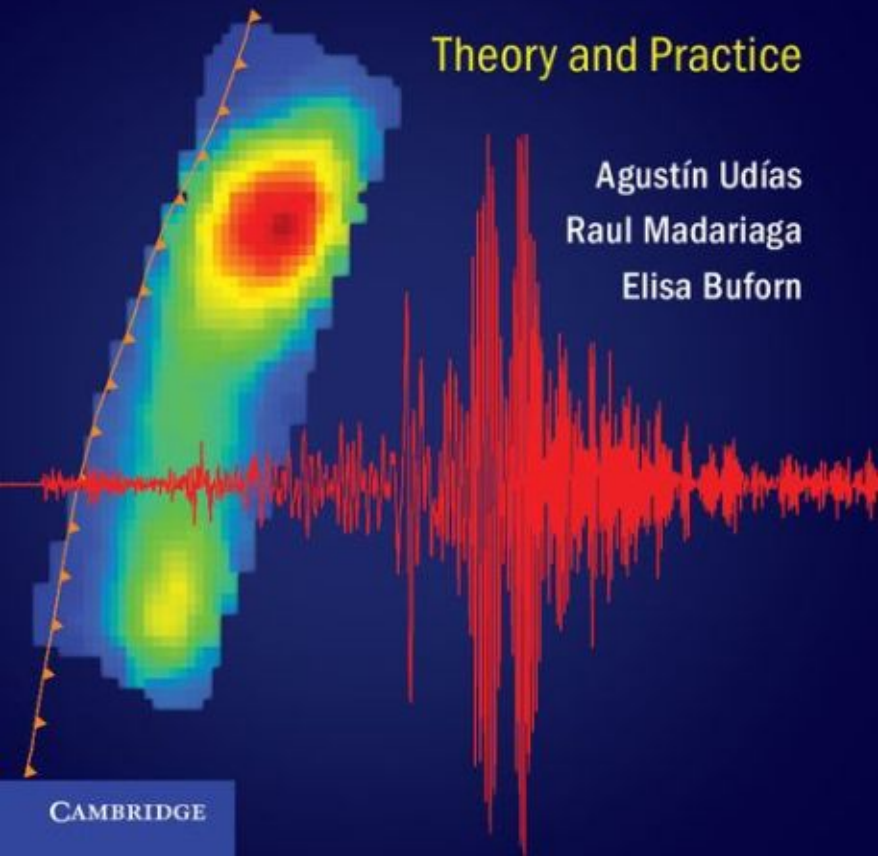
# Source Mechanisms of Earthquakes

Theory and Practice

Agustín Udías

Raul Madariaga

Elisa Buorn



CAMBRIDGE

# Source Mechanisms of Earthquakes

## Theory and Practice

---

Recent, disastrously large and tsunami-generating earthquakes, from Sumatra in 2004 to Chile in 2010 and Japan in 2011, have underlined the need to better understand the origins, dynamics and source mechanisms of earthquakes. This book presents an innovative new approach to studying source mechanisms, combining theory and observation in a unified methodology, with a key focus on the mechanics governing fault failures.

The authors explain source mechanisms by building from fundamental concepts, such as the equations of elasticity theory, to more advanced problems including dislocation theory, kinematic models and fracture dynamics. The theory is presented in a student-friendly form, using consistent notation throughout and with full, detailed, mathematical derivations that enable students to follow each step. The topics covered include point source models, the seismic moment tensor, the determination of point sources and source dimensions and kinematic extended sources.

The later chapters present widely used practical modeling methods for source-mechanism determination, linking clearly to the theoretical foundations. These chapters highlight the processing of digital seismological data and cutting-edge computer methods and are fully supported with up-to-date seismograms and illustrative data plots.

Providing a unique balance between application techniques and theory, this is an ideal guide for graduate students and researchers in seismology, tectonophysics, geodynamics and geomechanics and a valuable practical resource for professionals working in seismic hazard assessment and seismic engineering.

**Agustín Udías** is Emeritus Professor at the Universidad Complutense de Madrid (UCM). He is the author of many papers about seismicity, the seismotectonics of the Azores–Gibraltar region and the physics of seismic sources and has also written several textbooks including *Principles of Seismology* (Cambridge, 1999). Professor Udías has served as Editor-in-Chief of *Física de la Tierra* and the *Journal of Seismology*, and earlier as the Vice-President of the European Seismological Commission. He is a member of the Accademia Europeae, the Seismological Society of America and the American Geophysical Union, amongst other societies, and is a Fellow of the Royal Astronomical Society.

**Raúl Madariaga** is Emeritus Professor of Geophysics at the École Normale Supérieure (ENS) in Paris. During his career he has served as Director of the Seismological Laboratory of the Institut de Physique du Globe (IPG) and as Director of the Geology Laboratory of ENS. Professor Madariaga is a Fellow of the American Geophysical Union and has been awarded the Stefan Muller medal of the European Geophysical Society and also the H. F. Reid Medal, the highest award of the Seismological Society of America. He has been an editor of several

journals as well as a member of the US science Board and he is the author of 140 papers in leading scientific journals as well as several articles in earth science encyclopaedias.

**Elisa Buorn** is a Professor of Geophysics at UCM, teaching courses on geophysics, seismology, physics and numerical methods. She has published papers on topics ranging from source fracture processes and seismicity to the seismotectonics of the Ibero-Maghrebian region and the Azores–Gibraltar region and is the author of various textbooks including *Solved Problems in Geophysics* (Cambridge, 2012). Professor Buorn currently serves as Editor-in-Chief of *Física de la Tierra* and is on the Editorial Board of the *Journal of Seismology*. She has served on many international scientific committees and is a member of the Seismological Society of America, the American Geophysical Union, the Royal Astronomical Society and other distinguished societies.

# Source Mechanism of Earthquakes: Theory and Practice

---

AGUSTÍN UDÍAS

Universidad Complutense de Madrid

RAÚL MADARIAGA

École Normale Supérieure, Paris

ELISA BUFORN

Universidad Complutense de Madrid



CAMBRIDGE  
UNIVERSITY PRESS

**CAMBRIDGE**  
UNIVERSITY PRESS

University Printing House, Cambridge CB2 8BS, United Kingdom

Published in the United States of America by Cambridge University Press, New York

Cambridge University Press is part of the University of Cambridge.

It furthers the University's mission by disseminating knowledge in the pursuit of  
education, learning and research at the highest international levels of excellence.

[www.cambridge.org](http://www.cambridge.org)

Information on this title: [www.cambridge.org/9781107040274](http://www.cambridge.org/9781107040274)

© Agustín Udías, Raúl Madariaga and Elisa Buform 2014

This publication is in copyright. Subject to statutory exception  
and to the provisions of relevant collective licensing agreements,  
no reproduction of any part may take place without the written  
permission of Cambridge University Press.

First published 2014

Printed in the United Kingdom by XXXX

*A catalogue record for this publication is available from the British Library*

*Library of Congress Cataloguing in Publication data*

Udías Vallina, Agustín, author.

Source mechanisms of earthquakes : theory and practice / Agustín Udías, Universidad Complutense de  
Madrid (Spain), Raúl Madariaga, Ecole normale supérieure, Paris (France), Elisa Buform, Universidad  
Complutense de Madrid (Spain).

pages cm

ISBN 978-1-107-04027-4 (Hardback)

1. Faults (Geology) 2. Seismic event location. 3. Shear (Mechanics) 4. Geodynamics. 5. Seismic prospecting. I. Madariaga, Raúl, author. II. Buform, Elisa, 1954– author. III. Title.

QE539.2.S37U35 2014

551.2201–dc23

2013049910

ISBN 978-1-107-04027-4 Hardback

Cambridge University Press has no responsibility for the persistence or accuracy of  
URLs for external or third-party internet websites referred to in this publication,  
and does not guarantee that any content on such websites is, or will remain,  
accurate or appropriate.

# Contents

<i>Preface</i>	<i>page</i> ix
<b>1. Earthquakes and fault motion</b>	1
1.1. The origin of earthquakes	1
1.2. Faults in the Earth's crust	2
1.3. Geometry of a fault	5
1.4. Elastic rebound and the earthquake cycle	7
1.5. Energy, stress drop and seismic moment	9
1.6. Stick-slip motion on a fault	14
1.7. Seismicity and statistical properties of earthquakes	19
<b>2. Processing and analysis of recorded seismic signals</b>	22
2.1. Recorded and ground motion in time and frequency domains	22
2.2. Analogical and digital data	25
2.3. Removing the instrumental response	27
2.4. Processing a seismic signal	30
2.5. Displacement, velocity and acceleration	36
2.6. Continuous GPS observations	39
<b>3. Mathematical representation of the source</b>	41
3.1. Fundamental equations of motion for an elastic medium	41
3.2. Green's and Somigliana's tensors	44
3.3. Representation theorem	45
3.4. Somigliana's tensor for an infinite homogeneous isotropic medium	48
3.5. Green's tensor for an infinite homogeneous isotropic medium	52
3.6. Green's function for layered media	57
3.7. Focal region	59
3.8. Kinematic and dynamic models	61
<b>4. Point source models</b>	63
4.1. Point source approximation	63
4.2. Equivalent forces. Double couple	63
4.3. Shear fracture or dislocation	66
4.4. Point shear fracture in an infinite medium	69
4.5. The geometry of a shear fracture	77
4.6. Far-field displacements referred to the geographical axes	78

4.7. Source representation using the focal sphere	80
4.8. The source time function	81
4.9. Spectral properties of the source time function	86
4.10. Seismic energy radiation	88
<b>5. The seismic moment tensor</b>	<b>90</b>
5.1. Definition of the moment tensor	90
5.2. Eigenvalues and eigenvectors	93
5.3. Components of the moment tensor	94
5.4. Moment tensor and elastic dislocations	95
5.5. Moment tensor components referred to geographical axes	98
5.6. The point source moment tensor	99
5.7. The separation of the moment tensor	102
5.8. Higher-order moment tensors	105
5.9. Moments of the moment-rate distribution	106
<b>6. Determination of point source mechanisms</b>	<b>108</b>
6.1. Parameters and observations	108
6.2. The focal sphere	109
6.3. Fault-plane solutions from P wave polarities	110
6.4. Inversion of body wave forms	116
6.5. Empirical Green's functions	123
6.6. Moment tensor inversion	124
6.7. Centroid moment tensor inversion	132
<b>7. Kinematics of extended sources</b>	<b>135</b>
7.1. Source dimensions	135
7.2. Rectangular fault. Haskell's model	138
7.3. Bilateral rupture propagation	141
7.4. Oblique rupture propagation	142
7.5. Corner frequency	145
7.6. Directivity effects	148
7.7. Rupture nucleation, propagation and arrest	151
7.8. Kinematic models with variable slip on the fault plane	155
7.9. The circular kinematic model of Sato and Hirasawa	157
<b>8 Determination of source dimensions</b>	<b>163</b>
8.1. Parameters of kinematic extended source models	163
8.2. Analysis of seismic wave spectra	163
8.3. Directivity effects of Rayleigh waves	167
8.4. Effects of directivity on body wave form modeling	170
8.5. Apparent source time function	172
8.6. Far-field inversion of the slip distribution on the fault plane	173
8.7. Kinematic inversion of the near-field waves	181

<b>9. Simple dynamic models</b>	189
9.1. Kinematic and dynamic models	189
9.2. Static problem	190
9.3. Modes of propagating fractures	191
9.4. Circular fault. Static model	192
9.5. Circular fault. Brune's model	195
9.6. Scaling laws	200
<b>10. Dynamics of fracture. Homogeneous models</b>	205
10.1. Griffith's fracture model	205
10.2. Energy flow towards the fracture front for a growing crack	209
10.3. Stress singularities around the rupture front moving at constant speed	212
10.4. Spontaneous shear-fracture propagation	216
10.5. Friction models of fracture	220
10.6. Rupture of an expanding circular fault	223
10.7 Far-field displacements of a dynamic circular fault	227
<b>11. Fracture dynamics. Heterogeneous models</b>	232
11.1. The cohesive zone	232
11.2. The slip-weakening friction model	233
11.3. Friction laws	237
11.4. Determination of $G_c$ from seismic data	243
11.5. Nucleation and arrest of rupture	246
11.6. Barriers and asperities	250
11.7. Healing and rupture pulse propagation	253
11.8. Super-shear rupture velocity	254
<b>12. Modeling earthquakes using fracture dynamics</b>	259
12.1. Dynamic models	259
12.2. Modeling earthquakes in three dimensions	260
12.3. Rupture propagation on a planar uniform fault	263
12.4. A finite circular fault in a homogeneous medium	265
12.5. Shallow strike-slip rectangular fault	269
12.6. Spontaneous rupture on a realistic fault: the Landers 1992 earthquake	270
12.7. Rupture of a geometrically complex earthquake: the Izmit event of August 1999	275
12.8. Dynamic inversion of the 2008 Iwate intermediate-depth earthquake	276
12.9. Conclusion and perspectives	281
<i>References</i>	284
<i>Index</i>	300



## Preface

A key problem in seismology is the study of the processes that give rise to earthquakes. It is well established now that earthquakes, with rare exceptions, are caused by shear fracture on preexisting faults in the Earth. Thus, the modern study of earthquakes and their source mechanisms should be based on the application of dislocation theory and fracture mechanics; this is the point of view taken in this book. General textbooks of seismology have dedicated chapters to this subject, for example, Aki and Richards (1980); Ben Menahem and Singh (1981); Dahlen and Tromp (1998), Gubbins (1990), Lay and Wallace (1995) and Udiás (1999). A few books have been written specifically on the subject, for example, Kasahara (1981), Kostrov and Das (1988) and Scholz (1990). Each of these three books has a different approach: Kasahara presents the state of the study of earthquake mechanisms as it was 30 years ago, before modern developments, and does not give details of the mathematical developments. Scholz' approach is that of rock mechanics, with an emphasis on qualitative descriptions and applications to Earth faulting. Finally, Kostrov and Das (1988) gives an excellent presentation of earthquake dynamics, but it may be difficult for students to follow. None of these books includes a detailed presentation and discussion of practical methods for the determination of the earthquake mechanisms together with the theory on which they are based.

At present it is very common to find, in publications and on the web, results from different methods of determination of the source mechanisms of earthquakes, for example, centroid moment tensor (CMT) solutions. The use of these results is today standard practice in the study of tectonics and seismic hazard, often without knowledge of the methods and theory behind them. Thus the novel approach of this book is to present the theory of the source mechanisms of earthquakes and also the methods used for their determination in particular cases. The theory on which the methods are based is made clear. As nowadays digital data are used in the analysis of observations, the practical processing of seismograms, accelerograms and high-rate GPS data is also presented. A further novelty is the structure of the book as a textbook, that is, having in mind its use by students. Thus topics are presented in a gradual form, starting from the basic principles and developments and progressing to more advanced and difficult problems. In many cases mathematical developments are given in detail, and throughout the book a unified terminology and notation are used. This is an important point since in articles different authors use differing notation, and this makes it difficult, sometimes, to get a unified grasp of the subject. Above all, considerable efforts have been made towards clarity in the presentation and an emphasis on the fundamentals; therefore some more advanced and difficult problems have been omitted.

The book is divided into 12 chapters. An introduction, in which very basic concepts are explained (Chapter 1), is followed by a presentation of the basis of digital data processing,

an often neglected subject ([Chapter 2](#)). The fundamentals of the elastodynamic theory of earthquake source representation are given in detail in [Chapter 3](#). In the following chapters three types of source representation or model are considered. These are point sources, including the first-order moment tensor ([Chapters 4 and 5](#)), extended kinematic sources ([Chapter 7](#)) and dynamic sources, both homogeneous and heterogeneous ([Chapters 9–11](#)). In these last few chapters the more complex concepts of seismic source dynamics are presented. After the presentation of each type of source model, some methods used for determination of the corresponding model parameters from seismic wave observations are discussed, namely, point source inversion, including fault-plane solutions and moment tensor inversion ([Chapter 6](#)), the determination of source dimensions and slip distribution on the fault plane ([Chapter 8](#)) and the determination of dynamic parameters ([Chapter 12](#)). In these chapters, the methods are explained in detail and references are given to web addresses where computer programs for them can be found.

The authors' aim is that the book should be both a user-friendly text book and also a standard reference for source mechanism studies of earthquakes and their applications, for graduate students and researchers. An comprehensive list of references is given. The book is based on the long teaching and research experience of the authors.

The authors wish to thank to all our students, to whom we are indebted for their questions and suggestions. A. U. and E. B. specially thank C. Pro (University of Extremadura), S. Cesca (GFZ, Potsdam) and C. del Fresno (Instituto Geográfico Nacional, Madrid). R. M. thanks M. Lancieri (IRSN, France), S. Ruiz (University of Chile in Santiago), C. Holden (New Zealand) and S. Di Carli (France) for their help and Drs J. Virieux, K. B. Olsen, R. Archuleta, S. Peyrat, E. Fukuyama, T. Tada and H. Aochi for their long-standing collaboration on the dynamic modeling and inversion of earthquakes.

## 1.1. The origin of earthquakes

Humankind's experience of earthquakes has always given rise to shock and confusion. The ground beneath us, our basis of stability, is suddenly subject to shaking, bringing ruin to buildings and causing high numbers of casualties. Investigating the causes of these phenomena has interested human beings since antiquity. The first rational explanations, beyond mythical stories, were presented by Greek natural philosophers beginning in the sixth century BC. The most lasting theory of the Greek philosophers was presented by Aristotle (fourth century BC) in his book *Meteorologica*. By the word *meteors* ancient Greeks referred to a variety of phenomena which were believed to take place somewhere above the Earth's surface, such as rain, wind, thunder, lightning, comets and the Milky Way, or inside the Earth, such as earthquakes and volcanoes. Aristotle refuted the ideas proposed by previous authors, as Anaxagoras, Empedocles and Democritus, and proposed that the cause of earthquakes consisted in the shaking of the earth by dry heated underground exhalations or winds trapped in cavities of its interior, as they attempt to escape toward the exterior. This explanation was part of his general theory for "meteors", which, he proposed, were all caused by various types of exhalation of dry or humid, cold or hot, vapors or winds, which extended from the interior of the Earth to the Lunar orbit. This was a very popular theory, which was accepted with only minor changes until the seventeenth century. Roman authors such as Pliny and Seneca presented it in their encyclopedic works and medieval authors such as Albert the Great and St Thomas Aquinas wrote long commentaries on it.

The general reaction against Aristotelian physics, and the birth of modern science in the seventeenth century, gave rise to a new theory to explain the origin of earthquakes. Martin Lister in England and Nicolas Lemery in France proposed that earthquakes were caused by spontaneous explosions of flammable material accumulated underground in certain regions. The increasing use of mines in mining and military operations suggested this idea. The explosive theory was supported by Newton and Buffon and helped to define the concept of the focus of an earthquake as the location where the explosion took place.

The great Lisbon earthquake of 1755 created in Europe a widespread interest in the study of these phenomena and can be considered as marking the beginning of modern seismology. In 1760 John Michell, for the first time, related the ground-shaking due to earthquakes with the propagation through the Earth of elastic waves generated at the focus. Thomas Young, Robert Mallet and John Milne, among others, further developed this idea, laying the foundations of seismology. Mallet, in his study of the Naples earthquake of

1857, developed the theory of the seismic focus, from which elastic waves spread out in all directions. He connected the occurrence of earthquakes with changes in the Earth's crust, which often result in dislocations and fractures, though he did not abandon the explosive theory. Charles Lyell, in his foundational work on geology, related earthquakes to tectonic processes and volcanic activity. Edward Suess, Ferdinand Montessus de Ballore and Alfred Sieberg, among others, continued these studies, relating the occurrence of earthquakes to orogenic and tectonic processes. Systematic studies of field observations after the occurrence of earthquakes in the nineteenth century, such as those of George K. Gilbert (Owen, California, 1872), Bunjiro Koto (Nobi, Japan, 1891) and Richard D. Oldham (Assan, India, 1897) began relating earthquakes to motion along faults. With the increase of these field observations and precision in locating epicenters, the relation between earthquakes and faults became more evident. The cause of earthquakes began to be understood as the release by fracture of the tectonic stresses accumulated in the Earth's crust, as we now explain.

Francis Reid in 1910 presented the first mechanical model for the faulting process of earthquakes, in order to explain the observed ground fracture with horizontal displacement observed in the San Francisco earthquake of 1906. This earthquake marked a milestone in the development of earthquake source studies, as did the Lisbon earthquake for general seismology. Reid's theory, known as the *elastic rebound* theory, assumes that earthquakes take place by a fracturing of the Earth's crust with total or partial release of the elastic strain accumulated in a region owing to the stresses produced by tectonic processes. In his own words: "the difference between displacements in neighboring regions sets up elastic strains, which may become greater than the rock can endure; a rupture then takes place and the strained rock rebounds under its own elastic stresses until the strain is largely or wholly relieved" (Reid, 1911). With certain modifications Reid's basic insight, that earthquakes are caused by fractures in the Earth's crust induced by tectonic stress, still remains valid today. According to plate tectonic theory, developed between 1960 and 1970, tectonic stresses are ultimately related to the relative motion of lithospheric plates. An earthquake can be considered, then, to be produced by the rupturing of a certain part of the Earth's crust, with a relative displacement of its two sides and the release of the accumulated elastic strain, produced by the relative motion of lithospheric plates. A rupture of the crust is generally referred to as a *fault*. Owing to the confining pressure inside the Earth, faults are shear fractures; that is, motion takes place along the breaking surface.

## 1.2. Faults in the Earth's crust

---

Most earthquakes are of tectonic origin and take place on faults. Non-tectonic earthquakes, such as those of volcanic origin or induced by dams, may have different characteristics. Geological field observations show the presence of many fault traces exposed at the Earth's surface, with lengths which vary from some meters to many kilometers (Fig. 1.1). In general, observed fault traces are not continuous straight lines but have bends, bifurcations, offsets and other complexities. The non-continuous nature of observed faults has led



**Figure 1.1.** Surface rupture of the San Andreas fault, California. View along Carrizo Plains (US Geological Survey/Photo R. E. Wallace).

to the consideration that their nature might be fractal. The concept of a fault plane is, then, a useful simplification of a situation which involves non-planar geometry and various complexities. The depth extent at which faults break by brittle fracture generating earthquakes can be deduced from the depth of shallow earthquakes. From this evidence, it has been shown that brittle fracture extends only to about between 15 km and 20 km in depth. This shows that only the upper part of the crust has a brittle nature and can, in consequence, be fractured. This brittle upper part of the crust is called the *seismogenic* layer, that is, the layer capable of generating earthquakes. The lower part of the crust and the upper mantle, owing to the increase in temperature and pressure, behaves as a plastic material which can be deformed without breaking. This behavior of the lower crust and upper mantle has been confirmed from deep seismic reflection studies.

The limitation on the brittle depth imposes a condition on the fault-surface shape; the latter is roughly described by its aspect ratio  $L/W$  (length over width). For small earthquakes, with fracture lengths less than 20 km, there is no limitation to the propagation of fracture in all directions, so that the shape of faults is symmetrical, approximately circular or square, with aspect ratio near to unity. For large earthquakes the length is longer than the depth limit and so the shape will be rectangular or elliptical, with a longer length than width, and aspect ratio greater than unity. Very large crustal earthquakes have lengths extending for hundreds of kilometers and only a limited width, less than about 40 kilometers; their aspect ratios may be greater than 10. However, large earthquakes in subduction zones with lengths longer than 400 km may have widths of about 100 km. The shape of the fault depends, then, on the size and type of earthquake, with different shapes for small and large events.

A different problem is presented by the nature of earthquakes with foci at depths below 60 km. These earthquakes are produced in regions where tectonic processes have introduced crustal material inside the Earth's mantle. Intermediate-depth ( $50 \text{ km} < h < 200 \text{ km}$ )

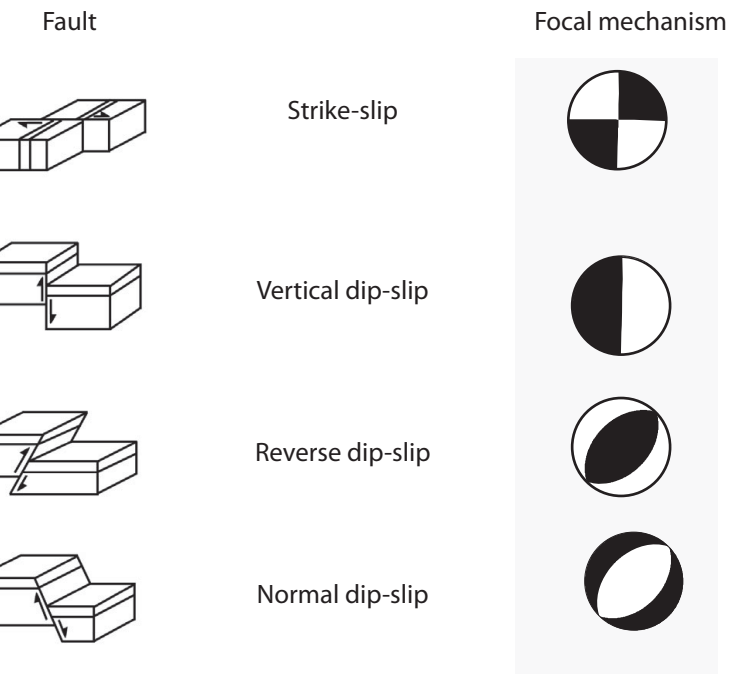


**Figure 1.2.** Types of fault and their focal mechanism diagrams.

and deep ( $200 \text{ km} < h < 700 \text{ km}$ ) earthquakes cannot be produced by brittle fracture, owing to the high temperature and pressure existing at those depths. Different processes, such as sudden phase transitions, have been proposed for them; however, they do occur on weakness surfaces similar to those of faults.

Faults can be classified according to their type of motion into *strike-slip* faults, where the motion is horizontal and parallel to the strike and *dip-slip* faults, where in cross-section the motion is in a vertical plane (see Fig. 1.2). Strike-slip faults are divided into right-lateral and left-lateral, according to the direction in which one side of the fault moves as seen from the other side. Dip-slip faults are divided into *normal* faults, with the hanging wall sliding downward with respect to the foot wall, and *reverse* faults, with motion in the opposite direction; the hanging wall moves upward with respect to the foot wall. Normal faults are also called *gravity* faults, because their motion results from a process driven by gravity. Reverse faults with a small dip angle are called *thrust* faults (Fig. 1.2). Combinations of horizontal and vertical motion result in *oblique* faults. Normal faults are caused by horizontal tension and reverse faults by horizontal pressure. In strike-slip faults the tension and pressure are both horizontal.

In general, earthquakes occur on preexisting fault planes although, naturally, at some time faults involve newly broken material. The material between the two moving surfaces of a fault is usually filled with crushed and highly deformed rocks, called *fault gouge*, in a zone that may be up to several meters wide in some places. This material is formed by the repeated differential movement of the two sides of the fault over a long time; this breaks and

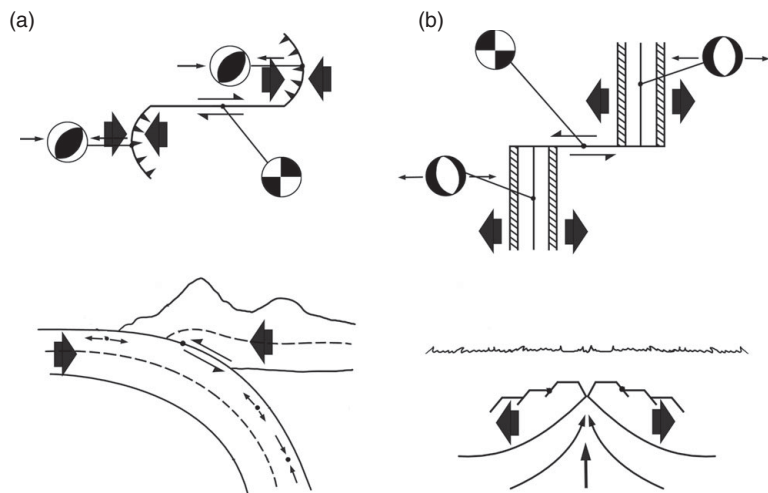


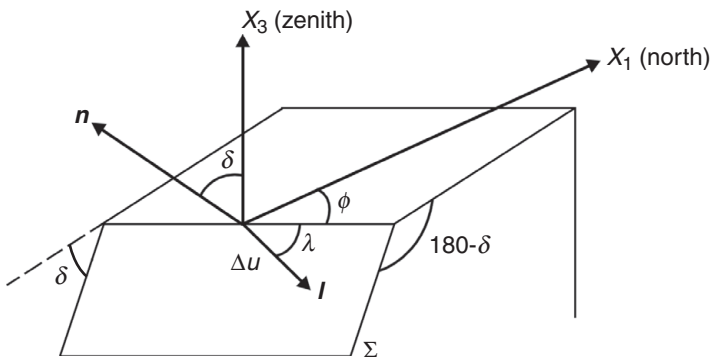
**Figure 1.3.** Plate boundaries and focal mechanisms: horizontal plans and vertical cross-sections. (a) Subduction: reverse and transform (strike-slip) faults. (b) Rift: normal and transform (strike-slip) faults. The large arrows show the stress directions. The directions of motion are represented by the small half-arrows.

shears the rock into a fine granular and powdery form, which can be altered by the addition of water into clays and sandy silts. Earthquakes do not happen at present on all observed geological faults; that is, not all faults observed today in the field are seismically active. On a given active fault, earthquakes of different size break partial sections of its surface. On a long fault several large earthquakes may be needed to break its whole extent. Faults can also move slowly without producing an earthquake; this type of motion is called *fault creep*.

The active factor responsible for movement along faults is the tectonic stress resulting from the relative motion of *lithospheric plates*, which are driven by the convective currents in the mantle. According to plate tectonics the Earth surface is divided into several plates (the main plates are the Eurasia, Africa, America, Pacific, Indo-Australia, Antarctic, Nazca and Arabia plates), which move relative to each other with velocities ranging from about 1 to 8 cm/year. The plate boundaries are, then, the places where most earthquakes occur (*interplate* earthquakes), though earthquakes also occur in the interior of plates (*intraplate* earthquakes). The types of boundary between plates can be reduced to three and at each of these a corresponding type of fault is predominant: where plates are separating from each other (at *extension zones*), faults are normal; where plates are colliding (at *collision* and *subduction zones*) faults are reverse; and, where plates slide horizontally over each other, faults are strike-slip (Fig. 1.3).

### 1.3. Geometry of a fault

A fault is defined as a rupture in the Earth's crust with a relative displacement of its two sides. The size of the fault is given by its area  $S$ , which for a rectangular fault is given by  $S = LW$ , where  $L$  is the length and  $W$  the width, and for a circular fault is given by  $S = \pi a^2$ , where  $a$  is the radius. These two approximations to the shapes of faults are very often used.

**Figure 1.4.**

Geometry of a shear fault. The fault orientation is given by either angles  $\phi$  (azimuth),  $\delta$  (dip) and  $\lambda$  (the rake or slip angle) or unit vectors  $n$  (normal to the fault plane) and  $I$  (in the slip direction). The fault slip is  $\Delta u$  and the fault surface is  $\Sigma$ .

The relative displacement of the two sides of the fault, or fault *slip*, is the vector  $\Delta u$ . In general,  $\Delta u(\xi_i, \tau)$  may vary in amplitude and direction over the fault plane, where position is specified by the vector  $\xi_i$ , and at each position  $\xi_i$  as a function of time  $\tau$ . It can be expressed as  $\Delta u I$ , where  $\Delta u$  is the fault slip amplitude and  $I$  is a unit vector in the direction of the slip. The time dependence is usually separated from the amplitude and direction, taking  $\Delta u = \Delta u(\xi_i) I_i(\xi_i)g(\tau)$ , where the time dependence  $g$  is taken to be the same for all points on the fault. The slip rate or velocity  $\Delta \dot{u}(\xi_i, t)$  can also be expressed as  $\Delta \dot{u}(\xi_i) I_i(\xi_i)f(\tau)$ , where  $f(\tau) = \dot{g}(\tau)$  is usually referred to as the *source time function* (STF). For very large earthquakes, such as those of Chile 1960 and Sumatra 2005, the length of faults can reach 1000 km. Fault slips are of the order of centimeters for small earthquakes and meters for large ones. In the San Francisco 1906 earthquake the observed displacement reached 6 m. The orientation of the fault plane is given by two angles (Fig. 1.4). The *azimuth*  $\phi$  is the angle between the trace of the fault (the intersection of the fault plane with the horizontal plane) and north ( $0^\circ \leq \phi \leq 360^\circ$ ); the angle is measured clockwise so that the fault plane dips to the right-hand side. The *dip*  $\delta$  is the angle between the fault plane and the horizontal plane at right angles to the trace ( $0^\circ \leq \delta \leq 90^\circ$ ). A third angle,  $\lambda$ , the *rake* or *slip* angle, defines the direction of the motion on the fault plane. It is given by the angle between the direction of slip and the horizontal, measured on the fault plane ( $-180^\circ \leq \lambda \leq 180^\circ$ );  $\lambda$  is negative for normal faults and positive for reverse faults. Since often the word “slip” is used to designate both  $\Delta u$  and  $\lambda$ , care must be taken not to confuse them. Thus the orientation of the motion of the fault is given by the three angles  $\phi$ ,  $\delta$  and  $\lambda$ .

The values of  $\delta$  and  $\lambda$  correspond to different types of fault. We have mentioned above (and see Fig 1.2) strike-slip faults, for which  $\delta = 90^\circ$  and  $\lambda = 0^\circ$ , dip-slip vertical faults, for which  $\delta = 90^\circ$  and  $\lambda = 90^\circ$  and dip-slip faults on an inclined plane, for which  $0^\circ < \delta < 90^\circ$  and  $\lambda = 90^\circ$ . According to the value of  $\lambda$ , on an inclined fault we can have horizontal motion ( $\lambda = 0^\circ, 180^\circ, -180^\circ$ ), vertical motion ( $\lambda = 90^\circ$ ) or inclined motion with horizontal and vertical components ( $-180^\circ < \lambda < 180^\circ$ ). If  $\lambda$  is negative then the fault is a normal fault and if positive it is a reverse fault. The angles  $\phi$ ,  $\delta$  and  $\lambda$  are shown on a stereographic projection of the fault plane in Fig. 1.5.

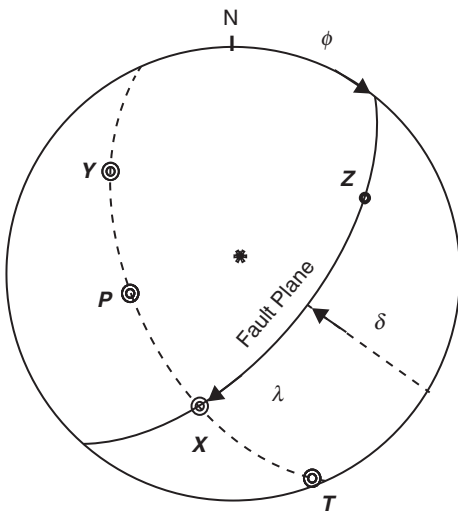


**Figure 1.5.** Stereographic projection of the fault plane: the angles  $\phi$ ,  $\delta$ ,  $\lambda$ , shown by arrows; the double-couple axes  $X$ ,  $Y$ ,  $Z$  (couples along  $X$  and  $Y$ ) and the axes of the principal stresses  $P$ ,  $T$ ,  $Z$  ( $P$ , pressure;  $T$ , tension).

## 1.4. Elastic rebound and the earthquake cycle

As we mentioned in the introduction, the most accepted model of the origin of earthquakes is the earthquake rebound model proposed by Francis Reid in 1910 (Reid, 1911). Following the earthquake that devastated the city of San Francisco in 1906, the American government charged a commission led by Reid, a professor at Johns Hopkins University in Baltimore, to evaluate the damage produced by the earthquake and to try to understand its origin. Using geodetic data that had been collected before and after the earthquake of 1906, he proposed a model that has become the basis of modern earthquake source studies.

Let us consider the simplified model of a crustal block, shown in Fig. 1.6, and assume that an earthquake has just occurred on the main fault, which runs across the middle of the block. During a certain period of time many aftershocks will occur on the fault itself and its immediate vicinity and a certain amount of post-seismic deformation will occur. After a certain time the activity will cease; we choose this time as the zero instant,  $t = 0$ , of our earthquake cycle. Then a slow continuous process of stress accumulation will start around the main fault from time  $t = 0$ . This stage in the fault progress is shown in Fig. 1.6a. As time passes, the slow movement of the plates, of the order of a few centimeters per year, will produce a pre-seismic deformation of the rocks that surround the fault. This deformation, shown in Fig. 1.6b, produces a generalized increase of the stress level around the fault.

An essential point with Reid's model is that plate motion does not produce deformation that is uniformly distributed over the plates. Reid and his colleagues proposed that the deformation around the fault was actually concentrated in a relatively narrow band some 40 km in width. This localization of deformation is an essential part of the elastic rebound theory. Without a mechanism that localizes deformation, there would be no earthquakes;

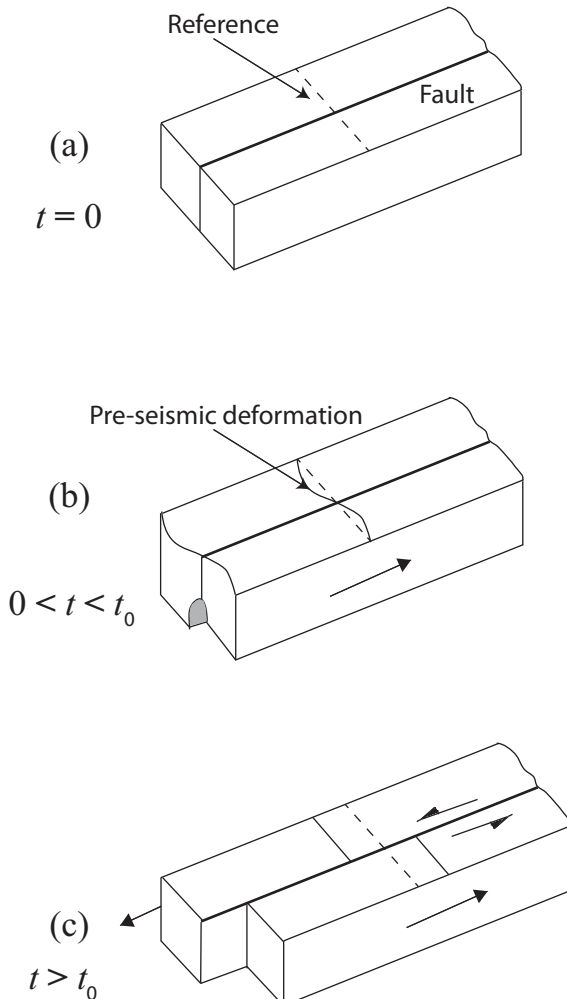


**Figure 1.6.** Schematic representation of the elastic rebound theory: (a) initial situation, at  $t = 0$ ; (b) pre-seismic deformation due to applied stress; (c) displacement after earthquake occurrence at time  $t_0$ .

the earth would deform continuously as the plates move. In Reid's time the internal structure of fault zones was practically unknown, but since then geodetic observations have improved significantly. We now know that the localization of deformation does occur because at depths greater than 15 or 20 km the crust reaches temperatures close to about 30% of the melting temperatures of the rocks that make up the crust, and at those temperatures rocks flow under stress and are no longer elastically deformed. Thus, the deeper part of the San Andreas fault, shown by the shaded area in Fig. 1.6b, undergoes continuous aseismic slip due to creep. Creep may be localized on the deep roots of the faults or may be spread over a large zone around the fault. In Fig. 1.6b we illustrate the former model.

Finally, once the deformation around the upper region near the fault is such that the stress across the fault is larger than its frictional resistance, an earthquake is triggered,

at time  $t = t_0$ , producing a sudden release of accumulated stresses on the fault (Fig. 1.6c). This sudden release of stresses produces a slip on the fault that is usually called *elastic rebound*. This is a way of expressing the idea that during the earthquake the brittle part of the crust slips very rapidly until the slowly accumulated stress is eliminated. In the idealized model shown at Fig. 1.6c, the two sides of the fault have slipped uniformly so that there is no stress left on the fault. In reality, of course, elastic rebound is not perfect and, once the earthquake has occurred, a period of slow post-seismic slip occurs. At the end of the current earthquake the entire cycle starts again with a slow accumulation of deformation near the surface and continuous slip at depth. The process we have just described is cyclic, although not necessarily periodic; it is what seismologists call the *earthquake cycle*, an endless repetition of slow loading and fast release of stresses on the fault zone.

Reid's model has been extensively tested from geodetic field observation in the last 40 years, starting with the classical work by Savage and Burford (1973) on the Parkfield segment of the San Andreas fault. Observation of the preseismic accumulation of stresses has now been extended to subduction zones, where, although the details are more complex, again the basic mechanism of the slow accumulation of deformation at shallow depths and its eventual release by elastic rebound has been observed after many large earthquakes.

## 1.5. Energy, stress drop and seismic moment

Motion on a fault happens when the applied shear stress on the fault plane overcomes the strength of the material or the friction which holds its two sides locked. The strength under the given conditions can be defined as the maximum stress that the material can support without suffering a permanent deformation or failure. The material has a plastic behavior if it suffers a permanent deformation without breaking and a brittle fracture behavior if it suffers permanent deformation by failure, with a break and a relative displacement of the two sides of the fault. We will consider always brittle fracture either of unbroken material or against friction on a preexisting fault.

Let us now consider a fault kept locked by friction. An earthquake happens when shear stress overcomes the static friction and displaces the two sides of the fault. After the earthquake the fault is locked again by friction forces. This simple model of the source can be used to define fundamental concepts such as energy dissipation, stress drop, fault slip, seismic moment and magnitude (Fig. 1.7).

Strain elastic energy accumulates in the region surrounding a fault, by tectonic processes; part of this energy is consumed in the production of an earthquake. The *total energy*  $E_T$  dissipated in an earthquake is given by

$$E_T = E_F + E_S + E_H \quad (1.1)$$

where  $E_F$  is the energy needed to create new fracture or to overcome the friction between the two sides of the fault,  $E_S$  is the energy dissipated into the surrounding medium in the form of elastic waves, called the *seismic energy*, and  $E_H$  is the energy dissipated by friction

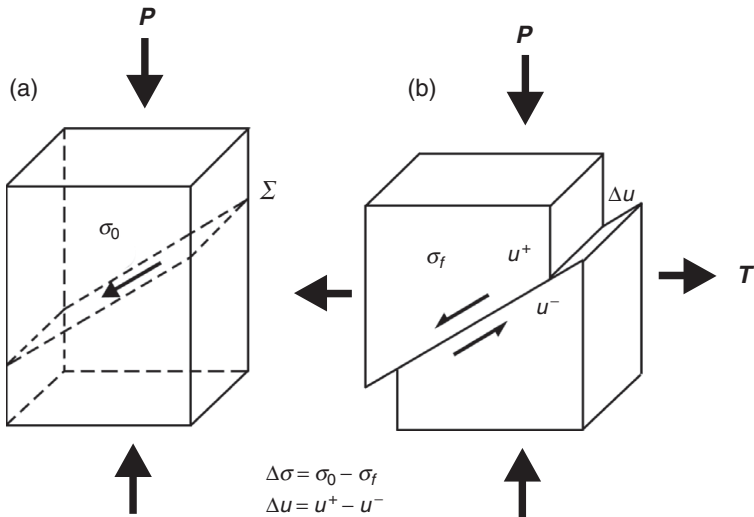


**Figure 1.7.** Schematic representation of acting stresses, (a) before and (b) after an occurrence on a shear normal fault with slip  $\Delta u$  and stress drop  $\Delta\sigma$ .

as heat at the fault surface or in non-elastic processes. The units used for energy are joules (SI) or ergs (cgs).

The energy  $E_S$  radiated as seismic waves, which propagate with velocity  $c$ , can be say, determined from the amplitudes of waves observed at a distance from the source, correcting first for the amplitude distribution at the source, the geometrical spreading of the wave front and the anelastic attenuation:

$$E_S = \int_{-\infty}^{\infty} c p \dot{u}(t)^2 dt \quad (1.2)$$

The energies  $E_F$  and  $E_H$  are dissipated during the time that the fracture process lasts,  $t_0 < t < t_f$ , where  $t_f$  is the final time, when motion stops;  $E_S$  is finally dissipated when all elastic waves in the Earth are attenuated by anelastic processes. Since the only part we can directly measure by analysing seismograms is the seismic energy  $E_S$ , we can express it as a fraction of the total energy, defining the *seismic efficiency coefficient*  $\eta$  by

$$\eta = \frac{E_S}{E_T} \quad (1.3)$$

The seismic efficiency coefficient  $\eta < 1$  measures the proportion of the total energy radiated as seismic waves.

From the point of view that earthquakes are caused by shear fracture, the size of an earthquake can be measured by its *seismic moment*  $M_0$ , introduced by Aki (1966) and given by

$$M_0 = \mu \Delta \bar{u} S \quad (1.4)$$

where  $\mu$  is the shear or rigidity modulus of the material at the fault,  $\Delta \bar{u}$  is the spatial average value of the final slip or displacement on the fault surface and  $S$  is the area of the fault surface;

$$\Delta\bar{u} = \frac{1}{S} \int_S \Delta u(\xi_i) dS \quad (1.5)$$

In SI units the seismic moment is given in newton meters (N m) and in cgs units in dyne centimeters (dyn cm). Since  $M_0$  depends on the area of the fault, the slip or displacement and the strength of the material, it constitutes a good physical measurement of the size of an earthquake.

In a simplified model of shear fracture, the relative slip  $\Delta u$  of the two sides of a fault is produced when the acting shear stress, at a given moment, exceeds the strength of the material or the friction that maintains the fault locked. If the shear stresses acting on the fault plane before and after the occurrence of an earthquake are  $\sigma_0$  and  $\sigma_f$ , we can define the difference between the two as the *stress drop*  $\Delta\sigma$  and the mean value of the two or *average stress*,  $\bar{\sigma}$ , by

$$\Delta\sigma = \sigma_0 - \sigma_f \quad (1.6)$$

$$\bar{\sigma} = \frac{1}{2}(\sigma_0 + \sigma_f) \quad (1.7)$$

The units of stress or pressure are pascals (SI) or bars (cgs). The initial stress  $\sigma_0$  represents the tectonic stress responsible for the strain in the focal region. Since  $\sigma_0$  and  $\sigma_f$  are the static initial and final values of the stress,  $\Delta\sigma$  is the static stress drop (we will call it later  $\Delta\sigma_s$ ), independently of the process which has connected the two values. The stress drop represents the part of the acting stress which is employed in producing the slip of the fault, so that  $\Delta u$  is related to  $\Delta\sigma$  (Fig. 1.7). In the same manner as the slip  $\Delta u$ , the stress drop  $\Delta\sigma$  may vary over the fault surface. A spatial average value can be defined as,

$$\Delta\bar{\sigma} = \frac{1}{S} \int_S \Delta\sigma(\xi) dS \quad (1.8)$$

If  $\sigma_f$  is zero, the stress drop is total and the relation between the stress drop and the average stress is  $\Delta\sigma = 2\bar{\sigma}$ . Owing to the friction between the two sides of the fault this is seldom the case and usually there is some residual or final stress  $\sigma_f$  acting after the motion on the fault ends.

In a simplified form, the total release of energy during the fracture process at an earthquake by the change of elastic potential energy  $\Delta W$  can be expressed as

$$E_T = \Delta W = \bar{\sigma} \Delta\bar{u} S = \bar{\sigma} S \Delta\bar{u} \quad (1.9)$$

where  $\bar{\sigma} S$  represents the force acting parallel to the fault plane. In terms of the seismic moment (1.4) we obtain

$$E_T = \frac{\bar{\sigma}}{\mu} M_0 \quad (1.10)$$

Substituting into this equation  $E_T = E_S / \eta$  from (1.3), we obtain

$$\eta\bar{\sigma} = \mu \frac{E_S}{M_0} \quad (1.11)$$

where  $\eta\bar{\sigma}$  is called the *apparent average stress*, which can be determined from the values of  $E_S$  and  $M_0$  obtained from observations of seismic waves.

If the stress drop is total then, substituting the stress drop into (1.10), we obtain

$$E_T = \frac{\Delta\bar{\sigma}}{2\mu} M_0 \quad (1.12)$$

This expression relates the total energy release in an earthquake to the seismic moment for total stress drop. Substituting this value of  $E_T$  into the expression for the seismic efficiency coefficient we obtain

$$\eta = \frac{2\mu E_S}{\Delta\bar{\sigma} M_0} \quad (1.13)$$

All the quantities on the right-hand side of the equation are seismological parameters that can be determined from observations. It is found that, for most shallow tectonic earthquakes (brittle events),  $\eta > 0.25$  and for very deep earthquakes  $\eta < 0.25$  (Kanamori, 2004).

If the stress drop is not total ( $\sigma_f \neq 0$ ), the average applied stress can be written as

$$\bar{\sigma} = \frac{\Delta\bar{\sigma}}{2} + \sigma_f \quad (1.14)$$

By substitution into (1.6) we obtain for the total energy

$$E_T = E_0 + \sigma_f \Delta\bar{u} S \quad (1.15)$$

where  $E_0$  is the total energy when the stress drop is total, as in (1.12). The energy lost by friction during the fracture process ( $E_R = E_F + E_H$ ) can be written in analogy with (1.9) as

$$E_R = \sigma_{fr} \Delta\bar{u} S \quad (1.16)$$

where  $\sigma_{fr}$  is the frictional stress at the fault. Thus, we can write for the seismic or radiated energy (see (1.1))

$$E_S = E_T - E_R = E_0 + \Delta\bar{u} S (\sigma_f - \sigma_{fr}) \quad (1.17)$$

In seismology it is often assumed that the final stress equals the friction stress ( $\sigma_f = \sigma_{fr}$ ); this is known as *Orowan's condition*. Then  $E_S = E_0$  and from (1.12) we can write, now substituting  $M_0$  by its value (1.4),

$$E_S = \frac{1}{2} \Delta\bar{\sigma} \Delta\bar{u} S \quad (1.18)$$

This expression shows that from the radiated energy we only have information about the stress drop, not about the stress acting on the fault during faulting. Substituting (1.9) and (1.18) into (1.3), the seismic efficiency coefficient is now given by

$$\eta = \frac{\Delta\bar{\sigma}}{2\bar{\sigma}} \quad (1.19)$$

From static crack considerations, in a shear fracture the average stress drop  $\Delta\bar{\sigma}$  can be considered to be proportional to the average displacement  $\Delta\bar{u}$  divided by  $L'$ , a length dimension of the fault. This can be explained by considering that  $\Delta\bar{u}/L'$  represents the

non-elastic deformation at the source which is proportional to the stress drop. For a circular fault this length dimension  $L'$  is equal to the radius while for a rectangular fault it is equal to the width of the fault. The average stress drop is then given by

$$\Delta\bar{\sigma} = C\mu \frac{\Delta\bar{u}}{L'} \quad (1.20)$$

where  $C$  is a non-dimensional factor which depends on the shape of the fracture (e.g.  $C = 7\pi/16$  for a circular fault). Then, for a circular fault of radius  $a$ , we can now write the average stress drop as

$$\Delta\bar{\sigma} = \frac{7\pi\mu}{16} \frac{\Delta\bar{u}}{a} \quad (1.21)$$

In terms of the seismic moment, substituting  $\Delta\bar{u}$  from (1.4),

$$\Delta\bar{\sigma} = \frac{7}{16a^3} M_0 \quad (1.22)$$

Often values of the stress drop are determined from values of the seismic moment and fault dimensions, using this type of relation. Since the fault radius is raised to the power 3 small errors in its determination will result in large errors in the obtained values of the stress drop. The seismic moment in terms of the stress drop and fault area (in this case  $S = \pi a^2$ ) is given by

$$M_0 = \frac{16}{7\pi^{3/2}} \frac{\Delta\bar{\sigma}}{S^{3/2}} \quad (1.23)$$

On taking logarithms we have

$$\log M_0 = \frac{3}{2} \log S + \log\left(\frac{16\Delta\bar{\sigma}}{7\pi^{3/2}}\right) \quad (1.24)$$

From this equation it follows that if the stress drop is constant for all earthquakes then  $\log S$  is proportional to  $2/3 \log M_0$ . This hypothesis was shown empirically to be valid for a large range of values of  $M_0$  (Kanamori and Anderson, 1975). For earthquakes of magnitudes larger than 5 ( $M_0 > 10^{18}$  N m), the observed values of  $\Delta\sigma$  are in the range 1–10 MPa, with mean value 6 MPa. This value is of the same order of magnitude as the value suggested by Tsuboi (1956) for the critical strain of the Earth's crust. Kanamori and Anderson (1975) suggested that earthquakes that take place at plate boundaries (interplate earthquakes) have lower stress drops (about 3 MPa) than those in plate interiors (about 10 MPa).

The measurement of the size of an earthquake, derived from observations of the radiated seismic waves, is traditionally represented by its magnitude (Gutenberg and Richter, 1942). There are several definitions of magnitude, according to the seismic waves used. Two of the most commonly used magnitudes are the *body wave magnitude*  $m_b$  and the *surface wave magnitude*  $M_s$ . The body wave magnitude is given by

$$m_b = \log\left(\frac{A}{T}\right) + \sigma(\Delta, h) \quad (1.25)$$

where  $A$  is the amplitude in micrometers (that is, microns,  $\mu\text{m}$ ) of the vertical component of P wave ground motion,  $T$  is the period in seconds and  $\sigma(\Delta, h)$  is a calibration

term which depends on epicentral distance and focal depth. The surface wave magnitude is given by

$$M_s = \log\left(\frac{A}{T}\right) + 1.66 \log \Delta + 3.3 \quad (1.26)$$

where  $A$  is the maximum amplitude of the Rayleigh wave ground motion in micrometers,  $T$  is the period (approximately 20 s) and  $\Delta$  is the epicentral distance in degrees. From these magnitudes the radiated seismic energy in joules can be estimated using the empirical relations of Gutenberg and Richter (1956)

$$\log E_s = 2.4m_b - 1.2 \quad (1.27)$$

$$\log E_s = 1.5M_s + 4.8 \quad (1.28)$$

The surface wave magnitude can be related to the seismic moment  $M_0$  in N m in terms of the apparent average stress, using (1.12),

$$\log M_0 = \frac{3}{2}M_s + 4.8 - \log\left(\frac{\eta\bar{\sigma}}{\mu}\right) \quad (1.29)$$

If  $\eta\bar{\sigma}$  is constant, we have a linear relation between  $\log M_0$  and  $M_s$  with slope equal to 3/2. Observations agree with this hypothesis although there is a certain dispersion in the data, especially for very large earthquakes, which may be due to the saturation of the  $M_s$  scale (Kanamori and Anderson, 1975).

Assuming constancy of the stress drop, Kanamori's *moment magnitude*  $M_W$  can be defined from (1.12), using the empirical relation between surface wave magnitude and seismic energy of Gutenberg and Richter and assuming a constant value of  $\Delta\sigma/\mu = 10^{-4}$ :

$$M_W = \frac{2}{3} \log M_0 - 6.07 \quad (1.30)$$

where  $M_0$  is given in N m. The moment magnitude  $M_W$ , widely used at present because it does not saturate at large values, is thus a value derived from the seismic moment, under the hypothesis of a constant stress drop, that satisfies the Gutenberg and Richter relation between surface wave magnitude and energy.

## 1.6. Stick-slip motion on a fault

Considering that the motion on a fault is controlled by friction between its two sides, we can model the process of rupture by chains of blocks coupled by horizontal springs sliding on a frictional surface, as first proposed by Burridge and Knopoff (1967). The simplest such model is that of a single block of mass  $M$  which rests on the frictional surface of an elastic medium and is connected to a spring which is driven slowly at a uniform velocity (Fig. 1.8). While the block is at rest the spring is stretched by the uniform motion of one of its ends at constant velocity  $v$ , so that the force exerted by the spring on the block is  $F = -Kx = -Kvt$ , where  $x = vt$  is the elongation or deformation of the spring. The block

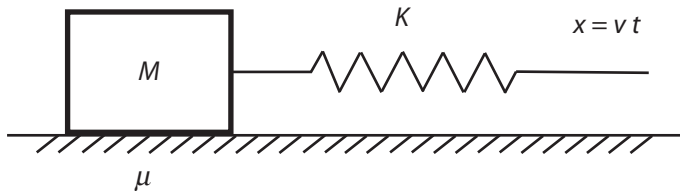


**Figure 1.8.** Sliding block driven by a spring with friction:  $M$ , mass;  $K$ , spring coefficient;  $\mu$ , coefficient of friction;  $v$ , driving velocity.

remains stationary until the force exerted by the spring overcomes that of friction. If the static friction force is  $\sigma_s$  ( $\sigma_s = \mu\sigma_n S$  where  $\mu$  is the static friction coefficient,  $\sigma_n$  is the normal stress and  $S$  is the area of the contact surface of the block), the block begins to move suddenly when  $F = -Kx_0 = -Kvt_0 = \sigma_s$ , where  $x_0$  is the elongation of the spring from an initial unstretched position, at  $t = 0$  and  $t_0$  is the time elapsed. During the motion, frictional energy is generated, part of which is radiated as seismic waves into the elastic medium and part of which is dissipated as heat. The initial process in which the spring is stretched without moving the block represents, in the context of earthquakes, the deformation or strain loading of the medium by tectonic forces. The velocity  $v$  with which the end of the spring is stretched represents the relative velocity of the tectonic plates. This velocity is of the order of centimeters per year; this is very small compared with the slip velocity in earthquakes, which is of the order of meters or centimeters per second. So in our analysis  $v$  is ignored during the motion of the block.

From the energy point of view, the elastic energy accumulated in the spring immediately before the block moves is

$$E_T = \frac{1}{2}Kx_0^2 = \frac{1}{2}K(vt_0)^2 \quad (1.31)$$

where  $x_0$  is the elongation of the spring before the block moves and  $t_0$  is the time elapsed. The block begins to move suddenly at  $t_0$  and continues moving against the *kinematic friction* stress  $\sigma_k$  until it stops at  $t_f$ , when the elongation of the spring is  $x_f$ ; then there is a static friction stress  $\sigma_f = Kx_f$ , where  $\sigma_k < \sigma_f < \sigma_s$ . During the time interval  $\Delta t = t_f - t_0$ , the block has moved a distance  $\Delta u = x_0 - x_f$ . The difference between the forces exerted by the spring before and after the motion is  $\Delta\sigma_s = \sigma_s - \sigma_f = K \Delta u = Kv \Delta t$ . The forces in the model represent the shear stresses (forces per unit area) acting on the fault plane. Thus,  $\Delta\sigma_s$  represents the static stress drop, that is, the difference in stress between the static situations before and after motion has occurred. Because of the sudden start of the motion of the block at  $t = t_0$  and its stop at  $t = t_f$ , regulated by friction, the process is called *stick-slip* motion. If the forces exerted by the spring on the block before and after the motion are  $\sigma_s = Kx_0$  and  $\sigma_f = Kx_f$  then the change in elastic potential energy after the motion has finished is given by, using (1.9),

$$\Delta W = E_T = \frac{1}{2}K(x_0^2 - x_f^2) = \frac{1}{2}(\sigma_s + \sigma_f) \Delta u \quad (1.32)$$

The energy radiated as seismic waves is represented by the difference between the total change in elastic potential energy minus the energy spent in moving the block against

friction and the energy dissipated by friction in the form of heat. From (1.1),  $E_S = E_T - (E_F + E_H)$ , which from (1.32) results in

$$E_S = \frac{1}{2}(\sigma_s + \sigma_f) \Delta u - \sigma_k \Delta \hat{u} \quad (1.33)$$

where  $E_F + E_H = \sigma_k \Delta \hat{u}$  and  $\sigma_k$  is the value of the kinematic or dynamic friction stress during the motion and  $\Delta \hat{u}$  is the average value of the displacement during the motion. This equation can also be written as

$$E_S = \frac{1}{2}\Delta\sigma_s \Delta u + \sigma_f \Delta u - \sigma_k \Delta \hat{u} \quad (1.34)$$

where  $\Delta\sigma_s = \sigma_s - \sigma_f$  represents the *static stress drop*. This is the energy that can be determined from seismological observations. From (1.33) we obtain, for the seismic efficiency factor,

$$\eta = 1 - \frac{2\sigma_k \Delta \hat{u}}{\Delta\sigma_s \Delta u + 2\sigma_f \Delta u} \quad (1.35)$$

The equation of motion for the displacement of the block,  $u(t) = x - x_0$ , for  $t \geq t_0$ , assuming that the block always moves in the positive direction between times  $t_0$  and  $t_1$ , is

$$M\ddot{u} = \sigma_s - Ku - \sigma_k = -Ku + \Delta\sigma_d \quad (1.36)$$

where  $M$  is the mass of the block,  $\sigma_k$  is, as before, the kinematic friction during the motion of the block, which usually depends on the block's velocity but is taken here to be constant, and  $\Delta\sigma_d = \sigma_s - \sigma_k$  is the *dynamic or kinematic stress drop*, that is, the stress drop during the motion. For simplicity we have assumed that there is no viscous damping due to friction during motion. This equation can be written as

$$\ddot{u} = -\omega_0^2 u + \frac{\Delta\sigma_d}{M} \quad (1.37)$$

where  $\omega_0^2 = K/M$  would be the free frequency of the system if it were left to oscillate. The dynamic stress drop  $\Delta\sigma_d$  is the net force that moves the mass of the block starting at  $t = t_0$ . A solution of (1.37) can be written as the sum of the solution for the homogeneous equation and of a particular solution, for  $t \geq t_0$ . The boundary conditions at  $t = t_0$  are  $u = \dot{u} = 0$ . Then the solution of (1.37) is given by

$$u(t) = \frac{\Delta\sigma_d}{K} [1 - \cos \omega_0(t - t_0)] \quad (1.38)$$

and the velocity  $\dot{u}(t)$  is given by

$$\dot{u}(t) = \frac{\omega_0 \Delta\sigma_d}{K} \sin \omega_0(t - t_0) \quad (1.39)$$

The block is assumed to stop at time  $t_f = t_0 + \pi/\omega_0$ , before the motion would be reversed by an increase in the friction to  $\sigma_f$  ( $\sigma_k < \sigma_f < \sigma_s$ ), so that we always have  $\dot{u} > 0$ . Since we want the block to move only in one direction, the block is thus stopped in a rather artificial manner, when its velocity is zero, before the direction of motion is

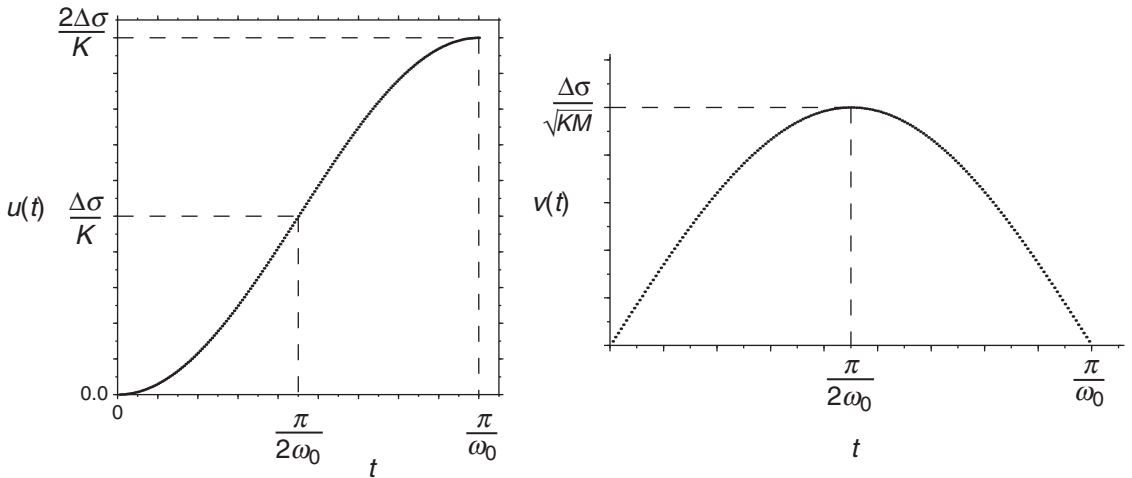


**Figure 1.9.** Displacement  $u(t)$  and velocity  $v(t)$  of a sliding block.

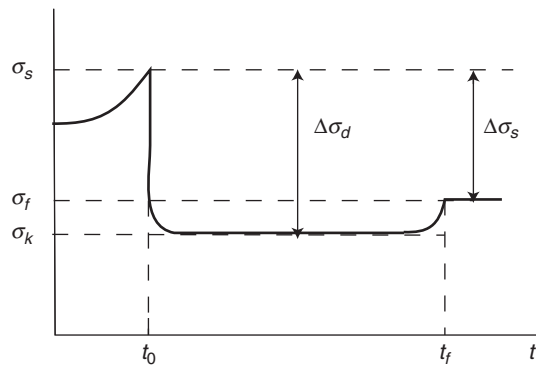


**Figure 1.10.** The stress acting on a block subject to friction as a function of time, before ( $t < t_0$ ), during ( $t_0 < t < t_f$ ) and after ( $t > t_f$ ) sliding:  $\Delta\sigma_d$ , dynamic stress drop;  $\Delta\sigma_s$ , static stress drop.

reversed; otherwise the block would oscillate back and forth. Then, the final displacement and velocity, at  $t = t_f$  are

$$u(t_f) = \frac{2 \Delta\sigma_d}{K} \quad (1.40)$$

$$\dot{u}(t_f) = 0 \quad (1.41)$$

The changes in  $u$  and  $\dot{u}$  with time are given in Fig. 1.9. The displacement increases from zero to a maximum value before the block stops. The velocity has a maximum value at the middle of the process and is zero at the end. The change in stress is given in Fig. 1.10. The stress drops from  $\sigma_s$  to  $\sigma_k$  when the block begins to move. As the block moves, the stress varies with the dependence of  $\sigma_k$  on  $\dot{u}$  (although here we have taken it to be constant) and finally increases to the value of the friction  $\sigma_f$  which stops the motion. Thus, during motion the dynamic stress drop  $\Delta\sigma_d$  is larger than the final static stress drop  $\Delta\sigma_s$ . In the time

interval  $\Delta t = t_f - t_0$  during which the block moves, the stretching of the spring due to the velocity  $v$  of its end is negligible and has not been taken into account, owing to its low value with respect to  $\dot{u}$ , as mentioned previously. After the motion has stopped, the block remains at rest while again the driving motion begins to stretch the spring. This process continues until the force exerted on the block increases from  $\sigma_1$  and again reaches the value  $\sigma_s$ ; then another sliding event happens.

This very simple model illustrates the process of generation of earthquakes. During the loading phase the velocity with which the end of the spring is stretched, while the block is at rest, represents the tectonic processes which accumulate elastic deformations on the fault region. These processes are finally related to the relative motion between lithospheric plates. An earthquake is produced when the strain in a region exceeds a certain threshold value ( $\sigma > \sigma_s$ ). Correspondingly, in the model the force exerted by the spring becomes greater than the static friction between the block and the surface. The sudden motion (stick-slip) of the block represents the occurrence of an earthquake. During the motion, the friction between the block and the surface produces radiation of seismic waves in the elastic medium and dissipation of energy in form of heat ( $E_S + E_R$ ). As in the case of earthquakes, the motion of the block in the model is stopped by friction, by raising its value above the level of the kinematic friction:  $\sigma_f > \sigma_k$ . Once the block has stopped, the spring slowly begins to be stretched again. This represents the beginning of a new *loading phase* or *earthquake cycle*. If we take for  $v$  the value of 1 cm/yr as the velocity of plate motion, it will take 100 years to accumulate enough strain to generate an earthquake with a maximum slip of 1 m, that is, corresponding to about  $M_W = 7$ . If  $v = 5$  cm/yr it will only take 20 years. This shows how the frequency of occurrence of earthquakes in a region is related to the velocity of relative motion between the tectonic plates.

McGarr and Fletcher (2003) showed that laboratory observations of stick-slip friction phenomena simulate well the rupture processes of all earthquakes in continental crustal settings. They show that maximum slip rates are several meters per second, independently of the seismic moment of the earthquakes and that the apparent stresses are limited to about 10 MPa (Fig. 1.11). Thus mechanism of stick-slip motion can be considered as a good simplified model for the fracture process in earthquakes even for large events.

In conclusion, earthquakes can be explained in terms of the motion which takes place on faults when the acting stress overcomes the resistance of the material, which can be expressed as a friction force. The driving force is the stress drop  $\Delta\sigma$  and the result is the slip or relative displacement of the two sides of the fault  $\Delta u$ . The size of an earthquake is given by its seismic moment  $M_0$ , which includes the slip, the fault area and the properties of the material represented by the shear modulus. The total energy release  $E_T$  is divided into the energy which produces the motion or fracture,  $E_F$ , the energy propagated as seismic waves,  $E_S$ , and the energy dissipated as heat,  $E_H$ . In seismology the study of the source mechanism of earthquakes is based on observations of the radiated seismic waves registered by seismographs in the near and far fields. The source is represented by physical-mathematical models in terms of the stress and slip on faults, from which, using the appropriate equations of continuous mechanics, the radiated seismic waves can be deduced. The parameters defining the source can then be determined by an inversion process from the observed wave field.

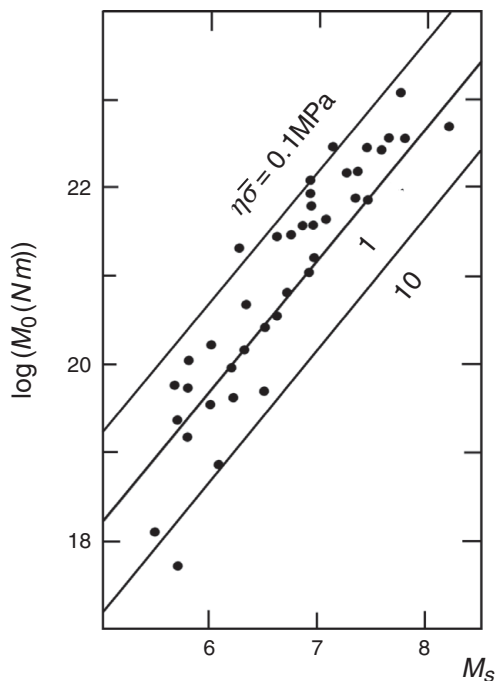


**Figure 1.11.** Relation between seismic moment  $M_0$  and surface wave magnitude  $M_s$ . The lines correspond to values of constant apparent average stress  $\eta\bar{\sigma}$ .

## 1.7. Seismicity and statistical properties of earthquakes

Earthquake statistics is a fully developed branch of earthquake studies. In the following we present a few fundamental statistical properties. The most important of these properties is that on any given volume of the earth, for individual faults as well as for the full Earth, large-magnitude earthquakes are much less frequent than small-magnitude ones. This property is expressed by the *Gutenberg–Richter* (G-R) law, which states that the logarithm of the number of earthquakes greater than a certain magnitude decreases linearly with magnitude (Gutenberg and Richter, 1954, pp. 17–19). The common way of expressing this property is as

$$\log N = a - bM \quad (1.42)$$

where  $N$  is the number of earthquakes larger than magnitude  $M$ ,  $a$  and  $b$  are constants and  $M$  is any one of the magnitude scales defined earlier. Here we consider that magnitude to be  $M_W$ , as defined by Hanks and Kanamori (1979); it is based on the seismic moment (1.30). For most seismic areas of the world where there is a sufficient range of magnitudes that the constant  $b$  can be determined with accuracy, it is observed that  $b$  is very close to 1. In Fig. 1.12 we show the G-R relation for two global seismicity catalogues. The first is the Centennial Catalogue collected by Engdahl and Villaseñor (2002), which covers the most

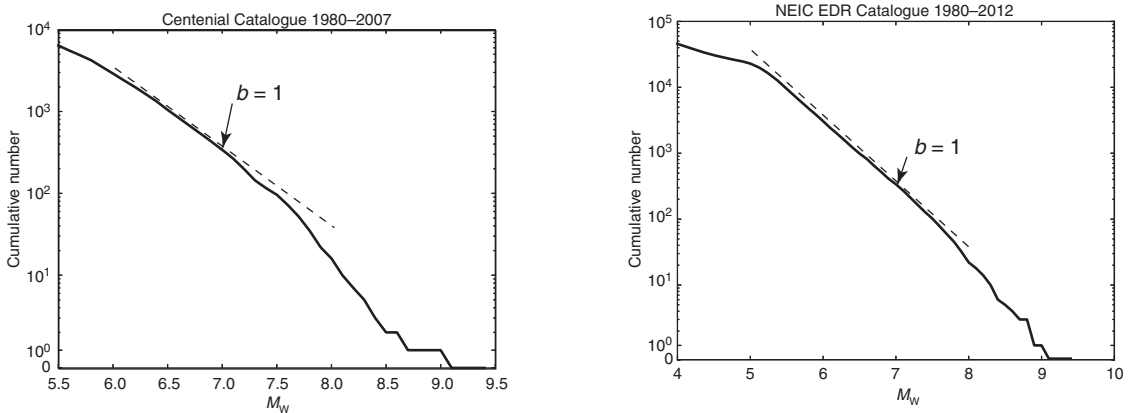


**Figure 1.12.** Cumulative number of earthquakes versus magnitude: left, Centennial Catalogue 1980–2007; right, NEIC EDR Catalogue 1980–2012. The slope for  $b = 1$  is shown.

significant worldwide earthquakes of the last century. We have chosen to plot the seismicity since 1980 because magnitude estimates for earlier earthquakes were not very accurate for events with magnitude larger than 7. Figure 1.12 shows, on the left, the cumulative number of earthquakes  $N$  for earthquakes between magnitudes 5.5 and 9.5. In the same figure, on the right, we plot the catalogue produced by the National Earthquake Information Center (NEIC) of the United States. The cumulative G-R distribution for earthquakes from January 1990 to September 2010 in the magnitude range 4 to 10 is shown. Both catalogues have slope  $b = -1$  for events with magnitudes between 6 and 7.5. For events with magnitudes smaller than 6 the Centennial Catalogue tends to saturate, while the cumulative number of earthquakes in the NEIC catalogue does not follow the  $b = 1$  line for magnitudes smaller than 5. This change in the slope of the GR law is most likely due to the incompleteness of these catalogues for small events, which are not well detected by the global networks. At large magnitudes, greater than 7.5, the logarithm of the number of events decreases with magnitude faster than linearly. This is an indication that there are relatively fewer larger events than the number predicted by the G-R relation. Two possible explanations of this deficiency of larger events are: (1) this is a real characteristic of the seismicity of the earth; or (2) the time span of the catalogues is too short, so that there are not enough large events in that period of time; if we had a catalogue that spanned a much longer period of time then the G-R law would be verified for all magnitudes. In either case there must be a maximum magnitude, and the distribution of those extreme events may deviate from the G-R law (see e.g. Wesnousky, 1998).

The other important property of earthquakes is *Omori's law*; it states that the number of aftershocks following a main shock decreases as an inverse power of time (Omori, 1894). In the most common version of this law a decrease inversely proportional to time is assumed, that is,

$$N(t) = \frac{A}{c + t} \quad (1.43)$$

where  $N(t)$  is the number of aftershocks per unit time step  $\Delta t$ , the interval between  $t$  and  $t + \Delta t$ ,  $c$  is a time constant that limits the growth of  $N$  at zero time and  $A$  is a constant that measures the level of aftershock activity. Actually the value of  $N(t)$  must be interpreted as the perturbation in seismicity produced by the main event. After a certain time the seismicity will return to a steady state that is usually defined as the background seismicity.

Finally, a less well-established property is the so-called *Båth* rule, which states that the largest aftershock of a major surface earthquake has a magnitude of the order of one unit less than that of the main event. For deep earthquakes, however, i.e. those at between 150 km and 600 km, the difference is between 2 and 4 ([Båth, 1965](#)). This rule failed for two very large recent earthquakes: the Maule, Chile earthquake with  $M_W = 8.8$  in 2010 and the Tohoku earthquake with  $M_W = 9$  in 2011. The largest aftershock that has occurred so far for Maule had a magnitude of only 7.3; it occurred on 23 March 2012, more than two years after the main event. The largest event that followed Tohoku had a magnitude of 7.8; it occurred a few minutes after the main event.

In earthquake statistics these three laws and rules can be combined to produce a model of seismicity that assumes that every earthquake in a series is a main event, with its own set of aftershocks following the *Båth* rule and the Omori law. The ensemble of earthquakes is then determined by a suite of main events given by the G-R law. These and more sophisticated models produce interesting statistical models, such as the so-called ETAS model of [Ogata \(1988\)](#). Seismic catalogues can be scanned to test different seismicity models.

## 2

# Processing and analysis of recorded seismic signals

## 2.1. Recorded ground motion in time and frequency domains

The determination of the mechanism of an earthquake is an inverse problem; that is, we obtain the parameters which define the mechanism from observations of the ground motion produced by seismic waves and recorded by *seismographs* at different locations on the Earth's surface. As a consequence, we first need to obtain the ground motion by processing and analysing the records of seismographs or *seismograms*. In this chapter we review some basic ideas about processing digital data from *broadband* seismograms, as digital data are most commonly used nowadays to obtain the characteristics of ground displacements. We include also some examples of this processing using Seismic Analysis Code (SAC) commands (Tapley and Tull, 1992).

We will first review briefly the fundamental equations relating recorded signals and ground motion. A seismogram is a time signal  $s(t)$ , recorded by a seismograph at a particular location at an epicentral distance  $Q$  from the source, corresponding to the motion of the ground from an incoming seismic wave and can be expressed as the convolution

$$s(t) = u(t) * f(Q, t) * I(t) \quad (2.1)$$

Here  $u(t)$  is the ground motion displacement at the source corrected for *geometrical spreading*, the free surface effects  $f(Q, t)$  correspond to *anelastic attenuation* along the ray path and  $I(t)$  is the *instrumental response* (the symbol  $*$  denotes the convolution operator) (Fig. 2.1).

If we apply a Fourier transform (FT) to equation (2.1) we obtain in the frequency domain

$$S(\omega) = U(\omega) F(Q, \omega) I(\omega) \quad (2.2)$$

and, solving for the displacement, we obtain

$$U(\omega) = \frac{S(\omega)}{F(Q, \omega) I(\omega)} \quad (2.3)$$

From equation (2.3) we can obtain an expression for the ground motion displacement  $u(t)$  in the time domain in terms of the FT of the recorded observations  $S(\omega)$ , using the inverse Fourier transform:

$$u(t) = \frac{1}{2\pi} \int_{-\infty}^{\infty} \frac{S(\omega)}{F(Q, \omega) I(\omega)} e^{i\omega t} d\omega \quad (2.4)$$

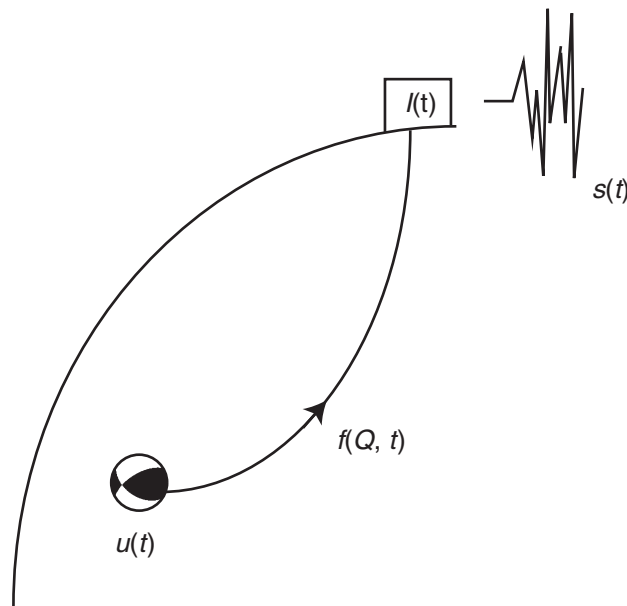


**Figure 2.1.** Relation between displacement at the source  $u(t)$ , and its recording at an observation point: ray path anelastic attenuation  $f(Q, t)$ , instrumental response  $I(t)$  and seismogram time signal  $s(t)$ .

To retrieve the displacement  $u(t)$  using equation (2.4) from the FT of the recorded seismogram  $S(\omega)$  it is necessary to know the FTs of the instrumental response  $I(t)$  and of the anelastic attenuation operator  $f(Q, t)$ .

The instrumental response of a seismometer is obtained by solving the equation of motion of its mass, given by Scherbaum (1996, pp. 48–58) or Udiás (1999, pp. 406–10):

$$\ddot{z} + 2\beta\omega_0\dot{z} + \omega_0^2 z = -\ddot{u} \quad (2.5)$$

where  $z(t)$  is the relative motion of the mass with respect to the frame of the instrument,  $\ddot{u}(t)$  is the ground acceleration,  $\beta$  is the *damping factor* (not to be confused with the S wave velocity) and  $\omega_0$  is the natural frequency of the undamped system. If we assume for  $u(t)$  a harmonic motion of frequency  $\omega$  and amplitude  $X$ , i.e.  $u(t) = X \sin(\omega t)$ , we obtain

$$\ddot{z} + 2\beta\omega_0\dot{z} + \omega_0^2 z = X\omega^2 \sin(\omega t) \quad (2.6)$$

The solution of this equation, ignoring the transient part, is

$$u(t) = Z \sin(\omega t - \varepsilon) \quad (2.7)$$

where  $Z$  and  $\varepsilon$  are the amplitude and phase of the relative motion of the mass with respect to the instrument frame, that is, the motion that is recorded or output signal. In the Fourier domain  $Z$  and  $\varepsilon$  are given by

$$Z = \frac{\omega^2 X}{\left[ (\omega_0^2 - \omega^2)^2 + (2\beta\omega\omega_0)^2 \right]^{1/2}} \quad (2.8)$$

$$\varepsilon = \tan^{-1} \left( \frac{2\beta\omega\omega_0}{\omega_0^2 - \omega^2} \right) \quad (2.9)$$

The *frequency transfer function*  $T(\omega)$  is defined as the Fourier transform of the output signal divided by the Fourier transform of the ground motion or input signal (Scherbaum, 1996, pp. 63–5). From (2.8) its amplitude and phase are given by

$$|T(\omega)| = \frac{Z}{X} = \frac{\omega^2}{[(\omega_0^2 - \omega^2)^2 + (2\beta\omega\omega_0)^2]^{1/2}} \quad (2.10)$$

$$\varepsilon = \tan^{-1} \left( \frac{2\beta\omega\omega_0}{\omega_0^2 - \omega^2} \right) \quad (2.11)$$

If instead of the Fourier transform we apply a Laplace transformation to the seismometer equation (2.5) we obtain

$$s^2 Z(s) + 2\beta\omega_0 s Z(s) + \omega_0^2 Z(s) = -s^2 X(s) \quad (2.12)$$

and now the transfer function is given by

$$T(s) = \frac{Z(s)}{X(s)} = \frac{-s^2}{s^2 + 2\beta\omega_0 s + \omega_0^2} \quad (2.13)$$

In terms of the Laplace transform, the transfer function (2.13) is characterized by its *zeros*, the roots of the numerator, and by its *poles*, the roots of the denominator. Thus equation (2.13) has two zeros equal to 0 and two complex conjugate poles, the roots of the polynomial in the denominator.

The *total magnification* of the system,  $V(\omega)$ , is given by the product of the *dynamic magnification*  $V_d(\omega)$  and the *static magnification*  $V_s$ :

$$V(\omega) = V_s V_d(\omega) \quad (2.14)$$

Here  $V_s$  is the amplification of the relative motion of the mass with respect to the frame of the instrument and depends on the type of seismograph;  $V_d(\omega)$  is the amplitude dynamic magnification of the seismometer for a harmonic input signal of frequency  $\omega$  and it is given by the transfer function  $T(\omega)$  (2.10):

$$V_d(\omega) = \frac{\omega^2}{[(\omega^2 - \omega_0^2)^2 + (2\omega\omega_0\beta)^2]^{1/2}} \quad (2.15)$$

The magnification of the system,  $V(\omega)$ , is the amplitude part of the instrument response  $I(\omega)$  in the frequency domain. The complete instrument response in the frequency domain is then given by

$$I(\omega) = V_s V_d(\omega) \exp ie(\omega) \quad (2.16)$$

The maximum value of the amplitude magnification is  $V_{\max}$ . This must not be confused with the *dynamic range* (DR), defined as the range between the maximum ( $A_{\max}$ ) and minimum ( $A_{\min}$ ) amplitudes that can be recorded by each system. Amplitudes greater than  $A_{\max}$  will be saturated (clipped) and amplitudes smaller than  $A_{\min}$  will not be recorded. The DR is measured in decibels and given as

$$\text{DR} = 20 \log \frac{A_{\max}}{A_{\min}} \quad (2.17)$$

The DR is in itself independent of the magnification. If we increase the magnification while keeping the same DR,  $A_{\max}$  will correspond to smaller amplitudes of ground motion. The system will be saturated for amplitudes larger than  $A_{\max}$  and we will lose information about those amplitudes. For example, if we have an analogical instrument where  $A_{\min}$  is 1 mm and  $A_{\max}$  is 10 mm (the peak to peak amplitude) then the DR is 40 dB. If  $V_{\max}$  is 1500, a ground motion of 10  $\mu\text{m}$  will be amplified to 15 mm but  $A_{\max}$  is only 10 mm and therefore the record will be saturated.

The anelastic attenuation effects in the frequency domain may be approximated by a linear operator (Deschamps *et al.*, 1980):

$$F(Q, \omega) = \exp \left( -\frac{\omega t'}{2Q} + i \frac{\omega t'}{\pi Q} \log \frac{\omega}{\omega_1} \right) \quad (2.18)$$

where  $Q$  is the *quality factor* and  $t'$  is the *travel time*. For epicentral distances between 30° to 90°,  $t'/Q$  is 1 for P waves and 4 for S waves;  $\omega_1$  is a reference frequency, normally  $2\pi$ .

## 2.2. Analogical and digital data

*Analogical* data result from the output of a seismograph, either mechanical or electromagnetic, corresponding to the three components of the ground motion (vertical, NS and EW). The graphical representation of the data provides an analogical record or seismogram. This was the type of seismological data that was available from the time when the first seismographs were installed, at the end of the nineteenth century, until about 1980, when *digital* instruments were introduced. Analogical records are continuous, so that before we can use them in digital computers they must be digitized. The digitization process has a number of limitations such as the length of the sampling interval, which depends on the graphical representation facility of the seismogram, and the errors which are easily introduced during this process. Let us suppose that an earthquake has been recorded, for example, at an analogical station of the WWSSN network. There will be two sets of records for this event: seismograms recorded by the *short period* (SP) instrument and by the *long period* (LP) instrument. In graphical seismograms the time representation of one minute in centimeters is different for the SP and LP instruments. For LP records the length is usually 1.5 cm or 3 cm and for SP records 6 cm, which limits the sampling rate,

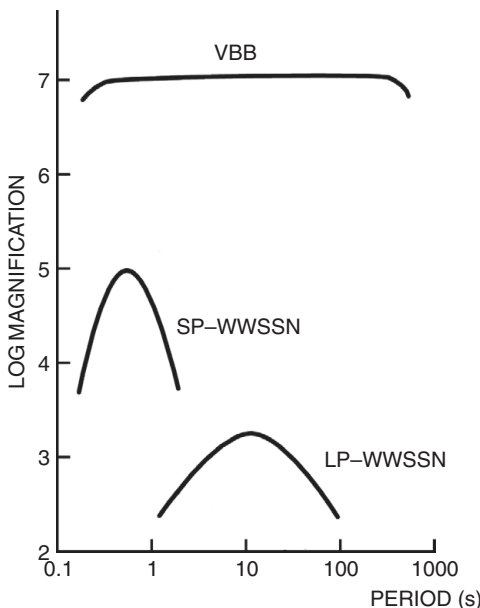


**Figure 2.2.** Magnification curves for WWSSN short period (SP), long period (LP) and broadband (VBB) seismographs.

commonly, to one sample per second. With the digital instruments we avoid this problem: modern instruments feed the continuous electric current output of an electromagnetic seismograph to an *analogue-to-digital* (AD) converter, which produces a digitized time series. The sampling rate can be as high as needed, depending on the AD converter. For this reason, at present most seismographic stations provide data in digital form. Another modern improvement in the instrumentation has been the substitution of SP and LP seismographs by broadband (BRB) instruments. Classic SP and LP instruments have a narrow amplification response, centered, for example, at one second (SP) and 15 seconds (LP), while broadband instruments have a flat response between a frequency of 20 Hz and a period of 1000 seconds or 1 mHz (Fig. 2.2). Thus, a single instrument substitutes the previous two. Owing to the general use of this new type of instrument, we will limit our considerations to the analysis of data from digital broadband seismographs.

The output data from current digital broadband instruments are provided by different channels with different sampling intervals and frequency bands; the most common currently in use are listed in Table 2.1.

The selection of the data channel depends on the type of data in which we are interested. If we want to analyse surface waves or the complete seismogram for a teleseismic event, we can use the LH channel, but if we want to study only a few phases, for example P or SH waves, it is more convenient to use the BH channel. For local or regional small earthquakes with a high-frequency content, we need higher sampling rates and so we use the SH or HH channels instead. An example of the three components of a broadband seismogram on the LH channel for a teleseismic event is given in Fig. 2.3.

The main difference between mechanical and electromagnetic instruments (digital instruments are electromagnetic) is the output, i.e. the seismogram. Mechanical

**Table 2.1**

Channel	Sampling rate (samples/s)	Time interval (s)
VH	1/10	10
LH	1/1	1
BH	20/1	0.05
HH/SH	50/1–100/1	0.02–0.01

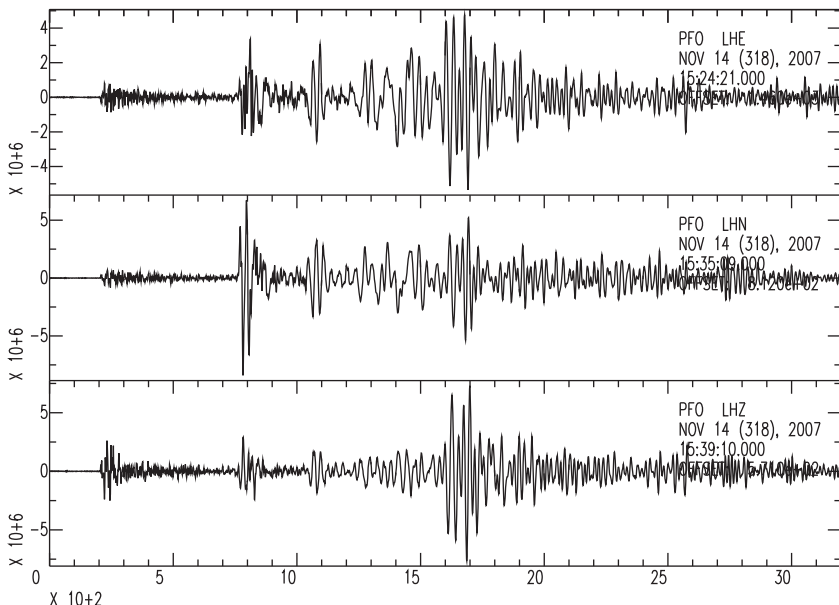


**Figure 2.3.** Broadband seismogram at the Pinyon Flat, California station of the Chile earthquake of 14 November 2007, magnitude  $M_W = 7.7$ . The east–west (LHE), north–south (LHN) and vertical (LHZ) components recorded on the LH channel are shown.

seismographs record the ground displacement  $u(t)$  while electromagnetic instruments record the ground velocity  $v(t)$ . Records from a mechanical seismograph (a Wiechert model) and from an electromagnetic seismograph (a BB Streckeisen model) at the same site are shown in Fig. 2.4. Since all modern seismographs are electromagnetic, in order to obtain the ground displacement  $u(t)$  we have to integrate the velocity signal.

## 2.3. Removing the instrumental response

The instrument response may be obtained in terms of the Laplace transform from the transfer function (2.13), by making the replacement  $s = i\omega$  (Scherbaum, 1996, pp. 63–5). The output amplitude of a digital instrument is given in digital units or *counts*. The correspondence between counts and displacements or velocities depends on the

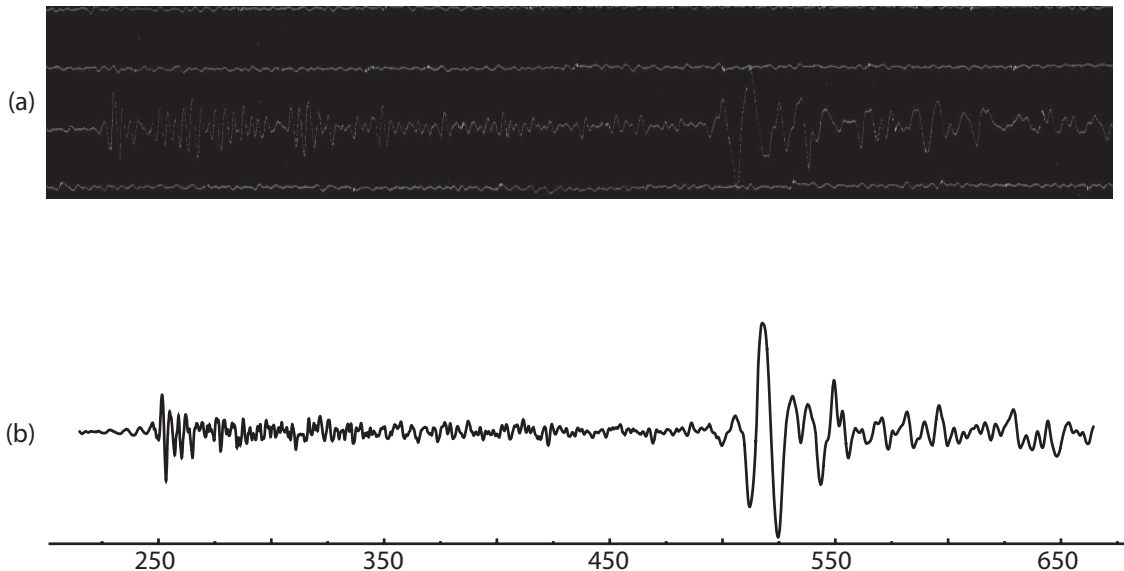


**Figure 2.4.** For comparison, (a) the displacement record (east–west component) of a Wiechert seismograph at the TOL (Toledo, Spain) station and (b) the velocity broadband seismograph record (east–west component) at the PAB (San Pablo, Toledo, Spain) station of the Aegean Sea earthquake with  $M_W = 6.1$ . The horizontal scale is in seconds.

instrument's amplification (a common equivalence is that approximately one count equals one nanometer displacement or, for velocity, one nanometer per second). The instrumental amplitude magnification of displacement is given by equation (2.15). In digital instruments the static magnification  $V_s$  is given by the *instrument constant*, which is the product of two terms,  $A_0$  (a *normalization factor*), given in  $\text{V}/(\text{ms}^{-1})$ , and the *sensitivity*  $D_s$ , given in  $\text{V}/\text{count}$ . As a consequence the total instrument response in its most general form, including the AD converter and filters, is a product of poles and zeros:

$$I(s) = A_0 D_s \frac{\prod_{j=1}^{N_z} (s - s_z)}{\prod_{j=1}^{N_p} (s - s_p)} \quad (2.19)$$

where  $N_z$  is the number of zeros and  $N_p$  the number of poles, and  $s_z$  and  $s_p$  are their respective values. The units in equation (2.19) for a velocity-sensitive seismograph are  $\text{counts}/(\text{ms}^{-1})$ .

From equation (2.1) we can obtain the ground motion  $u(t)$  if we know the instrument response  $I(t)$  and the attenuation  $f(Q, t)$ . As mentioned above, most seismographs are velocity instruments, that is, they record the ground velocity  $v(t) = \dot{u}(t)$ . The instrumental response for this kind of instrument is a velocity response,  $I_v(t)$ , so that we can modify equation (2.1) to the form

$$s(t) = v(t) * f(Q, t) * I_v(t) \quad (2.20)$$

If we take the FT of this equation, we obtain in the frequency domain

$$S(\omega) = V(\omega)F(Q, \omega)I_v(\omega) \quad (2.21)$$

Then, using the derivative property of the FT in this equation, we can write

$$S(\omega) = i\omega U(\omega)F(Q, \omega)I_v(\omega) \quad (2.22)$$

Solving for the FT of the ground displacement we get

$$U(\omega) = \frac{S(\omega)}{i\omega F(Q, \omega) I_v(\omega)} \quad (2.23)$$

Taking the inverse FT in equation (2.23), we obtain the ground displacement in the time domain,  $u(t)$ . In order to obtain the ground displacement from equation (2.22), however, we would need to remove the effect of the instrument, using the velocity instrument response, and afterwards integrate this equation to obtain  $u(t)$ . Another way to do this is to use the Laplace transform in terms of poles and zeros, (2.19); by adding a zero to the instrumental response we can obtain directly the ground displacement  $u(t)$ . The second option is more convenient because it implies fewer calculations. Adding a zero to a velocity instrumental response is equivalent to using the displacement instrumental response:

$$I_d(s) = sI_v(s) \quad (2.24)$$

**Figure 2.5** and **Table 2.2** show the amplitude response and the instrumental response for a BB seismograph. We observe that the instrument response is given in terms of its Laplace transform, in units of radians per second corresponding to the angular frequency  $\omega$ . If the units are Hz/s, the values correspond to the frequency  $f$ . In this case, in equation (2.19), we must add a factor  $(2\pi)^a$  with  $a = N_z - N_p$ .

The instrument of **Table 2.2** is a velocity instrument, so that to obtain the displacement response we have to add a zero to the transfer function, giving  $s = i\omega$ . Thus, the instrument

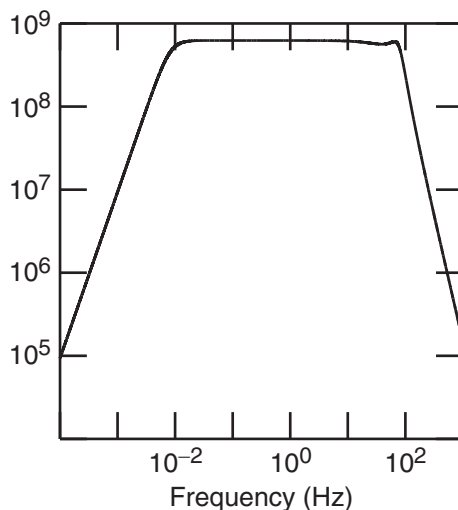


**Figure 2.5.** Magnification curve for the broadband seismograph of the CART (Cartagena, Spain, Western Mediterranean Network) station.

**Table 2.2****CHANNEL RESPONSE DATA**

Station: CART

Network: WM

Location: Cartagena Naval Base (Spain)

Channel: BHZ

Start date: 1997,345

End date: No Ending Time

| Response (Poles &amp; Zeros), CART ch BHZ |

Transfer function type: A [Laplace Transform (rad/s)]

Stage sequence number: 1

Response in units lookup: m/s - velocity in meters per second

Response out units lookup: V - volts

 $A_0$  normalization factor: 6.0077E+07

Normalization frequency: 1

Number of zeros: 2

Number of poles: 5

Complex zeros:

real imag real\_error imag\_error

0.000000E+00 0.000000E+00 0.000000E+00 0.000000E+00

0.000000E+00 0.000000E+00 0.000000E+00 0.000000E+00

Complex poles:

-3.700400E-02 3.701600E-02 0.000000E+00 0.000000E+00

-3.700400E-02 -3.701600E-02 0.000000E+00 0.000000E+00

-1.310400E+02 -4.672900E+02 0.000000E+00 0.000000E+00

-1.310400E+02 4.672900E+02 0.000000E+00 0.000000E+00

-2.513300E+02 0.000000E+00 0.000000E+00 0.000000E+00

| Channel Sensitivity, CART ch BHZ |

Stage sequence number: 0

Sensitivity: 6.150000E+08

Frequency of sensitivity: 2.000000E-02 HZ

response in displacement has three zeros and five poles. If we want the acceleration response we must remove a zero from [table 2.2](#), leaving one zero and five poles).

## 2.4. Processing a seismic signal

Processing a digital seismic signal is a necessary step previous to any seismological analysis, which involves a series of processes starting with data acquisition. Here we will present some of these processes: (1) instrumental deconvolution or removal of the instrument response in order to obtain the ground motion; (2) calculation of the amplitude spectrum; (3) determination of the radial and transverse components of horizontal motion and (4) determination of the particle motion; see the end of [section 2.4](#).

## Data acquisition

Nowadays, digital seismograms from broadband stations can be obtained from several data center web sites, for example, IRIS (Incorporated Research Institutions for Seismology, <http://www.iris.edu/hq>), GEOFON (<http://geofon.gfz-potsdam.de/geofon/>) and ORFEUS (<http://www.orfeus-eu.org>). The data are given in binary form; one of the most commonly used formats is the SEED (Standard for the Exchange of Earthquake Data) format. From these web sites one can also download the software necessary to process seismograms in SEED format. On the IRIS web site the program is called *rdseed* (an example is shown in Table 2.3). As this program is updated periodically, one should download the latest version.

In this example, chile.seed is the input file for the Northern Chile earthquake of 14 November 2007; it corresponds to the BHZ channel of station PFO (Pinyon Flat Observatory, Riverside, California), which we retrieved from the IRIS web site. The output file is given in SAC format, but seven other options are possible including an ASCII (American Standard Code for Information Interchange) file (option 6). There is an option to obtain the instrument response given by two files: the file RESP.AZ.PFO..BHZ file is the velocity instrument response for the PFO station on the BHZ channel (Table 2.2); the other format is in terms of poles and zeros and is given in the file SAC\_PZs\_AZ\_PFO\_BHZ\_...

**Table 2.3**

```

rdseed
<< IRIS SEED Reader, Release 4.7.5 >>
Input File (/dev/nrst0) or 'Quit' to Exit: chile.seed
Output File (stdout) :
Volume # [(1)-N] :
Options [acCsSpRtde] : d
Summary file (None) :
Station List (ALL) : PFO
Channel List (ALL) : BHZ
Network List (ALL) :
Loc Ids (ALL ["--" for spaces]) :
Output Format [(1=SAC), 2=AH, 3=CSS, 4=mini seed, 5=seed, 6=sac
ascii, 7=SEGY] : 1
Output file names include endtime? [Y/(N)] n
Output poles & zeroes ? [Y/(N)] y
Check Reversal [(0=No), 1=Dip.Azimuth, 2=Gain, 3=Both] : 0
Select Data Type [(E=Everything), D=Data of Undetermined State,
R=Raw waveform Data, Q=QC'd data] :
Start Time(s) YYYY, DDD, HH:MM:SS.FFFF :
End Time(s) YYYY, DDD, HH:MM:SS.FFFF :
Sample Buffer Length [2000000] :
Extract Responses [Y/(N)] : y
Writing AZ.PFO..BHZ, 132241 samples (binary), starting 2007, 318
15:47:03.4250 UT
Input File (/dev/nrst0) or 'Quit' to Exit: Quit

```

The seismogram in SAC binary format is given in the file 2007.318.15.47.03.4250.AZ.PFO..BHZ.R.SAC.

Sometimes data are given in miniSEED format; this is a seed file which does not have the header “file” and which contains information about the instrument response. In this case we can use the same code, but first we have to execute the following command: setenv ALT\_RESPONSE\_FILE dataless\_stn, where dataless\_stn is a header file that contains the station characteristics, such as the station coordinates, the instrument type etc. Other formats that can be retrieved with the rdseed programme are GSE (Group Scientific Experts), CSS (Center for Seismic Studies), SEISAN etc. We can make a conversion from these formats to the SAC format, for example, for the CSS format using the css2sac command, but we must include a file with the station characteristics.

### Instrumental deconvolution (removing the instrument response)

---

The first step in the analysis of recorded seismic waves is to obtain the ground motion  $u(t)$ . In order to obtain it we must remove the instrument response. As the seismograms have been obtained in SAC format we will use the SAC program to process the records. The list of commands for this process is given in [Table 2.4](#).

The command  $r\ file.SAC$  reads the data (the seismogram in SAC format) of the Chile earthquake at the station PFO and we may plot it, using the command  $p$  ([Fig. 2.6](#), top). The  $rmean$  command removes the mean and  $rtrend$ , a linear trend. The  $taper$  command applies a symmetric taper to each end of the data. The  $trans$  command removes the instrument response, which is given in displacements by the zeros and poles in  $SAC\_PZsfile$ ; it is plotted using the  $p$  command ([Fig. 2.6](#), middle). As a result of the deconvolution, low- and high-frequency noise beyond the frequency response of the instrument is introduced into the deconvolved signal. For this reason, a band pass Butterworth filter (the  $bp$  command) is applied to obtain the final displacement ground motion  $u(t)$  ([Fig. 2.6](#), bottom).

### Amplitude spectra

---

The frequency analysis of seismic waves is a fundamental tool in seismology. We can obtain the *amplitude spectra* of the ground motion  $u(t)$  by applying a Fourier transform.

**Table 2.4**

```
SAC> r 2007.318.15.47.03.4250.AZ.PFO..BHZ.R.SAC
SAC> p
SAC> rmean
SAC> rtrend
SAC> taper
SAC> trans from polezero subtype
SAC_PZs_AZ_PFO_BHZ_2004.056.18.43.30.0000_99999.9999.24.60.60.99999
SAC> p
SAC> bp n 3 corner 0.01 1
SAC> p
```

**Table 2.5**

```
SAC> cut a -50 300
SAC> r pfo_filt*
SAC> p
SAC> rmean
SAC> rtrend
SAC> taper
SAC> p
SAC> fft
SAC> psp am
SAC> xlim 0.001 4
SAC> xlog
SAC> ylog
SAC> xgrid on
SAC> ygrid on
SAC> psp am
SAC> bd sgf
SAC> psp am
SAC> sgftops f001.sgf pfo.esp
```

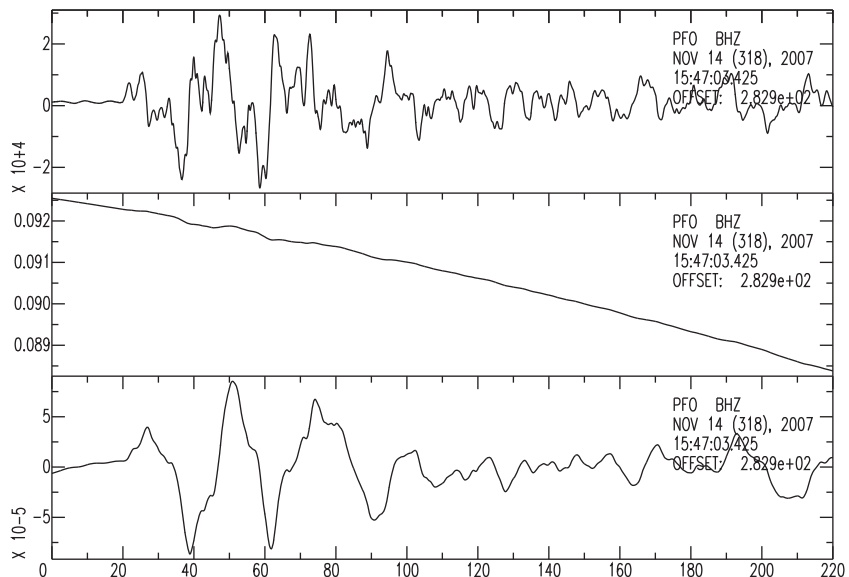
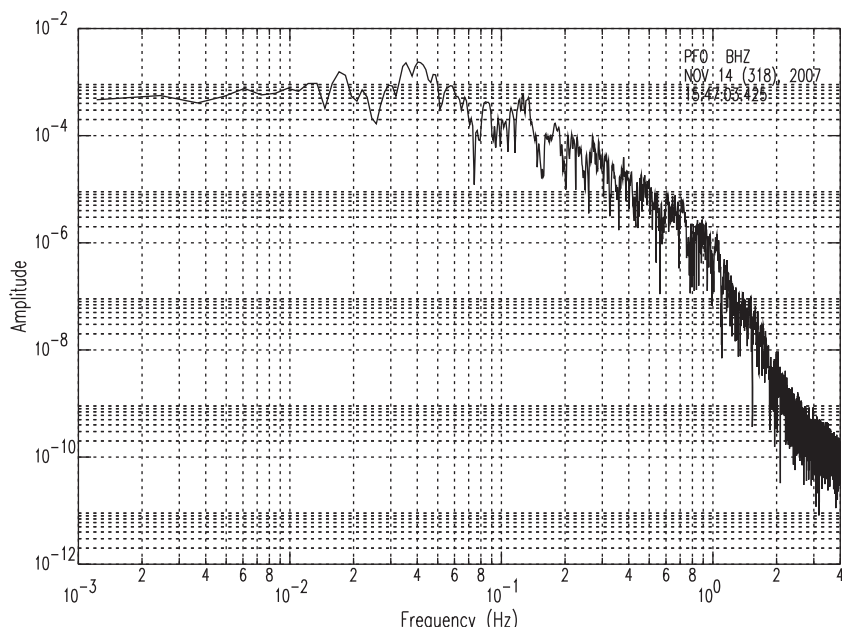


**Figure 2.6.** The ground motion displacement from the seismogram of Fig. 2.3, obtained by removal of the instrument response. Top: vertical component of the P waves showing the velocity in m/s versus time in seconds. Middle: displacement ( $10^{-4}$  m) without a filter. Bottom: displacement after the application of a Butterworth band pass filter.

The commands to perform the FT are given in [Table 2.5](#). In our example of the Chilean earthquake recorded at the PFO station, first we select a particular set of time intervals on the record (for the P wave), of size, for example, 350 s (we do this using the *cut* command). In our case the sampling rate is 20 samples/s so that we have a total of 7000 samples, which is close to  $8192 (2^{13})$ ; because of the requirements of the fast Fourier transform (fft) used in the program, it is important that the selected number of samples should be close to a value which is a power of 2 ( $2^N$ ). As before, we have to remove the mean and trend of the data and apply a taper. To estimate the Fourier transform we use the *fft* command and, to plot the amplitude spectra, the *psp am* command. We limit the frequency plot to the range 0.001 to 4 Hz using the *xlim* command. It is convenient to use a logarithmic plot (the *xlog* and *ylog* commands) and we can include a grid in the plot (the *xgrid* and *ygrid* commands). Finally, to obtain a ps file with the plot diagram, we use the *bd sgf* command and the *sgfstop* command ([Fig. 2.7](#)).

### Radial and transverse components

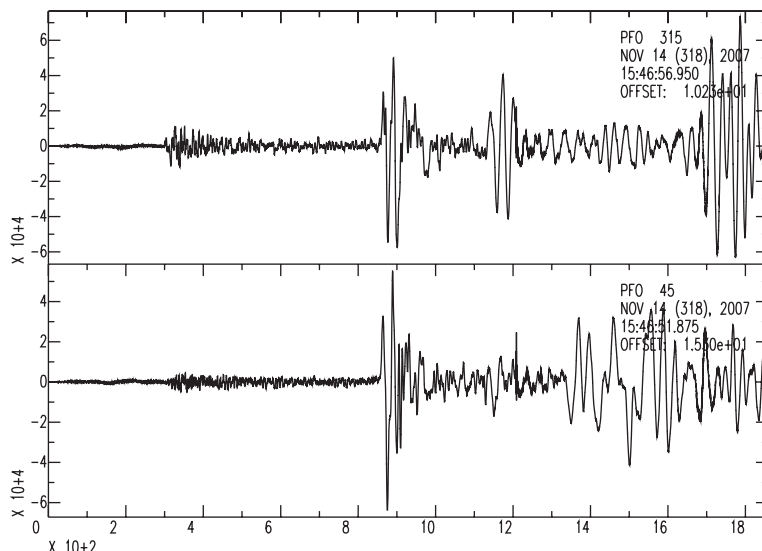
If we want to obtain the *radial* and *transverse* component of the horizontal ground motion in order to separate the P, SV and Rayleigh waves from the SH and Love waves, we have to rotate the horizontal components (NS and EW). For example, for the record of the Chilean earthquake at the PFO station, we use the *rotate* command to obtain the horizontal radial and transverse components. The sequence of commands is given in [Table 2.6](#). We read the data file in the order: first the NS component and then the EW component; we then remove the mean and the trend (*rmean* and *rtrend* commands) and we use the *rotate* command.



**Figure 2.7.** Amplitude spectrum of the P wave displacement for the seismogram of [Fig. 2.6](#).

**Table 2.6**

```
SAC> r 2007.318.15.46.56.9500.AZ.PFO..BHN.R.SAC
2007.318.15.46.51.8750.AZ.PFO..BHE.R.SAC
SAC> rmean
SAC> rtrend
SAC> taper
SAC> rotate to gcp
SAC> p1 r
SAC> bd sgf
SAC> p1 r
SAC> sgftops f001.sgf pfo_rotate.ps
```

**Figure 2.8.** Radial (top) and transverse (bottom) horizontal components of the seismogram of Fig. 2.3.

Finally, we can plot the result in graphics mode or obtain a ps file (using the `bd sgf` command). The result is shown in Fig. 2.8; in the radial component the larger amplitudes correspond to P and Rayleigh waves and in the transverse component to SH and Love waves.

### Particle motion

In many seismological applications it is important to determine the wave *particle motion*. To obtain the particle motion corresponding to a selected part of a seismogram on the horizontal plane, we use the commands given in Table 2.7. In this case we want to obtain the particle motion of the horizontal component of the S wave for the same record as

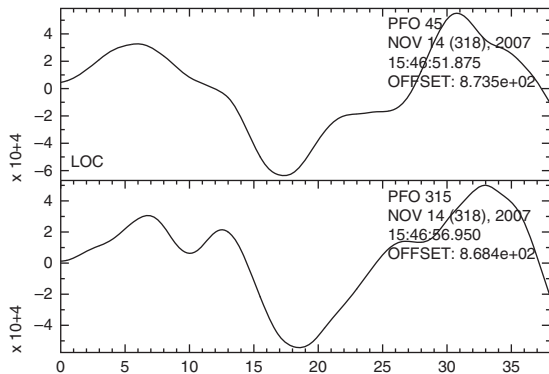
**Table 2.7**

```

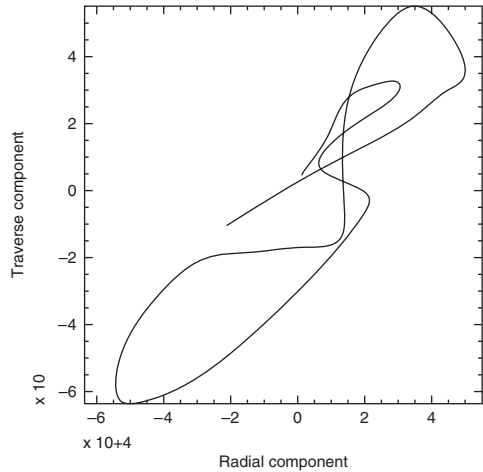
SAC> r pfo.bht pfo.bhr
SAC> rmean
SAC> rtrend
SAC> p1 r
SAC> plotpm
SAC> bd sgf
SAC> p1 r
SAC> plotpm
SAC> sgftops f001.sgf pfo_TR.ps
SAC> sgftops f002.sgf motion.ps

```

(a)



(b)

**Figure 2.9.**

Particle motion diagram and the horizontal components of the S wave of the seismogram of Fig. 2.3. (a) Radial and transverse components of the S wave. (b) The particle motion.

before. Previously we obtained the radial and transverse components and now we cut the seismogram in order to obtain the particle motion of the S wave. We read the transverse and radial components (using the *r* command), we remove the mean and trend (using the *rmean* and *rtrend* commands) and plot both components (Fig. 2.9a). The *plotpm* command gives a plot of the horizontal particle motion of the S wave (Fig. 2.9b). Finally we obtain the ps files with the *sgf* and *sgftops* commands.

## 2.5. Displacement, velocity and acceleration

The ground motion, which constitutes the observational data for the determination of the source mechanism, can be described in terms of displacement, velocity and acceleration. For harmonic motion their relation is

$$u(t) = A \cos \omega t \quad (2.25)$$

$$\dot{u}(t) = -A\omega \sin \omega t \quad (2.26)$$

$$\ddot{u}(t) = -A\omega^2 \cos \omega t \quad (2.27)$$

Mechanical seismographs directly record the relative displacement between the frame and mass of a pendulum, amplified by a system of levers (Fig. 2.4a). Such seismograms are still used in the examination of historical earthquakes. In about 1920 electromagnetic seismographs were introduced and rapidly substituted mechanical seismographs. In these instruments the relative velocity of the mass and frame is converted into a variable electric current proportional to this velocity. These seismograms, in analogue or digital form, represent the velocity of ground motion (Fig. 2.4b). As in the equation of motion the variable is the displacement  $u(t)$ ; to find it we have to integrate the seismograms, as we have already seen. In the previous sections we have described in some detail the processing of broadband digital seismograms.

Seismographs *saturate* and *clip* with the ground motion of large earthquakes, making their data unusable. For example, Fig. 2.10 shows a saturated (clipped) seismogram of an  $M_w = 6.4$  earthquake recorded by a broadband instrument at 40 km epicentral distance. To overcome this difficulty, *strong motion* instruments or *accelerographs* are used instead of seismographs to study large earthquakes in the near field. Accelerograms were originally very low sensitivity analogical instruments developed for the needs of earthquake

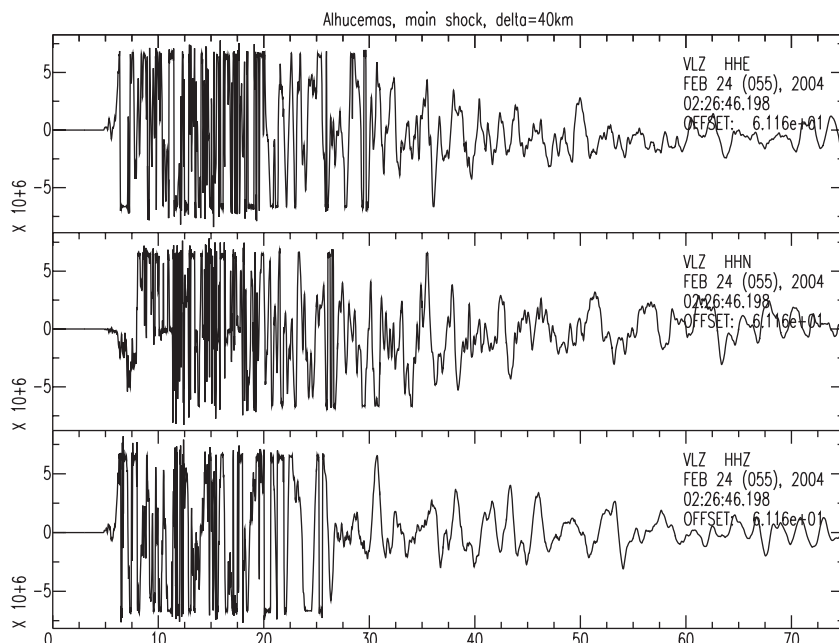


**Figure 2.10.** Clipped seismograms at broadband station VLZ (Velez Gomera, North Africa, Western Mediterranean Network) for the Alhoceima earthquake of 24 February 2004,  $M_w = 6$ , at 40 km epicentral distance. The east–west (HHE), north–south (HHN) and vertical (HHZ) components for the HH channel are shown.

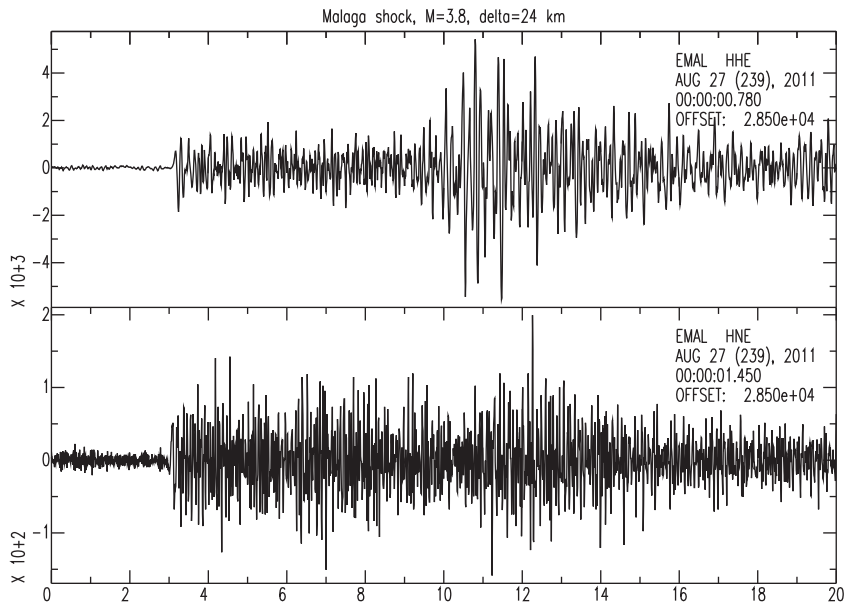


**Figure 2.11.** Velocity (HHE) and acceleration (HNE) seismograms for the east–west component for the EMAL (Malaga, Spain, Western Mediterranean Network) station from a local earthquake of  $M_W = 3.8$  at 24 km epicentral distance.

engineering. Their response is proportional to the acceleration, and they can record large accelerations up to several times the acceleration of gravity. Since the beginning of digital seismology in the late 1970s, accelerographs have also become digital; with these instruments it is possible to record the ground motion acceleration of large earthquakes at very short distances without saturation. By integration we can find the corresponding ground velocity and displacement. An important difference between velocity and acceleration records is in the frequency content: acceleration records have a broad range of high frequencies in comparison with ground velocity records (Fig. 2.11). Accelerographs still have two problems: they usually do not record continuously but are triggered with the arrival of strong motion, and they not always keep a well-calibrated time record synchronized to the Universal Time Coordinated (UTC) time by Global Position System (GPS) signals. Often seismologists have to determine the time corresponding to the records using cross-correlation or other error-prone techniques. Modern accelerometers, such as those that equip the K-net and KiK-net in Japan, use the same recording equipment as modern seismometers, providing excellent near-field records of large and intermediate-size events with accurate timing. Integrating accelerograms to obtain velocity and displacement is unfortunately not easy, particularly at low frequencies, because of problems with the rotation of the vertical axis of the instruments and a number of non-linear effects. Although there are many ways to obtain the correct ground motion from these instruments, this is still a difficult problem (see Boore *et al.*, 2002, for a detailed discussion).

Accelerometers have a very simple response, owing to the fact that the output is linearly proportional to the acceleration and there is no phase shift. Usually BB velocity records have a linear bandwidth from 0.01 to 50 Hz and a gain of 100–5000 V/(m s<sup>-1</sup>) and

accelerometers have a linear bandwidth from 0 to 100 Hz and a gain from 1 to 100 V/g, i.e.  $V/(10 \text{ m s}^{-2})$  (Havskov and Ottemöller, 2010). Actually, the low-frequency passband of accelerograms is limited by the total time-length of the records, usually a few hundred seconds. At present few accelerograms are recorded continuously. In general accelerometers have more instrument noise than other types of ground recording instrument (Fig. 2.10), but their large dynamic range is a clear advantage in recording moderate to large earthquakes in the near field without saturation.

In some cases accelerometers give records in ASCII format (normally called file.raw) and  $\text{cm/s}^2$  units; in this case there is no need remove the instrumental response. In other cases, such as the example of Fig. 2.11, both velocity and acceleration records are given in SEED format, which we have converted to SAC with amplitude units in counts. In this case we need to know the instrumental response to compute the ground velocity and acceleration. The instrumental response for acceleration has a similar form to that shown in Table 2.2.

## 2.6. Continuous GPS observations

---

As we have seen, seismographs and accelerographs provide respectively the velocity and acceleration of ground motion. Recently GPS has provided a different source of information about the ground motion produced by earthquakes. Being a global navigation satellite system, GPS estimates with high accuracy the position of a point with respect to a terrestrial reference frame. Determinations of the position of this point at different times provide a measurement of its displacement with respect to the reference frame. Thus displacements of ground motion can be obtained from successive positioning of the recording site. Two different methodologies are commonly used: *precise point positioning* and *differential positioning*. The data processing is quite complex and involves the use of methods such as the *modified sidereal filter* or the *regional filter* (Larson, 2009). The processing of GPS data is carried out by geodeticists and is not the particular concern of this textbook; therefore, we will not explain here the different methods for achieving this processing and their problems. Rather, we will assume that we have the GPS signal processed to include the necessary corrections, such as the baseline correction, ionospheric delays etc.

For geodynamic purposes, GPS data at time intervals of months or years have been used to determine the velocity of plate motion (Prawirodirjo and Bock, 2004) and the deformation that occurs during a seismic cycle. Since the late 1990s, GPS data, digitized at shorter time intervals, have been used for seismological purposes, measuring *co-seismic* displacements and giving what can be considered as a new type of seismogram (Larson, 2009). In the last few years the use of GPS in real-time seismometers has increased, owing to the development of the receiver's recording capacity to store and transfer data with high sampling rates. The use of high-rate GPS sampling (1 Hz, instead of 1 per 30 s) has opened the way to the use of GPS instruments to measure dynamic ground deformation during large earthquakes. The common sampling rate of GPS data used in seismology is at

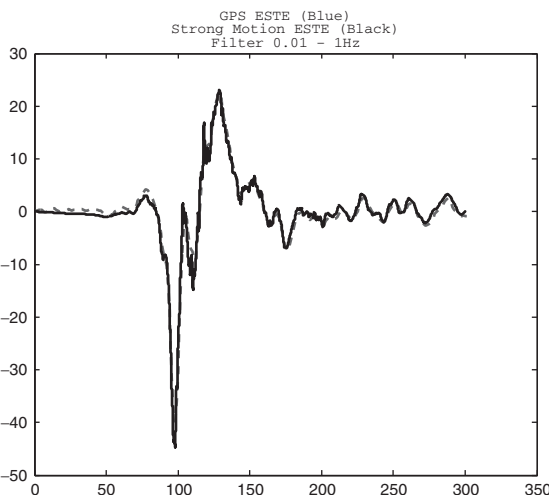


**Figure 2.12.** Horizontal component of the ground displacement from GPS observations (solid line) and, integrated, from an accelerograph (broken line) at the El Roble (Chile) station about 400 km epicentral distance from the Maule earthquake of 27 February 2010,  $M_W = 8.8$ , in south central Chile.

present, as mentioned above, 1 Hz but rates of 10 Hz, 50 Hz and higher are becoming available. These GPS data provide a direct measure of the ground displacement; this is an advantage over the velocity response seismographs or accelerographs, where displacements have to be found through integration with the possible introduction of errors. Since present GPS error margins in position are of the order of 1 cm, for seismological purposes only large displacements, of the order of a few cm, can be recorded. The use of GPS as a seismometer is limited, thus, to nearby large earthquakes ( $M_W > 7$ ) or to shallow-focus events of lower magnitudes and to some specific types of mechanism; GPS recordings correspond, generally, to surface waves. For example, the 2002 Denali shock ( $M_W = 7.9$ ) generated ground displacements that were well recorded at 3000 km distance in GPS stations, but other smaller earthquakes such as the 2003 San Simeon ( $M_W = 6$ ) and the 2009 L'Aquila ( $M_W = 6.3$ ) produced ground displacements observed at very-near-field GPS stations (Larson, 2009; Bilich *et al.*; 2008; Avallone *et al.*, 2011). When GPS and strong motion instruments are present at the same site it is possible to compare the ground displacement measured directly using GPS and the displacement computed by the integration of strong motion acceleration records. Figure 2.12 shows an example of the agreement between the ground displacement recorded by GPS and that integrated from a strong motion record, reported in the supplementary material of Vigny *et al.*, (2011). The data is from the multi-component station El Roble (ROBL) located at  $32.927^\circ$  S,  $71.015^\circ$  W, about 400 km north of the epicentre of the Maule earthquake of 27 February 2010 in south central Chile ( $36.29^\circ$  S,  $73.24^\circ$  W). Both components have been filtered in the frequency band from 0.01 to 1 Hz.

### 3.1. Fundamental equations of motion for an elastic medium

The study of the source mechanism of earthquakes has its foundations in the mathematical formulation of the theory of the generation and propagation of elastic waves. The starting point is the development of mechanical models for the processes involved in the generation of earthquakes and for the propagating medium, so that the appropriate equations can be established. These equations relate the elastic displacements produced by seismic waves recorded at observation points (seismograms) to the parameters which define the processes at the source. As a first approximation, the Earth can be considered as a continuous deformable medium. A continuous medium is an idealization of a real material in which the distance between two contiguous points can be made infinitesimally small. In this approximation the granular nature of the real materials of the Earth and their molecular and atomic discrete structures are not considered. In a continuous medium the term “particle” is used to mean a geometrical point without dimensions. The properties of the medium such as its density or elastic coefficients are considered to be piecewise-continuous functions of space.

The *displacement* at a point of a deformable medium is given by the vector  $\mathbf{u}(\mathbf{x}, t)$ . The deformation or strain within a deformable medium, if only infinitesimal deformations are considered, can be expressed by the *Cauchy tensor*  $e_{ij}$ , which, if  $\mathbf{u}$  varies continuously and slowly with position, is given in component form by

$$e_{ij} = \frac{1}{2} \left( \frac{\partial u_i}{\partial x_j} + \frac{\partial u_j}{\partial x_i} \right) = \frac{1}{2} (u_{i,j} + u_{j,i}) \quad (3.1)$$

Thus, a comma between the sub-indices indicates a partial derivative with respect to a space coordinate.

The motion at each point inside a volume  $V$  of a continuous body surrounded by an external surface  $S$  is determined by the forces acting in its interior and the stresses acting on its surface (Fig. 3.1). Newton’s second law, according to *Euler’s formulation*, is given in *sub-index notation* by

$$\int_S T_i(x_s, t) dS + \int_V F_i(x_s, t) dV = \frac{d}{dt} \int_V \rho v_i(x_s, t) dv \quad (3.2)$$

where  $T_i(x_s, t)$  are the stresses acting on each surface element  $dS$ ,  $F_i(x_s, t)$  are the forces per unit volume acting on each volume element  $dV$ ,  $\rho(x_s)$  is the density and  $v_i(x_s, t)$  is the

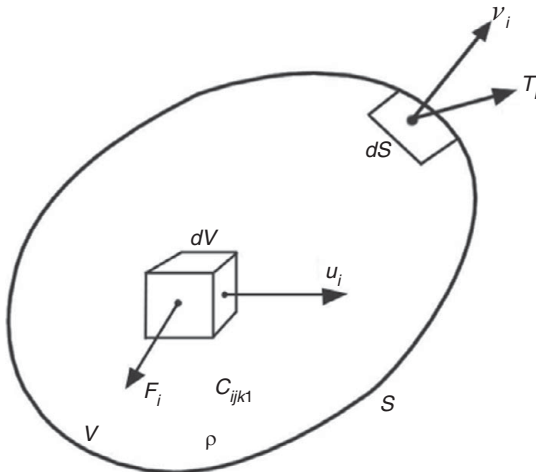


**Figure 3.1.** Elastic displacement vector  $u_i$ , force vector  $F_i$  per unit volume  $dV$  (the body force) and stress vector  $T_i$  on unit surface  $dS$  with normal vector  $v_i$ , for an elastic medium of volume  $V$ , density  $\rho$  and elastic coefficients  $C_{ijkl}$  surrounded by a surface  $S$ .

particle velocity. For infinitesimal deformations and very small velocities and changes in velocity, second-order terms can be neglected, the total derivative with respect to time can be approximated by the partial derivative and the Lagrangian formulation used. Replacing the vector  $T_i$  by Cauchy's stress tensor  $\tau_{ij}$  ( $T_i = \tau_{ij}v_j$ , where  $v_j$  is the normal to the surface element  $dS$  and repeated indices are summed according to the Einstein convention), and considering the density  $\rho$  to be constant with time, equation (3.2) can be written as

$$\int_S \tau_{ij}v_j dS + \int_V F_i dV = \int_V \rho \frac{\partial^2 u_i}{\partial t^2} dV \quad (3.3)$$

For an elastic medium, we express the stress in terms of the strain using Hooke's law,  $\tau_{ij} = C_{ijkl} e_{kl} = C_{ijkl} u_{kl}$ , where  $C_{ijkl}$  is the tensor of the *elastic coefficients*; this tensor has 81 components but, owing to symmetry considerations, only 21 are independent. We thus obtain the equation of motion in terms of the displacements:

$$\int_S C_{ijkl} u_{kl} v_j dS + \int_V F_i dV = \int_V \rho \frac{\partial^2 u_i}{\partial t^2} dV \quad (3.4)$$

Replacing the surface integral in (3.3) by a volume integral by means of Gauss's theorem, we obtain

$$\int_V \frac{\partial \tau_{ij}}{\partial x_j} dV + \int_V F_i dV = \int_V \rho \frac{\partial^2 u_i}{\partial t^2} dV$$

For an infinite medium we can then write the differential equation

$$\frac{\partial \tau_{ij}}{\partial x_j} + F_i = \rho \frac{\partial^2 u_i}{\partial t^2} \quad (3.5)$$

and, in terms of the displacements,

$$\frac{\partial}{\partial x_j} (C_{ijkl} u_k, l) + F_i = \rho \frac{\partial^2 u_i}{\partial t^2} \quad (3.6)$$

For an isotropic elastic medium the 21 independent components of  $C_{ijkl}$  are reduced to two,  $\lambda$  and  $\mu$ , called *Lamé's coefficients*;  $\mu$  is also called the *shear or rigidity modulus* (Udías, 1999, pp. 14–15). For most materials in the Earth's interior we can assume the so-called *Poisson condition*,  $\lambda = \mu$ . Putting  $C_{ijkl}$  in terms of  $\lambda$  and  $\mu$ , equation (3.6) becomes

$$\frac{\partial}{\partial x_j} [\lambda \delta_{ij} u_k, k + \mu (u_{i,j} + u_{j,i})] + F_i = \rho \frac{\partial^2 u_i}{\partial t^2} \quad (3.7)$$

For an isotropic homogeneous material, that is, for  $\lambda$  and  $\mu$  constant, we can write the differential equation of motion using index notation as

$$(\lambda + \mu) u_{k,k} + \mu u_{i,jj} + F_i = \rho \ddot{u}_i \quad (3.8)$$

or using vector rotation as

$$(\lambda + \mu) \nabla(\nabla \cdot \mathbf{u}) + \mu \nabla^2 \mathbf{u} + \mathbf{F} = \rho \ddot{\mathbf{u}} \quad (3.9)$$

Dividing equation (3.9) by  $\rho$  and substituting the values of the squared P wave velocity,  $\alpha^2 = (\lambda + 2\mu)/\rho$ , and the squared S wave velocity,  $\beta^2 = \mu/\rho$ , we obtain

$$\alpha^2 \nabla(\nabla \cdot \mathbf{u}) - \beta^2 \nabla \times (\nabla \times \mathbf{u}) + \frac{\mathbf{F}}{\rho} = \ddot{\mathbf{u}} \quad (3.10)$$

where we have used the relation between the Laplacian and the curl of the curl,  $\nabla \times \nabla \times \mathbf{a} = \nabla(\nabla \cdot \mathbf{a}) - \nabla^2 \mathbf{a}$ . In equation (3.10) we can see that the velocity  $\alpha$  is related to the divergence  $\nabla \cdot \mathbf{u}$ , that is, to changes in volume or radial displacements (P waves), and that velocity  $\beta$  is related to the  $\nabla \times \mathbf{u}$ , that is, to changes in rotation or transverse displacements (S waves).

According to *Helmholtz' theorem* the vector displacements  $\mathbf{u}$  and the forces  $\mathbf{F}$  can be represented by scalar and vector potentials (the vector potentials must have zero divergence), in the form

$$\mathbf{u} = \nabla \phi + \nabla \times \boldsymbol{\psi} \quad (3.11)$$

$$\mathbf{F} = \nabla \Phi + \nabla \times \boldsymbol{\Psi} \quad (3.12)$$

Equation (3.10) can now be separated into two equations, a scalar equation and a vector equation:

$$\alpha^2 \nabla^2 \phi + \frac{\Phi}{\rho} = \ddot{\phi} \quad (3.13)$$

$$\beta^2 \nabla^2 \boldsymbol{\psi} + \frac{\boldsymbol{\Psi}}{\rho} = \ddot{\boldsymbol{\psi}} \quad (3.14)$$

Because of the condition of null divergence for the vector potentials  $\boldsymbol{\psi}$  and  $\boldsymbol{\Psi}$ , equations (3.13) and (3.14) represent only three independent equations. This separation of the

equation of motion is very important because it greatly facilitates its solution. One must note that although the forces  $\mathbf{F}$  may be defined only inside a small volume, the potentials that represent them ( $\Phi$  and  $\Psi$ ) are defined in the whole volume considered.

### 3.2 Green's and Somigliana's tensors

In the study of earthquake mechanisms the force of gravity and the effect of the rotation of the Earth can be neglected (provided that very low frequencies are not considered) and the processes at the source can be described by systems of forces. In general, these forces  $\mathbf{F}(x, t)$  will be functions of space coordinates and time and will be defined inside a certain source volume or on a certain source surface. The most elementary system of forces is that formed by an unit impulsive force in space and time with an arbitrary direction. We can represent this type of force by means of *Dirac's delta function*:

$$F_i(x_k, t) = \delta(x_k - \xi_k) \delta(t - \tau) e_i \quad (3.15)$$

Thus, the equation describes a unit force in the direction of the unit vector  $e$  applied at the point  $\xi$  and time  $\tau$  that is zero outside this point and time (Fig. 3.2). If we substitute (3.15) into the equation of motion (3.3), we can obtain the solution for the corresponding elastic displacement  $u_i(x_k, t)$  at all points of the volume  $V$  surrounded by surface  $S$ . Since for every orientation of the force given by the vector  $e$  there is a different solution, we write the general solution for any orientation in the form of a second-order tensor  $G_{ni}(\xi_k, \tau, x_k, t)$  (see Fig. 3.2); the sub-index  $n$  indicates the direction of the force,  $i$  indicates the component of the displacement tensor for each force direction  $n$ ,  $x_k$  and  $t$  represent the point and time where the displacement is being evaluated;  $\xi_k$  and  $\tau$  represents the general point of space and time where the force is applied.

Replacing the stress in term of the derivative of the displacements, we can write equation (3.4) for an impulsive force at  $(\xi, \tau)$  in the form

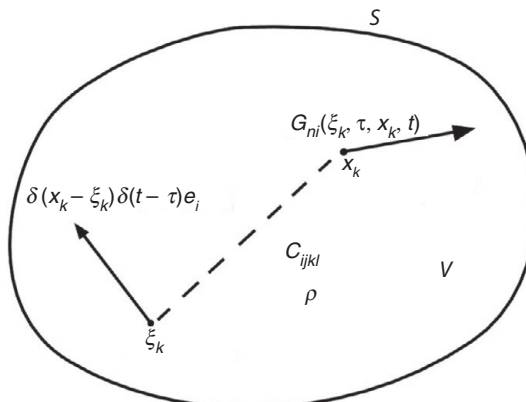


**Figure 3.2.** The displacement  $G_{ni}$  (Green's function) at a point  $x_k$  produced by a unit impulsive force with direction  $e_i$  at a point  $\xi_k$ .

$$\int_V \rho \ddot{G}_{ni} dV - \int_S C_{ijkl} G_{ni}, l v_j dS = \int_V \delta(x_s - \xi_s) \delta(t - \tau) \delta_{ni} dV \quad (3.16)$$

where  $\delta_{ij}$  is the Kronecker delta (it equals 1 for  $i = j$  and 0 for  $i \neq j$ ). For an infinite homogeneous medium, according to equation (3.6) we obtain

$$\rho \ddot{G}_{ni} - C_{ijkl} G_{nk}, l v_j = \delta(x_s - \xi_s) \delta(t - \tau) \delta_{ni} \quad (3.17)$$

The solutions of equations (3.16) and (3.17) represent the elastic displacements produced by an unit impulsive force in space and time. For this reason the tensor  $G_{ni}(\xi_k, \tau, x_k, t)$  which satisfies this equation is called the *Green's function* or *Green's tensor* of elastodynamics, defined as the response of the medium to an impulsive excitation (Morse and Feshbach, 1953, pp. 834–43). The form of this function depends on the characteristics of the medium, its elastic coefficients and its density. In the finite medium case) (3.16), it depends also on the shape and dimensions of the volume  $V$  and the boundary conditions on its surface  $S$ . For each medium there is a different Green's function, which defines how the medium reacts mechanically to an impulsive excitation and is therefore a proper characteristic of each medium.

A similar tensor can be derived for the displacements produced by a unit force acting at a point  $\xi_k$  in the static case, that is, when there is no time dependence. According to (3.16), putting  $F_i = \delta(x_s - \xi_s) \delta_{ni}$  the equation of motion becomes

$$-\int_S C_{ijkl} S_{ni}, l v_j dS = \int_V \delta(x_s - \xi_s) \delta_{ni} dV \quad (3.18)$$

and for an infinite homogeneous medium, according to (3.6)

$$-C_{ijkl} S_{nk}, l v_j = \delta(x_s - \xi_s) \delta_{ni} \quad (3.19)$$

The tensor  $S_{ni}(\xi_k, \tau, x_k, t)$  is called *Somigliana's function or tensor*. Green's and Somigliana's tensors are very important tools for the mathematical representation of the mechanism of earthquakes. These tensors represent the elastic displacements at  $(x, t)$  produced by an impulsive unit force acting at a arbitrary point and time  $(\xi, \tau)$  for the dynamic and static cases respectively.

### 3.3 Representation theorem

Since in seismology the observations are ground displacements, it is convenient to find an equation that gives us explicitly the displacements in terms of the source parameters. This can be obtained by means of the *representation theorem*, which is thus an important mathematical tool in the study of earthquake mechanisms (Aki and Richards, 1980, pp. 28–30). We begin with the consideration of two independent systems of forces  $f$  and  $g$ , acting in a medium of volume  $V$  surrounded by a surface  $S$ , where the stresses acting are  $T^u$  and  $T^w$  and the corresponding displacements are respectively  $u$  and  $w$  (Fig. 3.3). Multiplying the equation of motion (3.3) for each system by the displacements of the

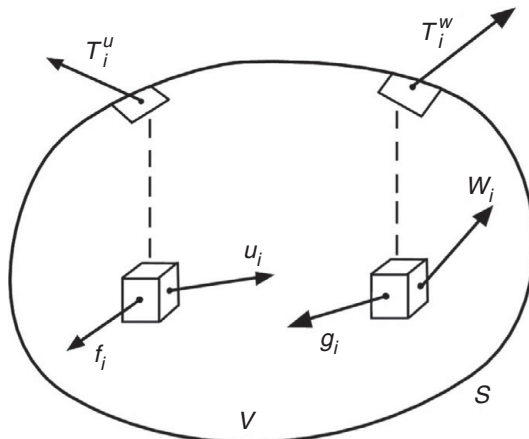


**Figure 3.3.** Elastic displacements  $u_i$  and  $w_i$  corresponding to body forces  $f_i$  and  $g_i$ , respectively, acting inside the volume  $V$  and stresses  $T_i^u$  and  $T_i^w$  acting on the surface  $S$ .

other, that is, the equation for  $\mathbf{u}$  by  $\mathbf{w}$  and that of  $\mathbf{w}$  by  $\mathbf{u}$ , subtracting the equations for the two systems and integrating in the time domain we obtain

$$\int_{-\infty}^{\infty} dt \int_V \rho(u_i \ddot{w}_i - w_i \ddot{u}_i) dV = \int_{-\infty}^{\infty} dt \int_V (u_i g_i - w_i f_i) dV + \int_{-\infty}^{\infty} dt \int_S (u_i T_i^w - w_i T_i^u) dS \quad (3.20)$$

This equation, known as the *Green–Volterra* generalization of *Betti's reciprocity theorem*, relates the displacements and accelerations produced by two systems of forces and stresses on the same volume, integrated over space and time. A particular case results if the displacements and velocities are null for all times previous to a given time, that is, if the forces and stresses begin to act at a given time and the displacements and velocities are zero before that time. This condition, which is satisfied by earthquakes, implies the *causality principle*, namely, that the medium is at rest until a given time when motion begins. In this case the first integral is zero and we have (Udías, 1999, pp. 25–28; Aki and Richards, 1980, pp. 28–30),

$$\int_{-\infty}^{\infty} dt \int_V (u_i g_i - w_i f_i) dV + \int_{-\infty}^{\infty} dt \int_S (u_i T_i^w - w_i T_i^u) dS = 0 \quad (3.21)$$

This is a very important result, since it allows the representation of the displacements due to a system of forces by those produced by a different system, provided that causality conditions are satisfied. With this relation we can represent the displacements due to a complicated system of forces in terms of those produced by a simpler one.

We can now select as one such system an impulsive force in time and space and its corresponding displacements given by Green's functions. We substitute for  $\mathbf{g}$  in (3.21) using an expression like (3.15) and for  $\mathbf{w}$  by  $\mathbf{G}$ , and express  $\mathbf{T}^w$  in terms of the derivatives of  $\mathbf{G}$ ,  $v_j$ , the normal to  $dS$ , and the elastic constants  $C_{ijkl}$  (replacing  $\mathbf{T}^u$  by  $\mathbf{T}$ ). Then, equation (3.21) becomes

$$\int_{-\infty}^{\infty} dt \int_V [u_i \delta(x_s - \xi_s) \delta(t - \tau) \delta_{in} - G_{ni} f_i] dV = \int_{-\infty}^{\infty} dt \int_S (G_{ni} T_i - u_i C_{ijkl} G_{nk, l} v_j) dS \quad (3.22)$$

The first term in the left-hand integral, according to the definition of the delta function, is equal to  $\mathbf{u}(\xi, \tau)$  and, by the symmetry of equation (3.22) with respect to  $\xi, \tau$  and  $\mathbf{x}, t$ , we can now write

$$\begin{aligned} u_n(x_s, t) &= \int_{-\infty}^{\infty} d\tau \int_V f_i(\xi_k, \tau) G_{ni}(\xi_k, \tau; x_s, t) dV(\xi_k) \\ &\quad + \int_{-\infty}^{\infty} d\tau \int_S [G_{ni}(\xi_k, \tau; x_s, t) T_i(\xi_k, \tau) \\ &\quad - C_{ijkl} u_i(\xi_k, \tau) G_{nk, l}(\xi_k, \tau; x_s, t) v_j(\xi_k)] dS(\xi_k) \end{aligned} \quad (3.23)$$

where  $\xi_k$  and  $\tau$  are the variables of integration. This expression is called the representation theorem. With this equation we can obtain the elastic displacements  $\mathbf{u}(\mathbf{x}, t)$  at every point inside a volume  $V$ , once we specify the forces  $\mathbf{f}$  acting at elements of volume  $dV$ , the stresses  $\mathbf{T}(\xi, \tau)$  acting on the surface  $S$  of the volume  $V$  and the displacements  $\mathbf{u}(\xi, \tau)$  at the same surface (see Fig. 3.4). The displacements  $\mathbf{u}(\mathbf{x}, t)$  are defined at every point of the medium; the forces  $\mathbf{f}(\xi, \tau)$  are defined inside  $V$  at  $dV(\xi)$  and the stresses  $\mathbf{T}(\xi, \tau)$ , displacement  $\mathbf{u}(\xi, \tau)$  and normal  $\mathbf{v}(\xi, \tau)$  are defined on the surface  $S$  at  $dS(\xi)$ . The Green's function  $G(\xi, \tau; \mathbf{x}, t)$  is a function of both  $\xi, \tau$  and  $\mathbf{x}, t$ .

Equation (3.23) allows us to determine the elastic displacements inside a medium produced by a system of forces acting per unit volume and a system of stresses and displacements specified on its surface if we know the Green's function of the medium. This means that we need only to solve the equation of motion once to obtain the Green's function. If the Green's function for a particular medium of volume  $V$ , with specified characteristics (its density and elastic coefficients) and boundary conditions on  $S$ , is known

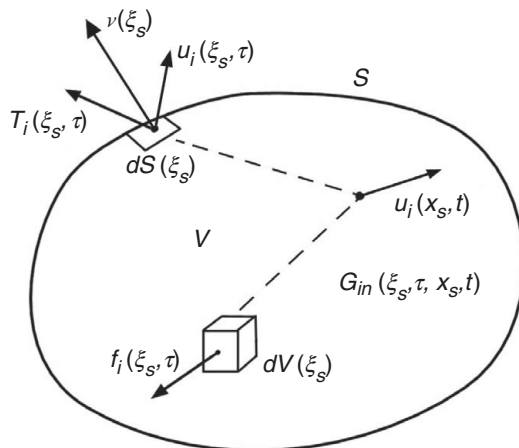


**Figure 3.4.** Elastic displacement  $u_i$  at point  $x_s$  and time  $t$  corresponding to a body force  $f_i$  and stress  $T_i$  acting at  $\xi_s$  and  $\tau$ , in a medium with Green's tensor  $G_{in}$ .

then we can determine, by means of equation (3.23), the elastic displacements due to any system of forces in  $V$  and stresses and displacements on  $S$ . In this expression the Green's function acts as a *propagator* since it propagates the effect of the forces, stresses or displacements from points and times defined by coordinates  $\xi$  and time  $\tau$ , to find the elastic displacements at  $x$  and  $t$ . We will see below how this equation is used in the representation of the earthquake mechanisms.

### 3.4. Somigliana's tensor for infinite homogeneous isotropic medium

The simplest case for which we can solve the equation of motion is that of an infinite homogeneous perfectly elastic isotropic medium. The equation of motion for the static case with an impulsive force is given by, according to (3.10),

$$\alpha^2 \nabla(\nabla \cdot \mathbf{u}) - \beta^2 \nabla \times \nabla \times \mathbf{u} = -\frac{1}{\rho} \delta(x) \mathbf{e} \quad (3.24)$$

where  $\delta(x)$  is the Dirac delta function for a force acting at the origin of coordinates in the direction of the unit vector  $\mathbf{e}$ . According to (3.11) and (3.12), we can express the displacements and forces in terms of the potentials,

$$\mathbf{u} = \nabla \phi + \nabla \times \psi \quad (3.25)$$

$$\mathbf{e} \delta(x) = \nabla \Phi + \nabla \times \Psi \quad (3.26)$$

By the substitution of (3.25) and (3.26) into (3.24) we obtain two equations, cf. (3.13) and (3.14):

$$\nabla^2 \phi = -\frac{\Phi}{\alpha^2 \rho} \quad (3.27)$$

$$\nabla^2 \psi = -\frac{\Psi}{\beta^2 \rho} \quad (3.28)$$

Let us consider first the force potentials  $\Phi$  and  $\Psi$ . We introduce a new vector potential function  $\mathbf{W}$  such that  $\Phi = -\nabla \cdot \mathbf{W}$  and  $\Psi = \nabla \times \mathbf{W}$ . Substituting into (3.26) and using the relation between the curl of the curl of a vector and the Laplacian, we obtain

$$\nabla^2 \mathbf{W} = -\delta(r) \mathbf{e} \quad (3.29)$$

where  $r$  is the distance from the point where the force is applied, in this case the origin ( $r = |x_i|$ ). Since one definition of the delta function is  $\delta(r) = -\frac{1}{4\pi} \nabla^2 \left( \frac{1}{r} \right)$  (Gel'fand and Shilov, 1964), we obtain

$$\mathbf{W} = \frac{1}{4\pi r} \mathbf{e} \quad (3.30)$$

We consider now the particular case when the force acts in the  $x_1$  direction, that is,  $\mathbf{e} = (1, 0, 0)$ . In this case, if  $\xi_i$  is the position vector of an arbitrary point then its distance to the origin where the force is acting is  $r = |\xi_i|$  and the potentials  $\Phi$  and  $\Psi$  are given by

$$\Phi(\xi_i) = -\nabla \cdot \mathbf{W} = -\frac{1}{4\pi} \frac{\partial}{\partial \xi_1} \left( \frac{1}{|\xi_i|} \right) \quad (3.31)$$

$$\Psi(\xi_i) = \nabla \times \mathbf{W} = \frac{1}{4\pi} \left( 0, \frac{\partial}{\partial \xi_3} \left( \frac{1}{|\xi_i|} \right), -\frac{\partial}{\partial \xi_2} \left( \frac{1}{|\xi_i|} \right) \right) \quad (3.32)$$

Let us consider now the displacement potentials  $\phi$  and  $\Psi$ . Equations (3.27) and (3.28) have the form of Poisson's equation. Therefore, the solution for the function  $\phi$  defined in the volume  $V$  can be given by (Morse and Feshbach, 1953, pp. 38–9),

$$\phi(x_i) = \frac{1}{4\pi\rho\alpha^2} \int_V \frac{\Phi(\xi_i)}{|x_i - \xi_i|} dV(\xi_i) \quad (3.33)$$

with a similar expression for the vector potential  $\Psi$ ; here  $x_i$  is the point where we evaluate  $\phi$ , and  $\xi_i$ , the variable of integration, represents the coordinates of the volume element  $dV$ . We should notice that, although the force is acting at a point (the origin), the potentials  $\Phi$  and  $\Psi$  which represent it are defined for all points of the volume considered, in our case for infinite space. By substitution of (3.31) into (3.33) we obtain for the potential  $\phi(x_i)$

$$\phi(x_i) = \frac{-1}{16\pi^2\alpha^2\rho} \int_V \frac{1}{|x_i - \xi_i|} \frac{\partial}{\partial \xi_1} \left( \frac{1}{|\xi_i|} \right) dV \quad (3.34)$$

For the case of an infinite medium we take as the volume  $V$  a sphere with center at  $x_i$  and radius  $r' = |x_i - \xi_i|$ , which we let allow to become infinite (Fig. 3.5). The volume integral is separated into a surface integral over the surface  $S$  of the sphere and an integral over  $r'$  from zero to infinity. The second integral can be changed into an integral over time, since  $r' = \alpha t$ , where  $\alpha$  is the velocity of P waves, so that  $dr' = \alpha dt$ . Then the integral in (3.34) becomes

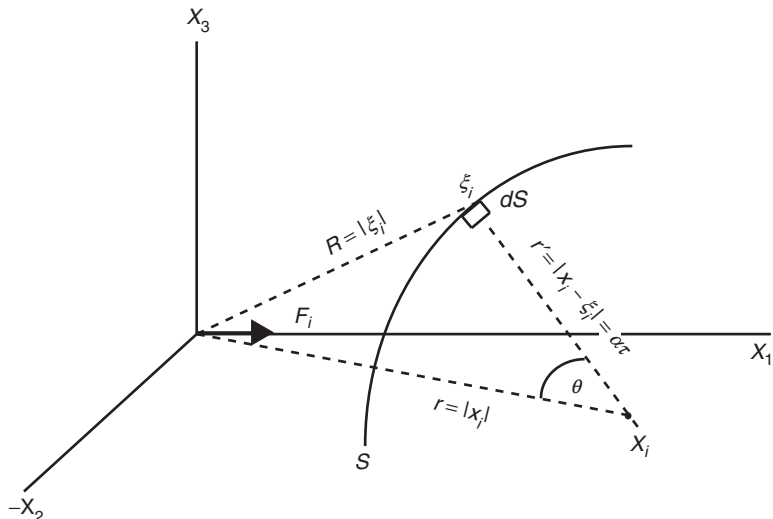


**Figure 3.5.** Spherical surface with center at  $x_i$  and radius  $\alpha t$  for the evaluation of integral (3.34) ( $\xi_i$  is the integration variable).

$$\int_0^\infty \frac{1}{\tau} \int_S \frac{\partial}{\partial \xi} \left( \frac{1}{|\xi_i|} \right) dS d\tau = \int_0^\infty \frac{1}{\tau} h d\tau \quad (3.35)$$

where  $h$ , after changing the order of integration and derivation and putting  $R = |\xi_i|$  (the distance from the origin to the point  $\xi$ ), is given by

$$h = \frac{\partial}{\partial \xi_1} \int_S \frac{dS}{R} \quad (3.36)$$

In this integral, since  $S$  is a sphere of radius  $r'$  we put  $dS = 2\pi r'^2 \sin \theta d\theta$  and writing, as before,  $r' = \alpha\tau$  we obtain

$$\int_S \frac{dS}{R} = 2\pi \alpha^2 \tau^2 \int_0^\pi \frac{\sin \theta d\theta}{R} \quad (3.37)$$

Using the cosine rule for the triangle with vertices at  $x_i$ ,  $dS$  and 0 (Fig. 3.5), we have

$$R^2 = r^2 + \alpha^2 \tau^2 - 2r\alpha\tau \cos \theta$$

where  $r = |x_i|$  is the distance from the point where we evaluate  $\phi$  to the origin of coordinates, where the force is acting, and  $r' = |x_i - \xi_i| = \alpha\tau$ , the distance from  $x$  to  $dS$  (Fig. 3.5). Taking the derivative of  $R$  (for a given  $x_i$ ,  $r$  is constant and on the surface of the sphere  $r'$  is also constant), we obtain

$$\sin \theta d\theta = \frac{R dR}{r\alpha\tau}$$

By substitution into (3.37) we obtain

$$\frac{2\pi\alpha\tau}{r} \int_0^\pi dR = \frac{2\pi\alpha\tau}{r} \int_{r-\alpha\tau}^{r+\alpha\tau} dR = \frac{2\pi\alpha\tau}{r} [r + \alpha\tau - (r - \alpha\tau)] \quad (3.38)$$

where we have used that, for  $\theta = 0$ ,  $R = r - \alpha\tau$  and, for  $\theta = \pi$ ,  $R = r + \alpha\tau$  (Fig. 3.5). Now, the value inside the square brackets in (3.38) depends on whether the origin ( $x_i = 0$ ) is either (a) inside or (b) outside  $S$ . In case (a),  $r < \alpha\tau$ , the term inside the parentheses is  $\alpha\tau - r$  and the contents of the square brackets equal  $2r$ ; in case (b),  $r > \alpha\tau$ , the term inside the parentheses is  $r - \alpha\tau$  and the contents of the square brackets equal  $2\alpha\tau$ . Then we have for (3.38)

$$\begin{aligned} \text{in case (a),} & \quad 4\pi\alpha\tau, \quad r < \alpha\tau \\ \text{in case (b),} & \quad \frac{4\pi\alpha^2\tau^2}{r}, \quad r > \alpha\tau \end{aligned}$$

When we substitute these values into equation (3.36) we obtain for  $h$

$$\begin{aligned} \text{in case (a),} & \quad h = 0 \\ \text{in case (b),} & \quad h = 4\pi\alpha^2\tau^2 \frac{\partial}{\partial \xi_1} \left( \frac{1}{r} \right) \end{aligned}$$

To take the derivative of  $1/r$  we put the force at an arbitrary point  $\eta_i$ ; then, instead of  $|\xi_i|$  we have  $|\xi_i - \eta_i|$  and instead of  $|x_i|$  we have  $|x_i - \eta_i|$ . Thus we obtain  $\partial/\partial\xi_i = -\partial/\partial\eta_i = \partial/\partial x_i$ . By substitution into equation (3.34), the potential  $\phi$  at point  $x_i$  is given by

$$\phi(x_i) = \frac{-1}{4\pi\rho} \frac{\partial}{\partial x_1} \left( \frac{1}{r} \right) \int_0^{r/a} \tau d\tau \quad (3.39)$$

where we have taken into consideration that, for  $\tau > r/a$ ,  $h = 0$ . After integrating we obtain

$$\phi(x_i) = \frac{-1}{8\pi\rho} \frac{r^2}{a^2} \frac{\partial}{\partial x_1} \left( \frac{1}{r} \right) = \frac{\gamma_1}{8\pi\rho a^2} \quad (3.40)$$

where we have substituted  $\gamma_1$ , the direction cosine of  $x_1$ , according to the relations

$$\begin{aligned} \frac{\partial r}{\partial x_i} &= \gamma_i \\ \frac{\partial}{\partial x_i} \left( \frac{1}{r} \right) &= -\frac{\gamma_i}{r^2} \\ \frac{\partial \gamma_i}{\partial x_j} &= -\frac{1}{r} (\gamma_i \gamma_j - \delta_{ij}) \end{aligned} \quad (3.41)$$

For the potential  $\Psi(x_i)$ , we proceed in a similar manner. We can write, as in (3.33),

$$\Psi(x_i) = \frac{1}{4\pi\rho\beta^2} \int_V \frac{\Psi(\xi_i)}{|x_i - \xi_i|} dV(\xi_i) \quad (3.42)$$

Substituting the value of  $\Psi$  from (3.32) and, following the same procedure as we used for  $\phi$ , we finally obtain

$$\Psi = \frac{r^2}{8\pi\rho\beta^2} \left[ 0, \frac{\partial}{\partial x_3} \left( \frac{1}{r} \right), -\frac{\partial}{\partial x_2} \left( \frac{1}{r} \right) \right] = \frac{1}{8\pi\rho\beta^2} (0, -\gamma_3, \gamma_2) \quad (3.43)$$

To find the displacements  $u_i(x_j)$  we apply equation (3.25) and find, for the force acting in the direction of  $x_1$ , the expression

$$u_i^1(x_j) = \frac{1}{8\pi\rho r} \left[ \left( \frac{1}{\beta^2} - \frac{1}{a^2} \right) \gamma_1 \gamma_i + \left( \frac{1}{a^2} + \frac{1}{\beta^2} \right) \delta_{1i} \right] \quad (3.44)$$

We can extend this result to the general situation, when the force is acting in a general direction defined by the sub-index  $j$ . The result is the tensor  $S_{ij}$ , where

$$S_{ij}(x_k) = \frac{1}{8\pi\rho r} \left[ \left( \frac{1}{\beta^2} - \frac{1}{a^2} \right) \gamma_j \gamma_i + \left( \frac{1}{a^2} + \frac{1}{\beta^2} \right) \delta_{ji} \right] \quad (3.45)$$

Somigliana's tensor  $S_{ij}$  is the basis for solutions of problems in elastostatics. This tensor represents the static displacement field produced in an infinite homogeneous isotropic elastic medium by the application of an impulsive force acting at the origin of coordinates in an arbitrary direction. This cannot be considered as the limit for constant time of the

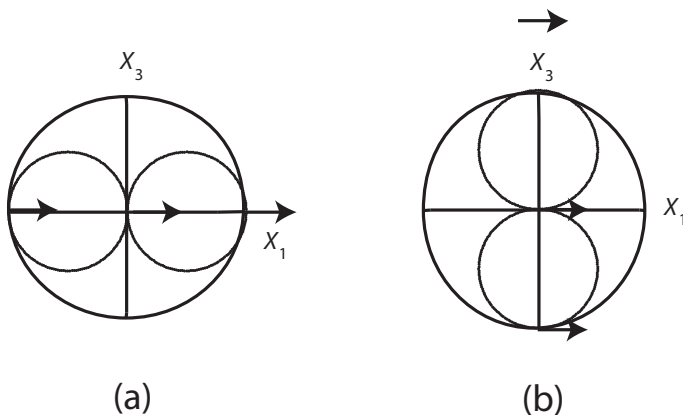


**Figure 3.6.** Normalized radiation pattern of Somigliana's tensor on the  $(x_1, x_3)$  plane for a force in the  $x_1$  direction: (a) radial displacement, (b) transverse displacements.

Green's function but as representing the direct solution of the equation of motion in the static case.

The solution (3.45) represents the distribution of static displacements around the focus; these decay with distance as  $1/r$ . The dependence on the azimuth is called the radiation pattern. If the force is in the  $x_1$  direction ( $e = 1, 0, 0$ ), the radiation pattern on the plane  $(x_1, x_3)$  at a unit distance, without the factor  $1/(8r\pi\rho)$ , can be easily found to be

$$\begin{aligned} S_{11} &= A \cos^2 \theta + B \\ S_{13} &= A \sin \theta \cos \theta \end{aligned}$$

where  $A = 1/\beta^2 - 1/\alpha^2$  and  $B = 1/\alpha^2 + 1/\beta^2$ . Separating the radial component  $S_{1r}$  and the transverse component  $S_{1\theta}$  we obtain

$$\begin{aligned} S_{1r} &= (A + B) \cos \theta \\ S_{1\theta} &= -B \sin \theta \end{aligned}$$

As expected, the static displacements for  $\theta = 0, \pi/2, \pi, 2\pi$  are in the same direction as the force (Fig. 3.6).

### 3.5. Green's tensor for infinite homogeneous isotropic medium

The solution in the dynamic case for the elastic displacements due to an impulsive source corresponds to the determination of the Green's tensor (Aki and Richards, 1980, pp. 70–7; Gershnik, 1996, pp. 514–26; Udiás, 1999, pp. 302–7). This is not, in general, an easy problem; it depends on the characteristics and the boundary conditions of the medium. As in the determination of Somigliana's tensor in the static case, the simplest solution of the dynamic case corresponds to an infinite homogeneous isotropic elastic medium. According to equations (3.10) and (3.17), the equation of motion for a force acting at the origin of coordinates and time  $t = 0$  is given by

$$\ddot{G}_{ij} - \alpha^2 \nabla(\nabla \cdot G_{ij}) + \beta^2 \nabla \times \nabla \times G_{ij} = \frac{1}{\rho} \delta(x_s) \delta(t) \delta_{ij} \quad (3.46)$$

As in the problem of Somigliana's tensor, we begin with the displacement  $\mathbf{u}(x, t)$  corresponding to a force in the direction of  $x_1$ , that is,  $\delta(t)\delta(x)(1,0,0)$ . In terms of the potentials, as in (3.27) and (3.28) we have now

$$\ddot{\phi} - \alpha^2 \nabla^2 \phi = \frac{\Phi}{\rho} \quad (3.47)$$

$$\ddot{\psi} - \beta^2 \nabla^2 \psi = \frac{\Psi}{\rho} \quad (3.48)$$

As for the Somigliana tensor, we introduce a vector potential  $\mathbf{W}$  such that that  $\Phi = -\nabla \cdot \mathbf{W}$  and  $\Psi = \nabla \times \mathbf{W}$ . The potential  $\mathbf{W}$  is the solution of Poisson's equation,  $\nabla^2 \mathbf{W} = -\delta(t) \delta(x)(1, 0, 0)$ , as in (3.29), and according to (3.30) is now given by

$$\mathbf{W}(\xi_i, t) = \frac{\delta(t)}{4\pi |\xi_i|} (1, 0, 0) \quad (3.49)$$

The potentials  $\Phi$  and  $\Psi$  can be derived from  $\mathbf{W}$  using equations (3.31) and (3.32), resulting in

$$\Phi(\xi_i, t) = \frac{\delta(t)}{4\pi} \frac{\partial}{\partial \xi_1} \left( \frac{1}{|\xi_i|} \right) \quad (3.50)$$

$$\Psi(\xi_i, t) = \frac{\delta(t)}{4\pi} \left[ 0, \frac{\partial}{\partial \xi_3} \left( \frac{1}{|\xi_i|} \right), - \frac{\partial}{\partial \xi_2} \left( \frac{1}{|\xi_i|} \right) \right] \quad (3.51)$$

Let us consider now the scalar potential  $\phi$ , which is the solution of (3.47). For the static case,  $\phi$  is independent of time and is the solution of Poisson's equation. It is given by (3.33). Introducing a time dependence, the solutions for  $\phi$  and  $\psi$  can now be written as

$$\phi(x_i, t) = \frac{1}{4\pi\alpha^2\rho} \int_V \frac{\Phi(t - r'/\alpha)}{r'} dV(\xi_i) \quad (3.52)$$

$$\psi_j(x_i, t) = \frac{1}{4\pi\beta^2\rho} \int_V \frac{\Psi_j(t - r'/\beta)}{r'} dV(\xi_i) \quad (3.53)$$

where  $r' = |x_i - \xi_i|$ ,  $x_i$  gives the coordinates of the point where we evaluate the displacements  $u_i$  and  $\xi_i$  those of the points where the potentials of the forces are defined, that is, all points in the volume  $V$ . We should remember that, although the force is concentrated at a point, the potentials which represent the force are defined over the whole volume. By substituting expression (3.50) into (3.52) and, as we did for Somigliana's problem (3.35), considering the volume  $V$  as a spherical surface  $S$  with center at  $x_i$ , where displacements are evaluated and the radius  $r'$  is  $\alpha\tau$  for  $\phi$  and  $r' = \beta\tau$  for  $\psi$ , and then letting the radius  $r'$  become infinite to cover the infinite space, we obtain

$$\phi(x_i, t) = \frac{1}{16\pi^2\rho\alpha^2} \int_0^\infty \frac{\delta(t - \tau)}{\tau} \int_S \frac{\partial}{\partial \xi_1} \frac{1}{|\xi_i|} dS d\tau \quad (3.54)$$

The value of the surface integral was evaluated in the previous section, in equations (3.35) to (3.39). We obtain, for  $r > \alpha\tau$  (for  $r < \alpha\tau$ , this integral is equal to zero)

$$\int_S \frac{\partial}{\partial \xi_1} \frac{1}{|\xi_i|} dS = 4\pi\alpha^2\tau^2 \frac{\partial}{\partial x_1} \frac{1}{r}$$

where  $r = |x_i|$ , as in Somigliana's problem is the distance from the origin where the force is applied to the point  $x_i$ , where the potential is evaluated (Fig. 3.5). By substitution into (3.54) we obtain

$$\phi(x_i, t) = \frac{1}{4\pi\rho} \frac{\partial}{\partial x_1} \frac{1}{r} \int_0^{r/\alpha} \tau \delta(t - \tau) d\tau \quad (3.55)$$

where we have taken into account that for  $\tau > r/\alpha$  the surface integral is zero. In a similar manner we obtain the expression for the vector potential  $\psi$ :

$$\psi(x_i, t) = \frac{1}{4\pi\rho} \left( 0, \frac{\partial}{\partial x_3} \frac{1}{r}, -\frac{\partial}{\partial x_2} \frac{1}{r} \right) \int_0^{r/\beta} \tau \delta(t - \tau) d\tau \quad (3.56)$$

Substituting the derivatives of  $1/r$  in terms of the direction cosines, as we did to obtain (3.40) and (3.43), we obtain

$$\phi(x_i, t) = \frac{1}{4\pi\rho r^2} \gamma_1 \int_0^{r/\alpha} \tau \delta(t - \tau) d\tau \quad (3.57)$$

$$\psi(x_i, t) = \frac{1}{4\pi\rho r^2} (0, \gamma_3, -\gamma_2) \int_0^{r/\beta} \tau \delta(t - \tau) d\tau \quad (3.58)$$

The displacements  $\mathbf{u}(x, t)$  are obtained using equation (3.25). These displacements constitute the Green's function for a force acting at the origin of coordinates in the direction of  $x_1$ , that is,  $G_{i1}$ ;

$$G_{i1} = \frac{1}{4\pi\rho} \left[ \frac{1}{r^3} (3\gamma_1\gamma_i - \delta_{1i}) \int_{r/\alpha}^{r/\beta} \tau \delta(t - \tau) d\tau + \frac{1}{\alpha^2 r} \gamma_1\gamma_i \delta(t - r/\alpha) - \frac{1}{\beta^2 r} (\gamma_1\gamma_i - \delta_{1i}) \delta(t - r/\beta) \right] \quad (3.59)$$

We can now generalize this result for a force acting in an arbitrary direction given by the sub-index  $j$ , in the form

$$G_{ij} = \frac{1}{4\pi\rho} \left[ \frac{1}{r^3} (3\gamma_j\gamma_i - \delta_{ji}) \int_{r/\alpha}^{r/\beta} \tau \delta(t - \tau) d\tau + \frac{1}{\alpha^2 r} \gamma_j\gamma_i \delta(t - r/\alpha) - \frac{1}{\beta^2 r} (\gamma_j\gamma_i - \delta_{ji}) \delta(t - r/\beta) \right] \quad (3.60)$$

This is the final expression for the Green's tensor for an infinite homogeneous isotropic elastic medium with P and S velocities  $\alpha$  and  $\beta$  and density  $\rho$ . This result together with that obtained for Somigliana's tensor constitute the basic building blocks for seismic source studies.

### 3.5.1. Separation of near and far field

We have seen that for Somigliana's tensor the amplitude of the displacements depends on distance as  $1/r$ . For Green's tensor (3.60) there are two dependences on distance: the first term decays as  $1/r^3$  and the second and third as  $1/r$ . Thus, the displacement represented by the first term attenuates more rapidly with distance than the second and third, and can only be observed very near the source. For this reason, it is called the *near field*. As this term depends on both  $\alpha$  and  $\beta$ , it is a displacement of mixed P and S motion. The second and third terms, with a dependence of  $1/r$ , constitute the *far field* and are formed by P and S waves which arrive separately. The expressions for the near and far fields (3.60) contain two parts: one, called the *radiation pattern*, depends on the direction cosines of the ray that connects the observation point and the source and expresses the spatial distribution of amplitudes; the other expresses their temporal dependence or wave form.

#### Near field

The time dependence of the near field can be rewritten (Knopoff, 1967) using Heaviside's step function  $H(t)$  in the form

$$\int_{r/\alpha}^{r/\beta} \tau \delta(t - \tau) d\tau = \int_{-\infty}^{\infty} \tau \delta(t - \tau) \left[ H\left(\tau - \frac{r}{\alpha}\right) - H\left(\tau - \frac{r}{\beta}\right) \right] d\tau \quad (3.61)$$

According to the properties of the step and delta functions the integral has the value

$$tH\left(t - \frac{r}{\alpha}\right) - tH\left(t - \frac{r}{\beta}\right)$$

The first term can be written as

$$tH\left(t - \frac{r}{\alpha}\right) = \left(t - \frac{r}{\alpha}\right)H\left(t - \frac{r}{\alpha}\right) + \frac{r}{\alpha}H\left(t - \frac{r}{\alpha}\right)$$

and a similar expression holds for the second term. In the above equation  $(t - r/\alpha)H(t - r/\alpha)$  is a *ramp function* of slope unity.

The time dependence of the near field can now be written as the sum of two terms, one depending on  $1/r^3$  and the other on  $1/r^2$ :

$$\begin{aligned} & \frac{1}{r^3} \left[ \left(t - \frac{r}{\alpha}\right)H\left(t - \frac{r}{\alpha}\right) - \left(t - \frac{r}{\beta}\right)H\left(t - \frac{r}{\beta}\right) \right] \\ & + \frac{1}{r^2} \left[ \frac{1}{\alpha}H\left(t - \frac{r}{\alpha}\right) - \frac{1}{\beta}H\left(t - \frac{r}{\beta}\right) \right] \end{aligned} \quad (3.62)$$

The factor multiplying  $1/r^3$  is the difference between two ramp functions and the factor multiplying  $1/r^2$  is the difference between two step functions of different amplitudes (Fig. 3.7). The term which depends on  $1/r^3$  has the form of a ramp function of unit slope

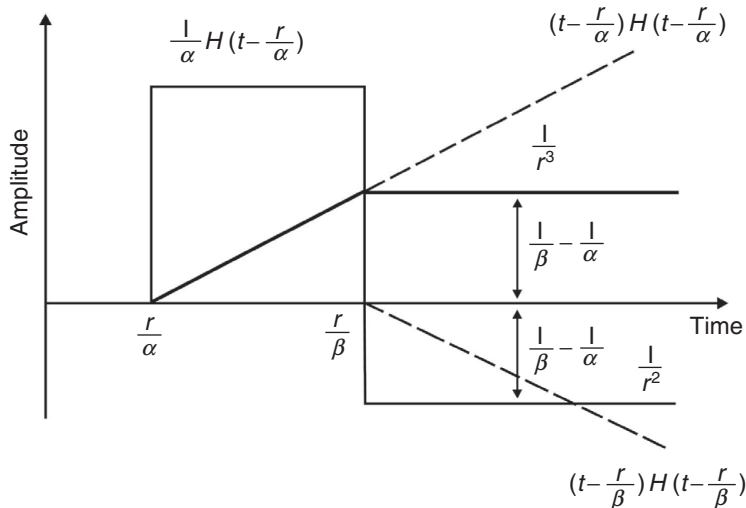


**Figure 3.7.** Near-field displacement Green's function for an infinite medium at a distance  $r$ , as a function of time.

beginning at  $t = r/\alpha$  and ending at  $t = r/\beta$ . From this time onward the displacement has a constant amplitude  $1/\beta - 1/\alpha$ . The part which depends on  $1/r^2$  is a step function of amplitude  $1/\alpha$  between times  $t = r/\alpha$  and  $t = r/\beta$ . From the latter time onward the amplitude is constant and equal to  $1/\alpha - 1/\beta$ . Thus the displacement in the near field has a static part, which remains constant with time.

The radiation pattern of the near-field term is given by  $3\gamma_i \gamma_j - \delta_{ij}$ . If the force is acting in the direction of  $x_1$  then the distribution of normalized amplitudes in the plane  $(x_1, x_3)$  is the following:

$$\begin{aligned} G_{11} &= 3\gamma_1 \gamma_1 - 1 = 3 \cos^2 \theta - 1 \\ G_{13} &= 3\gamma_1 \gamma_3 = 3 \cos \theta \sin \theta \end{aligned}$$

Separating the radial component  $G_{1r}$  and the transverse component  $G_{1\theta}$ , we have

$$\begin{aligned} G_{1r} &= 2 \cos \theta \\ G_{1\theta} &= -\sin \theta \end{aligned}$$

This is the same distribution as for Somigliana's tensor (Fig. 3.6). The maximum amplitudes are for  $\theta = 0, \pi$  and have the same direction as the force.

### Far field

The far field (the terms depending on  $1/r$  in equation (3.60)) is formed by two impulses (delta functions) which arrive separately at times  $t = r/\alpha$  and  $t = r/\beta$  (Fig. 3.8). These are the P and S waves observed at large distances from the source.

The radiation pattern is different for each type of wave. It is represented for the P wave by the term  $\gamma_i \gamma_j$  and for the S wave by the term  $\gamma_i \gamma_j - \delta_{ij}$ . For the case of a force acting in the direction of  $x_1$ , the distributions of the normalized amplitudes in the plane  $(x_1, x_3)$  for the P and S waves are the following:

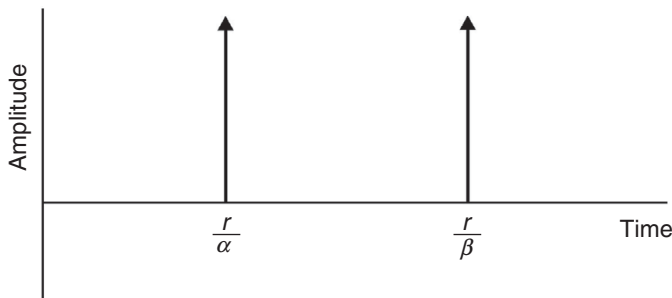


**Figure 3.8.** Far-field displacement Green's function for an infinite medium (P and S waves) at a distance  $r$ , as a function of time.

$$\begin{aligned} G_{11}^P &= \gamma_1 \gamma_1 = \cos^2 \theta \\ G_{13}^P &= \gamma_1 \gamma_3 = \cos \theta \sin \theta \\ G_{11}^S &= -\gamma_1 \gamma_1 + 1 = \sin^2 \theta \\ G_{13}^S &= -\gamma_1 \gamma_3 = -\cos \theta \sin \theta \end{aligned}$$

Separating the radial component  $G_r^P$  and the transverse component  $G_\theta^S$  corresponding to the P and S waves, we obtain

$$\begin{aligned} G_r^P &= \cos \theta \\ G_\theta^S &= -\sin \theta \end{aligned}$$

As expected, the displacements of the P waves are in the radial direction and those of the S waves are in a transverse direction. The radiation pattern around the source has in both cases two lobes, with the same distribution as in Somigliana's tensor (Fig. 3.6). For P waves the displacements are radial; in the right lobe they are outward, that is, they are compressions in the usual seismological terminology, and in the left lobe they are inward, that is, they are dilatations, with maxima at  $\theta = 0$  and  $\pi$ . For S waves the displacements are in the transverse direction converging toward the direction of the force in both lobes, with maxima at  $\theta = \pi/2$  and  $3\pi/2$ .

### 3.6. Green's functions for layered media

The Green's function for an infinite homogeneous isotropic elastic medium corresponds to the response of the most simple type of propagating medium. This can be useful in some cases, but more complex models are necessary to represent the structure of the Earth. The first model to be considered is that of a homogenous isotropic half-space, which takes into consideration the existence of a free surface of the Earth. The problem of the response of a half-space to an impulsive point source was first solved by Lamb (1904) and by Lapwood (1949). The main effect of the free surface is to generate surface Rayleigh waves. Using the scalar potentials  $\phi$  and  $\psi$  to represent the P and SV motion, the radial and vertical components of the of Rayleigh wave displacements at the free surface due to a unit point

source located at depth  $h$  can be written as (Aki and Richards, 1981, pp. 214–24; Gershanik, 1996, pp. 585–99)

$$G_r^R(r, t) \approx 2i\sqrt{\frac{2\pi\omega}{rc_R}} \frac{k_R \sqrt{k_R^2 - k_\beta^2}}{\omega\beta^2 F'(k_R)} \exp i\left[k_R(r - c_R t) - h\sqrt{k_R^2 - k_\beta^2} + \frac{\pi}{4}\right] \quad (3.63)$$

$$G_z^R(r, t) \approx 2\sqrt{\frac{2\pi\omega}{rc_R}} \frac{2k_R^2 - k_\beta^2}{\omega\beta^2 F'(k_R)} \exp i\left[k_R(r - c_R t) - h\sqrt{k_R^2 - k_\beta^2} + \frac{\pi}{4}\right] \quad (3.64)$$

where  $c_R$  is the velocity of Rayleigh waves ( $c_R = 0.92\beta$ ),  $k_R = \omega/c_R$  is the corresponding wave number, and

$$F'(k_R) = \left(2k_R^2 - k_\beta^2\right)^2 - 4k_R^2 \sqrt{k_R^2 - k_\alpha^2} \sqrt{k_R^2 - k_\beta^2}$$

A better approximation to the generation of seismic waves in the Earth is obtained by using models of plane or spherical layered media. In this form, one can obtain the P and S waves transmitted and reflected in the different layers and the two types of surface wave, the Rayleigh and *Love* waves. In the flat layered model the Earth is constituted by a number of horizontal layers, specified by their thickness and their P and S wave velocities and densities, overlying a half-space. The point source is located inside one of the layers. The problem is solved for the displacements at the free surface by summing the contributions of all P, SV and SH waves transmitted and reflected through the layers, plus those of the generated Rayleigh and Love waves. There are several methods to solve this problem; we briefly describe two of the most commonly used, the *reflectivity* and *normal mode* methods (Müller, 1985; Kennet, 2001).

The reflectivity method is based on integration of the reflection coefficients over the wave number in a layered medium (Fuchs and Müller, 1971; Müller, 1985; Kennet, 2001). In the presence of the free surface and the point source at a certain depth, the integration is carried out in two parts, namely, one using the reflection coefficients of the layers above the source and the other using those of the layers below. Similar to the reflectivity method are methods based on ray theory but with different approaches (for example, Helmberger, 1974; Chapman, 1978; Bouchon, 1981; Luco and Apsel, 1983).

Another approach to the problem for flat or spherical layered media is that of normal mode summation (Schwab *et al.*, 1984; Panza, 1985; Dahlen and Tromp, 1998, pp. 363–404). This method is most effective for the calculation of surface waves, but with the summation of a sufficiently large number of modes it can synthesize the complete seismogram including the body waves.

For an infinite homogeneous medium, the far-field displacements corresponding to the Green's function for a particular orientation of the force are impulsive P and S waves. For a homogeneous half-space, for a source at a certain depth we have to add the contribution of the Rayleigh waves generated at the free surface. Layered media with an increasing number of layers and an internal source produce increasingly complex signals, with contributions from the reflected and refracted P and S waves in the different layers and the dispersed trains of Raleigh and Love waves. The increasing complexity of the Green's functions corresponding to one layer over a half-space  $M_2$  and three layers over a

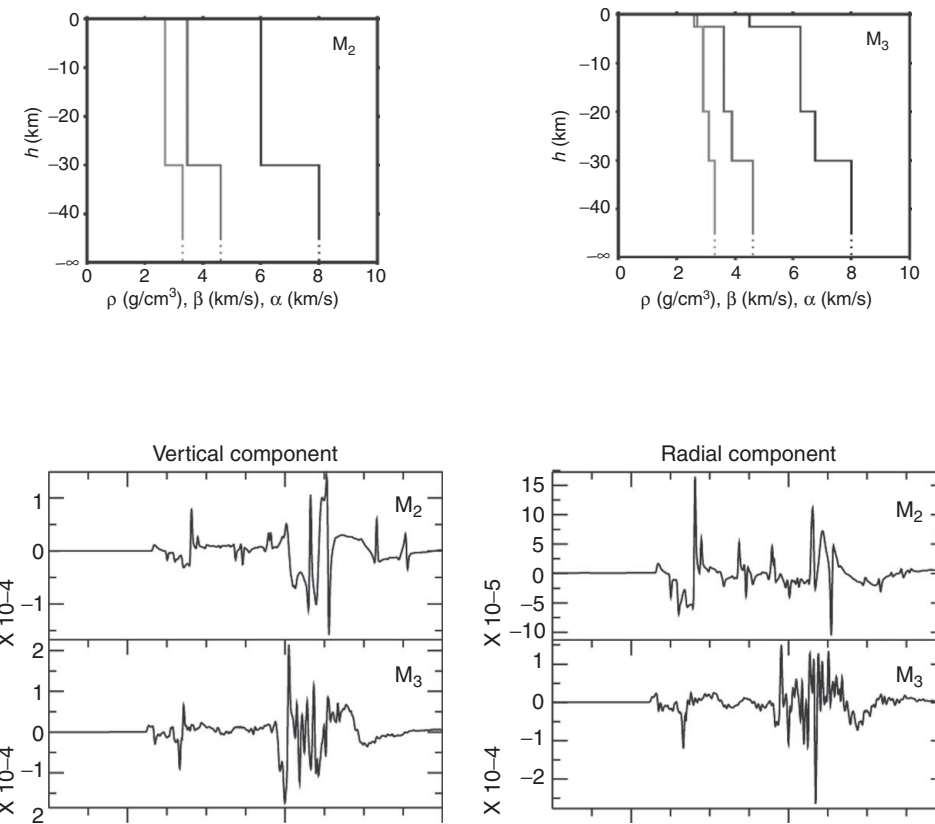


**Figure 3.9.** Example of vertical and radial components of the Green's function corresponding to two layered media,  $M_2$  and  $M_3$ . In the upper figures, shown left to right are the dependences of  $\alpha$ ,  $\beta$ , and  $\rho$  on  $h$ .

half-space  $M_3$  for a vertical force at a depth of 10 km is shown in Fig. 3.9. The Green's functions were determined by the reflectivity method.

### 3.7. Focal region

The processes which generate an earthquake take place at a particular location, called the source or *focal region*, which can be represented by a limited volume  $V_0$  inside the Earth. Let us consider a volume  $V$ , representing the Earth, surrounded by a surface  $S$ ; inside this volume there is a region of volume  $V_0$  surrounded by a surface  $\Sigma$ . Let us consider that the source processes are represented by a system of forces per unit volume defined inside volume  $V_0$  that are zero outside it and that  $\Sigma$  is the surface surrounding  $V_0$  at which certain stresses  $\mathbf{T}$  are also defined (Fig. 3.10); then we can write the equation of motion (3.3) in the form

$$\int_{V_0} F_i dV + \int_{\Sigma} T_i d\Sigma + \int_S \tau_{ij} v_j dS = \int_{V'} \rho \frac{\partial^2 u_i}{\partial t^2} dV \quad (3.65)$$

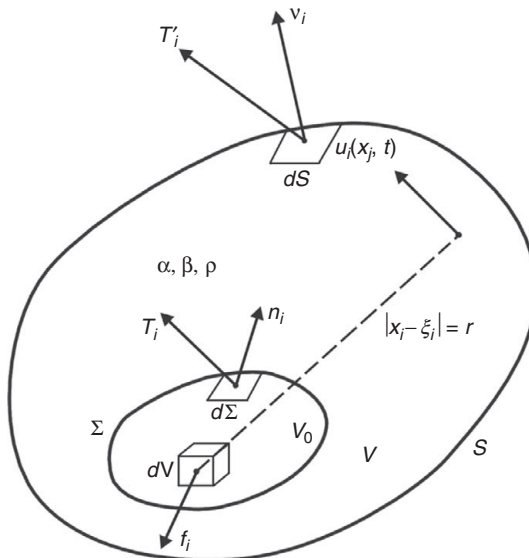


**Figure 3.10.** The displacement  $u_i$  in a medium of volume  $V$  and the stress  $T'_i$  on its surface  $S$  corresponding to a body force  $f_i$  acting on volume  $V_0$  and stresses  $T_i$  acting on a surface  $\Sigma$  of normal  $n_i$  surrounding  $V_0$ . The P and S wave velocities are  $\alpha$  and  $\beta$  and the density is  $\rho$ .

Using the representation theorem (Section 3.3), the definition of the focal region implies that the body forces are only defined inside the focal volume  $V_0$  and that the stresses  $\mathbf{T}$  and displacements  $\mathbf{u}$  must also be specified on the surfaces  $\Sigma$  and  $S$ . Then the elastic displacements outside the focal region are given by, according to (3.23),

$$\begin{aligned} u_n(x_s, t) = & \int_{-\infty}^{\infty} dt \int_{V_0} f_i G_{ni} dV + \int_{-\infty}^{\infty} d\tau \int_{\Sigma} (G_{ni} T_i - C_{ijkl} u_i G_{nk}, l n_j) dS \\ & + \int_{-\infty}^{\infty} d\tau \int_S (G_{ni} T'_i - C_{ijkl} u_i G_{nk}, l v_j) dS \end{aligned} \quad (3.66)$$

where  $\mathbf{n}$  is the normal to  $\Sigma$  and  $\mathbf{v}$  is the normal to  $S$ . If the conditions on the external surface  $S$  are homogeneous, the third integral is null. This is satisfied in an infinite medium. Then the elastic displacements outside the focal region are given by the conditions in the focal region specified by the values of  $\mathbf{f}$ ,  $\mathbf{T}$  and  $\mathbf{u}$ . Since earthquakes are caused by motion on faults, we can deform the focal volume  $V_0$  into a double-layer surface  $\Sigma$  with no volume between the layers. We define the discontinuity in displacement across the positive and negative sides of  $\Sigma$  as

$$\Delta u_i = u_i^+ - u_i^- \quad (3.67)$$

Then we write the elastic displacements in an infinite medium in terms of the distribution of forces  $\mathbf{f}$ , the discontinuity in displacement  $\Delta \mathbf{u}$  and the distribution stress  $\mathbf{T}$  defined over the surface  $\Sigma$  representing a fault surface (Fig. 3.11):

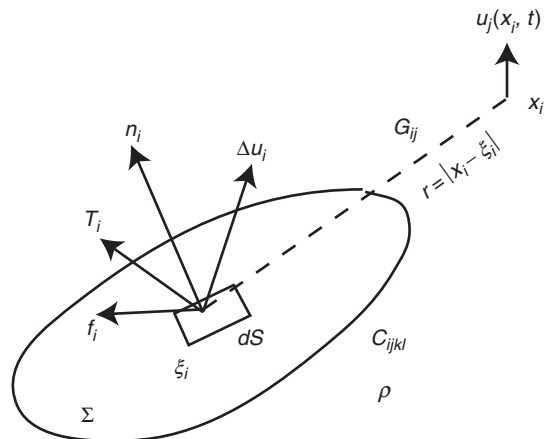


**Figure 3.11.** The displacement  $u_j$  in an infinite medium corresponding to forces  $f_i$  and stresses  $T_i$  per unit area acting on the fault surface  $\Sigma$ , and the displacement discontinuity  $\Delta u_i$  across the same surface.

$$u_n(x_s, t) = \int_{-\infty}^{\infty} d\tau \int_{V_0} f_i G_{ni} dV + \int_{-\infty}^{\infty} d\tau \int_{\Sigma} C_{ijkl} \Delta u_i G_{nk, l} n_j dS + \int_{-\infty}^{\infty} d\tau \int_{\Sigma} G_{ni} T_i dS \quad (3.68)$$

This equation shows how we can determine the elastic displacements at an arbitrary point of observation as a function of time, that is, the seismograms, if we know the conditions on the fault surface at the source defined by  $f$ ,  $T$  and  $\Delta u$ . This is known as the direct problem and allows the calculation of theoretical seismograms for a selected source if we know the Green's tensor of the medium,  $G_{ij}$ , and the source parameters  $f$ ,  $T$  and  $\Delta u$ . The inverse problem consists in determining the source parameters from the observed values of the elastic displacements at different points (the observed seismograms), assuming the known values of the Green's function for the medium.

## 3.8. Kinematic and dynamic models

Although in the general case displacements are given by the three terms on the right-hand side of equation (3.68), for practical applications we can select only one of them. Thus we have three ways of representing the source. First, we can represent it by forces per unit volume acting inside a certain source region  $V_0$  or by forces per unit surface area acting on a fault surface  $\Sigma$ . Since we know that these forces do not really exist they are called *equivalent forces*, that is, they are forces which generate elastic displacements equal to those generated by the physical processes that take place in the source of an earthquake. Then the elastic displacements can be written as

$$u_k(x_n, t) = \int_{-\infty}^{\infty} d\tau \int_{V_0} F_i(\xi_n, \tau) G_{ki}(\xi_n, \tau, x_n, t) dV \quad (3.69)$$

For a distribution of forces on a surface the elastic displacements are given by a similar surface integral over  $\Sigma$ .

We know that tectonic earthquakes are caused by the relative motion of one side of a fault relative to the other. This is a non-elastic displacement, since the sides of the fault suffer a permanent displacement and do not return to their initial position. Thus a fault can be represented by a *displacement dislocation*, that is, a discontinuity in displacement  $\Delta\mathbf{u}$  across a surface  $\Sigma$ . For this purpose we select the second term of [equation \(3.68\)](#). The elastic displacement field outside the source is represented in terms of non-elastic displacements at the source:

$$u_k(x_n, t) = \int_{-\infty}^{\infty} d\tau \int_{\Sigma} \Delta u_i(\xi_n, \tau) C_{ijsl} G_{ks, l}(\xi_n, \tau, x_n, t) n_j(\xi_n) dS \quad (3.70)$$

where  $\mathbf{n}$  is the unit vector normal to the fault surface at each point. Since we specify the displacements at the source, but not the stresses, this is a *kinematic model*, that is, we are describing the relative motion of the two sides of the fault without reference to the stresses which have caused it. Kinematic models are very useful in the study of earthquake sources of, since they establish a straightforward relation between the motion at the source and the elastic displacement field, that is, the observed seismograms, outside the source. The link between the two is the Green's function which describes the characteristics of the propagating medium. Moreover, in some cases, the final displacements at the source can be compared with direct field observations of the relative displacements produced on faults.

The third representation uses the stresses acting on the fault which are responsible for the non-elastic displacements. Some authors call these inelastic stresses the *stress glut* (see e.g. [Backus and Mulcahy, 1976b](#)). Using the third term of [equation \(3.68\)](#) we have, for the elastic displacement field,

$$u_k(x_n, t) = \int_{-\infty}^{\infty} d\tau \int_{\Sigma} T_i(\xi_n, \tau) G_{ik}(\xi_n, \tau, x_n, t) dS \quad (3.71)$$

Taking into account the conditions imposed on the stresses, this expression may be used to represent a *dynamic model*. The slip  $\Delta\mathbf{u}$  on the fault is produced by the stress drop  $\Delta\sigma$  [\(1.6\)](#) during the fault process. Dynamic models are more complicated than kinematic models since we have to specify the processes in terms of the stress drop, which take place at the fault as it breaks. In these models the motion at the fault is a consequence of the stress distribution, its changes along the fault with time (the stress drop) and the properties of the fault, especially the material strength and breaking friction. A complete dynamic description must, then, be able to describe the complete fracture process in terms of the specification of the stress conditions and the properties of the material of the focal region. In most cases solutions of dynamic models can be found only by numerical methods.

## 4.1. Point source approximation

The problem of finding the mechanism of an earthquake is considerably simplified if the finite size of the source is ignored, and the focal region is reduced to a point (Pujo and Herrmann, 1990). This so-called *point-source* approximation is valid if one considers observations which are at sufficiently large distances compared with the source dimensions and if the wavelengths of the observations are larger than the source dimensions. Putting the two conditions together, the requirement for the validity of the point-source approximation can be expressed as  $r\lambda \gg L^2$ , where  $r$  is the distance of the observation point from the source,  $\lambda$  is the wavelength and  $L$  is a typical dimension of the source.

The simplest point source model of earthquakes that can be studied is the *isotropic point source*, in which the source is considered as a point from which waves are propagated with equal amplitude in all directions. The five parameters defining this model are the space coordinates of the focus, usually given by the geographical latitude and longitude of the epicenter, and the focal depth, the origin time and a parameter indicating the energy release, that is, the magnitude or scalar seismic moment:  $\phi$ ,  $\lambda$ ,  $h$ ,  $t_0$ ,  $M_0$ . Since the parameters defining the location in space and time of the point source are determined from the first arrival times at observation points of waves of relatively short periods, they refer in fact to the location and time of the initiation of rupture on an extended source.

## 4.2. Equivalent forces. Double couple

The first mathematical formulation of earthquake mechanisms, presented by Nakano (1923), used the point source approximation. In this work Nakano, following ideas already developed in elastodynamic theory by Lamb (1904) and Love (1927), represented the source of an earthquake by a system of equivalent body forces acting at a point. Nakano solved the equation of motion (3.7), (3.8), substituting the force per unit volume  $F(\xi, t)$  by several systems of forces acting at a point. These systems of forces, which are functions of time, are designed so that they generate the same elastic wave field as that observed in earthquakes. The forces acting at a point can be considered as the limit of forces acting on the source volume  $V_0$  (cf. (3.65)) as it tends to zero (Fig. 3.10):

$$F_i(t) = \lim_{V_0 \rightarrow 0} \int_{V_0} F_i(\xi_k, t) dV \quad (4.1)$$

where  $\xi_k$  are the source point. Using the representation theorem in terms of the Green's function, the displacement field (3.69) produced by a system of forces acting at the origin of coordinates can be written as

$$u_i(x_s, t) = \int_{-\infty}^{\infty} F_k(\tau) G_{ki}(x_s, t - \tau) d\tau \quad (4.2)$$

The elastic displacements are given by the time convolution of the forces acting at the origin with the Green's function of the medium. The system of point forces most frequently used to represent the source of earthquakes is the *double couple* (DC), that is, two couples of forces having moments that are equal but in opposite directions and that are normal to each other. Thus there is no nett moment. This system is equivalent to two perpendicular *linear force dipoles* (with arms in the same directions as the forces) in opposite senses, acting at  $45^\circ$  to the couples (Fig. 4.1). The linear dipoles represent tension (positive) and pressure (negative) forces. These two systems are equivalent to a *shear fracture*, assumed to be the mechanism of tectonic earthquakes. For some time an alternative model proposed was that of a *single couple* (SC), but it was shown that this could not represent a shear fracture or any internal source, which must have zero total force and moment.

The elastic displacement due to a force couple can be derived from the displacement generated by a single force. If  $u_j^1$  are the displacements due to a force acting at the origin in the  $x_1$  direction, those due to a force couple in the  $(x_1, x_2)$  plane with forces in the positive and negative directions of  $x_1$  and whose arm is in the  $x_2$  direction are derived by performing a Taylor expansion for each force, displaced by  $s/2$  from the origin along the  $x_2$  axis. For the force in the positive direction of  $x_1$  and shifted by  $s/2$  from the origin in the positive direction of  $x_2$ , the elastic displacement is

$$u_j^+ = u_j^1 + \frac{s}{2} \frac{\partial u_j^1}{\partial \xi_2} \quad (4.3)$$

where  $\xi_i$  are as before the coordinates of the source point. For the force in the negative direction of  $x_1$  and shifted by  $s/2$  in the negative direction of  $x_2$ , the displacement,  $u_j^-$ , has a similar expression but with a negative sign in the first term. The sum of the two ( $u_j^{SC} = u_j^+ + u_j^-$ ) gives the displacement corresponding to a single couple (SC) with forces in the  $x_1$  direction and arm in the  $x_2$  direction:

$$u_j^{SC} = s \frac{\partial u_j^1}{\partial \xi_2} \quad (4.4)$$

For a double couple (DC) with couples in the  $x_1$  and  $x_2$  directions the displacements are given by

$$u_j^{DC} = s \left( \frac{\partial u_j^1}{\partial \xi_2} + \frac{\partial u_j^2}{\partial \xi_1} \right) \quad (4.5)$$

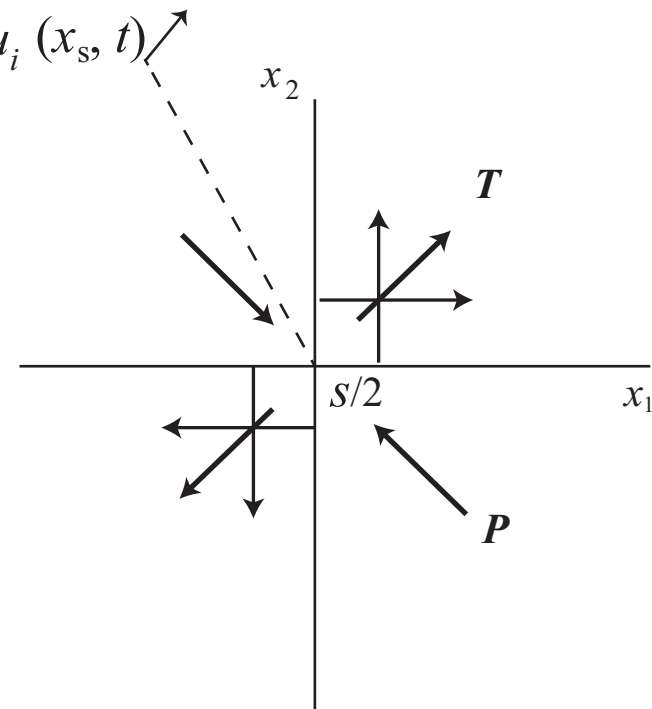


**Figure 4.1.** Double-couple point source model and the equivalent pressure ( $P$ ) and tension ( $T$ ) axes system.

Substituting (4.5) into equation (4.2), we obtain

$$u_j^{\text{DC}} = \int_{-\infty}^{\infty} M(\tau) \left( \frac{\partial G_{j1}}{\partial \xi_2} + \frac{\partial G_{j2}}{\partial \xi_1} \right) d\tau \quad (4.6)$$

where  $M(\tau) = sF(\tau)$  is the moment of each couple and is usually a function of time. For a DC point source in an arbitrary direction, with one couple with forces in the direction of the unit vector  $\mathbf{X}$  and arm in the direction of the unit vector  $\mathbf{Y}$ , and the second couple with forces in the direction of  $\mathbf{Y}$  and arm in the direction of  $\mathbf{X}$ , where  $\mathbf{X}$  and  $\mathbf{Y}$  are perpendicular, the displacements are

$$u_i^{\text{DC}}(x_s, t) = \int_{-\infty}^{\infty} M(\tau) (X_k Y_j + X_j Y_k) \frac{\partial G_{ik}(t - \tau)}{\partial \xi_j} d\tau \quad (4.7)$$

As mentioned above, linear dipoles (LDs) have forces and arms in the same direction. For two perpendicular linear dipoles with opposite signs in the directions of the  $x_1$  and  $-x_2$  axes, the equation corresponding to (4.5) is

$$u_j^{\text{LD}} = s \left( \frac{\partial u_j^1}{\partial \xi_1} - \frac{\partial u_j^2}{\partial \xi_2} \right) \quad (4.8)$$

As in (4.7), the equation corresponding to two perpendicular linear dipoles in the directions of the unit vectors  $-\mathbf{P}$  and  $\mathbf{T}$  representing the directions of the pressure and tension forces, is now

$$u_i^{\text{TP}}(x_s, t) = \int_{-\infty}^{\infty} M(\tau) (T_k T_j - P_j P_k) \frac{\partial G_{ik}(t - \tau)}{\partial \zeta_j} d\tau \quad (4.9)$$

where  $M(t) = -sP(t) = sT(t)$  is the moment of each linear dipole. If  $\mathbf{P}$  and  $\mathbf{T}$  are in the same plane as  $\mathbf{X}$  and  $\mathbf{Y}$  and at  $45^\circ$  to them, and if the moments are the same, equations (4.7) and (4.9) are equivalent (Fig. 4.1). The relation between the two systems is given by

$$\mathbf{P} = \frac{1}{\sqrt{2}} (\mathbf{X} - \mathbf{Y}) \quad (4.10)$$

$$\mathbf{T} = \frac{1}{\sqrt{2}} (\mathbf{X} + \mathbf{Y}) \quad (4.11)$$

$$\mathbf{Z} = \mathbf{X} \times \mathbf{Y} = \mathbf{P} \times \mathbf{T} \quad (4.12)$$

where  $\mathbf{Z}$  is the unit vector normal to the plane containing the forces. This vector is also known as  $\mathbf{B}$ , the null axis, because there is no component of force in its direction. In this way, for a DC point source we can define two orthogonal systems of axes in the directions of the vectors  $\mathbf{X}$ ,  $\mathbf{Y}$ ,  $\mathbf{Z}$  and  $\mathbf{P}$ ,  $\mathbf{T}$ ,  $\mathbf{Z}$  to specify the orientation of the source. We will see that the first system corresponds to the orientation of the motion of a point shear dislocation and the second to its corresponding principal axes of stress.

### 4.3. Shear fracture or dislocation

Since earthquakes are produced by the fracturing of the Earth's crust, as we saw in Chapter 1, it is appropriate to represent mechanically their source in terms of *fractures* or *dislocations* in an elastic medium. The theory of elastic dislocations was first developed by Volterra in 1907 and discussed by Love (1927). Among the first applications to the problem of seismic sources were those of Vvedenskaya (1956), Keylis-Borok (1956), Steketee (1958) and Knopoff and Gilbert (1960).

As already mentioned (Section 3.7), an earthquake source can be described by a *displacement dislocation* and, using the representation theorem, the elastic displacement field is given by equation (3.70). If the conditions for the point source approximation are fulfilled, this equation reduces to

$$u_n(x_s, t) = \int_{-\infty}^{\infty} S \Delta u_i C_{ijkl} G_{nk,l} n_j d\tau \quad (4.13)$$

where  $S$  is the area of the fault. For an isotropic medium, substituting the elastic coefficients as in (3.7) we obtain

$$u_n(x_s, t) = \int_{-\infty}^{\infty} S \Delta u [\lambda l_l n_l \delta_{ij} + \mu (l_i n_j + l_j n_i)] G_{ni,j} d\tau \quad (4.14)$$

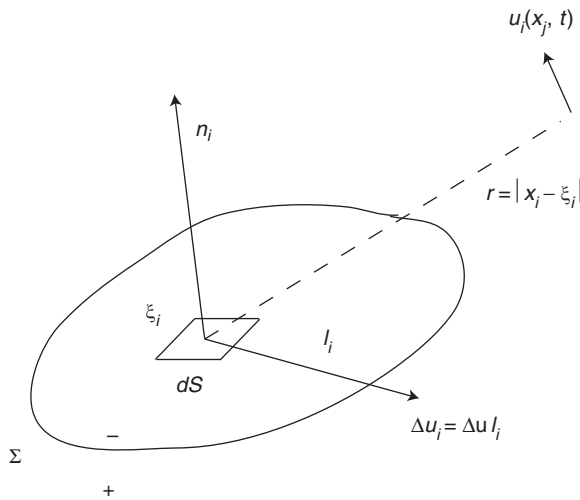


**Figure 4.2.** Shear-fault source model with slip  $\Delta\mathbf{u} = \Delta\mathbf{u}_i$  over surface  $\Sigma$ ;  $\mathbf{n} = \mathbf{n}_i$  and  $\mathbf{l} = \mathbf{l}_i$  are unit vectors respectively in the direction of the normal to the fault and in the direction of slip. The displacement is  $\mathbf{u} = \mathbf{u}_i$  at distance  $r$ .

where  $\mathbf{l}$  is a unit vector in the direction of the slip ( $\Delta\mathbf{u} = \mathbf{l}\Delta u$ ) and  $\mathbf{n}$  is a unit vector normal to the plane of fracture  $\Sigma$  (Fig. 4.2).

These two unit vectors, referred to the geographic system of coordinates (north, east, nadir), define the orientation of the fault motion. Since  $\mathbf{n}$  and  $\mathbf{l}$  are unit vectors, each has only two independent components, and so the orientation of the motion is given by four parameters. Expression (4.14) for  $i = j$  gives the component of the slip normal to the fault plane; the presence of such a component implies the existence of changes in volume at the source. If, however, motion takes place only parallel to the fault plane (a shear fracture or dislocation) then  $\mathbf{l}$  and  $\mathbf{n}$  are perpendicular ( $\mathbf{n} \cdot \mathbf{l} = 0$ ) and there are no changes of volume at the source. In this case the parameters representing the orientation of the point source are reduced to three, as we saw in section 1.3. From (4.14) the displacement field due to a point shear dislocation is given by

$$u_n(x_s, t) = \int_{-\infty}^{\infty} \Delta u S \mu (l_i n_j + l_j n_i) G_{ni,j} d\tau \quad (4.15)$$

where, as we saw in (1.4),  $\mu S \Delta u(t) = M_0(t)$  is the *scalar seismic moment*. The orientation of the source is now given by the three independent components of  $\mathbf{l}$  and  $\mathbf{n}$ . The elastic displacement field is given by the convolution of the seismic moment with the derivatives of the Green's function multiplied by a combination of the unit vectors in the direction of the slip,  $\mathbf{l}$ , and of the normal to the fault plane,  $\mathbf{n}$ .

Comparing equation (4.15) with (4.7) we see that the elastic displacements of a shear dislocation are the same as those of a double-couple system of forces with one couple in the direction of slip ( $\mathbf{X} = \mathbf{l}$ ) and the other in the direction of the normal of the fault plane ( $\mathbf{Y} = \mathbf{n}$ ). A point shear dislocation and a double couple are, then, *equivalent* point source representations. Since the latter representation is in turn equivalent to a

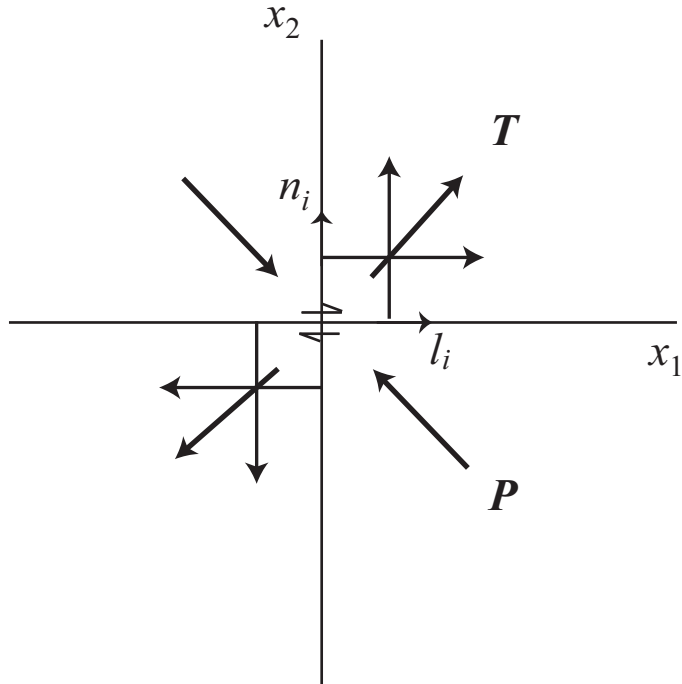


**Figure 4.3.** The correspondence between the double-couple (DC in the directions  $n_i$  and  $l_i$ ) and pressure–tension ( $P$  and  $T$ ) equivalent force systems and the shear-fault model, shown as half arrows in the direction  $l_i$ .

system of pressure and tension linear dipoles at  $45^\circ$ , this system is also equivalent to a point shear fracture (Fig. 4.3).

If  $\mathbf{l}$  and  $\mathbf{n}$  are constant with time then, substituting the seismic moment into (4.15), we obtain

$$u_n(x_s, t) = (l_i n_j + l_j n_i) \int_{-\infty}^{\infty} M_0(\tau) G_{ni,j}(t - \tau) d\tau \quad (4.16)$$

In terms of the  $\mathbf{P}$  and  $\mathbf{T}$  axes the displacements are given by

$$u_n(x_s, t) = (T_i T_j - P_i P_j) \int_{-\infty}^{\infty} M_0(\tau) G_{ni,j}(t - \tau) d\tau \quad (4.17)$$

The PT system represents in an ideal way the principal axes of stress acting at the fracture plane when there is no friction. The relation between the axes  $\mathbf{P}$ ,  $\mathbf{T}$  and the axes  $\mathbf{l}$ ,  $\mathbf{n}$  is given by equations (4.10) and (4.11), taking  $\mathbf{l} = \mathbf{Y}$  and  $\mathbf{n} = \mathbf{X}$ . This system, however, does not always correspond with the orientation of the acting stresses, because fracture takes place usually at preexisting faults, which may not be at a  $45^\circ$  angle to the stress direction. In a general form, the equivalence between displacement dislocations and double-couple body forces, for non-propagating or propagating extended sources, was shown by Burridge and Knopoff (1964).

## 4.4. Point shear fracture in an infinite medium

In equation (4.15) the displacement field of a point shear fracture (or equivalently a DC (4.7) or a PT (4.9) system of forces) is given in terms of the derivatives of the Green's function. In the case of an infinite homogeneous isotropic medium the latter are obtained by taking the derivative of (3.60) with respect to the source coordinate  $\xi_i$ :

$$\begin{aligned} \frac{\partial G_{ij}}{\partial \xi_k} = & \frac{1}{4\pi\rho} \left\{ \frac{1}{r^4} (15\gamma_i\gamma_j\gamma_k - 3(\gamma_i\delta_{jk} + \gamma_j\delta_{ik} + \gamma_k\delta_{ij})) \int_{r/\alpha}^{r/\beta} \tau \delta(t - \tau) d\tau \right. \\ & + \frac{1}{\alpha^2 r^2} (6\gamma_i\gamma_j\gamma_k - \gamma_i\delta_{jk} - \gamma_j\delta_{ik} - \gamma_k\delta_{ij}) \delta(t - r/\alpha) \\ & - \frac{1}{\beta^2 r^2} (6\gamma_i\gamma_j\gamma_k - \gamma_i\delta_{jk} - \gamma_j\delta_{ik} - 2\gamma_k\delta_{ij}) \delta(t - r/\beta) \\ & \left. + \frac{1}{r} \left[ \frac{1}{\alpha^3} \gamma_i\gamma_j\gamma_k \dot{\delta}(t - r/\alpha) - \frac{1}{\beta^3} (\gamma_i\gamma_j - \delta_{ij}) \gamma_k \dot{\delta}(t - r/\beta) \right] \right\} \end{aligned} \quad (4.18)$$

The displacements due to a point shear fracture or DC source are then given using (4.16), by substituting into it (4.18) for the derivatives of the Green's function and taking into account the properties of the delta function:

$$\begin{aligned} u_i = & \frac{1}{4\pi\rho} (l_j n_k + l_k n_j) \\ & \times \left\{ \frac{1}{r^4} (15\gamma_i\gamma_j\gamma_k - 3(\gamma_i\delta_{jk} + \gamma_j\delta_{ik} + \gamma_k\delta_{ij})) \int_{r/\alpha}^{r/\beta} \tau M_0(t - \tau) d\tau \right. \\ & + \frac{1}{\alpha^2 r^2} (6\gamma_i\gamma_j\gamma_k - \gamma_i\delta_{jk} - \gamma_j\delta_{ik} - \gamma_k\delta_{ij}) M_0(t - r/\alpha) \\ & - \frac{1}{\beta^2 r^2} (6\gamma_i\gamma_j\gamma_k - \gamma_i\delta_{jk} - \gamma_j\delta_{ik} - 2\gamma_k\delta_{ij}) M_0(t - r/\beta) \\ & \left. + \frac{1}{r} \left[ \frac{1}{\alpha^3} \gamma_i\gamma_j\gamma_k \dot{M}_0(t - r/\alpha) - \frac{1}{\beta^3} (\gamma_i\gamma_j - \delta_{ij}) \gamma_k \dot{M}_0(t - r/\beta) \right] \right\} \end{aligned} \quad (4.19)$$

Since for a shear fracture  $\mathbf{n}$  and  $\mathbf{l}$  are perpendicular ( $n_j l_k \delta_{jk} = 0$ ), this expression can be written as

$$\begin{aligned} u_i = & \frac{1}{4\pi\rho} \left( \frac{1}{r^4} \left[ 30\gamma_i(\gamma_j l_j)(\gamma_k n_k) - 6((\gamma_j l_j)n_i + (\gamma_k n_k)l_i) \right] \int_{r/\alpha}^{r/\beta} \tau M_0(t - \tau) d\tau \right. \\ & \left. + \frac{1}{\alpha^2 r^2} \left[ 12\gamma_i(\gamma_j l_j)(\gamma_k n_k) - 2((\gamma_j l_j)n_i - (\gamma_k n_k)l_i) \right] M_0(t - r/\alpha) \right) \end{aligned}$$

$$\begin{aligned}
& -\frac{1}{\beta^2 r^2} \left[ 12\gamma_i(\gamma_j l_j)(\gamma_k n_k) - 3((\gamma_j l_j)n_i - (\gamma_k n_k)l_i) \right] M_0(t - r/\beta) \\
& + \frac{1}{r} \left\{ \frac{1}{\alpha^3} 2\gamma_i(\gamma_j l_j)(\gamma_k n_k) \dot{M}_0(t - r/\alpha) - \frac{1}{\beta^3} \left[ 2\gamma_i(\gamma_j l_j)(\gamma_k n_k) - n_i(\gamma_j l_j) \right. \right. \\
& \left. \left. - (n_k \gamma_k)l_i \right] \dot{M}_0(t - r/\beta) \right\} \quad (4.20)
\end{aligned}$$

This expression is a sum of four terms; the first depends on  $1/r^4$ , the second and third on  $1/r^2$  and the fourth on  $1/r$ . The term which depends on  $1/r$  represents the far field and those which depend on the higher inverse powers of  $r$  form the near field. The distance at which each field predominates depends on the wavelength of the observations. The near field is only observed at distances of the order of a few wavelengths. For larger distances only the far field is observed. For a point source the far field condition can, then, be expressed as  $r/\lambda \gg 1$ . The amplitude of the displacements is proportional to the scalar seismic moment  $M_0(t)$  and its time rate  $\dot{M}_0(t)$ , whose time dependence must be specified. As we have seen, for a shear fracture model the scalar seismic moment is the product of the shear modulus, the slip and the area of the fault ( $M_0(t) = \mu \Delta u(t) S$ ), and for the equivalent force model it represents the moment of the force couples or of the linear dipoles ( $M_0 = sF(t)$ ).

#### 4.4.1. Near field

---

The *near field* of the displacements is formed by two terms, one depending on  $1/r^4$  and a second depending on  $1/r^2$ . The first is given by

$$\begin{aligned}
& \frac{1}{4\pi\rho} \frac{1}{r^4} (l_j n_k + l_k n_j) \left[ 15\gamma_i \gamma_j \gamma_k - 3(\gamma_i \delta_{jk} + \gamma_j \delta_{ik} + \gamma_k \delta_{ij}) \right] \\
& \times \int_{r/\alpha}^{r/\beta} \tau M_0(t - \tau) d\tau \quad (4.21)
\end{aligned}$$

This term attenuates with the highest inverse power of  $r$  and can only be observed at very short distances from the source. It depends on both  $\alpha$  and  $\beta$ , which means that it is formed by both P and S displacements. The second term, sometimes called the *intermediate field*, is given by

$$\begin{aligned}
& \frac{1}{4\pi\rho} \left\{ \frac{1}{\alpha^2 r^2} (l_j n_k + l_k n_j) (6\gamma_i \gamma_j \gamma_k - \gamma_i \delta_{jk} - \gamma_j \delta_{ik} - \gamma_k \delta_{ij}) M_0(t - r/\alpha) \right. \\
& \left. - \frac{1}{\beta^2 r^2} (l_j n_k + l_k n_j) (6\gamma_i \gamma_j \gamma_k - \gamma_i \delta_{jk} - \gamma_j \delta_{ik} - 2\gamma_k \delta_{ij}) M_0(t - r/\beta) \right\} \quad (4.22)
\end{aligned}$$

In this part of the field the displacements are separated into two motions, which start at different times that depend on the velocities of the P and S waves ( $t = r/\alpha$  and  $t = r/\beta$ ) and are proportional to the seismic moment  $M_0$ .

## Radiation pattern

The form of the *radiation pattern* can be obtained by taking a particular case when the fracture plane is on the  $(x_1, x_2)$  plane,  $\mathbf{n} = (0,0,1)$ , and the slip is in the  $x_1$  direction,  $\mathbf{l} = (1,0,0)$ , or equivalently a double couple with couples along the  $x_1$  and  $x_3$  axes. For the  $1/r^4$  term, putting  $\gamma_1 = \cos \theta$  and  $\gamma_3 = \sin \theta$ , where  $\theta$  is the angle between the  $x_1$  axis and the vector to the observation point, the distributions in the  $(x_1, x_2)$  plane of the  $u_1$  and  $u_3$  displacements are given by

$$\begin{aligned} u_1 &= 6A(5 \cos^2 \theta - 1) \sin \theta \\ u_3 &= 6A(5 \sin^2 \theta - 1) \cos \theta \\ A &= \frac{1}{4\pi\rho r^4} \int_{r/\alpha}^{r/\beta} \tau M_0(t - \tau) d\tau \end{aligned}$$

If the displacements are separated into a radial component  $u_r$  and transverse component  $u_\theta$ , we obtain

$$\begin{aligned} u_r &= 9A \sin 2\theta \\ u_\theta &= 6A \cos 2\theta \end{aligned}$$

The radial component  $u_r$  has maxima at  $\theta = \pi/4, 3\pi/4, 5\pi/4, 7\pi/4$ , is positive in the first and third quadrants, negative in the second and fourth quadrants and null at  $\theta = 0, \pi/2, \pi, 3\pi/2$ . The transverse component has maxima at  $\theta = 0, \pi/2, \pi, 3\pi/2$ , that are alternatively positive and negative, and it is null at  $\theta = \pi/4, 3\pi/4, 5\pi/4, 7\pi/4$  (Fig. 4.4). This distribution is consistent with the orientation of the equivalent system of compressive and tensional forces (PT) at  $45^\circ$  to the directions of the  $x_1$  and  $x_3$  axes.

For the term depending on  $1/r^2$  we need to separate the displacements which begin at  $t = r/\alpha$  and at  $t = r/\beta$ . For the radial and transversal components we obtain

$$\begin{aligned} u_r^\alpha &= 2B \sin 2\theta \\ u_\theta^\alpha &= B \cos 2\theta \end{aligned}$$

where

$$B = \frac{M_0(t - r/\alpha)}{2\pi\rho\alpha^2 r^2}$$

and

$$\begin{aligned} u_r^\beta &= 3C \sin 2\theta \\ u_\theta^\beta &= 3C \cos 2\theta \end{aligned}$$

where

$$C = \frac{M_0(t - r/\beta)}{4\pi\rho\beta^2 r^2}$$

The radiation pattern of the displacements for the parts which depend on  $\alpha$  and  $\beta$  are similar for the radial and transverse components. The azimuthal distribution has a pattern similar

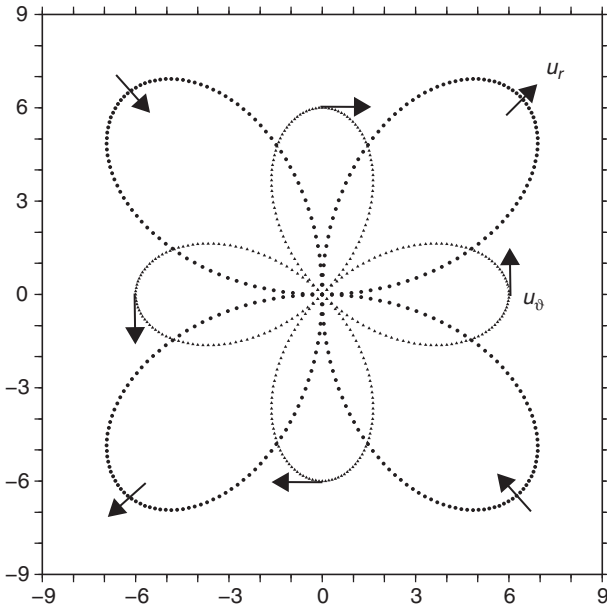


**Figure 4.4.** Radiation pattern distribution of the near-field displacement for the radial component  $u_r$  and the transverse component  $u_\theta$ .

to the displacements depending on  $1/r^4$  that we have seen above (Fig. 4.4). It is of interest, however, to note that the displacements which propagate with velocities  $\alpha$  and  $\beta$  and amplitudes depending on  $1/r^2$  have both radial and transverse components.

### Time function

The time dependence of the near-field displacements is governed by the *source time function*  $M_0(t)$ , the time history of the moment release which for a shear fracture represents the time history of the source slip  $\Delta u(t)$ . The part of the displacement which depends on the distance as  $1/r^4$  depends on time according to the integral in (4.18), while the part depending on  $1/r^2$  depends on time in the same way as the source time function.

Let us consider the simplest possible source time function, namely that given by Heaviside's step function,  $M_0(t) = M_0 H(t)$ . This implies that the slip at the source reaches its maximum value instantaneously and remains constant afterwards. The time dependence of the part of the displacement which depends on distance as  $1/r^4$  is given by the integral in (4.20), which, integrating by parts, can be written as

$$\begin{aligned} & M_0 \int_{r/\alpha}^{r/\beta} \tau H(t - \tau) d\tau \\ &= \frac{M_0}{2} \left[ \left( t^2 - \frac{r^2}{\beta^2} \right) H(t - r/\beta) - \left( t^2 - \frac{r^2}{\alpha^2} \right) H(t - r/\alpha) \right] \end{aligned}$$

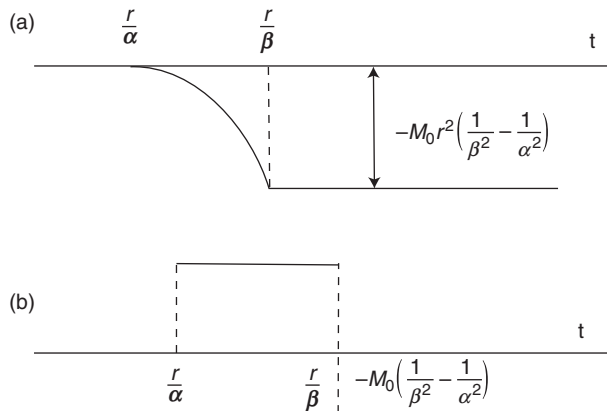


**Figure 4.5.** Time dependence of the near-field displacement of a double-couple point source with a step source time function, for distance dependences (a)  $1/r^4$  and (b)  $1/r^2$ .

The displacement begins at  $t = r/\alpha$  and increases with the square of the time until  $t = r/\beta$ . From this time on the displacement is constant with amplitude  $M_0[(r/\beta)^2 - (r/\alpha)^2]$  (Fig. 4.5a). The part which depends on  $1/r^2$  is the difference of two step functions, one which begins at  $t = r/\alpha$  with amplitude  $M_0/\alpha^2$  and the second which begins at  $t = r/\beta$  with amplitude  $M_0/\beta^2$  (Fig. 4.5b). From  $t = r/\alpha$  the displacement depends in both cases on  $1/r^2$ . The near field is, then, formed by permanent displacements with radial and transversal components, which begin with a first arrival with velocity  $\alpha$  and change character after a second arrival with velocity  $\beta$ .

The step function is a simplification of the source time function, since physically the slip at the source takes a time  $\tau_r$ , called the *rise time*, to reach its maximum value. This affects the form of the time dependence of the displacements, as we will see later in detail.

#### 4.4.2. Far field

The *far-field* displacements are given by the terms which decay with distance as  $1/r$ ; then can be separated into two parts, one that arrives with velocity  $\alpha$ , the P waves, and another with velocity  $\beta$ , the S waves:

$$u_i^P = \frac{1}{4\pi\rho\alpha^3 r} (l_j n_k + l_k n_j) \gamma_j \gamma_k \gamma_l \dot{M}_0 (t - r/\alpha) \quad (4.23)$$

$$u_i^S = \frac{-1}{4\pi\rho\beta^3 r} (l_j n_k + l_k n_j) (\gamma_i \gamma_j - \delta_{ij}) \gamma_k \dot{M}_0 (t - r/\beta) \quad (4.24)$$

Taking into account that  $\mathbf{n}$  and  $\mathbf{l}$  are perpendicular ( $n_k l_k = 0$ ), as in (4.20), we can also write

$$u_i^P = \frac{1}{4\pi\rho r} \left[ \frac{1}{\alpha^3} 2\gamma_i (\gamma_j l_j) (\gamma_k n_k) \dot{M}_0 (t - r/\alpha) \right] \quad (4.25)$$

$$u_i^S = \frac{1}{4\pi\rho r} \left[ \frac{-1}{\beta^3} (2\gamma_i (\gamma_j l_j) (\gamma_k n_k) - n_i (\gamma_j l_j) - (n_k \gamma_k) l_i) \dot{M}_0 (t - r/\beta) \right] \quad (4.26)$$

For the equivalent double-couple source with couples in the directions  $\mathbf{X}$  and  $\mathbf{Y}$  we put into equations (4.23)–(4.26)  $X_i = l_i$  and  $Y_i = n_i$ . In terms of the  $\mathbf{P}$  and  $\mathbf{T}$  axes, according to (4.9), (4.23) and (4.24), the displacements are given by

$$u_i^P = \frac{1}{4\pi\rho\alpha^3 r} (T_j T_k - P_k P_j) \gamma_j \gamma_k \gamma_i \dot{M}_0(t - r/\alpha) \quad (4.27)$$

$$u_i^S = \frac{-1}{4\pi\rho\beta^3 r} (T_j T_k - P_k P_j) (\delta_{ij} - \gamma_i \gamma_j) \gamma_k \dot{M}_0(t - r/\beta) \quad (4.28)$$

We should note that the interchangeability present in equations (4.23) and (4.24) regarding  $\mathbf{n}$  and  $\mathbf{l}$  does not exist in equations (4.27) and (4.28) for  $\mathbf{P}$  and  $\mathbf{T}$ . In both cases the displacements depend on the time derivative of the source time function. In the shear fracture model the displacements in the far field do not depend on the slip at the source but on the slip velocity or rate at the source. This means that the energy radiated towards the far field lasts only during the time that the source is moving; it ceases when the source stops.

### Radiation pattern

In the same way as for the near field, we now consider for the far field the distribution of amplitudes around the source, i.e. the radiation pattern. We will consider first the particular case of a fault in the  $(x_1, x_2)$  plane,  $\mathbf{n} = (0, 0, 1)$ , with slip in the  $x_1$  direction, that is,  $\mathbf{l} = (1, 0, 0)$ , and look for the amplitude distribution of far-field displacements in the  $(x_1, x_3)$  plane. Putting as before  $\gamma_1 = \cos \theta$  and  $\gamma_3 = \sin \theta$ , we obtain

$$\begin{aligned} u_1^P &= A \sin 2\theta \cos \theta \\ u_3^P &= A \sin 2\theta \sin \theta \end{aligned} \quad (4.29)$$

where

$$A = \frac{\dot{M}_0(t - r/\alpha)}{4\pi\rho\alpha^3 r}$$

and

$$\begin{aligned} u_1^S &= -B \cos 2\theta \sin \theta \\ u_3^S &= B \cos 2\theta \cos \theta \end{aligned} \quad (4.30)$$

where

$$B = \frac{\dot{M}_0(t - r/\beta)}{4\pi\rho\beta^3 r}$$

Transforming into radial and transverse components we obtain

$$u_r^P = A \sin 2\theta$$

$$u_\theta^S = B \cos 2\theta$$

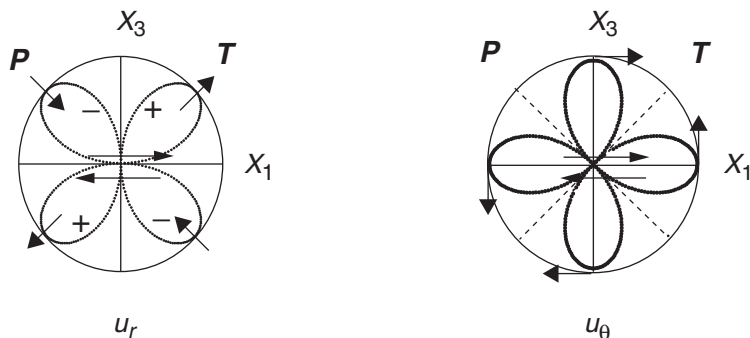


**Figure 4.6.** Radiation pattern distribution of the far-field displacement of a double-couple or shear-fracture point source for P ( $u_r$ ) and S ( $u_\theta$ ) wave amplitudes. The pairs of horizontal arrows indicate the direction of  $\Delta\mathbf{u}$ .

In the far field, the P waves have only a radial component and the S waves only transverse components. The radiation patterns for the P and S waves both have four *lobes* or *quadrants* (Fig. 4.6).

For the P waves the lobes have alternating directions of motion, either outward or positive (compressions) or inward or negative (dilatations), separated by two perpendicular nodal planes ( $x_1, x_2$ ) and ( $x_3, x_2$ ); the first (normal to  $\mathbf{n}$ ) corresponds to the *fault plane* and the second (normal to  $\mathbf{l}$ ) is called the *auxiliary plane*. The maximum amplitudes are at  $45^\circ$  to the directions of  $\mathbf{n}$  and  $\mathbf{l}$ , that is, in the directions of the  $\mathbf{P}$  and  $\mathbf{T}$  axes. For the S waves the motion changes direction in the lobes and points toward the  $\mathbf{T}$  axis and away from the  $\mathbf{P}$  axis. The maximum amplitudes coincide with the direction of  $\mathbf{n}$  and  $\mathbf{l}$  and nodal planes are at  $45^\circ$  to them.

In both cases the radiation pattern is symmetric and we can interchange  $\mathbf{n}$  and  $\mathbf{l}$  without changing the result. This is a consequence of the symmetry with respect to  $\mathbf{n}$  and  $\mathbf{l}$  in equations (4.23) and (4.24). For this reason the amplitude radiation patterns of the P and S waves cannot be used to distinguish between the fault plane and the auxiliary plane. This ambiguity is present in all methods used to determine the orientation of the point source mechanism from the far-field displacements of P and S waves. However, this ambiguity does not exist for  $\mathbf{P}$  and  $\mathbf{T}$ , which are always properly identified by the signs of the P wave displacements.

A useful concept in point-force focal studies is that of the *focal sphere*, a sphere of unit radius and constant velocity surrounding the focus (Fig. 2.1). A stereographic projection of the focal sphere is shown in Fig. 1.5 along with the location of the fault plane and the axes  $\mathbf{X}$ ,  $\mathbf{Y}$ ,  $\mathbf{P}$  and  $\mathbf{T}$ . A system of Cartesian coordinates  $(x_1, x_2, x_3)$  is defined, called the source system, with  $x_1$  in the direction  $\mathbf{l}$  and  $x_3$  in the direction  $\mathbf{n}$ , so that  $(x_1, x_2)$  is the fault plane and  $(x_1, x_3)$  the auxiliary plane. We use spherical coordinates  $(r, \theta, \phi)$ , with the  $\theta$  angle measured from  $x_3$  and  $\phi$  measured from  $x_1$  on the  $(x_1, x_2)$  plane. The direction cosines of the ray  $r$ , with respect to the source system for a point on the surface of the focal sphere, are

$$\gamma_1 = \sin \theta \cos \phi \quad (4.31)$$

$$\gamma_2 = \sin \theta \sin \phi \quad (4.32)$$

$$\gamma_3 = \cos \theta \quad (4.33)$$

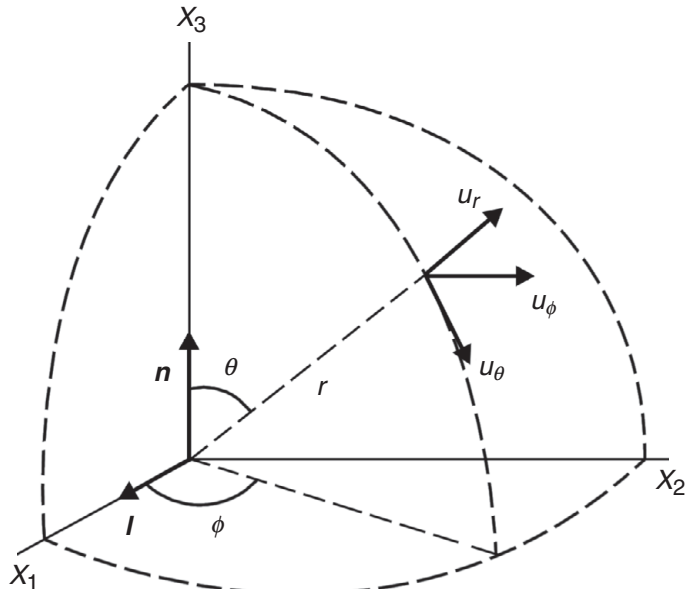


**Figure 4.7.** Orientation of the point source given by the unit vectors  $\mathbf{n}$  and  $\mathbf{l}$  and the corresponding displacements components  $(u_r, u_\theta, u_\phi)$  at distance  $r$ .

At each point of the spherical surface we define a system of Cartesian coordinates with unit vectors  $(\mathbf{e}_r, \mathbf{e}_\theta, \mathbf{e}_\phi)$  in the directions of the increments of  $r$ ,  $\theta$  and  $\phi$ . The components of the displacements in these directions correspond to P, SV and SH waves (Fig. 4.7) and are given by

$$\text{P : } u_r = A \sin 2\theta \cos \phi \quad (4.34)$$

$$\text{SV : } u_\theta = B \cos 2\theta \cos \phi \quad (4.35)$$

$$\text{SH : } u_\phi = -B \cos \theta \sin \phi \quad (4.36)$$

The *nodal planes* of the displacements of P waves occur for  $\theta = 90^\circ$ , which is the  $(x_1, x_2)$  plane, and  $\phi = 90^\circ$ , which is the  $(x_2, x_3)$  plane. The displacements of the SV motion have a nodal plane for  $\phi = 90^\circ$  (the  $(x_2, x_3)$  plane) and are null also for points of intersection of the surface of the focal sphere and the solid angles  $\theta = 45^\circ$  and  $135^\circ$ . The displacements in the SH motion have two nodal planes, for  $\theta = 90^\circ$  and  $\phi = 0^\circ$ .

### Time function

The time dependence of the displacements in the far field has the same form as the derivative of the source time function (see (4.23) and (4.24)) with separated arrivals for the P and S waves. As we have already seen, this means that the source radiates energy in the far field only during the time it is moving, the energy therefore depends not on the slip but on the slip velocity. This means that a source that moves very slowly will generate

very low amplitude waves in the far field. For the simplest case, when the source time function is a step function, the displacements at the far field have the form of impulses ( $dH(t)/dt = \delta(t)$ ). If at the source the slip  $\Delta u$  takes a time  $\tau_r$  (the rise time) to reach its maximum value then the impulses will have a certain width depending on the value of  $\tau_r$ . We will examine this question in [Section 4.8](#). We will see later that the widths of the P and S wave impulses also depend on the dimensions of the source.

## 4.5. The geometry of a shear fracture

The *geometry of a shear fracture* is defined by the two orthogonal unit vectors  $\mathbf{n}$  and  $\mathbf{l}$ ;  $\mathbf{n}$  is the normal to the fault plane and  $\mathbf{l}$  is the direction of slip. For the equivalent double-couple source the axes  $\mathbf{X} = \mathbf{l}$  and  $\mathbf{Y} = \mathbf{n}$  are each in the direction of one couple. The orientations of these two vectors  $\mathbf{l}$  and  $\mathbf{n}$  with respect to the geographical axes (north, east, nadir), can be expressed by the angles  $\theta_l$  and  $\theta_n$ , respectively, measured from the positive of  $x_3$  (the vertical) and the angles  $\phi_l$  and  $\phi_n$ , respectively, measured from  $x_1$  (north) on the horizontal plane ( $x_1, x_2$ ), so that the components of  $\mathbf{n}$  are

$$n_1 = \sin \theta_n \cos \phi_n \quad (4.37)$$

$$n_2 = \sin \theta_n \sin \phi_n \quad (4.38)$$

$$n_3 = \cos \theta_n \quad (4.39)$$

and similarly for those of  $\mathbf{l}$ . Since  $\mathbf{n}$  and  $\mathbf{l}$  are orthogonal unit vectors, only three of their components are independent. The same can be established for the  $\mathbf{T}$  and  $\mathbf{P}$  vectors in terms of the angles  $\theta_T$ ,  $\phi_T$ , and  $\theta_P$ ,  $\phi_P$ .

We saw in [Section 1.3](#) that the orientation of a fault is defined by three angles: the azimuth  $\phi$ , the dip  $\delta$  and the slip or rake  $\lambda$  ([Fig. 1.4](#)). The relations of  $\phi$ ,  $\delta$  and  $\lambda$  to the angles which define the geographical orientations of the vector  $\mathbf{n}$  and  $\mathbf{l}$  are given by ([Fig. 4.8](#))

$$\phi = \phi_n - \pi/2 \quad (4.40)$$

$$\delta = \theta_n \quad (4.41)$$

$$\lambda = \sin^{-1}(\cos \theta_l / \sin \theta_n) \quad (4.42)$$

The components of  $\mathbf{n}$  and  $\mathbf{l}$  referred to the geographical axes can now be written in term of  $\phi$ ,  $\delta$  and  $\lambda$  in the form

$$n_1 = -\sin \delta \sin \phi \quad (4.43)$$

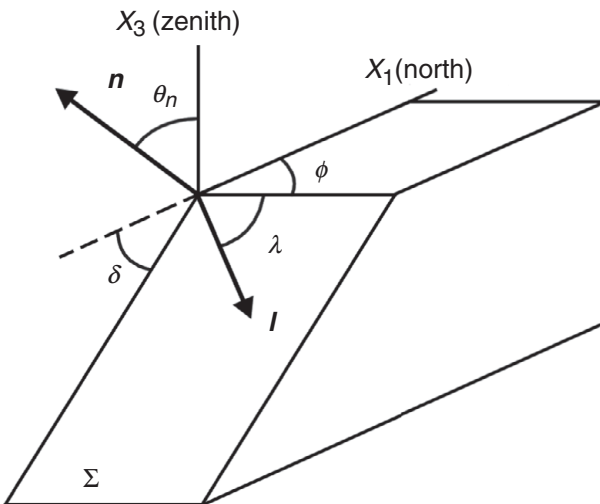
$$n_2 = \sin \delta \cos \phi \quad (4.44)$$

$$n_3 = -\cos \delta \quad (4.45)$$

$$l_1 = \cos \lambda \cos \phi + \cos \delta \sin \lambda \sin \phi \quad (4.46)$$

$$l_2 = \cos \lambda \sin \phi - \cos \delta \sin \lambda \cos \phi \quad (4.47)$$

$$l_3 = -\sin \lambda \sin \delta \quad (4.48)$$

**Figure 4.8.**

Correspondence between the unit vectors  $\mathbf{n}$  and  $\mathbf{l}$  and the angles  $\phi, \delta, \lambda$  defining the orientation of motion on a shear fault.

The orientation of the source is always given uniquely by only three parameters, namely,  $\phi, \delta, \lambda$  or  $\theta_n, \phi_n, \theta_l$  or  $\theta_P, \phi_P, \theta_T$ . The first choice implies that we have identified the fault plane correctly. Because there is always ambiguity between the  $\mathbf{l}$  and  $\mathbf{n}$  axes, that is, between the fault plane and the auxiliary plane, the values of  $\phi, \delta, \lambda$  must be given for both planes although the motion in one plane identifies the solution completely. The solution in terms of the stress axes does not have this ambiguity and the orientations of the  $\mathbf{P}$  and  $\mathbf{T}$  axes are uniquely defined.

## 4.6. Far-field displacements referred to geographical axes

Displacements of P waves and of the SV and SH components of S waves can be referred to the geographical axes through the direction of a seismic ray. If we consider points on the surface of the focal sphere, the rays are straight lines from its center. The direction cosines of a ray referred to the geographical coordinates (north, east, nadir) are given by

$$\gamma_1 = \sin i \cos \phi' \quad (4.49)$$

$$\gamma_2 = \sin i \sin \phi' \quad (4.50)$$

$$\gamma_3 = \cos i \quad (4.51)$$

where  $i$  is the *take-off angle* of the ray measured from the downward vertical (the nadir) and  $\phi'$  is the *azimuth* of the ray measured from north (Fig. 4.9). The displacement of the P wave is in the same direction as the ray, so its direction cosines are  $\gamma_i$ . The displacement of the SV component of the S wave is normal to the ray on the vertical plane, and that of

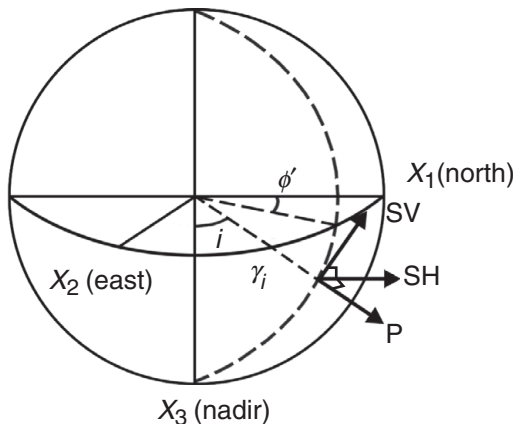


**Figure 4.9.** Geographical axes (north, east, nadir) at the focal sphere and the P, SH and SV displacements at a point on its surface for a ray leaving the source with take-off angle  $i$  and azimuth  $\phi'$  ( $\gamma_i$  are the direction cosines of the ray).

the SH component is normal to the ray on the horizontal plane. The direction cosines of a unit vector in the direction of SV and SH are

$$v_1 = \cos i \cos \phi' \quad (4.52)$$

$$v_2 = \cos i \sin \phi' \quad (4.53)$$

$$v_3 = -\sin i \quad (4.54)$$

$$h_1 = -\sin \phi' \quad (4.55)$$

$$h_2 = \cos \phi' \quad (4.56)$$

$$h_3 = 0 \quad (4.57)$$

Using equations (4.25) and (4.26) we can calculate the displacements for the P, SV and SH waves in terms of  $\mathbf{n}$  and  $\mathbf{l}$ , projecting onto the appropriate directions:  $\boldsymbol{\gamma}$  (P),  $\boldsymbol{v}$  (SV) and  $\boldsymbol{h}$  (SH):

$$u^P = 2A(\gamma_j l_j)(\gamma_k n_k) \quad (4.58)$$

$$u^{SV} = B[(n_j v_j)(\gamma_k l_k) + (n_j \gamma_j)(l_k v_k)] \quad (4.59)$$

$$u^{SH} = B[(n_j h_j)(\gamma_k l_k) + (n_j \gamma_j)(l_k h_k)] \quad (4.60)$$

where  $A$  and  $B$  are given by (4.29) and (4.30) and the Einstein summation convention is used.

The displacements in the P, SV and SH waves in terms of  $\mathbf{T}$  and  $\mathbf{P}$  are given from (4.27) and (4.28) by

$$u^P = A[(T_j \gamma_j)^2 - (P_j \gamma_j)^2] \quad (4.61)$$

$$u^{SV} = B\{(T_j v_j)(T_k \gamma_k) - (P_k v_k)(P_j \gamma_j) - [(T_k \gamma_k)^2 - (P_j \gamma_j)^2](\gamma_k v_k)\} \quad (4.62)$$

$$u^{\text{SH}} = B \{ (T_j h_j)(T_k \gamma_k) - (P_k h_k)(P_j \gamma_j) - [(T_k \gamma_k)^2 - (P_j \gamma_j)^2](\gamma_k h_k) \} \quad (4.63)$$

From equations (4.58) to (4.60) and (4.61) to (4.63) we can obtain the P, SV and SH displacements in terms of  $\mathbf{n}$  and  $\mathbf{l}$  or  $\mathbf{T}$  and  $\mathbf{P}$ , referring all the vectors involved to the geographical axes.

To express the P, SV and SH displacements in terms of  $\phi$ ,  $\delta$ ,  $\lambda$ , we substitute into (4.58)–(4.60) the components of  $\gamma$  (4.49)–(4.51),  $\mathbf{v}$  (4.52)–(4.54) and  $\mathbf{h}$  (4.55)–(4.57), referred to the geographical axes, and  $\mathbf{l}$  (4.46)–(4.48) and  $\mathbf{n}$  (4.43)–(4.45) in terms of  $\phi$ ,  $\delta$ ,  $\lambda$ , obtaining

$$\begin{aligned} u^{\text{P}} = A & \{ \sin^2 i [\cos \lambda \sin \delta \sin 2(\phi' - \phi) - \sin \lambda \sin 2\delta \sin^2(\phi' - \phi)] \\ & + \sin 2i [\sin \lambda \cos 2\delta \sin(\phi' - \phi) - \cos \lambda \cos \delta \cos(\phi' - \phi)] \\ & + \cos^2 i \sin \lambda \sin 2\delta \} \end{aligned} \quad (4.64)$$

$$\begin{aligned} u^{\text{SV}} = B & \left\{ \frac{1}{2} \sin 2i [\cos \lambda \sin \delta \sin 2(\phi' - \phi) - \sin \lambda \sin 2\delta (1 + \sin^2(\phi' - \phi))] \right. \\ & \left. + \cos 2i [\sin \lambda \cos 2\delta \sin(\phi' - \phi) - \cos \lambda \cos \delta \cos(\phi' - \phi)] \right\} \end{aligned} \quad (4.65)$$

$$\begin{aligned} u^{\text{SH}} = B & \left\{ \sin i [\sin \delta \cos \lambda \cos 2(\phi' - \phi) - \frac{1}{2} \sin 2\delta \sin \lambda \sin 2(\phi' - \phi)] \right. \\ & \left. + \cos i [\cos 2\delta \sin \lambda \cos(\phi' - \phi) + \cos \delta \cos \lambda \sin(\phi' - \phi)] \right\} \end{aligned} \quad (4.66)$$

These equations allow calculation of the far-field displacements of the P and S waves at a particular point specified by its distance, take-off angle and azimuth,  $(r, i, \phi')$ , generated by a point shear fracture or DC source, with a known orientation of the source,  $(\phi, \delta, \lambda)$ , and scalar seismic moment with known source time function  $M_0(t)$ .

## 4.7. Source representation using the focal sphere

We can use the concept of the focal sphere, introduced in section 4.4.2, to represent graphically the orientation of the source mechanism with respect to the geographical axes (north, east, nadir). The orientation of a point shear fracture or DC source is given by the  $\mathbf{n}$  and  $\mathbf{l}$  axes, the  $\mathbf{P}$  and  $\mathbf{T}$  axes or the  $\phi$ ,  $\delta$  and  $\lambda$  angles of orientation of the fault plane. As we have seen, the radiation pattern of the displacements of P waves has two mutually orthogonal nodal planes, which separate quadrants of compression and dilatation; each of these planes may represent the actual fault plane. On the focal sphere, then, we can represent the orientation of the source by plotting the axes  $\mathbf{n}(\theta_n, \phi_n)$ ,  $\mathbf{l}(\theta_l, \phi_l)$ ,  $\mathbf{P}(\theta_P, \phi_P)$  and  $\mathbf{T}(\theta_T, \phi_T)$  and the two possible fault planes identified by the angles  $(\phi, \delta, \lambda)$ . The  $\mathbf{T}$  axis is at the center of the compression quadrants and the  $\mathbf{P}$  axis is at the center of the dilatation quadrants. Usually these parameters are plotted on the stereographic horizontal projection of the lower hemisphere of the focal sphere, since observations at teleseismic distances correspond to rays radiated downward from the source (Fig. 4.10).

The distribution of the *polarity* quadrants (compressions and dilatations) of the P waves for the four types of faults discussed in section 1.3, namely, strike-slip and dip-slip, vertical, normal and reverse, on a horizontal and vertical projection, are shown in

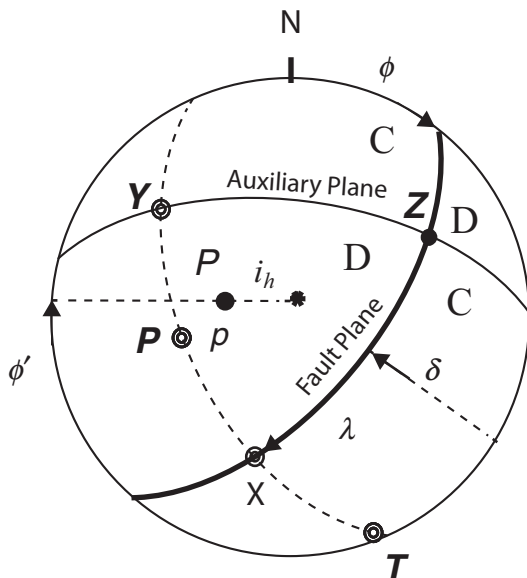


**Figure 4.10.** Stereographic projection of the lower hemisphere of the focal sphere, with the orientation of the fault plane ( $\phi'$ ,  $\delta$ ,  $\lambda$ ), the axes **X** ( $n$ ), **Y** ( $l$ ), **Z**, **P** and **T** and the location of an observation point  $p(i_h, \phi')$ . D, dilatations quadrants; C, compressions quadrants.

**Fig. 4.11.** The two nodal planes represent the possible fault planes. This type of representation, known as *beach ball*, is very useful since it allows a rapid recognition of the type of faulting present in an earthquake. Seismotectonic studies make wide use of this representation, plotted on a map, to interpret the orientation of earthquake mechanisms in relation to tectonic and geological features.

The beach ball type of representation can be used also to plot the polarities of the SH and SV components of the S waves. Now the nodal surfaces which separate regions of opposite polarity are not always planes. The horizontal projections of the distributions of P and SH waves corresponding to the four types of fault orientation are shown in Fig. 4.12.

## 4.8. The source time function

The *source time function* (STF) represents the time dependence of the seismic moment  $M_0(t)$  or, equivalently, for a shear fracture, of the slip  $\Delta u(t)$  at the source and is an important characteristic of the focal mechanism. We have seen that in the far field the elastic displacements (4.23) and (4.24) depend on the time derivative of the moment or *moment rate*,  $\dot{M}_0(t)$ . For this reason, it is convenient to model directly the moment rate; note that its time dependence by itself is often called the STF. We have already considered the simplest form of the STF, that is, the step function  $M_0(t) = M_0 H(t)$ . Use of this function

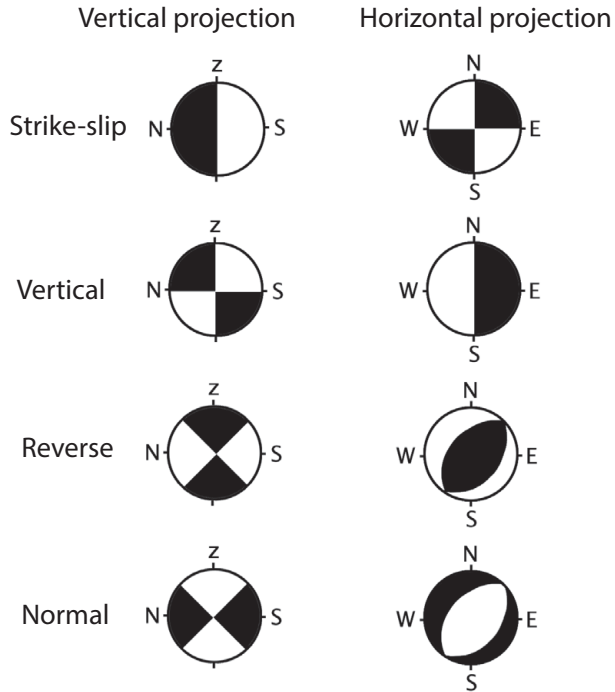


**Figure 4.11.** Vertical and horizontal projections of the P wave distribution on the focal sphere corresponding to strike-slip, vertical, reverse and normal faults. The black quadrants correspond to compressions and the white quadrants to dilatations.

implies that the moment reaches its maximum value  $M_0$  instantaneously at time  $t = 0$  and then remains constant (Fig. 4.13a). This means that once the fault has moved it does not return to its initial state. This instantaneous motion is not only unrealistic, but it produces a far-field displacement pulse ( $\dot{M}_0$ ) with the form of a Dirac function, which is mechanically unacceptable (Fig. 4.14a).

The solution to this problem is to introduce an STF that includes a rise time  $\tau_r$ , that is, the time taken by the slip to reach its maximum value, as already mentioned. An example of an STF of this type is the following:

$$M_0(t) = M_0 \left[ \frac{t}{\tau_r} H(t) - \frac{t - \tau_r}{\tau_r} H(t - \tau_r) \right] \quad (4.67)$$

The moment release begins at  $t = 0$  and increases linearly from  $t = 0$  to  $t = \tau_r$ , the time when it reaches its maximum value  $M_0$  (i.e. at the maximum of  $\Delta u$ ) and then stays constant (Fig. 4.13b).

For the model with a linear increase in the moment until the time  $\tau_r$  (4.67), the moment rate has the form of a rectangular impulse of duration  $\tau_r$  (Fig. 4.14b):

$$\dot{M}_0(t) = \dot{M}_0 [H(t) - H(t - \tau_r)] \quad (4.68)$$

In this model the moment or slip rate jumps instantaneously from zero to its maximum value  $\dot{M}_0$  and keeps this value during the time  $\tau_r$ , after which it stops abruptly (Fig. 4.14b).

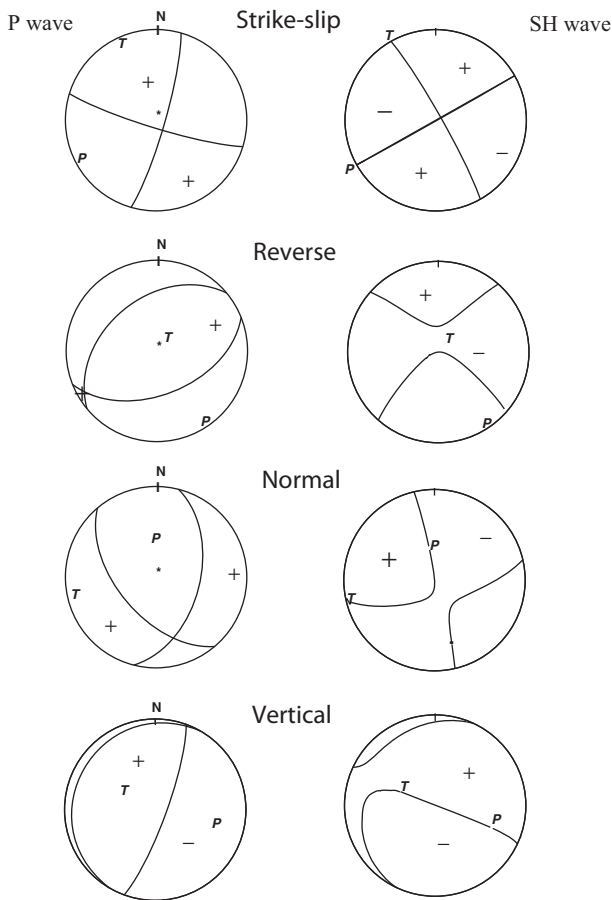


**Figure 4.12.** Horizontal projection of the radiation pattern of P and SH waves on the focal sphere corresponding to strike-slip, reverse, normal and vertical faults. Plus sign, positive amplitude; minus sign, negative amplitude.

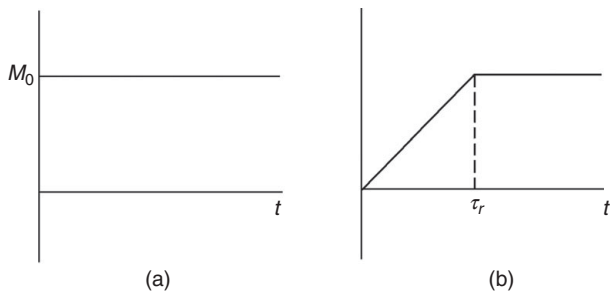


**Figure 4.13.** Seismic moment  $M_0(t)$  source time functions: (a) Heaviside step function; (b) linear increase with rise time  $\tau_r$ .

This source time function is not continuous, so that the ground velocity in the far field presents singularities at the beginning of the signal and at the end. The radiated energy from an earthquake is proportional to the square of the velocity field, so that a signal like (4.68) transports an infinite amount of energy. Therefore it is not an acceptable STF.

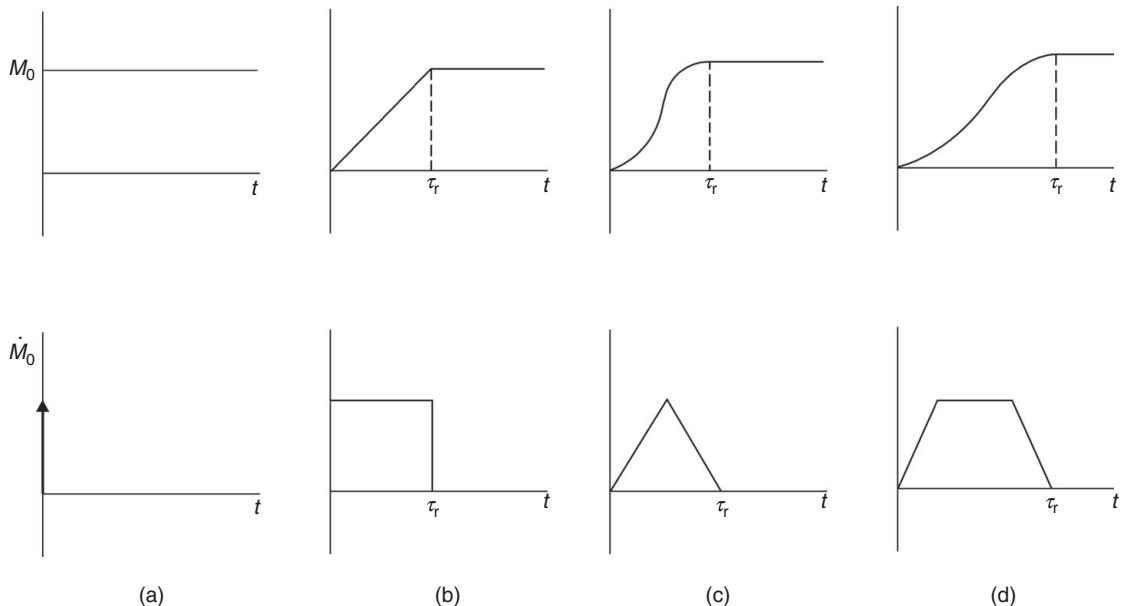


**Figure 4.14.** Four types of seismic moment  $M_0(t)$  and the corresponding moment-rate source time functions. (a) Heaviside step function; (b) linear increase; (c) continuous increase; (d) longer continuous increase. Moment rate  $\dot{M}_0(t)$ : (a) delta function; (b) boxcar; (c) triangle; (d) trapezoid.

A more realistic STF is one in which the moment rate or *slip velocity* is continuous, increasing from zero to a maximum value and then decreasing again to zero. An STF for a slip rate in which the increase and decrease in slip velocity are linear (the triangular shape) is given by

$$\begin{aligned}\dot{M}_0(t) &= M_0 \frac{4t}{\tau_r^2}, & 0 < t \leq \tau_r/2 \\ \dot{M}_0(t) &= M_0 \frac{4(\tau_r - t)}{\tau_r^2}, & \tau_r/2 < t \leq \tau_r\end{aligned}\quad (4.69)$$

and is equal to zero for times less than 0 and greater than  $\tau_r$ . The moment rate (4.69) increases from zero to its maximum value ( $2M_0/\tau_r$ ) in the interval from  $t = 0$ , to  $t = \tau_r/2$  and decreases again to zero in the interval from  $t = \tau_r/2$  to  $t = \tau_r$  (Fig. 4.14c). In the first part of the process the moment acceleration is positive and in the second negative.

Integrating (4.69) we may compute the moment function:

$$\begin{aligned}M_0(t) &= M_0 \frac{2t^2}{\tau_r^2}, & 0 < t \leq \tau_r/2 \\ M_0(t) &= M_0 \left[ \frac{2t(2\tau_r - t)}{\tau_r^2} - 1 \right], & \tau_r/2 < t \leq \tau_r \\ M_0(t) &= M_0, & \tau_r < t\end{aligned}\quad (4.70)$$

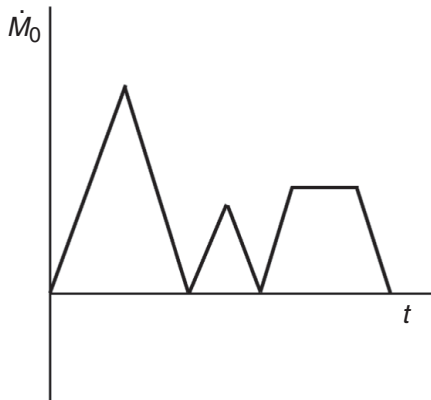


**Figure 4.15.** Example of a complex moment-rate source time function.

We observe that the moment function increases smoothly from zero to the maximum (or static) value  $M_0$  (Fig. 4.14c).

If we want to increase the duration of the source process we can use a STF of trapezoidal form in which the velocity maintains its maximum value during a certain time (Fig. 4.14d). A more complex type of point source can also be modeled by considering STFs consisting of several triangles or trapezoids each corresponding to a different subevent (Fig. 4.15). We must remember that in the point source model the only time parameter is the rise time  $\tau_r$ . This parameter can be used to model, using a point source, the total time duration of the fracture process over an extended source, although its meaning is not actually equivalent; in an extended source the total duration  $T$  of the fracture process depends on the dimension of the fault and the velocity of fracture propagation  $v$  ( $T = L/v$ ), while at each point of the fault there is a certain rise time  $\tau_r$ , which is the time it takes the slip to reach its maximum value at that point. Thus for an extended source  $T$  and  $\tau_r$  are in fact independent. Using the point source model we can consider  $\tau_r$  to represent  $T$ , in a certain way, but this is only a rough approximation and from this value we may not derive  $L$  by assuming a value of  $v$ .

Finally, we consider another very important source time function, which was proposed by Brune (1970) as a model of the radiation we can expect from a large variety of small earthquakes. In this model the moment is a continuous function of time:

$$M_0(t) = M_0[1 - (1 + t/\tau_r) e^{-t/\tau_r}] H(t) \quad (4.71)$$

where  $H(t)$  is the Heaviside function. This moment function has the following moment rate:

$$\dot{M}_0(t) = M_0 \frac{t}{\tau_r^2} e^{-t/\tau_r} H(t) \quad (4.72)$$

In this case the rise time  $\tau_r$  measures the duration of the source but the moment (4.71) continues to grow asymptotically to a value  $M_0$  after this time.

## 4.9. Spectral properties of the source time function

Some of the most useful and universal properties of source time functions are obtained in the *spectral domain*. The frequency dependence of the STF can be determined using its Fourier transform (FT). For a function of time  $f(t)$ , its Fourier transform  $F(\omega)$  is given by the pair of expressions

$$F(\omega) = \int_{-\infty}^{\infty} f(t) e^{-i\omega t} dt \quad (4.73)$$

$$f(t) = \frac{1}{2\pi} \int_{-\infty}^{\infty} F(\omega) e^{i\omega t} d\omega \quad (4.74)$$

In the absence of a rise time the STF is given by the step function  $H(t)$  and its amplitude FT decays with frequency as  $1/\omega$ . For the two STFs that are realistic, the triangular STF (4.69) (Fig. 4.16b) and Brune's signal (4.71) (Fig. 4.16a), we can compute their FTs, which are respectively

$$M_0(\omega) = \frac{M_0}{\omega} \left[ \frac{\tau_r \sin(\omega\tau_r/2)}{\omega\tau_r/2} \right] \exp[i(\omega\tau_r/2 - \pi/2)] \quad (4.75)$$

$$M_0(\omega) = \frac{M_0}{1 + \omega^2\tau_r^2} \quad (4.76)$$

In both cases the amplitude spectrum decays with frequency as  $1/\omega^2$  (Figs. 4.16c and 4.16d).

A property of the Fourier transform (4.73) of the moment rate function is that at low frequencies, when  $\omega \rightarrow 0$ ,

$$\lim_{\omega \rightarrow 0} \dot{M}_0(\omega) = M_0 \quad (4.77)$$

That is, at low frequencies the amplitude of the Fourier spectrum approximates the time integral of the STF and therefore the moment of the earthquake. The two source time functions (4.75) and (4.76) clearly exhibit this property.

As the frequency increases, at a frequency  $\omega_c = 1/\tau_r$  called the *corner frequency* the amplitude of the spectrum begins to decay as  $1/\omega^2$  (Fig. 4.16c). This dependence on frequency of the amplitude spectrum of the STF is a very general characteristic of seismic sources which have limited time duration. Since the displacements in the far field have the same time dependence as the moment rate, their amplitude spectra will also decay with frequency as  $1/\omega^2$ . This corresponds to the frequency decay of the amplitude spectra of many observed far-field body waves.

For a point source model with finite rise time  $\tau_r$ , the spectrum of the source time function  $\dot{M}_0$  can be approximated, in a general form, by a constant value for low frequencies and a high-frequency decay us  $1/\omega^2$  for frequencies greater than  $\omega_c$  (Aki, 1967; Brune 1970; Madariaga, 2009)

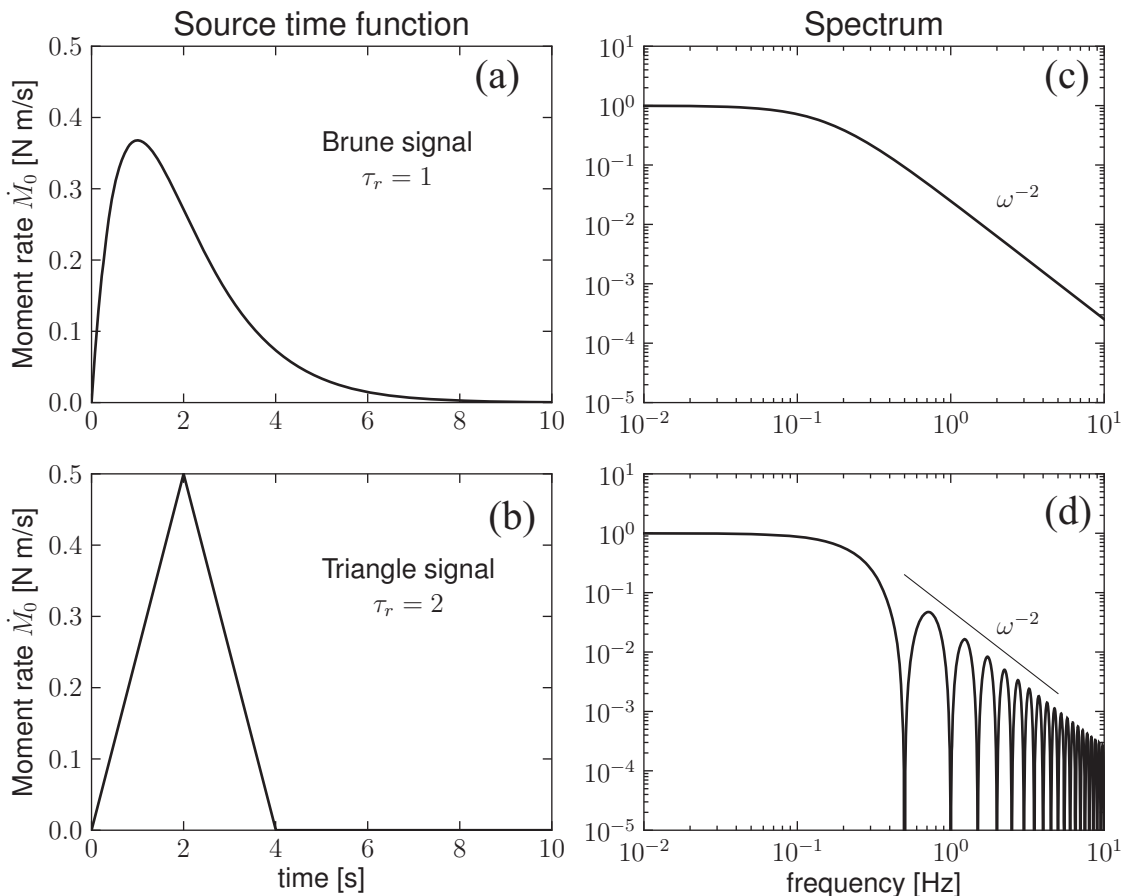


**Figure 4.16.** Fourier amplitude transform of moment-rate source time functions with rise time  $\tau_r$ : (a) Brune signal; (b) triangular signal; (c) spectrum of Brune signal; (d) spectrum of triangle signal

$$\dot{M}_0(\omega) = \frac{M_0}{1 + (\omega/\omega_c)^2} \quad (4.78)$$

where the corner frequency  $\omega_c$  is related to the inverse of the rise time,  $\omega_c \sim 1/\tau_r$ . The spectrum of the time derivative of (4.78) is related to the particle acceleration field that we will use to determine the radiated energy in the next section,

$$\ddot{M}_0(\omega) = \frac{i\omega M_0}{1 + (\omega/\omega_c)^2} \quad (4.79)$$

This has the same form as the spectrum of a time function of triangular shape (4.75) since it begins to decrease with frequency as  $1/\omega^2$  at  $\omega = \omega_c$ . It must be remembered that, for a point source, the only parameter which describes the duration of the process is the rise time  $\tau_r$ .

In conclusion, the parameters for a point source with rise time are nine, namely: three hypocentral coordinates and the origin time ( $\phi_0, \lambda_0, h, t_0$ ); three specifying the orientation

of the mechanism, assuming it to be a shear fault ( $\phi, \delta, \lambda$ ); the rise time  $\tau_r$  and the final or static value of the seismic moment  $M_0$ . The point source model provides information on the location and time of occurrence of an earthquake, its size, its mechanism, represented by the orientation of a shear fault or a double couple, and its source time duration.

## 4.10. Seismic energy radiation

The energy dissipated at an earthquake, as we saw in [Section 1.6](#), is divided into the energy dissipated in the focal region by non-elastic processes and heat and the energy radiated outside the source in the form of elastic waves. For a point source, the non-elastic processes are concentrated at a point. Considering an infinite homogeneous perfectly elastic isotropic medium, the elastic energy per unit volume outside the point source is given by the sum of the *kinetic energy*  $K$  and the *potential energy*  $U$  ([Madariaga, 2009](#))

$$K(t) + U(t) = \frac{\rho}{2} \dot{u}_i \dot{u}_i + \frac{1}{2} \tau_{ij} e_{ij} \quad (4.80)$$

In the far field it can be readily proven that the two terms in (4.80) are the same, so that in the far field the energy flux of elastic waves of velocity  $c$  across a surface whose normal is in the direction of the unit vector  $h_i$  is given by ([Hudson, 1980](#), p. 28)

$$\rho c |\dot{u}_i|^2 h_i \quad (4.81)$$

The total energy radiated by the point source across a spherical surface surrounding the source is the integral of the energy flows of the P and S waves across this surface:

$$E = \rho \int_S dS \int_{-\infty}^{\infty} \left( \alpha |\dot{u}_i^\alpha|^2 + \beta |\dot{u}_i^\beta|^2 \right) dt \quad (4.82)$$

where  $\dot{u}_i^\alpha$  and  $\dot{u}_i^\beta$  are the *particle velocities* of the P and S waves, respectively. For a point source we substitute the displacements by the time derivatives of expressions (4.23) and (4.24).

$$\begin{aligned} \dot{u}_i^P &= \frac{-1}{4\pi\rho\alpha^3 r} R_P \ddot{M}_0(t - r/\alpha) \\ \dot{u}_i^S &= \frac{-1}{4\pi\rho\beta^3 r} R_S \ddot{M}_0(t - r/\beta) \end{aligned}$$

where  $R_P$  and  $R_S$  are the radiation patterns of the P and S waves. For the part of the energy contained in the far-field radiation at a distance  $r$  we obtain, in terms of the parameters of the point source,

$$E = \frac{1}{16\pi^2 \rho r^2} \int_S \left( \frac{1}{\alpha^5} R_P^2 + \frac{1}{\beta^5} R_S^2 \right) \int_{-\infty}^{\infty} |\ddot{M}_0(t)|^2 dt \quad (4.83)$$

Now we integrate over the spherical surface  $S$  ( $dS = r^2 \sin \theta d\theta d\phi$ , where  $\theta$  and  $\phi$  are spherical coordinates centered on the point source). Defining the mean values  $\langle R_P \rangle$  and  $\langle R_S \rangle$  of the squared radiation patterns for P and S waves over the surface of the focal sphere as

$$\langle R_P^2 \rangle = \frac{1}{4\pi} \iint R_P^2(\theta, \phi) \sin \theta d\theta d\phi \quad (4.84)$$

with a similar expression for the S waves, we obtain

$$E = \frac{1}{4\pi\rho} \left( \frac{1}{\alpha^5} \langle R_P^2 \rangle + \frac{1}{\beta^5} \langle R_S^2 \rangle^2 \right) \int_{-\infty}^{\infty} |\ddot{M}_0(t)|^2 dt \quad (4.85)$$

The energy release is, then, proportional to the time integral of the square of the seismic moment acceleration function.

Expression (4.83) can be also computed in the spectral domain using Parseval's relation

$$\int_{-\infty}^{\infty} f^2(t) dt = \frac{1}{2\pi} \int_{-\infty}^{\infty} |F(\omega)|^2 d\omega = \frac{1}{\pi} \int_0^{\infty} |F(\omega)|^2 d\omega \quad (4.86)$$

which is valid for any real function  $f(t)$  and its corresponding Fourier transform  $F(\omega)$ . In terms of the source time function defined earlier we can write (4.83) in its most common form (Haskell, 1966; Boatwright, 1978):

$$E = \frac{1}{4\pi^2\rho} \left( \frac{1}{\alpha^5} \langle R_P^2 \rangle + \frac{1}{\beta^5} \langle R_S^2 \rangle^2 \right) \int_{-0}^{\infty} \omega^2 |\dot{M}_0(\omega)|^2 d\omega \quad (4.87)$$

We notice from (4.86) that the energy integral is finite if and only if the spectrum  $|\dot{M}_0(\omega)|$  decays faster than  $\omega^{-1}$  at high frequencies. This is a very strict requirement and it is the reason why the boxcar signal (4.68) is not an admissible source time function. We can finally compute the energy integral for a generic omega-squared source time function like that of (4.78):

$$E = \frac{1}{16\pi\rho} \left( \frac{1}{\alpha^5} \langle R_P^2 \rangle + \frac{1}{\beta^5} \langle R_S^2 \rangle^2 \right) M_0^2 \omega_c^3 \quad (4.88)$$

Thus for a general omega-squared far-field signal the radiated energy is proportional to the moment squared and to the cube of the corner frequency. This property is established simply on the basis of the general spectral form (4.78) of the radiated waves and not on a particular model of the source, as is sometimes assumed.

## 5.1. Definition of the moment tensor

In Chapter 4 we considered two equivalent point source models for earthquakes, namely, a shear fracture and a double-couple force system. Both can also be used to model extended sources by taking their distributions over a certain volume or surface. Considering all possible internal or indigenous sources, that is, those with zero total force and moment, it will be convenient to obtain a formulation for a more general type of source of which the double couple is a particular case. The *seismic moment tensor*  $M_{ij}$  represents precisely this general type of internal source. It can represent a point source or an extended source expressed as an integral over a certain source volume or source surface of an appropriate *moment tensor volume density*  $m_{ij}$  or *surface density*  $m'_{ij}$  (Jost and Hermann, 1989):

$$M_{ij} = \int_{V_0} m_{ij} dV = \int_{\Sigma} m'_{ij} dS \quad (5.1)$$

The seismic moment tensor was first proposed by Gilbert (1970), who related it to the total stress drop  $\Delta\sigma$  (1.6) which takes place at the earthquake source. Backus and Mulcahy (1976a, b) clarified that the moment tensor represents only the part of the internal stress change that is responsible for the non-elastic deformation of the source, that is, of the fracture process. It is important to remark that, up to this point, we have represented the source by either displacement dislocations  $\Delta\mathbf{u}$  or equivalent internal body forces  $\mathbf{F}$ . Now we will represent the source by internal stresses of non-elastic origin, in terms of the tensor  $M_{ij}$ , and show their relation to dislocations and body forces.

If we consider a perfect elastic medium in which only elastic processes occur then, in the absence of body forces, the equation of motion is given in differential form (3.4) by

$$\rho\ddot{u}_i = \tau_{ij,j} \quad (5.2)$$

where  $\tau_{ij}$  are the stresses of elastic origin.

In the real or physical situation, when an earthquake takes place, besides the elastic processes there are also non-elastic processes, that is, fracture and relative displacement of the material and heat production by friction. If we consider the total stresses  $\sigma_{ij}$  that are responsible for all processes in the medium, elastic and non-elastic, the equation of motion can be written as

$$\rho\ddot{u}_i = \sigma_{ij,j} \quad (5.3)$$

Now, we define the moment tensor density  $m_{ij}$  as the stress in excess of that which is purely elastic, the *stress glut* as it was called by Backus and Mulcahy: (1976a, b)

$$m_{ij} = \tau_{ij} - \sigma_{ij} \quad (5.4)$$

If we substitute (5.4) into (5.3), we obtain

$$\rho \ddot{u}_i = \tau_{ij,j} - m_{ij,j} \quad (5.5)$$

If we compare this expression with (5.2), we see that  $m_{ij}$  represents the part of the stresses related to the non-elastic processes. We also observe that  $m_{ij}$  acts as a source of seismic waves. Comparing (5.5) with (3.5) we obtain the relation between the moment tensor and internal body forces,

$$F_i = -m_{ij,j} \quad (5.6)$$

Equation (5.6) clarifies both the meaning of the moment tensor and that of the equivalent body forces. Both are related only to the stresses responsible for the non-elastic processes in the source and both have values only inside the source region  $V_0$ , that is, the region where there are non-elastic processes.

Considering the relation between the moment tensor and the body forces (5.6), we can express the elastic displacements using a Green's function, substituting (5.6) into (3.69):

$$u_i(x_n, t) = \int_{-\infty}^{\infty} d\tau \int_{V_0} [-m_{kj,j}(\xi_n, \tau) G_{ik}(\xi_n, \tau, x_n, t)] dV \quad (5.7)$$

Integrating by parts with respect to the spatial coordinates  $\xi$  and using Gauss's theorem in the first term thus obtained we get

$$u_i = \int_{-\infty}^{\infty} d\tau \int_{S_0} m_{kj} G_{ik} n_j dS + \int_{-\infty}^{\infty} d\tau \int_{V_0} m_{kj} G_{ik,j} dV \quad (5.8)$$

where  $S_0$  is the boundary of the source volume  $V_0$  and  $n$  is the normal to the boundary.

For an internal source the sums of all forces and of all moments inside the volume  $V_0$  must be identically zero; thus, by assuming that the volume  $V_0$  is large enough that  $m_{kj}$  is zero on its boundary, we obtain

$$u_i(x_n, t) = \int_{-\infty}^{\infty} d\tau \int_{V_0} m_{kj}(\xi_n, \tau) G_{ik,j}(\xi_n, \tau, x_n, t) dV_\xi \quad (5.9)$$

where  $m_{kj}$  is a symmetric tensor. If the moment tensor is defined on a surface  $\Sigma$ , we use  $m'_{ij}$ , the moment tensor density per unit surface and write (5.9) as a surface integral:

$$u_i(x_n, t) = \int_{-\infty}^{\infty} d\tau \int_{\Sigma} m'_{kj}(\xi_n, \tau) G_{ik,j}(\xi_n, \tau, x_n, t) dS \quad (5.10)$$

For a point source, equations (5.9) and (5.10) simplify to a time convolution of the moment tensor  $M_{ij}$  acting at the origin of coordinates ( $\xi = 0$ ) and the derivatives of the Green's function:

$$u_i(x_n, t) = \int_{-\infty}^{\infty} M_{kj}(\tau) G_{ik,j}(x_n, t - \tau) d\tau \quad (5.11)$$

Equations (5.9) and (5.10) for an extended source and (5.11) for a point source show that for a point source the elastic displacements outside the focal region can be derived from the moment tensor and the derivatives of the Green's function and for an extended source by integration over the source region ( $V_0$  or  $\Sigma$ ). Since we have not specified a particular form the moment tensor can represent a very general type of source, as we will see, and, according to (5.6), it corresponds to a general category of internal force systems provided that the net effect of their sum and the sum of their moments is null. The moment tensor is, then, a very convenient way of representing an earthquake source in a general form.

The physical meaning of the moment tensor can be understood by considering its relation to the equivalent body forces. In equation (3.69) the elastic displacements are given, in terms of the body forces, by

$$u_k(x_n, t) = \int_{-\infty}^{\infty} d\tau \int_{V_0} F_i(\xi_n, \tau) G_{ki}(\xi_n, \tau, x_n, t) dV \quad (5.12)$$

If we perform a Taylor expansion of  $G_{jk}$  about the origin ( $\xi = 0$ ), the first three terms are given by

$$G_{ik}(\xi_n) = G_{ik}(0) + \xi_j \frac{\partial G_{ik}}{\partial \xi_j} + \frac{1}{2} \xi_s \xi_j \frac{\partial^2 G_{ik}}{\partial \xi_s \partial \xi_j} + \dots \quad (5.13)$$

Substituting (5.13) into (5.12) we see that the first term is null by virtue of the requirement that the sum of internal forces must be zero, i.e.

$$\int_{V_0} F_i(0) G_{ki}(0, x_n) dV = 0 \quad (5.14)$$

If we stop the expansion at the second term, we obtain

$$u_i = \int_{-\infty}^{\infty} d\tau \int_{V_0} \xi_j F_k G_{ik,j} dV \quad (5.15)$$

By comparison of expression (5.15) with (5.9) we find that

$$m_{jk} = \xi_j F_k \quad (5.16)$$

The moment tensor density  $m_{jk}$  given by (5.16) corresponds to the first non-zero term in the Taylor expansion of (5.13) and thus is called the *first-order moment tensor*. Therefore, in equations (5.9), (5.10) and (5.11)  $m_{kj}$  represents the first-order moment tensor which is associated with the first derivatives of the Green's function. According to Backus and Mulcahy (1976a) this tensor corresponds to the *zero-order glut moment*, i.e. the or stress in excess of the elastic stress. We can also derive moment tensors of higher order, associated with higher derivatives of Green's functions, for example, the second-order moment tensor, corresponding to the third term in 5.13, represents the variations of the moment tensor with space and time, as we will see later.

According to (5.16) the components  $m_{ij}$  correspond to couples of forces or dipoles, with  $\xi$  corresponding to the arm and  $F$  to the force. The components  $m_{11}$ ,  $m_{22}$  and  $m_{33}$  are linear dipoles, without a moment, that is, the arms are in the same direction as the forces.

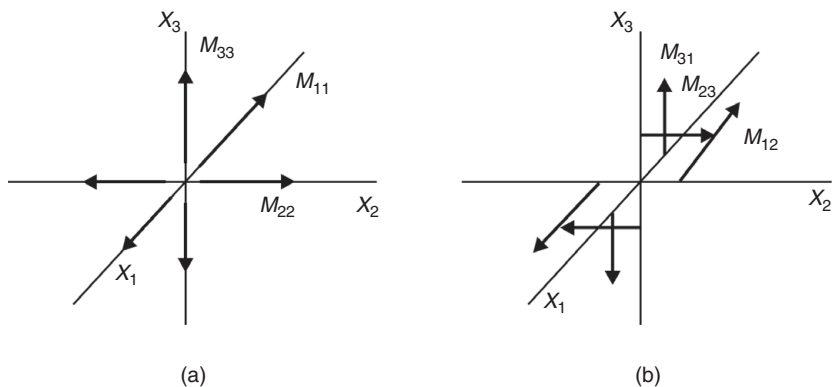


**Figure 5.1.** Components of the seismic moment tensor  $M_{ij}$ : (a) for  $i = j$ , (b) for  $i \neq j$  (only three components are shown).

The other components,  $m_{12}, m_{13}, m_{23}, m_{21}, m_{31}, m_{32}$ , have arms perpendicular to the forces and so are couples, with a moment (Fig. 5.1). The condition of zero net moment implies that the tensor is symmetric,  $m_{ij} = m_{ji}$ , that is, couples with opposite moments must be equal. For a particular medium, the Green's function represents displacements due to impulsive forces acting at a point; its derivatives represent displacements due to couples or dipoles of impulsive forces (Section 4.2). Thus, according to equations (5.9), (5.10) and (5.11), the elastic displacements are given by the convolution of the distributions of couples or dipoles of forces (represented by the moment tensor) with displacements due to couples or dipoles of impulsive forces (represented by derivatives of the Green's function). The components of the moment tensor  $M_{ij}$  are shown in Fig. 5.1.

## 5.2. Eigenvalues and eigenvectors

Since, as we have seen,  $M_{ij}$  is a symmetric tensor, its three *eigenvalues* are real and its three *eigenvectors* are mutually orthogonal. The eigenvalues and the corresponding eigenvectors of the moment tensor satisfy the equation

$$(M_{ij} - \delta_{ij}\sigma)v_j = 0 \quad (5.17)$$

The three eigenvalues  $\sigma_1, \sigma_2$  and  $\sigma_3$  are the roots of the cubic equation resulting from setting the determinant of (5.17) equal to zero,  $|M_{ij} - \delta_{ij}\sigma| = 0$ . By substituting each eigenvalue into (5.17), we obtain the three corresponding eigenvectors,  $v_k^1, v_k^2$  and  $v_k^3$ . In terms of the eigenvalues and the eigenvector components the moment tensor can be written as

$$M_{ij} = \sigma_1 v_i^1 v_j^1 + \sigma_2 v_i^2 v_j^2 + \sigma_3 v_i^3 v_j^3 \quad (5.18)$$

It is important to remark that this representation is unique when the eigenvalues are different. When two or more eigenvalues are identical, the definition of the corresponding

eigenvectors is non-unique but they can always be defined orthogonally in the corresponding vector subspace.

Since the moment tensor represents the non-elastic stresses acting at the source, its three mutually orthogonal eigenvectors correspond to the principal axes of the inelastic stress. With respect to these axes the moment tensor has the form

$$M_{ij} = \begin{pmatrix} \sigma_1 & 0 & 0 \\ 0 & \sigma_2 & 0 \\ 0 & 0 & \sigma_3 \end{pmatrix} \quad (5.19)$$

Thus, the moment tensor corresponds to three linear dipoles in the direction of these principal axes. If we order the eigenvalues by their values, so that  $\sigma_1 > \sigma_2 > \sigma_3$ , then  $\sigma_1$  correspond to the greatest stress,  $\sigma_2$  to the intermediate stress and  $\sigma_3$  to the least stress. We can, then, define the *differential stress*  $\sigma_d$  and the *stress ratio*  $R$ :

$$\sigma_d = \sigma_1 - \sigma_3 \quad (5.20)$$

$$R = \frac{\sigma_2 - \sigma_3}{\sigma_1 - \sigma_3} \quad (5.21)$$

The sum of the elements of the main diagonal in (5.19) is the first invariant of the tensor and has the same value for any reference system:

$$M_{11} + M_{22} + M_{33} = \sigma_1 + \sigma_2 + \sigma_3$$

This sum represents the inelastic dilatation or non-elastic change in volume per unit volume. We can thus define the *isotropic part* of the moment tensor as

$$\sigma_0 = \frac{1}{3}(\sigma_1 + \sigma_2 + \sigma_3) \quad (5.22)$$

If we subtract this quantity from the tensor  $M_{ij}$ , we obtain the *deviatoric tensor*  $M'_{ij}$ , the sum of whose diagonal elements is always zero; that is, it does not include changes in volume:

$$M'_{ij} = M_{ij} - \sigma_0 \delta_{ij} \quad (5.23)$$

The second term on the right-hand side of (5.23) is called the isotropic part of the moment tensor,  $M^0_{ij} = \sigma_0 \delta_{ij}$ . We can, then, separate any moment tensor into two parts:

$$M_{ij} = M^0_{ij} + M'_{ij} \quad (5.24)$$

where  $M^0_{ij}$  is the isotropic and  $M'_{ij}$  the deviatoric part.

### 5.3. Components of the moment tensor

The components of the moment tensor are expressed with respect to a coordinate system of reference, usually a geographic system with its origin at the focus of the earthquake, for example, the Cartesian coordinate system  $(x_1, x_2, x_3)$  or  $(x, y, z)$  positive in the directions

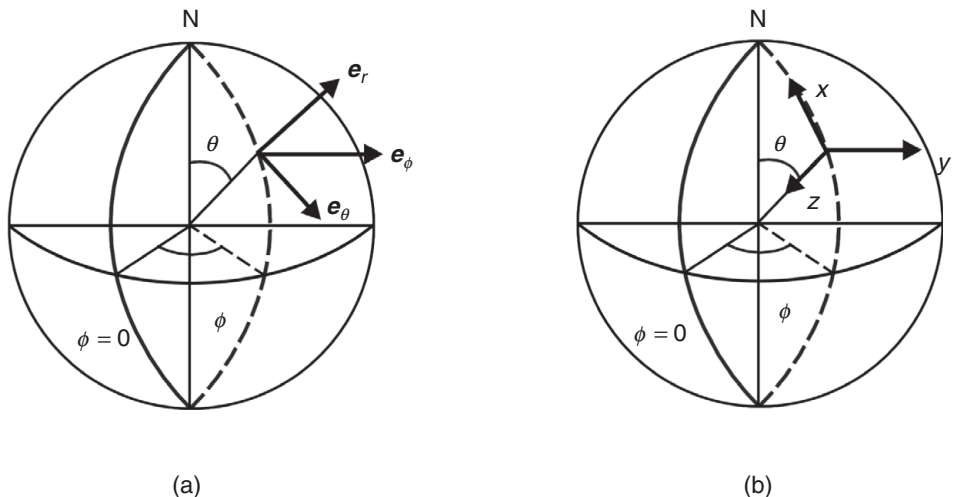


**Figure 5.2.** Systems of coordinates at the focus referred to the geocentric geographic system of the Earth. (a) System formed by the unit vectors  $(\mathbf{e}_r, \mathbf{e}_\theta, \mathbf{e}_\phi)$  in the direction of the spherical coordinates  $(r, \theta, \phi)$  (zenith, south, east). (b) System in the geographical directions  $(x, y, z)$  or (north, east, nadir).

north, east, nadir (Fig. 5.2) or north, west, zenith. Another system that is also used is referred to the geocentric spherical coordinates of the focus  $(r, \theta, \phi)$ , where  $r$  is in the radial direction,  $\theta$  is the geocentric colatitude and  $\phi$  the geocentric longitude. At the focus, the corresponding Cartesian coordinate system has unit vectors  $(\mathbf{e}_r, \mathbf{e}_\theta, \mathbf{e}_\phi)$  in the directions of positive increments in  $r, \theta, \phi$ . This system has positive axes in the directions zenith, south and east. The correspondences among the six components of the moment tensor in the three systems is as follows:

$$\begin{aligned} M_{11} &= M_{xx} = M_{\theta\theta} \\ M_{22} &= M_{yy} = M_{\phi\phi} \\ M_{33} &= M_{zz} = M_{rr} \\ M_{12} &= M_{xy} = M_{\theta\phi} \\ M_{13} &= M_{xz} = M_{\theta r} \\ M_{23} &= M_{yz} = -M_{\phi r} \end{aligned}$$

## 5.4. Moment tensor and elastic dislocations

If we compare equation (5.10) with (3.70), we can define the moment tensor density corresponding to a dislocation with slip  $\Delta\mathbf{u}$  on a surface  $\Sigma$  having normal  $\mathbf{n}$  as

$$m_{ij} = C_{ijkl}\Delta u_k n_l \quad (5.25)$$

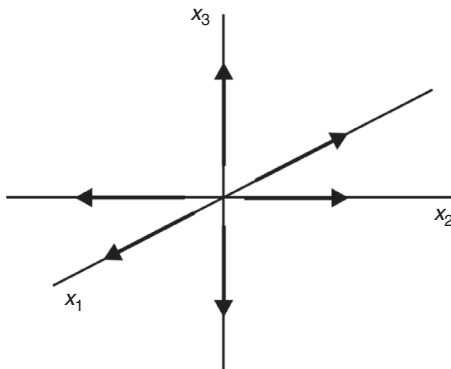


**Figure 5.3.** Example of an explosive source.

This is the most general definition of the moment tensor density in an elastic medium for a dislocation source of general type (see Cottrell and Bilby, 1949).

For an isotropic medium, if the direction of the slip is given by the unit vector  $\mathbf{l}$  then, according to (4.14), we have

$$m_{ij} = \Delta u [\lambda l_k n_k \delta_{ij} + \mu (l_i n_j + l_j n_i)] \quad (5.26)$$

From this expression we can find the moment tensor for various types of dislocation source by specifying the orientations of  $\mathbf{n}$  and  $\mathbf{l}$ .

### Explosive source

An *explosive source* may be considered as a sudden expansion along the three coordinate axes. In this case we need to consider only the isotropic part of the moment tensor. This situation can be represented by three linear dipoles, one along each axis (for each dipole  $\mathbf{l}$  and  $\mathbf{n}$  are in the same direction, that is,  $(1, 0, 0)$ ,  $(0, 1, 0)$  and  $(0, 0, 1)$ , respectively) (Fig. 5.3). The moment tensor density is the sum of the three and according to (5.26) is given by

$$m_{ij} = 3K \Delta u \begin{pmatrix} 1 & 0 & 0 \\ 0 & 1 & 0 \\ 0 & 0 & 1 \end{pmatrix} \quad (5.27)$$

where  $K = \lambda + \frac{2}{3}\mu$  is the *bulk modulus*. The sum of the elements of the principal diagonal, equal to  $9K\Delta u$ , represents the inelastic dilatation or increase in volume per unit volume (see, for a more general discussion, the classical work Eshelby, 1957).

### Tension fracture

For a *tension fracture* with fault plane  $(x_1, x_2)$ ,  $\mathbf{n} = (0, 0, 1)$  and  $\mathbf{l} = (0, 0, 1)$  (Fig. 5.4), the moment tensor density is given by

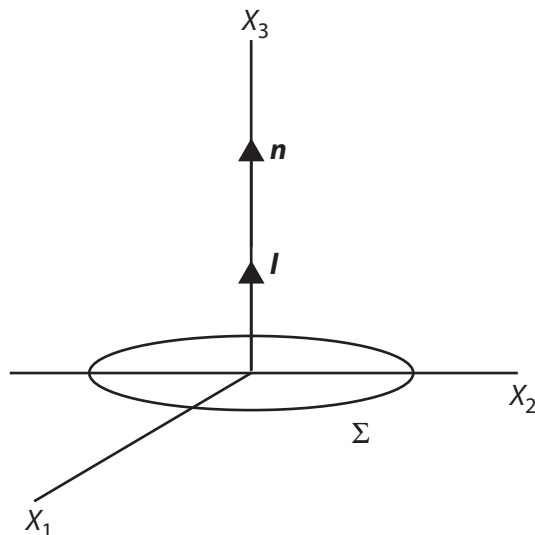


**Figure 5.4.** Example of a tension fracture ( $\mathbf{n} = \mathbf{I}$ ).

$$m_{ij} = \Delta u \begin{pmatrix} \lambda & 0 & 0 \\ 0 & \lambda & 0 \\ 0 & 0 & \lambda + 2\mu \end{pmatrix}$$

The change in volume is  $3K \Delta u$ . Referred to the principal axes, the tensor has the same form.

### Shear fracture

For a shear fracture, the slip  $\Delta \mathbf{u}$  lies on the fault plane, that is,  $\mathbf{n}$  and  $\mathbf{l}$  are perpendicular and, according to (5.26), the moment tensor density is

$$m_{ij} = \mu \Delta u (l_i n_j + l_j n_i) \quad (5.28)$$

For the particular case when the fault plane is the  $(x_1, x_2)$  plane, that is, its normal is  $\mathbf{n} = (0, 0, 1)$  and the slip is in the  $x_1$  direction,  $\mathbf{l} = (1, 0, 0)$  (Fig. 5.5) we obtain

$$m_{ij} = \mu \Delta u \begin{pmatrix} 0 & 0 & 1 \\ 0 & 0 & 0 \\ 1 & 0 & 0 \end{pmatrix}$$

The sum of the elements on the principal diagonal is null, indicating that there is no change in volume. The eigenvalues are  $(1, 0, -1)$  and the eigenvectors or principal axes are  $(1/\sqrt{2}, 0, 1/\sqrt{2})$ ,  $(0, 1, 0)$ ,  $(1/\sqrt{2}, 0, -1/\sqrt{2})$ . Referred to the principal axes the tensor is

$$m_{ij} = \mu \Delta u \begin{pmatrix} 1 & 0 & 0 \\ 0 & 0 & 0 \\ 0 & 0 & -1 \end{pmatrix}$$

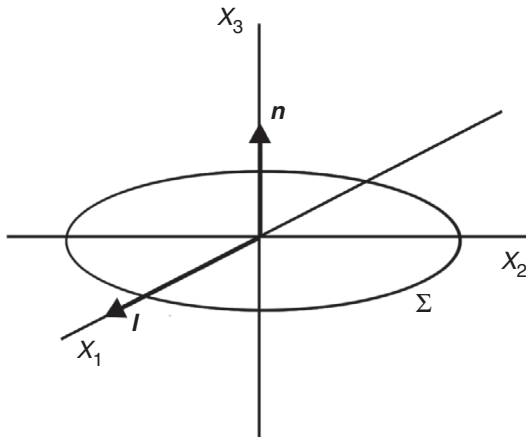


**Figure 5.5.** Example of a shear fracture ( $n_i l_i = 0$ ).

This tensor is equivalent to two linear dipoles of positive and negative sign, representing the tension and pressure forces, acting along the principal axes of stress given by the eigenvectors corresponding to eigenvalues  $\sigma_1 = 1$  and  $\sigma_3 = -1$ , that is, lying on the plane  $(x_1, x_3)$  at  $45^\circ$  to the direction of slip. These are, then, the pressure and tension axes,  $\mathbf{P}$   $(1/\sqrt{2}, 0, 1/\sqrt{2})$  and  $\mathbf{T}$   $(1/\sqrt{2}, 0, -1/\sqrt{2})$  (the axis corresponding to  $\sigma_2 = 0$  is the null or  $\mathbf{Z}$  axis  $(0,1,0)$ ). In terms of these axes the moment tensor is given by

$$m_{ij} = \mu \Delta u (T_i T_j - P_i P_j) \quad (5.29)$$

resulting in the same values for  $m_{ij}$ . This result is analogous to that found in [equation \(4.9\)](#) regarding the equivalence of a double couple and a system of pressure and tension forces at  $45^\circ$  to the couples. [Equation \(5.29\)](#) can be obtained from [\(5.18\)](#) by inserting  $\sigma_2 = 0$ ,  $\sigma_1 = -\sigma_3 = \mu \Delta u$ ,  $T_i = v_i^1$  and  $P_i = v_i^3$ .

## 5.5. Moment tensor components referred to geographical axes

The moment tensor components corresponding to a shear dislocation referred to geographical axes, as defined in [section 4.5](#), can be obtained by substituting in [equation \(5.28\)](#) the components of  $\mathbf{n}$ , as given in [\(4.37\)–\(4.39\)](#), and similar ones for  $\mathbf{l}$ . We obtain (omitting the factor  $\mu \Delta u$ )

$$\begin{aligned} m_{11} &= 2 \sin \theta_n \cos \phi_n \sin \theta_l \cos \phi_l \\ m_{22} &= 2 \sin \theta_n \sin \phi_n \sin \theta_l \sin \phi_l \\ m_{33} &= 2 \cos \theta_n \cos \theta_l \\ m_{12} &= \sin \theta_l \cos \phi_l \sin \theta_n \sin \phi_n + \sin \theta_l \sin \phi_l \sin \theta_n \cos \phi_n \\ m_{13} &= \sin \theta_l \cos \phi_l \cos \theta_n + \cos \theta_l \sin \theta_n \cos \phi_n \\ m_{23} &= \sin \theta_l \sin \phi_l \cos \theta_n + \cos \theta_l \sin \theta_n \sin \phi_n \end{aligned} \quad (5.30)$$

As we saw in section 4.5, a shear fracture can be specified by the angles  $\phi$ ,  $\delta$  and  $\lambda$  of the fault. Using the relations (4.43)–(4.48) of these angles with the components of  $\mathbf{n}$  and  $\mathbf{l}$  we obtain for the components of the moment tensor

$$\begin{aligned} m_{11} &= -\sin \delta \cos \lambda \sin 2\phi - \sin 2\delta \sin^2 \phi \sin \lambda \\ m_{22} &= \sin \delta \cos \lambda \sin 2\phi - \sin 2\delta \cos^2 \phi \sin \lambda \\ m_{33} &= \sin 2\delta \sin \lambda \\ m_{12} &= \sin \delta \cos \lambda \cos 2\phi + \frac{1}{2} \sin 2\delta \sin 2\phi \sin \lambda \\ m_{13} &= -\cos 2\delta \sin \lambda \sin \phi - \cos \delta \cos \phi \cos \lambda \\ m_{23} &= \cos 2\delta \sin \lambda \cos \phi - \cos \delta \sin \phi \cos \lambda \end{aligned} \quad (5.31)$$

The components of the moment tensor in equations (5.30) are the same if we interchange  $\mathbf{n}$  and  $\mathbf{l}$ , which reflects the ambiguity with respect to the fault plane and auxiliary plane. In equations (5.31) the components correspond to the plane selected as the fault plane and are the same as those calculated for the auxiliary plane.

## 5.6. The point source moment tensor

When the conditions specified in section 4.1 are fulfilled, i.e. when the wavelength  $\lambda \gg L^2/r$ , we can represent the source by a moment tensor acting at a point. According to (5.11), with the source at the origin of coordinates the displacements are given by

$$u_i(x_n, t) = \int_{-\infty}^{\infty} M_{kj}(\tau) G_{ik,j}(x_n, t - \tau) d\tau \quad (5.32)$$

In the frequency domain, taking the Fourier transform of (5.32) we obtain

$$U_i(x_n, \omega) = M_{kj}(\omega) G_{ik,j}(x_n, \omega) \quad (5.33)$$

In the frequency domain the displacements are linear products of the components of the moment tensor with the derivatives of the Green's function.

For an infinite homogeneous isotropic medium, according to (4.23) and (4.24) the displacements in the time domain for the P and S waves in the far field are given by

$$u_i^P = \frac{1}{4\pi\rho\alpha^3 r} \gamma_j \gamma_k \gamma_i \dot{M}_{jk}(t - r/\alpha) \quad (5.34)$$

$$u_i^S = \frac{-1}{4\pi\rho\beta^3 r} (\delta_{ij} - \gamma_i \gamma_j) \gamma_k \dot{M}_{jk}(t - r/\beta) \quad (5.35)$$

The elastic displacements depend on the time derivatives of the moment or moment rate. A simplifying assumption is that all components of the moment tensor have the same temporal dependence (corresponding to a *synchronous source*), so that we can write  $M_{ij}(t) = M(t)m_{ij}$ , where  $m_{ij}$  are the time-independent *normalized components* and  $M(t)$  is the total time-dependent scalar seismic moment. In the frequency domain we can write  $M_{ij}(\omega) = M(\omega)m_{ij}$ . A formal discussion of this separation can be found in Silver and Jordan

(1982). Only if the moment tensor corresponds to a shear fault or double couple (DC) do we obtain  $M(t) = M_0(t)$  and  $M(\omega) = M_0(\omega)$ , the scalar seismic moment defined in (1.4).

As in section 4.6, we can write the displacements in the P waves and the SV and SH components of the S waves in terms of geographical coordinates and the direction of the seismic ray ( $i, \phi'$ ) in terms of the components of the moment tensor:

$$\begin{aligned} u^P &= A[\sin^2 i (\cos^2 \phi' m_{11} + \sin^2 \phi' m_{22} + \sin 2\phi' m_{12}) \\ &\quad + \cos^2 i m_{33} + \sin 2i (\cos \phi' m_{13} + \sin \phi' m_{23})] \end{aligned} \quad (5.36)$$

$$\begin{aligned} u^{SV} &= B\left[\frac{1}{2} \sin 2i (\cos^2 \phi' m_{11} + \sin^2 \phi' m_{22} - m_{33} + \sin 2\phi' m_{12})\right. \\ &\quad \left.+ \cos 2i (\cos \phi' m_{13} + \sin \phi' m_{23})\right] \end{aligned} \quad (5.37)$$

$$\begin{aligned} u^{SH} &= B\left[\sin i \left(\frac{1}{2} \sin 2\phi' m_{22} - \frac{1}{2} \sin 2\phi' m_{11} + \cos 2\phi' m_{12}\right)\right. \\ &\quad \left.+ \cos i (\cos \phi' m_{23} - \sin \phi' m_{13})\right] \end{aligned} \quad (5.38)$$

where

$$A = \frac{\dot{M}(t - r/\alpha)}{4\pi\rho\alpha^3 r} \quad (5.39)$$

$$B = \frac{\dot{M}(t - r/\beta)}{4\pi\rho\beta^3 r} \quad (5.40)$$

Equations (5.36)–(5.40) give the displacements produced by a point source represented by a moment tensor of a general type. We can see from them that the displacements are linear combinations of the components of the moment tensor. It is possible, then, to determine the displacements from the observations by *linear inversion*. The main advantage of this formulation is that it relates the observations linearly to the parameters defining the orientation and amplitude of the source.

### 5.6.1. Temporal and frequency dependence

As already mentioned, it is often assumed that all components of the moment tensor have the same temporal dependence,  $M_{ij}(t) = M(t)m_{ij}$  and  $M_{ij}(\omega) = M(\omega)m_{ij}$ , where for a shear dislocation  $M(t) = M_0(t)$  and  $M(\omega) = M_0(\omega)$ . According to (5.39) and (5.40), the elastic displacements in the far field depend on the time derivative of the moment tensor or moment rate  $\dot{M}(t)$  and, for a shear dislocation,  $\dot{M}_0(t)$ . In the frequency domain we have  $\dot{M}(\omega) = \omega M(\omega)$  and  $\dot{M}_0(\omega) = \omega M_0(\omega)$ . As discussed in Chapter 4, in far-field wave form modeling it is often assumed that  $\dot{M}(t)$  is of a triangular or trapezoidal form and, for complex sources, a series of triangles of different sizes (Fig. 5.6). As we can see from (4.75) and (4.78), the Fourier transform of a time function of triangular form decays at high frequency as  $1/\omega^2$ . The scalar seismic moment  $M_0$ , which is a measure of the size of an earthquake, can be obtained by the integration of  $\dot{M}_0(t)$ . We remark that the same value of  $M_0$  will result from two different functions of the moment rate where one has a large amplitude and short

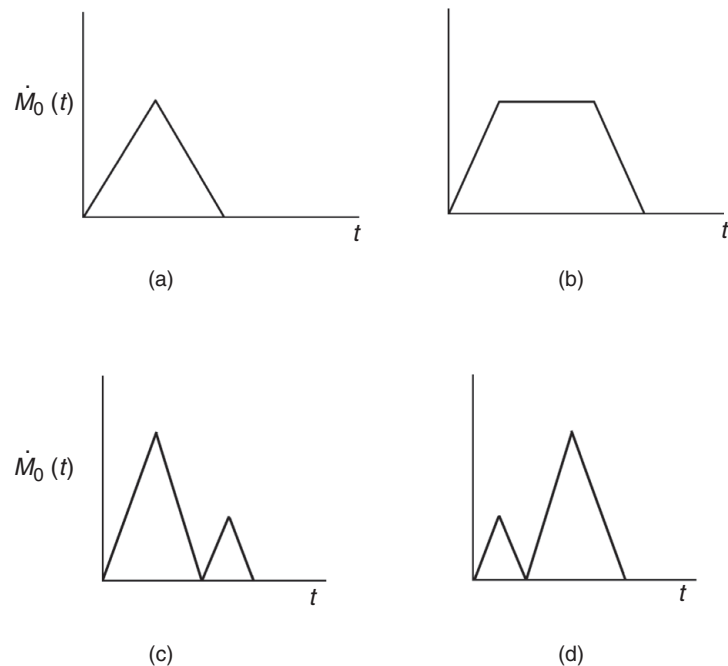


**Figure 5.6.** Temporal dependence of the moment rate for (a) triangular, (b) trapezoidal, (c) and (d) complex sources.

duration and the other has a smaller amplitude and longer duration. They represent two different ways to release the same amount of moment, over a shorter or longer time interval.

We must remember that we are dealing here with a point source representation, whereby the duration of the moment rate may be used as an approximate representation of the total duration of the rupture process of an extended source. This includes both the rise time  $\tau_r$  and the *rupture duration*  $t_r = L/v_r$ , where  $L$  is the source length and  $v_r$  is the *rupture velocity*). In a point source model, a complex moment-rate distribution varying with time may be considered as an approximate representation of the real extended source, that is, of both the time and space distribution of rupture. Thus we can represent the moment-rate release in a complex source by several triangles of different sizes (Fig. 5.6). The relative sizes of the triangle represents how the moment release takes place in time. In some cases, the larger part of the moment release takes place during the first part of the shock and a smaller part takes place later (Fig. 5.6c). In other cases there is first a small moment release and then, later, the main part (Fig. 5.6d). The small event can be considered as an aftershock in the first case and as a foreshock in the second. This form of modeling the source time function by that for a point source is a rather artificial way of representing some elements of the complex rupture process which takes place on an extended fault plane.

### 5.6.2. The centroid moment tensor

Use of the point source moment tensor implies that the moment tensor is acting at a point. This point is usually assumed to be the hypocenter. However, this may not be the most appropriate choice. The hypocenter location and origin time are obtained from the first

arrivals of P and S waves of relatively short period and thus correspond to the time and location of the beginning of rupture. Since all earthquakes have a certain finite size, the point of initiation of rupture need not be actually the best point source location, as was pointed out by Dziewonski *et al.* (1981). These authors introduced the source location and origin time as variables in their method of estimating the components of the moment tensor from observations of body and surface waves. Thus, they determined the point source location and origin time, which in fact corresponded not to the point and time of the initiation of rupture but to the *centroid* of the seismic moment distribution in space and time. The difference between the location of the initiation of rupture and the centroid can be significant except for very small earthquakes (Dziewonski and Woodhouse, 1983).

For a shear dislocation on a fault plane with slip in a constant direction, the coordinates and origin time of the centroid, for an isotropic medium with hydrostatic initial stresses, can be expressed as (Dahlen and Tromp, 1998, pp. 167–70)

$$x_j^C = \frac{1}{M_0} \int_{\Sigma} \mu \xi_j \Delta \dot{u} dS \quad (5.41)$$

$$t^C = \frac{1}{M_0} \int_0^t d\tau \int_{\Sigma} \mu \tau \Delta \dot{u} dS \quad (5.42)$$

or, in terms of the moment-rate density,

$$x_j^C = \frac{1}{M_0} \int_{\Sigma} \xi_j \dot{m} dS \quad (5.43)$$

$$t^C = \frac{1}{M_0} \int_0^t d\tau \int_{\Sigma} \tau \dot{m} dS \quad (5.44)$$

The position of the centroid can be considered as the best estimate of the spatial location of the point source, and the corresponding origin time as the best estimate of the time for the same source. These space and time coordinates do not refer to the point of initiation of rupture but to a weighted mean position of the source in space and time (Backus, 1977). Spatially, the centroid corresponds to the geometrical center of gravity of the fault surface with respect to the moment-rate distribution. The distance  $\Delta x$  between the hypocenter and the centroid depends on the location of the initiation of rupture on the fault plane and it may be approximately half the dimension of the fault plane ( $\Delta x = L/2$ ). The centroid origin time may be approximated by half the source duration  $\Delta t = L/(2v)$  even when the centroid and hypocenter coincide. The moment tensor located at the centroid is known as the *centroid moment tensor* (CMT). For the general case, a synchronous point source of this type is defined by 12 parameters (four for the location in space and time of the centroid, two for the scalar moment and rise time and six for the components of the moment tensor). If the source is deviatoric the parameters reduce to 11, and for a DC source to nine.

## 5.7. The separation of the moment tensor

As already mentioned, the moment tensor represents a very general type of seismic source. We can discuss the different types of source represented by the moment tensor by analysing

their eigenvalues. As would be expected, the most general type of moment tensor is that with different eigenvalues whose sum is not zero ( $\sigma_1 \neq \sigma_2 \neq \sigma_3$  and  $\sigma_1 + \sigma_2 + \sigma_3 \neq 0$ ). This source includes changes in volume and can be separated into its isotropic and deviatoric parts (see (5.24)). The sum of the eigenvalues represents an increase or decrease in volume, according to its sign. Earthquakes associated with volcanic eruptions can give rise to substantial volume changes. If the three eigenvalues are equal, the source represents a symmetrical explosion (for a positive sign) or implosion (for a negative sign). The deviatoric part represents a general type of deviatoric mechanism, not necessarily a shear fracture or double couple.

For sources without a net volume change ( $\sigma_1 + \sigma_2 + \sigma_3 = 0$ ) the moment tensor is purely deviatoric. Then only two of the eigenvalues are independent ( $\sigma_2 = -\sigma_3 - \sigma_1$ ). This condition is often imposed on tectonic earthquakes, since it is often assumed that the high compressive stress conditions inside the Earth do not allow for inelastic volume changes. For a shear fracture or double couple, the moment tensor is purely deviatoric and one of its eigenvalues must be zero and the other two equal with opposite signs ( $\sigma_2 = 0$  and  $\sigma_1 = -\sigma_3$ ).

Sources of tectonic earthquakes are normally thought to be shear fractures or nearly so. However, this need not always be the case; the possibility of some volume change in shear faulting cannot be completely ruled out. Methods for determining the moment tensor components from observations of seismic waves, when they do not impose any conditions on the eigenvalues, may result in solutions with some amount of volume change and a deviatoric part that does not correspond to a pure double couple. In these general cases it is convenient to separate the moment tensor into three parts, an isotropic part corresponding to changes in volume, a pure shear or DC part and a third part that may be of various kinds (Strelitz, 1989). This analysis is called the partition or separation of the moment tensor and can be expressed by writing

$$\mathbf{M} = \mathbf{M}_0 + \mathbf{M}_{DC} + \mathbf{M}_R \quad (5.45)$$

The partition of the deviatoric part  $\mathbf{M}' = \mathbf{M}_{DC} + \mathbf{M}_R$  is non-unique and can be made in several ways. The simplest is to separate this part into two double couples, *major* and *minor*. To do this we take into account that, for a purely deviatoric tensor,  $\sigma_2 = -\sigma_1 - \sigma_3$ ; we thus split the moment tensor into two sub-faults:

$$\begin{pmatrix} \sigma_1 & 0 & 0 \\ 0 & \sigma_2 & 0 \\ 0 & 0 & \sigma_3 \end{pmatrix} = \begin{pmatrix} \sigma_1 & 0 & 0 \\ 0 & -\sigma_1 & 0 \\ 0 & 0 & 0 \end{pmatrix} + \begin{pmatrix} 0 & 0 & 0 \\ 0 & -\sigma_3 & 0 \\ 0 & 0 & \sigma_3 \end{pmatrix} \quad (5.46)$$

For example, if the major DC, with scalar moment  $M_0 = \sigma_1$ , is on the  $(x_1, x_2)$  plane then the minor DC, with scalar moment  $M_0 = \sigma_3$ , is on the  $(x_2, x_3)$  plane, both with force couples at  $45^\circ$  to the principal axes.

Another commonly used separation is the sum of the best shear fault component plus a compensated linear dipole; the best shear fault solution is that which maximizes the DC part of the source. A solution for this problem was proposed by Knopoff and Randall (1970) in the form

$$\begin{pmatrix} \sigma_1 & 0 & 0 \\ 0 & \sigma_2 & 0 \\ 0 & 0 & \sigma_3 \end{pmatrix} = \begin{pmatrix} \frac{1}{2}(\sigma_1 - \sigma_3) & 0 & 0 \\ 0 & 0 & -\frac{1}{2}(\sigma_1 - \sigma_3) \\ 0 & 0 & -\frac{1}{2}(\sigma_1 - \sigma_3) \end{pmatrix} + \begin{pmatrix} -\frac{1}{2}\sigma_2 & 0 & 0 \\ 0 & \sigma_2 & 0 \\ 0 & 0 & -\frac{1}{2}\sigma_2 \end{pmatrix} \quad (5.47)$$

The first term on the right-hand side of the equation is a DC source with  $\mathbf{M}_0 = \frac{1}{2}(\sigma_1 - \sigma_3)$ . The second term is the *compensated linear vector dipole* (CLVD). Its physical meaning, as given by Knopoff and Randall, is a sudden change in the shear modulus in a direction normal to the fault plane, without change in volume. Then, the source represented by the sum of the two terms corresponds to a shear fracture in which, during the rupture process, the shear modulus in the focal region changes suddenly in a direction normal to the fault plane. This separation of the moment tensor is the one most commonly used.

The point source moment tensor can, then, be separated into three parts: one involving the changes in volume, a DC and a CLVD:

$$\mathbf{M} = \mathbf{M}_0 + \mathbf{M}_{\text{DC}} + \mathbf{M}_{\text{CLVD}} \quad (5.48)$$

This partition separates the effect of the shear fracture, considered to be the standard model for the source of earthquakes, from other effects which may be also present. In most problems concerning tectonic earthquakes, the isotropic part  $\mathbf{M}_0$  is assumed to be zero. In a deviatoric source the deviation from a pure DC is given by the *percentage of CLVD* present, by the ratio  $\delta = 100|\sigma_2|/|\sigma_1|$ .

When the moment tensor is obtained by the inversion of observations, the presence of non-DC components may be often due to errors in the observations and to propagation effects that have not been taken into account properly, rather than to processes at the source itself. There is always a certain amount of ambiguity in separating in the observations effects due to the source and those due to wave propagation. Perfect separation of these two effects is not always possible, because the propagating medium is not very well known. The presence of a CLVD component in the moment tensor affects the quadrant distribution of compressions and dilations of P waves. As the percentage of CLVD increases, the distribution becomes quite different from that of a pure DC source (see Fig. 5.7). The values of  $\delta$  normally observed are less than about 15%. Higher values of  $\delta$  usually point to problems in the determination of the moment tensor from the observed data or incorrect models for the propagating medium. However, in some cases they may represent actual deviations of the source from a pure DC type. The most likely candidates for actual non-DC sources would be deep earthquakes. Frohlich (2006, pp. 228–35) made a very complete study of this problem, concluding that, for a *typical deep earthquake*, errors may be the cause of much of the observed CLVD components. He admits, however, that in a few cases large CLVD components may not be attributable to systematic errors. According to Frohlich, the actual type of source represented by the CLVD components is not clear either, and it may be in effect the sum of two closely positioned and suitably oriented DC sources. If this were always true then the DC source would be the normal mechanism for all tectonic earthquakes at any depth.

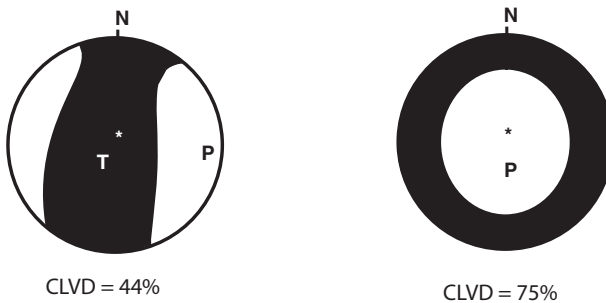


**Figure 5.7.** Representations on the focal sphere of sources corresponding to moment tensors with 44% or 75% of non-DC (CLVD) component.

## 5.8. Higher-order moment tensors

If we take into account more terms in the Taylor expansion (5.13), we obtain *higher-order moment tensors*. Taking only the first three terms, and remembering that the first is zero, equation (5.15) becomes

$$u_i = \int_{-\infty}^{\infty} d\tau \int_{V_0} (\xi_j F_k G_{ik,j} + \frac{1}{2} \xi_s \xi_n F_j G_{ij,sn}) dV \quad (5.49)$$

In terms of the moment tensor acting at a point, this expression can be written as (Doornbos, 1982)

$$u_i = \frac{\partial G_{ij}}{\partial \xi_k} * M_{jk} + \frac{\partial^2 G_{ij}}{\partial \xi_l \partial \xi_k} * \frac{\partial M_{jk}}{\partial \xi_l} \quad (5.50)$$

where the stars indicate time convolutions, and we have used that  $M_{ij} = \xi_j F_i$  and  $M_{ij,k} = \xi_k M_{ij}$ .

Equation (5.50) can be written as a sum of the temporal derivatives of the Green's function multiplied by the moment tensor (Doornbos, 1982; Dahm and Krüger, 1999). If we make the simplifying assumption that the components of the moment tensor density have a common space and time history, the first six terms can be written as

$$\begin{aligned} u_i = & \left[ G_{ij,k} - \Delta\tau \dot{G}_{ij,k} + \Delta\xi_l \dot{G}_{ij,kl} + \frac{1}{2} \Delta(\tau^2) \ddot{G}_{ij,k} \right. \\ & \left. - \Delta(\tau\xi_l) \ddot{G}_{ij,kl} + \frac{1}{2} \Delta(\xi_l \xi_m) \ddot{G}_{ij,klm} \right] M_{jk} \end{aligned} \quad (5.51)$$

where  $\Delta\tau = \tau - \tau_0$ ,  $\Delta\xi_l = \xi_l - \xi_{0l}$ ,  $\Delta(\tau^2) = (\tau - \tau_0)(\tau - \tau_0)$  etc. and  $\tau_0, \xi_{0l}$  are the time and point in space where the source is located. The number of parameters is now 24:  $\tau_0$  (1),  $\xi_{0l}$  (3),  $M_{ij}$  (6),  $\Delta\tau$  (1),  $\Delta\xi_l$  (3),  $\Delta(\tau^2)$  (1),  $\Delta(\tau\xi_l)$  (3),  $\Delta(\xi_l \xi_m)$  (6). If  $\tau_0$  and  $\xi_{0l}$  are the time and space coordinates of the centroid ( $t^C$  and  $x_i^C$ ) then  $\Delta\tau$  and  $\Delta\xi_l$  are zero, the parameters are reduced to 20 and equation (5.50) is simplified to

$$u_i = \left[ G_{ij,k} + \frac{1}{2} \Delta(\tau^2) G_{ij,k} - \Delta(\tau \xi_l) G_{ij,kl} + \frac{1}{2} \Delta(\xi_l \xi_m) \ddot{G}_{ij,klm} \right] M_{jk} \quad (5.52)$$

The parameters which appear in this equation are related to the time and space dimensions of the source about in relation to the centroid:  $\Delta(\tau^2)$  represents the time duration (the sum of the rise time and the rupture time);  $\Delta(\tau \xi_l)/\Delta(\tau^2) = v_l$ , the rupture vector velocity averaged over the source region (for a *symmetric bilateral rupture*,  $v_l = 0$ ) and  $\Delta(\xi_l \xi_m)$  is related to the size, shape and orientation of the final static region. As a consequence, the second-order terms of the moment tensor for a point source can be expressed by factors of the first-order tensor which indicate the time duration and space characteristics of the source. A more complete treatment of this subject can be found in Backus and Mulcahy (1977a, b) in terms of the different orders of the stress glut  $\Gamma_{ij}^n(\xi_l, \tau)$ .

## 5.9. Moments of the moment-rate distribution

Another approach to the problem is to consider the *moments* of different order of the distributions of the slip rate  $\Delta \dot{u}(\xi_i, \tau)$  or moment-rate release  $\dot{m}_{ij}(\xi_i, \tau)$  (Silver and Jordan, 1983; Das and Kostrov, 1997; McGuire *et al.*, 2001; McGuire, 2004).

We can define the time moments  $\eta^n(t_0)$  of order  $n$  of a function with respect to a reference time  $t_0$  as

$$\eta^n(t_0) = \int_{-\infty}^{\infty} (t - t_0)^n f(t) dt, \quad n = 0, 1, 2, \dots \quad (5.53)$$

Then, the zero- and first-order time and space moments of the moment rate distribution over the fault plane are given by

$$\eta^{0,0}(\tau) = \int_{\Sigma} \dot{m}(\xi_i, \tau) dS \quad (5.54)$$

$$\eta_j^{1,0}(\tau) = \int_{\Sigma} \xi_j \dot{m}(\xi_l, \tau) dS \quad (5.55)$$

$$\eta^{0,1}(\tau) = \int_{\Sigma} \tau \dot{m}(\xi_l, \tau) dS \quad (5.56)$$

where the superscripts refer to the space and time order of the moment rate, in that order. Using the zero-, first- and second-order moments of the moment-release distribution, integrated over the source volume  $V$  or fault surface  $\Sigma$  and source time duration  $t_d$ , and assuming a constant moment tensor during rupture, that is, that  $\dot{m}_{ij}(\xi_l, \tau) = \bar{m}_{ij} \dot{m}(\xi_l, \tau)$ , we can find the various source parameters.

The integral over the source surface  $\Sigma$  of  $\dot{m}(\xi_l, \tau)$  is the source time function. The zero-order moment  $\mu^{0,0}$  is the scalar seismic moment,

$$M_0 = \eta^{0,0} = \int_0^{t_d} \int_{\Sigma} \dot{m}(\xi_i, \tau) dS d\tau \quad (5.57)$$

The first-order moments with respect to space and time,  $\mu_i^{1,0}$  and  $\mu^{0,1}$ , define the coordinates and origin time of the centroid,

$$x_i^C = \frac{\eta_i^{1,0}}{\eta^{0,0}} = \frac{1}{M_0} \int_0^{t_d} \int_{\Sigma} \xi_i \dot{m}(\xi_i, \tau) dS d\tau \quad (5.58)$$

$$t^C = \frac{\eta^{0,1}}{\eta^{0,0}} = \frac{1}{M_0} \int_0^{t_d} \int_{\Sigma} \tau \dot{m}(\xi_i, \tau) dS d\tau \quad (5.59)$$

The second-order moments referred to the centroid give certain spatial and temporal dimensions of the source,

$$\mu_i^{1,1} = \int_0^{t_d} \int_{\Sigma} (\xi_i - x_i^C)(\tau - t^C) \dot{m}(\xi_i, \tau) dS d\tau \quad (5.60)$$

$$\mu_{ij}^{2,0} = \int_0^{t_d} \int_{\Sigma} (\xi_i - x_i^C)(\xi_j - x_j^C) \dot{m}(\xi_i, \tau) dS d\tau \quad (5.61)$$

$$\mu^{0,2} = \int_0^{t_d} \int_{\Sigma} (\tau - t^C)^2 \dot{m}(\xi_i, \tau) dS d\tau \quad (5.62)$$

The moment  $\mu_i^{1,1}$  is related to the rupture propagation,  $\mu_i^{2,0}$  to the space dimensions of the source and  $\mu^{0,2}$  to the time duration of the source process. If we compare with the terms in (5.52),  $\mu_i^{1,1}$  corresponds to  $\Delta(\tau\xi_l)$ ,  $\mu_{ij}^{2,0}$  to  $\Delta(\xi_i\xi_m)$  and  $\mu^{0,2}$  to  $\Delta(\tau^2)$ . From the moments defined in (5.60)–(5.62), we can find the *characteristic rupture length*  $L_c$ , the *characteristic duration*  $\tau_c$  and the *characteristic, or apparent rupture velocity*  $v_c$  (McGuire, 2004).

The characteristic rupture length  $L_c$  is given by the maximum value of  $x_c(\mathbf{n})$  (i.e. it corresponds to the largest eigenvalue of  $\mu_{ij}^{2,0}$ ), which is the characteristic dimension of the slip distribution in the direction of the unit vector  $\mathbf{n}$  and is defined by  $x_c^2(\mathbf{n}) = 4\mathbf{n}^T \boldsymbol{\mu}^{2,0} \mathbf{n}$  (here we have used bold notation for the tensor  $\boldsymbol{\mu}^{2,0}$ ; cf. (5.45));  $\tau_c^2 = 4\mu^{0,2}$  and  $v_c = L_c/\tau_c$ . The average velocity of the instantaneous spatial centroid is given by  $v_0 = \boldsymbol{\mu}^{1,1}/\mu^{0,2}$ . From this quantity we can find the *directivity ratio*  $|v_0|/v_c$ , which ranges from 0 for a perfectly symmetric bilateral rupture to 1 for a *unilateral rupture* with uniform slip (McGuire, 2004). The second-order moments of the moment-rate tensor are difficult to determine and are not often used in practice.

## 6.1. Parameters and observations

In general the determination of the source mechanisms of earthquakes consists in using seismic wave observations to determine by inversion the parameters of the model assumed to represent the source. The number of parameters depends on the complexity of the model that is used. The location of the source in space and time, usually given by the hypocenter and the origin time, is assumed to be previously known. The hypocenter parameters are the geographical latitude  $\phi_0$  and longitude  $\lambda_0$  of its projection onto the surface of the Earth at the *epicenter*, the depth  $h$  of the focus and the origin time  $t_0$ . These parameters are determined from the first arrivals of seismic waves and they correspond to the place and time of *nucleation* of the faulting process. For point models the source is usually assumed to be located at the hypocenter, except for the models that make use of the source centroid (section 5.6). In certain methods some location parameters, such as the depth, or, in the case of the centroid methods, all the location parameters are obtained simultaneously with the source mechanism. The size of the earthquake, given by its surface wave magnitude  $M_s$  (see (1.26)) and its body wave magnitude  $m_b$  (see (1.25)), is independently determined. However, the scalar seismic moment  $M_0$  can be either independently determined or evaluated at the same time as the mechanism. From the seismic moment one can obtain the moment magnitude  $M_W$  (1.30).

As we have seen in Chapters 4 and 5, the simplest models of the source mechanism are those which reduce the extension of the source to a point. This model is appropriate when we are observing the source from a very long distance compared with its dimensions and when the wavelengths used in the analysis are also long. More precisely, as defined in section 4.1, if  $L$  is the dimension of the source,  $R$  the distance from the observation point to the source and  $\lambda$  the wavelength then they must be such that  $R\lambda \gg L^2$ . For large earthquakes the dimensions of the source may introduce errors in the estimation of the point source orientation. If the mechanism is a shear fracture or dislocation, the point source orientation is given by the angles  $\phi, \delta, \lambda$  (section 4.5). For the equivalent double-couple force model, the orientation of the source is given by that of the two couples, that is, the axes  $X(\Theta_x, \Phi_x)$  and  $Y(\Theta_y, \Phi_y)$ , or by that of the pressure and tension axes,  $P(\Theta_P, \Phi_P)$  and  $T(\Theta_T, \Phi_T)$  (section 4.2). Since in each case the two axes are orthogonal, only three angles are needed, for example,  $\Theta_P, \Phi_P, \Theta_T$ . Including the seismic moment, the point shear fault time-independent source model is given by a set of four parameters,  $M_0, \phi, \delta, \lambda$  or  $M_0, \Theta_P, \Phi_P, \Theta_T$ .

The time dependence of the source is given by the source time function (STF)  $f(t)$ . This can be assumed to have a particular form, for example, a triangular shape, or it can be left

free to be determined in the inversion process. The duration of the source time function  $\tau_r$  must then be determined by inversion, together with the other parameters; in this case the total number of parameters for a shear fault point source is nine ( $M_0, \phi_0, \lambda_0, h, t_0, \phi, \delta, \lambda, \tau$ ).

An alternative, more general way, to represent a point source is by the first-order moment tensor  $M_{ij}$ . For the general case, when changes in volume are included, the number of independent elements of the tensor is six ( $M_{11}, M_{22}, M_{33}, M_{12}, M_{13}, M_{23}$ ). If the source is assumed to be purely deviatoric (no volume changes), there are five independent elements, since for such a source  $M_{11} + M_{22} + M_{33} = 0$ . A particular case is that of the moment tensor corresponding to a shear dislocation, for which the determinant of the tensor is zero. In the moment tensor formulation its components are functions of time. For a synchronous source all components have the same time dependence.

The observations used in the determination of the focal mechanism are the elastic displacements of the seismic waves recorded at several points on the surface of the Earth. They can be divided into free oscillations, body waves and surface waves. Ground displacements are obtained from seismograms that are now conveniently recorded in electronic digital form (Chapter 2). For earthquakes before about 1990, seismograms were recorded graphically and their analysis included a previous process of digitalization. Usually methods are separated into those which use body and surface waves and those which use the complete seismogram, and they can be carried out in the time or the frequency domain.

Since waves propagate from the source to the recording station, the mechanical properties of the Earth must be known previously. Owing to the heterogeneous nature and imperfect elasticity of the Earth, incomplete knowledge of its structure imposes limitations upon investigation of the source. There is, then, always a latent ambiguity about which characteristics of the seismic waves are due to the source and which are due to the propagating medium. There are ways to isolate these two effects from each other, but there is always a trade-off between the details of the source, which are to be determined, and those of the medium, which are supposed to be known. Simple models such as that of a point source, with observations at relatively long distances and low frequencies, are, in general, not very much affected by propagation effects. Standard models of the Earth's structure (such as the PREM or IASPEI models; see section 6.3.1 below), with distributions of the P and S velocities, the density and the anelastic coefficients as functions of the radius, are usually sufficient for most problems. Plane or spherically laterally homogeneous layered models are normally used, the first for regional distances (less than 1000 km) and the second for teleseismic distances. The presence of lateral inhomogeneities in the Earth may cause errors in the determination of the source parameters. To obtain more details about the fracture process in three dimensions at regional distances, crustal or lithospheric models are used.

## 6.2. The focal sphere

---

The focal sphere is a very useful concept, employed to correct for the heterogeneous nature of the Earth's structure, in many practical methods for determination of the orientation of the focal mechanism. It is a sphere of unit radius and homogeneous material properties

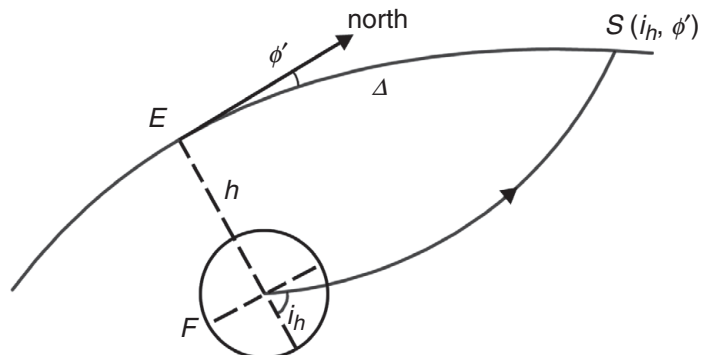


**Figure 6.1.** A ray path from the focus  $F$  at depth  $h$  with epicenter  $E$  to a station  $S$  at distance  $\Delta$  and the focal sphere. The azimuth is  $\phi'$  and the take-off angle is  $i_h$ .

surrounding the focus. The observation points on the surface of the Earth (stations) are projected onto points on the surface of the focal sphere, by tracing the trajectories of the rays back to the focus (ray back-tracing) (Fig. 6.1). If an observing stations  $S$  is located at distance  $\Delta$  from the epicenter and azimuth  $\phi$  ( $0^\circ$ – $360^\circ$ ), its projection onto the surface of the focal sphere is given by its azimuth  $\phi$  and take-off angle  $i_h$  ( $0^\circ$ – $180^\circ$ ), measured from the downward vertical (Fig. 6.1).

In order to determine the take-off angle  $i_h$  for a focus at depth  $h$ , corresponding to a given distance  $\Delta$ , the structure of the parts of the Earth through which the ray propagates must be known. For teleseismic distances ( $\Delta > 1000$  km),  $i_h$  can be calculated from the travel-time curves  $t(\Delta)$  using Snell's law,

$$\sin i_h = \frac{v_h}{r_h} \frac{dt}{d\Delta} \quad (6.1)$$

where  $r_h = R - h$ , with  $R$  the Earth's radius and  $v_h$  is the velocity at the focal depth. Errors in the value of this velocity result in errors in  $i_h$  and consequently in mislocation of the observations on the focal sphere. For local or regional distances ( $\Delta < 1000$  km), the determination of  $i_h$  requires knowledge of the velocity distribution in the crust and upper mantle of the region. In general, layered models with constant layer velocities or with linear velocity distributions are used. Models with velocity gradients are more convenient since they give a continuous relation of  $i_h$  with  $\Delta$ , whereas layers with constant velocities give a discontinuous relation. Once we have determined values of  $\phi$  and  $i_h$  for each observation point and located them on the surface of the focal sphere, the problem is reduced to that of a homogeneous medium. For each problem, a reliable solution requires a sufficient number of observations, distributed over azimuths and take-off angles, that the focal sphere is well covered.

### 6.3. Fault-plane solutions from P wave polarities

The first methods to determine the source mechanisms of earthquakes were based on observations of the polarity of the first P wave motion, that is, whether it is compressional

or dilatational in nature. The first authors to study this type of data were Omori and Galitzin, around 1905. Shida in 1917 was the first to recognize the alternating distribution of the polarities of P waves in four quadrants. The first operational method was proposed by Byerly (1928) and was solved in a graphical form. Byerly did not use the concept of the focal sphere to solve for the curvature of seismic rays in the Earth. He used instead what are known as the extended positions of the observations, that is, the exit points on the Earth's surface assuming that ray paths are straight lines. Projecting the extended positions onto a plane he was able to separate the four quadrants of P wave polarities and find the orientation of the two nodal planes of P motion, i.e. the possible fault planes. The method was simplified by the introduction of the focal sphere as developed by Honda and Ritsema, among others, in the 1950s. Using stereographic projections of the focal sphere such as Wulff and Schmidt nets, graphical solutions are found that separate compressions and dilatations by two orthogonal planes. Between 1950 and 1970 Russian seismologists used graphical methods extensively, adding to P wave polarities those of SV and SH waves. Because of the simplicity of the polarity data, fault-plane solutions are still widely used but graphical methods have been substituted by methods using computer programs (Udías, 1989).

Fault-plane methods are based on the quadrant distribution of the polarities of the far-field radiation pattern produced by a shear fracture or double-couple source (section 4.4.2). The quadrants with alternating signs (compressions and dilatations) are separated by two orthogonal planes. The signs of the first P wave motion are usually read from vertical-component seismograms (upward for compressions C, downward for dilations D). The methods consist of separating the four quadrants by two orthogonal nodal planes, one of which is the fault plane and the other of which is the auxiliary plane. Because of the symmetry of seismic radiation patterns with respect to the orientation of the normal to the fault plane  $\mathbf{n}$  and the direction of slip  $\mathbf{l}$ , as mentioned earlier the methods cannot distinguish between the two planes. They provide the orientation of the source model corresponding to either a point shear dislocation or a double couple (sections 4.2 and 4.4). The orientation of the mechanism is given by the orientation of the two planes (fault and auxiliary) in terms of the angles  $\phi, \delta, \lambda$  or of the axes  $X$  and  $Y$  of the double couple or of the orientation of the  $\mathbf{P}$  and  $\mathbf{T}$  (pressure and tension) axes. Because the two planes are orthogonal, the three angles defining one plane also define the orientation of the second plane, that is, the complete mechanism. Since the two pairs of axes  $X, Y$  and  $\mathbf{P}, \mathbf{T}$  are orthogonal unit vectors, their orientation is given in each case by only three axes,  $\Phi_x, \Theta_x, \Phi_y$  or  $\Phi_P, \Theta_P, \Phi_T$ .

### 6.3.1. Graphical methods

The most commonly used *graphical method* employs a stereographic projection of the focal sphere, usually Schmidt or equal-area net projection (Fig. 6.2). Since in most cases observations correspond to rays leaving the focus downward, the lower hemisphere of the focal sphere is projected onto the horizontal plane. For a down-going ray with take-off angle  $i_h$ , the point  $S$  on the surface of the lower hemisphere of the focal sphere projects as  $S'$  onto the horizontal plane, so that  $i_h$  varies from  $0^\circ$  to  $90^\circ$ . If there are stations very

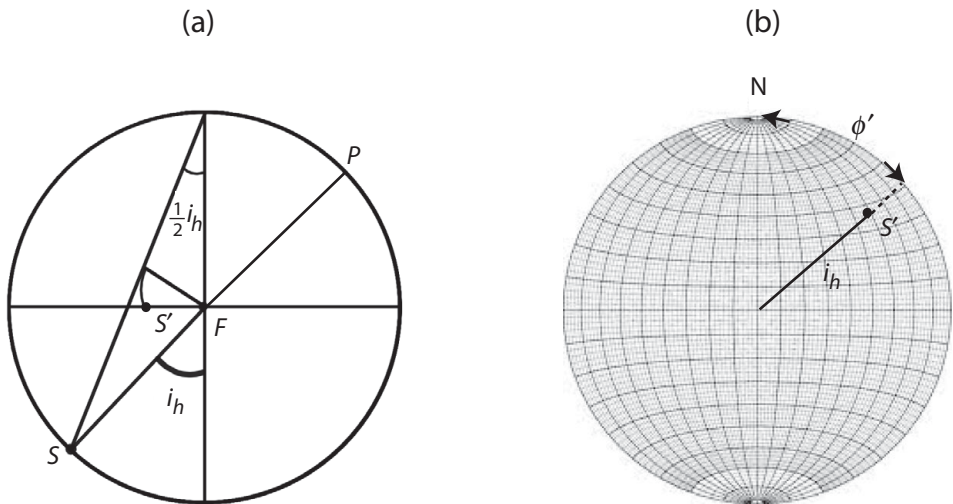
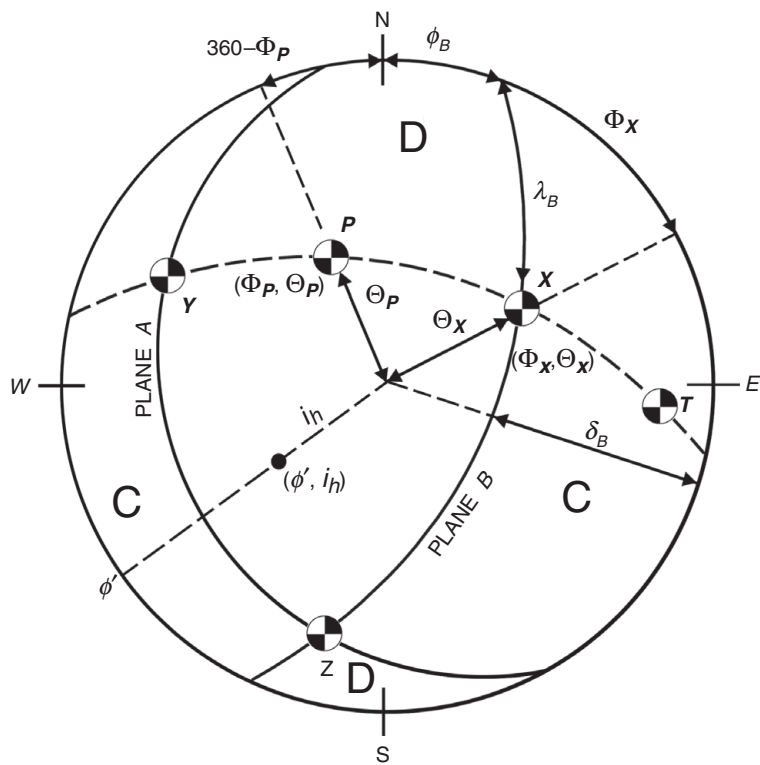


Figure 6.2.

Schmidt equal-area stereographic projection. (a) Point  $S$ , corresponding to a ray with take-off angle  $i_h$  at the lower hemisphere, projects as  $S'$  on to the horizontal plane. (b) Representation of the point  $S'$  ( $\phi', i_h$ ) ( $\phi'$ , azimuth;  $i_h$ , take-off angle) on the Schmidt net diagram.

close to the point source, or for very deep earthquakes at short distances, stations corresponding to up-going rays are projected first onto the lower hemisphere along the diameter of the focal sphere. A point  $P$  corresponding to an up-going ray is projected first onto  $S'$  on the upper hemisphere and then to  $S'$  on the lower hemisphere (Fig. 6.2). The lower hemisphere projects as a circle of unit radius. Points on the surface of the lower hemisphere defined by their azimuth and take-off angles ( $\phi', i_h$ ) project at  $(\phi', r)$ , where  $r = \sqrt{2} \sin(i_h/2)$ . Planes through the center project as great circles.

The data needed for the determination of a fault-plane solution are the polarities (compressions or dilatations) of the first P wave motion at a number of stations at different distances  $\Delta$  and azimuths  $\phi'$  from the source. The distances  $\Delta$  are converted into take-off angles  $i_h$ , so that each observation is defined at angles  $(\phi', i_h)$ . Observations are plotted on the stereographic projection with a different symbol for compressions and dilatations. Then a search is made for the set of two orthogonal planes that best separate compressions and dilatations into four quadrants. This is done by drawing first one plane (a great circle on the projection) and locating its pole (the normal through the center) and then drawing the second plane, such that it must pass through the pole of the first plane and its pole must be on the trace of the first plane. This ensures that the two planes are orthogonal (Fig. 6.3;  $X$  is the pole of plane  $A$  and  $Y$  is that of plane  $B$ ). The intersection of the two planes defines the  $Z$  axis. Usually several attempts are needed in order to separate all compressions and dilatations with a minimum number of inconsistencies. Once we have obtained the solution, we measure the orientation of the two planes in terms of angles  $\phi, \delta, \lambda$  and the orientations of the axes  $X, Y, P$  and  $T$  in terms of angles  $\Theta$  and  $\Phi$ . The  $P$  and  $T$  axes are at  $45^\circ$  from  $X$  and  $Y$ ;  $P$  is on the dilatation quadrant and  $T$  is on the compression



**Figure 6.3.** Representation on the Schmidt projection of the focal sphere for a shear fault (DC) mechanism: nodal planes  $A$  and  $B$ ; force axes  $X$  and  $Y$ ; principal stress axes  $P$  and  $T$ ; null axis  $Z$ ; observation point  $(\phi', i_h)$ ; D dilatation quadrants; C compression quadrants;  $\phi_B$ ,  $\delta_B$ ,  $\lambda_B$ , strike, dip and slip angles defining orientation and motion on plane  $B$ ;  $\Theta_X$ ,  $\Phi_X$  and  $\Theta_P$ ,  $\Phi_P$ , spherical coordinates corresponding to the axes  $X$  and  $P$ .

quadrant. We can see that all four axes are on the same plane (the plane of the forces) and normal to the  $A$  and  $B$  planes (Fig. 6.3). The quality of the solution is given by the score, which is the quotient of the number of correctly placed observations, that is, observations lying within the quadrants, assigned to their polarity, and the total number of observations.

The process that we have described can be also performed on the screen of a computer by using an interactive program. An example of such a program implements the following steps (Buform, 1994: <http://www.ucm.es/info/Geofis/g-sismolo/G-Sismolo.html>): first enter observations with station names, azimuth  $\phi'$ , take-off angle  $i_h$  and P wave first-motion polarity, 1 for compression and -1 for dilatation. The values of  $\phi'$  and  $i_h$  must be found previously from the geographical coordinates of the stations and the epicenter and the focal depth.

For teleseismic distances, values of  $\phi'$  and  $i_h$  may be obtained in several ways. For example, if data are in SAC format then from the header we can obtain the azimuth and epicentral distance in degrees. The take-off angle may be estimated from the IASPEI (Kennet and Engdahl, 1991) or PREM (Dziewonsky and Anderson, 1981) models using the ray parameter  $p = dt/dA$  (see, for example, the *ttimes* program available at <http://www.iris.edu/software/downloads/processing>).

Alhoceima 24-02-2010

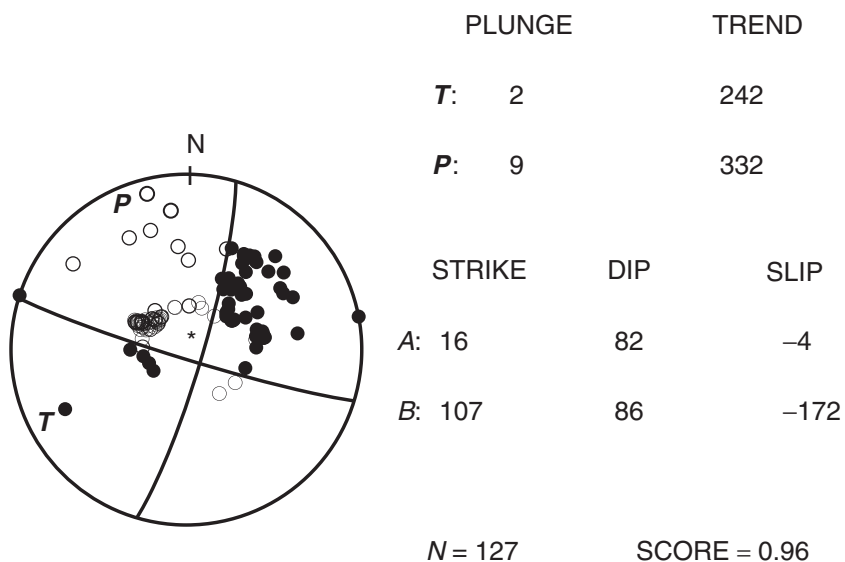


**Figure 6.4.** Graphical fault-plane solution from P wave polarities (the open circles show dilatations and the solid circles show compressions) for the Alhoceima (Morocco) earthquake of 24 February 2010 given by the orientation of the  $\mathbf{T}$  and  $\mathbf{P}$  axes and of the nodal planes  $A$  and  $B$ .

For regional distances, detailed lithospheric models are necessary in order to estimate  $i_h$ ; for example, a plane layered model with linear distribution of velocities can be used (<http://www.ucm.es/info/Geofis/g-sismolo/G-Sismolo.html>). The program locates first the observations on the screen using an equal-area projection. To begin the process, a first trial solution is given by specifying the orientation of  $\Phi_x$ ,  $\Theta_x$ ,  $\Phi_y$  or  $\Phi_P$ ,  $\Theta_P$ ,  $\Phi_T$ , or  $\phi$ ,  $\delta$ ,  $\lambda$ . The program draws the two planes on the screen together with the observations and determines the score of the solution. By successive approximations the trial solution is updated, until the solution with the maximum score is found. The program gives the solution in terms of the orientations of the  $X$ ,  $Y$ ,  $\mathbf{P}$  and  $\mathbf{T}$  axes and of the planes  $A$  and  $B$  (Fig. 6.4).

### 6.3.2. Numerical methods and computer programs

Since 1960, with the development of digital computers several methods for the numerical determination of fault-plane solutions have been proposed. The first algorithm was proposed by Knopoff (1961) who used a central projection in which the nodal planes project as straight lines. The function to be maximized was given by

$$\Psi = \sum_{i=1}^N \log \frac{1}{2} \left[ 1 + \operatorname{erf} \left( \frac{U_{ri}}{\alpha} \right) \operatorname{sgn} U_{ri} R_i \right] \quad (6.2)$$

where  $U_{ri}$  is the expected amplitude at station  $i$  from source orientation  $r$ ,  $R_i$  is the P wave polarity at station  $i$ ,  $\alpha$  is a constant noise level and  $\text{erf}$  is the error function. The maximization of  $\Psi$  was done by an iterative procedure, starting with some initial orientation of the source and proceeding until convergence was achieved. The problem was reformulated by Kasahara (1963) using spherical coordinates on the focal sphere. The basic ideas of Knopoff and Kasahara were applied in a computer program developed by Wickens and Hodgson (1967), in which they maximized the score of the solution (which is related to the number of consistent observations), defined as

$$S = \left| \frac{\sum_{i=1}^N w_i \operatorname{sgn} u_i^P \operatorname{sgn} p_i \pm D}{\sum_{i=1}^N w_i} \right| \quad (6.3)$$

where  $N$  is the number of observations,  $\operatorname{sgn} u_i^P$  gives the signs of the theoretical amplitudes and  $\operatorname{sgn} p_i$  those of the observations,  $D$  is a parameter based on the sign changes between successive trials and  $w_i$  is a weighting function that depends on the expected amplitudes,

$$w_i = |2u_i^P(1 - |u_i^P|)| + 0.3 \operatorname{sgn} u_i^P \quad (6.4)$$

The maximization process was performed by a systematic rotation of the two orthogonal nodal planes through all possible values in a search for the orientation that maximizes the score. The procedure was carried out first with a coarse grid, and then with a finer subgrid around the best 20 trials. The program could also weight the stations on the basis of their past performance. This program was used extensively in the Dominion Observatory, Canada, in a reevaluation of the fault-plane solutions for the period 1928 to 1962.

There are several computer programs that carry out a fault-plane solution. A computer program widely used at present was proposed by Reasenberg and Oppenheimer (1985): <http://earthquake.usgs.gov/research/software/index.php>. The program is based on an algorithm which uses the minimization of an L1 misfit (absolute value) function given by

$$F^i = \frac{\sum_{k=1}^N |p_o^k - p_t^{i,k}| w_o^k w_t^{i,k}}{\sum_{k=1}^N |w_o^k - w_t^{i,k}|} \quad (6.5)$$

where  $N$  is the number of observations,  $p_o^k$  the observed polarity at station  $k$  (0.5 for compressions and  $-0.5$  for dilatations),  $p_t^{i,k}$  is the theoretical polarity at station  $k$  corresponding to source model  $i$  (0.5 for compressions and  $-0.5$  for dilatations),  $w_o^k$  is the observation weights estimated and assigned to the data and  $w_t^{i,k} = [A(i,k)]^{1/2}$ , is the square root of the normalized theoretical P wave amplitudes at station  $k$  corresponding to model  $i$  (this downweights observations near the nodal planes). The program compares the observed polarity  $p_o^k$  at station  $k$  with that calculated for a given orientation  $i$  of the source,  $p_t^{i,k}$ . The orientation of the source is given by the three angles  $\phi, \delta, \lambda$  of one nodal plane. The program searches for a minimum in  $F^i$  by systematically changing the angles

$\phi, \delta, \lambda$ , first at increments of  $20^\circ$  and then, around the minimum thus found, by increments of  $5^\circ$  over an interval of  $45^\circ$  for  $\phi$  and  $\delta$  and of  $10^\circ$  over an interval of  $30^\circ$  for  $\lambda$ . A perfect fit corresponds to  $F^i = 0$  and a total misfit to  $F^i = 1$ . The program determines the variance of  $F^i$  and the 90 percent confidence limits, from which it estimates the uncertainties in the parameters of the solution.

A probabilistic formulation of the problem was first proposed by Keilis-Borok *et al.* (1972) using a *maximum likelihood* method. Following this approach, a method and computer program were developed by Brillinger *et al.*, (1980) and Udiás and Buforn (1988) that use the maximization of a likelihood function to find the orientation of the mechanism and its variance for individual and joint solutions for several earthquakes. The probability of observing a compression at station  $i$  is expressed as a function of the theoretical normalized amplitude  $A_i(\Phi_T, \Theta_T, \Phi_P)$  expected from an orientation of the  $T$  and  $P$  axes of the source given by

$$\pi_i = \gamma + (1 + 2\gamma)\zeta[A_i(\Phi_T, \Theta_T, \Phi_P)] \quad (6.6)$$

where  $\gamma$  is a small constant ( $0 \leq \gamma \leq \frac{1}{2}$ ) that accounts for reading errors and  $\zeta$  is the normal cumulative distribution function. The maximum likelihood estimates of the parameters of the orientation of the source are obtained by maximizing the function

$$L = \sum_{i=1}^N \log \frac{1}{2} |1 - (2\pi_i - 1)Y_i| \quad (6.7)$$

where  $Y_i$  are the observed P wave polarities and  $N$  is the number of observations. Because  $L$  is a differentiable function of the source orientation parameters  $\Phi_T, \Theta_T, \Phi_P$ , many efficient routines are available for the maximization. The computer program uses an iterative process from a given initial solution. Standard errors of the estimates of the solution are determined and methods for testing the hypotheses concerning the parameter values are applied. The program can be used for the determination of joint solutions for a number of earthquakes ( $k = 1, 2, \dots, M$ ) in the same region, if we expect them to have similar fault planes by introducing a parameter  $\rho_k$  which acquires larger values if the events have similar solutions. The computer program for individual solutions calculates the parameters of the orientation of the source with standard errors and the score of the solution and represents them graphically (Fig. 6.5): <http://www.ucm.es/info/Geofis/g-sismolo/G-Sismolo.html>.

## 6.4. Inversion of body wave forms

A widely used method to determine point source mechanisms is based on the analysis of the *body wave forms* and is usually known as *wave form inversion*. The method consists of the comparison of body (P and SH) wave forms observed at various azimuths around the focus with those calculated for a point source model. The model is found by minimizing the difference between the observed and theoretical wave forms. According to (4.16), for

## S. Vicente Cape 12-02-2007

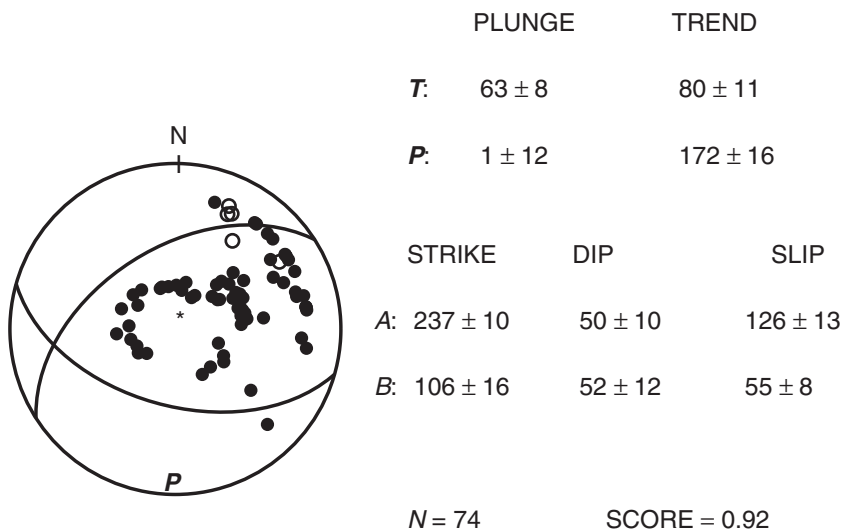


**Figure 6.5.** Numerical fault-plane solution, from the polarities of P waves (open circles, dilatations; black circles, compressions), using the MECSTA program for the San Vicente Cape earthquake of 12 February 2007; the solution is given by the orientation of the **T** and **P** axes and of the nodal planes **A** and **B**, with errors.

a point shear dislocation the seismic wave displacements are given by the convolution of the source parameters with the derivatives of the Green's function of the medium. Thus, we need to calculate the Green's functions before we can determine the mechanism. In applications to observations at local or regional distances, with waves traveling through the crust and upper mantle, we need to compute the Green's functions for the appropriate structure, usually approximating the latter by layered media. This problem is more difficult because of the heterogeneity of the crustal structure. For observations at teleseismic distances ( $\Delta > 30^\circ$ ), the problem can be simplified by the use of the Green's function computed using ray theory for a spherically isotropic medium (section 3.5). The parameters which define the point source model are the orientation of the sources mechanism, given by the angles  $\phi, \delta, \lambda$  of shear fracture, the source time function (STF), the variation of the moment rate with time  $f(t)$ , the scalar seismic moment  $M_0$  and the focal depth  $h$  (Deschamps *et al.*, 1980; Kikuchi and Kanamori, 1982, 1991; Nabelek, 1984; MacGraffey *et al.*, 1991).

Let us consider first the simplest case, that of P waves when we only have the direct wave; this would correspond to a very deep earthquake for which the reflected pP and sP waves would arrive separately and so do not interfere with the direct wave. One way to solve the problem is to use the Green's function computed by ray theory in a vertically layered isotropic medium. The far-field displacements of P waves for a point source shear dislocation in an infinite homogeneous medium are given by (4.23). The components of the vectors **n** and **l** can be expressed in terms of the fault angles  $\phi, \delta, \lambda$  according to

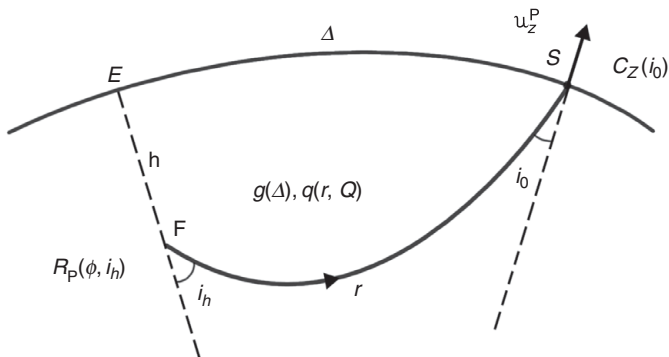


**Figure 6.6.** Ray path of the direct wave from focus \$F\$ (epicenter \$E\$) to station \$S\$ for a deep earthquake at depth \$h\$: \$R^P(\phi, i\_h)\$, radiation pattern; \$\Delta\$, epicentral distance; \$r\$, distance along the ray; \$i\_h\$, take-off angle; \$i\_0\$, incident angle; \$u\_z^P\$, vertical component of the P wave displacement; \$g(\Delta)\$, geometrical spreading; \$q(r, Q)\$, anelastic attenuation; \$C\_z(i\_0)\$, free surface correction.

(4.43)–(4.48). The moment rate \$\dot{M}\_0\$ can be expressed in terms of the seismic moment and the STF: \$\dot{M}\_0(t) = M\_0 f(t)\$. The direction cosines \$\gamma\_i\$ of the ray that arrives at the station can be computed in terms of the azimuth \$\phi\_s\$ and take-off angle \$i\_h\$; see (4.49)–(4.51). The vertical component of a direct P wave at an observation point on the surface of the Earth computed using ray theory can be written as (Fig. 6.6) (Deschamps *et al.*, 1980)

$$u_z^P = \frac{M_0 f(t - r/\alpha)}{4\pi\rho\alpha^3} R_P(\phi, \delta, \lambda, i_h) \frac{g(\Delta)}{\alpha} q(r, Q) C_z(i_0) \quad (6.8)$$

where \$r\$ is the distance along the ray from the focus to the station, \$R\_P(\phi, \delta, \lambda, i\_h)\$ is the radiation pattern for P waves (Section 4.4.2) with \$\phi\$ the azimuth at the focus measured from the trace of the fault (here, we use \$\phi = \phi\_{\text{station}} - \phi\_{\text{fault}}\$), \$i\_h\$ the take-off angle of the ray at the source and \$i\_0\$ the angle of incidence of the ray at the station; \$g(\Delta)\$ is a factor accounting for geometrical spreading, \$\Delta\$ is the angular distance from epicenter to station and \$\alpha\$ is the Earth's radius. Furhter more,

$$g(\Delta) = \left( \frac{\rho_h \alpha_h \sin i_h}{\rho_0 \alpha_0 \sin \Delta \cos i_0} \frac{di_h}{d\Delta} \right)^{1/2} \quad (6.9)$$

where the sub-index 0 refers to values at the station and the subindex \$h\$ to values at the focus. The anelastic attenuation is given by

$$q(r, Q) = \exp\left(\frac{-\omega r}{2\alpha Q}\right) \quad (6.10)$$

where \$Q\$ is the quality factor. The correction \$C\_z(i\_0)\$ due to the effect on the amplitudes of the free surface at the observing point is given by

$$C_z(i_0) = \frac{2 \cos i_0 \cos j_0}{\cos^2 2j_0 + (\beta/\alpha)^2 \sin 2i_0 \sin 2j_0} \quad (6.11)$$

In terms of  $\phi$ ,  $\delta$ ,  $\lambda$  the radiation pattern of the P waves is given by

$$R_P = A(3 \cos^2 i_h - 1) - B \sin 2i_h - C \sin^2 i_h \quad (6.12)$$

and that of the SV waves by

$$R_S = -\frac{1}{2}A \sin 2i_h - B \cos 2i_h - \frac{1}{2}C \sin 2i_h \quad (6.13)$$

with

$$A = \frac{1}{2} \sin \lambda \sin 2\delta \quad (6.14)$$

$$B = \sin \lambda \cos 2\delta \sin \phi + \cos \lambda \cos \delta \cos \phi \quad (6.15)$$

$$C = \sin \delta \cos \lambda \sin 2\phi - \frac{1}{2} \sin \lambda \sin 2\delta \cos 2\phi \quad (6.16)$$

For a simple source the STF  $f(t)$  in (6.8) is assumed to have a triangular or trapezoidal form, and for a complex source it is assumed to be given by a combination of triangular or trapezoidal functions (Section 4.8). For a simple source the duration of the source corresponds to its rise time, and for a complex source to the sum of all the individual rise times. It is important to remember that if we assume a point source then the STF duration corresponds to the time interval of release of energy, not to the dimension of the source.

For the more frequent case of a shallow point source, we have to consider the contribution of the reflected waves pP and sP together with the direct P wave to obtain the complete wave form, adding these terms to obtain synthetic seismograms (Fig. 6.7). Thus, the complete wave form of the displacement at the surface is the sum of P, pP and sP waves, which, using the Green's function computed using ray theory in a stratified medium, is given by (Deschamps *et al.*, 1980)

$$\begin{aligned} u_z^P &= \frac{M_0}{4\pi\rho\alpha^3} \frac{g(\mathcal{A})}{a} G(r, Q) C_z(i_0) \\ &\times [R_P(\phi, i_h) f(t - t_p) \\ &+ R_P(\phi, \pi - i_h) V_{pR} f(t - t_p - \Delta t_{pP}) \\ &+ R_S(\phi, \pi - j_h) V_{sR} f(t - t_p - \Delta t_{sP})] \end{aligned} \quad (6.17)$$

The first term corresponds to the direct wave, the second to the pP wave and the third to the sP wave (Fig. 6.7). The quantities  $R_P$  and  $R_S$  are the normalized radiation patterns for the P and SV waves (4.64) and (4.65). For the pP and sP waves, rays take off from the focus in the upward direction and correspond to incidence angles  $\pi - i_h$  and  $\pi - j_h$ . According to Snell's law,  $\sin j_h = (\beta/\alpha) \sin i_h$ . The delays of the pP and sP waves with respect to the arrival time  $t_p$  of the P wave are calculated using the approximation that the direct and reflected rays have the same take-off angles at the focus and the surface; see Fig. 6.7a. Then from  $F$  and  $F'$  the travel times of the three rays are the same, and the delay time of the pP wave is

$$\Delta t_{pP} = t_{pP} - t_p = \frac{l_1 + l_2}{\alpha} = \frac{2h \cos i_h}{\alpha} \quad (6.18)$$

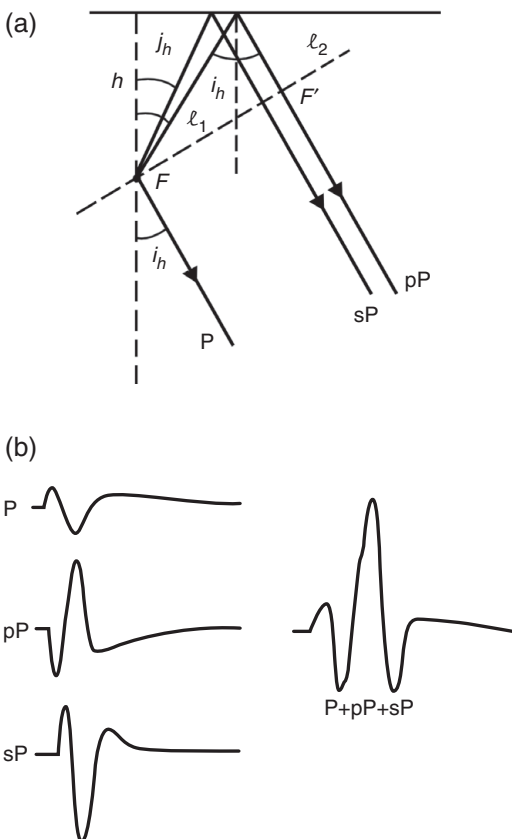


**Figure 6.7.** (a) Paths of rays leaving a shallow focus  $F$  at depth  $h$ : P: direct wave; pP, reflected P wave; sP, reflected wave converted from S to P;  $i_h$ , take-off angle of P wave;  $j_h$ , take-off angle of S wave. (b) Pulses at a station of the waves P, pP and sP, and their sum.

and that of the sP wave is

$$\Delta t_{\text{sP}} = t_{\text{sP}} - t_{\text{P}} = h \left( \frac{\cos j}{\beta} + \frac{\cos i_h}{\alpha} \right) \quad (6.19)$$

In equation (6.17)  $V_{\text{pP}}$  and  $V_{\text{SP}}$  are the reflection coefficients at the free surface for an incident P and reflected P wave, and an incident SV and reflected P wave. The observed P wave is the sum of the three waves (Fig. 6.7b).

In practice, for S waves the horizontal components are first rotated to obtain the radial and transverse components, corresponding to horizontal SV and SH waves. Usually only the SH component of the S wave is used. If we are using stations at epicentral distances  $30^\circ$ – $90^\circ$ , the attenuation effect may be considered as constant and it is enough to multiply equation (6.17) by a factor 1 for P waves and a factor 4 for S waves.

A more general approach, which can be applied to earthquakes at teleseismic and regional distances, uses the Green's functions determined for spherical or plane layered

media for the calculation of the *synthetic seismograms*. For the far-field approximation the six Green's functions can be written in terms of three functions of the ray parameter  $I_k(p)$ , called the *elementary seismograms*, and functions depending on the azimuth between the source and the station (Sipkin, 1982; Koch, 1991; Dahm, 1996):

$$g_{ij} = I_1(p_i) a_{1j}(\phi_i) + I_2(p_i) a_{2j}(\phi_i) + I_3(p_i) a_{3j}(\phi_i) \quad (6.20)$$

where  $i = 1, 2, 3$  refers to the components of the displacement and  $j = 1-6$ . The azimuthal functions  $a_{kj}(\phi_i)$  for the vertical and radial components (P and SV) are given by

$$\begin{aligned} a_{1j} &= \frac{1}{2} (\delta_{1j} \cos^2 \phi + \delta_{3j} \sin^2 \phi) + \frac{1}{2} \delta_{2j} \sin 2\phi \\ a_{2j} &= \delta_{4j} \cos \phi + \delta_{5j} \sin \phi \\ a_{3j} &= \frac{1}{2} \delta_{6j} \end{aligned}$$

and for the transverse motion (SH) they are

$$\begin{aligned} a_{1j} &= \frac{1}{2} (\delta_{1j} - \delta_{3j}) \sin 2\phi - \delta_{2j} \cos 2\phi \\ a_{2j} &= \delta_{4j} \sin \phi - \delta_{5j} \cos \phi \\ a_{3j} &= 0 \end{aligned}$$

The elementary seismograms  $I_k(p)$  for layered media can be calculated by several methods, as seen in section 3.6. For epicentral angular distances less than  $30^\circ$ , the attenuation  $Q$  should be taken into account (in this case we cannot use the approximations 1 for P waves and 4 for SH waves); we need to use specific values for each region.

In practice, after we have calculated the synthetic seismograms there are two ways of proceeding. In the first we convolve the calculated or theoretical ground displacement  $u^T(t)$  with the attenuation and the instrument response to obtain, according to (2.1), a synthetic seismogram which we compare with the observed seismogram. Since each station has a different instrument response, it is more convenient to remove the specific instrument effect for each observed seismogram and to convolve them with a common instrumental response for all the observations. The synthetic seismograms  $u^T(t)$  are also convolved with this common instrumental response and then a comparison is made between the synthetic and observed seismograms.

Alternatively, we can work directly with the synthetic ground displacements  $u^T(t)$ , corrected only by an attenuation factor, and compare them with the observed ground displacements obtained by removing the instrumental response from the observed seismograms. The latter method is less stable in the presence of seismic noise, especially at low frequencies.

In order to carry out the inversion we need to choose a set of observations, that is, the seismograms, and to fix a number of parameters in order to start the inversion. The length of the selected part of the seismogram must be sufficient to include all the phases used in the inversion. For example, at teleseismic distances, if we use body waves then the time window must include the entire P or SH wave trains (that is, the P, pP, sP waves etc.) and so its duration depends on the magnitude and focal depth of the shock. For example, for a

moderate ( $M_W < 7.0$ ) shallow earthquake ( $h < 30$  km) a time window of 40 s is enough, but for a deep earthquake ( $h > 500$  km) we need a time window of about 250 s. The initial parameters to start the process of inversion are the preliminary values of the fault-plane orientation (strike, dip and slip), the depth, the scalar seismic moment and the STF. The STF is usually a triangle for a simple source and several triangles for complex sources (normally we give the half triangle time duration).

The observations are selected from the P and SH waves at different azimuths within the accepted range of distance. A solution is sought which minimizes the misfit  $\chi$  between the observed and theoretical wave forms by changing the parameters of the model, namely  $\phi$ ,  $\delta$ ,  $\lambda$ ,  $f(t)$ ,  $M_0$  and  $h$ :

$$\chi = \sum_{j=1}^N \sum_{k=1}^L \left( u_{jk}^O - u_{jk}^T \right)^2 \quad (6.21)$$

where  $u_{jk}^O$  are the observed and  $u_{jk}^T$  the theoretical wave amplitudes at station  $j$  corresponding to time  $k$ ,  $L$  is the number of amplitudes at time or frequency values of the wave form or spectrum at each station (the same for all stations) and  $N$  is the number of stations. The number of observations is then  $LN$ . The source parameters are  $M_0$ ,  $\phi$ ,  $\delta$ ,  $\lambda$ ,  $f_i$ ,  $i = 1, \dots, P$  and  $h$ ; that is, there are  $5+P$ , where  $P < L$ ; the  $f_i$  are the discretized values of  $f(t)$  and the source duration is  $t_d$ .

The procedure used to find the set of source parameters that minimize the misfit  $\chi$ , (6.21), varies for different approaches. Usually an iterative procedure is used starting from some initial values. In the first step the values of depth are changed within some pre-established range and, for each value, the other parameters are found. The depth is then selected that corresponds to a minimum in the misfit (Fig. 6.8). This value of  $h$  corresponds to the centroid depth and may be different from the hypocentral depth. In the second step, this fixed value of depth is used in order to refine the inversion of the other parameters ( $M_0$ ,  $\phi$ ,  $\delta$ ,  $\lambda$ ,  $f_i$ ). The object of having two steps is to reduce the number of unknowns to be determined at each step of the process. A problem with such methods is the non-uniqueness of the solution and the possible existence of several relative minima in the solution space, especially if the algorithm does not do a complete fine search in this space.

Moreover, there may exist a certain ambiguity between the STF and depth. Normally we fix the STF to obtain the correct depth and then, in the second step, we vary the STF to obtain the minimum misfit. However, it is sometimes possible to obtain the same synthetic seismogram by using a simple STF at a shallow depth or a more complex STF at a greater depth.

It is important to remember that the body wave amplitude depends on the radiation pattern, which varies according to the take-off angle with respect to the faulting mechanism of the ray reaching the recording station. For rays leaving the source near a nodal plane their amplitudes will be small. For large earthquakes ( $M_W > 7$ ) this is not a problem, because the signal amplitudes are larger than the noise level. For lower magnitudes ( $5.0 < M_W < 7.0$ ), however, the noise may be very large; in this case the observed amplitudes of the P and SH waves will depend on the relative orientation of the station and the fault planes. In general, strike-slip mechanisms are difficult to model since the take-

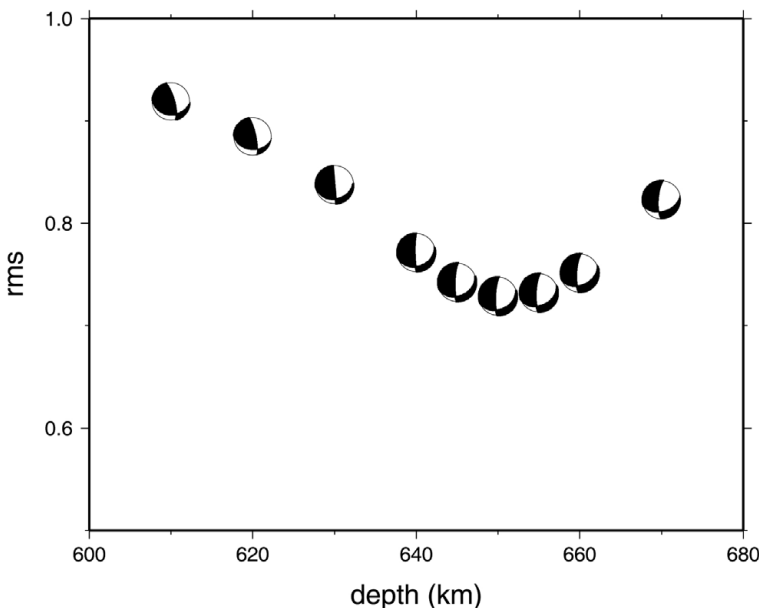


**Figure 6.8.** Plot of the root mean square misfit versus depth of the source mechanism, obtained from inversion of the body waves for the Spanish deep earthquake of 11 April 2010. The minimum occurs at 650 km.

off angles for rays arriving at teleseismic distances (between  $30^\circ$  and  $90^\circ$ ), correspond to low amplitudes for most azimuths (Fig. 4.12). However, for dip-slip mechanisms, such as thrust faulting, these stations have large amplitudes for all azimuths for P waves and for some azimuths for SH waves.

For small earthquakes, for which amplitudes are low, we need to use observations at regional distances. The methodology is similar but to compute the Green's functions we need a detailed crustal model for each region. Inversion can be carried out in the time or frequency domain but, owing to path effects, errors in the crustal model can produce errors in the estimation of focal depth (Cesca *et al.*, 2006).

## 6.5. Empirical Green's function

At regional distances (100 to 1000 km), owing to the heterogeneity of the crust and upper mantle structure, it is difficult to separate source effects from path effects in the observed seismograms. To model wave forms at those distances we need very detailed crustal models to generate the Green's functions. In many cases, however, owing to the presence of lateral inhomogeneities, the use of models with homogeneous layers together with the reflectivity method or the generalized ray method to model synthetic seismograms may be inappropriate. One way to solve this problem is to use *empirical Green's functions* (EGFs) (Hartzell, 1978). This requires Green's functions to be obtained empirically for the region in question. To use this method we need two

earthquakes with same hypocenter, recorded at the same station and with similar wave forms and differences in magnitude from 1 to 2.5 units. We assume that the seismogram of the smaller earthquake represents an EGF that can be used to determine the mechanism of the larger shock.

Let  $s_1(t)$  be the seismogram of the larger shock and  $s_2(t)$  that of the smaller one; then, according to equation (2.1),

$$\begin{aligned}s_1(t) &= u_1(t)*f(t, Q)*I_1(t) \\ s_2(t) &= u_2(t)*f(t, Q)*I_1(t)\end{aligned}\quad (6.22)$$

If we assume that for the smaller shock the STF has approximately the form of a delta function,  $f(t) = \delta(t)$ , then its seismogram  $s_2(t)$  can be used as the Green's function for the larger one.

Bearing in mind equation (6.17), if we apply a Fourier transform to equations (6.22) and divide the two equations we then obtain, since  $F_2(\omega)$  is equal to unity,

$$\frac{S_1(\omega)}{S_2(\omega)} = \frac{U_1(\omega)}{U_2(\omega)} = \frac{M_{01} F_1(\omega)}{M_{02} F_2(\omega)} = \frac{M_{01}}{M_{02}} F_1(\omega) \quad (6.23)$$

From this equation we can obtain the STF for the larger shock,  $F_1(\omega)$ . This STF is called the *apparent source time function* (ASTF) and it can vary from one station to another if directivity effects are present (Fig. 6.9). Also, the EGF may be used to obtain synthetic records for larger-magnitude earthquakes by convolution of the EGF with the STF of the larger shock.

## 6.6. Moment tensor inversion

In Section 5.6 we studied the representation of a point source in terms of the first-order moment tensor. According to (5.32) and (5.33) the seismic wave displacement can be expressed in the time domain as a convolution and in the frequency domain as the product of the components of the moment tensor with the derivatives of the Green's function of the medium. For an infinite homogeneous isotropic medium the displacements in the P, SV and SH waves can be written in terms of very simple linear equations for the components of the moment tensor, namely, (5.36), (5.37) and (5.38). The mechanism defined by the six components of the moment tensor represents a very general form of point source including changes in volume. If these are excluded ( $M_{11} + M_{22} + M_{33} = 0$ ), the source is purely deviatoric and the independent components are reduced to five (see section 5.7). The moment tensor can be normalized and, for a synchronous source in the time domain, we can express it as  $M_{ij}(t) = M_0 f(t) m_{ij}$  or, in the frequency domain,  $M_{ij}(\omega) = M_0 f(\omega) m_{ij}$ . Here  $M_0$  is the scalar seismic moment only when the moment tensor is a simple shear fracture or double-couple (DC) source. Several methods have been proposed for inversion of the moment tensor, using body wave forms, surface waves or the complete seismogram, both at teleseismic and regional distances (see, for example, Mendiguren, 1977; Kanamori and Given, 1981; Stump

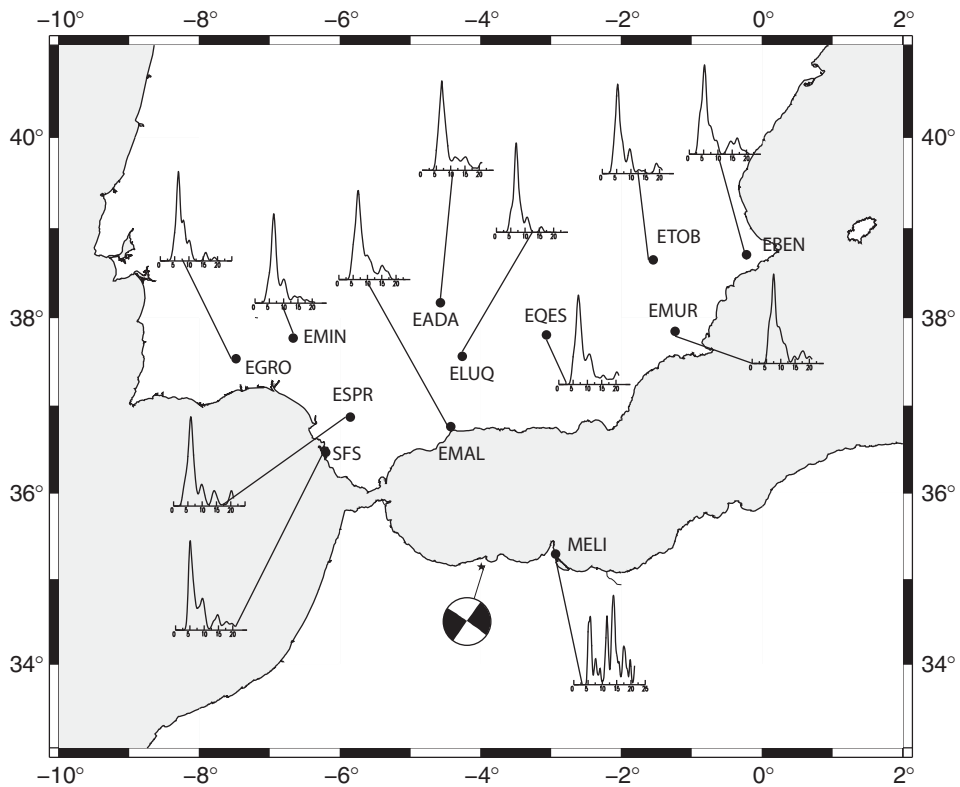


**Figure 6.9.** Solution of wave form analysis for the point source mechanism of the Chile earthquake of 25 March 2012. Agreement between the observed (gross) and synthetic (thin) of P and SH wave pulses, source time function and mechanism with P wave polarities. Scalar seismic moment  $M_0$  (N m) and moment magnitude  $M_W$ .

and Johnson 1977; Strelitz, 1978; Sipkin, 1986 and 1994; Dahm, 1996; Cesca *et al.*, 2010 and, for a review, Jost and Hermann, 1989). Most methods assume that the source is purely deviatoric and synchronous, so that it is defined by the five components of  $m_{ij}$ , plus  $M_0$  and  $f(t)$ . The solution obtained for the moment tensor can then be separated into DC and CVLD parts, as we saw in section 5.7.

The determination of the seismic moment tensor can be carried out either in the time or frequency domain. In the frequency domain the real and imaginary parts of the spectrum are linear functions of the moment tensor components but not of the spectral amplitude. If we solve the problem in the frequency domain using only the amplitude spectra, we lose the information about the polarities of the seismograms. In this case a comparison with the observed seismograms is necessary in order to obtain the correct values for the  $P$  and  $T$  axes. It is generally assumed that all components of the moment tensor have the same time or frequency dependence (i.e. a synchronous source). In some cases the time dependence is assumed to be known. The derivative of the Green's function for each location can be reduced to six so-called *excitation functions* for each component of the displacement. The Green's functions depend on the Earth model, the

location of the point source and the receiver position. For observations at  $k$  stations with one component, we can write [equation \(5.32\)](#) as

$$u^k(r, t) = \sum_{i=1}^6 g_i^k(r, t) * m_i(t) \quad (6.24)$$

in the time domain, and as

$$u^k(r, \omega) = \sum_{i=1}^6 g_i^k(r, \omega) m_i(\omega) \quad (6.25)$$

in the frequency domain. These expressions can be written in matrix form as

$$\mathbf{u} = \mathbf{G} * \mathbf{m} \quad (6.26)$$

and

$$\mathbf{u} = \mathbf{G} \mathbf{m} \quad (6.27)$$

where  $\mathbf{u}(u_j^k)$  is one component of the observed wave displacement at station  $k$  ( $k = 1-N$ ), located at position vector  $\mathbf{r}$ , corresponding to times  $t_j, j = 1-L$  or frequencies  $\omega_j, j = 1-L$  ( $L$  is the same for all stations);  $G_{ij}^k$  are the six excitation functions ( $i = 1-6$ ) for a given medium (usually a layered medium), which are a function of the location of the source and of the observation point, corresponding to times  $t_j, j = 1-L$  or frequencies  $\omega_j, j = 1-L$ ; and  $m_{ij}$  ( $i = 1-6$ ) are the six components of the moment tensor  $\mathbf{m}$  ( $m_1 = m_{11}, m_2 = m_{22}, m_3 = m_{33}, m_4 = m_{12}, m_5 = m_{13}, m_6 = m_{23}$ ), at times  $t_j, j = 1-P$  or frequencies  $\omega_j, j = 1-P$  ( $P < L$ ). For purely deviatoric sources  $m_1 + m_2 + m_3 = 0$ . For a synchronous moment tensor the time dependence is the same for all components. At each station the wave displacements are sampled at  $L$  times or frequency values. If we have  $N$  stations then there are  $LN$  equations to solve for the six or five components of the moment tensor, each for  $P$  time or frequency values, that is,  $6P$  or  $5P$  unknowns. For a synchronous source, as mentioned before, all components of the moment tensor are assumed to have the same time or frequency dependence and thus the unknowns are  $6+P$  or  $5+P$  in number. Since the number of observations  $LN$  is larger than the number of unknowns  $6P$  or  $6+P$ , the problem can be solved for the model vector  $\mathbf{m}$  in different forms ([Tarantola, 1987](#); [Menke, 2012](#)). For example, by a least square's procedure,

$$\mathbf{m} = (\mathbf{G}^T \mathbf{G})^{-1} \mathbf{G}^T \mathbf{u} \quad (6.28)$$

where the superscript  $T$  denotes a matrix transpose and the superscript  $-1$  indicates a matrix inverse. Or, using Lanczos' generalized inverse, the solution is given in the form

$$\mathbf{m} = (\mathbf{U}^T \mathbf{A} \mathbf{V}) \mathbf{u} \quad (6.29)$$

where  $\mathbf{U}$  and  $\mathbf{V}$  are matrices formed by the eigenvectors of  $\mathbf{G}^T \mathbf{G}$  and  $\mathbf{G} \mathbf{G}^T$  respectively and  $\mathbf{A}$  is a diagonal matrix formed by the eigenvalues of  $\mathbf{G}^T \mathbf{G}$ . Unfortunately this solution can almost never be computed because the matrix  $\mathbf{G}^T \mathbf{G}$  is almost always ill conditioned, that is, its inverse cannot be computed in a computer with finite digital precision. The reason is that this matrix invariably contains a set of very small eigenvalues that produce large

errors when the inversion procedure is carried out. To reduce such uncertainties produced by small eigenvalues of the matrix  $\mathbf{G}^T \mathbf{G}$  one adds additional conditions for the solution of (6.28), as discussed in inverse problem theory (see e.g. Tarantola, 1987; Menke, 2012). The most common method is to add a correlation matrix that imposes a set of bilinear relationships between the elements of the model vector  $\mathbf{m}$ . This is equivalent to requiring that the model vector satisfies the additional linear relations  $\mathbf{C}\mathbf{m} = 0$  as closely as possible. The result is

$$\mathbf{m} = (\mathbf{G}^T \mathbf{G} + \theta \mathbf{C}^T \mathbf{C})^{-1} \mathbf{d} \quad (6.30)$$

where  $\theta$  is a Lagrange multiplier and  $\mathbf{C}^T \mathbf{C}$  is a correlation matrix. The Lagrange multiplier can take any value, so that for very small  $\theta$  the effect of the correlation matrix is very small while for larger values of the multiplier the correlation dominates. In many practical applications  $\theta$  is called the damping coefficient, and the matrix  $\mathbf{C}^T \mathbf{C}$  is called the smoothing matrix because its main effect is to reduce small eigenvalues of the least squares solutions, thus reducing fast variations of the elements of  $\mathbf{m}$ . A typical example of a smoothing operator, used in many applications, is the minimum norm of the model vector  $\mathbf{m}$ . This is obtained when  $\mathbf{C}^T \mathbf{C} = \mathbf{I}$  because it is equivalent to adding the conditions  $\mathbf{m} = 0$  to the inverse problem. In general, the use of this condition is enough to stabilize the inverse problem (6.28).

In practice the formal inversion given by equations (6.28) and (6.29) is seldom used. In its place the solution is often found by minimizing the misfit between the synthetic and observed seismograms, equation (6.24), by a systematic search for the values of the moment tensor components.

Because of the properties of the convolution of two functions, equation (5.32) can also be given, for the far-field displacements, as

$$u_i = g_{ik} * \dot{M}_k \quad (6.31)$$

This equation can now be written in the form of equations (6.24) and (6.25), where the  $g_{ik}$  are Green's functions and the  $\dot{M}_k$  are the time derivatives of the moment tensor.

The solution obtained for the moment tensor can then be separated into its isotropic, double couple and CVLD components, as explained in section 5.7.

## Body wave forms

As we did for the inversion of body wave forms for a point shear fracture model, we will consider first an isolated direct P wave, as we might have in the case of a very deep earthquake. According to (5.36) and (6.8) the far-field displacement of the P waves at a distance  $\Delta$  from the source can be written, using the Green function's for an infinite homogeneous medium, as

$$\begin{aligned} u_z^P(t) = & A \cos i_0 [\sin^2 i_h (\cos^2 \phi' m_{11}(t) + \sin^2 \phi' m_{22}(t) \\ & + \sin 2\phi' m_{12}(t)) + \cos^2 i_h m_{33}(t) \\ & + \sin 2i_h (\cos \phi' m_{13}(t) + \sin \phi' m_{23}(t))] \end{aligned} \quad (6.32)$$

where  $\phi'$  is the azimuth of the station,  $A$  is given by

$$A = \frac{M_0 f(t - r/\alpha) g(A)}{4\pi\rho\alpha^3} q(r, Q) C_z(i_0) \quad (6.33)$$

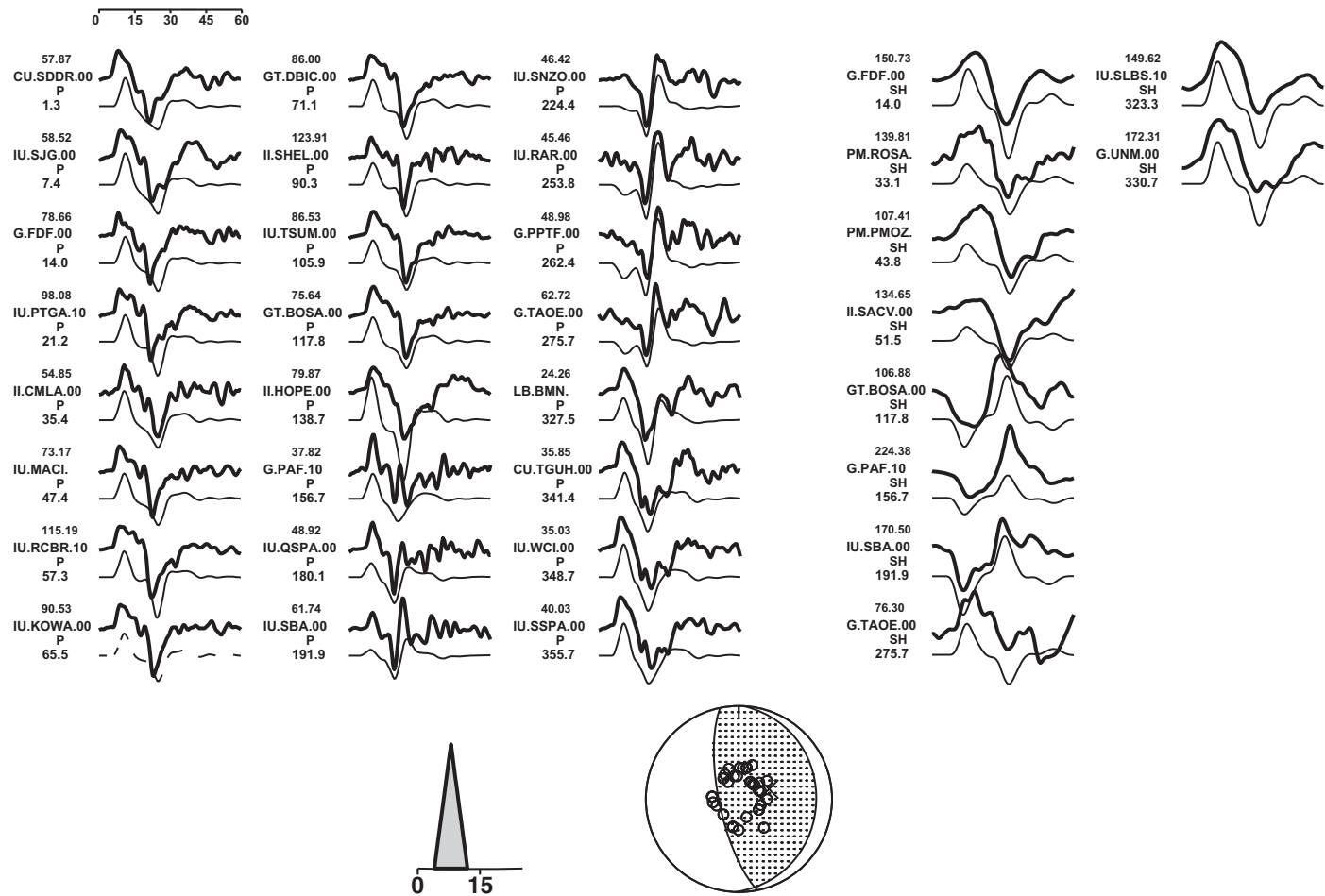
and for a synchronous source all components of the moment tensor have the same time dependence. The various quantities in (6.32) were defined after (6.8).

For a general wave form we have to consider the sum of the P, pP and sP waves, as we did in (6.17). The result is an expression very similar to (6.17), substituting  $R_P(\hat{\phi}, \delta, \lambda, i_h)$  and  $R_S(\hat{\phi}, \delta, \lambda, i_h)$  (where  $\hat{\phi} = \phi_{\text{station}} - \phi_{\text{fault}}$ ) by (5.36) and (5.37) without the constants  $A$  and  $B$ . If the problem is solved in the frequency domain, we change  $f(t - r/\alpha)$  to its Fourier transform  $f(\omega) \exp(-i\omega r/\alpha)$ . If the number of observations comprises  $L$  samples in time or frequency at  $N$  stations, i.e.  $u_j(t_k)$  for  $j = 1-N$  and  $k = 1-L$  then we have  $LN$  equations of the type (6.24) or (6.25) that must be solved for the  $6L$  unknowns  $M_{ij}(t_k)$  or  $M_{ij}(\omega_k)$ ,  $k = 1-L$  or, for a synchronous source,  $6 + L$  unknowns. If the source is assumed to be purely deviatoric, we can substitute  $m_{33} = -m_{11} - m_{22}$ . The misfit between the observations and the theoretical displacements calculated from the obtained solution can be found by again using a least squared expression such as (6.21).

In the general case, for a complex medium we have to define first the Earth's lithospheric and mantle structure and then calculate the Green's functions (Kikuchi and Kanamori, 1982; Nabelek, 1984). Normally a layered medium is used, defined by the height  $h_i$  of layer  $i$ ,  $\alpha_i$  and  $\beta_i$ , its P and S velocities, and its density  $\rho_i$ . Other methods for regional distances use the reflectivity method (Müller, 1985) to generate the Green's functions for specific crustal models. In some methods different lithospheric models for the source and the stations can be used. Once we have generated the Green's functions for the medium, we can convolve them with the derivatives of the moment tensor in (6.27) to find the body wave forms (<http://www.eri.u-tokyo.ac.jp/ETAL/KIKUCHI/>). An example of the results of inversion at teleseismic distances of P and SH waves is shown in Fig. 6.10. Herrmann's programs (<http://www.eas.slu.edu/eqc/eqccps.html>) use body and surface waves and three different sets of Green's functions: one for teleseismic distances, great circle angular distances between  $35^\circ$  and  $95^\circ$  and depths down to 790 km, and two others for regional distances up to 2190 km and depths from the surface down to 69 km. One regional-distance set is for a craton model and the other is for a tectonic structure (<ftp://ftp.eas.slu.edu/pub/rbh/PROGRAMS.330/NP330.Apr-03-2009.tgz> and tutorial: <ftp://ftp.eas.slu.edu/pub/rbh/MomentTensor/MomentTensor-Course.pdf>). Other methods for regional distances use the reflectivity method (Müller, 1985) to generate the Green's functions from specific crustal models for each region.

As already mentioned, most so-called *inversion methods* do not solve the problem using equations (6.28) or (6.29) but usually generate synthetic displacements  $u_i^T$  corresponding to a given moment tensor; these are then compared with the observed data. Using difference methods the solution is found for the moment tensor that minimizes the misfit or difference between the synthetic and observed data, as in equation (6.21). The obtained moment tensor is then separated into DC and CLVD parts (Fig. 6.11). When we obtain solutions with a high percentage of CLVD, this may be an indication that the lithospheric model was not correct, or the result of errors in the numerical method used to minimize the sum of the squares of the residuals, not necessarily a property of the source. Normally, as mentioned earlier, inversion methods use a fixed depth and then carry out iterative

## Chile 25 March 2012



$$M_O \text{ (N m)} = 0.198 \times 10^{20} \quad M_W = 6.80$$

**Figure 6.10.**

Empirical apparent source time functions (ASTFs) at different broadband stations in south Iberia and Northern Africa from the Alhoceima earthquake (Morocco) on 24 February 2010 (The time scales are in seconds).

## Colombia 30-09-2012

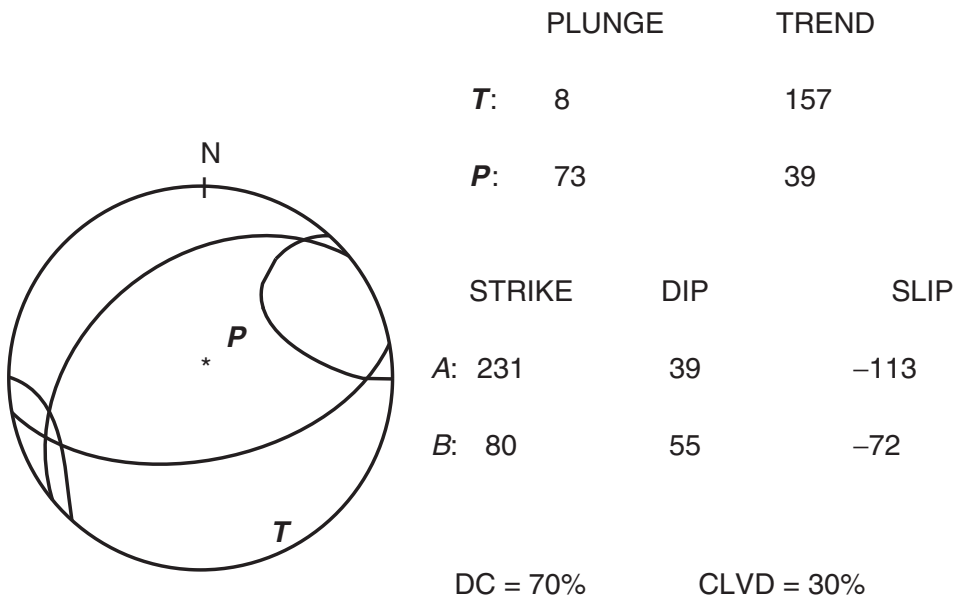


**Figure 6.11.** Results of moment tensor inversion for the Colombia earthquake of 30 September 2012, with components 70% DC and 30% CLVD.

inversions using different depths inside an interval. The solution with the lowest rms value is identified as corresponding to the correct depth. Some methods use the minimization of a combination of different fit parameters, such as rms, CLVD etc.

In some cases, if the observed seismograms have complex wave forms then it is possible to model them using several events at different depths and with different fault-plane orientations. The total solution, that is, the sum of all individual solutions, will then correspond to a non-DC source. In this way, it is possible to obtain a good fit between the observed and synthetic data, but the solution, formed from different events with different mechanisms, may not be realistic, from a seismotectonic point of view.

### Surface waves

Other methods for moment tensor determination use the inversion of the spectral amplitudes of Rayleigh waves (Mendiguren, 1977; Kanamori and Given, 1981; Romanowicz, 1982). The vertical component of the Rayleigh wave spectrum recorded at a distance  $r$  and azimuth  $\phi$  can be written as

$$U(r, \phi, \omega) = S(\omega)I(\omega) e^{ir\omega/c} e^{-\gamma r} A_0(\omega, \phi) e^{\Phi_0(\omega, \phi)} \quad (6.34)$$

where  $S(\omega)$  and  $I(\omega)$  are corrections for propagation and instrument effects,  $c$  and  $\gamma$  are the average phase velocity and attenuation coefficient and  $A_0$  and  $\Phi_0$  are the amplitude and phase at the source.

The real and imaginary parts of the displacement spectrum at the source are linear functions of the moment tensor components  $M_{ij}(\omega)$  and of the Fourier transforms of the Green's functions or *excitation functions*. For a purely deviatoric source (with only five independent components of the moment tensor), the real and imaginary parts of the displacements are given by

$$\begin{aligned}\text{Re}(\omega, \phi) = & -(M_{11} + M_{22})(G_1 - G_2) - (M_{11} - M_{22})G_2 \cos 2\phi \\ & + 2M_{12}G_1 \sin 2\phi\end{aligned}\quad (6.35)$$

$$\text{Im}(\omega, \phi) = M_{13}G_3 \cos \phi + M_{23}G_3 \sin \phi \quad (6.36)$$

where  $G_i(\omega, h)$  are the excitation functions in the frequency domain ( $h$  is the depth of the focus). If we use the vertical component of the Rayleigh waves at  $N$  stations, the real and imaginary parts of their spectra at  $L$  values of frequency constitute  $2LN$  equations such as (6.35) and (6.36), to be solved for  $5P$  unknowns (given  $P$  spectral values of the moment tensor) or  $5+P$  unknowns for a synchronous source. A simplification can be introduced by assuming for the moment tensor a known function of time. The solution can be found by a least squares procedure. The excitation functions  $G_i$  depend on frequency and focal depth. Since focal depth is usually a poorly constrained parameter, in order to avoid errors that it may introduce into the determination of  $M_{ij}$  solutions are found for different values of  $h$ . This is done by determining the misfit (equation (6.21)) between the observed and theoretical values as a function of focal depth and, finally, selecting the value of  $h$  that minimizes the misfit.

For the spectral amplitudes, the problem is non-linear and can be solved by linearization using the form

$$A(\omega, m_i) = A(\omega, m_i^0) + \sum_{i=1}^6 \left( \frac{\partial A}{\partial m_i} \right)_{m_i^0} \delta m_i \quad (6.37)$$

where  $A(\omega, m_i)$  are the observed spectral amplitudes corrected for propagation and instrument effects,  $m_i^0$  are initial values of the six components of the moment tensor and  $\delta m_i$  are the corrections found at each iteration, so that  $m_i^k = m_i^{k-1} + \delta m_i$ . The unknown  $m_i$  are found by an iterative process until a minimum of the misfit (6.21) between the observed and the theoretical wave-forms is found.

Thio and Kanamori (1995) carried out an inversion at regional distances in the frequency domain using the complex spectra of surface waves recorded at different stations. The seismograms are first corrected for propagation effects. The corrected spectra of Rayleigh and Love waves are then given by

$$\begin{aligned}V_R(\omega) = & -P_R \left[ M_{xy} \sin 2\phi - \frac{1}{2}(M_{yy} - M_{xx}) \cos 2\phi \right] - \frac{1}{2}S_R(M_{yy} - M_{xx}) \\ & + iQ_R(M_{yz} \sin \phi + M_{xz} \cos \phi)\end{aligned}\quad (6.38)$$

$$\begin{aligned}V_L(\omega) = & -P_L \left[ \frac{1}{2}(M_{xx} - M_{yy}) \sin 2\phi - M_{xy} \cos 2\phi \right] \\ & + iQ_L(M_{yz} \cos \phi - M_{xz} \sin \phi)\end{aligned}\quad (6.39)$$

where  $V_L(\omega)$  and  $V_R(\omega)$  are the corrected spectra at the source,  $P_L$ ,  $P_R$ ,  $Q_L$ ,  $Q_R$ , and  $S_R$  are the excitation functions and  $\phi = \phi_{\text{sta}} - \phi_{\text{fault}}$ .

These equations may be written in matrix form as

$$\mathbf{v} = \mathbf{A} \mathbf{m} \quad (6.40)$$

where  $\mathbf{A}$  is a matrix that contains the excitation functions and the azimuthal terms,  $\mathbf{m}$  is a vector formed as before by the moment tensor elements  $M_{ij}$  and  $\mathbf{v}$  is a vector comprising the real and imaginary parts of the spectral data (the observations). To reduce the noise, a group velocity window (say between 2.5 and 4.5 s) can be applied to the observed and synthetic data before computation of the Fourier transform. Once the full wave forms have been computed, inversion of moment tensor can be carried out. This method is valid if the source dimension and duration are small compared with the epicentral distance and the period of the surface waves. For events with  $M_W > 6$  directivity effects, due to the dimensions of the source, must be taken into account. The excitation functions are estimated for different crustal models on the basis of dispersion curves and different focal depths. The inversion of the moment tensor components is carried out by solving equation (6.40) for  $\mathbf{m}$  in a least squares sense.

There are some methods for earthquakes at regional distances that use the full seismogram. For example, the KIWI tools (<http://kinherd.org/>) of Cesca *et al.* (2010) use the entire bandpass-filtered seismogram in order to fit the flat part of the spectra at low frequencies and to stabilize the inversion process. The inversion can also be carried out in the frequency domain, fitting amplitude spectra (Romanowicz, 1982; Dahm *et al.*, 1999). The observed amplitude spectra are inverted to find the best point source parameters (Fig. 6.12), but with this approach there is an ambiguity in the polarities, because the phases are not included and it is necessary to carry out a second inversion in the time domain in order to retrieve the correct polarities. After the first step of the inversion, the strike, dip, rake, scalar moment and centroid depth are estimated and the STF is fixed.

## 6.7. Centroid moment tensor inversion

---

As we saw in section 5.6, the hypocentral and origin times obtained from the first arrivals of body waves may not give the best point source location for the determination of the components of the moment tensor. Thus, as mentioned earlier, the concept of the location and origin time of the centroid was introduced (Dziewonski *et al.*, 1981; Dziewonski and Woodhouse, 1983). In the *centroid moment tensor inversion* method we seek to determine the location and origin time of the centroid together with the moment tensor components. In order to do this, following Dziewonski *et al.* (1981), we begin with the seismograms (for body and/or surface waves) recorded at several stations and perform a linear inversion of the moment tensor in the time domain using the known hypocentral coordinates and origin time (see equation (6.21)). This solution is taken as the initial estimate of the moment tensor. Then, in a second step,

## Aquila Main shock 06-04-2009

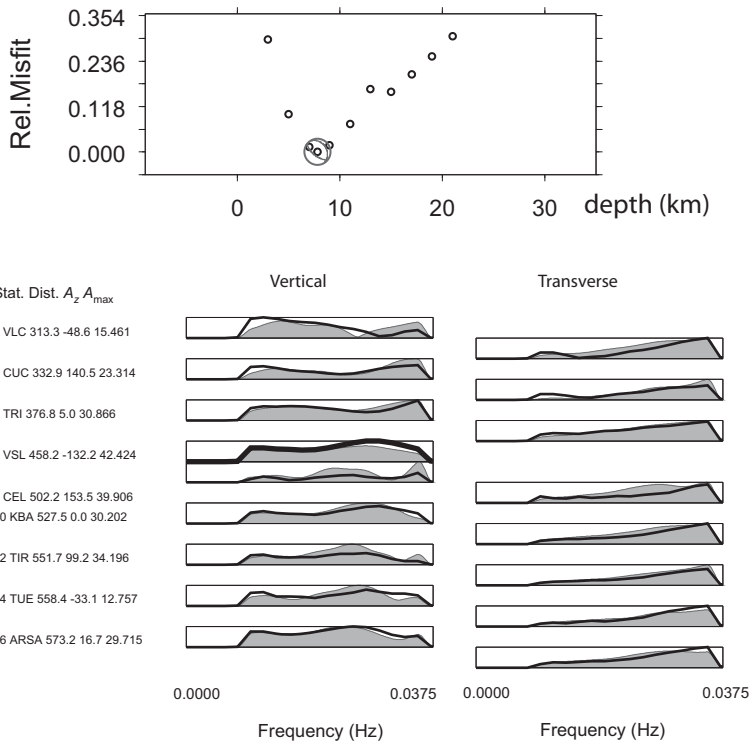


**Figure 6.12.** Inversion of the moment tensor from the body wave spectra at regional distances for the Aquila, Italy earthquake of 6 April 2009 using KIWI tools. At the top, the relative misfit versus depth. Below, the synthetic (shaded) and observed (bold-line) amplitude spectra for the closest stations, for the vertical and transverse components (courtesy of S. Cesca). The station distances are in km.

expression (6.21) for station  $k$  is expanded for small perturbations of the location, origin time and moment tensor components in the form

$$u_k = u_k^0 + b_k \delta r_s + c_k \delta \theta_s + d_k \delta \phi_s + e_k \delta t_s + \sum_{i=1}^6 g_{ki}^0 \delta m_i \quad (6.41)$$

where

$$\begin{aligned} b_k &= \sum_{i=1}^6 \frac{\partial g_{ki}^0}{\partial r_s} m_i^0 & c_k &= \sum_{i=1}^6 \frac{\partial g_{ki}^0}{\partial \theta_s} m_i^0 \\ d_k &= \sum_{i=1}^6 \frac{\partial g_{ki}^0}{\partial \phi_s} m_i^0 & e_k &= \sum_{i=1}^6 \frac{\partial g_{ki}^0}{\partial t_s} m_i^0 \end{aligned}$$

In (6.41)  $u_k^0$  are the wave displacements at station  $k$  corresponding to the initial estimates,  $r_s$ ,  $\theta_s$ ,  $\phi_s$  and  $t_s$  are the centroid source coordinates and origin time,  $g_{ki}$  are the excitation

Global CMT Catalogue  
 Search criteria:  
 Start date: 2012/3/25 End date: 2012/3/25  
 $-90 \leq \text{lat} \leq 90$     $-180 \leq \text{lon} \leq 180$   
 $0 \leq \text{depth} \leq 1000$     $-9999 \leq \text{time shift} \leq 9999$   
 $6 \leq \text{mb} \leq 10$     $6 \leq \text{Ms} \leq 10$     $6 \leq \text{Mw} \leq 10$   
 $0 \leq \text{tension plunge} \leq 90$     $0 \leq \text{null plunge} \leq 90$

#### Results

-----  
 201203252237A NEAR COAST OF CENTRAL CHILE



Date: 2012/3/25 Centroid Time: 22:37:20.9 GMT  
 Lat= -35.31 Lon= -72.41  
 Depth= 33.8 Half duration= 8.8  
 Centroid time minus hypocenter time: 14.9  
 Moment Tensor:  $\text{Expo}=26\ 2.920\ -0.038\ -2.880\ 0.415\ -5.190\ -0.474$   
 $M_w = 7.1\ mb = 6.5\ Ms = 7.1$  Scalar Moment =  $5.98e+26$   
 Fault plane: strike=20 dip=16 slip=112  
 Fault plane: strike=177 dip=76 slip=84

**Figure 6.13.** Centroid moment tensor (CMT) solution for the Chile earthquake of 25 March 2012. (Goran Ekstrom's global CMT project.)

functions and  $m_i$  are the six components of the moment tensor. The superscript 0 refers to the initial estimates. The problem is solved for the corrections  $\delta r$ ,  $\delta\theta$ ,  $\delta\phi$ ,  $\delta t$ ,  $\delta m_i$ , by an iterative process, beginning with the initial solution already obtained, until a solution is found which minimizes the misfit between the observed seismograms and the theoretical seismograms (6.20). Until 2006 this method was applied on a routine basis at Harvard University for all earthquakes with  $M_w > 5.0$ , using data from digital stations. The determination of moment tensors is nowadays continued by the global centroid moment tensor (CMT) project ([www.globalcmt.org](http://www.globalcmt.org)) led by Goran Ekstrom (see (Fig. 6.13)). Centroid moment tensors are also routinely calculated by the National Earthquake Information Center of the US Geological Survey (<http://neic.usgs.gov/equarchives/sopar/>).

## 7.1. Source dimensions

The first attempts to take into account the *extended dimensions* of an earthquake source considered as models spherical cavities of finite radius with a certain distribution of stress on their surface (Jeffreys, 1931, Nishimura, 1937). These studies showed that the duration of the radiated wave pulses depends on the radius of the cavity. Ben Menahem (1961), (1962) described *extended sources* in terms of distributions of single- and double-couple force systems propagating with a certain rupture velocity on a rectangular fault plane and determined the displacement field of the radiated body and surface waves. Berckhemer (1962) studied the duration of seismic pulses generated by shear dislocations on a *circular fault* of finite radius with a fracture propagating from its center. In a classical paper, Burridge and Knopoff (1964) studied the propagation of shear dislocations and showed that they were equivalent to a system of propagating double couples.

Following Burridge and Knopoff (1964) an *extended kinematic source* can be described either as a point displacement dislocation or a double-couple source propagating with a finite *rupture velocity* on a surface of finite area. Let us start with the expressions for the far-field displacement produced by a point dislocation, and let the point propagate radiating waves as it moves (Ben Menahem and Singh 1981, pp. 229–52; Aki and Richards, 1980, pp. 799–812). We consider a point shear dislocation that produces a slip  $\Delta u_i(\xi_i, t) = \Delta u(\xi_i, t) l_i(\xi_i, t)$ , where  $l_i$  is the unit vector in the direction of slip. We assume that the slip propagates from the point  $\xi_i = 0$  (the origin of coordinates is the point where the rupture begins) over a distance  $L$ , with constant velocity  $v$  in one direction along a surface  $\Sigma$  (Fig. 7.1). The velocity of propagation of the slip discontinuity corresponds to the rupture velocity and is assumed to be less than the shear wave velocity ( $v < \beta$ ), that is, we are treating subsonic fractures (a frequently adopted value is  $0.7 \beta$ ). The far-field displacement of the P waves at a point  $x_s$  and time  $t$ , in an infinite medium, can be written using the expression for the radiation from a point moment-rate source ((4.23) for P waves and (4.24) for shear waves). We assume, following (1.4), that for a point source the moment-rate element is  $dM_0 = \mu \Delta u dS$ , so that the far-field displacement associated with a P wave is given in sub-index notation by

$$u_i^P(x_s, t) = \frac{\mu}{4\pi\rho\alpha^3} \int_{\Sigma} \frac{R_P(n_k, l_k, \gamma_k)}{r} \Delta \dot{u}\left(\xi_l, t - \frac{r}{\alpha}\right) dS \quad (7.1)$$

where  $R_P(n_k, l_k, \gamma_k)$  is the radiation pattern, which depends on the orientation of the dislocation ( $n_k, l_k$ ) and the position of the observation point relative to each point of

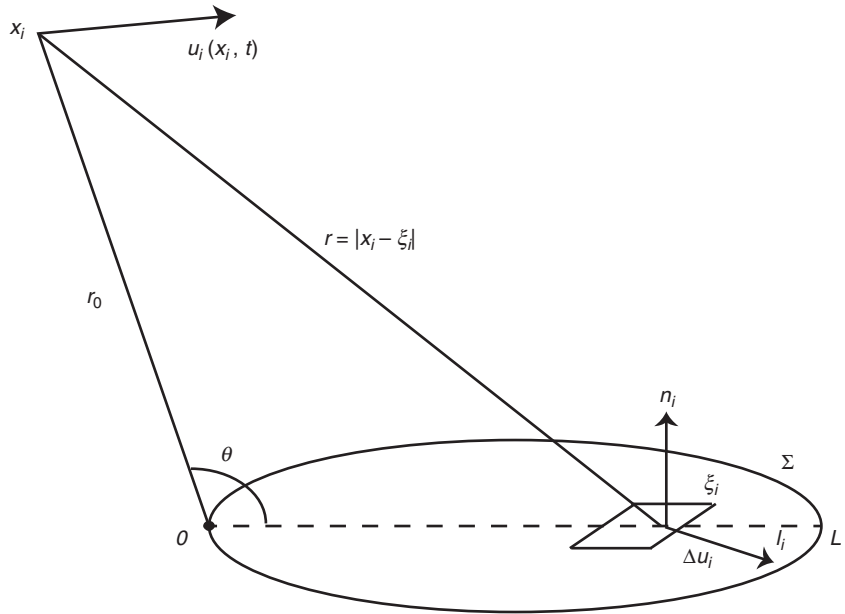


**Figure 7.1.** Elastic displacement  $u_i$  at point  $x_i$  a distance  $r_0$  from the origin  $O$  corresponding to an extended source of dimension  $L$  with slip  $\Delta u_i$  in the direction of unit vector  $l_i$  over the surface  $\Sigma$  with normal  $n_i$  ( $\xi_i$  lies on the surface  $\Sigma$ ).

the source (given by direction cosines  $\gamma_k$ ). The distance from the observation point  $x$  to the point  $\xi$  where the slip  $\Delta u(\xi, t)$ , with direction  $l$ , is occurring at time  $t$  is  $r = |x_i - \xi_i|$ . We assume now that the fault surface  $\Sigma$  extends along a line from  $\xi_i = 0$  to a maximum distance  $L$  that represents the length of the fault surface.

We will now assume that we are observing the earthquake in the far field, so that the distance  $r$  and the radiation pattern  $R_P$  may be considered to be constant. As already discussed, far-field conditions are achieved when the dominant wavelength  $\lambda \gg L^2/r_0$ , where  $L$  is the size of the source and  $r_0$  is the distance from the hypocenter to the point of observation. We can then simplify (7.1) to:

$$u_i^P(x_s, t) = \frac{\mu}{4\pi\rho\alpha^3} \frac{R_P(n_k, l_k, \gamma_k)}{r_0} \int_{\Sigma} \Delta u \left( \xi_l, t - \frac{r}{\alpha} \right) dS \quad (7.2)$$

Expressing the distance  $r$  from the current source point to the observation point in terms of a Taylor expansion about  $r_0 = |x_i|$ , we obtain

$$r = r_0 + \xi_i \frac{\partial r}{\partial \xi_i} + \frac{1}{2} \xi_j \xi_j \frac{\partial^2 r}{\partial \xi_k \partial \xi_k} + \dots \quad (7.3)$$

with the derivatives evaluated at  $r = r_0$ . According to (3.41)  $\partial r / \partial \xi_i = -\gamma_i$ , where  $\gamma_i$  are the direction cosines of  $r$  with respect to  $r_0$ ; keeping only the first-order term, we obtain

$$r = r_0 - \xi_i \gamma_i$$

Since the first term that is neglected in this approximation is  $|\xi_i|^2/r_0$ , and the maximum value of  $|\xi_i|$  is  $L$ , the approximation given by (7.4) below is valid for displacements of

wavelength  $\lambda$  and distance  $r_0$ , such that  $\lambda r_0 \gg L^2$ . The wave form of the P wave displacement given in (7.2) can thus be written as

$$u^P(t) = \frac{1}{4\pi\rho\alpha^3} \frac{R_P(n_k, l_k, \gamma_k)}{r_0} \mu \int_{\Sigma} \Delta\dot{u} \left( \xi_i, t - \frac{r_0 - \xi_i \gamma_i}{\alpha} \right) dS \quad (7.4)$$

In order to simplify the notation, in the following we will write (7.4) in the form

$$u^P(t) \approx \mu \int_{\Sigma} \Delta\dot{u} \left( \xi_i, t - \frac{r_0 - \xi_i \gamma_i}{\alpha} \right) dS \quad (7.5)$$

omitting the factor in front of the integral in (7.4). The time Fourier transform of (7.5) is

$$U^P(\omega) \approx e^{-i\omega r_0/\alpha} \mu \int_{\Sigma} i\omega \Delta U(\xi_i, \omega) e^{i\omega \gamma_i \xi_i / \alpha} dS \quad (7.6)$$

where we have used the properties that the Fourier transform of  $\Delta\dot{u}(t)$  is  $\Delta\dot{U}(\omega) = i\omega \Delta U(\omega)$  and that  $\text{FT}[f(t - r_0/\alpha)] = e^{-i\omega r_0/\alpha} F(\omega)$ . Substituting  $\omega/\alpha = k$ , the wave number, we obtain,

$$U^P(k) \approx e^{-ir_0k} \mu \int_{\Sigma} i\alpha k \Delta U(\xi_i, \alpha k) e^{i\gamma_i \xi_i k} dS \quad (7.7)$$

In this equation the Fourier transform of the displacements  $U^P(k)$  has the form of a spatial transform, over the fault surface  $\Sigma$ , of the temporal transform of the slip  $\Delta U(k)$ . In the exponential,  $k\gamma_i$  is the wave number in the direction of the vector defined by the direction cosines  $\gamma_i$ . If the dependence on time of the slip is that of a step function,  $\Delta u(\xi_i, t) = \Delta u(\xi_i) H(t)$ , its transform is  $\Delta U(\xi_i, k) = \Delta u(\xi_i)/(iak)$  and, substituting into (7.7) we obtain,

$$U^P(k) \approx e^{-ir_0k} \mu \int_{\Sigma} \Delta u(\xi_i) e^{i\gamma_i \xi_i k} dS \quad (7.8)$$

If we take the low-frequency limit ( $k \rightarrow 0$ ), we obtain

$$U^P(0) \approx \mu \int_{\Sigma} \Delta u(\xi_i) dS \approx \mu \bar{\Delta u} S \approx M_0 \quad (7.9)$$

At low frequencies, tending to zero, the spectral amplitudes of the far-field displacement become asymptotically proportional to the seismic moment. Adding in the proportionality factor in equation (7.4), which has been omitted, we get

$$U^P(0) = \frac{1}{4\pi\rho\alpha^3} \frac{R_P(n_k, l_k, \gamma_k)}{r_0} M_0 \quad (7.10)$$

For a finite source of surface  $\Sigma$ , the spectral displacement (7.8) at high frequencies ( $k \rightarrow \infty$ ) tends to zero with an inverse power law that is determined in a very complex way by the discontinuities of  $\Delta u$ . In practice, however, the form of the amplitude spectra of displacements corresponding to a source with finite dimension is well established from seismic observations, as follows. At low frequencies the spectrum  $U(\omega)$  is constant up to a certain value of frequency, where it begins to decrease. As we will show later, this value of frequency is inversely proportional to the size of the source. At the high-frequency end,

amplitudes tend to zero. The envelope of the spectrum decays at high frequencies with an inverse-power frequency dependence, with power values between 3/2 and 3 but in most cases near to two (i.e. we have  $\omega^{-2}$ ). The source dimensions limit the spectrum of the displacements to a finite frequency range. The larger the source dimensions, the lower the frequency limit of the displacement spectra. These general results are valid for any shape and temporal dependence of the source and are common characteristics for all sources of finite dimensions for which the slip starts from zero at a certain point of space and time and ends after a *finite* time, producing a *finite* total seismic moment  $M_0$ . These results are similar to those obtained for the spectra of the waves radiated from a point-source with an STF with finite rise time (section 4.8). The rise time of the point source can thus be considered as an approximate representation of the time duration of an extended source for which  $\tau_r \approx L/v$ .

## 7.2. Rectangular fault. Haskell's model

A simple kinematic source model of finite dimension is that of a *rectangular fault* of length  $L$  and width  $W$ . A slip front  $\Delta u$  propagates with constant velocity  $v$  along the  $L$  direction (the slip appears instantaneously across the width  $W$ ). This simple model was first proposed by Haskell (1964) and is usually known as the *Haskell model* of the source. It is interesting to note that Haskell considered several other models, defined by cross-correlations of the slip distributions. Let us call  $\xi$  the coordinate along the fault length, which varies from 0 to  $L$ , and let us assume, for simplicity that the slip  $\Delta u(\xi, t)$  has only one component, parallel to the direction of  $\xi$  (Fig. 7.2). According to the propagation of the fracture, Faults are called *unilateral* if they propagate only in one direction (from 0 to  $L$ ) and *bilateral* if they propagate each way (for example, from 0 to  $L/2$  and from 0 to  $-L/2$ ). For a unilateral fracture, according to (7.5), assuming that the radiation pattern and distance do not change significantly with position on the fault in (7.1), the far-field displacements of the P waves can be written as

$$u^P(x_i, t) \approx W \int_0^L \Delta u \left( \xi, t - \frac{r_0 - \xi \cos \theta}{\alpha} \right) d\xi \quad (7.11)$$

where  $\theta$  is the angle between  $r_0$ , the line from the origin of the fault ( $\xi = 0$ ) to the observation point, and the strike of the fault ( $\gamma = \cos \theta$ ). If  $\phi$  is the azimuth of the fault,  $\phi'$  the azimuth of the observation point and  $i_h$  the take-off angle of the ray then  $\cos \theta = \sin i_h \cos(\phi' - \phi)$ .

If we assume that a uniform slip front moves along the fault with constant velocity  $v$  then  $\Delta u(\xi, t) = \Delta u(t - \xi/v)$ , so that we can write (7.11) in the simpler form

$$u^P(x_i, t) \approx W \int_0^L \Delta u \left( t - \frac{r_0}{\alpha} - \frac{\xi}{\alpha} \left( \frac{\alpha}{v} - \cos \theta \right) \right) d\xi \quad (7.12)$$

If we make the substitution

$$d = \frac{r_0}{\alpha} + \frac{\xi}{\alpha} \left( \frac{\alpha}{v} - \cos \theta \right) \quad (7.13)$$

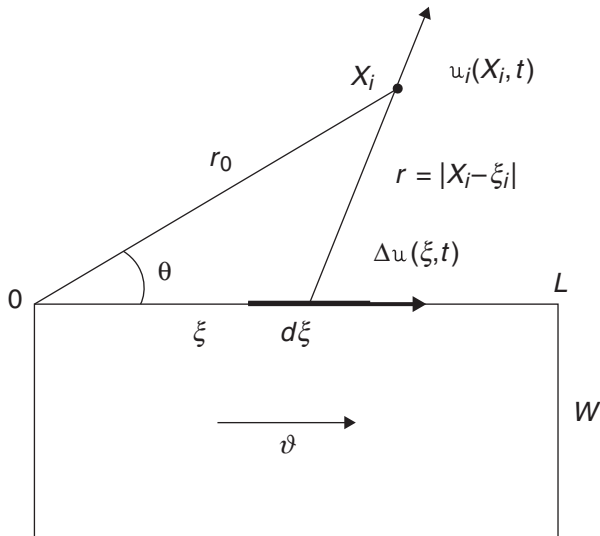


**Figure 7.2.** Haskell's model of a vertical rectangular fault of length  $L$  and width  $W$ , with slip  $\Delta u$  and constant fracture propagation velocity  $v$ . The elastic displacement is  $u_i$  at the point  $x_i$  at a distance  $r_0$  from the origin 0; the  $\xi$  coordinate is along the length  $L$ .

then the Fourier transform of  $u^P(x_i, t)$  is

$$U^P(x_i, \omega) \approx W \int_0^L d\xi \int_{-\infty}^{\infty} \Delta \dot{u}(t-d) e^{-i\omega t} dt \quad (7.14)$$

If  $\Delta U(\omega)$  is the transform of  $\Delta u(t)$  then that of  $\Delta \dot{u}(t)$  is  $i\omega \Delta U(\omega)$  and that of  $\Delta u(t-d)$  is  $\Delta U(\omega) \exp(-i\omega d)$ , so that in (7.14) we have

$$\int_{-\infty}^{\infty} \Delta \dot{u}(t-d) e^{-i\omega t} dt = i\omega \Delta U(\omega) e^{-i\omega d} \quad (7.15)$$

Therefore, equation (7.14) becomes

$$U^P(x_i, \omega) \approx iW\omega \Delta U(\omega) e^{-i\omega r_0/\alpha} \int_0^L \exp\left[-i\frac{\xi\omega}{\alpha}\left(\frac{\alpha}{v} - \cos\theta\right)\right] d\xi \quad (7.16)$$

To evaluate the integral in (7.16), we make the substitution

$$b = -(\omega/\alpha)(\alpha/v - \cos\theta)$$

and obtain

$$\int_0^L e^{ib\xi} d\xi = \frac{2}{b} \sin\left(\frac{bL}{2}\right) \exp\left(i\frac{bL}{2}\right) = L \frac{\sin X}{X} \exp(iX) \quad (7.17)$$

where

$$X = \frac{bL}{2} = -\frac{\omega L}{2\alpha} \left(\frac{\alpha}{v} - \cos\theta\right) \quad (7.18)$$

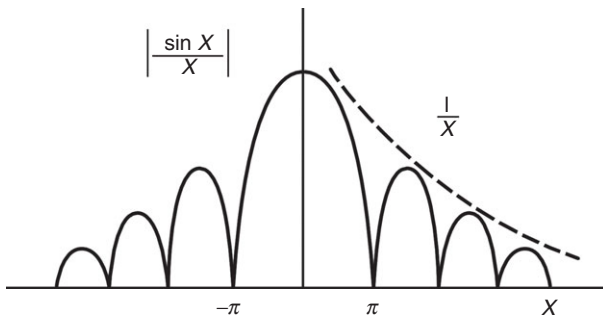


**Figure 7.3.** Form of the function  $(\sin X)/X$ .

The final form for the transform of the far-field displacements of P waves, according to (7.16), adding in the factors in (7.1), considering  $R_P$  to be constant over the surface  $S = LW$  and setting  $i = e^{i\pi/2}$ , gives

$$U^P(x_i, \omega) = \frac{\mu S \omega \Delta U(\omega) R_P(n_k, l_k, \gamma_k)}{4\pi \alpha^3 \rho r_0} \frac{\sin X}{X} \exp\left[-i\left(\frac{\omega r_0}{\alpha} - X - \frac{\pi}{2}\right)\right] \quad (7.19)$$

The amplitude spectrum of the P wave far-field displacements is given in terms of the seismic moment by

$$|U^P(x_k, \omega)| = \frac{R_P(n_k, l_k, \gamma_k) |M_0(\omega)| \omega}{4\pi \alpha^3 \rho r_0} \left| \frac{\sin X}{X} \right| \quad (7.20)$$

where  $M_0(\omega) = \mu S \Delta U(\omega)$  is the Fourier transform of the seismic and is a function of the time dependence of the source time function (STF). The amplitude spectrum depends on the factor  $(\sin X)/X$ . This function has a maximum value of unity at  $X = 0$ , it has zeros for  $X$  equal to integer multiples of  $\pi$  and its envelope decreases as  $1/X$  when  $X > 1$  (Fig. 7.3). For fixed values of  $L$  and  $\theta$  the variable  $X$  depends on frequency  $\omega$ : for low frequencies, as  $\omega$  tends to zero, the factor  $(\sin X)/X$  equals unity and for high frequencies it tends to zero, its envelope decreasing as  $1/\omega$ .

The form of the amplitude spectrum of the displacements (7.20) depends also on the form of  $M_0(\omega)$ , the Fourier transform of the STF. We discussed in section 4.8 the forms of the Fourier transforms of several STFs. As an example, for the simplest case, when  $M_0(t) = M_0 H(t)$ , we have  $M_0(\omega) = \Delta u/(i\omega)$ . Substituting into (7.20), the amplitude spectrum at the low-frequency limit is proportional to the seismic moment  $M_0$ , and for high frequencies it decreases as  $1/\omega$ . In this case the slip takes its maximum value instantaneously. If there is a rise time  $\tau_r$ , as in equations (4.70) and (4.71), the transforms of the STF are given by (4.75) and (4.76). In both cases, on substituting into (7.20) it can be seen that the amplitude spectrum decreases at high frequencies as  $1/\omega^2$ . This is the same result as that obtained for the point source, but now the value of  $\omega$  from which the spectrum begins to decrease, the corner frequency, depends also on the dimension of the source  $L$ , which governs the value of  $X$  (see (7.18)). For a point source the duration is given only by the rise time  $\tau_r$ ; for an extended source there is also the total duration of the rupture process, given by  $t_r = L/v$ . In the case of an extended source  $\tau_r$  and  $t_r$  are different and independent of each other. As the rupture front moves with velocity  $v$ , the rise time  $\tau_r$  may either be constant for all points or

vary from one point to another. It is also important to distinguish between the slip velocity or slip rate  $\Delta\dot{u}$  and the rupture velocity  $v$ , and to remember that  $\Delta\dot{u}$  has values different from zero at each point of the fault surface only in the time interval,  $0 < t < \tau_r$ . Since for kinematic models the rise time and the total duration are independent, the motion may stop at each point of the fault independently of the arrest of the rupture at the edges of the fault. In conclusion, in an extended kinematic model we have introduced three new source parameters:  $L$ , the fault length,  $W$ , the fault width, and  $v$ , the rupture velocity, which, added to the nine parameters of the point source defined in section 6.1) gives 12 parameters.

### 7.3. Bilateral rupture propagation

We consider now *bilateral propagation*, when a rupture moves in two opposite directions on the fault plane simultaneously (Fig. 7.4). Rupture begins at the origin and then propagates with velocity  $v_1$  in the positive direction for a distance  $L_1$  and in the negative direction with velocity  $v_2$  for a distance  $L_2$ . The total length of the fault is  $L = L_1 + L_2$  and the total duration of rupture is  $\tau_r = L_1/v_1 + L_2/v_2$ . The orientation of the mechanism is assumed to be the same for the ruptures in both directions and the radiation pattern is assumed to be constant. The distances from the observation point to moving points on each side of the fault are now given by  $r_1 = r_0 - \xi_1 \cos \theta$  and  $r_2 = r_0 + \xi_2 \cos \theta$ . The integral in (7.12) for the Fourier transform of the P wave displacement of is now replaced by two integrals, one over  $\xi_1$  from 0 to  $L_1$  and the other one over  $\xi_2$  from 0 to  $L_2$ . Using the unilateral result (7.19) for each direction of propagation, we get

$$U^P(x_i, \omega) = \frac{\mu W \omega R_P}{4\pi\rho\alpha^3 r_0} \left\{ \Delta U_1 L_1 \frac{\sin X_1}{X_2} \exp\left[-i\left(\frac{\omega r_0}{\alpha} - X_1 - \frac{\pi}{2}\right)\right] + \Delta U_2 L_2 \frac{\sin X_2}{X_1} \exp\left[-i\left(\frac{\omega r_0}{\alpha} - X_2 - \frac{\pi}{2}\right)\right] \right\} \quad (7.21)$$

where  $R_P$  is the radiation pattern, considered to be constant,  $\Delta u_1$  and  $\Delta u_2$  are the slip amplitudes at the two sides of the rupture and their Fourier transforms are  $\Delta U_1$  and  $\Delta U_2$ ; the variables  $X_1$  and  $X_2$  are related to  $L_1$  and  $L_2$  by

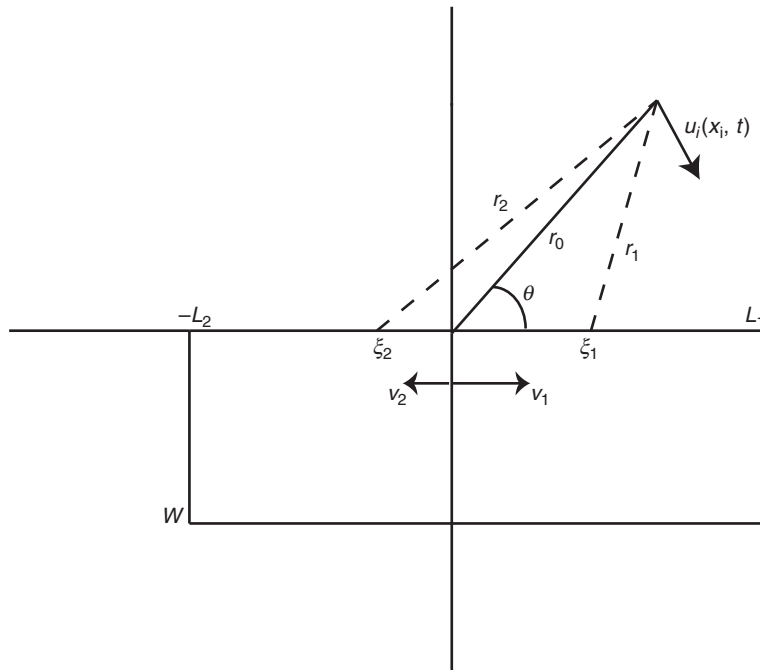
$$X_1 = -\frac{\omega L_1}{2\alpha} \left( \frac{\alpha}{v_1} - \cos \theta \right) \quad (7.22)$$

$$X_2 = -\frac{\omega L_2}{2\alpha} \left( \frac{\alpha}{v_2} + \cos \theta \right) \quad (7.23)$$

In terms of the seismic moment we have

$$U^P(x_i, t) = \frac{R_P \omega}{4\pi\rho\alpha^3 r_0} \left( M_1 \frac{\sin X_1}{X_2} e^{iX_1} + M_2 \frac{\sin X_2}{X_1} e^{iX_2} \right) \exp\left[-i\left(\frac{\omega r_0}{\alpha} - \frac{\pi}{2}\right)\right] \quad (7.24)$$

where  $M_1 = \mu WL_1 \Delta U_1$  and  $M_2 = \mu WL_2 \Delta U_2$  are the seismic moments from each side of the rupture and the total seismic moment  $M_0 = M_1 + M_2$ .

**Figure 7.4.**

Bilateral rupture propagation on a vertical fault of length  $L_1 + L_2$  with different rupture velocities  $v_1$  and  $v_2$  in each direction. The elastic displacement is  $u_i$  at the point  $x_i$ , a distance  $r_0$  from the origin;  $\xi_1$  and  $\xi_2$  are the coordinates along the lengths  $L_1$  and  $L_2$ .

Since the modulus of the sum of two complex quantities

$$g = ae^{ib} + ce^{id}$$

is given by

$$|g|^2 = a^2 + c^2 + 2ac \cos(b - d)$$

we have that the amplitude spectrum of the P wave displacements for a bilateral fault is given by

$$|U^P(x_k, \omega)| = \frac{R_P \omega}{4\pi\rho\alpha^3 r_0} \left[ \left( M_1 \frac{\sin X_1}{X_1} \right)^2 + \left( M_2 \frac{\sin X_2}{X_2} \right)^2 + 2M_1 M_2 \frac{\sin X_1}{X_1} \frac{\sin X_2}{X_2} \cos(X_1 - X_2) \right]^{1/2} \quad (7.25)$$

## 7.4. Oblique rupture propagation

The result obtained in section 7.2 for a unilateral rupture propagating along the length of the fault can be easily extended to a rupture that propagates obliquely with respect to the horizontal direction. We follow the work of Hirasawa and Stauber (1965), changing their

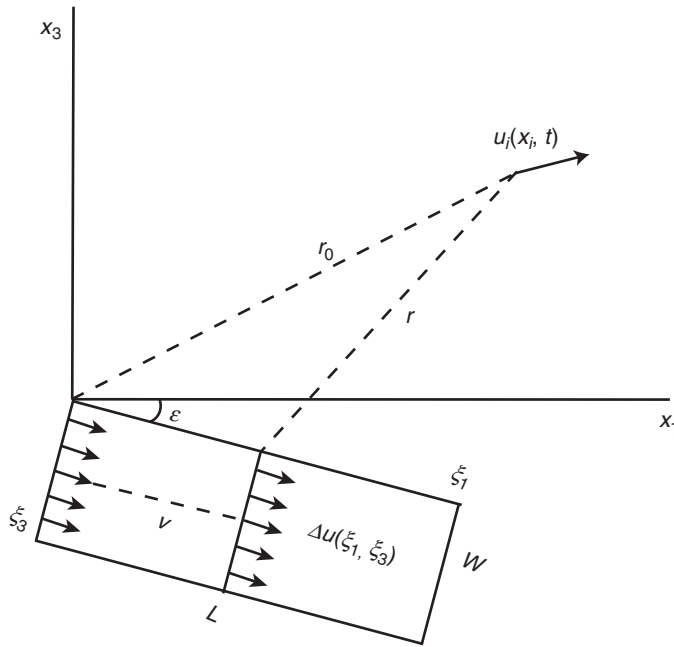


**Figure 7.5.** Rupture propagation along an inclined rectangular fault of length  $L$  inclined at angle  $\varepsilon$ . The variables are as in Fig. 7.2.

notation to agree with that used in section 7.2 and using as the propagating point source a shear dislocation of arbitrary time dependence  $\Delta u(t)$ . We consider a rectangular fault of length  $L$  and width  $W$  in the  $(x_1, x_3)$  plane inclined at an angle  $\varepsilon$  with respect to the horizontal ( $x_1$  corresponds to the strike of the fault) (Fig. 7.5). On the rupture plane we introduce coordinates  $(\xi_1, \xi_3)$  along the directions of the length and width, respectively. Rupture propagates in the  $\xi_1$  direction with constant velocity  $v$ . Using the approximation (7.4) the distance  $r$  from a point on the fault plane of coordinates  $(\xi_1, \xi_3)$  to an observation point  $(x_1, x_2, x_3)$ , if  $W/r_0 < L/r_0 < 1$  where  $r_0^2 = x_1^2 + x_2^2 + x_3^2$ , can be written as

$$r = r_0 - \frac{x_1}{r_0} (\xi_3 \sin \varepsilon + \xi_1 \cos \varepsilon) - \frac{x_3}{r_0} (\xi_3 \cos \varepsilon - \xi_1 \sin \varepsilon) \quad (7.26)$$

The expression for the P wave displacement corresponding to (7.12) is

$$u_i^P \approx \int_0^L \int_0^W \Delta u \left( t - \frac{r_0}{v} + \frac{1}{v} \left[ \xi_1 \left( x_1 \cos \varepsilon - x_3 \sin \varepsilon - \frac{\alpha}{v} \right) + \xi_3 \left( x_1 \sin \varepsilon + x_3 \cos \varepsilon \right) \right] \right) d\xi_3 d\xi_1 \quad (7.27)$$

According to Hirasawa and Stauder (1965) we now change the Cartesian coordinates of the observation point to spherical coordinates  $(r_0, \theta', \phi')$  with  $\theta'$  measured from the  $x_2$  axis and  $\phi'$  from the  $x_1$  axis counter-clockwise, so that

$$\begin{aligned} x_1 &= r_0 \gamma_1 = r_0 \sin \theta' \cos \phi' \\ x_2 &= r_0 \gamma_2 = r_0 \cos \theta' \\ x_3 &= r_0 \gamma_3 = -r_0 \sin \theta' \sin \phi' \end{aligned}$$

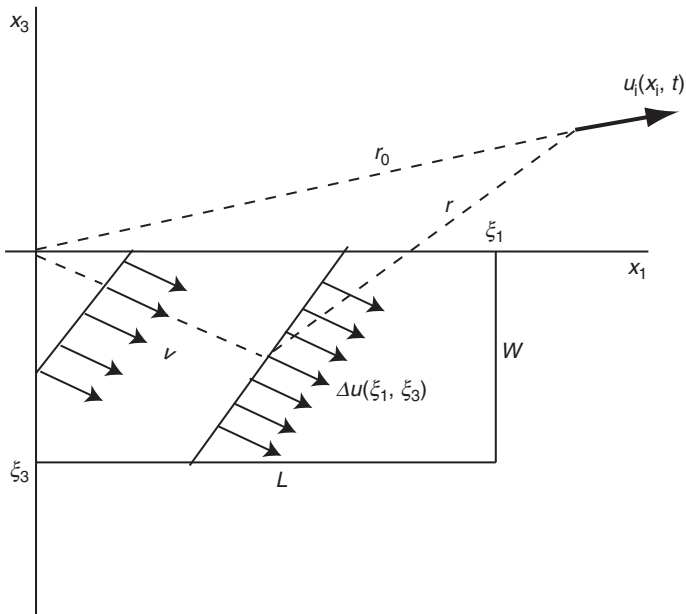


**Figure 7.6.** Oblique rupture propagation on a vertical rectangular fault. The variables are as in Fig. 7.2.

Taking the Fourier transform and proceeding as in the previous case, but now with a double integral over  $\xi_1$  and  $\xi_3$ , we obtain for the radial component of the P wave displacements

$$U^P(r_0, \theta, \phi, \omega) = \frac{R(n_i, l_i, \theta, \phi) \omega M_0(\omega)}{4\pi\rho\alpha^3 r_0} \frac{\sin X}{X} \frac{\sin Z}{Z} \exp\left[-i\left(\frac{\omega r_0}{\alpha} + X + Z\right)\right] \quad (7.28)$$

where

$$X = \frac{L\omega}{2\alpha} \left[ \frac{\alpha}{v} - \sin \theta' \cos (\phi' - \varepsilon) \right] \quad (7.29)$$

$$Z = \frac{W\omega}{2\alpha} \sin \theta' \sin (\phi' - \varepsilon) \quad (7.30)$$

The amplitude spectrum of the P waves (cf. (7.19)) is given by

$$\left| U^P(r_0, \theta', \phi', \omega) \right| = \frac{R(n_k, l_k, \theta', \phi') |M_0(\omega)| \omega}{4\pi\rho\alpha^3 \rho r_0} \left| \frac{\sin X}{X} \right| \left| \frac{\sin Z}{Z} \right| \quad (7.31)$$

The amplitude spectrum depends now on the components of the rupture propagation in the  $x_1$  and  $x_3$  directions and on the relative position of the observation point with respect to the orientation of the fault plane.

We consider now the case when the rupture propagation is oblique to the  $L$  and  $W$  directions on the fault plane (Fig. 7.6). We consider, as before, that the fault is in the  $(x_1, x_3)$  plane and  $L$  and  $W$  are in the  $x_1$  and  $x_3$  directions, respectively. Let the rupture propagation make an angle  $\varepsilon$  with  $x_1$ . The rupture velocity  $v$  has now two components, in the  $\xi_1$  and  $\xi_3$  directions, namely  $v_1$  and  $v_3$  ( $v^2 = v_1^2 + v_3^2$ ), both constants so that the rupture front is a straight line. The P wave displacement is now given by

$$u_i^P \approx \int_0^L \int_0^W \Delta \dot{u} \left( t - \frac{r_0}{\alpha} - \frac{\xi_1}{\alpha} \left( \frac{\alpha}{v_1} - \sin \theta' \cos \phi' \right) - \frac{\xi_3}{\alpha} \left( \frac{\alpha}{v_3} - \sin \theta' \sin \phi' \right) \right) d\xi_3 d\xi_1 \quad (7.32)$$

The amplitude spectra of the P waves has the same form as in equation (7.31) where now the values of  $X$  and  $Z$  in (7.29), (7.30) are replaced by

$$X = \frac{L\omega}{2\alpha} \left( \frac{\alpha}{v_1} - \sin \theta' \cos \phi' \right) \quad (7.33)$$

$$Z = \frac{W\omega}{2\alpha} \left( \frac{\alpha}{v_3} - \sin \theta' \sin \phi' \right) \quad (7.34)$$

The amplitude spectrum has the form of a product of two  $(\sin x)/x$  functions, one depending on  $L$  and  $v_1$  and the other on  $W$  and  $v_3$ . For very low frequencies both tend to unity. The corner frequency depends now on both  $L$  and  $W$ .

## 7.5. Corner frequency

In general, if we plot the logarithm of the amplitude spectrum with respect to the logarithm of the frequency, its form is flat from frequencies close to zero up to a certain frequency  $\omega_c$ , called the *corner frequency*. From this frequency to higher frequencies the envelope of the amplitude spectrum is a straight line with slope proportional to some power of the frequency, generally between 1.5 and 3 (Fig. 7.7). This form of spectrum is produced by the combined effect of the source dimensions and the rise time. If in equation (7.19) we consider the particular case  $\theta = \pi/2$  and a corner frequency corresponding to  $X = \pi/2$ , we obtain  $\omega_c = \pi v/L$ , that is, the corner frequency is proportional to the inverse of the source length. The corner frequency is actually an approximation to the equivalent width of the

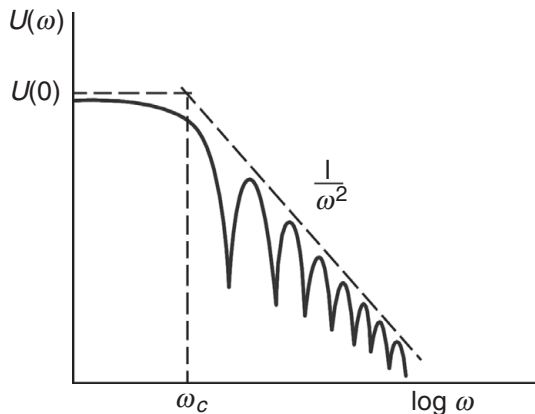


**Figure 7.7.** Ideal amplitude spectrum of displacement corresponding to a finite extended source;  $\omega_c$  is the corner angular frequency.

spectrum. Since the finite length of the fault results in displacement pulses with a certain finite duration, the corner frequency is determined by the general inverse relation between the duration of the time pulse and that of its spectrum (Bracewell, 1965, pp. 148–56).

Haskell's model for a unilateral fault and an STF with finite rise time predicts a displacement spectrum with a corner frequency which is inversely proportional to the length of the fault and which decays with frequency according to  $1/\omega^2$ . Savage (1972) studied Haskell's model for a bilateral fault. For the particular case in which the fault starts at  $x = 0$  and moves with same velocity  $v$  from 0 to  $L/2$  and from 0 to  $-L/2$ , with the same value of slip ( $M_1 = M_2 = M_0$ ), the dependence of the amplitude spectrum is, according to (7.25),

$$|U(\omega)|^2 = A^2 |\omega M_0(\omega)|^2 \left[ \left( \frac{\sin X}{X} \right)^2 + \left( \frac{\sin X'}{X'} \right)^2 + 2 \frac{\sin X}{X} \frac{\sin X'}{X'} \cos(X - X') \right] \quad (7.35)$$

$$A = \frac{R_p}{4\pi\alpha^3 r_0}$$

where

$$\begin{aligned} X &= \frac{\omega L}{4\alpha} \left( \cos \theta - \frac{\alpha}{v} \right) \\ X' &= \frac{\omega L}{4\alpha} \left( \cos \theta + \frac{\alpha}{v} \right) \end{aligned}$$

Let the moment-rate spectral function be that of Brune defined by (4.76)

$$|\dot{M}_0(\omega)| = |\omega M_0(\omega)| = \frac{M_0}{1 + \omega^2 \tau_r^2} \quad (7.36)$$

Substituting into (7.35), we find that the displacement amplitude spectrum depends on the values of  $L$  and  $\tau_r$  and decays as  $1/\omega^2$  at high frequencies, because the terms that depend on  $X$  and  $X'$  decay as  $1/\omega^2$  at high frequencies. Savage (1972) related the rise time  $\tau_r$  in (7.36) to the width of the fault, so that  $\tau_r = W/(4.6v)$ ; that is, the slip begins at each point as the rupture front passes, and it continues until the rupture front is further away than the nearest edge of the fault surface.

The displacement spectrum (7.35) has two corner frequencies. The lower corresponds to the frequency at which the amplitude begins to decrease and depends on the length of the fault  $L$ . According to (7.35) it is approximately given for P waves by

$$\omega_1 = \frac{2\alpha \left[ (\alpha/v)^2 + \cos^2 \theta \right]^{1/2}}{L \left[ (\alpha/v)^2 - \cos^2 \theta \right]} \quad (7.37)$$

The second corner frequency – determined by (7.36) – depends on the rise time  $\tau_r$  or width  $W$  and is given by (Savage, 1972)

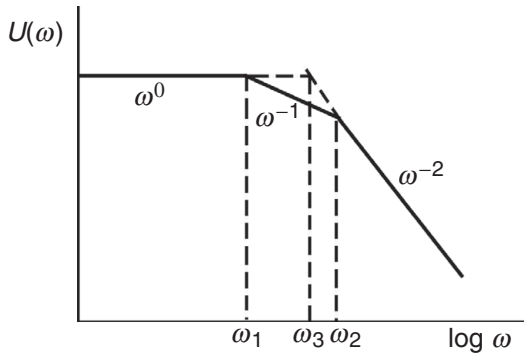


**Figure 7.8.** Corner frequencies  $\omega_1$ ,  $\omega_2$ ,  $\omega_3$  in the amplitude spectrum of the displacement corresponding to a rectangular fault according to Savage's model (1972).

$$\omega_2 = \frac{1}{\tau_r} = \frac{4.6v}{W} \quad (7.38)$$

In a logarithmic plot of the spectrum the amplitude decreases as  $1/\omega$  between  $\omega_1$  and  $\omega_2$  and as  $1/\omega^2$  for frequencies higher than  $\omega_2$ . The intersection between the constant amplitudes and the  $1/\omega^2$  asymptote defines what may be called a third corner frequency,  $\omega_3$  (Fig. 7.8). If  $L$  and  $W$  are approximately equal then  $\omega_1$  and  $\omega_2$  are approximately the same and there is a single corner frequency,  $\omega_3 = \sqrt{\omega_1 \omega_2}$ . For long and narrow sources such that  $L > W$  then  $\omega_1 < \omega_2$ .

The values of the corner frequencies for P and S waves were computed by Savage; for the particular value  $v = 0.9\beta$  of the rupture speed, they are:

P waves	S waves
$\omega_1 = 1.2a/L$	$\omega_1 = 3.6\beta/L$
$\omega_2 = 2.4a/W$	$\omega_2 = 4.1\beta/W$
$\omega_3 = 1.7a/\sqrt{LW}$	$\omega_3 = 3.8\beta/\sqrt{LW}$

Aki (1967) studied the displacement spectral shape using the statistical model presented by Haskell (1966), who described the source in statistical rather than deterministic terms. In this approach the source is modeled as a swarm of acceleration and deceleration pulses that propagate along the fault as a group with mean velocity  $v$ . Instead of  $L$  (length) and  $\tau_r$  (rise time) the parameters used are  $k_L$  and  $k_T$ , whose inverses are the correlation length and correlation time, respectively. This statistical source model, proposed by Haskell (1966), is

$$\Phi(x, t) = \Phi_0 e^{k_L |x|} (1 - k_T |t - x/v|) e^{-k_T (t - x/v)} \quad (7.39)$$

Aki and Richards (1980, pp. 819–25) discussed two possible models for the dependence of the spectrum of far-field seismic wave displacements, namely, the  $\omega$ -square and  $\omega$ -cube models. The latter is a special case of the model suggested by Haskell. Assuming similarity between large and small earthquakes, Aki concluded that the  $\omega$ -square model gives more satisfactory results. The far-field displacement spectrum of this model is given by

$$U(\omega) = \frac{U(0)}{1 + (\omega/\omega_c)^2} \quad (7.40)$$

This is the same as Brune's model, defined in (4.76), where  $\omega_c$  is the corner frequency and  $U(0)$  is the asymptotic value of the spectral displacements at low frequencies, which is proportional to the scalar seismic moment  $M_0$  times the constant  $A$  defined in (7.35).

## 7.6. Directivity effects

The second effect of the seismic source finiteness is *directivity*. This causes a modification of the observed amplitudes of the displacement spectrum; they now depend on the location of the observation point with respect to the direction of source propagation. The amplitudes for a unilateral Haskell model depend according to (7.20) on the factor  $(\sin X)/X$ , where  $X$  depends in turn on the angle  $\theta$ , i.e. the orientation of the observation point with respect to the strike of the fault (7.18). For wavelengths that are very long compared to the dimensions of the source ( $\lambda \gg L$ ) the factor  $(\sin X)/X$  is very close to unity, so that there is no directivity and the radiation pattern is that corresponding to a point source. For wavelengths of the order of the source dimensions or shorter, the amplitudes are strongly affected by directivity. They have a maximum at  $\theta = 0$ , that is, when the observation point is in the direction of source propagation, and a minimum when  $\theta = \pi$ , that is, in the opposite direction to rupture propagation (Fig. 7.9). The figure shows that the directivity effects are larger in the S waves. This directivity corresponds to the focusing of the energy in the direction of rupture propagation and is a phenomenon that occurs in all models of finite propagating sources.

The directivity effect can be isolated by taking the quotient of the spectral amplitudes of waves leaving the source in opposite directions (rays at angles  $\theta$  and  $\theta + \pi$ ). This quotient, called the *directivity function*  $D(\omega)$ , was introduced by Ben Menahem (1961). According to (7.19) and (7.17) the directivity function, for a unilateral fault, is given by

$$D(\omega) = \frac{\sin [(\omega L/2c)(c/v - \cos \theta)] (c/v + \cos \theta)}{\sin [(\omega L/2c)(c/v + \cos \theta)] (c/v - \cos \theta)} \quad (7.41)$$

where  $c$  is the velocity of the waves considered (either P, S or surface waves). This function has a series of maxima and minima for frequencies which depend on the values of  $L$  and  $v$ , and it can be used to determine these values. In practice it is easier to use with Rayleigh waves, since in this case  $\theta$  represents the azimuth of the station with respect to the strike of the fault. An example of the directivity function as a function of frequency for two different values of  $L$  is given in Fig. 7.10. The frequency corresponding to the first maximum and the intervals between maxima are proportional to  $1/L$ . For a vertical strike-slip fault the directivity function has a simple form that can be generalized to quotients of pairs of stations separated by an arbitrary angle  $\alpha$  in the following form (Udías, 1971):

$$D_\alpha(\omega) = \frac{\sin [(\omega L/2c)(c/v - \cos \theta)] (c/v + \cos \theta) \sin 2\theta}{\sin [(\omega L/2c)(c/v + \cos (\theta + \alpha))] (c/v - \cos \theta) \sin 2(\theta + \alpha)} \quad (7.42)$$

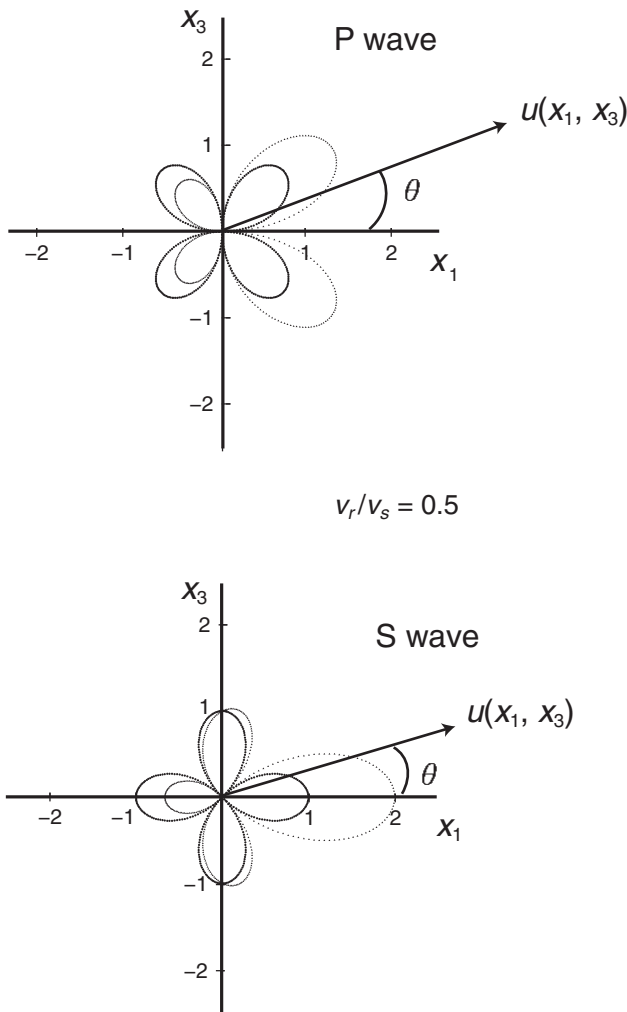


**Figure 7.9.** Directivity effect in the radiation pattern of P and S waves for an extended fault with a fracture propagating in the  $x_1$  direction (dotted line) and that for a point source (solid line) (Pro, 2002)

Directivity also affects the duration of the observed body wave pulses. If the STF is a triangle, the duration  $t_d$  of the pulses observed at different observation points around the source varies as

$$t_d = \frac{L}{v} - \frac{L \cos \theta}{c} \quad (7.43)$$

where

$$\cos \theta = \cos(\phi' - \phi_r) \sin i_h \quad (7.44)$$

and  $c$  is the wave velocity ( $\alpha$  for P waves and  $\beta$  for S waves),  $\phi'$  is the azimuth of the station,  $\phi_r$  the azimuth of the direction of rupture and  $i_h$  the take-off angle at the

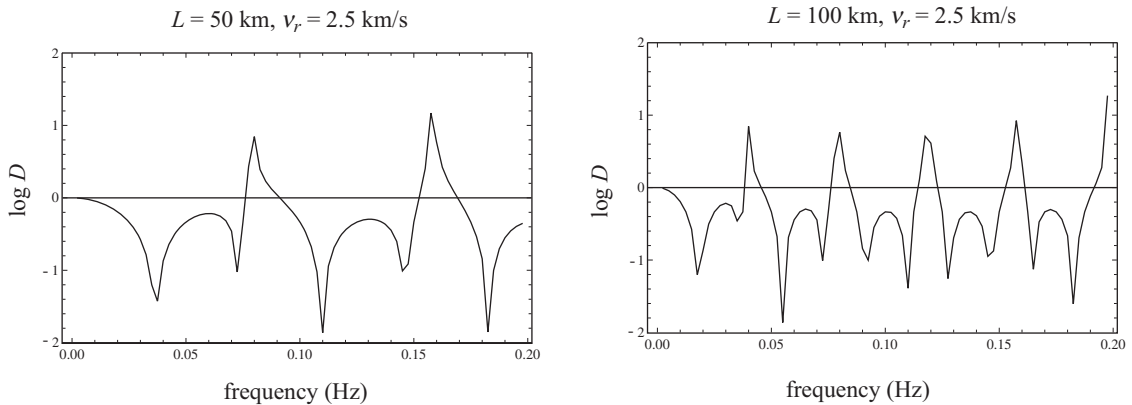


**Figure 7.10.** Influence of the length of the fault (50 km and 100 km) on the directivity function  $D$  (Pro, 2002).

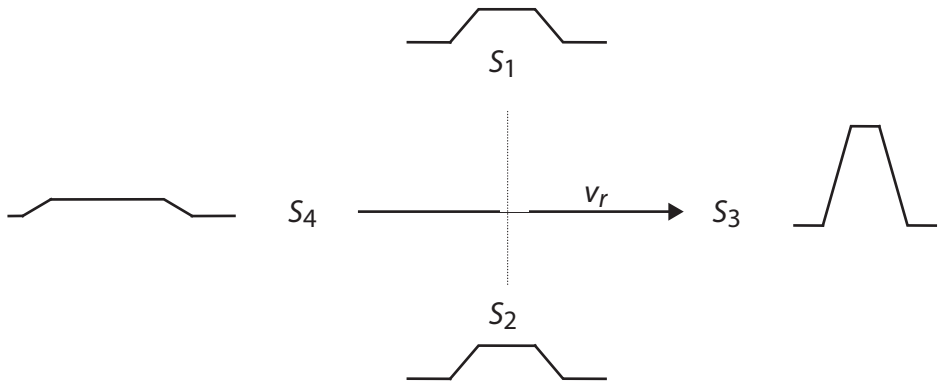


**Figure 7.11.** Variation of the width and amplitude of the wave pulse for a propagating source as a function of the azimuth of the observation point with respect to the direction of fault propagation:  $S_3$ , directivity station;  $S_4$ , anti-directivity station.

focus. The duration of the pulses at a point located in the direction of rupture propagation,  $\theta = 0$  (the directivity station) will be shorter than those received at locations in the opposite direction ( $\theta = \pi$ ). Observations at points perpendicular to the direction of rupture propagation ( $\theta = \pi/2$ ) are not affected (Fig. 7.11). The directivity effect may be used to determine the direction of rupture propagation by comparing the duration of the body wave pulses in different directions around the fault. The azimuth for which the pulses are the shortest indicates the direction of rupture propagation. The observation of directivity in body wave pulses is difficult because this is a high-frequency phenomenon, a domain in which scattering and multi-path phenomena affect the displacement spectral amplitudes. Nowadays, directivity is usually determined by direct modeling of body wave forms, as we will discuss in Chapter 8.

## 7.7. Rupture nucleation, propagation and arrest

The models we have discussed have several limitations (Aki and Richards, 1980, pp. 812–19). For instance they do not properly model the effects of the beginning of rupture, often called *nucleation*, because in these models rupture appears instantaneously across the fault; nor do they model satisfactorily the *cessation* or *arrest* of rupture, which determines the high-frequency spectral decay (Madariaga, 1977). The first attempt to include both effects was the *elliptical kinematic rupture* model proposed by Savage (1966). In his model Savage considered an elliptical fault in which rupture begins at one of the foci and stops when it reaches the border of the ellipse. In order to understand the effect of rupture nucleation and arrest we simplify this model to a circular fault of radius  $a$ , where the slip  $\Delta u$ , which is constant for all points, begins at the center, propagates radially with constant velocity  $v$  (giving circular rupture fronts) and stops when it reaches the circular border. We define a polar coordinate system  $(\rho, \phi)$  centered on the nucleation point, where  $\rho$  is the radius, the origin is at the center of the fault and  $\phi$  is measured from  $x_1$ . Savage further assumed that the slip depended only on  $\rho$  and its time dependence was a step function with no rise time, so that the slip as a function of radius and time can be written in the simple form

$$\Delta u(\rho, t) = \Delta u H\left(t - \frac{\rho}{v}\right) [1 - H(\rho - a)] \quad (7.45)$$

At the center of the fault ( $\rho = 0$ ) the slip jumps instantaneously at  $t = 0$  from zero to  $\Delta u$ . For other points on the fault the slip is zero until the rupture arrival time  $t_r = \rho/v$ , when it suddenly jumps to  $\Delta u$ . The rupture stops instantaneously at the radius  $\rho = a$ , so that for  $\rho \geq a$  the slip is zero for all values of  $t$  (Fig. 7.12).

We will consider only observations at a point on the  $x_3$  axis, that is, directly above the center of the fault at a distance  $r_0$  (Fig. 7.13). The displacement wave form of P waves can be computed, again using (7.1) and (7.2); we get

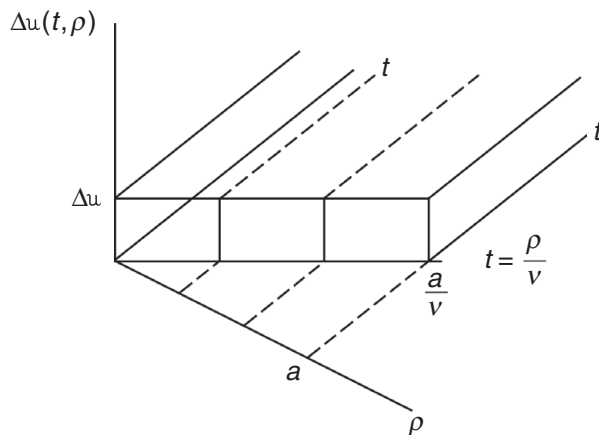


**Figure 7.12.** The slip as a function of time and distance inside the fault for Savage's model (1966) of the initiation and arrest of rupture.

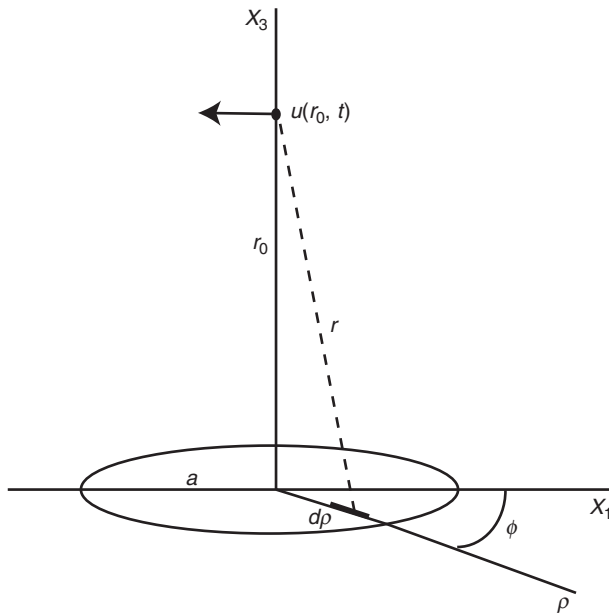


**Figure 7.13.** A circular fault and the displacement  $u$  at an observation point on a perpendicular axis at a distance  $r_0$  from the center of the fault.

$$u(r_0, t) = \int_0^{2\pi} \int_0^a \Delta \dot{u} \left( \rho, t - \frac{r(\rho, \phi)}{a} \right) \rho d\rho d\phi \quad (7.46)$$

where  $r(\rho, \phi)$  is the distance from the observation point to the current point  $(\rho, \phi)$  on the fault. Along the axis of the fault, for  $r_0 \gg a$  we can use the approximation  $r = r_0$ , so that after integration over  $\phi$  we have

$$u(r_0, t) = 2\pi \int_0^a \Delta \dot{u} \left( t - \frac{r_0}{a} \right) \rho d\rho \quad (7.47)$$

Taking the time derivative of (7.45) and substituting into (7.46), the displacement is given by

$$u(r_0, t) = 2\pi \Delta u H \left( t - \frac{r_0}{a} \right) \int_0^a \delta \left( t - \frac{r_0}{a} - \frac{\rho}{v} \right) [1 - H(\rho - a)] \rho d\rho \quad (7.48)$$

Since the integrand is zero outside the interval  $(0, a)$ , we can evaluate (7.48) using the the relation

$$\int_{-\infty}^{\infty} f(x) \delta(ax - b) dx = \frac{1}{a} f \left( \frac{b}{a} \right) \quad (7.49)$$

so that we obtain

$$u(r_0, t) = 2\pi \Delta u v^2 \left( t - \frac{r_0}{a} \right) H \left( t - \frac{r_0}{a} \right) \left[ 1 - H \left( v \left( t - \frac{r_0}{a} \right) - a \right) \right] \quad (7.50)$$

According to this expression,

$$u(r_0, t) = 0, \quad \text{for } t \leq \frac{r_0}{\alpha} \quad \text{and} \quad t \geq \frac{r_0}{\alpha} + \frac{a}{v}$$

whereas

$$u(r_0, t) = 2\pi \Delta u v^2 \left( t - \frac{r_0}{\alpha} \right), \quad \text{for } \frac{r_0}{\alpha} < t < \frac{r_0}{\alpha} + \frac{a}{v}$$

Displacement begins at  $t = r_0/\alpha$  and increases linearly with time until  $t_s = r_0/\alpha + a/v$ , which is the time when the fracture stops at the border. For times longer than  $t_s$  the displacement drops to zero. Thus  $t_s$  is the arrival time of the signal produced by the cessation of rupture at the border  $\rho = a$ , which is called the *stopping phase*. Since at that time the displacement drops discontinuously to zero, the ground velocity and acceleration become unbounded impulses, a very unlikely feature for a seismic pulse as discussed in [Chapter 4](#). The high-frequency radiation from Savage's elliptical crack is dominated by the stopping phases rather than by the initiation of rupture, when the radiation is much weaker. This is a common feature, which we will encounter in the dynamic models to be discussed later in this book.

In Savage's model, the slip jumps instantaneously from zero to its maximum value as the fracture propagates outwards from its nucleation point. The corresponding slip velocity is an impulse which propagates in the same way until it reaches the border of the fault. Other models of the time dependence of the slip may be considered, such as those used in [section 4.8](#), which involve a finite rise time  $\tau_r$ . For example, Savage proposed a linear increase of the slip during the rise time  $\tau_r$ . The slip can then be written as

$$\Delta u(\rho, t) = \Delta u H\left(t - \frac{\rho}{v}\right) [1 - H(\rho - a)] \left[ H(t) \frac{t}{\tau_r} - H(t - \tau_r) \frac{t - \tau_r}{\tau_r} \right] \quad (7.51)$$

The slip velocity is now a rectangular pulse of duration  $\tau_r$  that begins at the rupture time  $t' = \rho/v$  when the rupture arrives at points of radius  $\rho$  on the fault. The motion at each point of the fault ceases after a time  $\tau_r$  (the rise time) independently of the final arrest of rupture at time  $t_r = a/v$ .

Since the far-field displacements depend on the slip velocity  $\Delta \dot{u}$ , as shown by [\(7.1\)](#), certain models specify directly the slip-rate distribution over the fault. Among many possible circular fault models we choose the following one, in which the slip velocity is expressed as follows:

$$\Delta \dot{u}(\rho, t) = \Delta V \left[ H\left(t - \frac{\rho}{v}\right) - H\left(t - \frac{a}{v}\right) \right] H(a - \rho) \quad (7.52)$$

In this model the slip velocity jumps instantaneously to a constant value  $\Delta V$  at each point of the fault, when the rupture front arrives (at a time  $t' = \rho/v$ ), remains constant as long as  $t < a/v$  and ceases for  $t \geq a/v$ . This means that the slip velocity persists on every point of the fault until the fracture stops at the border,  $\rho = a$  ([Fig. 7.14](#)). This model does not have a rise time. In it, the information that rupture is arrested at the border of the fault reaches each point inside the fault instantaneously. This is a very unrealistic model, which can be improved by assuming that the stopping phases propagate inside the fault at a finite speed (for example, at the P wave speed): thus, we write

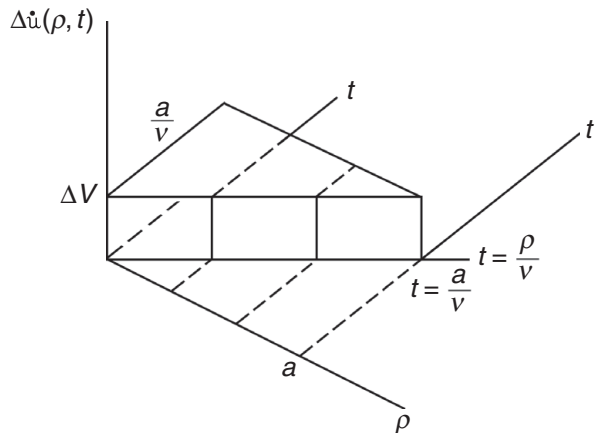


**Figure 7.14.** The slip velocity  $\Delta\dot{u}$  as a function of time and distance inside a circular fault of radius  $a$  and rupture velocity  $v$  for a model with initiation and arrest.

$$\Delta\dot{u}(\rho, t) = \Delta V \left[ H\left(t - \frac{\rho}{v}\right) - H\left(t - \frac{a}{v} - \frac{a - \rho}{a}\right) \right] H(a - \rho) \quad (7.53)$$

so that the slip velocity drops to zero at each point of the fault when a P wave arrives from the fault border. This wave is called the *healing front*, since it heals the fault by stopping its motion, starting from the border and towards the center. Another possible kinematic model is that of a circular fault which ruptures from the center to the border ( $\rho = a$ ) and then contracts back to the center at the same speed (Molnar *et al.*, 1973):

$$\Delta\dot{u}(\rho, t) = \Delta V \left[ H\left(t - \frac{\rho}{v} + \frac{a}{v}\right) - H\left(t + \frac{\rho}{v} - \frac{a}{v}\right) \right] H(a - \rho) \quad (7.54)$$

In these kinematic models the maximum slip is not reached until motion on the fault stops. Even more realistic kinematic models can be introduced by specifying that the slip velocity starts when rupture arrives at the point  $t' = \rho/v$ , then increases to a maximum value and finally decreases to zero, after a certain rise time  $\tau_r$  (see section 4.8, (4.70)). In this case there is no need for a healing front, since motion ceases at each point of the fault after a fixed rise time  $\tau_r$ . For rise times shorter than the total rupture time,  $\tau_r < a/v$ , the motion has the form of a propagating pulse of time width  $\tau_r$ , which heals itself as it propagates from the center to the edge of the fault  $r = a$ . This kind of slip rate model is frequently observed in narrow strike-slip faults and commonly called a *Heaton pulse* in the seismological literature (see Heaton, 1990, for further details).

In most kinematic source models the rise time  $\tau_r$  and the total duration of rupture  $t_r = L/v$  or  $t_r = a/v$  are considered to be independent. If both are equal,  $\tau_r \approx t_r$ , then the slip rate  $\Delta\dot{u}$  at individual points of the fault stops or heals once the total fracture is finished. Since this involves a requirement that information from the arrest of the fault at its border propagates instantaneously to all points of the fault, more realistic models, as we have seen, propose healing fronts to propagate from the edges of the fault at a certain fixed velocity, thus causing the arrest of motion. If  $\tau_r < t_r$  then motion at each point heals at time  $t = \tau_r$ , independently of the time when fracture ends. If the rise time is less than, say, 15% of the

fracture duration then  $\Delta\dot{u}$  propagates as a Heaton pulse over the fault plane, healing itself after a time equal to the rise time at each point. Motion takes place only over a limited band of the fault surface, and this band progresses with the velocity of fracture propagation.

## 7.8. Kinematic models with variable slip on fault plane

From a kinematic point of view, a complete description of the rupture process on a fault of finite dimensions requires that the slip be specified as a function of space and time for each point of the fault plane (Hartzell and Heaton, 1983). Let us assume that the fault plane is of rectangular form, of length  $L$  and width  $W$  with normal  $\mathbf{n}$ . For simplicity, we select the fault plane to be on the  $(x_1, x_3)$  plane, that is,  $\mathbf{n} = (0, 1, 0)$  and the rupture to propagate in the  $x_1$  direction with constant rupture velocity  $v$ . The points on the fault plane are given by coordinates  $(\xi_1, \xi_3)$  with respect to the origin, taken at a reference point on the fault plane (usually the hypocentre or the centroid of the moment tensor distribution) (Fig. 7.15). For such a model the far-field displacement of the P waves at a point  $x_i$  in an infinite medium is given by (7.1):

$$u^P(x_i, t) = A \int_0^L \int_0^W \frac{1}{r} R_p(n_k, l_k(\xi_j), \gamma_k(x_i, \xi_j)) \Delta\dot{u} \left( \xi_1, \xi_3, t - \frac{r}{v} \right) d\xi_3 d\xi_1 \quad (7.55)$$

$$A = \frac{\mu}{4\pi\rho\alpha^3}$$

where  $r = |x_i - \xi_i|$  is the distance from a point on the fault to the observation point  $\xi_i$ . The direction cosines of the vector  $\mathbf{r}$  are  $\gamma_j$  and  $R_p$  is the radiation pattern for a point moment

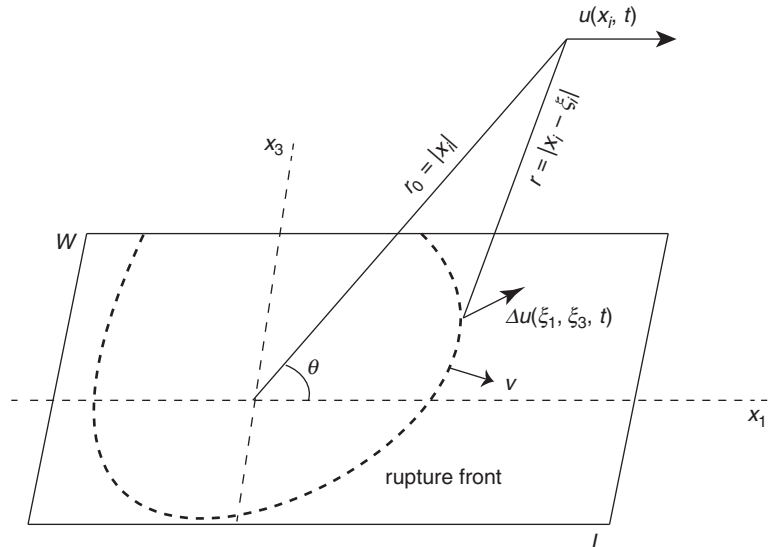


**Figure 7.15.** Displacement  $u$  at a distance  $r_0$  from the origin and distribution of the slip  $\Delta u$  as a function of position on a rectangular shear fault with velocity of propagation  $v$ .

tensor source situated at  $\xi_i$ . For a shear fracture  $l_k(\xi_j)$ , the direction of slip is normal to  $n_k$  ( $l_k n_k = 0$ ). An expression similar to (7.55) can be written down for the S waves.

Introducing the far-field approximation  $r = r_0 - \xi_j \gamma_j$ , defined before (7.4), and assuming that the rake or direction of the slip  $l_k$  is constant over the fault plane, we obtain as, cf. (7.12), the simplified expression

$$u^P(x_i, t) = \frac{AR_P(n_k, l_k, \gamma_k)}{r_0} \int_0^L \int_0^W \Delta\dot{u} \left( \xi_1, \xi_3, t - \frac{r_0}{\alpha} - \frac{\xi_i \gamma_i}{\alpha} \right) d\xi_3 d\xi_1 \quad (7.56)$$

where  $r_0 = |x_i|$  is the distance to the observer measured from the origin of coordinates on the source. Finally, we assume that the rupture speed  $v$  is finite on the fault plane and that the rupture front arrives at the point  $(\xi_1, \xi_3)$  at time  $t'(\xi_1, \xi_3)$ . If rupture begins at the origin ( $\xi_j = x_i = 0$ ) at time  $t = 0$ , the first arrival at  $x_i$  is at  $t = r_0/\alpha$ , so that we can write

$$\Delta\dot{u} \left( \xi_1, \xi_3, t - \frac{r_0}{\alpha} + \frac{\xi_i \gamma_i}{\alpha} \right) = \Delta\dot{u} \left( \xi_1, \xi_3, t - t'(\xi_i) + \frac{\xi_1 \gamma_1}{\alpha} \right) \quad (7.57)$$

Then, we can write (7.56) in the form

$$u^P(x_i, t) = \frac{AR_P(n_k, l_k, \gamma_k)}{r_0} \int_0^L \int_0^W \Delta\dot{u} \left( \xi_1, \xi_3, t - \frac{r_0}{\alpha} - t'(\xi_j) + \frac{\xi_i \gamma_i}{\alpha} \right) d\xi_3 d\xi_1 \quad (7.58)$$

A similar expression can be written down for the SH and SV components of the S wave. Equation (7.58) gives the far-field wave forms of P waves from a rectangular fault, where the slip is constant in direction but changes in amplitude over the fault. Rupture begins at the selected origin point and spreads with variable or constant rupture velocity. The distribution of the amplitude of the slip rate  $\Delta\dot{u}(\xi_i, t)$  is a function of position on the fault plane and time, sometimes referred to as the slip-rate history but more frequently as the source time function. The time in (7.58) is measured from the arrival time  $t'(\xi_1, \xi_3)$  of the rupture front at that point. A frequent assumption is that the slip dependence with time is the same for all points of the fault, separating the slip as a function of position from the local source time function, i.e.

$$\Delta\dot{u} \left( \xi_1, \xi_3, t - \frac{r_0}{\alpha} - t'(\xi_j) + \frac{\xi_i \gamma_i}{\alpha} \right) = D(\xi_1, \xi_3) f \left( t - \frac{r_0}{\alpha} - t'(\xi_j) + \frac{\xi_i \gamma_i}{\alpha} \right) \quad (7.59)$$

where  $f(t)$  is the source time function and  $D$  the slip distribution.

Let us finally assume that the direction of slip, that is,  $l_j(\xi_k)$ , varies over the fault plane, but it is always contained in the fault plane. If we describe the orientation of the rupture at each point of the fault by the angles  $(\phi, \delta, \lambda)$  (see section 1.3), since the fault plane is fixed then  $\phi$  and  $\delta$  are constant and  $\lambda(\xi_k)$ , the slip direction or rake, varies for each point of the fault. Expression (7.58) becomes

$$u^P(x_i, t) = \frac{A}{r_0} \int_0^L \int_0^W R_P(\phi_f, \delta, \lambda(\xi_j), \gamma_j) \Delta\dot{u} \left( \xi_1, \xi_3, t - \frac{r_0}{\alpha} - t'(\xi_j) - \frac{\xi_i \gamma_i}{\alpha} \right) d\xi_3 d\xi_1 \quad (7.60)$$

The radiation pattern  $R_P$  is now different for each point of the fault, as it depends on the value of  $\lambda(\xi_k)$ . Equation (7.60) gives the far-field wave forms of P waves from a rectangular

fault in which the slip direction changes along the fault. A similar expression can be written down for the SH and SV components of the S waves.

The problem can be also formulated in terms of the seismic moment-rate tensor density representing a shear fracture. If the slip direction is constant over the fault, equation (7.58) can be written as

$$u^P(x_i, t) = \frac{R_P(m_{ij})}{4\pi\rho\alpha^3 r_0} \int_0^L \int_0^W \dot{m} \left( \xi_1, \xi_3, t - \frac{r_0}{\alpha} - t'(\xi_j) - \frac{\xi_i \gamma_i}{\alpha} \right) d\xi_3 d\xi_1 \quad (7.61)$$

where  $\dot{m}(\xi_i, t)$  is the distribution of the moment rate or moment release over the fault plane with time. If the rake of the slip,  $\lambda(\xi_i)$ , is allowed to vary on the fault plane then, according to the relations between the components of the moment tensor and the angles  $(\phi, \delta, \lambda)$  (equations (5.31)), we can write (7.60) as

$$u^P(x_i, t) = \frac{1}{4\pi\rho\alpha^3 r_0} \int_0^L \int_0^W R_P(m_{ij}(\xi_j), \gamma_j) \dot{m} \left( \xi_1, \xi_3, t - \frac{r_0}{\alpha} - t'(\xi_j) - \frac{\xi_i \gamma_i}{\alpha} \right) d\xi_3 d\xi_1 \quad (7.62)$$

In this expression the amplitude of the moment rate and the components of the moment tensor vary over the fault plane, but the moment tensor is constrained to be that corresponding to a shear rupture on the specified fault plane, that is, only the slip angle varies in direction. For a synchronous source all components of  $m_{ij}$  have the same time dependence and usually the time dependence is the same for all points on the fault. Similar expressions to (7.61) and (7.62) can be written down for the SH and SV components of the S waves.

Equations (7.58)–(7.62) can be used in the forward problem to calculate the synthetic body wave forms due to a very general distribution of slip rate or moment rate on the fault, whether the slip has a fixed orientation or changes its rake. The orientation and dimensions of the fault plane and the location of the initiation of rupture must be assumed to be known. In the inverse problem the above equations can be used to determine the distribution of slip rate or moment rate and slip orientation on a specified fault plane from a set of observations of body wave forms. The equations (7.58)–(7.62) define kinematic models of the source in which the slip-rate amplitude and its orientation vary from point to point and with time on a specified fault plane, as the rupture front propagates from the point of initiation to the borders with constant or variable rupture velocity.

## 7.9. The circular kinematic model of Sato and Hirasawa

The models presented in sections 7.2–7.4 have the property that the slip has the same value everywhere on the fault. In such a model a point just inside the border of the fault slips by a finite amount  $\Delta u$ , while a point situated just outside the border of the fault does not slip at all. These models are not acceptable from a continuous-mechanics point of view because at the border the continuity of matter is violated. This produces stress concentrations around the border of the fault that have non-integrable singularities and store an infinite amount of strain energy (see Madariaga and Olsen, 2000, for further discussion). A mechanically acceptable model requires that the slip decreases continuously to zero at

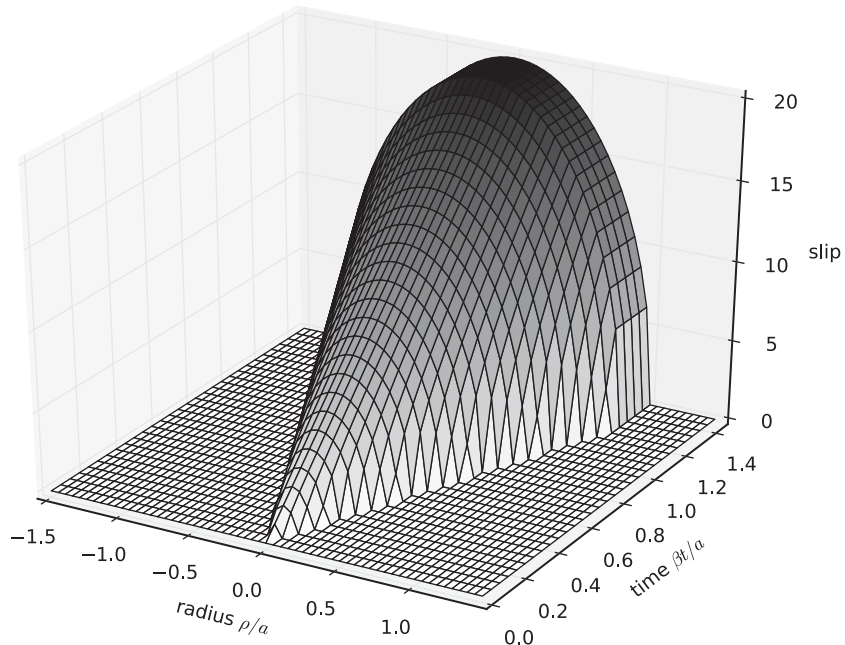


**Figure 7.16.** The slip on a circular fault of radius  $a$  as a function of time and distance in the model of Sato and Hirasawa (1973).

the fault edge as discussed in the previous section. As we will see in Chapter 9, the proper solution is to consider a crack or fracture model near the edge of the fault.

A model that is mechanically acceptable but still kinematic was presented by Sato and Hirasawa (1973), who were the first to introduce some elements of earthquake dynamics into kinematic models. This model will serve as an example for the estimation of seismic radiation from fracture models; for this reason we present it in detail. These authors considered a circular fault of radius  $a$  in which rupture propagates from the center of the fault outwards with constant rupture velocity  $v$  (Fig. 7.16). The slip on the fault is no longer constant as in Savage's (1966) model but is a function of the stress drop over the fault; Sato and Hirasawa (1973) assumed that the slip has the same form as that of a circular (coin-shaped) shear crack subject to a static stress drop  $\Delta\sigma$ . Since the radius of the fault at time  $t$  is  $vt$ , they assumed the following slip distribution:

$$\Delta u(\rho, t) = \frac{24\Delta\sigma v}{7\pi\mu} \sqrt{t^2 - \frac{\rho^2}{v^2}} H\left(t - \frac{\rho}{v}\right) [1 - H(\rho - a)], \quad t < a/v \quad (7.63)$$

where  $\rho$  is the radial distance. In this model it is assumed that the slip distribution, or crack shear displacement, for a circular crack under uniform shear stress holds for each time during the rupture process. At a point of radius  $\rho$  on the fault, slip begins at  $t = \rho/v$  and increases parabolically with time until  $t = a/v$ . The slip on the fault heals instantaneously at all points when the rupture front reaches the border ( $t = a/v$ ). The final static slip once fracture has stopped ( $t > a/v$ ) is given by

$$\Delta u(\rho, t) = \frac{24\Delta\sigma}{7\pi\mu} \sqrt{a^2 - \rho^2} [1 - H(\rho - a)] \quad (7.64)$$

This is the slip distribution over a coin-shaped circular crack; it has its maximum at the center of the fault and decreases to zero at the border ( $\rho = a$ ). This solution will be discussed in more detail in [Chapter 9](#). Near the edge of the fault the slip decreases as the square root of the distance from the border.

The radiation from this circular kinematic model can be computed very easily using the far-field approximation to equation (7.1):

$$u_i^{P,S}(x_s, t) = \frac{1}{4\pi c^3 \rho} \frac{R_{P,S}(n_k, l_k, \gamma_k)}{r} \Omega_{P,S}(t, \theta) \quad (7.65)$$

where the wave speed  $c$  stands for the P or S wave velocity depending on the type of wave under consideration. In (7.65)  $\Omega_{P,S}$  is the *apparent moment rate* observed in the azimuthal direction  $\theta$  and is given by

$$\Omega_c(t, \theta) = 2\pi\mu \int_{\Sigma} \Delta \dot{u} \left( \rho, t - \frac{r_0}{c} - \frac{\rho}{c} \sin \theta \right) \rho d\rho \quad (7.66)$$

where we notice that for a circular crack the scalar product  $\xi_i \eta_i = \rho \sin \theta$ . In (7.66) we have made the usual far-field approximation defined by (7.4). Taking the time derivative of the slip distribution (7.63) and inserting it into (7.66) we obtain

$$\begin{aligned} \Omega_c(t, \theta) &= \frac{24\Delta\sigma}{7} a^2 v \frac{2}{[1 - (v^2/c^2) \sin^2 \theta]^2} \frac{v^2 t^2}{a^2}, \quad 0 < t < t_1 \\ \Omega_c(t, \theta) &= \frac{24\Delta\sigma}{7} a^2 v \frac{1}{2(v/c) \sin \theta} \left[ 1 - \frac{v^2 t^2}{a^2 [1 + (v/c) \sin \theta]^2} \right], \quad t_1 < t < t_2 \end{aligned} \quad (7.67)$$

where  $t_1 = (a/v)[1 - (v/c) \sin \theta]$  is the travel time of the first stopping phase, that is, the wave emitted from the point on the circle of radius  $a$  that is closest to the observation point;  $t_2 = (a/v)[1 + (v/c) \sin \theta]$  is the arrival time of the second stopping phase, emitted by points situated on the opposite side of the circular fault.

The far-field displacement and velocity have a number of interesting and important properties, which we will review very briefly. The amplitude of the far-field displacement ([Fig. 7.17a](#)) at  $t = 0$  grows as the square of time, so that the initial motion emitted by the fault is weak compared with the stopping phases, which we now discuss. When the first stopping phase arrives at  $t = t_1$  the displacement is continuous, but it has a discontinuous first derivative in time. The value of the apparent moment rate  $\Omega_c$  at that point is given by

$$\Omega_c(t = t_1, \theta) = \frac{24\Delta\sigma}{7} v a^2 \frac{2}{[1 + (v/c) \sin \theta]^2} \quad (7.68)$$

At time  $t = t_2$  the signal returns to zero and again has a discontinuous time derivative. The integral of the signal  $\Omega_c$  is equal to the scalar seismic moment of the earthquake:

$$M_0 = \int_0^{t_2} \Omega_c(t, \theta) dt = \frac{16}{7} \Delta\sigma a^3 \quad (7.69)$$

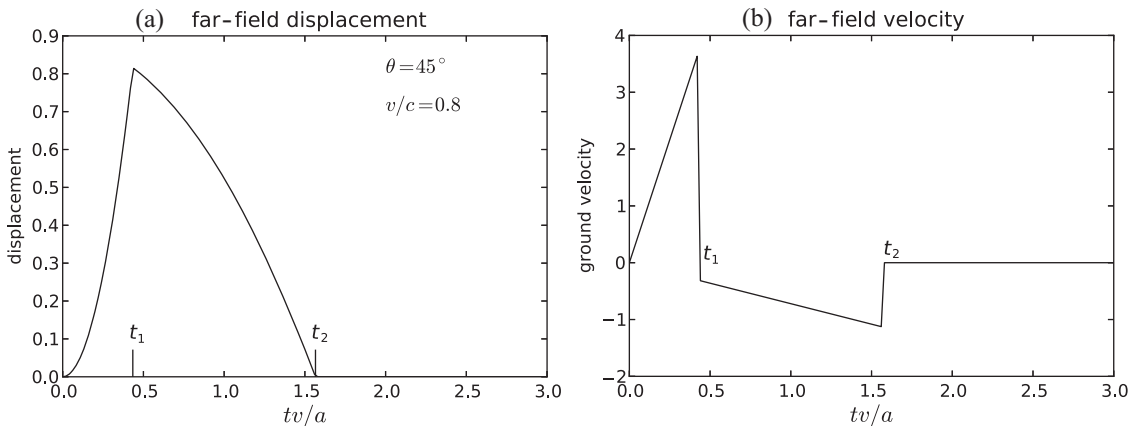


**Figure 7.17.** (a) Far-field displacement and (b) far-field velocity pulse as a function of time for the model of Sato and Hirasawa (1973).

and is independent of the azimuth of radiation  $\theta$ . The value of the seismic moment in (7.69), already given in (1.22), is what is expected for a circular crack, according to Eshelby (1957) and Sato and Hirasawa (1973).

The far-field velocity pulse (Fig. 7.17b) is obtained by taking the time derivative of (7.67). The most important features of the velocity pulse are the two jumps in velocity associated with the arrival time of the stopping phases at times  $t_1$  and  $t_2$ . These can be computed from the time derivative of (7.67), and we obtain

$$\begin{aligned}\Delta\dot{\Omega}(t = t_1, \theta) &= -\frac{24}{7} \Delta\sigma a v^2 \frac{1}{(v/c) \sin \theta} \frac{1}{[1 - (v/c) \sin \theta]^2} \\ \Delta\dot{\Omega}(t = t_2, \theta) &= \frac{24}{7} \Delta\sigma a v^2 \frac{1}{(v/c) \sin \theta} \frac{1}{[1 + (v/c) \sin \theta]^2}\end{aligned}\quad (7.70)$$

The amplitudes of these jumps in velocity are proportional to the radius  $a$  of the fault times the square of the rupture velocity. This is a common feature, which we find in all source models based on fracture dynamics. When ruptures propagate very slowly they produce no high-frequency waves, and for faster ruptures their amplitude increases as the rupture velocity squared.

## Spectral properties

Computing the Fourier transform of the far-field displacement (7.67) is straightforward, but the result is very unwieldy and difficult to interpret; it is easier to compute the spectrum numerically from the exact expressions (7.67). We observe in Fig. 7.18 that the spectrum has the same features as those already described several times for the Brune spectral model. The most important feature is that at low frequencies we have

$$\tilde{\Omega}(0, \theta) = \frac{16}{7} \Delta\sigma a^3 = M_0 \quad (7.71)$$

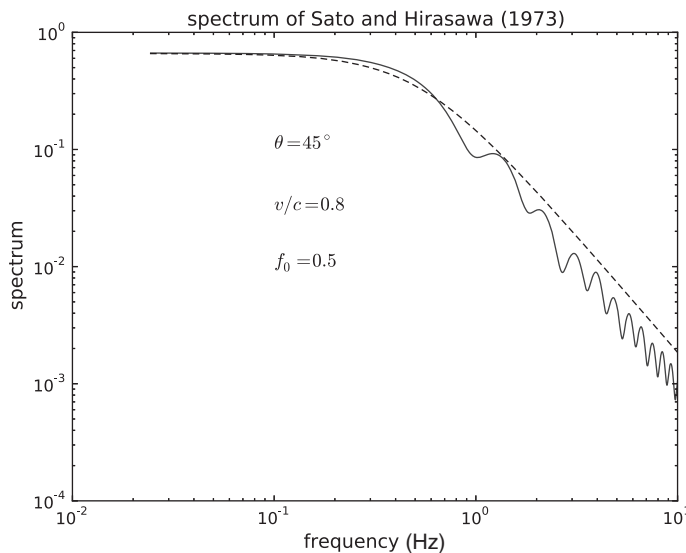


**Figure 7.18.** Far-field amplitude spectrum of displacement for the model of Sato and Hirasawa (1973).

Thus, as expected, the low-frequency limit of the spectrum of the far-field displacement is equal to the seismic moment and is independent of the radiation angle  $\theta$ . At high frequencies the radiation is also easy to compute; it has two terms, associated with the stopping phases at  $t_1$  and  $t_2$  shown in Fig 7.17. The high-frequency spectrum is given by

$$\tilde{\Omega}(\omega, \theta) = \frac{24}{7} \Delta\sigma a^3 \frac{1}{(v/c) \sin \theta} \left\{ \frac{\exp(-i\omega t_1)}{[1 - (v/c) \sin \theta]^2} + \frac{\exp(-i\omega t_2)}{[1 + (v/c) \sin \theta]^2} \right\} \frac{v^2}{\omega^2 a^2} \quad (7.72)$$

We observe again that while at low frequencies the radiation is independent of position in the focal sphere, high frequencies are strongly affected by *focusing* (corresponding to the inverse  $\sin \theta$  term) and directivity. The far-field spectrum of the Sato and Hirasawa (1973) model behaves like the inverse squared model of Brune (1970), in that the amplitude decays as  $\omega^{-2}$  at high frequencies. The decay of the spectrum at high frequencies is not smooth, however, as in Brune's model because it has a pattern of interferences between the two stopping phases that is similar to that already discussed for the stopping phases of the bilateral Haskell model. Peaks and troughs occur when the two exponentials in (7.72) are roughly in phase or in opposition of phase, i.e. when  $\omega(t_1 - t_2) = (2\omega a/c) \sin \theta = n\pi$ .

### Corner frequency

As we saw in section 7.5, and as will be further explained in section 9.4, Brune (1970) introduced the concept of the corner frequency. According to this model the far-field displacement spectrum is controlled by a frequency that is inversely proportional to the source radius. This model has become the standard method to determine the equivalent radius of the seismic source and, from this radius, the average stress drop on the fault. Sato and Hirasawa (1973) evaluated the relation between the corner frequency observed in

Figure 7.18 and the size of the fault. For that purpose they averaged the corner frequencies computed for different values of azimuth  $\theta$ . Although the relation depends on the rupture velocity  $v$  we can approximate the corner frequency of S waves by

$$\omega_c = C_s \frac{\beta}{a} \quad (7.73)$$

where  $C_s$  is a numerical coefficient that varies from 1.57 for a rupture velocity  $v = 0.5\beta$  to 1.99 for  $v = 0.9\beta$ . This coefficient is significantly smaller than that proposed by Brune (1970), i.e.  $C_s = 2.34$ .

### Directivity and focusing

The expressions (7.70) for the stopping phases in the time domain and their high-frequency spectra (7.72) demonstrate two main features of the radiation from a finite fault at high frequencies. The first is its directivity, expressed by the terms in the denominator, which are inversely proportional to the directivity factor already discussed in section 7.6 for Haskell's model. The only difference is that now the directivity is expressed in terms of the polar angle  $\theta$  instead of the cosine of the direction of take-off as in Haskell's model.

The second important feature, less well known in seismology, is the focusing due to the circular shape of the radiator. This is expressed by the term  $\sin \theta$  in the denominator. Along the axis of the fault ( $\theta = 0$ ) the radiation is very strong and decreases with increasing angle  $\theta$ . The radiation from a circular fault is modulated by these two competing effects, focusing in the direction perpendicular to the fault and directivity along the fault.

## 8.1. Parameters of kinematic extended source models

The theory of *kinematic extended models* of the source, presented in Chapter 7, is the foundation for the development of methods to determine from the analysis of seismic waves the parameters that define such models. Although faults of any shape can be studied kinematically, most often the fault is assumed to be planar with simple external geometry: a rectangle, a circle or an ellipse. For a rectangular source the parameters are the length  $L$ , width  $W$ , rupture velocity  $v_i$  and the distribution of the slip and slip rate on the fault. For circular faults the parameters are the radius of the fault  $a$ , the rupture speed  $v$  and the distribution of the slip and slip rate on the fault plane. The orientation of the extended source is defined by that of its normal vector  $n_j$ . If it were not a plane, the normal would change in direction with its position vector  $\xi_i$ , i.e. it would have to be written as  $n_j(\xi_i)$ , corresponding to a warped surface.

The rupture velocity  $v_i(\xi_j)$  may be assumed to be constant or to change in amplitude and direction over the fault plane. The slip  $\Delta u_j(\xi_i, t)$  and the slip rate  $\Delta \dot{u}_j(\xi_i, t)$  are functions of position on the fault plane and of time. For pure shear sources,  $\Delta u_j(\xi_i, t)$  and  $n_j$  are always perpendicular. Alternative parameters can be introduced such as the maximum values of the amplitude of the slip and slip rate,  $\Delta u_{\max}$  and  $\Delta \dot{u}_{\max}$ , and the position on the fault plane where these maxima are located. The time dependence of the slip includes the value of the rise time  $\tau_r(\xi_i)$ , which may change over the fault plane. This would imply that fracture does not propagate uniformly but accelerates and decelerates as it propagates on the fault plane and may even stop and restart at some places. Boundary conditions must be added to ensure that  $\Delta u_j(\xi_i, t)$ ,  $\Delta \dot{u}_j(\xi_i, t)$  and  $v_i(\xi_i)$  become zero at the boundaries of the fault.

In this chapter we will present some methods which have been developed to determine the parameters of extended seismic sources from the analysis of seismic waves.

## 8.2. Analysis of seismic wave spectra

As we discussed in section 7.5, the finite dimensions of the source determine the shape of the amplitude spectrum of seismic waves, which has a flat part at low frequencies, proportional to the seismic moment, and decays at high frequencies as  $\omega^{-\gamma}$ , where  $\gamma$  is generally very close to 2. The low- and high-frequency asymptotes intersect at the corner frequency  $\omega_c$ , which is inversely proportional to the characteristic fault dimension (Fig. 7.7). When

the spectrum is drawn on a logarithmic scale it can be fitted by two straight lines, a flat one at the low frequency and another of slope  $\gamma \cong -2$  at high frequencies. According to equation (7.20) the scalar seismic moment  $M_0$  can be determined from the mean value of the low-frequency part of the amplitude spectrum of body and surface waves.

The observations used in spectral studies are seismograms (Chapter 2), from which we need to remove the instrument response in order to obtain the ground motion  $u(t)$ . Then we correct for all the factors that affect wave amplitudes in their propagation from the source to the observation point (Chapter 6). Finally, we can compute the seismic moment in terms of the spectrum of P waves as

$$M_0 = \frac{U_z^P 4\pi\rho\alpha^3 R_T q(r, Q_\alpha)}{g(\Delta) C_z(i_0) R_P(\phi, \delta, \lambda, i_h)} \quad (8.1)$$

Where  $U_z^P$  is the mean value of the low-frequency spectral amplitude of the vertical component of the ground displacement produced by P waves at a particular seismic station,  $\rho$  is the density,  $\alpha$  is the P wave velocity at the source,  $R_T$  is the Earth's radius,  $q(r, Q)$  is the anelastic attenuation,  $g(\Delta)$  is the geometric spreading factor,  $\Delta$  is the epicentral distance,  $C_z(i_0)$  is the effect of the free surface, where  $i_0$  is the incident angle at the station, and  $R_P$  is the radiation pattern of the P waves. For SH waves the equation is similar to (8.1) but with the replacements  $U_{SH}$ ,  $\beta$ ,  $q(r, Q_\beta)$ ,  $R_{SH}$  and  $C_{SH}(j_0)$ . For Rayleigh waves the relation is

$$M_0 = \frac{U_z^R (2\pi R)^{1/2} \exp(\gamma_R R)}{k_R^{1/2} N_z(R, h) R_R(\phi, \delta, \lambda)} \quad (8.2)$$

where  $U_z^R$  is the mean spectral amplitude for the low-frequency vertical components of the Rayleigh waves,  $R$  is the epicentral distance in km,  $\gamma_R$  is the attenuation factor,  $k_R$  is the wave number,  $N_z(R, h)$  is the excitation factor for depth  $h$  and  $R_R$  is the Rayleigh wave radiation pattern. Expressions (8.1) and (8.2) can be simplified by approximating some factors.

From the corner frequency, defined in section 7.5, we can determine an approximation to the dimensions of the source (Hanks and Wyss, 1972). For a circular fault, according to Brune's model (see section 9.4 below), the radius  $a$  of the fault can be obtained from the corner frequency of the S wave spectrum by

$$a = \frac{2.34\beta}{2\pi f_c^S} \quad (8.3)$$

It is also possible in some cases to determine the radius  $a$  from the corner frequency of the P wave spectrum:

$$a = \frac{2.34\beta}{2\pi f_c^P} \quad (8.4)$$

However, in general this expression is incorrect (see Madariaga, 1976, and section 9.5).

For a rectangular fault of length  $L$  and width  $W$  the relation between  $L$ ,  $W$  and the corner frequency of P waves has never been studied in detail for dynamic models. However, for kinematic rectangular faults (section 7.5) we find

$$\sqrt{LW} = \frac{1.7\alpha}{2\pi f_c^P} \quad (8.5)$$

and for S waves

$$\sqrt{LW} = \frac{3.8\beta}{2\pi f_c^S} \quad (8.6)$$

The circular model is applicable to small-to-moderate-magnitude earthquakes ( $M_W < 6$ –6.5), with dimensions smaller than the seismogenic layer (20 km) so that the fault can grow unimpeded in all direction. For larger earthquakes the fault length is greater than the thickness of the seismogenic layer and the source is better approximated by the rectangular model with  $L > W$ . For such large-source models it is common to invert the observed seismograms in order to determine the slip distribution, a method usually called finite-source inversion. We will study it in [section 8.6](#).

Once we have obtained  $M_0$  and the fault dimensions from the spectra of body or surface waves, we can obtain the *average value of the slip*  $\Delta\bar{u}$  over the fault area  $S$ , given by

$$\Delta\bar{u} = \frac{M_0}{\mu S} \quad (8.7)$$

where for a circular fault  $S = \pi a^2$  and for a rectangular fault  $S = LW$ . We can also obtain the *average value of the stress drop*  $\Delta\bar{\sigma}$ , which, for a circular fault (1.23), is

$$\Delta\bar{\sigma} = \frac{7}{16} M_0 \left( \frac{\pi}{S} \right)^{3/2} \quad (8.8)$$

Thus, we can use the spectra of body waves to obtain estimates of the scalar seismic moment and the fault dimensions, and from them determine the average values of the slip and stress drop. This is a very simple and straightforward method to estimate these parameters, although sometimes the results are conditioned by the approximations used to derive these equations, especially by Brune's formula for the relation between the source radius and corner frequency. We show an example in [Fig. 8.1](#), showing P waves observed at a station located at teleseismic distance 3945 km from an earthquake of focal depth 650 km. As the seismogram corresponds to the BHZ channel (20 samples/s) (see [Chapter 2](#)), we have used a time window of 50 s. In terms of the digital data there are 1000 points, that is, a number very close to a power of 2 ( $2^{10} = 1024$ ). It is important to remember that the FFT algorithm, used by most programs to compute the Fourier transform, is based on the properties of the powers of 2; thus it is desirable that the length of the window of our signal data should be close to but less than a power of 2. For example, if we chose a length of 257 points instead of 256 ( $2^8$ ), the algorithm used to estimate the FFT will automatically fill the signal with zeros to obtain the next power of 2 ( $2^9 = 512$ ), that is, it will be padded with 255 zeros. The spectra would then be calculated for a signal with about 50% zeros.

The amplitude spectrum in [Fig. 8.1](#) was computed from the digital data following the steps described in [section 2.4](#)). First the instrument response was removed in order to obtain the ground displacement  $u(t)$ , then the time window was, tapered to remove other seismic phases, multiple reflections or scattered waves (coda) and finally the Fourier transform, was computed.

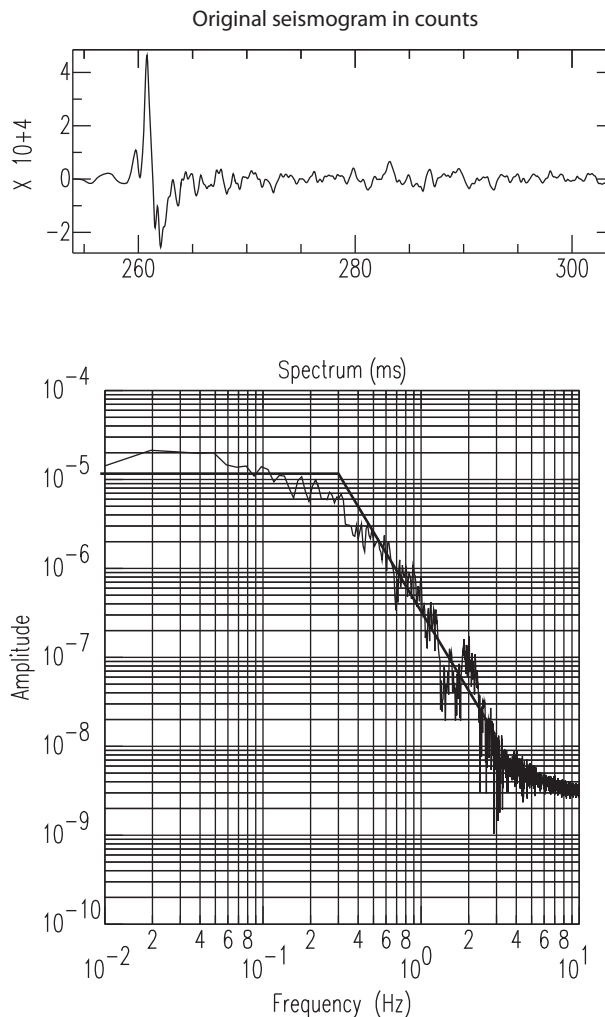


**Figure 8.1.** Amplitude spectrum of P waves observed at an epicentral distance 3945 km for a deep earthquake ( $h = 650$  km) with magnitude  $M_W = 6.2$ .

According to Fig. 8.1 the flat part of the spectra has amplitude  $U_z^P = 10^{-5}$  ms. As the focal depth is 650 km, we take the values  $\rho = 4.35$  g/cm<sup>3</sup> and  $\alpha = 10.5$  km/s. The value of the radiation pattern for the orientation of the station (in this case 0.65) can be determined from the focal mechanism, but if we do not know it then we can assume an average value of 0.7. It is important to remember that to estimate the moment  $M_0$  we should avoid nodal stations. The correction for geometrical spreading ( $g(\Delta)/R_T$ ) may be obtained using some specific programme to estimate it or it can be found directly from equation (6.9). In this case the value

$$\left( \frac{di_h}{d\Delta} \right) = \frac{d^2 t}{d\Delta^2}$$

may be obtained from the travel-time curves for the IASPEI or PREM models (Kennet and Engdahl, 1991; Dziewonski and Anderson, 1981). In cases where we do not have these tables we can approximate geometrical spreading by the inverse of the hypocentral distance, an approximation that is often used in practical applications. Using these values we obtain that the scalar seismic moment from P waves is equal to  $3.5 \times 10^{18}$  N m and that the moment magnitude from (1.30) is  $M_W = 6.2$ . From the corner frequency ( $f_c = 0.3$  Hz), using equation (8.4) we obtain, for the radius of a circular fracture,  $a = 13$  km. Finally, from these values and expressions (8.7) and (8.8) we can compute the average slip and stress drop,  $\Delta\bar{u} = 4$  cm and  $\Delta\bar{\sigma} = 0.7$  MPa.

An important practical problem to consider is the length of the seismogram or time window used to estimate the spectra. For body waves it must contain only P or S pulses. For large earthquakes at teleseismic distances this is not generally a problem but for small earthquakes at regional distances it is important. With modern digital instruments we can avoid this problem using data with high-rate sampling (for example, channels with 100 samples/s).

At regional distances we must use accurate values for the various corrections, especially for the attenuation corrections. In Fig. 8.2 we show the seismogram and amplitude spectrum for a regional earthquake in southern Spain (epicentral distance 70 km and depth 6 km). In this case, we use a shorter time window (12 seconds), density  $2.7$  g/cm $^3$  and P wave velocity 6 km/s. From the value of the flat part of the spectrum,  $2 \times 10^{-5}$  m/s, the obtained scalar seismic moment is  $M_0 = 7.3 \times 10^{15}$  N m and, from the 2 Hz corner frequency, we obtain  $a = 1$  km,  $M_W = 4.5$ ,  $\Delta\bar{u} = 5.8$  cm and  $\Delta\bar{\sigma} = 3$  MPa.

Normally we estimate the scalar seismic moment  $M_0$  from several stations with different azimuths and take the average of these values. It is important to recall from spectral analysis that we can estimate independently  $M_0$ , from the flat part of the spectra, and the dimensions, from the corner frequency, and from these values calculate the average slip and stress drop. The corner frequency may be also used as an indicator for filtering seismograms. If records are noisy then it may be necessary to filter them, but it is important to avoid the loss of seismic information. The corner frequency may be used for this purpose as it corresponds to the maximum frequency that must be used to filter the seismogram. If we filter the seismogram using a frequency lower than the corner frequency, we would lose information.

### **8.3. Directivity effects on Rayleigh waves**

---

Besides the dimensions an important parameter in kinematic extended models is the rupture velocity  $v_r$ , which is much more difficult to invert. For instance, in the classical Brune model (8.3) there is no way to determine the rupture speed. A possible way to determine rupture speed is to use surface waves, especially for shallow strike-slip faults. As we saw in (7.41) the directivity function  $D(\omega)$  for unilateral faulting depends on both  $L$  and  $v_r$ , so it can be used for their determination. Once we have found  $L$  and  $v_r$ , we can determine the total duration of the rupture process  $T = L/v_r$ , which is in general different from the rise time  $\tau$ .

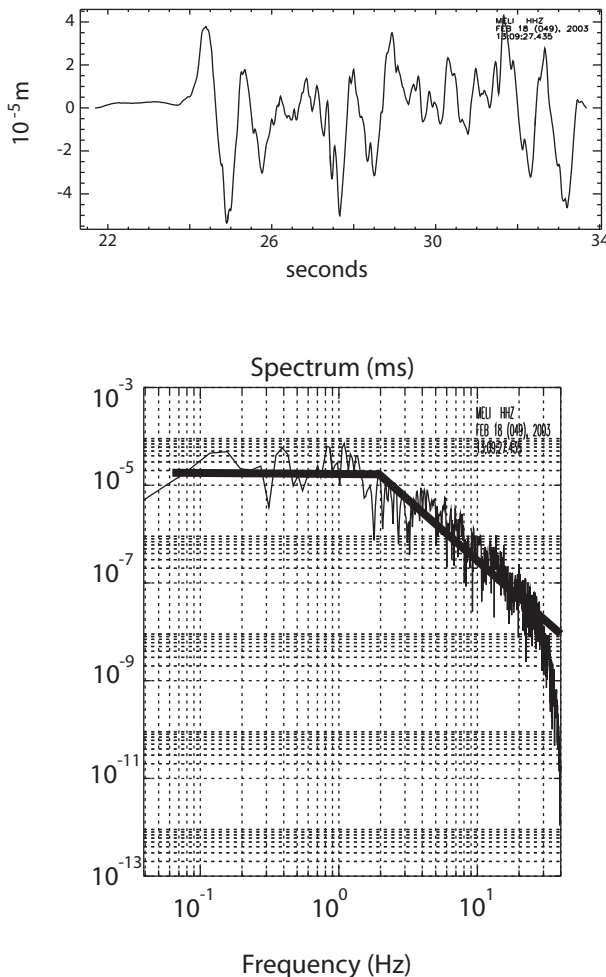


**Figure 8.2.** Amplitude spectrum of P waves observed at a station at 70 km epicentral distance from an earthquake at 6 km depth with magnitude  $M_W = 4.5$ .

The simplest case to obtain information about  $L$  and  $v$  from the directivity is to use Rayleigh waves recorded at stations separated by an azimuth of  $180^\circ$  from earthquakes with a vertical strike-slip mechanism (7.41). The directivity function  $D(\omega)$  has a number of maxima and minima. The first maximum corresponds to a frequency

$$f_{\max}^1 = \frac{c}{L(c/v_r + \cos \theta)} \quad (8.9)$$

Thus for constant  $v_r$ , the frequency of the first maximum or minimum is inversely proportional to the source length  $L$ : for small  $L$  the first spectral peak is at a higher frequency than for longer  $L$  (Fig. 7.10). Using equation (8.9) we can obtain the values of  $L$  and  $v_r$ . For the Kulun earthquake in China (14 November 2001,  $M_W = 7.8$ ), with a strike-slip focal mechanism, we estimated the amplitude spectrum for the Rayleigh waves recorded at

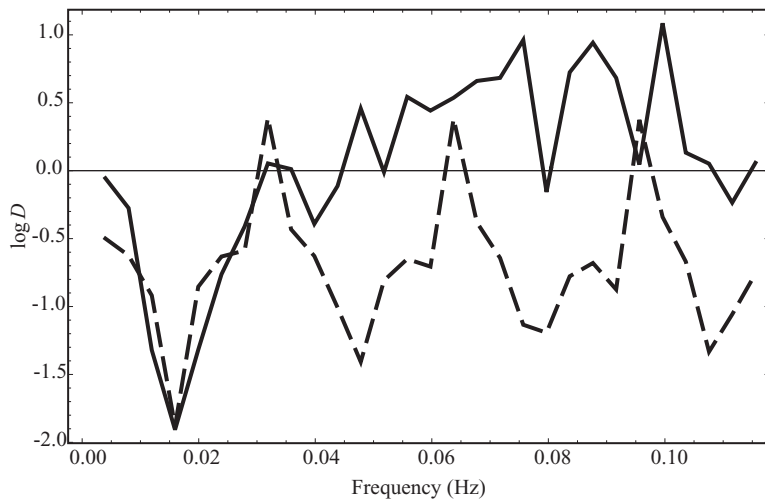


**Figure 8.3.** Observed directivity function (continuous line) for stations OBN and WRAB with an  $180^\circ$  azimuth between them, for the Kulun (China) earthquake of 14 November 2001,  $M_W = 7.8$ , and the corresponding theoretical directivity function (broken line) for a source of length 425 km and rupture velocity 3.9 km/s (Courtesy of C. Pro).

stations OBN and WRAB, with azimuths that differ by almost  $180^\circ$ . We corrected them for attenuation and divided them to obtain the directivity  $D(\omega)$ . In Fig. 8.3, we plot the logarithm of the directivity function  $D$ . From the fault-plane solution (with planes striking at  $272^\circ$  and  $182^\circ$ ) we chose the plane striking at  $272^\circ$  as the rupture plane. We observe that the first minimum corresponds to a frequency  $f = 0.016$  Hz, and if we assume that  $v_r = 3.9$  km/s we obtain a fault length  $L = 425$  km. In order to obtain the direction of rupture propagation we estimated the theoretical function  $D$  for these values of  $v_r$  and  $L$  and for the two possible propagation directions,  $92^\circ$  and  $272^\circ$ . From a comparison between theoretical and observed data we chose as the rupture propagation direction the azimuth  $92^\circ$  (the broken line in Fig. 8.3) (the rms of the difference between the theoretical and observed values of  $D$  is equal to 0.74).

The frequency interval between two consecutive extreme values of the directivity function for constant  $v_r$  decreases for larger values of  $L$  (Fig. 7.10). For constant  $L$  the frequency of the first extreme value of  $D(\omega)$  depends directly on  $v_r$  and also the frequency interval between two extreme values. Since  $v_r$  varies little, say, between 1.5 and 3.5 km/s, its effect on  $D(\omega)$  is small, so that this method is not very efficient for finding its value (Pro, 2002). Moreover, there is an ambiguity, because  $L$  and  $v_r$  are not independent (see (8.9)). For example, in the case of the Kulun earthquake (Fig. 8.2), if we assume a different rupture velocity ( $v_r = 2.8$  km/s) we obtain a length  $L = 240$  km. To reduce this ambiguity, we can use the directivity function from different pairs of stations and, using the same value of  $v_r$ , we must obtain the same  $L$  in all pairs of stations. Therefore, from the directivity, besides finding estimates for  $L$  and  $v_r$  we can also identify the rupture plane and the sense of rupture propagation. Unfortunately this method is restricted to shallow horizontal earthquakes with stations in both azimuths.

## 8.4. Effects of directivity on body wave form modeling

Directivity effects are also present in body wave forms and they can also be used to determine fault dimensions. The dependence of the P wave forms on the length of the fault  $L$  and the rupture velocity  $v_r$ , through the variable  $X$ , is shown in equation (7.19). As we saw in (7.43) the width of the body wave pulses  $t_d$  depends on both these quantities. A simple way to demonstrate the effect of directivity on body wave forms is to use a discrete model consisting of a sum of  $N$  point sources whose motion propagates along a line of length  $L$  with velocity  $v_r$ , so that  $L = \Delta x(N - 1)$  where  $\Delta x$  is the interval between the point sources (Fig. 8.4) (Pro, 2002). The displacement of the P wave  $u(r, t)$  at an observation point at distance  $r$  from the origin of the rupture line is the sum of the displacements produced by the point sources radiating at the corresponding delayed times:

$$u(r, t) = \sum_{k=1}^N u_k(r_k, t - t_k) \quad (8.10)$$

where  $t_k$  is the arrival time at the observation point at distance  $r_k$  of a pulse emitted by the point source located at  $x_k = (k - 1) \Delta x$ . According to (7.13),  $t_k$  is given by

$$t_k = \frac{r}{\alpha} + \frac{x_k}{\alpha} \left( \frac{\alpha}{v} - \cos \theta \right) \quad (8.11)$$

where  $\theta$  is the angle formed by the line of sources and the line from the origin to the observation point (Fig. 8.4) and  $\alpha$  is the P wave velocity. If the line of sources is horizontal then

$$\cos \theta = \cos \phi \sin i_h \quad (8.12)$$

where  $\phi$  is the azimuth measured from the source line to the observation point and  $i_h$  is the take-off angle at the source. If each elementary source point has a different seismic moment  $m_k$ , the far-field displacement of the P wave at a distance  $r$  can be written as

$$u^P(r, t) = \frac{R_P(\phi, i_h)}{4\pi\rho\alpha^3 r} \sum_{k=1}^N m_k f(t - t_k) \quad (8.13)$$

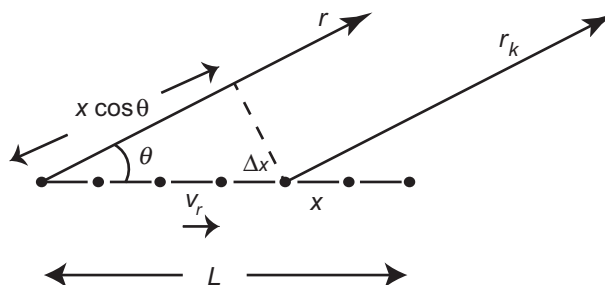


**Figure 8.4.** Schematic view of a source line of length  $L$  and rupture velocity  $v_r$  and observations at distance  $r$  and azimuth  $\theta$ .

where  $f(t - t_k)$  is the *apparent source time function* (ASTF) corresponding to the  $k$ th point source at each observation point and varies from one station to another depending on their location.

In practice there are different ways to generate the ASTF. For example, we can use triangles with base  $\tau_r$ , the rise time. If we assume a constant rupture velocity, the rise time must satisfy the condition (Herrero, 1994)

$$\tau_r = \frac{\Delta x}{v_r}$$

If the rupture velocity is variable then we must introduce the condition  $\tau_r > \Delta x/v_r$ .

If we want to change the time duration of each triangle as a function of the azimuth of station  $j$ , then we write

$$\tau_{rj} = \tau_r \left(1 - \frac{v}{\alpha} \cos \theta_j\right) \quad (8.14)$$

If the seismic moments  $m_k$  are all equal, the time function at station  $j$  has a trapezoidal form with duration  $\tau_j'$ :

$$\tau_j' = \frac{L}{v_r} \left(1 - \frac{v_r}{\alpha} \cos \theta_j\right) \quad (8.15)$$

The ASTF for station  $j$  is given by

$$f_j(t - t_k) = \sum_{k=1}^N m_k f(\tau_r, t - T_{jk}) \quad (8.16)$$

where  $T_{jk}$  is the delay at station  $j$  due to the source  $k$ :

$$T_{jk} = \frac{x}{v_r(k)} - \frac{x}{\alpha} [\cos(\phi_j - \phi_{rup})] \sin i_h \quad (8.17)$$

Here  $\phi_{rup}$  is the azimuth of the direction of rupture propagation.

At observation points located in the direction of the source line ( $\theta_j = 0^\circ$  corresponding to the *directivity stations*) and in the backward direction ( $\theta_j = 180^\circ$ , corresponding to the *anti-directivity stations*), the time function is shortened or lengthened with respect to those located in a direction perpendicular to the source line. An example of the directivity effect on the body waves is shown in Fig. 8.5. We generated synthetic P wave forms without taking into account the directivity effect (the continuous lines) and with directivity effects (the dotted lines). The method used to generate such synthetic seismograms is similar to the methods described in section 6.4; the only change we need to make is to replace the STF with equation (8.16). Two stations (EST1 and EST2) are normal to the rupture plane ( $272^\circ, 89^\circ, -4^\circ$ ), EST3 station is a directivity station and STS4 is in the opposite (anti-directivity) direction. In Fig. 8.5 the effect of directivity on the amplitude and duration of the pulse may be observed at the EST3 and EST4 stations.

In practice, when considering the directivity effect in body wave form modeling, we estimate values of the linear dimension  $L$  of a source with constant fracture velocity  $v_r$ . The procedure followed is to minimize the misfit between the observed and synthetic

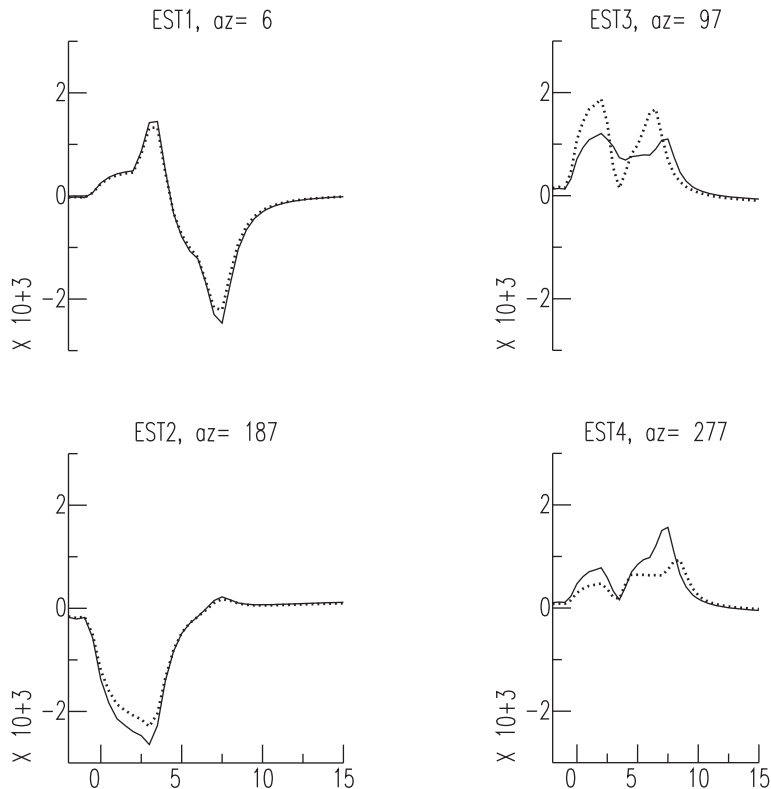


**Figure 8.5.** Theoretical P wave forms from an extended source propagating observed at four azimuths (dotted lines) and from a point source (continuous lines). Stations EST1 and EST2 at  $90^\circ$  from the propagation direction do not show any directivity effect; EST3 is a directivity station (shorter pulse) and EST4 an anti-directivity station (longer pulse).

wave forms by changing the values of  $L$  and  $v_r$ . Observations from a sufficient number of different stations distributed around the source must be used, so that the directivity effects are clearly observed. Directivity effects are only observed for sufficiently large earthquakes, that is those for which  $M_W > 6$ .

## 8.5 Apparent source time function

As discussed above, directivity has a direct influence on the apparent source time function (ASTF) observed at a station this effect modifies the shape of the ASFT at different azimuths. Thus, stations with azimuths perpendicular to the fault are not affected by directivity, but those with azimuths along the direction of propagation of the rupture (the directivity stations) have shorter ASTFs than stations in the opposite direction (the anti-directivity stations) (see equation (8.15) and Fig. 7.11). This effect can be observed by comparing the ASTFs at different stations (Fig. 6.9). From these effects on the ASTF we can obtain estimates of the typical source dimension  $L$  and rupture velocity  $v_r$ . If we assume a constant  $v_r$  then, as mentioned earlier, we can invert both  $L$  and  $v_r$  because we have

**Table 8.1**

```

qdp off
title "stack of 9 BB records pP"
sss
addstack file1
addstack file2
addstack file3
addstack file4
addstack file5
addstack file6
addstack file7
addstack file8
addstack file9
tw -5 15
sumstack

```

$n$  ( $n > 2$ ) equations and two unknowns. But if the rupture velocity varies then it is impossible to solve the system (we have  $n$  equations and  $n + 1$  unknowns).

A useful way to detect directivity effects in body wave signals is by using *stack methodology*. For intermediate-depth and deep earthquakes this is a very effective method (Houston *et al.*, 1998). The idea is based on the use of teleseismic P wave data (epicentral distances between  $30^\circ$  and  $90^\circ$ ) recorded at arrays of stations located at different azimuths with respect to the source (avoiding the azimuth normal to the fracture). We compute the stack (sum) of all the available records in each array. The stack reduces the noise produced by incoherent reverberations at stations. The procedure is: first remove the instrument response at each station to obtain the ground motion  $u(t)$ ; discard noisy stations; carefully line up the P waves at the first break or at a prominent sharp feature early in the waveform; then sum up the records. We can normalize and filter them if necessary. As an example of this method, in Table 8.1 we present an SAC macro designed to perform the stacking. The result is given in Fig. 8.6a.

The *sss* command indicates that we start the stack signal processing. The *addstack* command adds a new file (*file1*) to the stack file list. The *tw* command sets the time window limits for subsequent stack summations (for other details see Chapter 2). The directivity effect is observed in the stack for directivity stations (Fig. 8.6b, right), with shorter time duration, and for the stack of anti-directivity stations, with longer time duration (Fig. 8.6b, left). A comparison between the results for the two stacks shows the effect of the direction of propagation.

## 8.6. Far-field inversion of the slip distribution on fault plane

A widely used method to study a source mechanism having finite dimensions is to determine the *slip distribution* on the fault plane from the inversion of body wave forms. The number of unknown variables of an extended model begins with those for a point

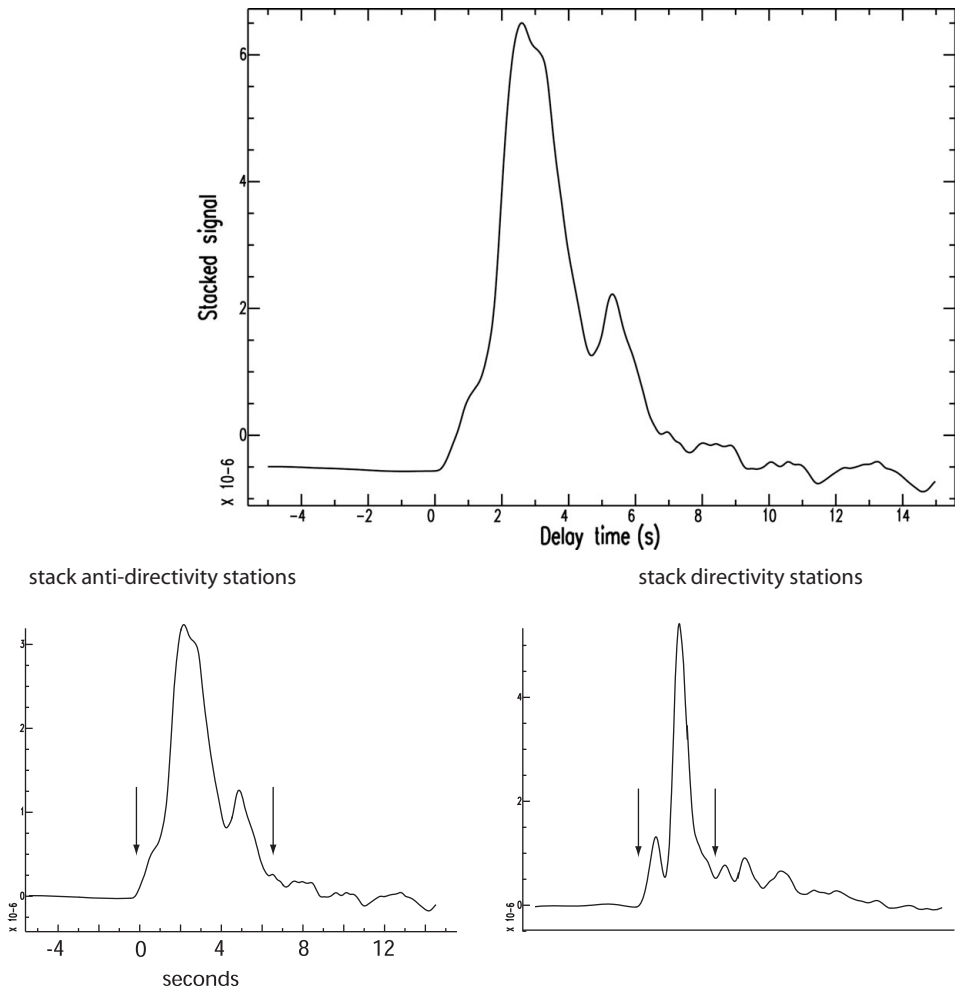


**Figure 8.6.** (a) Apparent source time function (ASTF) obtained from a stack of nine stations. (b) On the left, stacks of anti-directivity stations (wide pulse) and, on the right, stacks of directivity stations (narrow pulse).

source: the fault-plane orientation ( $\phi, \delta, \lambda$ ), the depth  $h$ , the scalar seismic moment  $M_0$  and the source time function  $f(t)$ ; to these we must add the dimensions  $L$  and  $W$ , the rupture velocity  $v_r$  and the distribution of the slip rate  $\Delta\dot{u}$  over the fault plane. Among the most frequently used methods to invert far-field waves are those developed by Kikuchi and Kanamori (1982, 1991), Hartzell and Heaton (1983), Archuleta (1984) and Fukuyama and Irikura (1986) among others.

Body wave forms depend from the slip rate at the source. For an extended source, we can obtain the average slip as a function of time, in terms of the scalar seismic moment, the source area and the rigidity of the material  $m$ . To obtain the slip and slip-rate distributions on a finite rectangular fault plane we divided it into subfaults with area  $A_j$  and assume that the slip is non-uniform and variable in time and space (Fig. 8.7). As a consequence the slip rate at the  $j$ th subfault may be written as

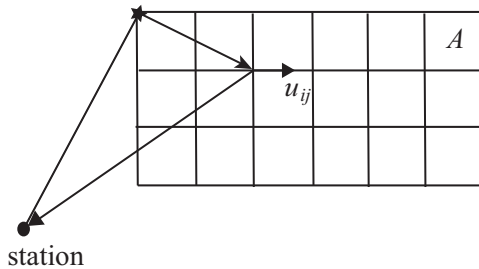


**Figure 8.7.** Division of fault plane into cells for the determination of the distribution of the slip  $u_{ij}$ , showing the location of the station.

$$\Delta i_j(t) = \frac{\dot{M}_j(t)}{\mu A_j} \quad (8.18)$$

where  $\dot{M}_j(t)$  is the scalar seismic moment rate of the  $j$ th subfault. A similar relation can be written for  $\Delta u_j$  in terms of  $M_j$ .

As we saw in section 6.4, the moment rate at each subfault can be written in terms of the source time function  $f(t)$  as

$$\dot{M}_j(t) = M_j f_j(t) \quad (8.19)$$

with the implicit requirement that

$$\int_0^{\tau_r} f(t) dt = 1 \quad (8.20)$$

where  $\tau_r$  is the rise time of the source time function, i.e. for  $t > \tau_r$  the source time function  $f$  is zero.

For an extended source we assume that the slip and moment on the fault are variable in time and space (Fig. 8.7). The standard procedure to model extended sources is to assume a finite rectangular fault plane divided into a set of contiguous subfaults of area  $A_j$  and with moment  $M_j$  and source time function  $f_j(t)$ . The slip rate at each subfault is

$$\Delta i_j(t) = \frac{M_j f_j(t)}{\mu A_j} \quad (8.21)$$

where  $M_j$  is the scalar seismic moment of the  $j$ th subfault and  $f_j(t)$  is the corresponding source time function (Chen and Xu, 2000). The seismic wave radiated at the far field by a moment-tensor point source was discussed in section 6.4. For shallow far-field sources we have to include not just the direct P wave emitted by the source but also the pP and sP waves reflected by the free surface (see (6.17)–(6.19)). For extended sources, for each of the phases P, pP and sP the ASTF observed at the  $i$ th station may be written, cf. (8.16), as the sum of the contributions from each subfault:

$$f_i(t) = \sum_{j=1}^N m_j f_j(\tau_r, t - \tau_{ij}) \quad (8.22)$$

where  $m_j = M_j/M_0$  is the scalar seismic moment at the  $j$ th subfault normalized by the total scalar seismic moment  $M_0$ . The term  $\tau_{ij}$  is the time delay observed at the station  $i$  between the arrival time of the wave from the origin and the arrival time of the signal from subfault  $j$ .

These equations, or some variation on them, are used to generate synthetic wave forms  $u_s(t)$ , which are then compared with the observations  $u_0(t)$  using the standard L2 norm (also known as the misfit),

$$\chi_2 = \sum_i \int_0^{\infty} [u_{0i}(t) - u_{si}(t)]^2 dt \quad (8.23)$$

where we sum over all time in each seismogram and over all the available stations  $i$ . We begin by assuming some initial values of  $L$  and  $W$  according to the earthquake magnitude. The rectangular fault is divided into a number  $N \times M$  of subfaults of equal area  $A$ , so that  $(N \times M)A = LW$  (Fig. 8.7). The displacement at a station is given by the sum of the contributions of each elementary subfault.

For the motion on the fault to stop at its border a boundary condition must be added forcing  $\Delta\dot{u}$  to diminish to zero as it approaches the limits of the fault. The locations where higher values of  $\Delta\dot{u}$  are found correspond to the presence of *asperities* in the inhomogeneous dynamic model (see section 11.6 below).

For a shear fracture, if the rake of the slip direction changes over a fault plane with fixed orientation, we let the rake angle  $\lambda$  vary together with the slip amplitude. To avoid inconsistencies in the direction of slip over the fault surface,  $\lambda$  is only allowed to change over a certain range around a given initial value.

In theory, we could retrieve all the parameters involved in the slip distribution over the fault plane from the inversion of body waves, but in practice some parameters are fixed and the inversion is carried out only for a few of them. For example, information about the dimensions of the fault must be assumed from other considerations. Normally, in a first step we obtain the fault-plane orientation and depth using a point source model. Fixing these values, we perform an inversion for the distribution of the slip rate on an extended source. From this inversion we obtain the moment rate and source dimensions. One of the most robust methods for this type of inversion is the Kikuchi and Kanamori algorithm (<http://www.eri.u-tokyo.ac.jp/ETAL/KIKUCHI>) for body waves at teleseismic distances ( $30^\circ$ – $90^\circ$ ). The amount of slip and the slip time history are determined at each grid point, using a fixed rupture velocity, and from these values we obtain synthetic seismograms. The solution is found by minimizing the fit between synthetic and observed data using (8.23). Normally, different sized grids, rupture velocities, time of the initiation or onset of rupture etc., are tested. It is important to take into account that the grid size and rise time are related to the rupture velocity. For example, if we use a grid that is  $30 \times 30 \text{ km}^2$  and a rupture velocity equal to  $3 \text{ km/s}$ , the maximum rise time is  $10 \text{ s}$ . It is important also to note that the grid size and rise time will depend on the magnitude of the earthquake. For a  $M_W = 6$  earthquake we can use a  $5 \times 5 \text{ km}^2$  grid and a rise time equal to  $1 \text{ s}$ , but for larger shocks we must increase these values. When the orientation of the fault is not known from the tectonic context, we can check which of the two possible source mechanism fault planes produces a slip distribution that has the minimum misfit between the synthetic and observed seismograms.

As an example we present the solution for the  $M_W = 6.6$  earthquake that occurred near the city of Concepcion in Chile on 5 March 2010. (This was an aftershock of the great  $M_W = 8.8$  Maule earthquake of 27 February 2010.) We used the 22 P and 13 SH wave forms (Fig. 8.8) and inverted them using the Kikuchi and Kanamori algorithm. We used a  $32 \times 32 \text{ km}^2$  fault divided into 16 subfaults of  $8 \times 8 \text{ km}^2$ . The rupture velocity was taken to be 3 km/s and the scalar seismic moment  $1.1 \times 10^{19} \text{ N m}$ .

The slip distribution is quite simple, with a single maximum. The maximum slip is 0.54 m and is located at the center of the fault, with the horizontal N–S plane as the rupture plane. To arrive at this solution several grid sizes, nucleation points and rupture velocities were tested. Finally we chose the solution that corresponds to the minimum misfit (0.2018) between the synthetic and observed seismograms.

Earthquakes may have more complex distributions than the one shown in Fig. 8.8, with several maxima of the slip over the fault plane. An example is shown in Fig. 8.9 for the  $M_W = 8.8$  Maule megathrust earthquake in Chile of 27 February 2010. In this case the overall fault dimensions were  $500 \times 90 \text{ km}^2$  and the grid size was  $45 \times 45 \text{ km}^2$ . These are substantially larger than those used to model the aftershock of 5 March 2012 shown in Fig. 8.8, because of the much larger magnitude of the Maule earthquake. The time window used in the inversion was 180 s as against the 40 s window used for the 5 March 2010 aftershock. The misfit is 0.3487, larger than in Fig. 8.8 owing to the use of a longer time window. We obtained a bilateral rupture over a nearly horizontal plane oriented roughly in the N–S direction. We observed that the rupture starts at a point at the center of the plane and then propagates towards the north and south. The distribution of slip shows that the rupture consisted of two patches, the larger located to the north with a maximum slip of 13.45 m. The slip distribution over the fault plane may be interpreted in terms of the presence of two asperities (Chapter 11). A slip distribution with several asperities, as in Fig. 8.9, may be interpreted as a *complex rupture*.

The time distribution of the slip rate as it progresses over the fault plane is known as the *slip-rate history*. An example for the Maule 2010 earthquake in Chile, given in Fig. 8.10, was obtained from the slip distribution over the rupture plane shown in Fig. 8.9. We divided the rupture time duration into intervals of 25 s. At the top we show the beginning of the rupture; the star corresponds to the nucleation point. After 25 s the rupture propagation is bilateral, with rupture fronts moving in the north and south directions. Rupture continues in both directions for a total time of about 75 s. After this time, propagation to the south practically stops, but it continues to the north. It stops finally 150 s after the beginning of rupture. The maximum slip occurs between 50–100 s.

It is important to realize that all these methods have some limitations and ambiguities. Sometimes we can find different slip distributions that give similar misfits (8.23) and then we must use other information, such as geodetic slip vectors, geological evidences etc., to choose the rupture plane.

For regional distances there are methods, such as *Kiwi* (Kinematic Waveform Inversion) (Heimann, 2011, <http://kinherd.org>), which provide synthetic seismograms for finite source models and perform moment-tensor kinematic extended source inversion. The inversion is typically carried out following a multi-step approach (Cesca *et al.*, 2010) in which both amplitude spectra and displacement wave forms are fitted. Amplitude spectra inversion is

## CHILE 05-03-10

$M_0 = 0.110E+20 \text{ N m}$ ,  $M_W = 6.6$

$h = 18.0 \text{ km}$ , var. = 0.2018, max. slip = 0.54 m

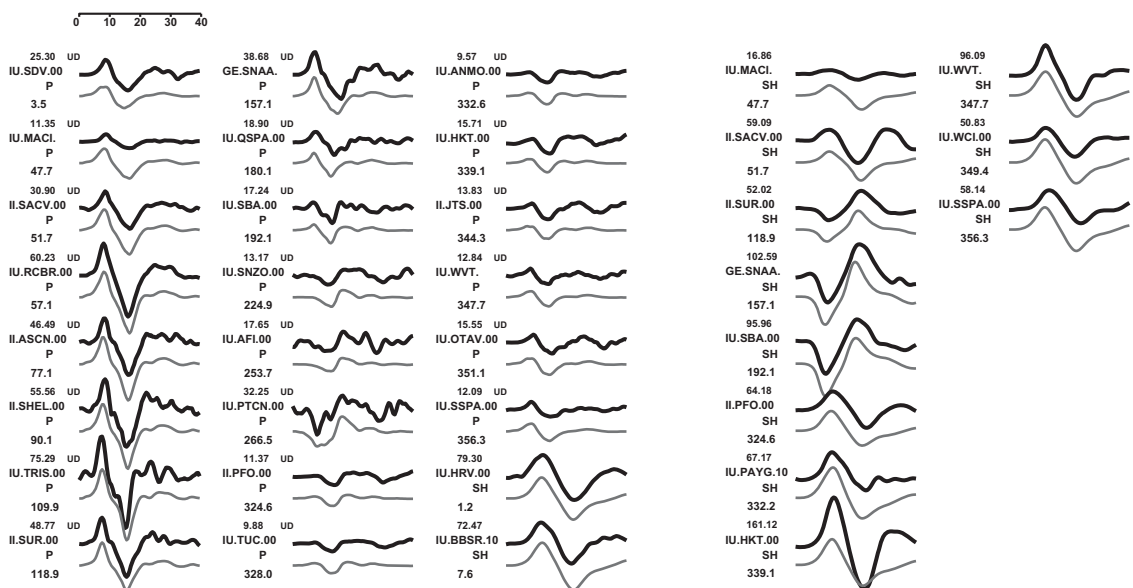
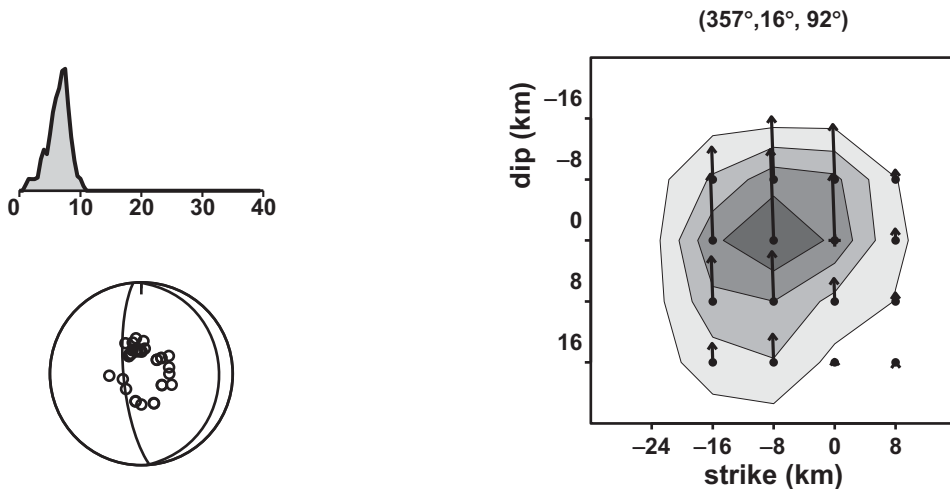


**Figure 8.8.** Determination of the distribution of slip over the fault plane for the Chile earthquake of 5 March 2010,  $M_W = 6.6$  with a single asperity. Top left, source time function and fault-plane solution; top right, the distribution of slip over the fault plane. Bottom, the observed (boldface) and synthetic (lightface) P and SH wave forms.

## CHILE 2010 Main shock

$$M_0 = 0.176 \times 10^{23} \text{ N m}, \quad M_W = 8.8$$

$$h = 25.0 \text{ km}, \quad \text{var.} = 0.3487, \quad \text{max. slip} = 13.45 \text{ m}$$

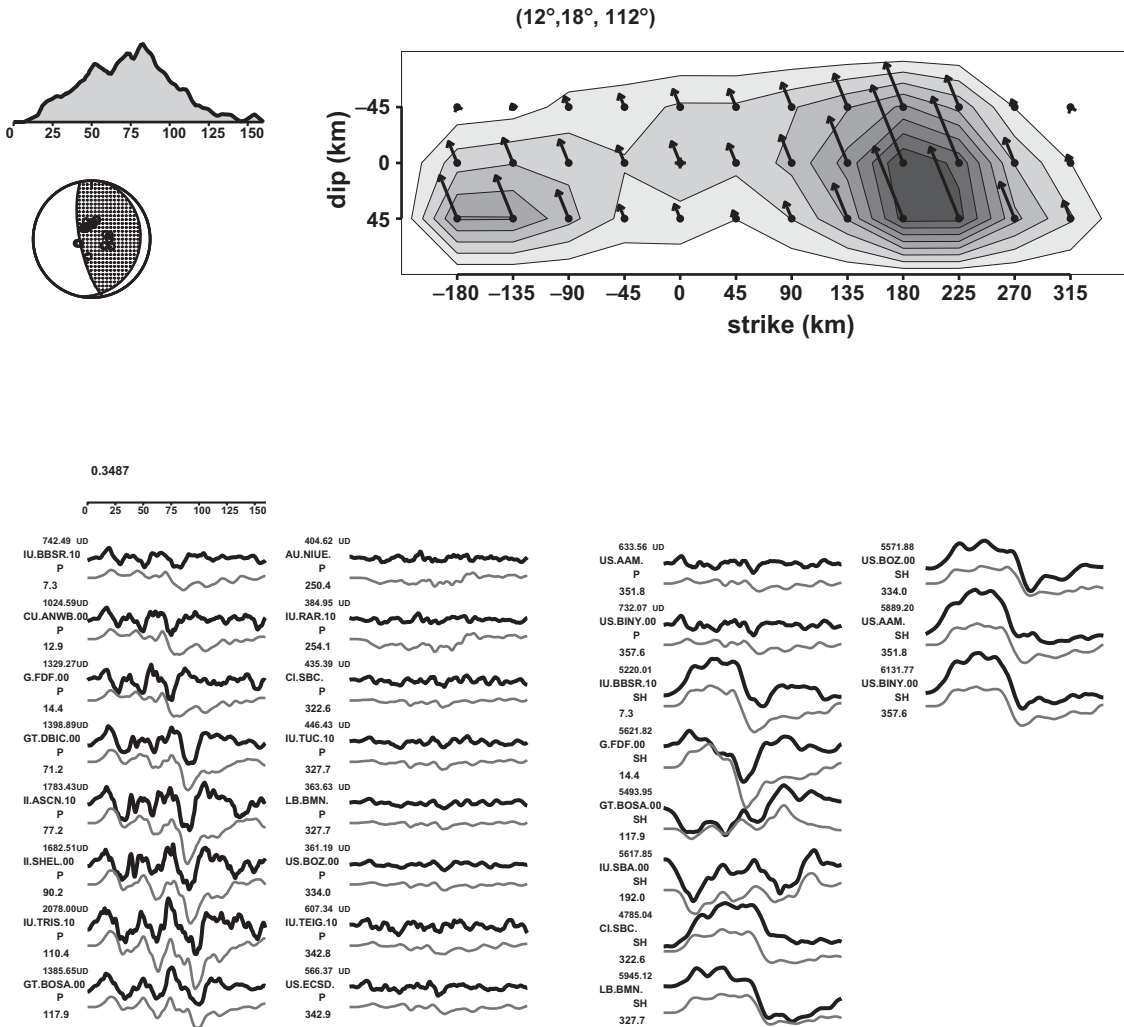


**Figure 8.9.** Determination of the distribution of slip over the fault plane for the Chile earthquake of 27 February 2010,  $M_W = 8.8$  (the main shock), which was a complex rupture with two asperities. Top left, the source time function and fault plane solution; top right, the distribution of slip over the fault plane. Bottom, the observed (boldface) and synthetic (lightface) P and SH wave forms.

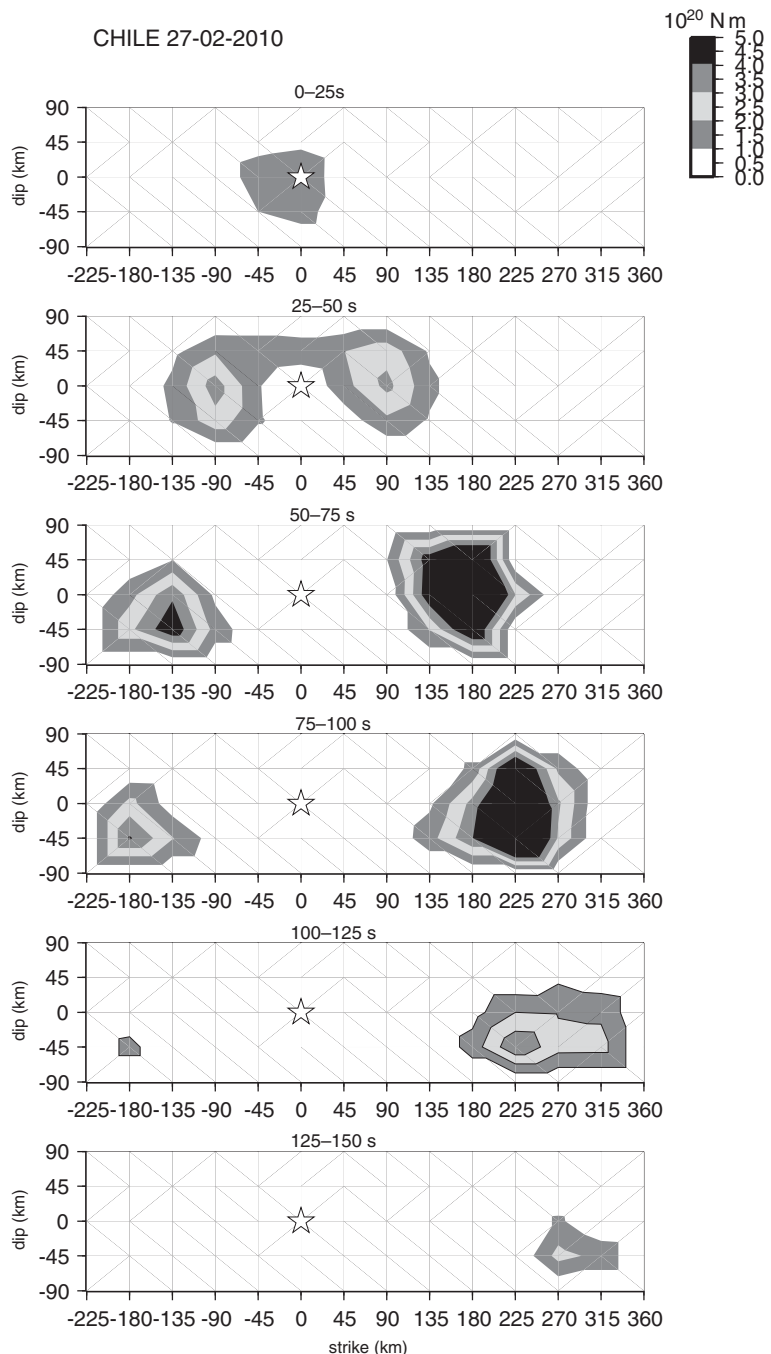


**Figure 8.10.** Time history for the Chile earthquake main shock (27 February 2010) obtained from the slip distribution in Fig. 8.9.

typically used at a first step, because of its better performance when a simplified Earth velocity model is assumed, and also to handle trace misalignment. Since amplitude spectra inversion alone cannot resolve the focal mechanism polarity, this is fixed at a later stage, by using an analysis of the wave form fit in the time domain. Higher frequencies are used at a later stage to invert for simplified finite source models, in order to derive important source parameters such as the rupture size, rupture velocity and main rupture direction (directivity). In Fig. 8.11 we show results corresponding to the application of this method to the L'Aquila main shock. At top left is the fault-plane solution used for the orientation of the rupture plane on the inversion ( $127^\circ$ ,  $63^\circ$ ,  $-101^\circ$ ); at top right the dimensions of the source as a semicircular fault of 20 km radius. Below this, the relative misfits for the radius and rupture velocity are shown. At the bottom we show the synthetic and observed seismograms for the vertical (left) and transverse (right) components.

There are other methods, such as those based on the use of a pre-calculated catalogue of the theoretical Green's functions for a region (Dreger and Helmberger, 1993; Dreger, 1994). These methods are based on non-negative least squares inversion for finite source parameters, given a source mechanism. Smoothing and moment minimization constraints are applied. All these methods provide the slip distribution, average slip and fault dimensions and resolve the fault-plane ambiguity.

## 8.7. Kinematic inversion of the near-field waves

---

An important method for the study of seismic sources and their rupture processes is kinematic finite source inversion using *near-field records* (section 3.5.1). This method uses accelerograms recorded in the near field to determine the distribution of slip and the rupture process of large shallow earthquakes. The main problem in the near field is to compute the accelerograms produced by an elementary fault of arbitrary orientation and position. In the previous section we saw that one can use ray theory methods, by assuming that the Earth is either homogeneous or has a smoothly varying structure. In the near field, wave propagation is affected by the strong variation of seismic wave velocities and density as a function of depth and by wave trapping in the shallow layers of the Earth. Studies of seismic waves have shown that near-field wave propagation can be modeled using a variety of techniques for frequencies lower than 1 Hz. At higher frequencies seismic waves are strongly scattered by local heterogeneities in the crust and mantle, so that modeling seismic waves, even if we knew the source, would be a formidable challenge. For this reason seismologists have limited the study of near-field records to frequencies lower than 1 Hz, with typical wavelength longer than 2 km.

In principle, modeling waves in the near field up to 1 Hz is within the reach of modern numerical methods for the simulation of seismic waves. Unfortunately the structure of the Earth is not very well known in most of the seismogenic areas of the world. For this reason simplified methods developed in the early 1980s are still very much in use. These methods assume that the Earth is a layered medium with known properties. For such a medium, usually called one dimensional, we may assume that the effect of lateral

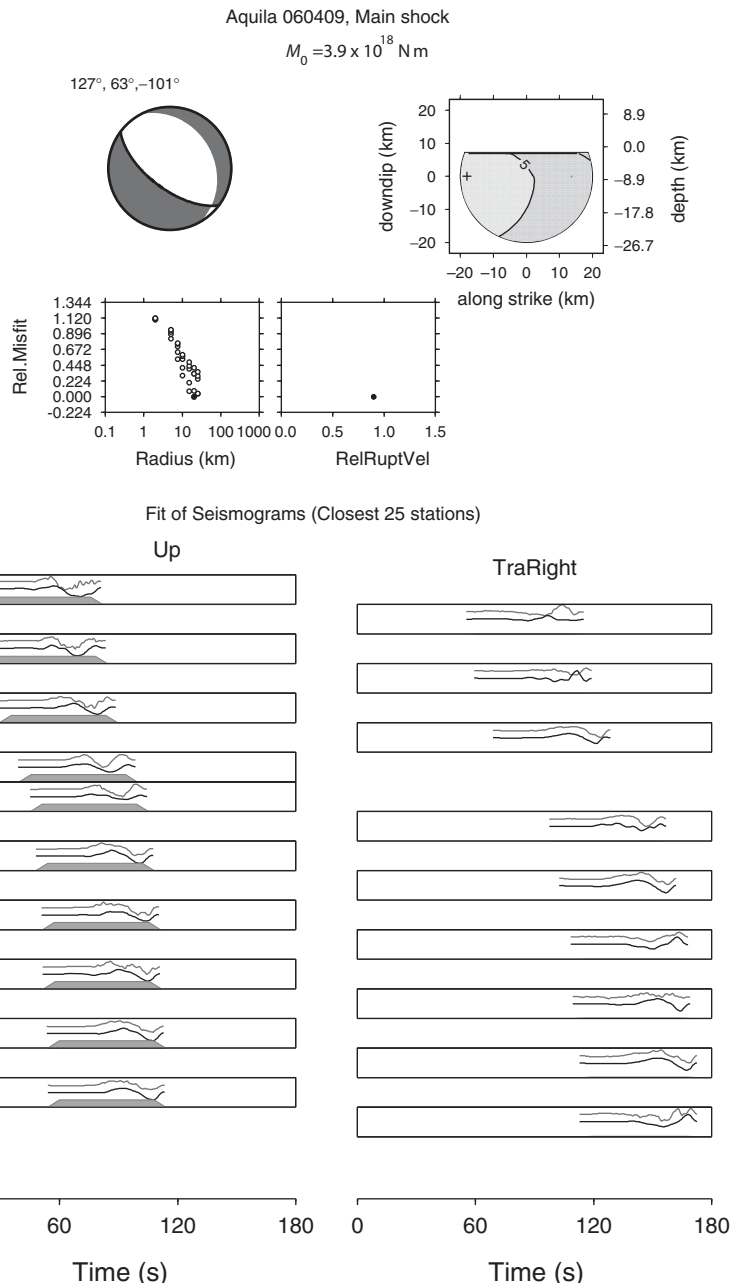


**Figure 8.11.** Source inversion from data at regional distances using KIWI tools for the Aquila, Italy earthquake of 6 April 2009. Top, the fault-plane solution, rupture area and slip amplitude distribution. Middle, relative misfit with radius of fault and rupture velocity. Bottom, observed (lightface) and synthetic (boldface) vertical and transverse components of seismograms (courtesy of S. Cesca).

variations of the seismic wave velocity and density are less important than the vertical variations. With this assumption it is simple to compute synthetic seismograms for frequencies from 0 to 1 Hz (static to 1 s period) using various techniques, which we will briefly describe.

In the simplest models, no longer in common use it is assumed that the Earth is a simple half space having constant properties. In this case we can use the expressions developed in section 7.8, including the corrections for attenuation, free surface response and the variation of radiation pattern with position on the fault. The next degree of sophistication is to use ray methods, taking into account a few well-chosen rays such as the direct waves, the waves reflected by the Moho, etc. This technique, proposed by Spudich and Frazer (1984) and by Bernard and Madariaga (1984) is fast, but with modern computers it is just as fast, and easier to compute, complete wave fields in a vertically stratified medium. There are two methods that are widely used to compute wave propagation in such media. Both use a *wave number and summation* method that works in a medium approximated by a one-dimensional vertical variation in velocity and density. Two variations of these methods are used in the simulation of global seismograms: (1) the vertical integration is performed using a numerical technique such as finite differences or finite elements; (2) the seismograms are computed using a stack of uniform layers.

Numerical integration of the frequency–wave number equations using a finite element integration of the vertical equations was proposed by Olson *et al.* (1984). This is the so-called DWFE method used by Archuleta (1984) to model the Imperial Valley earthquake of 1979. The layered stack method was introduced by Haskell and Thompson (Udías, 1999, Chapter 11) and has been the most common technique used to simulate wave propagation in the Earth for the last 50 years. Haskell’s original method, using layered matrices, is known to have problems at high frequencies; these were corrected in the 1980s by Luco and Apsel (1982) and by Kennet (1981), who proposed the use of interface matrices and simple *exponential propagators* inside the layers. This method, adapted to a spherical geometry, opened the way to the computation of large-scale synthetic seismograms. In source seismology this method was used by Bouchon (1981, 1982) to compute numerical seismograms in the frequency–wave number domain by Fourier transform inversion. Numerical inverse Fourier transforms pose a number of problems, which can be solved by deforming contours into the complex frequency plane. We will not enter into the details of this technique here; we just refer to the original papers by Bouchon (1982) and recommend the use of the software package *AXITRA* by Coutant (1990), which can compute complete seismograms from static (0 Hz) to 1 Hz and higher frequencies ([http://www.orfeus-eu.org/software/seismo\\_softwarelibrary.html](http://www.orfeus-eu.org/software/seismo_softwarelibrary.html)).

These numerical methods provide a Green function’s that gives the displacement produced at the observer by a point-like moment located at an arbitrary position in the fault (sections 3.5 and 5.1). We can write the  $\ell$ th component of the seismogram produced by each patch in the simple form

$$u_\ell(x_i, t) = \int_0^\infty G_{\ell j k}(x_i, \xi_i, t - \tau) \dot{M}_{jk}(\xi_i, \tau) d\tau \quad (8.24)$$

where  $\dot{M}_{jk}$  is the moment-rate tensor at the source position  $\xi_i$  and the observer is located at the point  $x_i$ . The moment-rate tensor can be written as the product of the moment tensor times a source time function  $f$  that contains a time delay  $\tau(\xi_i)$ :

$$\dot{M}_{jk}(t) = M_{jk}(\xi_i)f(t - \tau(\xi_i)) \quad (8.25)$$

where  $M_{jk}$  is the moment tensor of the source located at position  $\xi_i$ .

In seismic source inversions it is usually assumed that the source time function is independent of position on the source and that the time delay for the initiation of slip at a point on the fault is a known function. The most frequent assumption is that the rupture velocity across the fault is constant or has few discrete jumps. Once  $\tau(\xi_i)$  is fixed, the problem of determining the moment tensor  $M_{jk}$  as a function of position on the fault is linear. In more advanced inversion methods it is possible to use a *multi-window* method, where the source time function is split into several windows of finite duration. Inversion of the amplitude of the source time function is carried out for each window.

In order to simplify the expressions that follow let us assume that the fault is planar, so that the moment can be written as a constant normalized tensor  $m_{jk}$  times the scalar seismic moment. Then (8.25) becomes

$$\dot{M}_{jk}(t) = m_{jk}M_0(\xi_i)f(t - \tau(\xi_i)) \quad (8.26)$$

and (8.24) is reduced to

$$u_\ell(x_i, t) = g_\ell(x_i, \xi_i, t - \tau(\xi_i))M_0(\xi_i) \quad (8.27)$$

where

$$g_\ell(x_i, \xi_i, t) = \int_0^\infty G_{\ell j k}(x_i, \xi_i, t - \tau) m_{jk}f(\tau) d\tau \quad (8.28)$$

is a Green's function and  $f(t)$  is a finite source time function. Often  $g_\ell$  contains also filters to eliminate high frequencies and/or numerical noise. In the following we assume that  $g_\ell$  has been computed numerically or that we have a simple analytical approximation for it.

Let us finally assume that we divide the fault into a fixed set of *rectangular patches* as shown in Fig. 8.7. Let the total number of patches be  $M$ . The seismograms observed at a position  $x_i$  are digitalized as a set of  $k$  points, usually a power of 2, so that, summing the contributions of all patches, we can write (8.27) as

$$u_\ell(x_i, t_k) = \sum_{j=1}^M g_\ell(x_i, \xi_j, t_k - \tau(\xi_j))M_0(\xi_j) \quad (8.29)$$

The inverse problem consists in determining the  $M$  values of the moment at each patch  $i$  from the data, the  $n$  digital seismograms  $u(x_i, t_k)$ . Thus we have a total of  $N = nk$  data points. This is clearly a linear inverse problem with  $N$  data points and  $M$  unknowns. Usually the number of data points  $N$  is much larger than the number of slip patches  $M$ . Thus the problem is apparently overdetermined, but in reality the points in the seismograms are not independent and the seismograms themselves are not always independent of each other. For this reason, solving the inverse problem requires using the modern inverse

techniques already discussed in section 6.6 for moment tensor inversion. Let us first proceed to solve (8.29) by standard least squares inversion methods. Since the number of data points is larger than the number of unknowns we can solve that problem by least squares using the L2 norm defined in (8.23). In order to write the problem at hand in the standard notation of linearized inverse problems we introduce the following notation. Let  $\mathbf{d}$  be a vector of length  $N$  that contains all the data points at the  $n$  stations and the  $k$  digital points. Let  $\mathbf{m}$  be a vector of length  $M$  that contains the moments  $M_0$  at the  $M$  patches. Then (8.29) can be written as in section 6.6 in the standard form

$$\mathbf{u} = \mathbf{G}\mathbf{m} \quad (8.30)$$

where  $\mathbf{u}$  are the observations and the  $N \times M$  matrix  $\mathbf{G}$  contains the Green's functions  $g_{\ell}$  defined in (8.28). Using the norm (8.23) between the observed and synthetic seismograms we find that the least squares solution of (8.30) is

$$\mathbf{m} = (\mathbf{G}^T \mathbf{G})^{-1} \mathbf{G}^T \mathbf{d} \quad (8.31)$$

Equation (8.31) provides a solution to the problem of the inversion of near-field seismograms. Unfortunately, as we saw in section 6.6, this solution can almost never be computed because the matrix  $\mathbf{G}^T \mathbf{G}$  is almost always ill conditioned, that is, its inverse cannot be computed in a computer with finite digital precision. The reason is that this matrix invariably contains a set of very small eigenvalues, which produce large errors when (8.31) is inverted. The inverse problem for finite source inversion has a particularity that can help to stabilize the solution. Since we have assumed that the orientation of slip on the fault does not vary from patch to patch, the solutions of (8.31) that are of interest to us are such that the moment tensors for each patch are all positive. Obtaining a least squares solution with *positivity constraints* is a standard problem in linear algebra, for which standard routines exist, such as the so-called NNLS method (non-negative least squares). Generally, the positivity constraint regularizes the inversion at long wavelengths but it does not suppress the high-frequency noise due to poorly controlled small eigenvalues.

As mentioned above, the least squares problem of near-field inversion is almost always ill posed, and the various strategies used to obtain a solution all introduce a large number of artifacts that may or may not reflect how the moments of the patches that make up the source actually differ from each other. This is an important concern for the interpretation and comparison of the various approaches to inversion. The approach we have just described is based on the standard methods used to solve *linearized inverse problems*, which we strongly favor. There are other techniques used in geophysics that have been tested in inversion, for instance the use of criteria other than the least squares criterion leading to (8.31). Some authors have used other norms to compare synthetic and observed seismograms; some are norms in the mathematical sense and others, based on so-called *semblance operators*, are norms only in the neighborhood of the solution. Yet other authors propose global inversion methods, so that the source is divided not into rectangles but into more general shapes (circles, ellipses) which may overlap in space. We will not discuss those approaches because they are still in the development stages. The conclusion is that near-field inversion is a powerful approach to obtain elaborate kinematic models of the source but, like many other geophysical inverse problems, it does not have a *unique*

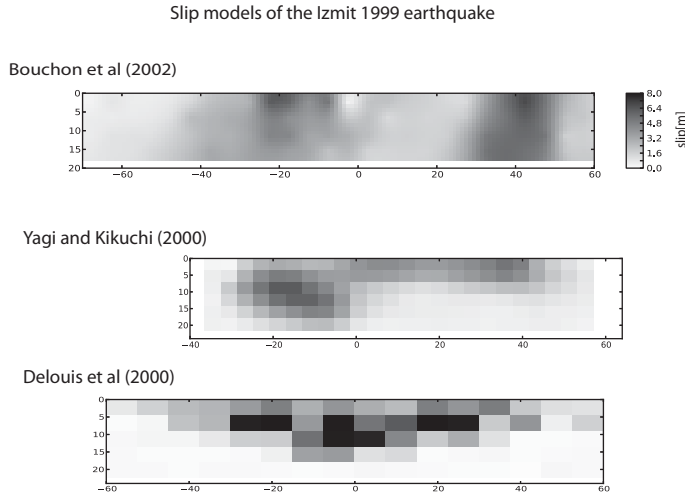


**Figure 8.12.** Slip distribution obtained for the Izmit earthquake 1999 using different types of data. From top to bottom: strong-motion data, far- and near-field seismic data and far-field and INSAR data.

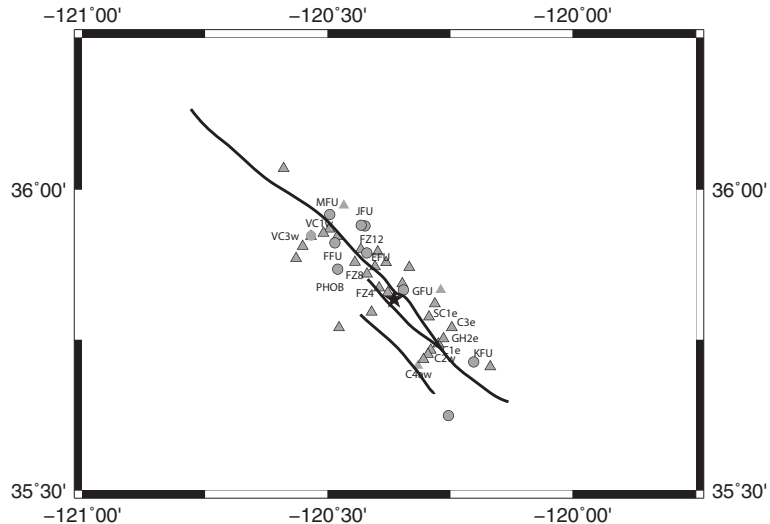


**Figure 8.13.** Distribution of strong motion stations (triangles analogical, circles digital) available for the Parkfield earthquake (28 September 2004). The star is the epicenter of the earthquake. Main faults are shown with black lines.

*solution*. Thus additional conditions have to be imposed, leading to possible confusion because many earthquakes have *multiple sources*. As an example, we show in Fig. 8.12 the solutions obtained for the Izmit earthquakes of 1999 by different authors using different types of data. These include, at the top, the far-field and InSAR data of Delouis *et al.* (2000), in the middle, the far- and near-field seismic data of Yagi *et al.* (2000) and, at the bottom, the strong motion data of Bouchon *et al.* (2002). It is clear that only the central patch of this event is well determined by inversion; to what extent the other patches are

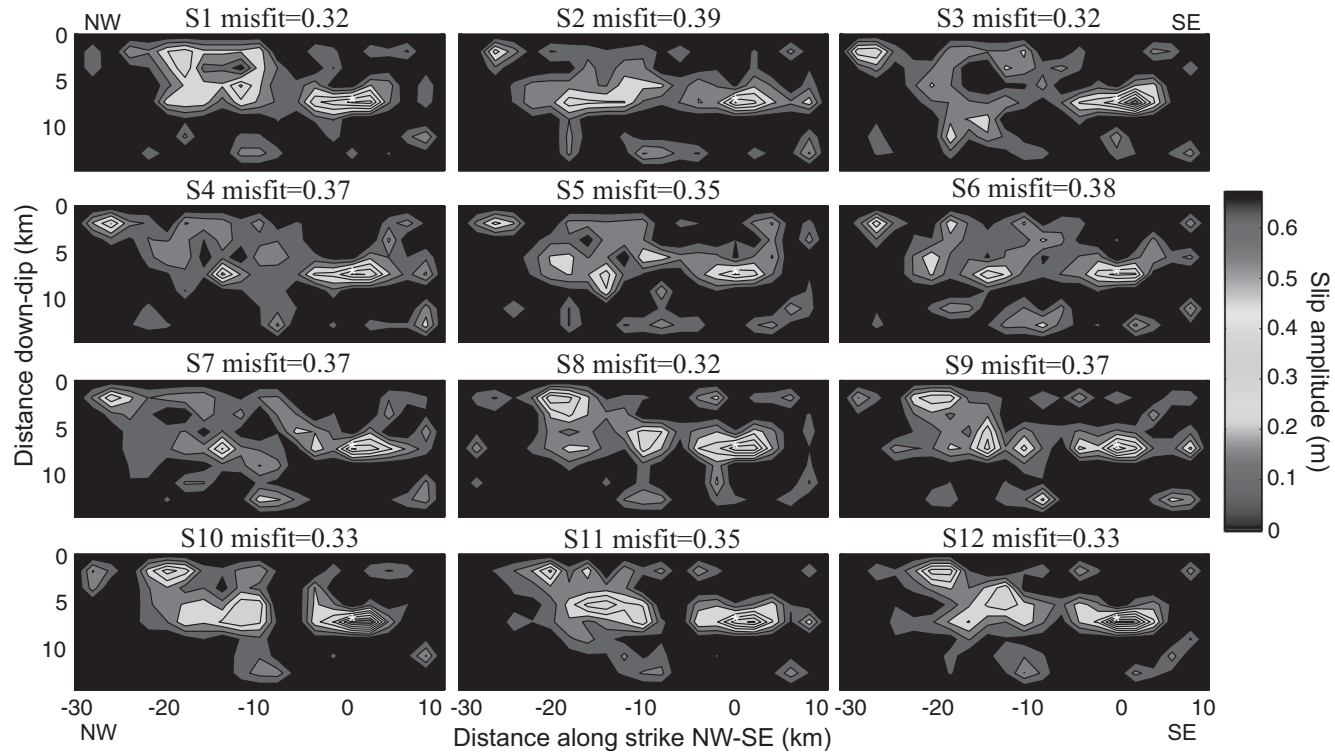


**Figure 8.14.** Slip amplitude distribution on the fault obtained by Custodio *et al.* (2005) for the Parkfield earthquake (28 September 2004) from the kinematic inversion of the strong motion data. The goodness of the fit is indicated by the values printed after the model name.

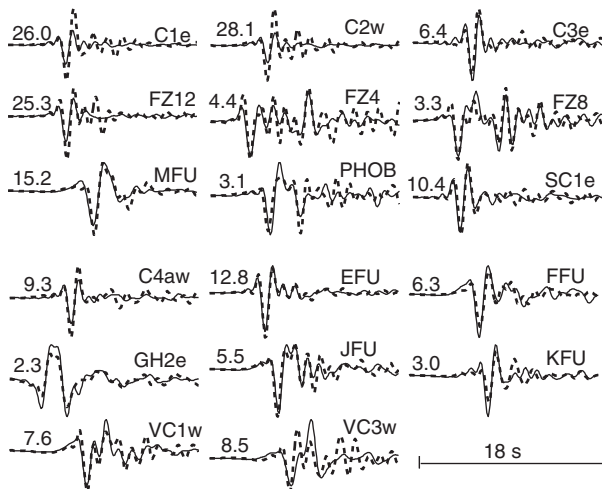


**Figure 8.15.** Synthetic (dashed line) and observed (continuous line) seismograms obtained at the stations shown in Figure 8.13. The slip distribution used to generate the synthetics is that of model S1 in figure 8.14 (modified from Custodio *et al.*, 2005).

needed depends on the weighting of the different data sets in the inversion and on the smoothing constraints used in the inversion.

Finally, an example is presented that is based on one of the best-studied earthquakes, the Parkfield earthquake of 28 September 2004, which was recorded by a set of digital and analogical accelerograms. Unfortunately not all the records had a time trace, a common situation until recently; many accelerograms used for the study of strong motion in earthquake engineering used not to continuously record a time trace synchronized by GPS or by an internet connection. In those cases the accelerograms, once digitized, had to be given a reference time by some cross-correlation technique with the stations that had time traces. This was a difficult procedure because the records had to be filtered before cross correlation. The accelerograms were inverted by Custodio *et al.* (2005), who used a total of 43 records in the inversion. These stations were divided into a series of data sets, some of which were used directly for the inversion; others were used to test the results of the inversion. In Fig. 8.13 we show a subset of the stations used to invert the slip distribution. The results of the inversion, the slip distributions on the fault, are shown in Fig. 8.14; slip results obtained from 12 different sets of near-field displacement records are shown. It can be seen that some robust common features emerge from this study but that, depending on the particular set of stations used in the inversion, there remain significant differences in the details of the resulting slip distributions. The fit of the synthetics to the observed strong motion records is shown in Fig. 8.15. Both the observed and synthetic records were filtered in the frequency band from 0.16 to 1 Hz. This is a relatively narrow band that could have been extended to lower frequencies, but then not all the data could have been used.

The inversions reveal that the slip amplitude was less than 0.65 m and define two principal areas of slip, one located close to the hypocenter of the event and another located 10 to 20 km northwest of the hypocenter, at a depth between 2 and 8 km.

## 9.1. Kinematic and dynamic models

Kinematic models for the source of earthquakes, the type of model that we have considered up to this point, describe the time-dependent distribution of the slip  $\Delta u_i(t)$  on a fault and are a simplified representation of the real fracture process. In kinematic models the rupture propagates at a constant or variable speed and is made to stop at the fault limits. A number of arbitrary factors are introduced into these models, some of which lead to physical inconsistencies at, for example, the borders of the fault. In spite of these limitations, kinematic models provide essential information about the seismic source, such as the fault orientation, source dimensions and slip distribution on the fault plane. However, the physical occurrence of an earthquake provides a *dynamic problem*: the slip on the fault has to be considered as a consequence of the stress conditions and the strength of the material in the focal region. Dynamic models of the generation of earthquakes take into consideration these conditions and are based on the theory of the generation and propagation of fractures or *cracks* in stressed media. From this point of view, the mechanism of tectonic earthquakes may be represented by a shear fracture produced when the stress acting overcomes the strength of the material and/or the friction between the two sides of a preexisting fault. A fracture initiates at a point of the fault where the stress acting on the fault plane exceeds a critical value, then it propagates with a certain rupture velocity and finally stops when the mechanical conditions impede its further propagation. A complete *dynamic model* must, then, include the whole fracture process, that is, its initiation or nucleation, propagation and arrest, and must be derived from the stress conditions and the properties of the material in the focal region. The two determining factors are the stresses acting on the focal region due to tectonic processes derived from the motion of lithospheric plates and the mechanical properties of the rocks in the region. Since seismic fractures generally take place on preexisting faults, important factors are the conditions between the two sides of the fault, mainly friction.

Among the first studies of fracture dynamics applied to earthquakes sources were those of Eshelby (1957), Keylis-Borok (1959), Kostrov (1964, 1966), Burridge (1969), Freund (1972b) and Madariaga (1976). These studies were based on the work on fractures in crystals and metals published between 1920 and 1950 by A. A. Griffith, G. R. Irwin and A. T. Starr. In this chapter we will consider some simple dynamic problems.

## 9.2. Static problem

The fracture of materials involves processes at the molecular, crystal and rock level, but important information can be obtained by considering an ideal continuous elastic body. As a first step to understanding the relation between the applied stress and the slip on a fault we consider the *static problem*, that is, the situation after fracture has taken place. Let us consider the two-dimensional problem of a shear crack located on the plane  $x_3 = 0$  that moves along a strip of infinite length in the  $x_2$  direction and width  $2a$  in the  $x_1$  direction. We solve for the shear displacements  $u_2$  inside the crack and the shear stress  $\tau_{32}$  outside, at points along the  $x_1$  axis (Fig. 9.1) (Knopoff, 1958; Aki and Richards 1980, p. 856). Let the shear stress acting on the medium before fracture be uniform and equal to  $\sigma_0$  and let the stress inside the fault ( $|x_1| < a$ ) be zero after faulting has taken place. Then the *static drop of stress* inside the fault is  $\Delta\sigma = \sigma_0$ . In the absence of body forces the equation of motion for the static case is, from (3.5),

$$\frac{\partial \tau_{ij}}{\partial x_j} = 0 \quad (9.1)$$

with boundary conditions  $\tau_{32} = \sigma_0$  for  $|x_1| \gg a$  and  $\tau_{32} = 0$  for  $|x_1| < a$ . We assume that linear elasticity applies everywhere outside the fault; then equation (9.1) can be written in terms of the shear displacements  $(0, u(x_1, x_3), 0)$ :

$$\frac{\partial^2 u}{\partial x_1^2} + \frac{\partial^2 u}{\partial x_3^2} = 0 \quad (9.2)$$

Following Knopoff (1958) we introduce the complex variable  $z = x_1 + ix_3$  on the  $(x_1, x_3)$  plane. Then the solution of the Laplace equation (9.2) is the real or imaginary part of a complex analytic function  $f(z)$ . Let  $u(z)$  be its imaginary part:

$$f(z) = v(z) + iu(z)$$

Since  $f(z)$  satisfies the Cauchy–Riemann conditions, it is a solution of the Laplace equation

$$\frac{\partial^2 f}{\partial x_1^2} + \frac{\partial^2 f}{\partial x_3^2} = 0 \quad (9.3)$$

For our two-dimensional *antiplane crack*, taking into account the boundary conditions, we can write down a particular solution of (9.3) of the form

$$f(z) = \frac{\sigma_0}{\mu} \sqrt{z^2 - a^2} \quad (9.4)$$

which can be easily verified to satisfy equation (9.3). Then we can write the solution for the displacement  $u(z)$  as

$$u(x_1, x_3) = \frac{\sigma_0}{\mu} \operatorname{Im} \sqrt{z^2 - a^2}$$

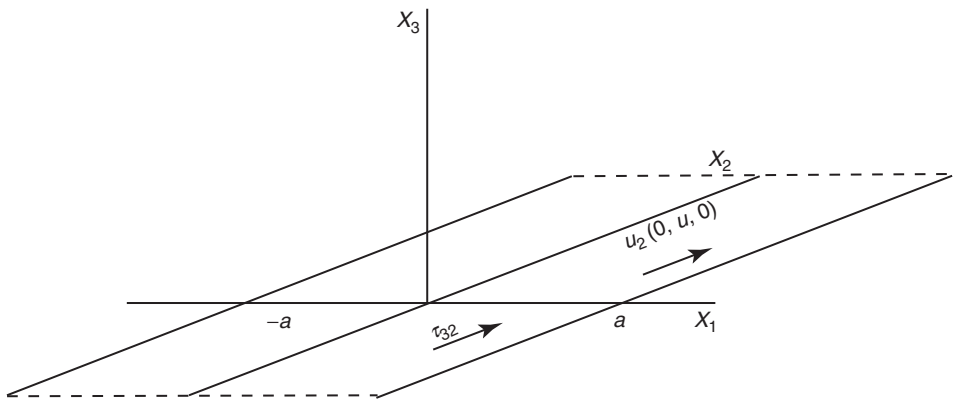


**Figure 9.1.** Shear rupture, on the plane  $(x_1, x_2)$ , of infinite length in the  $x_2$  direction and propagating in the  $x_1$  direction with slip  $u_2$  and acting stress  $\tau_{32}$ .

For points on the fault plane,  $x_3 = 0$  and  $|x_1| < a$ , we get

$$u(x_1, 0) = \frac{\sigma_0}{\mu} \sqrt{a^2 - x_1^2} \quad (9.5)$$

The shear stress is then given by

$$\tau_{32} = \mu \frac{\partial u}{\partial x_3} = \sigma_0 \operatorname{Im} \frac{iz}{\sqrt{z^2 - a^2}} = -\sigma_0 \operatorname{Re} \frac{z}{\sqrt{z^2 - a^2}}$$

For  $x_3 = 0$  and  $|x_1| > a$ , outside the crack, we obtain

$$\tau_{32}(x_1, 0) = \frac{\sigma_0 x_1}{\sqrt{x_1^2 - a^2}} \quad (9.6)$$

The displacement (9.5) has its maximum value ( $u_{\max} = a\sigma_0/\mu$ ) at the center of the crack ( $x_1 = 0$ ) and the stress becomes infinite from the outside at the edge of the crack ( $|x_1| = a$ ) (Fig. 9.2). This situation, which is not physically possible since no material can sustain an infinite stress, results from the fact that the stress drops to zero inside the fault and must increase unlimitedly outside its edge, where the material is perfectly elastic. This situation arises in perfect brittle fractures where the material is broken and free of stress inside the fault and unbroken and perfectly elastic outside its edge. We will see in later chapters how to take into account the finite mechanical resistance of materials.

### 9.3. Modes of propagating fractures

A very important aspect of fracture mechanics is how fractures propagate. As the fracture front advances the material becomes fractured; behind the fracture front the stress becomes zero for a total stress drop or has a residual value which depends on the friction conditions

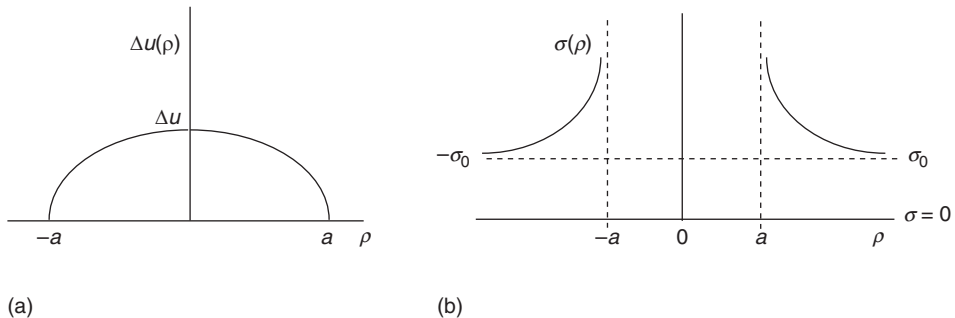


Figure 9.2.

Rupture: the static case. (a) The distribution of the slip  $\Delta u$  inside the fault. (b) The distribution of the stress outside the fault.

between the two sides of the fault. In a brittle fracture, ahead of the fracture front the material is continuous and elastic and behind the fracture front it is fractured, with a discontinuous displacement or slip. It is of interest to consider the relation between the direction of slip and that of fracture propagation. We will consider first a simple case in which a fracture propagates with a constant velocity  $v$  and the stress acting has a constant value far from the fault region. The fracture front is unlimited in the  $x_2$  direction and advances with velocity  $v$  in the  $x_1$  direction.

The relation between the direction of the slip on the fracture front and the direction of rupture propagation defines three modes of fracture. *Mode I* corresponds to tensile or tensile fracture: the slip  $\Delta \mathbf{u}$  is normal to the fracture plane and to the direction of fracture propagation. As a fracture propagates the two sides of the fault separate from each other and in this case the stress drop is always total, that is, behind the fracture front the stress is zero (Fig. 9.3a). In seismology, Mode I has little application, tectonic earthquakes are known to be produced by shear fractures: inside the Earth the confining pressure is generally so large that it allows only shear motion on faults. *Modes II* and *III* correspond to shear fracture, in which slip is contained on the fault plane. In Mode II, in-plane fracture, the direction of slip is the same as that of fracture propagation (Fig. 9.3b). In Mode III, antiplane fracture, the direction of slip is perpendicular to that of fracture propagation (Fig. 9.3c). For observations along the  $x_1$  axis, in Mode II the motion is given by  $\Delta u_1$  and we have radiation of P and SV waves, whereas in Mode III the motion is given by  $\Delta u_2$  and we have only SH waves. The situation in Mode III allows for simpler solutions for the displacement field.

## 9.4. Circular fault. Static model

Let us now consider a more realistic static problem, that of a circular fault of radius  $a$ . We consider conditions where by the slip is constrained inside the fault, i.e.  $u(\rho) = 0$  for  $\rho \geq a$ , and is a maximum at the center of the fault,  $u(0) = \Delta u_{\max}$ . The stress far from the fault

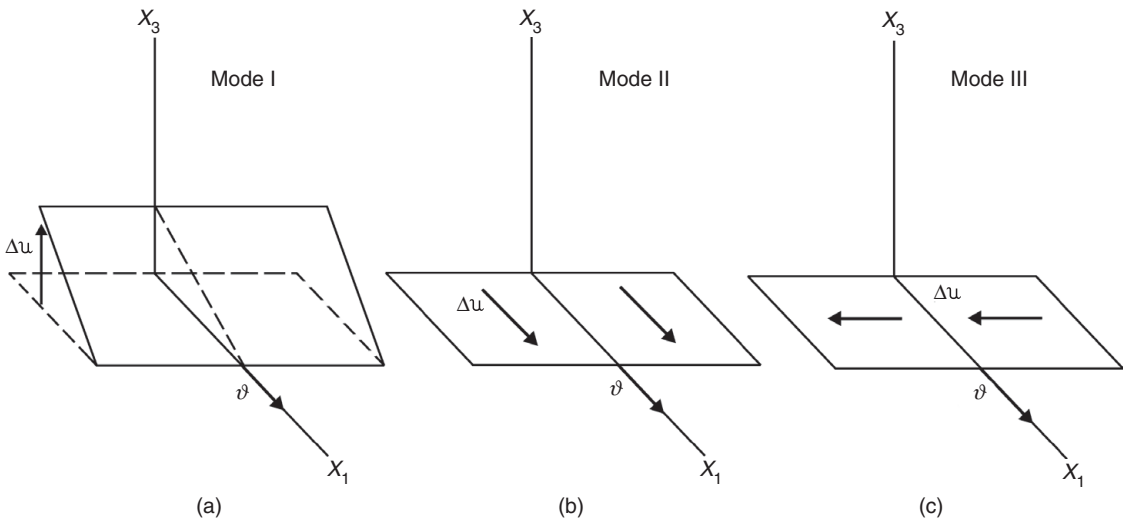


**Figure 9.3.** Three modes of propagation of a rupture:  $\Delta u$ , slip;  $v$ , rupture propagation velocity.

has a constant value,  $\sigma_0$ , and is zero inside the fault,  $\sigma(\rho) = 0$  for  $\rho < a$  (Eshelby, 1957; Keylis-Borok, 1959). Under these conditions, a solution for the slip inside the fault ( $\rho < a$ ) for Poisson ratio 0.25, as in equation (9.5) can be written

$$\Delta u(\rho) = \frac{24}{7\pi} \frac{\Delta\sigma}{\mu} \sqrt{a^2 - \rho^2} \quad (9.7)$$

where  $\Delta\sigma = \sigma_0$  (Fig. 9.2a). The relation between the static stress drop and the maximum slip at the center of the fault is

$$\Delta u_{\max} = \frac{24}{7\pi} \frac{\Delta\sigma}{\mu} a \quad (9.8)$$

This solution also applies to situations in which the stress inside the fault does not drop to zero during slip. This occurs when faulting occurs under friction, the most common situation in earthquake dynamics. In this case the stress drop is the difference between the initial stress  $\sigma_0$  and the final stress  $\sigma_f$  under friction.

The stress outside the circular fault ( $\rho > a$ ) can be computed using the method proposed by Eshelby (1959) but the computations are too complex to reproduce here. If the complete field is needed then numerical methods based on Okada's (1992) formulae (Toda *et al.*, 2011) are more appropriate to find the stress field of the circular crack. The main feature of the stress field around a circular crack is that it is not cylindrically symmetric about the axis of the fault. The reason is that under shear the crack is in Mode II deformation in the direction of application of the stress and it is in Mode III deformation in the direction transverse to the initial stress. If we let the initial stress be oriented along the  $x$  axis and the normal to the fault be along the  $z$  axis, the stress field of the circular crack presents singularities of the inverse square

root type along the circumference of the crack. In cylindrical coordinates  $(\rho, \phi)$ , on the plane of the fault we get

$$\sigma_{xz}(\rho, \phi) \approx (K_{II} \cos \phi + K_{III} \sin \phi) \frac{1}{\sqrt{2\pi}} \frac{1}{\sqrt{\rho - a}} \quad \text{for } \rho > a \quad (9.9)$$

where  $K_{II}$  and  $K_{III}$  are the in-plane and antiplane *stress-intensity factors* (see section 10.1 below), respectively. Thus around the fault the stresses are square root singular, with an intensity that depends on the two coefficients

$$K_{II} = \frac{16}{7\sqrt{\pi}} \frac{1}{1+\nu} \Delta\sigma a^{1/2} \quad \text{and} \quad K_{III} = \frac{16}{7\sqrt{\pi}} \Delta\sigma a^{1/2}$$

where  $\nu$  is Poisson's modulus. For the value  $\nu = 0.25$  normally used in seismology, the Mode II stress intensity factor is  $4/3$  times the Mode III intensity factor. In summary, as in the two-dimensional example of section 9.2 the slip has a simple expression; it is a maximum at the center of the fault ( $\rho = 0$ ) and decreases smoothly to zero near the edges of the fault (Fig. 9.2a). Associated with this decrease in slip, inverse square root singularities appear at the edge of the fault ( $\rho = a$ ). Far from the fault ( $\rho \gg a$ ), the stress remains equal to the initial stress  $\sigma(\rho) = \sigma_0$  (Fig. 9.2b). The corresponding displacement inside the fault is proportional to the stress drop, a maximum at its center and zero at the border (Fig. 9.2a).

We can now compute the average displacement over the fault area, which is given by

$$\Delta\bar{u} = \frac{1}{S} \int_S \Delta u \, dS \quad (9.10)$$

Substituting (9.7) we obtain

$$\Delta\bar{u} = \frac{48 \Delta\sigma}{7\mu S} \int_0^a \rho \sqrt{a^2 - \rho^2} \, d\rho = \frac{16a^3 \Delta\sigma}{7\mu S} \quad (9.11)$$

Putting  $S = \pi a^2$ , the relation between the average displacement and the stress drop is

$$\Delta\bar{u} = \frac{16}{7\pi} \frac{\Delta\sigma}{\mu} a \quad (9.12)$$

so that the seismic moment is given in terms of the stress drop by

$$M_0 = \mu \Delta\bar{u} S = \frac{16}{7} \Delta\sigma a^3 \quad (9.13)$$

This expression has been presented already, in (1.22).

If the stress drop is not constant over the fault plane, we can define its average value over the fault area as

$$\Delta\bar{\sigma} = \frac{1}{S} \int_S \Delta\sigma(\rho, \phi) \sqrt{1 - \rho^2/a^2} \rho \, d\rho \, d\phi \quad (9.14)$$

where  $(\rho, \phi)$  are the cylindrical coordinates inside the fault (Madariaga, 1979). Substituting  $\Delta\bar{\sigma}$  for  $\Delta\sigma$  in equation (9.12), we obtain the relation between the average displacement and

the average stress drop on the fault and, substituting into (9.13), the seismic moment in terms of the average stress. These are very useful simple relations between the parameters of a circular fault derived from the static case.

## 9.5. Circular fault. Brune's model

Rectangular fault models are appropriate for earthquakes in which the length is larger than the width. This is commonly the case for large strike-slip earthquakes if the rupture remains limited to a finite depth inside the Earth's crust, but for smaller earthquakes the rupture is completely contained in the crust, the length and width are similar in size and the shape of the fault can be approximated by a circle, as we saw in section 1.2. A commonly used model for a circular fault of finite dimensions is that presented by Brune (1970, 1971). *Brune's model* can be considered as a simple dynamic model, since it is based on the sudden application of a shear stress pulse to a circular fault of finite radius. Because the stress pulse is applied instantaneously over the entire fault area, there is no fracture propagation. The sudden shear stress drop inside the fault generates a plane SH wave which propagates with velocity  $\beta$  perpendicular to the fault plane of radius  $a$  (Fig. 9.4). If we denote by  $\Delta\sigma$  *Brune's effective stress*, that is,  $\Delta\sigma = \sigma_0 - \sigma_f = \varepsilon\sigma_0$  is the difference between the tectonic stress and the frictional stress (for a total stress drop  $\Delta\sigma = \sigma_0$ , and  $\varepsilon = 1$ ), and if we let  $\Delta v$  be the shear displacement on the fault plane (that is, for  $x \rightarrow 0$ , where  $x$  is the distance normal to the fault), we can follow Brune's derivation in a simplified form as follows. Let us consider a shear stress pulse with time dependence given by a step function which propagates perpendicularly to the fault with velocity  $\beta$ ,

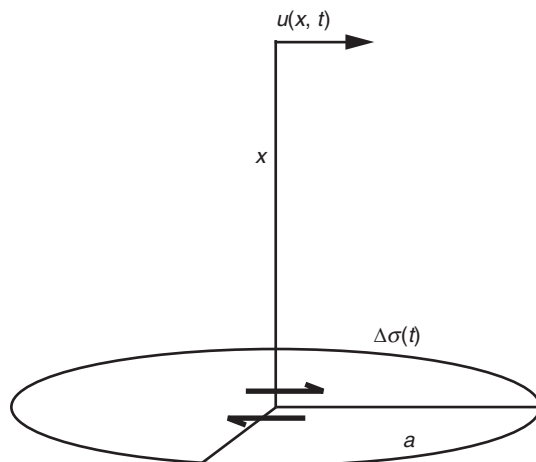


**Figure 9.4.** Rupture on a circular fault: Brune's model.

$$\Delta\sigma(x, t) = \Delta\sigma H\left(t - \frac{x}{\beta}\right) \quad (9.15)$$

The shear displacement  $u$  associated with this stress pulse can be computed by integration of (9.15), since in this case  $\Delta\sigma = \mu \partial u / \partial x$ :

$$u\left(t - \frac{x}{\beta}\right) = \frac{\Delta\sigma}{\mu} \int H\left(t - \frac{x}{\beta}\right) dx = \frac{\Delta\sigma}{\mu} \beta t H\left(t - \frac{x}{\beta}\right)$$

On the fault, when  $x \rightarrow 0$ , we have

$$u(t) = \frac{\Delta\sigma}{\mu} \beta t H(t) \quad (9.16)$$

Thus, at a point inside the fault, the displacement increases linearly with time until the effects of the boundary ( $r = a$ ) reach the point and stop the linear increase. Since the Fourier transform of the ramp function is

$$\text{FT}[tH(t)] = i\pi \frac{d}{d\omega} [\delta(\omega)] - \frac{\beta \Delta\sigma}{\mu \omega^2}$$

The Fourier transform of (9.16), ignoring the imaginary part, is given by

$$U(\omega) = -\frac{\beta \Delta\sigma}{\mu \omega^2} \quad (9.17)$$

The influence of the finite dimension of the source (of radius  $a$ ) can be introduced by considering that the effects of the edges of the fault are appreciable only for times not larger than  $\tau = a/\beta$  and that the velocity goes to zero for larger values of time. Then the displacement near the fault (the near-field) is given approximately by

$$u(t) = \frac{\Delta\sigma}{\mu} \beta \tau (1 - e^{-t/\tau}) \quad (9.18)$$

and the velocity by

$$\dot{u}(t) = \frac{\Delta\sigma}{\mu} \beta e^{-t/\tau} \quad (9.19)$$

According to Brune, the amplitude Fourier transform of (9.18) can be written as

$$|U(\omega)| = \frac{\Delta\sigma}{\mu} \beta \frac{1}{\omega (\omega^2 + \tau^{-2})^{1/2}} \quad (9.20)$$

For the far-field radiation, the effects of diffraction at the edges of the fault are approximated by introducing the factors  $f$  and  $\omega_c$  (we use the current notation  $\omega_c$  for the corner frequency instead of Brune's  $\alpha$ ). The far-field displacements of S waves at distance  $r$  can be written in a similar way to (9.18):

$$u(t) = f \frac{\Delta\sigma a}{\mu r} R_S \beta \left(t - \frac{r}{\beta}\right) \exp\left[-\omega_c \left(t - \frac{r}{\beta}\right)\right] \quad (9.21)$$

where  $R_S$  is the S wave radiation pattern. The amplitude of the Fourier spectrum of  $u(t)$  is given by

$$|U(\omega)| = f \frac{\Delta\sigma a}{\mu r} R_S \beta \frac{1}{\omega^2 + \omega_c^2} \quad (9.22)$$

This Fourier spectrum has the form already discussed in [section 4.9](#).

The values of  $f$  and  $\omega_c$  are chosen so that the energy radiated to the far field at high and low frequencies is consistent with the energy that would be radiated by an instantaneous circular shear crack. Taking into consideration the average displacement of a circular dislocation of radius  $a$  in terms of the stress drop, given by [\(1.21\)](#) and [\(1.22\)](#), and comparing the expression [\(9.22\)](#) for the low-frequency limit ( $\omega \rightarrow 0$ ) with the spectra of the far-field S wave radiation for a double couple, Brune obtained

$$f = \frac{4}{7\pi} \left( \frac{\omega_c a}{\beta} \right)^2 \quad (9.23)$$

Substituting this value of  $f$  into the spectrum [\(9.22\)](#) and using the expression [\(9.13\)](#) for the moment, we get, in the low-frequency limit,

$$|U(0)| = \frac{4}{7\pi\beta r} R_S \frac{\Delta\sigma}{\mu} a^3 \approx \frac{1}{4\pi\rho\beta^3 r} R_S M_0 \quad (9.24)$$

This is the far-field displacement at low frequencies for a double-couple source with moment  $M_0$ , where the radiation pattern has been assumed to be equal to 1. In addition, since the observed values of  $f$  are close to 1, Brune assumed that  $f = 1$  was a sufficient approximation, so that the corresponding value of  $\omega_c$  is

$$\omega_c = \sqrt{\frac{7\pi\beta}{4a}} = 2.34 \frac{\beta}{a} \quad (9.25)$$

and the amplitude spectrum [\(9.22\)](#) is finally given by

$$|U(\omega)| = \frac{1}{4\pi\rho\beta^3 r} R_S M_0 \frac{\omega_c^2}{\omega^2 + \omega_c^2} \quad (9.26)$$

Since the corner frequency  $\omega_c$  is inversely proportional to the source radius  $a$ , this expression shows that the far-field displacement spectrum depends on the radius of the fault. As discussed in [section 4.9](#), Brune's spectrum [\(9.26\)](#) has a flat part for low frequencies and decays as  $\omega^{-2}$  at high frequencies ([Fig. 7.7](#)). The radius of the fault is given in terms of the corner frequency by

$$a = \frac{2.34\beta}{\omega_c} \quad (9.27)$$

This approximate relation has been used by many authors to determine the fault dimensions from the spectra of S waves. It is probably correct for small crustal earthquakes up to magnitudes of the order of 6. The dimensions of earthquakes with these magnitudes are less than about 20 km, that is, less than the total thickness of the seismogenic layer. In these

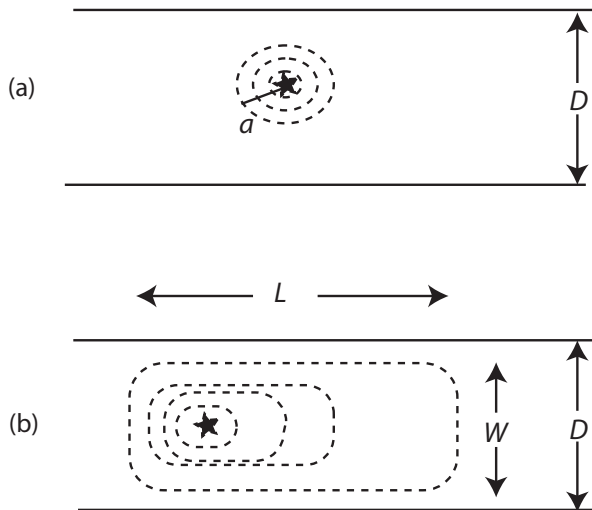


**Figure 9.5.** (a) Circular fault (radius  $a$ ) corresponding to a small earthquake; (b) rectangular fault corresponding to a large earthquake:  $L$ , length;  $W$ , width;  $D$ , thickness of seismogenic layer.

cases fractures start at a point and grow unhindered in all directions, giving a near-circular shape ( $L = W$ ) (Fig. 9.5a). Larger earthquakes may have a larger length in comparison to their width ( $L > W$ ), which is limited to the thickness of the seismogenic layer; they are better approximated by a rectangular fault (Fig. 9.5b).

### Energy balance for Brune's circular model

A very important and still poorly understood issue in seismology is the *energy balance* of earthquakes. Brune's circular crack model has the very useful property that all relevant energies can be computed exactly.

For a circular crack, the static slip produces a total *strain energy release* that can be directly computed from the slip distribution (9.7):

$$\Delta W = \int_S \bar{\sigma} \Delta u \, dS \quad (9.28)$$

where  $\bar{\sigma} = \frac{1}{2}(\sigma_0 + \sigma_f)$  is the average stress acting on the fault when slip occurs. See also the introductory discussion of section 1.6. This energy,  $\Delta W$ , actually is dissipated in two ways: first, as frictional energy (mostly heat),

$$\Delta F = \int_S \sigma_f \Delta u \, dS \quad (9.29)$$

and, second, as elastic energy  $\Delta U$ , which is partly dissipated as radiation energy and partly used to make the rupture grow:

$$\Delta U = \frac{1}{2} \int_S \Delta\sigma \Delta u \, dS \quad (9.30)$$

Thus we have  $\Delta W = \Delta U + \Delta F$ . In a perfect fault, corresponding to the so-called *Orowan model*, all the available strain energy  $\Delta U$  is converted into seismic waves (see e.g. Savage and Wood, 1971). Such a model assumes that no energy is used to produce the circular fracture. In a circular crack model the total strain energy can be directly computed from the slip distribution (9.7) since  $\Delta\sigma$  is assumed to be constant:

$$\Delta U = \frac{1}{2} \Delta\sigma \times \frac{16}{7\pi} \frac{\Delta\sigma}{\mu} a \times \pi a^2 = \frac{8}{7} \frac{\Delta\sigma^2}{\mu} a^3 \quad (9.31)$$

We can now compare the strain energy (9.31) with the seismic energy actually radiated by Brune's model. The latter can be computed using the expression (4.87); for S waves we get

$$E_s = \frac{1}{16\pi\mu} \langle R_s^2 \rangle M_0^2 \frac{\omega_c^3}{\beta^3} = \frac{2.34}{7} 4 \langle R_s^2 \rangle \frac{\Delta\sigma^2}{\mu} a^3$$

where we have written  $M_0$  and  $\omega_c$  in terms of the stress drop  $\Delta\sigma$  and the radius of the fault,  $a$ . Finally we use the root mean square averaged radiation pattern  $\langle R_s^2 \rangle = 0.4$  to find that

$$E_s = 0.535 \frac{\Delta\sigma^2}{\mu} a^3 = 0.47 \Delta U \quad (9.32)$$

This value is cited by Brune (1970) in his equation (39). Defining the radiation efficiency (Husseini and Randall, 1976) as  $\eta_r = E_s/\Delta U$ , Brune's model gives an efficiency of 47%. This corresponds to about half the maximum possible radiated energy, which is found in the Orowan model, as mentioned above. Where does the rest of the available energy go? It goes into *fracture energy*, the amount of energy that is used to create the fault surface. This was not taken into account by Brune (1970) because he assumed that the fault broke instantaneously, at time  $t = 0$ . A better model of the energy partition will be presented in the following chapters.

As discussed in Section 1.6, seismologists originally defined the efficiency as the ratio

$$\eta = \frac{E_s}{\Delta W}$$

of the radiated energy and the total strain energy change  $\Delta W$ . Unfortunately  $\Delta W$  cannot be measured from seismic observations alone. It is better to define the apparent stress defined as (Wyss and Brune, 1968)

$$\sigma_a = \eta \bar{\sigma} = \mu \frac{E_s}{M_0}$$

While neither the efficiency  $\eta$  nor the average stress can be computed from seismic observations their product, the apparent stress, can be computed from the ratio of the radiated energy and the seismic moment. For Brune's model we have

$$\sigma_a = 0.466 \Delta\sigma \quad (9.33)$$

## 9.6. Scaling laws

Earthquakes occur with very different sizes, from very small ones that can only be detected by extremely sensitive instruments to very large ones that produce catastrophic damage and ground rupture along many hundreds of kilometers. We have seen how the earthquake sources can be represented by models which are given in terms of a small number of parameters. It was realized by Aki (1967) that not all these parameters were independent; some could be related to a few fundamental ones. Parameters which define the location in space and time ( $\phi_0, \lambda_0, h, t_0$ ) and the orientation of the source ( $\mathbf{l}, \mathbf{n}$ ) are independent of earthquake size, so they are not included in this consideration. We can then see whether it is possible to establish *scaling laws* among the parameters which are related to the size of earthquakes, so that some parameters can be expressed in terms of other more fundamental ones (Madariaga and Olsen, 2002).

The parameters which define the size of an earthquake are the scalar seismic moment  $M_0$ , which is proportional to the area of the fault, and the average slip on its surface. The moment magnitude  $M_W$  defined in (1.30) is proportional to the logarithm of the energy released at the source (Hanks, 1977). In terms of their seismic moment earthquakes range roughly between  $10^8$  to  $10^{23}$  N m (with  $M_W$  between  $-1$  and  $9$ ), that is, over 15 orders of magnitude. We have seen that from the dynamic point of view the slip  $\Delta u$  on the fault surface is produced by a drop in the acting stress  $\Delta\sigma$ , which can be considered to be, for this reason, the most fundamental parameter (Scholz, 1990, pp. 202–11).

The first seismic scaling law was introduced by Aki (1967) from considerations about the shape of the spectrum and the various magnitude scales that were in common use at the time. His argument was that these magnitude scales could be reconciled if it was assumed that all earthquakes shared the seismic wave spectrum, with a flat part at low frequencies and an  $\omega^{-2}$  decay of amplitude at high frequencies. Thus, Aki in 1967 assumed that earthquake spectra were of the Brune type (9.26). He then compared the spectra of earthquakes of different sizes and concluded that the corner frequency was inversely proportional to the size of the earthquake, let us call it  $L$ , and that the moment was proportional to the stress drop times the cube of the source length and the inverse of the cube of the corner frequency, that is,

$$M_0 \approx \Delta\sigma L^3 \approx \Delta\sigma \omega_c^{-3} \quad (9.34)$$

Comparing earthquakes of different sizes occurring in similar tectonic areas he found that the scaling relation implied that, within an order of magnitude, the stress drop  $\Delta\sigma$  was essentially the same for all earthquakes. This is the most basic result of earthquake dynamics. It implies that earthquakes can be represented by self-similar fracture models, that is, models in which the parameters of events of different size differ only by a scale factor which the size  $L$  of the fault. Aki (1967) found that, basically, the size of earthquakes (given by  $M_W$  and  $M_0$ ) scales with the cube of the fault length  $L$ . By straightforward dimensional analysis from the definition of moment it can be concluded that the average slip on the fault  $\Delta\bar{u}$  must also be proportional to  $L$ . We have already found this result for a circular fault, see equation (9.12),

if the static stress drop  $\Delta\sigma$  is taken to be essentially constant for all earthquakes; for constant  $\Delta\sigma$  the proportionality between  $L$  and  $\Delta\bar{u}$  can be expressed as

$$\Delta\bar{u} \approx \frac{\Delta\sigma}{\mu} L \quad (9.35)$$

Observations show that  $\Delta\sigma$  varies only between 1 and 10 MPa while  $L$  varies from some meters to hundreds of kilometers.

Kanamori and Anderson (1975) introduced similarity conditions relating the length  $L$ , width  $W$ , average slip  $\Delta\bar{u}$ , rupture velocity  $v_r$ , and rise time  $\tau_r$ . They studied the *aspect ratio* of the fault,  $C_1 = W/L$ , the ratio of slip to fault length for constant stress drop,  $C_2 = \Delta\bar{u}/L$ , and the ratio of the duration of rupture and the fault size (the *dynamic similarity*),  $C_3 = v_r\tau_r/L$ . From the first and second ratios they derived that the seismic moment is proportional to the cube of the length:  $M_0 \approx L^3$  (as we have already found for a circular fault, see (9.13)). Dynamic similarity implies that the dynamic stress drop  $\Delta\sigma_d$  is constant for large earthquakes. The apparent average stress  $\sigma_a$ , (1.11), is also considered to be constant and this results in proportionality between the seismic energy and the fault length cubed:  $E_s \approx L^3$ . The latter relation will be discussed in more detail in a later section.

We have seen that fracture in small earthquakes ( $M_W < 6$ ) is uninhibited by the thickness of the seismogenic layer (about 25 km) and is more or less circular (Fig. 9.5a). Thus for small earthquakes the slip increases linearly with the length. Large strike-slip earthquakes produce long fractures which have constant width  $W$  (the width of the seismogenic layer), breaking the whole seismogenic layer and varying in length up to hundreds of kilometers with an aspect ratio  $L/W$  larger than about 3 (Fig. 9.5b). For these earthquakes there is a tendency for the slip  $\Delta u$  to attain a constant maximum value of about 10 meters, so that the proportionality between  $L$  and  $\Delta u$  is not completely preserved. Large subduction earthquakes, however, can have larger widths of up to 100 kilometers and lower aspect ratios. Cowie and Scholz (1992) did an exhaustive search for the scaling of slip with fault size, concluding that slip seemed to scale with fault length rather than fault width. A different conclusion was reached by Romanowicz (1992) who found that observations of large strike-slip earthquakes indicated that slip scaled with fault width. Many other authors looked for this relationship in geological, seismic and geodetic data, reaching contrasting conclusions. Although several very large strike-slip earthquakes have occurred in recent years, such as the Denali earthquake of 2002 in Alaska, the Kunlun earthquake of 2002 in Tibet and the 2013 earthquake in the Indian ocean off Sumatra, there is no general agreement whether observations support that the slip for large earthquakes actually scales with  $L$  or with  $W$  (Bodin and Brune, 1996).

Since the area of the surface of the fault is proportional to  $L^2$ , according to (9.13) (for a circular fault) we can relate the size of an earthquake, given by its seismic moment, to the fault length, which thus becomes the fundamental parameter, in the form

$$M_0 \approx \Delta\sigma L^3 \quad (9.36)$$

As mentioned above, it was shown by Hanks (1977) that most earthquakes have fairly constant stress drops between 1 MPa and 10 MPa. In Fig. 9.6 we show a collection of observations of the moment and length of many earthquakes in many different

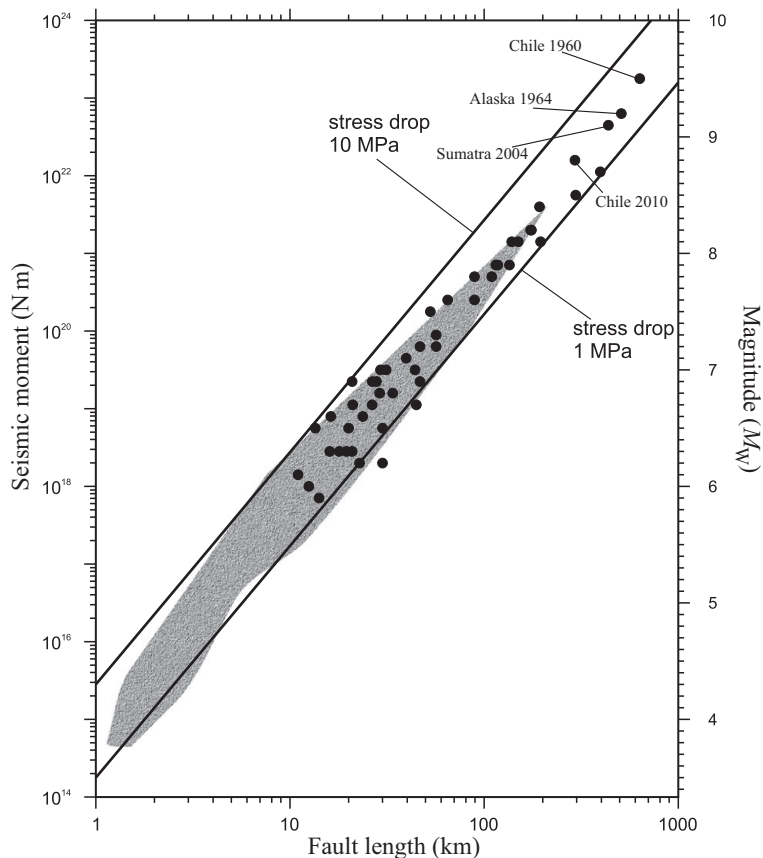


**Figure 9.6.** Relation between seismic moment, magnitude  $M_W$  and fault length for earthquakes with widely varying magnitudes. The grey zone is the area where most earthquakes lie. The dots are significant earthquakes.

environments, including very recent events of large magnitude. The moments reported in Fig. 9.6 stretch over 10 orders of magnitude. The same relation applies to smaller earthquakes but it is often more difficult to determine the fault length for those events. As in the case of the relation between slip and fault length, the relation between seismic moment and length is considered by some authors to be different for small and large earthquakes: Shimazaki (1986) showed that for Japanese earthquakes a difference exists in the scaling of the seismic moment with fault length between large and small earthquakes. Earthquakes with seismic moment less than  $10^{19}$  N m scale with  $L^3$  and those with moments larger than  $10^{19}$  N m scale with  $L^2$ . It seems, however, that, while for small and moderate-size earthquakes seismic moments do scale with  $L^3$ , for large earthquakes there is a large scatter in the data, so that it is not certain which relation exists. Scholz (1990, 2007) summarized the situation, separating three size regimes for different relations between  $L$  and  $W$ , with different scaling relations, namely: (1)  $L < W$ ,  $\Delta u \approx L$ ,  $M_0 \approx L^3$ ; (2)  $W < L < 10W$ ,

$\Delta u \approx L$ ,  $M_0 \approx L^2 W$ ; (3)  $L > 10W$ ,  $\Delta u \approx W$ ,  $M_0 \approx LW^2$ . Most events belong to regimes (1) and (2); events in regime (3) are very rare. Assuming a constant stress drop it is possible to derive a relationship between maximum (or average) slip for earthquakes and their seismic moment:  $\Delta u \approx M_0^{1/3}$  (Somerville *et al.*, 1999; McGarr and Fletcher, 2003).

The static scaling law (9.36) establishes a relation between the seismic moment and the length of the earthquake that is a fundamental property of earthquake sources. Associated with the spatial dimensions of faults, represented by their length  $L$  (or width  $W$ ) there is a temporal dimension:  $t_r$ , the time duration of the complete fracture process. This time dimension depends on the velocity of rupture  $v_r$ , which may vary over the fault surface ( $t_r = L/v_r$ ). The velocity of rupture is a difficult parameter to determine experimentally. An average value over the whole rupture can be expressed as a fraction of the shear wave velocity  $\beta$  at the source, which is a material property. Thus,  $t_r$  can be expressed as

$$t_r = \frac{L}{\beta} \quad (9.37)$$

Substituting into (9.36), this relation implies that the seismic moment scales with the cube of the source duration:

$$M_0 \approx t_r^3 \quad (9.38)$$

Another temporal dimension is given by the rise time  $\tau_r$ , the time that it takes for the slip to reach its maximum value at each point of the fault (in general  $\tau_r < t_r$ ). However, it is not clear how  $\tau_r$  scales with other parameters of the source. For long strike-slip earthquakes, Heaton (1990) proposed that the rise time was independent of the size of the earthquake and that seismic ruptures seemed to behave like pulses of finite width running along the fault. Although there is substantial evidence in favour of the pulse model it is not universally accepted, especially for subduction-zone earthquakes.

In Table 9.1 we present typical values of  $M_0$ ,  $L$ ,  $T$  and  $\Delta u$  for earthquakes of different moment magnitude  $M_W$ . Moment and moment magnitude are related by expression (1.30); the rest are computed from (9.36), (9.38) and (9.35) assuming that  $\Delta\sigma = 3$  MPa. The numbers are rounded.

## Energy scaling

This is a crucial issue in seismology and one for which we have no definite answer yet. If we follow the circular shear crack model, we observe that strain energy scales as follows:

$$\Delta U = \frac{8}{7} \frac{\Delta\sigma^2}{\mu} a^3 \quad (9.39)$$

while moment scales as  $M_0 \sim \Delta\sigma a^3$ . Thus two quantities that have the same dimensions ( $J = N\text{ m}$ ) scale differently, one as  $\Delta\sigma$  and the other as  $\Delta\sigma^2$ , meaning that some additional phenomenon is not taken into account in the scaling of the simple circular crack model. We can now recall relation (9.32), according to which the radiated energy scales as

**Table 9.1.** Average values of moment, length, duration and slip for earthquakes of different moment magnitude  $M_W$ .

Magnitude $M_W$	Moment $M_0$ (N m)	Length $L$ (km)	Duration $T$ (s)	Slip $\Delta u$ (m)
10	$10^{24}$	1000	300	100
9	$3 \times 10^{22}$	300	100	30
8	$10^{21}$	100	30	10
7	$3 \times 10^{19}$	30	10	3
6	$10^{18}$	10	3	1
5	$3 \times 10^{16}$	3	1	0.3
4	$10^{15}$	1	.3	0.1

$$E_s = 0.535 \frac{\Delta\sigma^2}{\mu} a^3 \quad (9.40)$$

It is clear now that the circular crack model has additional features that were not taken into account in the instantaneous crack model. These differences in the energy and in the moment are not obvious because, as already mentioned, the usual earthquake model assumes that  $\Delta\sigma$  is the same for all earthquakes. We can finally produce a simple scaling law between energy and moment for Brune's model, based on the relationship (4.88):

$$E_S = 0.00796 \frac{M_0^2 \omega_c^3}{\mu \beta^3} = 1.9739 \frac{M_0^2 f_c^3}{\mu \beta^3} \quad (9.41)$$

where  $f_c$  is the corner frequency in Hz. This relationship can be used to test whether Brune's model applies to a particular earthquake or perhaps to a suite of seismic events. The numerical coefficient in (9.41) was computed for Brune's model; in fact it can be computed for any kinematic or dynamic model, as we will see in the following chapters.

## 10.1. Griffith's fracture model

In the previous chapter we studied a simple circular earthquake model proposed by Brune (1970). In that model the amount of radiated energy was about 45% of the strain energy released by the elastic body, so where does the rest of the energy go? It goes into the creation of the *fracture surface* or fault. This energy is released near the edge or tip of the fault, that is, the place where the material passes from being unbroken to being broken (Kostrov and Das, 1988, pp. 53–62). In the case of a homogeneous, continuous, perfectly elastic material, the material ahead of the fracture front is continuous and elastic and behind the front it is discontinuous (broken). In a tensional fracture (mode I, see section 9.3), when the two sides of the fracture become separated by a *crack-opening displacement*  $\Delta u$ , the stress behind the front is zero and the stress drop is total. This situation is usually the one considered in engineering applications. Alan Griffith in 1921 introduced the first elements of *brittle fracture* in his work on the fracture of metals. At that time it was generally accepted that the strength of a material was about one tenth of the value of Young's modulus. However, in practice, from laboratory experiments it was known that the critical strength at which material fracture occurred was about a thousand times lower. Griffith made the hypothesis that the presence of small cracks lowered the strength of the material, causing it to fracture long before it reached its theoretical *breaking strength*. He assumed that the surface energy dissipated by the forming of a new crack surface is equal to the resistance to *crack growth*. To create a new unit area of fracture a certain amount of energy per unit surface,  $\gamma$ , was necessary, which he called the effective *specific surface energy*. He assumed that  $\gamma$  was a material constant. According to Griffith, for the crack to grow by a new surface element  $\delta S$ , it was necessary to provide it with an amount of energy equal to  $2\gamma\delta S$  (the factor 2 is for the two sides of the fracture).

The criterion of fracture can then be stated in the following form: under quasistatic driving stresses greater than a certain critical value, fracture will grow satisfying the virtual energy balance condition

$$\delta W - \delta U - 2\gamma\delta S = 0 \quad (10.1)$$

where  $\delta W$  is the work done by the applied external stresses,  $\delta U$  is the change in strain energy produced by the crack-opening displacement of the fracture and, as we saw above,  $2\gamma\delta S$  is the energy required for the creation of the new fracture surface  $\delta S$ .

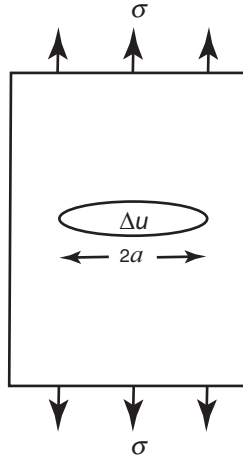


**Figure 10.1.** Thin plane with a crack of size  $2a$  and displacement  $\Delta u$  under tensional stresses  $\sigma$ .

Griffith studied several problems in the strength of materials in order to determine the stresses needed to overcome the resistance of a fault of certain size to growth. Let us consider the simplest case, that of a very thin planar plate with a slit of size  $2a$  in its middle, as shown in Fig. 10.1. Tensional stresses  $\sigma$  are applied in the direction normal to the crack. Under the plane stress conditions appropriate for a thin plate, the crack-opening displacement is

$$\Delta u(x) = \frac{4\sigma}{E} \sqrt{a^2 - x^2} \quad (10.2)$$

where  $E$  is Young's modulus and  $a$  is the crack length (Broberg, 1999, section 4.6). The relations between  $E$ , the elastic coefficients  $\lambda$  and  $\mu$  and Poisson's ratio  $\nu_p$  are

$$\mu = \frac{E}{2(1 + \nu_p)}, \quad \lambda = \frac{Ev_p}{(1 - 2\nu_p)(1 + \nu_p)}$$

In (10.2),  $x$  is the position along the crack. When this crack appears, under a certain applied stress  $\sigma$ , the medium releases an amount of internal energy equal to

$$\Delta U = \frac{1}{2} \sigma \overline{\Delta u} = \pi \frac{\sigma^2}{E} a^2 \quad (10.3)$$

which, by Griffith's hypothesis, must balance the surface energy  $2\gamma a$ . If the stress  $\sigma$  is at the critical level  $\sigma_c$  then  $\Delta U = 2\gamma a$  and the crack may extend. We find that the critical stress is (Broberg, 1999, p. 582)

$$\sigma_c = \sqrt{\frac{2E\gamma}{\pi a}} \quad (10.4)$$

This calculation applies to a thin plate under plane stress loading. In geophysics we are more interested in plane strain conditions, which are appropriate for a body that extends infinitely in the direction along the crack axis. In that case the critical stress is

$$\sigma_c = \sqrt{\frac{2\mu\gamma}{\pi(1-v_p)a}}$$

where  $\mu$  is the elastic rigidity coefficient.

Griffith's theory is based on the global energy balance for a crack inside a perfectly elastic medium; its use in practical applications is difficult because computing the energy balance is often more difficult than solving for the stress field around a crack of general shape. George R. Irwin in the 1950s introduced the concept of the *stress intensity factor*,  $K_I$ , which is a measure of the stress field intensity near the tip of an ideal crack in a linear elastic material. For the thin plate studied by Griffith, the stress near the tip of a crack subjected to tension has the form

$$\sigma = \frac{K_I}{\sqrt{2\pi r}} \quad (10.5)$$

where  $K_I$  is the stress intensity factor for Mode I. Definition (10.5) means that the stress field near the tip decreases as the inverse square root of the distance  $r$  from the tip of the crack. According to Irwin (1957), the stress intensity factor  $K_I$  is given by

$$K_I = \Delta\sigma\sqrt{a/2} \quad (10.6)$$

Associated with the stress intensity factor is the *energy release rate*  $G_c$  ("rate" meaning here per unit surface), defined as the amount of energy per unit surface area that is available to extend the fault quasistatically;  $G_c$  can be computed by integrating the strain energy along a small circular path around the crack tip. Actually, as shown by Eshelby (1957) and Rice (1968), the energy release rate in an elastic medium can be computed by taking any path that surrounds the crack tip. Thus  $G_c$  is a path-independent property of static fractures. For Mode I, under a plane strain,

$$G_c = \frac{1-v_p}{\mu} K_I^2 \quad (10.7)$$

It is important to remark that this relation is valid for the definition of stress intensity in (10.5). In the past other normalizations were used that led to slightly different definitions of  $G_c$  (for instance, Kostrov and Das, 1988, do not include  $\pi$  under the square root in (10.5)).

The concepts of Griffith and Irwin are easily extended to shear faults under Mode II (in-plane) or Mode III (antiplane) fracture. In section 9.2 we studied the stress and displacement fields around a simple Mode III crack under plane strain. The main difference from the tension crack is that, since the fault is not necessarily stress free after it slipping occurs, we have to take into account both the initial and final stresses  $\sigma_0$  and  $\sigma_f$ . Then the amount of strain energy available to expand the crack is given by

$$\Delta U = \frac{1}{2} \Delta\sigma \Delta\bar{u} \quad (10.8)$$

where  $\Delta\bar{u}$  is the average value of the slip inside the fault (9.5) multiplied by 2. Taking the average of that expression we get

$$\Delta\bar{u} = \frac{\Delta\sigma}{\mu} \frac{1}{a} \int_{-a}^a 2\sqrt{a^2 - x^2} dx = \pi \frac{\Delta\sigma}{\mu} a$$

so that the strain energy released per unit area is

$$\Delta U = G_c^* = \frac{\pi}{2} \frac{\Delta\sigma^2}{\mu} a \quad (10.9)$$

where  $G_c^*$  is the *static energy release rate* (the static energy release per unit area) due to the displacement inside the crack and has the same form as (10.7), the expression for  $G_c$  in the Griffith crack case.

As for the plane stress tensional crack we can write the energy release rate for a Mode III crack as

$$G_c^* = \frac{K_{III}^2}{2\mu} \quad (10.10)$$

where  $K_{III}$ , the stress intensity factor for mode III cracks, is given by the same expression as (10.6).

For mode II, a similar argument can be used. For a stress drop  $\Delta\sigma$ , the strain energy release on the fault is

$$\Delta U = \frac{\pi}{2} \frac{\Delta\sigma^2}{\mu} (1 - v_p) a$$

and the stress field ahead of the crack tip is

$$K_{II} = \Delta\sigma \sqrt{a/2} \quad (10.11)$$

Thus, the energy release rate is

$$G_c^* = (1 - v_p) \frac{K_{II}^2}{2\mu} \quad (10.12)$$

The critical energy release rate for any mode occurs when  $G_c$  is exactly equal to the energy needed to create new fracture surface,

$$G_c = 2\gamma \quad (10.13)$$

The crack propagates when  $G_c > 2\gamma$ . In classical fracture mechanics  $\gamma$  is considered to be a material property and has been evaluated for many materials. For earthquakes, as we will shortly see, it is not clear whether it is a material property or the result of internal processes near the rupture front that undergo adjustment depending on the size of the earthquake.

Irwin extended Griffith's theory to ductile materials in which a certain amount of energy for plastic deformation  $\gamma_p$  around the crack must be added to the purely elastic energy release  $\gamma$  used for creating a new surface.

## 10.2. Energy flow towards the fracture front for a growing crack

In the previous section we studied the conditions for the formation of a crack under *quasistatic* conditions. Once the energy release rate  $G_c$  is large enough the crack or fault will start to grow and a certain amount of energy will be absorbed by the fracture front as it propagates along the fault. Let us consider the simplest case, that of a homogeneous perfectly elastic medium in which a crack propagates with *constant rupture velocity* under the action of certain applied stresses. In a continuous elastic medium in which there are no cracks nor any other types of source, energy conservation within a volume  $V$  surrounded by a surface  $S$ , in the absence of sources of heat and heat dissipation across the surface, can be expressed as

$$\frac{d}{dt}(W - T - U) = 0 \quad (10.14)$$

where  $W$  is the work done by the external stresses  $\tau_{ij}$  acting on the surface  $S$ ,  $T$  is the kinetic energy and  $U$  is the elastic strain energy in the volume  $V$  (Fig. 10.2). There is no difficulty in applying (10.14) to other types of source, but we do not want to distract ourselves from the study of the origin of fracture energy. The complete energy conservation equation was discussed by Kostrov and Das (1988).

In an elastic solid with no body forces,  $W$ ,  $T$  and  $U$  are given by (Udias, 1999, pp. 18–19)

$$W = \int_S u_i \tau_{ij} n_j dS \quad (10.15)$$

$$T = \int_V \frac{1}{2} \rho \dot{u}_i \dot{u}_i dV \quad (10.16)$$

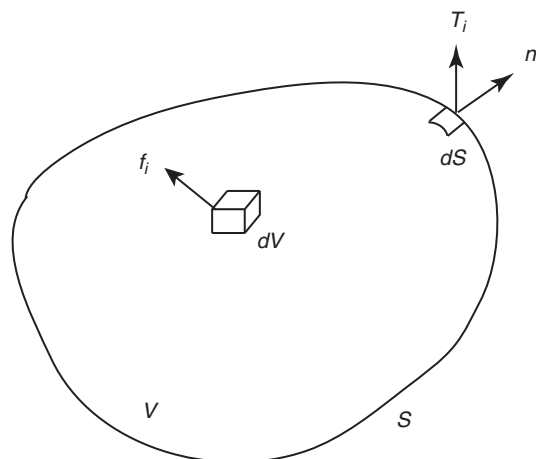


**Figure 10.2.** Elastic body of volume  $V$  surrounded by surface  $S$ , with forces  $f_i$  acting per unit volume and stresses  $T_i$  acting per unit surface.

$$U = \int_V \frac{1}{2} \tau_{ij} e_{ij} dV = \int_V \frac{1}{2} C_{ijkl} e_{ij} e_{kl} dV \quad (10.17)$$

Substituting into (10.14) we obtain

$$\frac{d}{dt} \left[ \int_S \tau_{ij} n_j u_i dS - \int_V \left( \frac{1}{2} \rho \ddot{u}_i \dot{u}_i + \frac{1}{2} C_{ijkl} e_{ij} e_{kl} \right) dV \right] = 0 \quad (10.18)$$

Taking time derivatives, transforming the surface integral into a volume integral by Gauss's relation and substituting the equation of motion  $\tau_{ij,j} + f_i - \rho \ddot{u}_i = 0$ , we obtain

$$\int_V (\tau_{ij} \dot{e}_{ij} - C_{ijkl} e_{ij} \dot{e}_{kl}) dV = 0 \quad (10.19)$$

The rate of energy transfer due to the external stresses acting on the medium is equal to the time rate of change of the strain energy.

We can also proceed by starting from the equation of motion in the absence of body forces, defined in (3.4):

$$\rho \ddot{u}_i = \tau_{ij,j}$$

Taking the scalar product of both sides of this equation by the particle velocity and integrating over the volume  $V$  we get

$$\int_V \rho \ddot{u}_i \dot{u}_i dV = \int_V \tau_{ij,j} \dot{u}_i dV \quad (10.20)$$

Then we notice that

$$\int_V \frac{\partial}{\partial x_j} (\tau_{ij} \dot{u}_i) dV = \int_V (\tau_{ij,j} \dot{u}_i + \tau_{ij} \dot{u}_{i,j}) dV = \int_V (\tau_{ij,j} \dot{u}_i + \tau_{ij} \dot{e}_{ij}) dV$$

since  $\tau_{ij} e_{ij} = \tau_{ij} u_{i,j}$ . So, (10.18) can be reorganized as follows:

$$\int_V \frac{\partial}{\partial x_j} (\tau_{ij} \dot{u}_i) dV = \int_V \tau_{ij} \dot{e}_{ij} dV + \int_V \rho \ddot{u}_i \dot{u}_i dV \quad (10.21)$$

We can now use Gauss's theorem to convert the right-hand side into a boundary integral:

$$\int_V \frac{\partial}{\partial x_j} (\tau_{ij} \dot{u}_i) dV = \int_S \tau_{ij} \dot{u}_i n_j dS$$

where  $n_i$  is the normal to  $S$  pointing out of the elastic body  $V$ . Finally, using the elastic constitutive relation we arrive at equation (10.19):

$$\frac{d}{dt} \int_S \tau_{ij} u_i n_j dS = \frac{d}{dt} \left[ \int_V \left( \frac{1}{2} \rho \ddot{u}_i \dot{u}_i + \frac{1}{2} C_{ijkl} e_{ij} e_{kl} \right) dV \right] \quad (10.22)$$

That is, in the absence of body forces, heat sources and heat dissipation, at any instant of time  $t$  the rate of working of the boundary forces is equal to the rate of change of the kinetic and strain energy inside the elastic body.

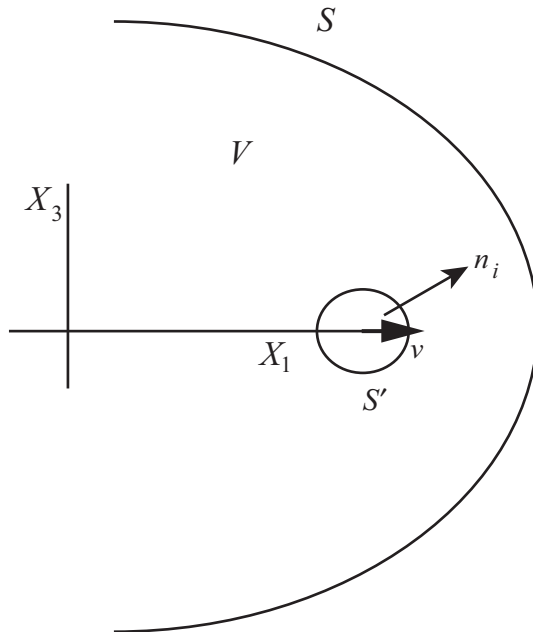


**Figure 10.3.** Rupture propagating inside an elastic body with velocity  $v$ , with a small surface  $S'$  of normal  $n_i$  and volume  $V$  surrounding the rupture tip or edge.

Let us now consider the two-dimensional problem of a fracture located on the plane  $x_3 = 0$  that extends without limit in the  $x_2$  direction on the plane. We assume for simplicity that the stress drop is total, so that  $\sigma_f = 0$ . The rupture front situated at the origin in Fig. 10.3 moves at constant velocity  $v$  in the direction  $x_1$  under the action of applied stresses (we assume that no body forces are acting) on a medium of volume  $V$  surrounded by a surface  $S$ . Let a small surface  $S'$  surround the tip of fracture (Kostrov, 1964; Freund, 1972b, 1979). In order to represent the fracture edge, we take the limit as the surface  $S'$  shrinks to zero. As we have already proved above, the rate of work done by the stresses acting on the boundaries  $S + S'$  is equal to the change in the kinetic plus elastic potential energy in the volume  $V$  enclosed between the two surfaces (10.14).

As the crack advances, mechanical energy flows through  $S'$  from the unbroken part of the material to produce new fracture surface. Let us now separate the energy flow rate  $\dot{W}$  through the external surface  $S$  from the flow rate across the small surface  $S'$  that surrounds the crack tip. Since we have assumed that the crack surfaces are free of stress we can rewrite (10.14) as

$$\dot{W} = \dot{T} + \dot{U} + \dot{F} \quad (10.23)$$

where  $\dot{F}$  is the energy flow per unit time entering the *crack tip* from the rest of the body. We remark that this has the opposite sign to that of the rate of work on the surface  $S$  because, while  $W$  is work done on the body  $V$ ,  $F$  is the energy flow per unit time into the crack tip. When the crack tip is fixed ( $v = 0$ ) the energy flow into the tip is given by

$$\dot{F} = - \lim_{S' \rightarrow 0} \int_{S'} \tau_{ij} \dot{u}_i n_j \, dS \quad (10.24)$$

which can be derived immediately from (10.20).

When the crack advances at speed  $v$  into the unbroken material, we have to consider the flux in kinetic and elastic potential energy through the surface  $S'$ . The flux of kinetic and elastic energy can be computed by noting that when the crack tip moves at speed  $v$  the total time derivative is  $d/dt = \partial/\partial t + v\partial/\partial x$ , so that we obtain (Freund, 1979; Aki and Richards, 1980, p. 862)

$$\dot{F} = - \lim_{S' \rightarrow 0} \int_{S'} \left[ \tau_{ij} \dot{u}_i n_j + \frac{1}{2} (\tau_{ij} \dot{u}_{i,j} + \rho \dot{u}_i \dot{u}_i) v n_1 \right] dS \quad (10.25)$$

The first term is the rate of work done by the material outside  $S'$  on the material inside  $S'$  and is given by the product of the stresses acting on  $S'$  and the particle velocity. The second term is the sum of the elastic strain energy and the kinetic energy of the material particles which cross the surface  $S'$  as they propagate into the unbroken material with velocity  $v$ . We notice that (10.25) is the energy flux into the crack tip per unit time. For a crack running at constant rupture velocity  $v$ ,

$$\dot{F} = G_c v \quad (10.26)$$

This shows that when a crack advances at a constant or slowly varying rupture speed it requires an energy flow per unit time defined by (10.24).

### 10.3. Stress singularities around a rupture front moving at constant speed

In the previous section we computed the amount of energy that flows into the crack tip when rupture advances at a constant speed. In order to compute explicitly the energy flow into the tip we need to find the details of the stress field near the tip of the rupture front. There many approaches to compute the general features of this stress field. Here we will examine in detail the propagation of a sharp two-dimensional antiplane crack running at constant speed.

We are interested in a simple crack moving along the  $x_1$  axis, perpendicularly to the  $x_3$  axis, as shown in Fig. 10.4. Displacement occurs in the  $x_2$  direction. The only components of displacement and stress that are relevant in this problem are  $u_2$ ,  $\sigma_{12}$  and  $\sigma_{13}$ . In coordinates fixed in the elastic medium with uniform properties the seismic waves generated by this crack satisfy the wave equation

$$\frac{1}{\beta^2} \frac{\partial^2 u_2}{\partial t^2} = \frac{\partial^2 u_2}{\partial x_1^2} + \frac{\partial^2 u_2}{\partial x_3^2} \quad (10.27)$$

where the shear wave speed is  $\beta$ . If the crack moves at constant speed  $v$  in the direction of positive  $x_1$  and the stress loading follows the crack at the same speed then we can simplify

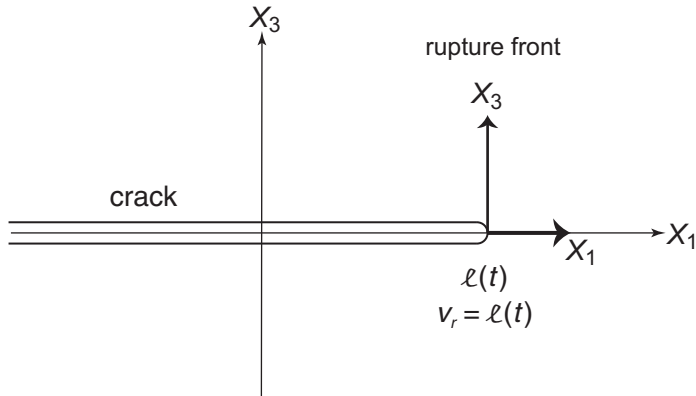


**Figure 10.4.** A crack moving along the axis  $x_1$ . The position of the crack tip is given by  $l(t)$  and the rupture velocity is  $v_r$ .

the solution of the problem by using moving coordinates. Following Ida (1972) and Burridge and Halliday (1977), this problem can be solved using a transformation to steady-state variables (Fig 10.4),

$$x_1 - vt = X_1 \quad \text{and} \quad \sqrt{1 - (v^2/\beta^2)}x_3 = X_3$$

In this coordinate system the equation of motion (10.27) can be rewritten as

$$\frac{\partial^2 u_2}{\partial X_1^2} + \frac{\partial^2 u_2}{\partial X_3^2} = 0 \quad (10.28)$$

In order to obtain (10.28) we used the property that in steadily moving coordinates  $v\partial_{x1} = \partial_t$ . Thus, the solution of the steady-state crack reduces to the solution of Laplace equation (10.28) for a static antiplane crack, for which we have already found a solution, in section 9.1. We will solve equation (10.28) with crack boundary conditions on  $X_3 = 0$ ; letting  $X = X_1$ , they are given by

$$\begin{aligned} u_2(X, 0) &= 0 \quad \text{for } X > 0 \\ \sigma_{23}(X, 0) &= -\Delta\sigma(X) \quad \text{for } X > 0 \end{aligned} \quad (10.29)$$

for the displacement and stress on the fault plane.

The first boundary condition expresses the fact that there is no displacement (and therefore no slip discontinuity) ahead of the crack tip situated at  $X = 0$ . The second boundary condition states that inside the broken crack ( $X < 0$ ) the stress is exactly equal to the stress drop. These boundary conditions define a mixed boundary value problem, which can be solved by a number of methods using complex potentials or integral equations. We adopt here the latter approach. For any slip distribution in the crack  $X < 0$  we can write down a boundary integral that expresses the stress field on the fault in terms of the slip distribution:

$$\sigma_{23}(X, 0) = -\frac{\mu}{2\pi} \sqrt{\frac{1 - v^2}{\beta^2}} P \int_{-\infty}^0 \frac{\partial D_2(\xi)}{\partial \xi} \frac{d\xi}{X - \xi} \quad (10.30)$$

where  $D_2(X) = u_2(X, 0^+) - u_2(X, 0^-)$  is the slip discontinuity inside the crack zone  $X < 0$ . The symbol P indicates that the principal value of the integral should be taken (Ida, 1972, equation 1). Expression (10.30) can be derived from the representation theorem of Burridge and Knopoff (1964). Equation (10.28) can be inverted in order to express the slip distribution as a function of the stress drop inside the crack. This solution is attributed to several creators of fracture dynamics. It is based on a theorem shown by Muskhelishvili (1973). The result (Ida, 1972, equation 10) is

$$\dot{D}_2(X, 0) = -\frac{2\nu}{\pi\mu} \frac{1}{\sqrt{1-\nu^2/\beta^2}} \frac{1}{\sqrt{-X}} \text{P} \int_{-\infty}^0 \frac{\sqrt{-\xi}}{X-\xi} \Delta\sigma(\xi) d\xi \quad \text{for } X < 0 \quad (10.31)$$

This equation expresses the slip rate  $\dot{D}_2$  as a function of the stress drop inside the crack. We remark that, for  $\dot{D}_2$  to be finite, the integral over the stress drop on the right-hand side has to have a finite value.

A companion expression, useful for studying the friction, relates the stress field outside the crack (i.e. for  $X > 0$ ) to the stress inside the crack:

$$\sigma_{23}(X, 0) = -\frac{1}{\pi} \frac{1}{\sqrt{X}} \int_{-\infty}^0 \frac{\sqrt{-\xi}}{X-\xi} \Delta\sigma(\xi) d\xi \quad \text{for } X > 0 \quad (10.32)$$

(Ida 1972, eq. 13). We notice the remarkable similarity between the two expressions (10.31) and (10.32). The slip rate  $\dot{D}_2$  inside the crack and the stress field outside are expressed in terms of the stress drop. We have now the complete solution for the antiplane shear crack propagating along a flat unlimited fault at constant speed. Similar, but much more involved, expressions can be found for in-plane cracks (Fossum and Freund, 1975; Kostrov, 1975).

## Stress intensity factor and energy release rate

Near the crack tip, close to  $X = 0$ , it is possible to simplify equations (10.31) and (10.32) under the condition that the stress drop  $\Delta\sigma$  inside the crack is sufficiently well behaved. We find from (10.32) that the stress near the crack tip for a Mode III fracture has the form

$$\sigma_{23}(X, 0) = \frac{1}{\sqrt{2\pi}} \frac{1}{\sqrt{X}} K_{\text{III}} \quad \text{as } X \rightarrow 0^+ \quad (10.33)$$

and from (10.31) the corresponding slip rate behaves as follows:

$$\dot{D}_2(X, 0) = \frac{1}{\sqrt{2\pi}} \frac{1}{\sqrt{-X}} V_{\text{III}} \quad \text{as } X \rightarrow 0^- \quad (10.34)$$

where

$$V_{\text{III}} = \frac{2\nu}{\mu} \frac{1}{\sqrt{1-\nu^2/\beta^2}} K_{\text{III}} \quad (10.35)$$

is the *velocity intensity factor*.

We notice that (10.33) has the same form as the stress field near the tip of a static crack, (10.5). The main difference is that the stress intensity factor is now

$$K_{\text{III}}(X, 0) = \sqrt{\frac{2}{\pi}} \int_{-\infty}^0 \frac{\Delta\sigma(\xi)}{\sqrt{\xi}} d\xi$$

Equations (10.33) and (10.34) are the most important results of dynamic fracture theory for earthquake studies. They show that both the stress and velocity fields present *inverse square root singularities* at opposite sides of the crack tip. These singularities constitute a fundamental property of a *running crack*; they appear because of the mixed boundary conditions (10.29) on the two sides of the crack tip.

The slip near the tip of the crack can be computed by integrating (10.34):

$$D_2(X, 0) = \frac{2}{\sqrt{2\pi}} V_{\text{III}} \sqrt{-X} \quad \text{as} \quad X \rightarrow 0^- \quad (10.36)$$

This is one of the best-known and characteristic features of fractures: the slip presents a square root discontinuity near the rupture front. For a running crack we can now compute the energy release rate  $G_c$ , that is, the amount of energy absorbed by unit advance of the crack tip. Using an argument of Kostrov and Nikitin (1970) and Palmer and Rice (1973) we find that

$$G_c = \frac{K_{\text{III}}^2}{2\mu\sqrt{1 - v^2/\beta^2}} \quad (10.37)$$

Comparing the expressions for  $G_c$  for static fracture, (10.10), and for dynamic fracture, (10.37), we observe that

$$G_c = G_c^* g(v) \quad (10.38)$$

where  $g(v)$  is a function of the propagating velocity,

$$g(v) = \frac{1}{\sqrt{1 - v^2/\beta^2}} \quad (10.39)$$

and  $G_c^*$  is the *static stress intensity factor* for the same stress field.

These expressions lead to a paradox. When the rupture speed approaches the shear wave speed, the velocity intensity factor  $V_{\text{III}}$ , the slip amplitude and the energy release rate  $G_c$  tend to infinity unless the stress intensity factor  $K_{\text{III}}$  tends to zero as the crack speed reaches its terminal value, which is actually the case for cracks moving in a time-independent stress field as will be shown in section 10.4.

As the fracture propagates, the stress ahead of the fracture front (in the unbroken part) becomes infinite and drops abruptly to zero behind the rupture front (in the broken part). The displacement discontinuity in the broken part behind the front has the typical form; it is proportional to the square root of the distance to the rupture front. These two results are analogous to those found in the static problem. The stress singularity at the rupture front shows that a homogeneous model, that is, one in which the material is continuous and

elastic right ahead of the fracture, can only be a useful approximation to real fractures, where the stress near the crack tip must be limited by plasticity, friction or other local processes.

The expressions for  $G_c$  for the other modes of fracture were given by (Rice, 1980; Kostrov and Das, 1988, p. 80):

$$G_1 = \frac{v \sqrt{1 - v^2/\alpha^2} K_I^2}{2\mu\beta^2 R(v)} \quad (10.40)$$

$$G_2 = \frac{v \sqrt{1 - v^2/\beta^2} K_{II}^2}{2\mu\beta^2 R(v)} \quad (10.41)$$

$$R(v) = 4\sqrt{1 - v^2/\beta^2} \sqrt{1 - v^2/\alpha^2} - (2 - v^2/\beta^2)^2$$

where  $K_I$  and  $K_{II}$  are the stress intensity factors for modes I and II, respectively,  $\alpha$  and  $\beta$  are the P and S wave velocities. For modes I and II, (10.40) and (10.41) imply that the velocity of crack propagation is in the range  $0 < v < v_R$  ( $v_R$ , the Rayleigh wave velocity, is a root of  $R(v) = 0$ ). For mode III, however, (10.37) implies that admissible velocity range is  $0 < v < \beta$ . Generally, fractures give a combination of the three modes. In seismology, earthquakes are produced in general by shear fractures with no crack opening displacement, so that  $K_I = 0$ . We should mention here that under special conditions Mode II cracks can propagate at speeds higher than the shear wave speed (Freund, 1979, Broberg, 1999).

## 10.4. Spontaneous shear-fracture propagation

We will consider now the effect of fracture propagation at variable speeds on the slip inside the fault and on the stress field outside it (Kostrov, 1964, 1966). For simplicity we will consider the two-dimensional problem of an antiplane crack on the plane  $(x_1, x_3)$ . The slip and displacement for such a crack are in the  $x_2$  direction; we will denote the displacement by  $u$  and the slip by  $\Delta u$ . The rupture front extends to infinity in the  $x_2$  direction and propagates in the positive  $x_1 = x$  direction (Fig. 10.5). The position of the fracture edge at a given time is given by  $x_1 = l(t)$ . The instantaneous rupture velocity is  $v = dl/dt$ . Points inside the fracture zone at a given time  $t$  are  $x_1 < l(t)$ ; and outside  $x_1 > l(t)$ . For pure shear motion and displacements in the  $x_2$  direction, the relevant stress components are

$$\sigma_{12} = 2\mu e_{12} = \mu \frac{\partial u}{\partial x_1}$$

$$\sigma_{32} = 2\mu e_{32} = \mu \frac{\partial u}{\partial x_3}$$

In this case the equation of motion (3.4) in the absence of body forces ( $F_i = 0$ ) reduces to the wave equation and can thus be written as

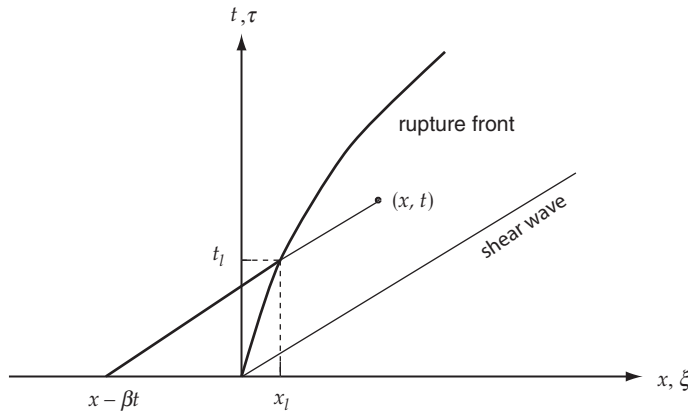


**Figure 10.5.** The rupture front in time and space and the position  $x_l$  of the fracture edge at time  $t_l$ .

$$\frac{1}{\beta^2} \frac{\partial^2 u}{\partial t^2} = \frac{\partial^2 u}{\partial x_1^2} + \frac{\partial^2 u}{\partial x_3^2} \quad (10.42)$$

where  $\beta$  is the shear wave velocity. Equation (10.42) has the form of a wave equation for  $u$  in two spatial dimensions. Its solution, in terms of a Green's function GF, for points along the  $x$  axis ( $x = x_1$ ; see Fig. 9.1) can be written as

$$u(x, t) = \int_{-\infty}^{\infty} dt \int_S GF(x, t, \xi, \tau) \sigma(\xi, \tau) dS \quad (10.43)$$

where  $x$  and  $t$  are the position and time of the point at which we want to determine the displacement and  $\sigma = \sigma_{23}$  is the stress on the fault plane. The displacement  $u(x, t)$  is continuous and equal to zero outside the fault (ahead of the fault edge) and discontinuous and equal to  $\Delta u(x, t)$  inside the fault. The Green's function (GF) for this problem can be found by adding an impulsive force,  $f = \delta(\xi - x)\delta(\tau - t)$ , to equation (10.42). The Green's function for a two-dimensional problem can be written as (Aki and Richard, 1980, p. 885),

$$GF(x, t, \xi, \tau) = \frac{1}{2\pi} \frac{H[(\xi - x) - \beta(\tau - t)]}{\sqrt{(\xi - x)^2 - \beta^2(\tau - t)^2}} \quad (10.44)$$

where  $H$  is the Heaviside step function. Following Kostrov (1966) we solve for the displacement or slip inside the fault,  $\Delta u(x, t)$ , for  $x < l(t)$ , and for the stress ahead of the crack tip ( $x > l(t)$ ). Substituting (10.44) into (10.43), we obtain for points along the  $x$  axis, inside the fault,

$$\Delta u(x, t) = \frac{1}{\pi} \int_S \frac{\sigma(\xi, \tau) d\xi d\tau}{\sqrt{(\xi - x)^2 - \beta^2(\tau - t)^2}} \quad \text{for } x < l(t) \quad (10.45)$$

where  $x$  and  $t$ , are an arbitrary location and time and  $S$  is the surface in the  $(\xi, \tau)$  plane where the square root in the denominator of (10.45) is real. This is called the

dependence domain and it is bounded by the two backward characteristic lines that start from the point  $(x, t)$ .

We impose now on the plane  $x_3 = 0$  the condition  $\Delta u = 0$  for points outside the fault, i.e. for  $x > l(t)$ . For this purpose we split (10.45) into two terms, one that contains the unknown stress  $\sigma = \sigma_{23}$  ahead of the crack tip and another that contains the known stress drop  $\Delta\sigma$  inside the fault:

$$\int_{S_{\text{out}}} \frac{\sigma(\xi, \tau) d\xi d\tau}{\sqrt{(\xi - x)^2 - \beta^2(\tau - t)^2}} = \int_{S_{\text{in}}} \frac{\Delta\sigma(\xi, \tau) d\xi d\tau}{\sqrt{(\xi - x)^2 - \beta^2(\tau - t)^2}} \quad (10.46)$$

where the domains of integration  $S_{\text{in}}$  and  $S_{\text{out}}$  refer respectively to the region where the stress is known inside the crack and the region where it is to be determined by solving (10.46). This is an integral equation for the unknown stress field  $\sigma$  outside the crack in terms of the known one  $\Delta\sigma$  inside. According to Kostrov (1966), we can solve this integral equation using Abel's theorem, so that, for  $x > l(t)$ ,

$$\sigma(x, t) = \frac{1}{\pi \sqrt{x - l(t)}} \int_{x + \beta t}^{l(t)} \frac{\Delta\sigma(\xi, t + (x - \xi)/\beta) \sqrt{l(t) - \xi}}{x - \xi} d\xi \quad (10.47)$$

where  $t$  is the solution of  $\beta t - x = \beta\tau - l(\tau)$ . In this expression the stress becomes infinite at the fracture edge,  $x = l(t)$ , when approached from the outside. This is the same property as we found in the static case. For points outside the crack near the edge,  $x \rightarrow l(t)$ , expression (10.47) can be approximated by

$$\sigma(x, t) \approx \frac{K_{\text{III}}(t)}{\sqrt{2\pi} \sqrt{x - l(t)}} \quad (10.48)$$

where  $K_{\text{III}}(t)$  is the stress intensity factor which we have already found for static Mode III cracks; see (10.10). From (10.47), when  $x \rightarrow l(t)$  we find that  $K_{\text{III}}$  is given by

$$K_{\text{III}}(t) = \sqrt{1 - l(t)/\beta} \int_{l(t) - \beta t}^{l(t)} \frac{\Delta\sigma[\xi, t + (\xi - l(t))/\beta] d\xi}{\sqrt{l(t) - \xi}} \quad (10.49)$$

For the case of constant rupture velocity,  $\dot{l}(t) = v$  and  $l = vt$ , we can write (10.48) in the standard form (10.33):

$$\sigma(x, t) \approx \frac{K_{\text{III}}(t)}{\sqrt{2\pi} \sqrt{x - vt}}$$

where the stress intensity factor is given by

$$K_{\text{III}}(t) = \sqrt{1 - v/\beta} \int_{vt - \beta t}^{vt} \frac{\Delta\sigma[\xi, t + (\xi - vt)/\beta] d\xi}{\sqrt{vt - \xi}} \quad (10.50)$$

It can be seen that the stress intensity factor is an integral of the applied stress weighted by the inverse square root of the distance from the crack tip. We observe now that if the rupture velocity approaches zero then  $K_{\text{III}}$  approaches an integral that we call the equivalent static stress intensity. Thus

$$K_{\text{III}}(t) = \sqrt{1 - v/\beta} K_{\text{III}}^* \quad (10.51)$$

The factor  $\sqrt{1 - v/\beta}$  shows that for an *antiplane fracture* the stress intensity factor decreases to zero as the rupture velocity  $v$  approaches the shear velocity  $\beta$  of the medium. This is the terminal velocity for Mode III cracks. Finally, from (10.50) we observe that, for a sharp crack with square root stress intensity and moving at speed  $v$ , the stress decreases as the velocity increases. For the particular case when the stress drop is constant,  $\Delta\sigma = \Delta\sigma_0$ , independently of  $\zeta$  and  $\tau$ , we obtain for the stress intensity factor

$$K_{\text{III}}(t) = 2\sqrt{1 - v/\beta} \sigma_0 \sqrt{\beta t} \quad (10.52)$$

We can now find the velocity intensity factor for a mode III crack, by inserting (10.51) into (10.35):

$$V_{\text{III}} = \frac{2v}{\mu} \frac{1}{\sqrt{1 - v^2/\beta^2}} K_{\text{III}} = \frac{2v}{\mu} \frac{1}{\sqrt{1 + v/\beta}} K_{\text{III}}^* \quad (10.53)$$

which shows that as the speed increases towards its terminal value, the velocity intensity remains finite while the stress intensity (10.51) decreases to zero.

Finally we can compute the energy release rate from (10.37):

$$G_c = \frac{K_{\text{III}}^2}{2\mu\sqrt{1 - v^2/\beta^2}} = \sqrt{\frac{1 - v/\beta}{1 + v/\beta} \frac{(K_{\text{III}}^*)^2}{2\mu}} \quad (10.54)$$

which is the most frequently used expression for the energy release rate by a fast-moving crack.

At the crack edge ( $x = l(t) = vt$ ) the slip is zero (Fig. 10.6a) and the slip velocity diverges as the inverse square root of the distance from the tip of the fault (Fig. 10.6b). The stress concentration has the same inverse square root behavior ahead of the crack tip as in the static case (Fig. 10.6c). These inverse square root singularities occur because the stress is assumed to drop abruptly immediately behind the rupture front. The appropriate way to remove these singularities is to introduce a *friction law* that has a finite length scale, for instance, slip-weakening or rate-and-state friction, as will be discussed in the next section.

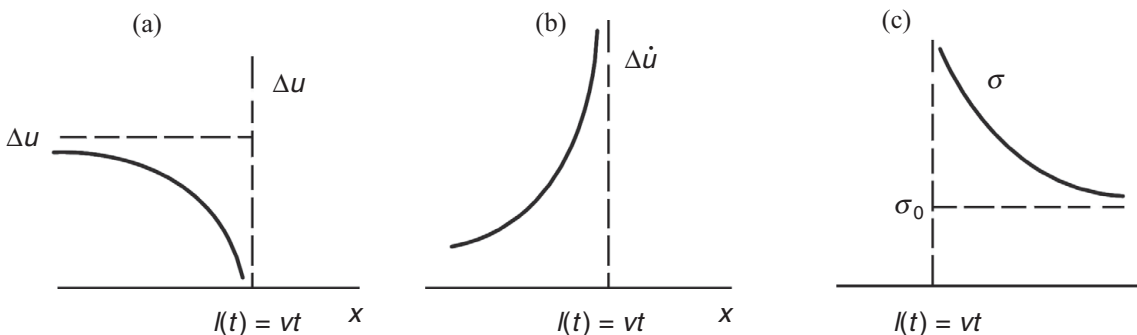


**Figure 10.6.** (a) The slip  $\Delta u$ , (b) the slip velocity  $\Delta \dot{u}$  inside the fault and (c) the stress  $\sigma$  outside the fault, in relation with the rupture front location  $l(t)$ .

The expressions (10.50)–(10.53) show, in a compact form, the behavior near the fracture edge of the stress outside the fault and the slip and slip velocity inside the fault, for an *antiplane propagating crack* with constant rupture velocity. It must be noted that, for homogenous conditions, once the rupture begins it never stops except at infinity. The singularities in the slip velocity and the stress at the fracture edge, as it advances ( $x = vt$ ), are associated with the energy absorbed as the fracture is produced. This corresponds to energy flow from the unbroken part to generate new rupture surface at the fault edge, as we have seen before.

## 10.5. Friction models of fracture

We have considered fracture as a process in which a previously unbroken material breaks under the action of applied stress. An alternative model which can be used to represent the phenomenon of fracture under shear is based on *rock friction*. We consider the shear stress acting on a preexistent fault with its two sides kept locked by the action of friction between them. The sides begin to move when the applied stress overcomes the resistance of friction. Burridge and Knopoff (1967) pioneered the first models in which friction was introduced to explain the behavior of dynamic rupture. Their model was composed of a chain of blocks coupled by horizontal springs sliding on a surface with friction, which delays the motion of the blocks. The blocks move in a stick-slip fashion as explained in section 1.6. In a shear fault the friction stress acts parallel to the surface of the fault and the two sides are kept locked by the *static friction stress*  $\sigma_s$ ,

$$\sigma_s = \mu_s \sigma_n \quad (10.55)$$

where  $\mu_s$  is the coefficient of static friction and  $\sigma_n$  is the normal stress. When the applied stress overcomes the static friction ( $\sigma > \sigma_s$ ), the two sides of the fault begin to move. This is resisted by the *kinematic friction stress*  $\sigma_k$ ,

$$\sigma_k = \mu_k \sigma_n \quad (10.56)$$

where  $\mu_k$  is the coefficient of kinematic or dynamic friction. In the simplest case, when the two sides of the fault begin to slide the friction stress drops from  $\sigma_s$  to  $\sigma_k$  instantly at time  $t = t_0$ , and the displacement between the two sides passes from zero to  $\Delta u$  (Fig. 10.7a). The effective or dynamic stress drop employed in producing the motion is

$$\Delta\sigma_d = \sigma_s - \sigma_k \quad (10.57)$$

Physically this instantaneous drop of friction is not possible; there must be a finite region near the crack tip where stress decreases from  $\sigma_s$  to  $\sigma_k$ . As proposed by Ida (1973) and Palmer and Rice (1973), the displacement  $\Delta u$  inside that zone increases from zero to a critical value  $D_c$  (Fig. 10.7b). At this point the two sides begin to slide, opposed only by the kinematic friction. The energy expended during this time interval is given roughly by  $\frac{1}{2}(\sigma_s - \sigma_k)D_c$ .

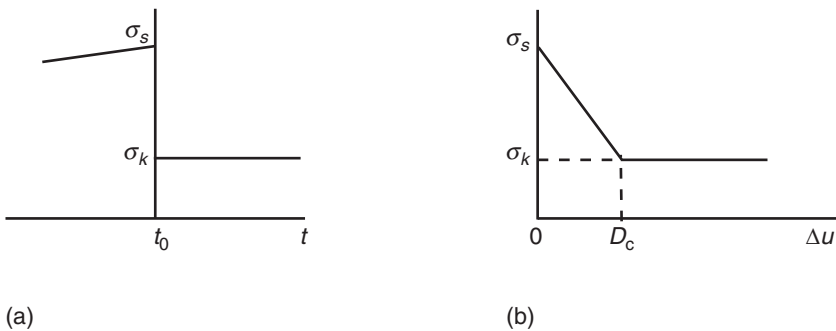


**Figure 10.7.** (a) Instantaneous stress drop from static friction  $\sigma_s$  to kinematic friction  $\sigma_k$ . (b) Dependence of the stress drop on the slip  $\Delta u$ ;  $D_c$  is the critical slip.

We can relate the friction model to the rupture model, identifying the energy spent by the system to initiate motion in the friction model with the energy that it takes to create a new element of rupture surface in the fracture model or driving force  $G_c$  (Ida, 1971; Rice, 1980; Olsen and Madariaga, 2000; Kanamori and Brodsky, 2004), given by

$$G_c = \frac{1}{2}(\sigma_s - \sigma_k)D_c \quad (10.58)$$

Equating this value of  $G_c$  with the strain energy released by a Mode III crack of length  $a$ , defined by (10.9), we obtain the *condition for initiation of fracture* under antiplane stress,

$$\frac{\pi a \sigma^2}{\mu} = D_c \Delta \sigma_d \quad (10.59)$$

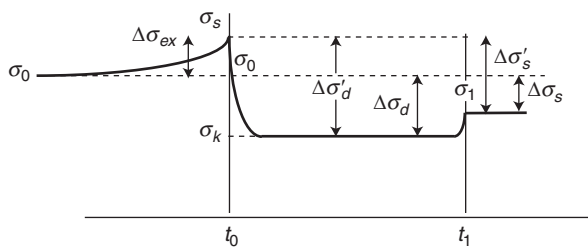
This equation relates, in a simplified way, the applied stress needed to create a new rupture surface in the fracture model to the effective stress drop and critical distance in the friction model. A similar expression can be obtained for mode II.

In the friction model the time process can be briefly summarized, in a simplified form, as follows (section 1.6). The tectonic stress  $\sigma_0$  acting on the fault increases slowly until it reaches a value greater than the static stress  $\sigma_s$ , also called the peak shear stress  $\sigma_u$ , that is, the highest stress the fault may sustain without moving. Once the stress reaches  $\sigma_s$  the fault starts to move, resisted now by the kinematic friction stress  $\sigma_k$  (Fig. 10.8a). The dynamic stress drop available to displace the two sides of the fault is  $\Delta\sigma'_d = \sigma_s - \sigma_k$ . Sometimes this is called the breakdown stress drop (Day, 1982; Mikumo, 1992). The dynamic stress drop, or effective stress in Brune's (1970) terms, is defined as the difference between the tectonic stress acting before rupture starts and the kinematic stress during the motion,  $\Delta\sigma_d = \sigma_0 - \sigma_k$ . The strength excess over the tectonic stress at the beginning of motion, or fracture strength, is defined as  $\Delta\sigma_{ex} = \sigma_s - \sigma_0$ . Then we can write the relation  $\Delta\sigma_d = \Delta\sigma'_d - \Delta\sigma_{ex}$ .

It is important to consider the relation between the tectonic stress  $\sigma_0$ , the stress at which slip begins,  $\sigma_s$ , and the kinematic frictional stress  $\sigma_k$ , which acts when the fault is in motion, and to define the non-dimensional parameter  $S$  (Das and Aki, 1977b):

(a)

Partial stress drop model



(b)

Slip overshoot model

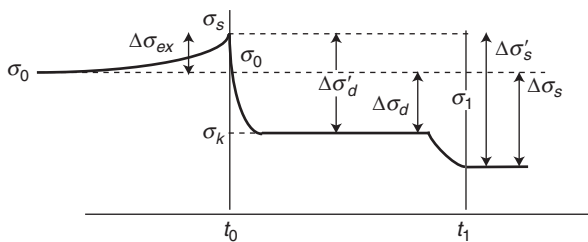


**Figure 10.8.** (a) Dependence of stress on time in the friction model of fracture. Ambient tectonic stress,  $\sigma_0$ ; static or maximum stress before fracture,  $\sigma_s$ ; kinematic stress during fracture,  $\sigma_k$ ; stress at stop of fracture,  $\sigma_1 > \sigma_k$ ; dynamic stress drop,  $\Delta\sigma'_d = \sigma_s - \sigma_k$  or  $\Delta\sigma_d = \sigma_0 - \sigma_k$ ; static stress drop,  $\Delta\sigma_s = \sigma_0 - \sigma_1$  or  $\Delta\sigma'_s = \sigma_s - \sigma_1$ ; stress excess,  $\Delta\sigma_{ex} = \sigma_s - \sigma_0$ . (b) Dependence of stress on time in the friction slip overshoot model of fracture,  $\sigma_1 < \sigma_k$ .

$$S = \frac{\sigma_s - \sigma_0}{\sigma_0 - \sigma_k} \quad (10.60)$$

which can also be written as  $S = \Delta\sigma_{ex}/\Delta\sigma_d$ , the ratio of the fracture strength and the dynamical stress drop. In terms of the breakdown stress drop,  $\Delta\sigma'_d = \sigma_s - \sigma_k$ ,

$$1 + S = \frac{\Delta\sigma'_d}{\Delta\sigma_d} \quad (10.61)$$

This expression represents the ratio of the stress change which occurs across the rupture edge and the stress drop measured from the tectonic stress.

The previous definitions apply while slip is still active. When rupture propagation stops and the fault heals, the stress continues to change in order to remove any transient wave propagation effects. Two situations may occur, as illustrated schematically in Figure 10.8. As assumed by certain authors, notably Brune (1970), the final stress will increase to a value  $\sigma_1 > \sigma_k$  greater than the kinematic friction stress. In this case the final static stress drop is the difference between the initial (0) and final (1) static states, i.e.  $\Delta\sigma_s = \sigma_0 - \sigma_1$  (Fig. 10.8a). In this case the dynamic stress drop or effective stress is larger than the static drop ( $\Delta\sigma'_d > \Delta\sigma_s$  and  $\Delta\sigma_d > \Delta\sigma_s$ ).

In the circular crack model, which we will discuss in the next section, the final stress drop is always less than the kinematic friction, so that  $\Delta\sigma_d < \Delta\sigma_s$ . This situation is illustrated in Figure 10.8b. There is a certain ambiguity in the literature about whether the reference stress level for measuring stress drop is  $\sigma_0$  or  $\sigma_s$ . After the fault is locked, the stress may continue to accumulate until again it reaches a value greater than  $\sigma_s$ , in which case the fault will move again. This situation occurs frequently, when rupture propagates as pulses of slip (Cochard and Madariaga, 1996).

## 10.6. Rupture of an expanding circular fault

In Chapter 9 we discussed in detail the circular earthquake model of Brune (1970). We noticed that Brune assumed that rupture occurs instantaneously along the crack, so the process of fracture was not properly modeled. A more realistic model for a circular earthquake source is a shear fault that expands at *constant subsonic velocity*  $v$  under constant stress conditions (Madariaga, 1976); this model has some features similar to those of the Sato and Hirasawa (1973) model already discussed, in section 7.9. The main difference is that after the initial rupture, the propagation slip will continue on the fault until the arrival of stopping phases emitted by the edges of the fault. In more advanced earthquake models the rupture velocity should be allowed to change as the crack propagates. For many earthquakes, however, the circular crack propagating at constant speed provides a sufficient model for the computation of fundamental properties such as size and stress drop. We now discuss this model in detail.

We consider an infinite homogeneous isotropic elastic medium, for which the equation of motion is given by (3.5) with no body forces ( $\mathbf{F} = 0$ ). The problem is formulated in terms of stresses and particle velocities using the equation of motion and Hooke's law for an isotropic medium (Madariaga, 1976; Virieux and Madariaga, 1982):

$$\rho \frac{\partial v_i}{\partial t} = \frac{\partial \sigma_{ij}}{\partial x_j} \quad (10.62)$$

$$\frac{\partial \sigma_{ij}}{\partial t} = \lambda \frac{\partial v_i}{\partial x_i} \delta_{ij} + \mu \left( \frac{\partial v_i}{\partial x_j} + \frac{\partial v_j}{\partial x_i} \right) \quad (10.63)$$

These equations can be solved numerically by a finite difference method, which discretizes them in a cylindrical or cubic grid. At the time when this model was first studied, computer resources were very limited so that several simplifying assumptions were needed. The most important was that, while the crack was expanding, the slip on the fault was everywhere parallel to the applied stress. Although we know that this approximation is not completely correct, modern studies have shown that the assumption is reasonable (Bizzarri and Cocco, 2003). If the slip on the fault is everywhere parallel to a coordinate axis then the problem (10.62), (10.63) can be reduced to a cylindrical one and solved numerically with a specific numerical technique. Nowadays, however, it is just as simple to use a straightforward cubic grid, as proposed by Madariaga *et al.* (1998) for finite differences.

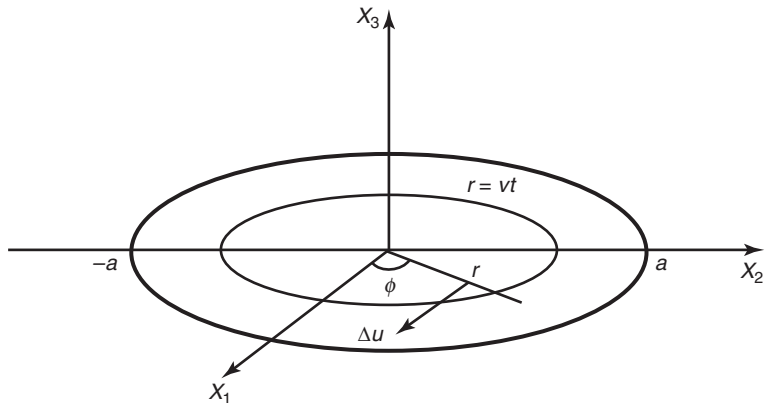


**Figure 10.9.** Growing circular fault model on the  $(x_1, x_2)$  plane. The polar coordinates  $r, \phi$  lie on the fault plane. The velocity of fracture propagation is  $v$ .

Since we are assuming that the material properties and the initial stress field are homogeneous, once the rupture begins to propagate it would continue to propagate without limit. If we want the model fracture to come to a stop when the radius takes a particular value  $a$ , we have to impose this as a boundary condition, that is, the motion stops at  $r = a$  when  $t = a/v$ . Let the fault plane be  $x_3 = 0$ , and let the shear stress act in the  $x_1$  direction ( $\sigma_{13} = \sigma$ ) (Fig. 10.9). The displacements are continuous outside the fault and discontinuous inside it. Before rupture initiation ( $t < 0$ ) the fault is subjected to a uniform state of stress at large distances from the fault. On the fault plane the stress can be separated into a normal component  $\sigma_{33}^0$  and a shear stress  $\sigma_{13}^0 = \sigma^0$ . At  $t = 0$ , the shear stress acting on the fault is considered to be sufficient to initiate rupture. The slip at the fault is resisted by kinematic friction between the two sides of the fault with constant kinematic friction coefficient  $\mu_k$ . Thus, the frictional stress on the fault is

$$\mathbf{T}_f = -\mu_k \sigma_{33}^0 \mathbf{e}_1 = -\sigma_k \mathbf{e}_1 \quad (10.64)$$

where  $\mathbf{e}_1$  is a unit vector in the direction of the slip velocity.

We can simplify the solution of the equations of motion (10.62), (10.63) by remarking that the shear crack problem is symmetric about the fault plane. On the fault plane, the displacements  $u_1$  and  $u_2$  are discontinuous inside the fault and zero outside it. They are thus antisymmetric about the plane  $x_3 = 0$ . The vertical displacement  $u_3$ , however, is symmetric with respect to the plane of the fault  $x_3 = 0$  and is generally different from zero on this plane. The symmetries of the stress field can be derived from the symmetries of displacement, the most important being that the shear stresses  $\sigma_{13}$  and  $\sigma_{23}$  on the fault are both symmetric while the normal stress  $\sigma_{33}$  is antisymmetric. Thus, on the upper half space we impose the following boundary conditions on the fault at  $x_3 = 0$ :

$$\begin{aligned} \sigma_{31} &= \sigma_0 - \sigma_k = \Delta\sigma_d && \text{for } r < vt, \text{ inside the fault} \\ \Delta u &= 0 && \text{for } r > vt, \text{ outside the fault} \end{aligned} \quad (10.65)$$

where  $r^2 = x_1^2 + x_2^2$  and  $\Delta\sigma_d$  is the kinematic stress drop. Brune (1970) used the term “effective stress” for the kinematic stress drop.

While rupture is still proceeding we can solve for the slip rate inside the fault exactly, using the self-similar slip distribution found by Kostrov (1964). The slip inside the fault before rupture stops is given by

$$\Delta u = C(v) \frac{\Delta\sigma_d}{\mu} \sqrt{(vt)^2 - r^2} \quad \text{for } r < vt \quad (10.66)$$

where  $C(v)$  is a constant that depends on the rupture speed. Actually,  $C(v)$  is very close to unity for the entire rupture velocity range from zero to the Rayleigh wave speed. Taking the derivative with respect to time, the slip velocity can be written for constant  $\Delta\sigma_d$  as

$$\Delta \dot{u} = C(v) \frac{\Delta\sigma_d}{\mu} \frac{v^2 t}{\sqrt{(vt)^2 - r^2}} \quad \text{for } r < vt \quad (10.67)$$

which shows that, as in all crack models, just behind the propagating rupture front ( $r = vt$ ) the slip velocity field has an inverse square root singularity.

The rupture in the model is brought to a stop artificially when  $r = a$ . In Fig. 10.10 we show the numerical solution for the slip as a function of position and time obtained for a circular fracture that propagates at 80% of the shear wave speed. The elastic medium has P-wave speed 6.2 km/s, shear wave speed 3.52 km/s and density 2.7 g/cm<sup>3</sup>; thus the rupture speed  $v$  is 2.534 km/s. We assumed that the kinematic (or effective) stress drop  $\Delta\sigma_d$  was 40 MPa. As observed in the figure, once the rupture reaches the final radius  $a = 20$  km, it stops growing instantaneously. This generates three healing phases, which propagate inward from the edge of the crack with velocities  $\alpha$ ,  $\beta$  and  $c_R$ , the Rayleigh wave speed. In Fig. 10.10 the slip distribution is plotted along the  $x_1$  axis. A very similar distribution can

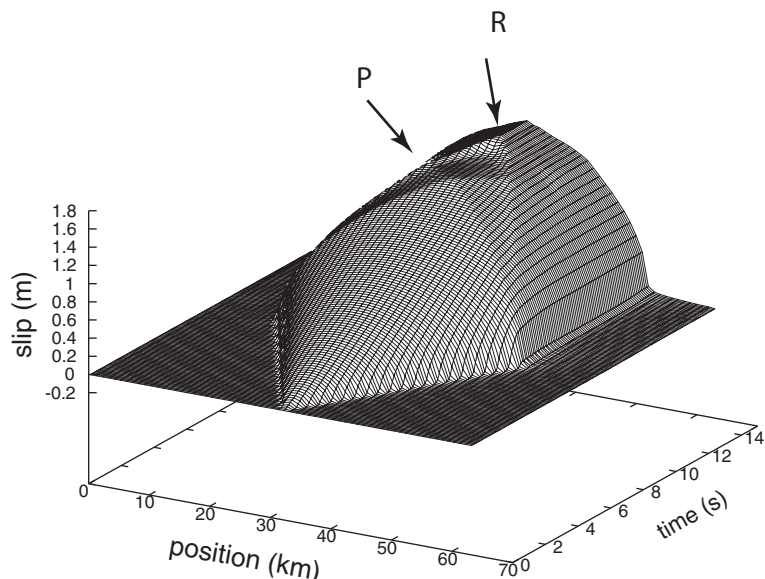


**Figure 10.10.** Numerical solution for the slip as a function of position and time for a circular fracture propagating at 80% of the shear wave speed. The healing phases have P and Rayleigh wave velocities.

be plotted along the  $x_2$  axis; differences appear only after the arrival of the P healing phase because along the  $x_2$  axis the P wave is very weak, almost null. Thus, even for this very simple model, the slip distribution is not cylindrically symmetric on the fault plane once the rupture front interacts with the borders of the fault. Our numerical calculation takes into account these asymmetries.

Once the healing phases reach the center of the fault, the slip reduces rapidly and it ceases completely once the Rayleigh waves have crossed each other. This healing occurs because after the Rayleigh waves the slip rate becomes negative, reversing the sense of the friction. At that point we assume that the slip inside the fault,  $\Delta\dot{u}$ , comes to a halt; we say that the fault heals. At healing, however, the stress field around the fault is still changing and is not in equilibrium with the slip on the fault. For this reason we let the model system evolve for a while and compute the final state of stress inside the fault. It turns out that for a circular shear crack the static stress drop  $\Delta\sigma_s$  is larger than the kinematic stress drop  $\Delta\sigma_d$ , as discussed at the end of section 10.5. The final slip on the fault after rupture stops can be approximated by the static solution for a circular crack,

$$\Delta u_f(r) = \frac{24}{7\pi} \frac{\Delta\sigma_s}{\mu} \sqrt{a^2 - r^2} \quad \text{for } r < a \quad (10.68)$$

Although the final slip, when computed numerically with high resolution, is not exactly of the elliptical shape predicted by the static solution (10.66), equation (10.68) is a good approximation for many purposes. Computations for many simulations at different speeds show that for a circular shear crack the static stress drop  $\Delta\sigma_s$  is always larger than the dynamic stress drop  $\Delta\sigma_d$ . For instance, for a crack running at  $v = 0.9\beta$ , Madariaga (1976) found that  $\Delta\sigma_s = 1.2 \Delta\sigma_d$ . For the example shown in Fig. 10.10, which was computed using a very fine rectangular grid, the final static stress drop is not uniform but is still about 15% higher than the kinematic stress drop (the effective stress in Brune's terms).

Finally, we can compute the seismic moment released by the circular crack model of Fig 10.10: it is  $M_0 = 4.9 \times 10^{19}$  N m, which is equivalent to a moment magnitude  $M_W = 7.0$ .

## Energy balance of the circular shear fault

We mentioned earlier that Brune (1970) made a crude approximation to the radiation from a circular shear crack by equating (see (9.18) and (9.26)) the high-frequency energy flow in the direction perpendicular to the fault to that observed in the far field. The self-similar circular crack model provides a simple way to compute the energy balance. For that purpose we use the *self-similar circular crack model* of Kostrov (1964), in which the crack grows at constant speed  $v$  from an initial point as was assumed in the initial part of our numerical solution; see Fig. 10.9. As shown by Madariaga (1976), the total energy released by fracture growth, called  $E_F$ , is

$$E_F = 2\pi \int_0^a G_c(r, v) r dr$$

where  $G_c(r, v)$  is the energy release rate computed for a self-similar circular crack growing at constant speed  $v$ . Omitting the details, we find that

$$E_F = \frac{\pi}{3} g(v) \frac{\Delta\sigma_d^2}{\mu} a^3 \quad (10.69)$$

where  $g(v)$  is a smoothly varying function of rupture velocity that has a complex expression, given by Madariaga (1976). A misprint in the original expression was corrected by Ide (2002). The rupture-velocity-dependent factor  $g(v)$  decreases monotonically from 1 at  $v = 0$  to 0.1 at  $v = 0.9\beta$ . The most important feature of (10.69) is that the total energy spent in propagation of the circular rupture grows in proportion to the cube of the radius. This is a consequence of the property of the self-similar shear cracks that the stress intensity factor grows in proportion to the square root of the radius of the fault as the radius increases. The quantity  $G_c(r)$ , which is proportional to the square of the stress intensity, grows as the radius as the fault expands. Thus  $G_c$  for a circular shear crack is not a constant but a function of radius.

Recalling from Chapter 9 that the strain energy release by a circular crack with final slip (9.39) is

$$\Delta U = \frac{8}{7} \frac{\Delta\sigma_s^2}{\mu} a^3 \quad (10.70)$$

we observe that strain energy also grows as the cube of the radius but also in proportion to the static stress drop squared. Thus the radiated seismic energy  $E_s = \Delta U - E_F$  also grows as the cube of the source radius.

The obvious consequence of the energy balance is that, for a circular shear crack growing at constant rupture speed, the energy release rate  $\gamma$  is not a material constant as assumed in the Griffith model of fracture. Either faults do not propagate at a constant rupture speed but adjust their speed to produce a constant energy release rate or, simply,  $\gamma$  is not a material property.

## 10.7. Far-field displacements of a dynamic circular fault

Up to this point we have discussed the main features of the slip distribution produced by a propagating circular fault. Now we will consider the relation between the elastic-wave radiation field and the dynamic process at the source. The far-field P or S wave displacements produced by a circular crack in a homogenous medium can be computed from the distribution of slip velocity  $\Delta\dot{u}$ , according to (7.1) and (7.5). For the circular shear crack the far-field P and S waves are given by

$$u^{P,S}(r_i, t) = \frac{\mu}{4\pi\rho c^3} \frac{1}{r} R_c \int_{\Sigma} \Delta\dot{u} \left( r', \phi, t - \frac{r}{a} + \frac{r_i r'_i}{c} \right) dS' \quad (10.71)$$

where the superscripts P, S indicate whether a P or an S wave is being modeled;  $c$  stands for the P or the S wave speed, according to which wave is being computed. As shown in Fig. 10.11,  $r_i$  is the position vector from the origin to the observation point  $(r, \theta, \phi)$  with  $\theta$  the polar angle of the vector  $r_i$  measured from the vertical to the fault;  $\phi$  is its

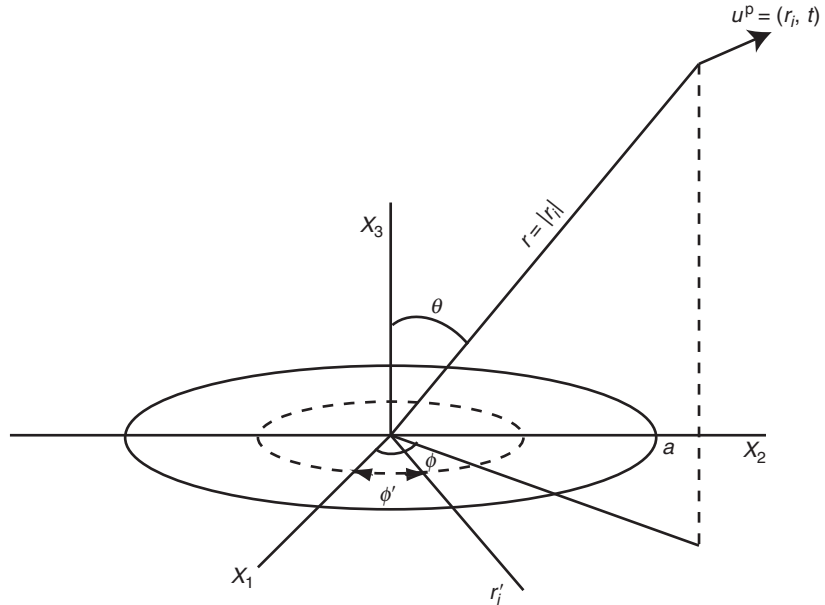


**Figure 10.11.** Displacement  $u^P$  observed at a point P located in the far field of a circular shear crack. The point is located at distance  $r$  from the fault and has an azimuth  $f$  with respect to the  $x_1$  axis.

azimuth and  $r'_i$  is the vector to the point of the fault where the fracture front is located at each time;  $(r', \phi')$  are polar coordinates on the fault plane;  $dS' = r'dr'd\phi'$ ;  $R_c$  is the radiation pattern corresponding to a shear-fault point source at the center of the fault, which we consider to be a function only of the location of the observation point; thus  $R_c = R_c(r, \theta, \phi)$ . The numerical evaluation of (10.71) poses no problem once the slip-rate distribution  $\Delta\dot{u}$  has been computed numerically. For analytical calculations there is a slight difficulty in integrating the slip velocity singularity at the rupture front  $r' = vt$ , but this can be done easily using a change of variables (Kostrov, 1964).

We are also interested in the spectrum of the radiated waves because most studies of earthquake parameters are done using this spectrum. We take the Fourier transform of (10.71) to the frequency domain:

$$U^{P,S}(r_i, \omega) = \frac{1}{4\pi\rho c^3} \frac{1}{r} R_c \Omega_0(\theta, \phi, \omega) e^{-i\omega r/c} \quad (10.72)$$

where  $\theta$  and  $\phi$  are the polar coordinates of a unit vector in the direction of the observer situated at  $r_i$  and  $\Omega_0(\theta, \phi, \omega)$  is the Fourier transform of the seismic moment rate as observed at a unit distance from the source in the direction defined by  $\theta$  and  $\phi$ :

$$\Omega_0(\theta, \phi, \omega) = \mu \int_{\Sigma} \Delta\dot{U}(r', \phi', \omega) \exp(i\omega\tau_c(\theta, \phi, r', \phi')) dS' \quad (10.73)$$

where  $\Delta\dot{U}(r', \phi', \omega)$  is the Fourier transform of  $\Delta\dot{u}(r', \phi', t)$  and the time delay in the exponent is

$$\tau_c(\theta, \phi, r', \phi') = \frac{r'}{c} \cos \theta \sin (\phi - \phi') \quad (10.74)$$

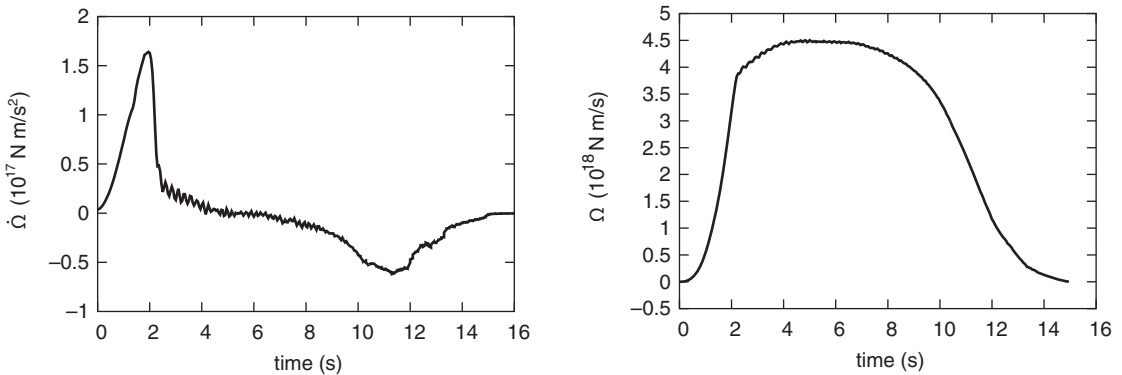


**Figure 10.12.** Far field radiation from a circular shear crack. Left, the velocity pulse and right the displacement pulse observed in the far field of a circular fault of 20 km radius and rupture velocity 2.534 km/s.

Finally, the amplitude of the far-field P and S waves in the frequency domain can be written according to (10.71) as

$$|U^{P,S}(r_i, \omega)| = \frac{1}{4\pi\rho c^3} \frac{1}{r} R_c |\Omega_0(\theta, \phi, \omega)| \quad (10.75)$$

and in the time domain as

$$u^{P,S}(r_i, t) = \frac{1}{4\pi\rho c^3} \frac{1}{r} R_c \Omega_0(\theta, \phi, t - r/\alpha) \quad (10.76)$$

where  $\Omega_0(\theta, \phi, t - r/\alpha)$  is the inverse Fourier transform of  $\Omega_0(\theta, \phi, \omega)$  (10.75). The source time function  $\Omega_0$  contains all the time dependence of the S wave far-field signal and it is often called the *far-field pulse*. Finally, we notice that, as expected, at low frequencies the time delay term in (10.75) tends to 1, and so, from (10.73),

$$\lim_{\omega \rightarrow 0} \Omega_0(\theta, \phi, \omega) = M_0 \quad (10.77)$$

since  $\Delta \dot{U}(r', \phi', 0) = \Delta u(r', \phi', 0)$  and therefore  $\Omega_0(\theta, \phi, 0) = \mu \int_S \Delta \dot{U}(r', \phi', 0) dS' = M_0$ , where  $U$  is the Fourier transform of  $u$ . Thus at low frequencies the source time function is the seismic moment of the source.

We used (10.76) to compute the far-field radiation from the circular crack model shown in Fig. 10.10. The far-field signal  $\Omega_0$  computed for angles  $\theta = 60^\circ$  and  $\phi = 0$  is shown in Figure 10.12. The displacement amplitude is given in units of moment rate and the duration of the signal is about 12 s, which is approximately twice the time for the rupture to cross the fault radius of 20 km at a rupture speed  $v = 2.534$  km/s. In the figure we plot the far-field velocity pulse (left) and the far field displacement pulse (right). These were computed by taking the numerical derivative of the displacement pulses and using a filter to remove the poorly modeled frequencies above 10 Hz.

In Fig. 10.13 we show the spectrum of  $\Omega_0$  for the shear waves corresponding to (10.73). We can distinguish three regions in the far-field displacement spectrum. In the first region, corresponding to low frequencies, the spectrum is flat with a value proportional to the

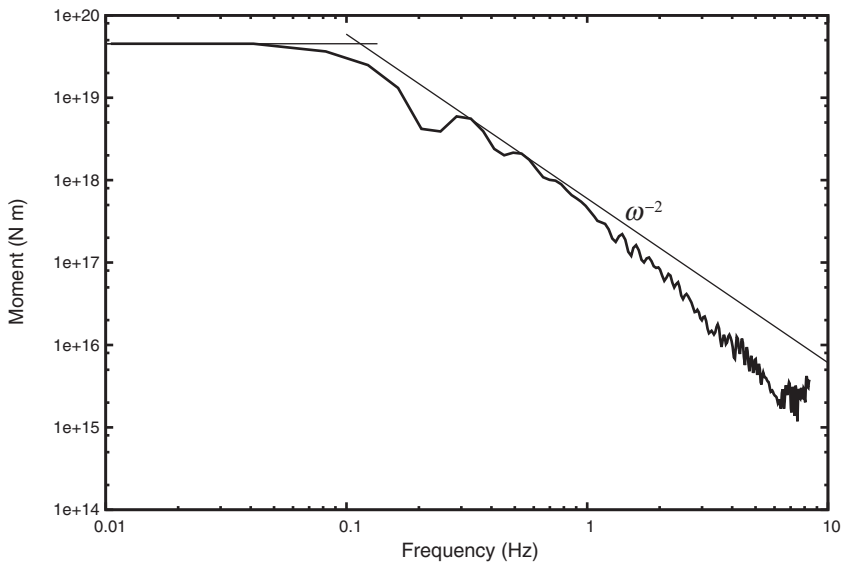


**Figure 10.13.** Far field spectrum of the shear waves radiated by a circular shear crack of radius 20 km and rupture velocity 2.534 km/s. This is the amplitude Fourier spectrum of the far field displacement pulse of [Figure 10.12](#).

seismic moment  $M_0 = 4.9 \times 10^{19}$  N m, as the fault appears as a point source. In the second region, corresponding to intermediate frequencies, the shape of the spectrum is controlled by the size of the fault. In this region the envelope of the spectrum has a decay rate that depends on the azimuth of the observation point. At high frequencies, beyond the corner frequency, we observe that the spectrum decays as  $\omega^{-2}$ . These results are similar to those obtained for Brune's model ([Chapter 9](#)). This high-frequency decay, inversely proportional to the square of the frequency, is controlled by the discontinuities of the seismic pulse, in particular by the *stopping phases*. These are better seen more easily in the time domain velocity pulses shown on the left of [Fig. 10.12](#). As we can see, the most important stopping phase is observed at time  $t_1 = 2$  s, near which the far-field velocity drops substantially in amplitude. This is the first stopping phase and comes from the edge of the fault closest to the observer. The second stopping phase, located at  $t_2 = 11.5$  s, is less remarkable than the first because it is emitted by the far edge of the fault. This stopping phase suffers a phase shift (corresponding to a Hilbert transform) when it crosses the axis of the fault. More details were presented by Madariaga ([1977](#)), who found asymptotic approximations for these stopping phases.

The complicated form of the envelope of the spectrum shown in [Fig. 10.13](#) depends on both  $\theta$  and  $\phi$ . This makes it difficult, in practice, to provide a single value of the corner frequency as a function of radius and rupture velocity. The corner frequency, as we have seen, is usually determined as the intersection of two straight lines fitted to the spectrum in the low- and intermediate-frequency parts. Owing to the complexity of the shape of the spectrum at intermediate and high frequencies even in this simple dynamic model, the value of the corner frequency is not unique. A general property of the amplitude spectra is

that the corner frequencies of P waves are higher than those of S waves. This reflects the fact that in the time domain the S wave pulses are longer than those of the P waves. For  $v = 0.9\beta$  and  $\alpha/\beta = 1.732$ , the values for the corner frequencies of P and S waves are

$$\omega_c^P = 1.16\alpha/a \quad (10.78)$$

$$\omega_c^S = 1.32\beta/a \quad (10.79)$$

The corner frequency for S waves is smaller by a factor 0.56 than the value proposed by Brune ( $\omega_c^S = 2.34\beta / a$ ; see (7.73) and (9.27)) for an instantaneous circular fault. Comparing with the values given by Savage (1972) (section 7.5) for a kinematic model, setting, for a circular fault,  $L = W = a$  and  $\omega_1 = \omega_2$ , we have

$$\omega_c^P = 1.3\alpha/a \quad (10.80)$$

$$\omega_c^S = 3.8\beta/a \quad (10.81)$$

The corner frequency for P waves in this model is similar to that of Savage, but for S waves it is lower by a factor 0.35. Even for this rather simple model of dynamic rupture, the form of the spectra of body waves in the far field is complex, and so average values such as (10.78) or (10.79) should be used with care.

In the previous chapter we studied the propagation of rupture in a material that we assumed to be otherwise unbroken, continuous and perfectly elastic outside the fracture. A direct consequence of these assumptions is that the stress and slip rate present inverse square root singularities as we approach the tip of the crack. These two singularities result from approximations that need to be corrected, since no material of finite strength can sustain infinite stresses or slip at an infinite rate. Moreover, homogeneous models cannot explain the nucleation and arrest of rupture nor the super-shear rupture speeds that sometime occur in earthquake ruptures. To avoid these problems we need to introduce heterogeneities into the medium. These will explain the beginning of the fracture process and its arrest and will also eliminate the singularities of stress and slip rate at the rupture edge.

### 11.1. The cohesive zone

We start with a study of the singularities at the edge of a propagating fracture. In order that the values of the stress and slip rate near the rupture front be finite it is necessary to introduce a transition zone where the material behaves inelastically. Barenblatt (1959a, b, 1962) proposed that the stresses immediately ahead of the fracture front should be regularized by the action of *cohesive forces*, which hold together the material while it is in the process of being broken. These forces are distributed in the vicinity of the rupture front and may be considered as a material property. They are analogous to the attractive or cohesive forces exerted on a liquid molecule by neighboring molecules which explains their name. The transition zone where these forces act is called the *cohesive zone* and its dimension  $d$  must be small compared with the size of the fracture (Fig. 11.1). At the front of the cohesive zone the opposite sides at the edge of the crack are smoothly joined and the stresses remain finite. Let us consider a very simple model of a cohesive zone of length  $d$  where the cohesive stresses are constant and equal to  $\sigma_c$ , which is a compressive stress that opposes the opening of the cohesive zone. Generally, the cohesive stress  $\sigma_c$  is larger than the acting stress  $\sigma_0$  (Fig. 11.1). Behind the cohesive zone, at distance  $d$  from the tip, the tensional stresses drop to zero. Barenblatt (1959b) showed that for the stresses to be finite ahead of the crack tip, the stress intensity produced by the cohesive forces beyond the crack must exactly balance the stress concentration produced by the external load on the crack. The cohesive zone model was subsequently extended for general shapes of the stress distribution inside the cohesive zone by many authors, the best known being Dugdale (1960).

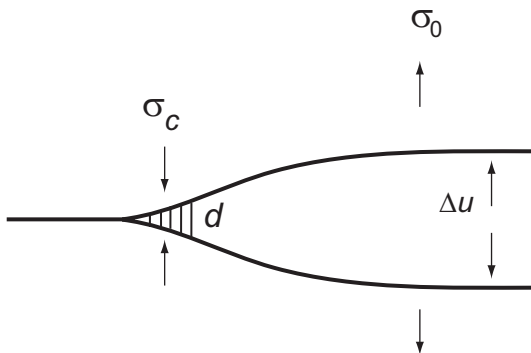


**Figure 11.1.** Cohesive zone model for a Mode I crack. The fault is opened by a tension stress  $\sigma$ . The crack opening displacement is  $\Delta u$ . The cohesive zone of length  $d$  is subjected to a cohesive stress  $\sigma_c$ .

## 11.2. Slip-weakening friction models

For shear cracks in Modes II and III an extension of the idea of a cohesive zone was proposed by Ida (1972, 1973) and, independently for quasistatic faults, by Palmer and Rice (1973). These authors proposed that, as in Barenblatt's model, behind the rupture front there is a *slip-weakening* zone where the friction decreases (weakens) as the slip increases. This reduction in friction depends on the distribution of the slip  $\Delta u$  between the two sides of the fault, so that friction in the slip-weakening zone is a non-linear function of  $\Delta u$ . The slip-weakening model proposes that the shear stress near the fault tip diminishes gradually as slip increases (Rice, 1980), a phenomenon observed in laboratory experiments on friction. The most important feature of the slip-weakening model is the length scale  $d$ , the *cohesive zone length*, which is independent of the load on the crack and thus introduces a smoothing scale into the fracture problem.

For an antiplane fault (Mode III), a simplified slip-weakening model can be described in the following way (Ida, 1973; Andrews, 1976). The elastic medium is subjected to a uniform initial stress  $\sigma_0$ . Rupture begins when the stress near the fracture edge increases to the peak or static friction value  $\sigma_s$  (Fig. 11.2a). Ahead of the rupture front, the stress  $\sigma_0$  is less than the static stress friction; at the rupture front itself the stress is exactly equal to the static friction and then decreases over a distance  $d$ , the width of the slip-weakening zone, until it reaches the dynamic or kinematic friction  $\sigma_k$ . As discussed in section 10.5, seismologists often use the term *strength excess* for the difference between the static friction  $\sigma_s$  and the ambient tectonic stress  $\sigma_0$ , i.e.  $\Delta\sigma_{\text{ex}} = \sigma_s - \sigma_0$  and the term *dynamic stress drop* for the difference between the initial stress and the kinematic friction, i.e.  $\Delta\sigma = \sigma_0 - \sigma_k$ . As shown in Fig. 11.2b, when the slip  $\Delta u$  increases, the friction  $\sigma_c(\Delta u)$  decreases until a critical value  $\Delta u = D_c$  is reached at which  $\sigma_c = \sigma_k$ . The critical value  $D_c$  is usually called the *critical slip-weakening distance*.

Let us consider a steady Mode III rupture that propagates with constant velocity  $v$  in the direction of  $x_1$ . According to section 10.3, the stress field ahead of the rupture front has an inverse square root singularity of intensity  $K_{\text{III}}$ , given by (10.33). We eliminate the

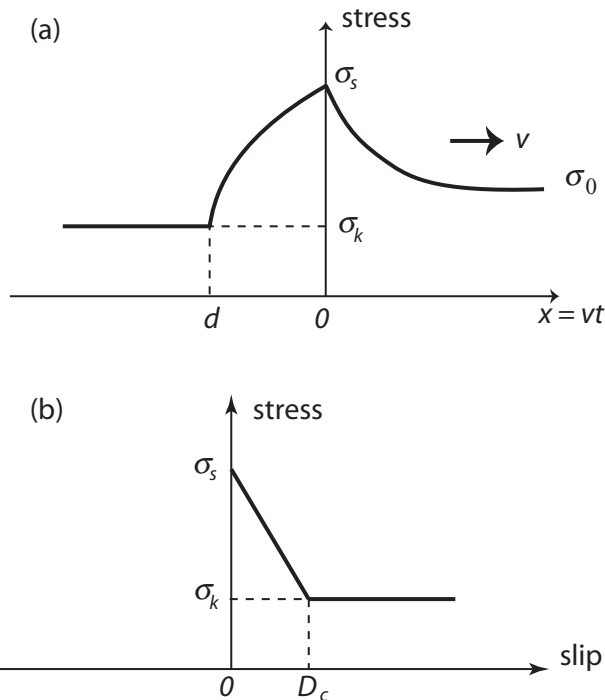


**Figure 11.2.** Slip-weakening zone, as in Ida's model, for a shear fault. (a) Stress distribution as a function of position for a crack moving at constant velocity to the right of the figure. The initial stress is  $\sigma_0$  and the peak friction is  $\sigma_s$ . Behind the slip-weakening zone, the friction drops to the kinematic friction  $\sigma_k$ . (b) The linear slip-weakening friction law plotted as a function of the slip on the fault;  $D_c$  is the critical slip distance and  $d$  is the cohesive zone length

singularity in this stress concentration with an identical but negative stress intensity factor that depends only on the friction stresses  $\sigma_c$  in the slip-weakening zone:

$$K_{III} = \sqrt{\frac{2}{\pi}} \int_{-d}^0 \frac{\sigma_c [\Delta u(\xi)]}{\sqrt{-\xi}} d\xi \quad (11.1)$$

where  $\xi = x_1 - vt$  is a coordinate moving with the rupture front. As the width  $d$  of the cohesive zone is small and limited to the immediate vicinity of the fracture edge, it does not affect the value of the applied stress  $\sigma_0$ . We notice that  $K_{III}$  is computed for stress drops considered as positive. For the right-hand side of (11.1) to match this value of  $K_{III}$ ,  $\sigma_c$  must be a positive stress increase.

Let us now analyse two common slip-weakening models used in the literature. The first is Barenblatt's model, in which the friction inside the cohesive zone is assumed to be uniform and equal to  $\sigma_c$ . The integral (11.1) can be computed exactly, giving

$$K_{III} = 2\sigma_c \sqrt{\frac{2d}{\pi}} \quad (11.2)$$

We can now compute the energy release rate  $G_c$  by substituting the stress intensity (11.2) into equation (10.37) for the energy release rate of a Mode III rupture moving at constant speed  $v$ ; we obtain

$$G_c = \frac{4}{\pi \sqrt{1 - v^2/\beta^2}} \frac{\sigma_c^2 d}{\mu} \quad (11.3)$$

This equation establishes the relation between  $G_c$ ,  $d$ ,  $\sigma_c$  and the rupture speed  $v$ . As we have seen,  $G_c$  is the energy provided from the unbroken part of the material to create a unit new rupture surface. From (11.3) we can now find the relation between the size  $d$  of the slip-weakening zone and the critical slip-weakening distance  $D_c$ . Noting that for the constant friction model  $G_c = \sigma_c D_c$ , we obtain from (11.3) the following relation between  $d$  and  $D_c$ :

$$D_c = \frac{4}{\pi \sqrt{1 - v^2/\beta^2}} \frac{\sigma_c}{\mu} d \quad (11.4)$$

This expression shows that the width  $d$  of the cohesive zone depends linearly on the slip-weakening distance and inversely on the friction stress. It also shows that as the rupture velocity  $v$  increases towards the terminal speed  $\beta$ , the shear wave velocity, the dimension of the slip-weakening zone  $d$  shrinks to zero for finite  $D_c$ . This phenomenon, first noticed by Andrews (1976) for mode II cracks, implies that as the rupture front approaches the terminal speed the expression (11.4) becomes incorrect, because the stress intensity factor near the rupture front decreases to zero. Other terms in the expression for the expansion of stresses near the rupture front become dominant. The constant cohesive stress in Barenblatt's model eliminates the stress concentration at the tip of the crack but it does not solve the problem of infinite stresses, because the stresses near the trailing edge of the slip-weakening zone have logarithmic singularities. For this reason Barenblatt's model cannot be used in the numerical modeling of earthquakes.

The most common friction model used in seismology is the *linear slip-weakening model* proposed by Ida (1972). Unfortunately it is not possible to find simple closed-form expressions for the slip-weakening distance  $d$  in terms of the friction law parameters for this model. If the slip-weakening process is linear as a function of the slip  $\Delta u$ , we can write the friction in the cohesive zone as

$$\sigma_c(\Delta u) = \sigma_s - (\sigma_s - \sigma_k) \frac{\Delta u}{D_c} \quad \text{for } \Delta u < D_c \quad (11.5)$$

For  $\Delta u$  greater than  $D_c$ , the two sides of the fault slide at constant kinematic friction  $\sigma_k$  (Fig. 11.2b). The energy release rate for the linear slip-weakening model is then (10.58)

$$G_c = \frac{1}{2} (\sigma_s - \sigma_k) D_c \quad (11.6)$$

This is the energy necessary to create a unit of fresh fault surface on the two sides of the fault. Inserting (11.5) into (11.1), we get a non-linear integral equation that has to be solved for  $d$  as a function of  $D_c$ . There is no exact solution for this problem, but it is not difficult to solve it numerically with a boundary integral equation technique. The result is

$$D_c = \frac{0.68}{\sqrt{1 - v^2/\beta^2}} \frac{\sigma_c}{\mu} d \quad (11.7)$$

Palmer and Rice (1973) proposed a simpler model which does not correspond to a specific slip-weakening model but can be easily computed numerically. In the model of Palmer and Rice (1973) it is assumed that  $\sigma_c$  varies linearly, between  $\sigma_s$  and  $\sigma_k$ , with the distance  $\xi$  inside the cohesive zone, that is, for  $\xi < d$ . The relation between  $d$  and  $D_c$  is

$$D_c = \frac{16}{9\pi\sqrt{1 - v^2/\beta^2}} \frac{\sigma_c}{\mu} d \quad (11.8)$$

which differs from the value for the constant-friction model (11.3) by a factor of 9/4 (for further details see Rice, 1980, and Palmer and Rice, 1973). The relation (11.8) between the friction parameters is almost the same as that for the linear slip weakening case, (11.7). Thus, we can write the solution for a very general slip-weakening model in the compact form

$$D_c = C_c \frac{1}{\sqrt{1 - v^2/\beta^2}} \frac{\sigma_c}{\mu} d \quad (11.9)$$

where  $C_c$  is a shape factor of order 1 that depends on the details of the slip-weakening friction law. This was verified for the different slip-weakening models considered by Ida (1972).

In Fig. 11.3 we present a numerical solution for the slip-weakening zone of a Mode III crack moving at constant sub-shear speed. The solution was obtained by a two-dimensional

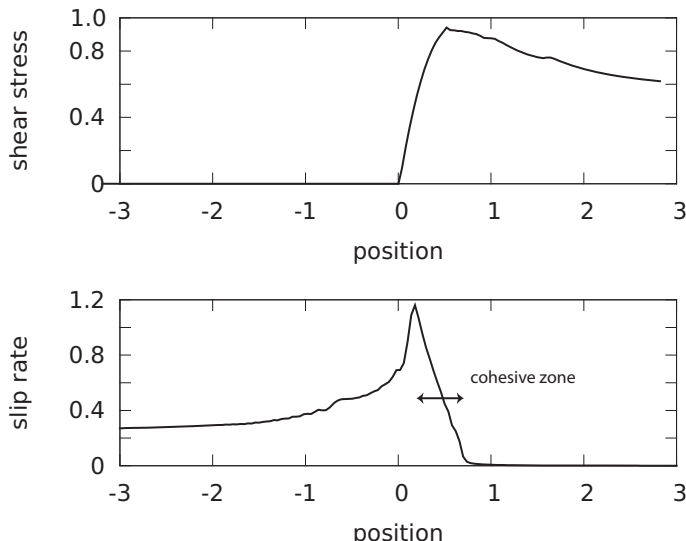


**Figure 11.3.** Slip-weakening zone computed for a Mode III fault moving at constant velocity. Upper panel, the stress field; Lower panel, the corresponding slip-rate field as a function of position in coordinates moving with the rupture front. The slip-weakening zone extends from 0.3 to 0.8 in non-dimensional units.

version of the velocity–stress finite difference method proposed by Virieux and Madariaga (1982). Figure 11.3 was extracted from a rupture simulation that started from a finite asperity and then broke indefinitely at sub-shear velocity. In the upper panel of Fig. 11.3 we show the stress field associated with the rupture front located at the origin in coordinates moving with the rupture front. In the lower panel we show the corresponding slip rate as a function of position. We have used non-dimensional units for the velocity and stress plots in which the position  $\xi$  is normalized by  $\Delta\sigma/(\mu D_c)$ , the stress by  $\Delta\sigma$  and the slip rate by  $\Delta\sigma/(\mu\beta)$ . We observe that the stress is finite at the rupture front  $x = 0$  and so is the slip-rate field. The slip-weakening zone extends over  $0 < x < d$ . We observe also a common property of slip-weakening models: the peak stress occurs at the rupture front while the peak slip rate appears at the trailing edge of the slip-weakening zone (Mikumo *et al.*, 2003).

For a rupture in mode II that propagates with constant velocity  $v$ , the relation, similar to (11.8) and (11.9) is (Aki and Richards, 1980, Chapter 15)

$$D_c = C_c \frac{1}{C(v)} \frac{\sigma_c}{\mu} d \quad (11.10)$$

where

$$C(v) = \frac{(4\beta^2/v^2) \left[ \sqrt{1 - v^2/\alpha^2} \sqrt{1 - v^2/\beta^2} - (1 - v^2/2\beta^2)^2 \right]}{\sqrt{1 - v^2/\beta^2}} \quad (11.11)$$

which, for values of the rupture speed  $v$  close to 0, approaches unity. The expression  $C(v)$  contains the Rayleigh function in the numerator, so it decreases to zero when  $v$  approaches the Rayleigh wave velocity. As a consequence, the terminal velocity for regular sub-shear Mode II faults is the Rayleigh wave speed. As in the Mode III case, (11.10) implies that when the rupture speed approaches the terminal speed the length of the cohesive zone  $d$  shrinks to zero (Andrews, 1976).

## 11.3. Friction laws

As we have seen (section 11.2 and Chapter 10), dynamic rupture on shear faults is entirely controlled by the friction that holds together the two sides of a preexisting fault. As rupture propagates along the fault the coefficient of friction falls from a certain peak or static friction  $\mu_s$  to a lower value, usually called the *kinematic* or *dynamic friction*  $\mu_k$ , at which rapid slip takes place. The static and kinematic friction stresses were shown in Fig. 11.2. The mechanical process by which the friction drops from static to kinematic is the subject of intense research, with significant discrepancies present in what has been reported in the literature (Marone, 1998; Dieterich, 2007; Ohnaka, 2013). In spite of these differences it is important to realize that all these friction laws introduce a well defined length scale that defines the size of the transition zone from static to kinematic friction. In the previous section we discussed the slip-weakening friction law; this is obviously an

oversimplification of reality because aseismic slip occurs well before the peak stress is reached, as can be observed in many subduction zones and on the San Andreas fault. The results of many experiments in the laboratory indicate that friction laws can be expressed as a function of the slip, the slip rate or velocity and a number of state variables, in the general scalar form  $\sigma(\Delta u, \Delta \dot{u}, \theta_n)$ , where it is assumed that the stress and slip are in the same direction. We are not going to provide details about friction here; instead we refer to the recent book by Ohnaka (2013), in which they are discussed in detail.

## Velocity weakening

Laboratory experiments on the friction between metals and other materials indicate that the friction on a fault is strongly affected by the slip rate. The original velocity-weakening model was introduced by Burridge and Knopoff (1967) in their study of the slip stability of interactive blocks pulled by springs. This is a classical model of simple slip instability, often called the BK model. The general phenomenology is that at high velocity the friction decreases inversely with the slip rate. In order to avoid problems at very low velocity this friction law must be regularized at the origin by the introduction of a cut-off speed  $v_c$ . We express the rate-weakening friction law as (Burridge and Knopoff, 1964; Carlson and Langer, 1989; Cochard and Madariaga, 1994):

$$\sigma(\Delta \dot{u}) = \sigma_s \frac{v_c}{v_c + \Delta \dot{u}} + \sigma_k \quad (11.12)$$

where  $\sigma_s$  is the limiting friction when the slip rate decreases to zero and  $v_c$  is a characteristic or critical slip velocity. At high slip rates (large  $\Delta \dot{u}$ ),  $\sigma$  decreases to its kinematic value,  $\sigma_k$ . As  $\Delta \dot{u}$  decreases the friction increases, reaching a static value  $\sigma_1 > \sigma_k$ , and motion stops. These types of friction law allow rupture propagation that is controlled by the initial or tectonic stress field  $\sigma_0$ , the static friction resistance  $\sigma_s$ , the kinematic friction  $\sigma_k$  and the characteristic slip velocity  $v_c$ . A detailed study of the consequences of this friction law for faults surrounded by a continuous homogeneous elastic medium was carried out by Cochard and Madariaga (1994) and Zheng and Rice (1998).

## Velocity-and-slip-weakening models

The slip- and rate-weakening models can be combined in order to include a dependence of friction on both the slip and slip rate. An example of such a friction law was introduced by Cochard and Madariaga (1996), who proposed the following friction model:

$$\begin{aligned} \sigma(\Delta u, \Delta \dot{u}) &= \left[ \sigma_s - (\sigma_s - \sigma_k) \frac{\Delta u}{D_c} \right] && \text{for } \Delta u < D_c \\ \sigma(\Delta u, \Delta \dot{u}) &= \left[ \sigma_s + \sigma_s \frac{v_c}{v_c + \Delta \dot{u}} \right] && \text{for } \Delta u > D_c \end{aligned} \quad (11.13)$$

where  $\sigma_v$  is the shear stress at the critical slip velocity  $v_c$ . In this case the friction diminishes with increasing slip and decreases with increasing slip velocity (displacement-weakening

and velocity-weakening friction). Because of its simplicity, this model has been used by many authors to explain several properties of friction laws. However, in an attempt to explain the properties of repeating earthquakes on the San Andreas fault, Johnson and Nadeau (2005) proposed the law

$$\sigma(\Delta u, \Delta \dot{u}) = - \left[ \sigma_s - (\sigma_s - \sigma_k) \frac{\Delta u}{D_c} + \sigma_v \frac{\Delta \dot{u}}{v_c} \right] \quad (11.14)$$

where as before  $\sigma_v$  is the shear stress at the critical slip velocity  $v_c$ . In this case the friction diminishes with increasing slip and increases with increasing slip velocity (displacement-weakening and velocity-strengthening friction). This friction law produces stable ruptures.

### Rate-and-state friction

To explain unstable slip on a seismic fault, Dieterich (1979a, b) proposed that the friction coefficient  $\mu$  depends logarithmically on the duration of contact of the asperities,  $t$ :

$$\mu = \mu_0 + a \ln(bt + 1) \quad (11.15)$$

In turn,  $t$  was quantified as a certain length scale  $L$  divided by the slip rate,

$$\mu = \mu_0 + a \ln\left(b \frac{L}{V} + 1\right) \quad (11.16)$$

where  $V$  is the slip rate, which we write as  $V$  instead of  $\Delta \dot{u}$  because this is the notation in general use in rock mechanics;  $\mu_0$  is an initial or reference value of the friction coefficient,  $L$  is an experimental slip distance, which depends on the roughness of the fault and  $a$  and  $b$  are constants that should be determined experimentally. In many publications the characteristic length is called  $D_c$ , but this may produce confusion with the slip-weakening distance, which, as we will show, is different from  $L$ . Ruina (1983) proposed a more general formulation of these laws, introducing the concept of internal state variables  $\theta_n$  which represent the memory of previous sliding on the surface or physical conditions such as the surface temperature on the fault. A simplified version of Dieterich's law, with only one internal state variable  $\theta$ , can be written as (Dieterich, 2007; Rubin and Ampuero, 2005) the *rate-and-state-dependent law*

$$\sigma = \sigma_n \left( \mu_0 + a \ln \frac{V}{v_c} + b \ln \frac{v_c \theta}{L} \right) \quad (11.17)$$

where  $\sigma$  is the friction shear stress,  $\sigma_n$  is the normal stress,  $v_c$  is a reference slip rate, at which  $\mu_0$  is measured, and  $L$  is the characteristic sliding distance. As presented in (11.17), the rate-and-state friction law is problematic at low speeds because the friction is undefined for slip velocities  $V$  close to 0, which is unphysical. To regularize (11.17) near  $V = 0$ , several approaches have been followed; these usually consist in adding a constant to the argument of the logarithms in (11.17) (Dieterich, 2007).

The time evolution of the internal variable can be expressed in several ways. The simplest is the so called *slip law*, whose evolution equation is

$$\frac{d\theta}{dt} = -\frac{V\theta}{L} \ln \frac{V\theta}{L} \quad (11.18)$$

In the slip law the state variable has the dimension of time and measures the duration of contact of the asperities. Many authors call (11.18) the *Dieterich–Ruina law*. Ruina proposed another evolution law, which gives very similar results for simple experiments:

$$\frac{d\theta}{dt} = 1 - \frac{V\theta}{L} \quad (11.19)$$

This is the so-called *aging* or *Ruina–Dieterich friction law*. The main difference between these two evolution laws occurs when the slip rate  $V$  becomes much smaller than the ratio  $L/\theta$ . In this limit the slip law (11.18) tends to zero, so that the state variable does not vary when the slip rate tends to zero. At zero nominal slip the state variable does not evolve; this is the reason why (11.18) is called the slip law. For the aging law, however, for small  $V$  we have  $V d\theta/dt = 1$ , so that in this case the state variable is proportional to the lapse time. This is the reason why it is called the aging law.

Under steady-state conditions ( $d\theta/dt = 0$ ) the state variable  $\theta_s$  for both evolution laws is given by

$$\theta_s = -b \ln \frac{V}{v_c} \quad (11.20)$$

The corresponding steady state friction  $\sigma_{ss}$  can be computed by inserting (11.20) into (11.17), giving

$$\sigma_{ss} = \sigma_n \left[ \mu_0 + (a - b) \ln \frac{V}{v_c} \right] \quad (11.21)$$

which means that the steady-state friction stress decreases logarithmically with increasing slip rate if the coefficient  $a < b$ . Under these circumstances the rate-and-state friction is unstable and produces weak (logarithmic) slip-weakening as the velocity increases. For  $a > b$ , on the contrary, the steady-state friction increases with increasing slip rate and the friction law is slip-strengthening, promoting stable slip.

The slip-rate-weakening behavior of the rate-and-state friction laws is illustrated in Fig. 11.4. A mass is moved at constant speed  $V_0$  over a substratum under the action of the Dieterich–Ruina friction law. The stress is at the steady state given by (11.21) with velocity  $V = V_0$ . At distance  $d = 0$ , the sliding speed is suddenly increased to  $V_1$ . The reaction of the interface is immediately to increase the friction by an amount

$$\Delta\sigma = \sigma_n a \ln \frac{V_1}{V_0} \quad (11.22)$$

This is the so-called *direct effect of rate-and-state friction* and is controlled by the parameter  $a$ . As the slider moves at the increased rate over the substratum, (11.18) or (11.19) comes into action, and the state variable  $\theta$  evolves to a new steady state over a distance of the order of  $L$ . As shown in Fig. 11.4, the friction between the slider and the substratum decreases when  $b > a$  until it reaches a new steady state defined by (11.21) with velocity  $V = V_1$ . In Fig. 11.4 we also show a second instantaneous slip-velocity change,

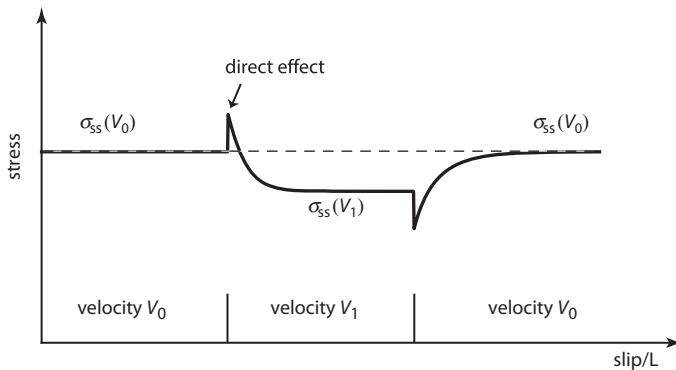


**Figure 11.4.** Rate and state friction law: response to velocity change. Initially the block moves at constant speed  $V_0$  under the control of a rate-and-state friction law. Friction is *steady state* and equal to  $\sigma_{ss}(V_0)$ . The velocity is suddenly increased to  $V_1$  producing an instantaneous increase in friction, the so-called direct effect. For a distance of the order of the characteristic length scale  $L$ , friction decreases to a new steady state value  $\sigma_{ss}(V_1)$ .

this time a decrease in velocity from  $V_1$  to  $V_0$ . Again the friction decreases instantly by the direct effect and then increases for a distance of order  $L$  until it returns to the steady state corresponding to the speed  $V = V_0$ .

Rate-and-state friction has been much used to study the phenomenology of seismicity, slow seismic events, earthquake nucleation and simple earthquakes in two dimensions, using a variety of numerical techniques. There are unfortunately no simple analytical solutions, and numerical simulations with rate-and-state parameters drawn from laboratory examples are very difficult to carry out at the scale of real earthquakes. The earlier attempts to model rupture propagation were due to Okubo (1989), who found that ruptures under rate-and-state friction were very similar to those computed using slip-weakening friction laws. Using more accurate numerical techniques, Cocco and Bizzari (2002) showed that a fault under rate-and-state friction, with the aging law for the evolution for state, produces a rupture front that looks almost like a linear slip-weakening, with a critical distance  $D_c$  that is roughly given by

$$D_c = L \ln(V_{\max}/V_{\min}) \quad (11.23)$$

where  $V_{\max}$  is the maximum slip rate reached during the dynamic rupture; this is of the order of 1 m/s;  $V_{\min}$ , however, is the slip rate at the peak frictional stress (the static friction of slip-weakening models), which is usually of the order of a few  $\mu\text{m/s}$  for typical values of the parameters  $a$ ,  $b$  and  $L$ . Thus for most models  $D_c$  is of the order of 10 to 20 times the intrinsic length  $L$ .

In Fig. 11.5 we show the steady-state behavior of the combined rate-and-state and aging friction laws (see (11.17) and (11.19)). We computed the propagation of a Mode III rupture controlled by rate-and-state friction using a staggered-grid finite difference method (Virieux and Madariaga, 1982). Rupture was initiated from a small asperity and then we let the rupture run for a significant distance until it reached a steady state at a speed of about 90% of the shear wave velocity. We then computed the stress and slip distributions across the

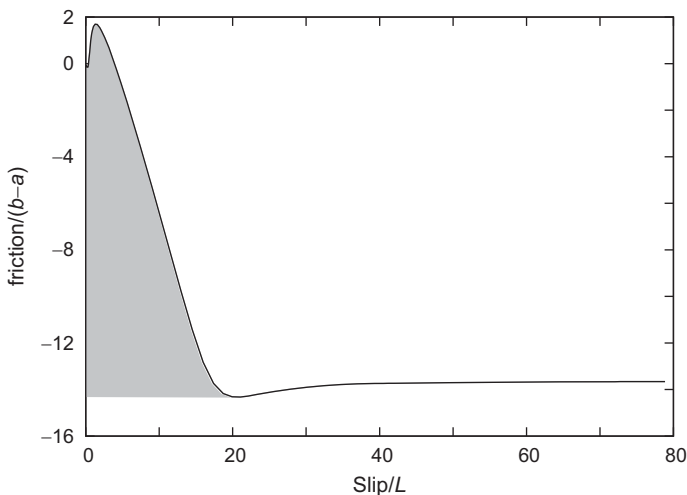


**Figure 11.5.** Slip-weakening behavior of the rate-and-state friction law at high velocities. The figure shows the decrease in stress as a function of slip on the fault near the rupture front.

fault at that time. Plotting stress against slip we found the result shown in Fig. 11.5; here the stress is normalized by  $b - a$  and the slip is normalized by the characteristic length  $L$ . The similarity between this curve and that of Ida's linear slip-weakening model (see Fig. 11.2) is striking. We will not go into more detail here, but it is not difficult to show that at high speeds the state-dependent term in the friction law (11.17) actually becomes a slip-weakening term (Dieterich, 2007). For the aging law, the stress drop is about ten times  $b - a$ , and the slip-weakening distance is about 10 times the characteristic length  $L$ .

The main problem with classical rate-and-state friction in earthquake dynamics is that the experimental values of the parameters  $a$ ,  $b$  are typically of the order of 0.01 to 0.02 and  $L$  is of the order of a few microns. For typical values of  $b - a = 0.01$  and for values of the normal stress  $\sigma_n$  of the order of 100 MPa, the friction drops are of the order of 1%–10% of the low-speed friction. Thus the stress drops are of the order of 1 MPa for 100 MPa effective compressional stress. This amounts to a very small reduction of friction during the dynamic phase of rupture, whereas in fact there is ample evidence that at high slip rates the friction decreases to about 0.1 (Tsutsumi and Miyamoto, 1997). An even more serious problem is that the experimental values of  $L$  are very small. For  $L$  a few microns,  $D_c$  (see (11.23)), according to Cocco and Bizzarri (2002), will be only a fraction of a millimeter. This is far smaller than the values of  $D_c \sim 7$ , estimated for earthquakes of  $M_W$  which are of the order of a few centimeters. A frequent solution is to assume that  $L$  is of the order of a few millimeters in actual earthquake faults, but as far as we know there is little experimental evidence for this change in scale.

### Rate weakening revisited

It is not clear whether rate-and-state friction laws with logarithmic velocity sensitivity (11.22) are appropriate to model friction at the large slip rates, of the order of 1 m/s,

observed in natural earthquakes. A large number of friction experiments by Tsutsumi and Miyamoto (1997), Han *et al.* (2007), Mizoguchi *et al.* (2007), Di Toro *et al.* (2011), Goldsby and Tullis (2011) and many others indicate that at high velocities of the order of m/s and long slip distances, of the order of a meters or so, the friction drops to much lower values than those predicted by rate-and-state friction using the values of  $a$ ,  $b$  and  $L$  measured in rock mechanics experiments. Some authors refer to this as enhanced rate dependence, but it is actually very similar to the initial proposition by Burridge and Knopoff (1967) that at high speeds the friction is inversely proportional to the slip rate (11.12). Whether the friction decreases inversely with the slip rate or at a certain power of the slip rate is important for the massive production of melt and phase transformation that occurs while faults are slipping at seismic velocities. Several recent attempts to include more complex effects in friction have been reported in the literature; for instance, Noda *et al.* (2009) and Brantut and Rice (2011) considered the effects of pore-fluid pressurization on cracks propagating at constant velocity.

Currently, although some authors prefer to use rate-and-state friction for modeling the dynamic stage of earthquakes, many others consider that the uncertainties in the parameters  $a$ ,  $b$  and  $L$  do not justify using such a complex frictional framework for earthquake dynamics. The advantage of the rate-and-state formulation, however, is that it contains a natural way to take into account simultaneously the fast (earthquake) and slow (creep) regimes of a seismogenic fault (Kaneko *et al.*, 2010). Recently Barbot *et al.* (2012) used the rate-and-state framework to model the seismicity of the Parkfield region in California, but they did not use laboratory-derived values for the characteristic length  $L$ ; rather, they used  $L$  in the 4 to 8 mm range so that the equivalent value of  $D_c$  was in the cm range, which agrees with the values obtained by inversion from seismic observations. The rate-and-state framework has the clear advantage that unbreakable barriers, regions that cannot break during an earthquake, can be modeled as rate-strengthening areas where  $a - b > 0$ .

## 11.4. Determination of $G_c$ from seismic data

---

Dynamic earthquake modeling is possible only if we have appropriate estimates of the parameters that constitute the friction law. As we have seen, in practice, at high rupture speeds all the common friction laws reduce to slightly modified versions of the slip-weakening friction of Ida (1972). There have been several independent attempts to determine the friction law parameters from seismic observations but it is still a very difficult problem, fraught with problems of resolution and trade-offs between the parameters. The current consensus is that it is possible to make approximate estimations of the energy release rate  $G_c$  but that individual values of the static friction and the slip-weakening distance cannot be determined with accuracy, owing to the limited frequency band used in inversions (e.g. Guatteri and Spudich, 2000; Tinti *et al.*, 2005a).

The earliest estimates of the energy release rate  $G_c$  were made in the 1970s using a method proposed by Husseini *et al.* (1975), which consists of determining the energy release rate required to stop the propagation of a seismic rupture. Aki (1979) used this

method to estimate the fracture energy required to stop the 1966 Parkfield earthquake near the town of Cholame on the San Andreas fault in Central California. He obtained a value of  $G_c = 80 \text{ MJ/m}^2$ , which was several orders of magnitude larger than the values measured in the laboratory. Brace and Walsh (1962) had reported values of  $G_c$  of the order of 0.1 to 10 kJ/m<sup>2</sup>. Aki (1979) attributed this very large value the absorption of energy over a large zone surrounding the rupture front, not just over a thin film covering the fault surface. Although this method can be used to obtain rough values of  $G_c$  it proved to be insufficiently accurate and was soon replaced by another approach, pioneered by Mikumo and colleagues, who used kinematic inversions to generate dynamic models of earthquakes. This approach was used by Fukuyama and Mikumo (1993) to model the Izu Oshima earthquake near the Izu peninsula in Honshu, Japan. From the kinematic inversion they could determine the stress excess  $\sigma_s - \sigma_k$  and the average stress drop  $\sigma_0 - \sigma_k$  for this event (see the definitions in section 10.5). Their numerical simulations of the earthquake were not accurate enough to estimate  $D_c$ . A similar method was used by Olsen *et al.* (1997) to estimate the energy release rate at different spots on the fault of the Landers earthquake of 1992; they found values of  $G_c = 9.6 \text{ MJ/m}^2$  for this  $M_W = 7.3$  event. This method led to dynamic inversion, as will be discussed in more detail in Chapter 12.

In 1997, Bouchon (1997) and Ide and Takeo (1997) used kinematic inversions to determine the stress field on the fault for several earthquakes in California and Japan. Although kinematic inversions involve several assumptions that are not always compatible with rupture dynamics, the inverted stress and slip fields provide a way to determine all the parameters of the friction law. Ide and Takeo (1997) found that the peak stress drop  $\sigma_s - \sigma_k$  of the Kobe earthquake was variable, with larger values at depth, but on the average it was about 4 MPa while  $D_c$  was of the order of 0.8 to 1 m, so that the energy release rate was about 2 MJ/m<sup>2</sup>. Thus two very different techniques used for two shallow strike-slip earthquakes of similar magnitude gave similar values of the energy release rate. The method of Ide and Takeo has been much improved and several limitations have been identified (Guatteri and Spudich, 2000, Tinti *et al.*, 2005a, b, 2009). Foremost is the fact that kinematic inversions are performed using a limited frequency band so that neither  $d$  (the size of the cohesive zone) nor  $D_c$  can be accurately resolved. This problem is of course intrinsic to seismological observations; small length scales are difficult to resolve with seismic waves because of scattering due to the heterogeneity of the earth at frequencies above 1 Hz. Tinti *et al.* (2005a, b) computed the energy release rate  $G_c$  for a large number of events, reaching the conclusion that  $G_c$  scales with moment to the power 1/3. The energy release rates they found for the Landers and Kobe earthquakes were essentially the same as those found by Olsen *et al.* (1997) and Ide and Takeo (1997), respectively.

Another technique that can be used to estimate the energy release rate is energy balance. We saw in section 10.6 that according to a rough energy balance for a seismic source, the available energy release  $\Delta U$  is equal to the sum of the radiated energy  $E_s$  and the energy spent in fracture growth,  $E_F$ . Assuming that the latter is constant over the fault we can estimate  $G_c$  from

$$G_c = \frac{E_F}{S} = \frac{\Delta U - E_s}{S} \quad (11.24)$$

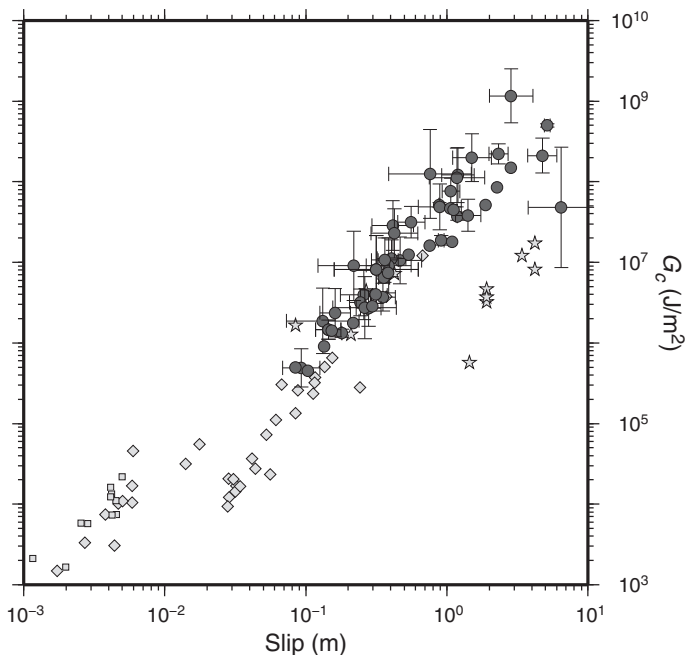


**Figure 11.6.** Energy release rate  $G_c$  as a function of slip determined for a selected set of earthquakes modeled with Brune's omega-squared spectrum. Data: stars, triangles and diamonds from Abercrombie and Rice (2005), inverted triangles from Ide *et al.* (2003) and circles with error bars from Lancieri *et al.* (2012).

where  $S$  is the source area. Since using (10.70)  $\Delta U$  can be computed from the static slip distribution, which is one of the best-determined source properties, the main uncertainty in (11.24) is the radiated energy. Expression (11.24) was used by Abercrombie and Rice (2005) and Lancieri *et al.* (2012) to estimate  $G_c$  for many earthquakes that had been studied using Brune's model (section 10.6). Figure 11.6 shows a review of the results recently obtained by these authors and by Ide *et al.* (2003). There is clearly a scaling of the energy release rate with the slip of the earthquake, but the method has many trade-offs and large uncertainties, especially for the estimation of the radiated energy. Methods used to determine  $G_c$  are improving constantly, and dynamic inversion should provide even better results given an appropriate estimation of the uncertainties.

In spite of many technical problems in estimating the radiated energy, if (11.24) is correct then it leads to a very fundamental property of earthquakes. Since both  $\Delta U$  and  $E_s$  scale with the cube of the fault radius, and  $S$  scales with the square, then  $G_c$  must be proportional to the radius of the fault. Thus, a general energy balance requires that  $G_c$  is a function of the size of the earthquake. The physical reason why  $G_c$  is not the same for all earthquakes is that larger earthquakes produce significant inelastic deformation in a much larger zone around the rupture front than do smaller ones (see Aki, 1979, and Andrews, 1976). This conclusion is inescapable if we accept the energy balance implied by (11.24).

## 11.5. Nucleation and arrest of rupture

The friction models presented in the previous sections explain the transition from static friction at the edge of a propagating fault to kinematic friction inside the fault. As we will see, the cohesive zone (Kostrov and Das, 1988, pp. 61–62) plays a fundamental role in the initiation of rupture. To initiate rupture it is necessary that a very small *initial stress bump* or *asperity* is present in the fault interface. Aseismic slip develops in the bump, transferring stresses to its surroundings. This bump region must be of a size such that the fault produces just enough strain energy release to initiate rupture (Yamashita and Ohnaka, 1991). If we apply the slip-weakening model to the breakdown zone, slip starts at a point where the stress reaches the peak or static friction level. At that point slip begins and friction decreases, following the slip-weakening friction model. Initially the stress drop is small but it transfers stresses outside the slipping area that contribute to spreading the fault even further. This process is initially stable and continues to progress slowly until the friction at some point in the fault has dropped to the kinematic value (Fig. 11.2b). This indicates that unstable seismic slip is preceded by stable slip in a limited area of dimension  $L_c$ , which is usually called the nucleation zone. Thus the stable slip which precedes seismic unstable dynamic rupture is a manifestation of the nucleation process.

The stable initial nucleation zone eventually becomes large enough that, at some point near its center, the friction drops to its kinematic value  $\sigma_k$ . This is followed by an accelerating progression of the breakdown zone up to a critical state when the slip reaches the critical value  $D_c$ , beyond which dynamic instability occurs and rupture starts to produce seismic waves (Ohnaka, 2013). From that point the two sides of the fault slide, resisted only by the kinematic friction (or dynamic friction)  $\sigma_k$ . The nucleation zone is limited to the area where rupture proceeds stably and quasistatically and extends from the point where the first failure occurs to the region beyond which unstable rupture begins. We can write the relation (11.10) between  $D_c$  and the initial size  $L_c$  of a shear crack where the stress is everywhere at the peak  $\sigma_s$ , i.e. at very low rupture speeds  $v \sim 0$ , in the form

$$\frac{D_c}{L_c} = C_c \frac{\Delta\sigma_d}{\mu} \quad (11.25)$$

where  $C_c$  is a constant that depends on the details of the slip-weakening. According to Ohnaka (2000), the moment of an earthquake is related to both the critical slip-weakening distance  $D_c$  and the size of the nucleation zone  $L_c$ , in the form  $M_0 \approx D_c^3$  and  $M_0 \approx L_c^3$ . This means that a large earthquake requires for its inception a large nucleation zone and a large critical slip. Thus small and large earthquakes would differ from their very onset. This hypothesis is used in earthquake early warning systems.

Actually, most earthquakes nucleate at average stresses that are below the peak stress  $\sigma_s$ . In that case the size of the nucleation zone can be estimated by the critical crack length  $L_c$  at which the available energy released equals the energy absorbed by the creation of new fracture (Andrews, 1976). For a two-dimensional Mode II crack we have

$$L_c = \frac{8(\lambda + \mu)}{\pi(\lambda + 2\mu)} \frac{\mu G_c}{(\sigma_0 - \sigma_k)^2} \quad (11.26)$$

For a Mode III antiplane crack under linear slip-weakening we can substitute  $G_c$  from (11.6) to get

$$L_c = 4 \frac{\mu(\sigma_s - \sigma_k)D_c}{(\sigma_0 - \sigma_k)^2} \quad (11.27)$$

A similar expression was obtained by Day (1982) for the critical radius  $R_c$  in a circular crack:

$$R_c = \frac{7\pi\mu(\sigma_s - \sigma_k)D_c}{24(\sigma_0 - \sigma_k)^2} \quad (11.28)$$

Dynamic rupture will initiate if stress is concentrated, and reaches the value of the breaking strength  $\sigma_s$ , in a small zone and if a large stress drop  $\Delta\sigma_d$  occurs there.

The models discussed above are for specific geometries. A more general approach was proposed by Madariaga and Olsen (2000, 2002), who remarked that all the previous conditions of rupture initiation could be expressed by a single parameter  $\kappa$  defined by

$$\kappa = \frac{(\sigma_0 - \sigma_k)^2 R}{\mu(\sigma_s - \sigma_k)D_c} \quad (11.29)$$

where  $R$  is the radius of the minimum asperity size or other characteristic length of the nucleation zone. In fact  $\kappa$  is a measure of the ratio of the available strain energy  $\Delta U$  released by the nucleation zone (10.5) and the energy release rate  $G_c$  required by the slip-weakening model (11.6); that is, it represents the ratio of the elastic potential energy in the fault region and the energy needed to create new rupture surface. In general  $\Delta U$  and  $G_c$  can be written as

$$\Delta U = \frac{1}{2} \Delta \bar{u} \Delta \sigma \quad (11.30)$$

$$G_c = \frac{1}{2} (\sigma_s - \sigma_k) D_c \quad (11.31)$$

where  $\Delta \bar{u}$  is the average slip on the fault,  $\Delta \sigma$  is the dynamic stress drop,  $\sigma_s$  is the static friction or peak stress and  $D_c$  is the slip weakening distance. Then, dropping numerical constants,  $\kappa$  is given by

$$\kappa = \frac{\Delta U}{G_c} = \frac{\Delta \bar{u} \Delta \sigma_d}{\sigma_s D_c} = \frac{\Delta \sigma_d^2 a}{\mu(\sigma_s - \sigma_k) D_c} \quad (11.32)$$

where we have used equation (10.9) for  $\Delta \bar{u}$  and  $a$  is the radius of the initial asperity. The parameter  $\kappa$  has a critical value  $\kappa_c$  such that for  $\kappa > \kappa_c$  rupture grows indefinitely but for  $\kappa < \kappa_c$  rupture stops and does not grow beyond the break of the initial asperity. The critical value  $\kappa_c$  depends on the geometry of the model but is of the order of unity.

The phenomenology of rupture nucleation in faults controlled by the rate-and-state model of friction is much richer because slip occurs at very low rates and depends on the past history of the fault. A simple approach to nucleation is to study the instability of a block-and-spring model with spring stiffness  $k$ . Rice and Ruina (1983) found that the block slider becomes unstable for values of the spring stiffness smaller than a critical value defined by

$$k_c = \sigma_n \frac{b - a}{L} \quad (11.33)$$

The critical stiffness is positive only for  $a < b$ , i.e. in the unstable regime. For stiffness  $k < k_c$  the slider enters a limit cycle that is controlled by the friction law but also by the mass of the slider. The critical stiffness can be related to the initial size of the asperity needed to start rupture by noting that, roughly speaking,  $k$  is inversely proportional to the size of the initial asperity. More accurate values for the initiation of rupture under rate-and-state friction were derived by Rice *et al.* (2001), who found that in a fault that has a broad spectrum of heterogeneities there is a critical wavelength. The critical wave number ( $\kappa = 2\pi/\lambda$ ) is just  $k_c$  as defined above, (11.33), with a modification that depends on the initial slip rate but which is rather small. These very simple models are needed to understand the initiation of rupture under rate-and-state friction. It is important to emphasize that under rate-and-state friction the interface has a memory of previous slow and fast slip events, changes in state, etc. and that nucleation has many aspects that a simple initially uniform model of state variable may not be able to capture. There has been extensive discussion of rupture nucleation under rate and state friction; see Dieterich (1992), Ampuero and Rubin (2008) and Rubin and Ampuero (2005).

An alternative model of the nucleation of fracture is that of the *coalescence of arrays of cascading micro-earthquakes*. This model presupposes the preexistence of microcracks, generally oriented obliquely to the compressional stresses in some region of the medium, before the beginning of faulting (Fig. 11.7). These microcracks interact and coalesce among themselves producing an initial fracture along a surface, which propagates into the unfaulted medium by inducing microcrack growth at its front (Reches and Lockner, 1994). Microcracking is usually attributed to the inhomogeneous structure of brittle rocks. From this point of view, a fault cannot be considered as an isolated individual element, but as a fault zone, that is, a zone of increased crack density with respect to the adjacent medium (Kame and Yamashita, 1997). The resulting propagating fracture can be considered as a single crack with dimensions larger than those of the preexisting microcracks in the medium.

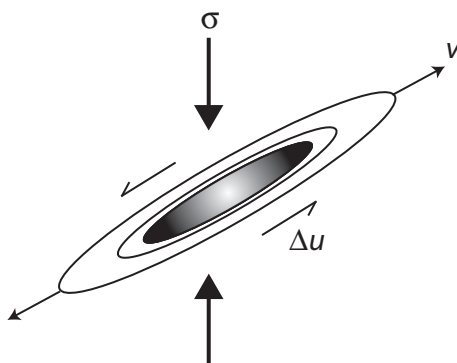


**Figure 11.7.** A small crack (shaded area) oriented at an angle with respect to the prevailing stress field.

## Seismological models of nucleation

The previous models are mechanical models for the transition from the quasistatic initiation of fracture to unstable propagation. Seismologists often observe foreshocks and long initial phases for many earthquakes and, since high-dynamic-range seismometers and accelerometers have become common, these observations have also become common. Ellsworth and Beroza (1995) reported evidence that the initial instants of nucleation of different earthquakes had certain common features. They proposed two possible models explaining the origin of these foreshocks, the *pre-slip patch* model and the *cascade* model, illustrated in Fig. 11.8. In the first model a nucleation zone undergoes very slow slip in preparation for a future earthquake; in the cascade model, a series of interacting events occur in a cascade of increasing-size events. At present, observations do not seem to favor either model but, probably, a mixture of the two. The main problem here is that the observation of a slow pre-slip phase will still be very difficult in spite of the improvements in GPS and other geodetic techniques that are expected in the near future. There is an additional seismological problem, in that detecting smaller events is a difficult task in many areas around the world. Bouchon *et al.* (2012) recently examined evidence for the systematic presence of foreshocks, for interpolate events larger than  $M_W = 6$  in California, Japan and Alsaka. Their conclusion was that close to 70% of these earthquakes presented precursors with variable time advances with respect to their main

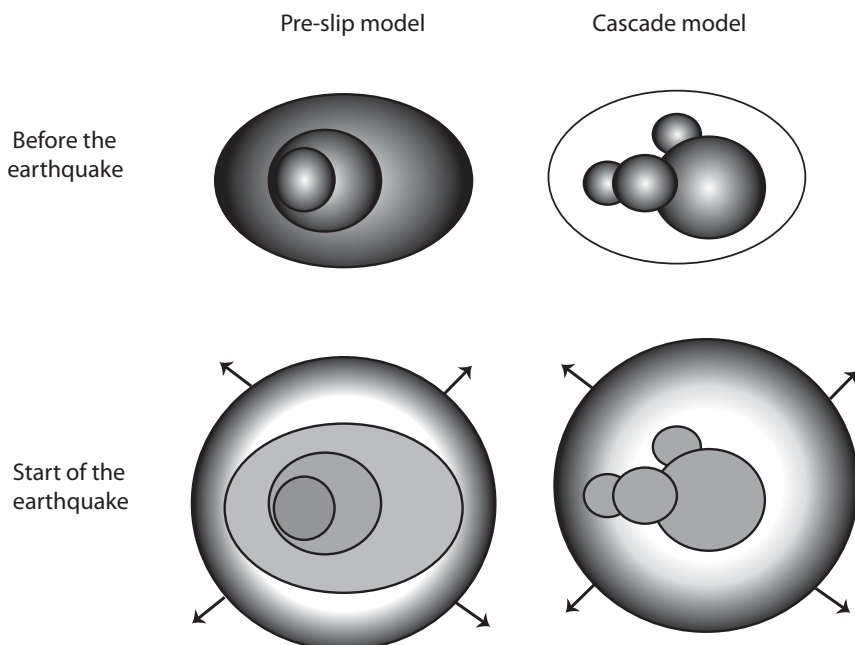


**Figure 11.8.** Pre-slip and cascade models of rupture nucleation, proposed by Ellsworth and Beroza (1995). In the pre-slip model slow slip occurs in the source area, triggering small events before the large earthquake begins. In the cascade model a series of small interacting events occur in the nucleation zone until the large event begins.

shocks. This information cannot be used for prediction because of the very large variability of magnitude and time delays but it provides information about the processes that occur before large events.

### Arrest of seismic ruptures

---

The arrest of a fracture is an effect of the presence of inhomogeneities on the fault. As we have already noted, if conditions are homogeneous then once a fracture starts it will continue to propagate indefinitely. In order to stop a rupture there must be places on the fault where the friction and geometrical conditions are different from those that allowed it to propagate. Two alternative possibilities may result in the arrest of a propagating fracture (Husseini *et al.*, 1975). One is the presence of a large discontinuous increase in fracture strength such that the stress concentration produced by rupture propagation can no longer overcome the strength of the material. This constitutes a fracture energy barrier. The barrier may be due to a continuous or discontinuous increase in the strength over a certain distance. The other possibility is the presence of an area of very low stress, where the stress falls below the value needed to provide an energy release rate sufficient to keep the fracture propagating. These two situations correspond to those arising in the two models of fault complexity that will be discussed in the next section, namely, barriers and asperities.

Another fundamental element in fracture arrest is the presence of geometrical complexities in the fault plane such as bends, offsets (jogs and steps), joints, bifurcations, duplexes etc. (Scholz, 1990, pp. 147–52). *Jogs* occur when the line of deviation of the fault from the slip plane is normal to the slip vector and *steps* occur if the deviation is parallel. Both jogs and steps present impediments to rupture propagation and may cause fault arrest. Some authors propose that rupture initiates at one geometrical irregularity on a fault and ends at another. However, large earthquakes may break through several of these fault irregularities. *Bends* and *bifurcations* on a crack can also occur in a homogeneous medium, if the crack tip growth changes direction (Kame and Yamashita, 1999a, b; Aochi and Madariaga, 2003; Adda Bedia and Madariaga, 2008). When this occurs the spontaneous arrest of rupture may follow.

## 11.6. Barriers and asperities

---

It is obvious from the observation of natural faults that the faulting process cannot be homogeneous. Actually, faults cross rocks of various strengths, often change direction and present bends, joints and bifurcations. The analysis of observed elastic wave forms radiated from earthquakes, especially for the high-frequency radiation in the near field, also reveals greater complexity than would be expected from simple homogeneous fractures. Two end-member models were proposed to explain earthquake complexity, namely, models with *barriers* and models with *asperities* (Madariaga, 1979). In the barrier model such complexity results from permanent features on the fault plane, which give rise to variations in strength and also control nucleation, arrest and wave radiation. In the asperity model the

complexity results from the initial stress conditions on the fault zone; the stress is a consequence of previous seismic or aseismic activity and may be under dynamic control. This type of complexity is continuously evolving so that its features are continuously created and destroyed.

### The barrier model

---

The barrier model of complex fracture postulates the existence of barriers on the fault surface which interact with rupture propagation (Das and Aki, 1977a; Aki, 1979, 1984). Fracture takes place under uniform conditions of stress but rupture resistance, static friction or strength is variable in the material. Zones on the fault surface with high values of strength form barriers which slow down or impede fracture propagation. Barriers are specified by their strength and dimensions and can be divided into weak and strong types. If the barrier dimensions are large compared with the instantaneous crack size at the time of encounter then crack propagation will stop. If the barrier dimensions are small then the crack tip and the barrier interact in different ways depending on the relative values of the tectonic stress  $\sigma_0$  and the barrier strength  $\sigma_b$ . If the tectonic stress is high ( $\sigma_0 > \sigma_b$ ), the barrier is broken and fractures continues. If the tectonic stress is low ( $\sigma_0 < \sigma_b$ ), the crack tip may stop at the barrier or may jump across it, leaving it unbroken. The barrier may break later owing to an increase in dynamic stress. The process accumulates stress on unbroken barriers, which will break later producing aftershocks. Once the rupture process is finished over the entire fault plane, the stress has been released in the fractured zones and has accumulated in the barriers left unbroken. For a large earthquake there may be many barriers that are left unbroken after the main shock but will break in successive aftershocks. Using the concept of the *arrest of fracture* by a strong barrier (Husseini *et al.*, 1975) and the characteristics of the cohesive zone and the slip-weakening model, we can associate the dimension  $d$  of the cohesive zone with the barrier dimensions, taking a quasistatic view of rupture arrest. We can also associate the critical slip  $D_c$  with the slip necessary to break the bond between the two sides of the fault in the barriers. For slips below this value the barriers are left unbroken.

### The asperity model

---

The asperity model was first proposed by Kanamori and Stewart (1978) in their study of the 1976 Guatemala earthquake. They observed a very complex P wave form, which led them to assume a complex source of 10 subevents, separated by space intervals of 14 to 40 km over a total length of 250 km which took about 2 minutes to break the entire fault plane. The complex nature of the source or multiple events had been observed before for large earthquakes (Wyss and Brune, 1967). Kanamori and Stewart (1978) proposed that the heterogeneity of the fracture process was produced by the successive breaking of several zones of greater strength, or asperities. This implies that before the earthquake the fault had a heterogeneous distribution of stress, with zones of high strength values (asperities) surrounded by unloaded regions. This situation was achieved by foreshocks and slow slip episodes. The breaking of the strong zones or asperities, where high stresses

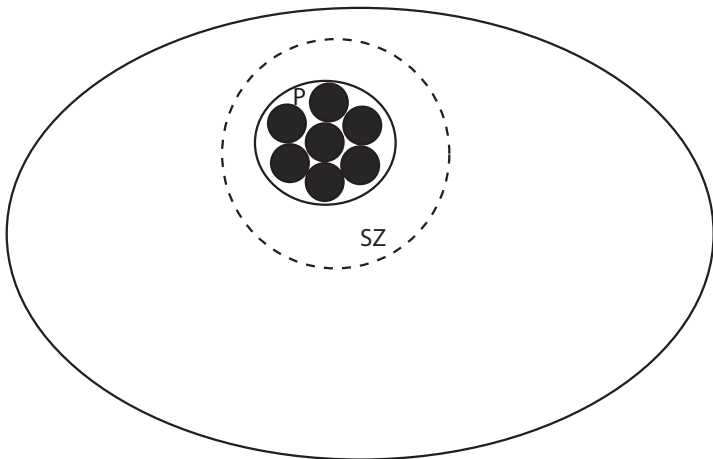


**Figure 11.9.** Asperity model of Johnson and Nadeau (2002, 2005): P, asperity patch; SZ, shadow zone.

have accumulated, constitutes the occurrence of a main large earthquake; its complexity is due to the fracture of several asperities.

The asperity model can then be summarized in the following manner (Madariaga, 1979). On the fault plane, owing to pre-seismic slip or foreshocks there are patches of stress concentration or asperities. The main earthquake releases these stress concentrations and a smooth final state of stress results over the whole fault surface.

Johnson and Nadeau (2002, 2005) studied a model of a fault in which asperities are grouped together in a patch  $P$ . On the fault outside the asperity patch the material is weaker and continually creeps in response to tectonic stress. Surrounding the asperity patch there is a zone of slip deficit with respect to the creeping area, which is called the shadow zone (SZ). This zone has a strength that is small compared with that of the asperity patch (Fig. 11.9). The individual asperities, the asperity patch and the shadow zone are assumed to be of circular shape. An earthquake occurs when the asperity patch breaks as the shear traction exceeds a critical value. Failure takes the form of a cascade process in which the break of one asperity transfers stress to those nearby that have not yet broken and leads to their breaking. It begins with the asperities at the edge of the patch, where the stress concentration is a maximum, and extends to other asperities in the patch, first to those at the periphery of the patch and then to those in the center, similarly to the model with a single asperity of Das and Kostrov (1983). After all the asperities in the patch have broken, failure extends out over the shadow zone, releasing the slip deficit accumulated there.

Aki (1984) discussed the main features of the earthquakes generated by these two models. In the asperity model of earthquakes there are stable asperities on the fault surface, which break repeatedly in major earthquakes. In the barrier-type model of earthquakes fracture takes place between strong stable barriers, which do not break; between them are weaker barriers which break in different patterns. The first type of earthquake has a characteristic amount of slip and the second a characteristic fault length. The barrier model explains the occurrence of aftershocks, as barriers left unbroken break later on, and the asperity model explains the occurrence of foreshocks, as small shocks break the zone

surrounding an asperity. Since both phenomena are present, a combination of the two models is probably the most realistic solution. Foreshocks or small shocks before the occurrence of a major shock produce heterogeneity on the fault surface, leaving the areas of high strength (the asperities) to be broken by the main shock. After the main shock has occurred, parts of the fault surface remain as unbroken concentrations of stress (barriers), so that they break later producing aftershocks. We may conclude that the stress or strength distribution on the fault surface must be heterogeneous both before and after the occurrence of earthquakes, so that both foreshocks and aftershocks are produced.

Inhomogeneous conditions on the fault plane can also be modeled by assuming that the static friction coefficient  $\mu_s$  and the kinematic friction coefficient  $\mu_k$  vary along the fault plane (Mikumo and Miyatake, 1978, 1995; Mikumo, 1994). When the applied stress  $\sigma_0$  at some point of the fault exceeds the static friction ( $\sigma > \sigma_s$ ), motion begins. Mikumo and Miyatake (1978, 1995) assumed in their numerical models that the static friction over the fault plane has a normal statistical distribution while the kinematic friction, which in reality might vary slightly from place to place, is assumed to be constant. The distribution of friction on the fault plane leads to distributions of the static and dynamic stress drops. The heterogeneity of the fracture process is finally assigned to a variable distribution of the stress drop over the fault.

## 11.7. Healing and rupture pulse propagation

As we saw in section 7.7, in kinematic extended models the rise time  $\tau_r$  and the total duration of fracture  $T = L/v$  are determined independently. Depending on the relation between  $\tau_r$  and  $T$ , the motion  $\Delta i$  at each point of the fault stops or “heals” when the total fracture process is over, or it takes place only over a limited band of the fault surface, which progresses with the velocity of fracture propagation (Heaton, 1990). In dynamic models the healing is controlled by the friction law used to model earthquakes. Classical slip weakening contains no mechanism that can produce healing; rate-weakening friction, however, can abruptly heal the slip on the crack, as shown by Cochard and Madariaga (1994, 1996). This has led to the consideration of two types of rupture model, namely, the *crack-like* model (Kostrov, 1964), where the motion continues behind the fracture front until the fault itself comes to a stop at its border, and the *pulse-like* model (Heaton, 1990), where the motion stops, or heals spontaneously, behind the fracture front as it propagates.

The propagation of self-healing rupture pulses has been studied by several authors (Heaton, 1990; Cochard and Madariaga, 1994; Beeler *et al.*, 1994; Zheng and Rice, 1998; Nielsen and Madariaga, 2003). Actually, self healing rupture pulses were introduced into fracture mechanics by Yoffe (1951), who showed that under shear a pulse of finite length could propagate on an infinite fault at sub-shear speeds both in Mode II and Mode III. In Fig. 11.10 we show an example of a Yoffe–Heaton pulse propagating along a two-dimensional fault. As in Fig. 11.3 this simulation was computed using a velocity–stress finite difference method with the same parameters. The upper panel in Fig. 11.10 shows the stress field associated with the rupture front located at the origin, in coordinates

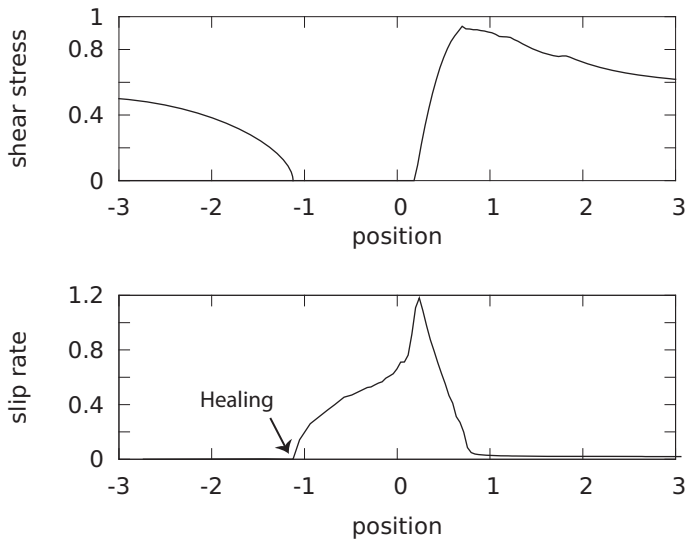


**Figure 11.10.** A rupture pulse propagating along a Mode II fault. Upper panel, the shear stress and, lower panel, the slip rate ahead of and behind the rupture front (at zero position). In this particular case the slip was artificially healed after a certain time behind the rupture front and then propagated at constant velocity as a pulse.

moving with the rupture front. The lower panel shows the corresponding slip rate as a function of position. The slip rate behaves initially as for the crack solution of Fig. 11.3 and then at a non-dimensional distance  $-1.2$  it reduces to zero. Once the slip rate has reduced to zero the stress increases behind the healing front, as observed in the analytical solutions computed by Nielsen and Madariaga (2003) for a self-similar model. The main change with respect to Fig. 11.3 is that a healing front was forced to start once the fault was propagating at almost constant speed. Nielsen and Madariaga (2003) studied the two-dimensional antiplane (Mode III) fracture problem, where rupture and healing are allowed to occur spontaneously. Since no energy is needed to produce healing, though it is needed to create new rupture area, once healing starts it propagates without further energy dissipation and there is no stress or slip-rate singularity associated with it. To initiate the healing phase will then propagate persistently under homogeneous conditions.

## 11.8. Super-shear rupture velocity

In a classical contribution Andrews (1976) studied the propagation of an in-plane (Mode II) rupture along a flat preexisting fault. As the fracture developed it accelerated until it reached a velocity that was close to the Rayleigh wave velocity, which had always been considered as the limiting speed for Mode II rupture propagation. Suddenly, in his numerical model, a secondary rupture front appeared close to the shear wave front. Further examination of the simulation by Andrews showed that the secondary rupture was created

by a strong peak of shear wave stress that propagated ahead of the rupture front. This front was actually created at the beginning of rupture once the initial fault was nucleated. A closer examination, and numerical solutions, showed that the shear wave had a peak stress value of 1.77 times the stress drop in the crack. This was sufficient for certain slip-weakening friction conditions to start a secondary rupture front that propagated at a speed faster than that of the shear wave. Intersonic velocities are domain-bounded by two particular speeds, the so-called *Eshelby velocity*, that is,  $c_E = \sqrt{2\beta}$ , and the P wave velocity. It is interesting that super-shear ruptures had been predicted previously in the dislocation literature by Weertmann (1967). Andrews (1976) studied fully the problem of a shear crack that started from a small initial source patch of length  $L_c$  and then propagated spontaneously under uniform initial stress and rupture resistance. The key parameter is the S-ratio defined in (10.60), that is, the ratio between strength excess and stress drop introduced by Das and Aki (1977b). Andrews showed that for values of  $S < 1.77$  the rupture could become super-shear by the creation of a so-called *daughter fracture* near the shear wave front. Although there have been several reports of super-shear rupture speeds, notably from Archuleta (1984) and Spudich and Cranswick (1984) for the Imperial Valley earthquake, super-shear velocities remained difficult to observe, mainly because they could only be detected by strong motion instruments located very close to the fault.

A turning point in the study of super-shear ruptures occurred around 1999 when Rosakis *et al.* (1999) showed that super-shear ruptures occurred in laboratory specimens of homalite. Almost simultaneously, near-field observations of super-shear rupture were made in Turkey during the Izmit earthquake (Bouchon *et al.*, 2001), although a super-shear shock was observed in only one accelerometer. Even stronger evidence for the occurrence of super-shear rupture in natural faults was provided by Bouchon and Vallée (2003), who found evidence for a long super-shear rupture in the propagation of the big  $M_W = 8.1$  Kunlunshan earthquake of 2001. More recently Vallée *et al.* (2008) found additional evidence of the Kunlun super-shear shock in high-frequency seismic waves observed by a temporary network in Tibet. In 2002 another large strike-slip event occurred in Alaska, the Denali earthquake, for which a clear super-shear signal was reported by Dunham and Archuleta (2004). Since then strong evidence has accumulated for super-shear propagation in these events, but it remains a rare observation. A possible explanation for the scarcity of super-shear bursts is that they can only occur in shallow strike-slip faults with relatively smooth fault topographies, so that super-shear propagation occurs over a long segment of the fault. Short bursts of super-shear rupture velocities have been inferred for other events, for instance, for the Landers earthquake of 1972 by Olsen *et al.* (1997) but short bursts are much more difficult to distinguish from other heterogeneities in rupture propagation.

As mentioned above, Rosakis (1999) observed super-shear ruptures in laboratory experiences with Mode II cracks in homalite, a transparent material where high-speed pictures of isochromatic fringes clearly permitted the identification of super-shear shock waves. More recently there have been a large number of observations of super-shear propagation. In Rosakis *et al.* (1999). It was reported that super-shear shocks had been generated under typical conditions for real earthquake generation. Passelègue *et al.* (2013) observed the super-shear propagation of Mode II ruptures in rock samples using very small accelerometers.

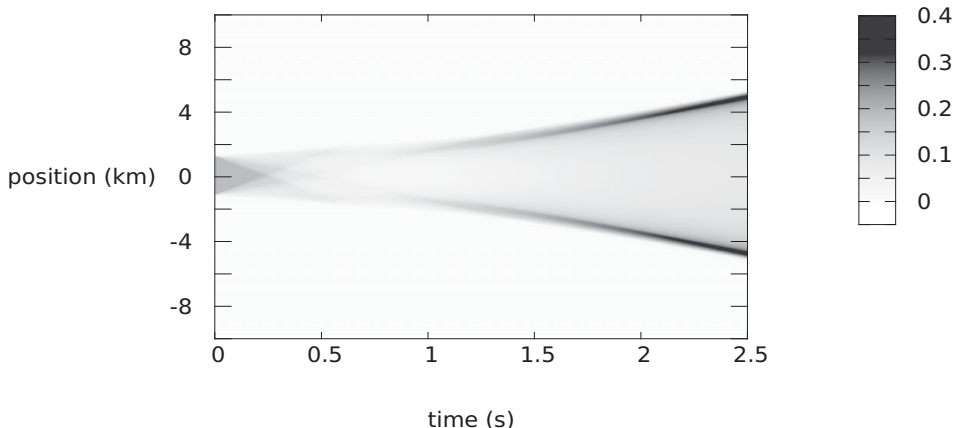


**Figure 11.11.** A sub-shear spontaneous rupture in Mode II. The rupture starts at a small initial asperity. After a relatively long nucleation time, a rupture propagating at a very high sub-shear velocity emerges. In this case the non-dimensional number  $S = 1.22$ .

In order to illustrate the differences between sub- and super-shear ruptures we modeled a simple two-dimensional fault where rupture is initiated by a high-stress asperity. All the parameters in the various computations were kept the same except for the initial stress.

The properties of the uniform elastic medium were as follows:  $\alpha = 5480$  m/s,  $\beta = 3164$  m/s and  $\rho = 3000$  kg/m<sup>3</sup>. With those properties the elastic rigidity  $\mu = 30$  GPa. The initial asperity was computed using Andrews' (1976) expression (11.26); we chose  $L_c = 2.4$  km. The rupture was modeled using the finite difference method proposed by Virieux and Madariaga (1982) for Mode II cracks. We modeled the friction using Ida's (1972) linear slip-weakening model with fixed parameters  $\sigma_s - \sigma_k = 4.0$  MPa and  $D_c = 0.05$  m, so that the energy release rate  $G_c = 0.1$  MJ/m<sup>2</sup>. The slip velocity on the fault plane is shown in Fig. 11.11 for a sub-shear rupture and in Fig. 11.12 for a rupture that becomes super-shear at time 1.2 s. The control parameters for these two rupture models are as follows:

$$\text{sub-shear, } \sigma_0 - \sigma_k = 1.8 \text{ MPa, } S = 1.22, \kappa = 1.30 \quad (11.34)$$

$$\text{super-shear, } \sigma_0 - \sigma_k = 2.5 \text{ MPa, } S = 0.60, \kappa = 2.5 \quad (11.35)$$

Here  $S$  and  $\kappa$  are the non-dimensional parameters of seismic rupture defined earlier in (10.60) and (11.29). In Fig. 11.12 for the super-shear rupture we observe that a daughter rupture is generated ahead of the sub-shear crack front at about 1.2 s. Behind the super-shear rupture front we observe a strong Rayleigh wave, as predicted by theoretical arguments. It is possible to compute sub-shear ruptures for values of  $\kappa$  closer to unity, but then the rupture initiation process becomes very long.

Finally, in Fig. 11.13 we show the most remarkable features of super-shear ruptures. This figure is a snapshot of the stress field surrounding the fault as it propagates at super-shear speed. We have plotted the shear stress because this is the field component that more closely resembles the figures of Rosakis *et al.* (1999). The super-shear front appears as the

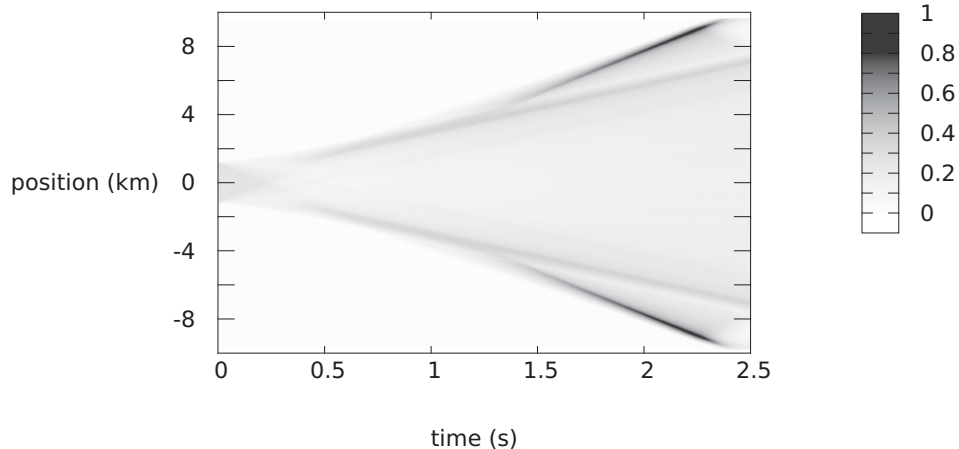


**Figure 11.12.** A super-shear transition in a spontaneous rupture in Mode II. After 1.2 s a daughter rupture propagating at super-shear velocity appears for non-dimensional  $S = 0.60$ .

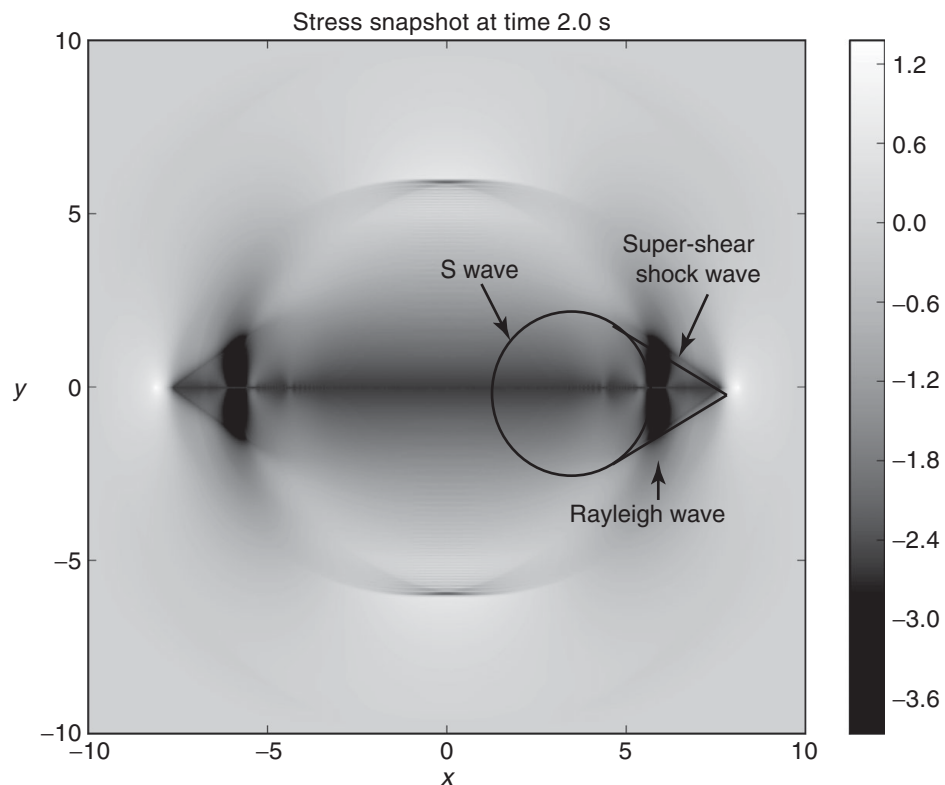


**Figure 11.13.** Cross-section of a super-shear fault showing the distribution of shear stress at time 2 s in Fig. 11.12. The rupture front is situated at the tip of the triangular regions delimited by the super-shear plane waves. Behind the super-shear shock wave a strong Rayleigh wave propagates.

two straight lines (plane waves) at each side of the figure emanating from the tip of the rupture. These plane waves connect to a circular S wave emitted at the instant when the rupture front jumped ahead of the shear wave. As mentioned above, from Fig. 11.12 we observe that the super-shear transition occurred at time 1.2 s and at 4 km distance from the origin of the rupture. Behind the rupture front, as an inheritance of the original sub-shear rupture front, we observe a very large Rayleigh wave, as predicted by all theoretical models of super-shear rupture (Xia *et al.*, 2004).

## 12.1. Dynamic models

The theory of the dynamic fracture process at an earthquake source was presented in Chapters 9 to 11. This theory is the basis for the development of methods for the study of earthquake dynamics. Kinematic models, as we have seen, describe the source of an earthquake in terms of the space–time distribution of slip on a certain fault surface. Dynamic models relate the slip to the stresses acting on the fault. Thus, the source is described in terms of the distribution of stress and friction and the elastic properties of the material. Kinematic inversion methods are at present routinely applied to study sufficiently large earthquakes ( $M_W > 5.5$ ) using strong motion, regional and teleseismic data. Dynamic models are significantly more involved and can be applied only to recent earthquakes that have been well recorded in the near field by strong motion data. For example, such studies have been applied to the earthquakes of Landers (1992), Kobe (1995), Chi Chi (1999), Izmit (1999) and Tottori (2000).

Earthquakes are three-dimensional phenomena that are very complex to model because of the interplay of the two fracture modes Mode II (in-plane) and Mode III (antiplane) and the presence of singularities near the border of the fault. There seems to be no way to obtain analytical solutions for shear rupture propagation in three dimensions, so that even for the simplest problems we have to resort to numerical simulation. A wide range of numerical methods is available including finite difference methods in three dimensions (Harris and Day, 1993; Mikumo and Miyatake, 1995; Madariaga *et al.*, 1998; Cruz-Atienza and Virieux, 2004), as well as finite element techniques (Duan and Oglesby, 2006; Ma *et al.*, 2008; Duan, 2010), high-order spectral element techniques (Kaneko *et al.*, 2010) and unstructured discontinuous element methods (Tago *et al.*, 2012). Advanced numerical methods together with the availability of fast parallel computers have opened the way to the study of accurate dynamic rupture models.

Our purpose is not to review those techniques but to obtain insights about the interaction of seismic ruptures with their environment, and most of all generate synthetic seismograms that can be efficiently compared to observed seismograms. In addition to volumetric methods such as finite differences and finite elements it is possible to use boundary integral equation methods that relate the stresses to the slip and slip rate on the fault surface by means of the Green's function of the medium. These methods can be used to model faults with complex geometries but only on uniform elastic media or in homogenous half spaces (Fukuyama and Madariaga, 1998; Aochi *et al.*, 2000).

## 12.2. Modeling earthquakes in three dimensions

We will study rupture propagation along a planar fault 435,11 embedded in a heterogeneous elastic isotropic medium. The elastic properties of the Earth model may be heterogeneous, may include a free surface etc. We use the velocity–stress formulation of elastodynamics (Madariaga, 1976) which was presented in section 10.6. We add to equation (10.63) the source terms for forces  $f_i$  and for moment  $m_{ij}$ , obtaining

$$\rho \frac{\partial v_i}{\partial t} = \frac{\partial \sigma_{ij}}{\partial x_j} + f_i \quad (12.1)$$

$$\frac{\partial \sigma_{ij}}{\partial t} = \lambda \frac{\partial v_i}{\partial x_i} \delta_{ij} + \mu \left( \frac{\partial v_i}{\partial x_j} + \frac{\partial v_j}{\partial x_i} \right) + \frac{\partial m_{ij}}{\partial t} \quad (12.2)$$

where  $v_i$  and  $\sigma_{ij}$  are the particle velocity and stress tensor, respectively;  $\rho$  is the density and  $\lambda$ ,  $\mu$  are the elastic properties, which can be spatially varying;  $f_i$  is a distribution of body forces and  $m_{ij}$  is the distribution of moment tensor sources. In our model we assume the  $f_i$  to be zero everywhere, and the moment tensor density is computed numerically from the solution of the frictional boundary conditions. Earthquake rupture propagation is entirely controlled by the properties of friction between the sides of the fault, as discussed in some detail in Chapter 11. The most commonly used friction laws are slip-weakening and rate-and-state friction. There is no particular difficulty in using rate-and-state friction in numerical modeling but the cost of implementation is still very high (Barbot *et al.*, 2012). Actually, as discussed in section 11.4, from the point of view of earthquake dynamics these two models of friction are equivalent (Okubo, 1989; Cocco and Bizzarri, 2002).

The first model that we shall study is rupture propagation along a planar fault that we choose to lie along the plane  $x_3 = 0$  (Fig. 12.1). Friction controls the initiation and propagation of rupture and the healing of faults. Because of the equivalence of the friction laws at high slip rates, in the following we will use the slip-weakening friction law, in which the slip is zero until the total stress reaches a peak value of static friction that we denote  $\sigma_s$ . Once this stress has been reached, the slip  $\Delta u$  starts and the friction decreases until it reaches a residual or kinematic friction  $\sigma_k$ :

$$\sigma(\Delta u) = \sigma_s - (\sigma_s - \sigma_k) \frac{\Delta u}{D_c} \quad \text{for } \Delta u < D_c \quad (12.3)$$

where  $D_c$  is the slip-weakening distance and  $\sigma_s$ ,  $\sigma_k$  are the static and kinematic friction, respectively. For  $\Delta u > D_c$  the stress drop is total, so that  $\sigma = \sigma_k$ . This friction law has been extensively used in numerical simulations of rupture, by Andrews (1976), Day (1982) and many others. Without loss of generality, and for simplicity of the numerical simulations, we will measure all stresses with respect to the kinematic friction  $\sigma_k$ . This is equivalent to assuming that  $\sigma_k = 0$  in (12.3). It is an important property of linear dynamic ruptures that the slip, energy balance and seismic radiation depend only on the stress change, not on the absolute stress levels. In other words we can add to (12.1) any stress field that is in equilibrium with its sources because the seismic waves generated

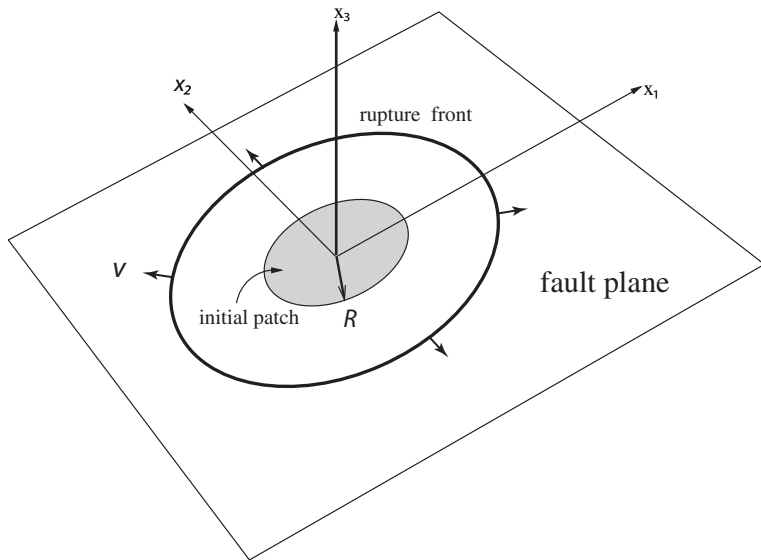


**Figure 12.1.** Geometry of a simple rupture propagating along a flat fault embedded in a three-dimensional elastic medium. Rupture starts from an initial small circular asperity patch of radius  $R$  and propagates indefinitely.

by the fault ignore the presence of preexisting stresses in the elastic medium. Seismic waves only interact with preexisting stress in the fault zone or if the wave propagation is non-linear.

The most important feature of the friction law (12.3) is that in order to propagate rupture along the fault plane the elastic medium surrounding the fault has to provide a fracture energy per unit surface equal to the energy release rate,

$$G_c = \frac{1}{2}(\sigma_s - \sigma_k)D_c \quad (12.4)$$

The value of  $G_c$  was initially considered to be an intrinsic property of faults that controlled the rupture speed, as is often assumed in fracture dynamics. In earthquakes, however, there is substantial evidence that  $G_c$  scales with size of the event, as discussed in section 11.4. We will solve (12.1) together with the friction boundary conditions (12.3) in an elastic medium with radiation conditions at infinity and subject to a heterogeneous initial stress field  $\sigma_0$ . This initial stress field includes both tectonic loading and the residual stress field left from previous earthquakes on the fault or on neighboring faults.

### Numerical method

An essential requirement for the study of dynamic faulting is an accurate and robust method for the numerical modeling of seismic sources. A very satisfactory method for modeling seismic ruptures on relatively flat faults embedded in mildly heterogeneous elastic media is the fourth-order formulation of the finite difference velocity–stress method (Madariaga, 1976; Madariaga *et al.*, 1998; Virieux and Madariaga, 1982). The most

important parameter in the finite difference modeling of wave propagation is the Courant–Friedrichs–Lowy (CFL) non-dimensional constant

$$H = \beta \Delta t / \Delta x \quad (12.5)$$

This expression involves the ratio of the temporal and spatial steps, where  $\beta$  is the shear wave velocity. We systematically used  $H < 0.3$  in our calculations, although in theory  $H < 0.6$  is sufficient. We refer to the papers cited above for further discussion of the numerical method. An important issue with finite differences is the implementation of boundary conditions. As discussed by Andrews (1999) there are two ways to impose the friction boundary conditions: the first splits the fault surface into two and treats each side of the fault differently (Madariaga, 1976); the second is a continuous approach that models the source by a stress glut or inelastic strain (Madariaga *et al.*, 1998). The split-nodes method is the only one that can be used in finite element methods, especially in their high-order and discontinuous versions. For finite differences the technique of split nodes was carefully reviewed by Dalguer *et al.* (2009). This and other numerical methods were tested in the Southern California Earthquake Center (SCEC) (Harris *et al.*, 2009).

## Scaling

---

The equations of motion (12.1), (12.2) contain no length or stress scale except for the size of possible elastic wave heterogeneities. For uniform elastic media the stress and length scales are determined by the boundary conditions and the initial stress field. Rupture propagation is completely controlled by the complex nonlinear interaction of the following:

1. the initial stress field  $\sigma_0$ ;
2. the parameters  $D_c$ ,  $\sigma_s$ ,  $\sigma_k$ , of the friction law (12.3).
3. the length scales that define the geometry of the fault.

We have already discussed the problem of the scaling of rupture nucleation in section 11.5. Like any other non-linear problem in physics the solutions of the earthquake dynamics are controlled by a number of non-dimensional parameters, which can be defined from appropriate dimensional analysis of the equations and boundary conditions. For earthquake dynamics, the problem defined by (12.1)–(12.3) includes two non-dimensional numbers, which have been well identified. These are the stress ratio, introduced by Das and Aki (1977b) and discussed in section 10.5,

$$S = \frac{\sigma_s - \sigma_0}{\sigma_0 - \sigma_k} \quad (12.6)$$

and the energy ratio  $\kappa$  proposed by Madariaga and Olsen (2002) and discussed in section 11.5 (see equation (11.29))

$$\kappa = \frac{(\sigma_0 - \sigma_k)^2 R}{\mu(\sigma_s - \sigma_k) D_c} \quad (12.7)$$

The ratio  $S$  is closely related to the transition from sub- to super-shear rupture propagation (section 11.8), while  $\kappa$  controls the initiation of rupture and the overall qualitative nature of

the rupture. It is possible to derive other parameters from the equations of motion, for instance the ratio of the overall dimension of the fault and the average fault slip, but they have not been discussed in the literature yet.

## 12.3. Rupture propagation on a planar uniform fault

We will study the *spontaneous propagation of rupture* along a planar fault subject to a slip weakening friction law (12.3). As discussed in section 11.5, the nucleation of rupture requires the initial development of a nucleation zone of finite size where the stress is high enough to overcome frictional resistance. There are several strategies to initiate rupture in numerical fault models: the most common is to introduce a *circular* or *rectangular patch* on the fault that is ready to break when the initial applied stress is larger than the static friction. It is also possible to initiate rupture by imposing an initial zone that breaks self-similarly at constant rupture speed (Andrews, 1976).

Let us assume that rupture starts from a small circular asperity of radius  $R$  that is ready to break, i.e. it is loaded with stress that is just slightly larger than the static friction and is surrounded by an unbounded fault surface loaded at a constant stress level (Fig. 12.1); the friction (12.3) is uniform everywhere on the fault plane. This is certainly the simplest model for an earthquake. Since we are mainly interested in the parameters that control rupture propagation we do not include, for the moment, any stopping mechanism. It is frequently assumed that the Kostrov (1964) solution for a self-similar circular fault is an adequate model of this problem, and it has been used extensively in the literature to simulate the initial radiation from a seismic source (Sato and Hirasawa, 1973; Madariaga, 1976). In fact this model cannot be correct, as pointed out by Kostrov (1964): the energy release rate in the in-plane, Mode II, direction and in Mode III are different. Additional discussion of this can be found in Kostrov and Das (1988).

As an example we will consider a model in which we used the following parameters. The elastic medium has velocities  $\alpha = 6400$  m/s,  $\beta = 3520$  m/s and  $\rho = 2700$  kg/m<sup>3</sup>. Thus the elastic rigidity  $\mu$  was 33.5 GPa. We modeled the elastic medium as a cube of  $(320)^3$  elements of size 200 m. The time step was 0.01 s, so that the CFL constant  $H = \beta\Delta t/\Delta x$  defined in (12.5) was 0.176. This is rather small, but it provides stability against absorbing boundary conditions. The parameters of the slip-weakening friction law were  $\sigma_s - \sigma_k = 8$  MPa and the slip weakening distance was 0.2 m, so that the energy release rate was  $G_c = 0.8$  J/m<sup>2</sup>.

In Fig. 12.2 we show the result of the numerical simulation for an initial asperity of radius  $R = 4$  km and a relatively high value of dynamic stress drop  $\sigma_0 - \sigma_k$ , 6 MPa. The non-dimensional numbers are  $S = 0.25$  and  $\kappa = 2.68$ . This figure illustrates most of the important features that are observed in the modeling of simple rupture on unbounded fault surfaces. Rupture starts from the initial circular asperity and accelerates rapidly, becoming elongated in the in-plane direction (the horizontal direction in Fig. 12.2). At time  $t = 100\Delta t$ , the second row in Fig. 12.2, we observe a certain diffusion of the rupture front near the in-plane direction. This is the onset of the super-shear instability. At times greater than 100 ( $t = 120\Delta t$  and  $t = 140\Delta t$ ), the rupture front acquires an elliptical shape with two protrusions (we call

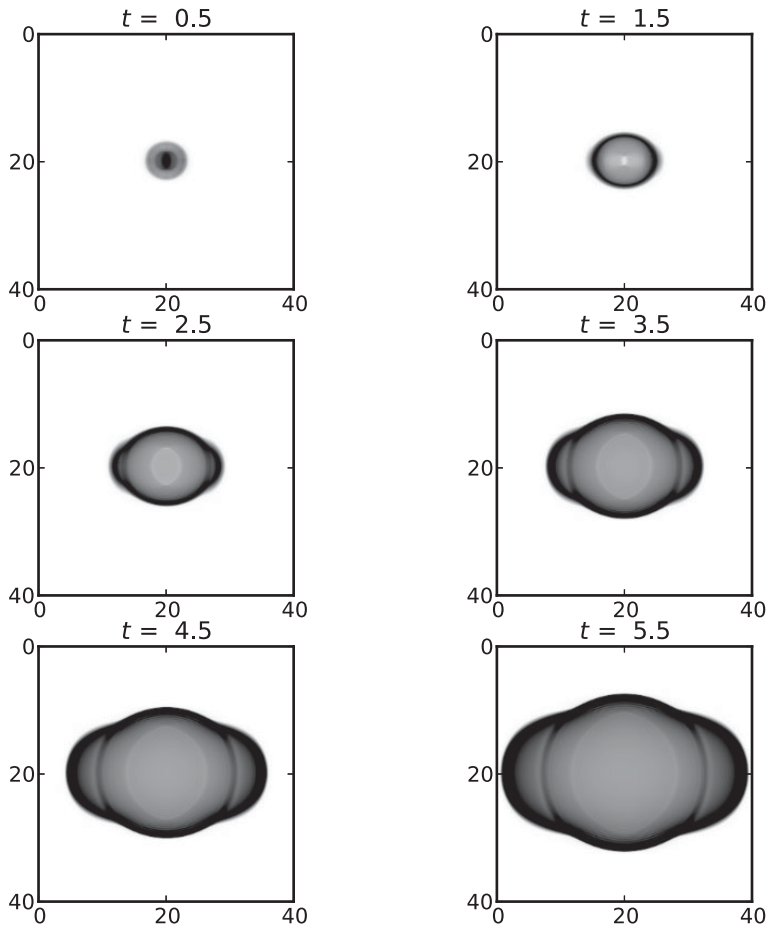


**Figure 12.2.** Rupture growth of a shear fault on a flat uniform fault embedded in a homogeneous elastic medium. The higher values of slip rate are darker. Rupture starts from a small finite initial asperity and then grows initially at sub-shear velocity in all spatial directions. After 2.5 s, the rupture in the in-plane (horizontal) direction jumps to a speed higher than that of the shear waves. After 3.5 s, a supershear front detaches from the Rayleigh wave.

them “ears”) elongated in the in-plane direction (the bottom row in Fig. 12.2). The transition from sub-shear to super-shear rupture in three dimensions is different from that studied by Andrews (1976) and discussed in section 11.8. The rupture front in three dimensions does not jump ahead of the S wave as it does in two dimensions; rather, it becomes initially unstable along the in-plane direction and then the instability propagates laterally along the rupture front. There is no discontinuity of the rupture front and, at least at the level of resolution that we currently have, we do not observe regions where the slip is arrested temporarily between the arrival of the super-shear and sub-shear rupture fronts. We observe clearly that there is a peak in the slip rate associated with the super-shear front and another associated with the older sub-shear front, i.e. the Rayleigh wave that propagates from the origin along the surface of the crack. It is perhaps important to remark that this Rayleigh wave has the same speed as the free surface Rayleigh wave but has different boundary conditions (Madariaga, 1977). The slip rate

decreases between the two fronts, but it does not decrease to zero as in Andrews (1976) in-plane rupture simulations.

### Why the super-shear “ears”?

Although the rupture front crosses the Rayleigh wave velocity in a continuous fashion, its local rupture velocity jumps discontinuously. This is the origin of the ears: the rupture front behaves like a wave front that has entered a region of higher velocity. The rupture-front velocity can be computed directly from the numerical simulations; it equals the so-called *Eshelby wave velocity*  $c_E = \sqrt{2}\beta$ . At the intersection between the super-shear front and the sub-shear rupture, which is propagating approximately at the Rayleigh wave speed, the angle is  $\phi = \arctan(0.914/1.44) = 32.9^\circ$ . It is important to note that the rupture speed does not take values in the “forbidden range” from the Rayleigh to the Eshelby wave velocity. This behavior has recently been verified by the very fine numerical resolutions of Bizzarri and Das (2012).

In conclusion, a three-dimensional rupture that is triggered from a circular asperity propagates initially self-similarly but rapidly becomes faster in the Mode II direction. The fault becomes increasingly elliptical as the speed increases. At some distance from the origin, controlled by the values of the non-dimensional parameters  $S$  and  $\kappa$ , the rupture makes a transition to super-shear velocity. The super-shear transition starts in the Mode II direction and then progresses laterally along the rupture front, maintaining a constant angle between the border of the super-shear front and the sub-shear front. In two dimensions the non-dimensional parameter  $S$  (12.6) plays a dominant role because the super-shear transition is dominated by the jump of the rupture to the shear stress peak. In initially circular ruptures we did not find a clear dependence on  $S$ , although we recall that  $S$  is contained implicitly in  $\kappa$ . It is interesting to note that, as the rupture grows, the velocity concentration near the rupture front increases but the stress concentration does not, because the rupture adjusts to exactly balance the energy flow to the slip-weakening zone and the energy release rate required for the rupture to advance. This behavior is quite different from that of faults expanding at fixed rupture speed, as in the self-similar model of Kostrov (1964).

## 12.4. A finite circular fault in a homogeneous medium

The circular crack model proposed by Brune (1970) to explain the omega squared behavior of the radiated spectrum was discussed in section 10.6. This model is widely used to obtain information about seismic sources and it is important to evaluate how it changes for a full dynamic simulation. In Chapter 10 we computed spectra for models that initially grew self-similarly until rupture stopped at a prescribed circular border. In this section we study the spontaneous propagation of rupture away from the circular asperity presented in the previous section and the arrest of rupture at an unbreakable circular barrier. The main purpose of this study is to show the role of stopping phases and healing phases for simple geometries.

We will use the same elastic medium and friction laws as those discussed in section 12.3. The space and time steps will also be the same: 200 m and 0.01 s, respectively with CFL constant  $H = 0.178$  ( $H$  is defined in (12.5)). The main difference from the previous model is that we introduce an unbreakable barrier, concentric with the initial asperity, with radius 20 km. It would be interesting to study cases where the initial asperity or hypocenter is not located at the center of the circle. These and other models will be part of the inversion method to be discussed in section 12.8. Since we are interested in comparing spontaneous rupture simulations with the quasidynamic circular crack model of section 10.6, we use a stress drop of 4.5 MPa so that the rupture does not become super-shear in our simulation. The values of the non-dimensional parameters are  $S = 0.78$  and  $\kappa = 1.71$ . Snapshots of the slip rate are shown in Fig. 12.3 at several successive instants of time measured in seconds.

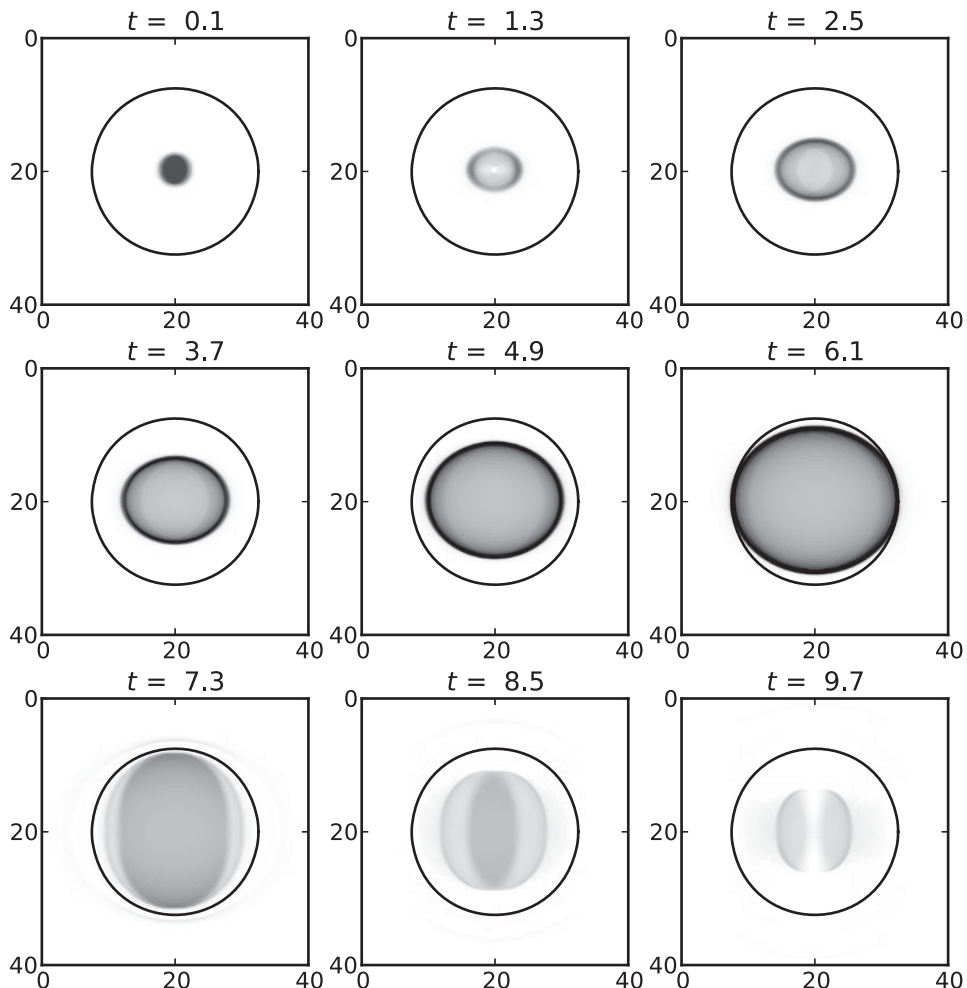


**Figure 12.3.** Snapshots of the slip rate on a finite circular crack of 20 km radius with a fixed border. The darker regions show higher slip rates. The rupture propagation is sub-shear. The non-dimensional parameter values are  $S = 0.78$  and  $\kappa = 1.71$ . The rupture reaches the border at 6.1 s and at 7.3 s the stopping phase propagates inwards.

We observe that after 2.5 s the rupture becomes spontaneously elongated in the horizontal direction, which is also the direction of the initial stress. In this direction Mode II prevails. In the transverse (vertical) direction the slip is in Mode III. Thus, as already remarked by Das (1980) and Day (1982), the rupture tends to grow faster in the in-plane direction, which is dominated by Mode II. At time  $t = 6.1$  s, the rupture has reached the unbreakable border of the fault in the in-plane direction and at time  $t = 7.3$  s the stopping phases generated by the top and bottom edges of the fault are moving toward the center of the fault. The snapshots after  $t = 8.5$  s show the stopping phases propagating inward from all directions. The slipping patches in the darker regions are now elongated in the antiplane direction, owing to slower healing. At time  $t = 9.7$  s, the in-plane stopping phases (moving in the vertical direction) have already reached the center of the fault and crossed each other. However, the slip rate has decreased to such small values that it may be contaminated with numerical noise.

### Radiation from a spontaneous circular crack

We have studied the radiation from a circular crack using several approximations, starting with the self-similar kinematic model of Sato and Hirasawa (1973) in section 7.9. This was followed by the instantaneous circular rupture modeled by Brune (1970) in section 9.5 and, finally, by the quasidynamic model of Madariaga (1976) in section 10.6. These circular crack models are widely used to study seismic radiation.

How much does *spontaneous rupture* affect the circular crack models? To respond to this question we computed the seismic radiation from the dynamic model. As for the quasidynamic model, there are significant differences in the seismic signal pulses radiated in different directions of space. To illustrate this variability we show in Fig. 12.4 the radiation in two directions of space: along the Mode II direction and along the transverse or

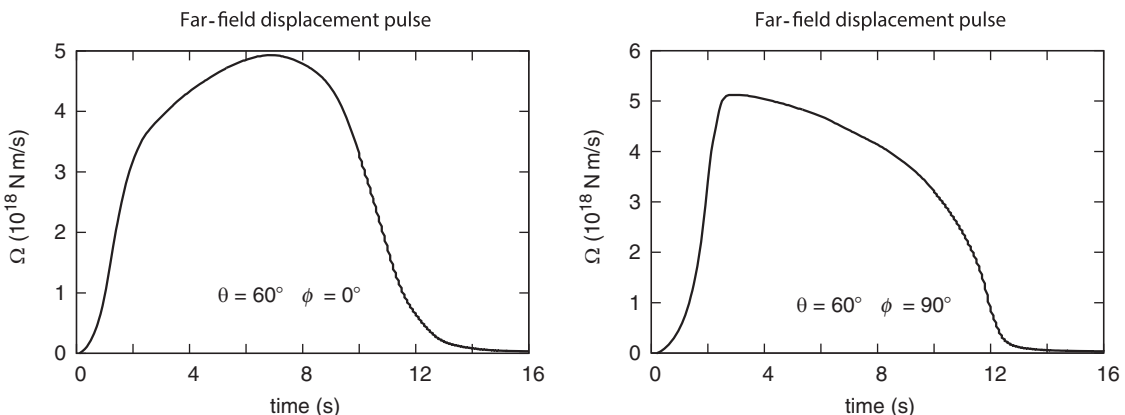


**Figure 12.4.** Radiation by the spontaneous circular fault of Fig. 12.3. Far field displacement pulses are shown for two direction of space.  $\theta = 60^\circ$  is the polar angle measured from the fault normal and  $\phi$  is the azimuth measured from the  $x_1$  axis, the in-plane direction. On the left far field pulse along the in-plane (Mode II) direction. On the right, the far field pulse radiated along the anti-plane (Mode III) direction.

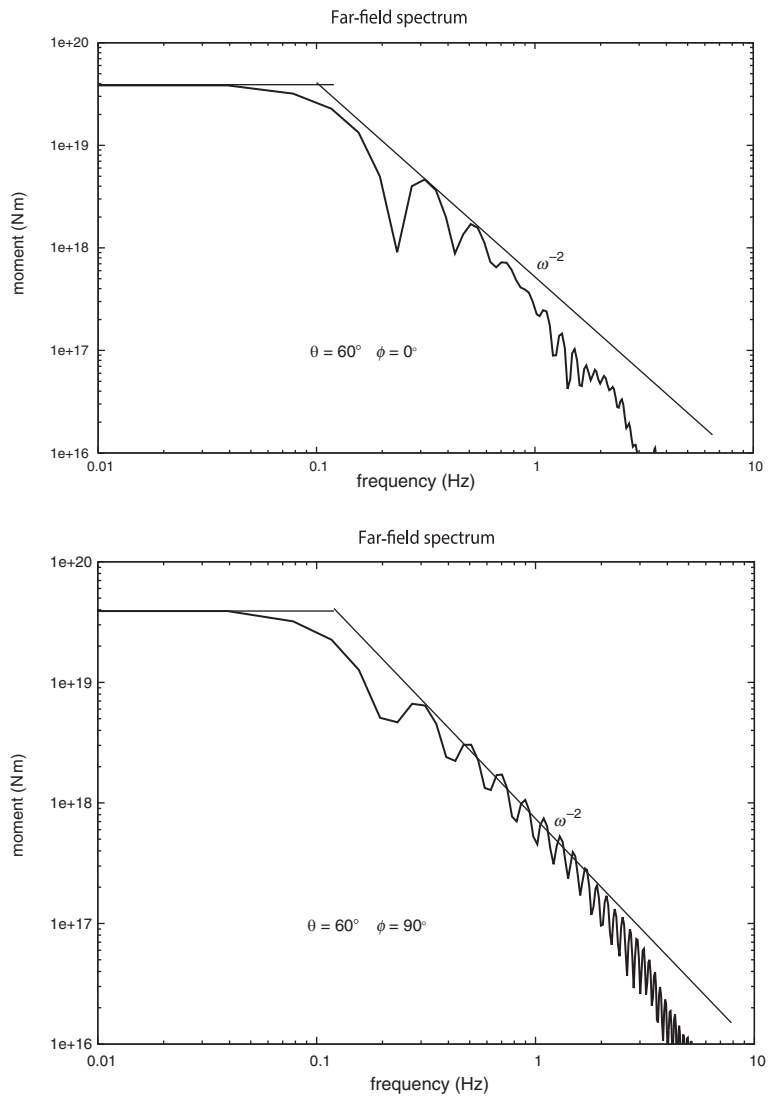


**Figure 12.5.** Amplitude spectra of the far field pulses shown in Fig. 12.4. The top spectrum corresponds to the pulse on the left of Fig. 12.3; the bottom figure is the spectrum of the pulse on the right of Fig. 12.4. In spite of the difference in shape of the time-domain signals, the spectra have the same Brune (1970) spectral shape.

Mode III direction. The angles  $\theta$  and  $\phi$  are the polar angle measured from the normal to the fault plane and the azimuth measured from the direction of slip on the fault ( $x_1$  in Fig. 12.1). The displacement signals in two different directions ( $\phi = 0^\circ$  and  $\phi = 90^\circ$ ) are shown in Fig. 12.4. Both have roughly the same duration, of about 10 s, but are quite different because one (for  $\phi = 90^\circ$ ) has a larger displacement at the beginning of the signal while the other is stronger near the end. The reason is that the stopping phases, the abrupt changes in slope in the figures, have different relative weights. This difference is in turn due to the directivity, which is large in the forward direction ( $\phi = 0^\circ$ ) and minimal in the

transverse direction ( $\phi = 90^\circ$ ) (section 7.6, Fig. 7.11). The corresponding amplitude spectra are shown in Fig. 12.5, which, as predicted by Aki (1967) and Brune (1970), have the typical  $\omega^{-2}$  spectral decay at high frequencies. We can compare the signals of Fig. 12.4 with those emitted by the quasidynamic model, shown in Fig. 10.12. They are similar, but the relative weight of the *stopping phases* is again different. The spectra of Fig. 10.13 and Fig. 12.5 are very similar: they have the same spectral shape and the corner frequencies vary from 0.1 to 0.12 Hz, the quasidynamic model having the highest corner frequency. It is not surprising that very different time-domain signals produce similar spectra. The reason is that the spectra are dominated by the stopping phases, which carry the information about *rupture arrest*. Although arrest is faster in the in-plane direction, the difference in arrival time of the stopping phases is not very large, so that the main features of the spectrum are preserved. It is possible to study the variation in the corner frequency as a function of the polar or azimuthal angles, but the effect of moving the initiation point with respect to the circular border is much more important.

## 12.5. Shallow strike-slip rectangular fault

In this section we study a longitudinal rupture model that is very realistic for shallow strike-slip earthquakes such as those in California, China or Turkey. We consider a shallow rectangular vertical strike-slip fault model limited above by a free surface and at the bottom of the seismogenic layer by an unbreakable barrier (Fig. 12.6). The elastic medium properties are the same as before, i.e.  $\alpha = 6.4$  km/s,  $\beta = 3.52$  km/s,  $\rho = 2700$  kg/m<sup>3</sup> and  $\mu = 33.5$  GPa. We use the same slip-weakening friction law as in the circular crack simulation, with  $\sigma_s - \sigma_k = 8$  MPa and  $D_c = 0.2$  m, so that  $G_c = 0.8$  J/m<sup>2</sup>. The area modeled has size  $32 \times 64 \times 64$  km<sup>3</sup> with absorbing boundary conditions on all sides except at the top, where we use symmetry to simulate a stress-free surface. A fault of length 44 km extends from the free surface to a depth  $W = 12$  km. We assume that the entire fault plane is subject to a constant initial stress field  $\sigma_0$  such that the dynamic stress drop  $\sigma_0 - \sigma_k = 4.5$  MPa, the same value as for the circular crack of the previous section. Rupture starts from an initial asperity of radius  $R = 4$  km, a size large enough to initiate rupture. In Fig. 12.6 we show the slip-rate field on the fault as a function of time elapsed since the beginning of rupture. We observe that during the first 3 s the rupture fills the region between the surface and the level  $W$ . Then, after a few seconds, a unilateral rupture propagates in the longitudinal direction with a sub-shear speed. At about 7 s the rupture process stabilizes, and we observe a rupture pulse propagating along the fault at almost constant velocity. The width of the pulse is not uniform with depth: it is thin at the bottom of the fault and wider near the surface. The healing or stopping phases that propagate at the rear of the pulse have the same horizontal velocity as the rupture front, producing a model that is quite similar to Haskell's dislocation except that the width of the pulse is variable with depth. This pulse is in very good agreement with the observations reported by Heaton (1990), who deduced from a number of kinematic inversions of shallow earthquakes that they propagated as pulses, as discussed in section 11.7.

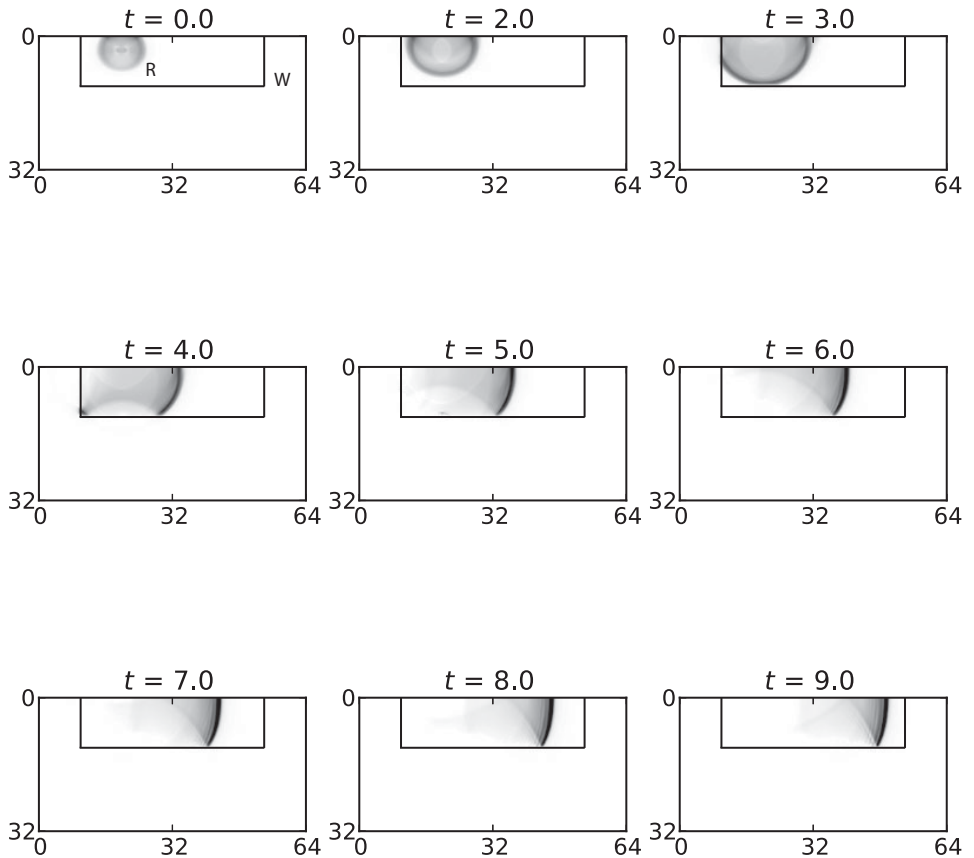


**Figure 12.6.** Snapshots of the slip rate on a shallow rectangular fault with width  $W = 12$  km. The darker regions show higher slip rates. The rupture propagation is sub-shear. After 5 s, a rupture pulse appears spontaneously and propagates along the fault without change as in a Heaton (1990) pulse.

The shallow strike-slip problem of Fig. 12.6 has actually three length scales:  $R$ , the radius of the initial rupture patch;  $W$ , the width of the rectangular fault; and  $D_c$ , the slip-weakening distance of the friction law. The scales  $R$  and  $D_c$  control rupture initiation while  $W$  and  $D_c$  control rupture propagation along the fault. Since the ratio  $W/D_c$  is constant, rupture becomes steady and propagates without change along the fault. This will not be the case, of course, for faults with variable stress drop or variable frictional properties.

## 12.6. Spontaneous rupture on a realistic fault: the Landers 1992 earthquake

Let us consider now the dynamic modeling of a shallow strike-slip earthquake in California. Olsen *et al.* (1997) proposed a dynamic rupture model of the  $M_W = 7.3$  Landers earthquake of 28 June 1992 in southern California and computed synthetic seismograms at several

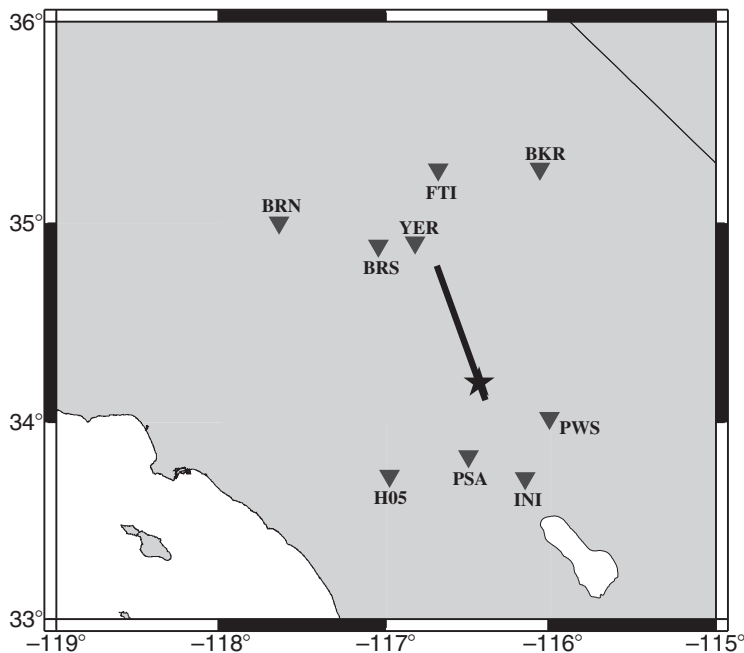


**Figure 12.7.** Landers ( $M_W = 7.3$ ) earthquake of 28 June 1992. The simplified fault trace is shown by the bold straight line, the star shows the epicenter and the inverted triangles the location of the strong motion stations used by Peyrat *et al.* (2001) to invert data to find the source.

strong motion sites near the earthquake fault (Fig. 12.7). Their dynamic model was based on the kinematic inversion of this event by Wald and Heaton (1994), who used seismic and geodetic data as input. Olsen *et al.* (1997) used a method proposed by Bouchon (1997) and Ide and Takeo (1997) to compute the stress-change field from the slip distribution obtained by kinematic inversion methods. This technique provides a stress-change image that must be converted to either an initial stress model or a friction model.

Since the radiation depends only on the elastic changes that occur at the source there is an ambiguity about the initial stress and rupture resistance; this was discussed in detail by Peyrat *et al.* (2001). The most common approach is to assume that the stress drop maps the initial stress on the fault and that after the earthquake the stress on the fault is essentially uniform. This corresponds to the asperity model discussed in section 11.6. Another approach is possible (Peyrat *et al.*, 2001), in which the variations in stress drop are converted into variations in the static friction. In this case rupture occurs only in the areas where the stress is larger than the static friction.

Peyrat *et al.* (2001) inverted the near-field accelerograms by a trial-and-error method, assuming an asperity model where the initial stress was variable on the fault but the rupture resistance (friction) was uniform over the fault plane. The accelerograms were filtered at 0.5 Hz (2 s), so that the model contains wavelengths down to about 5 km. Inversion was started using the initial stress field computed by Olsen *et al.* (1997) from the slip model determined by Wald and Heaton (1994). The initial stress field is shown in the upper panel

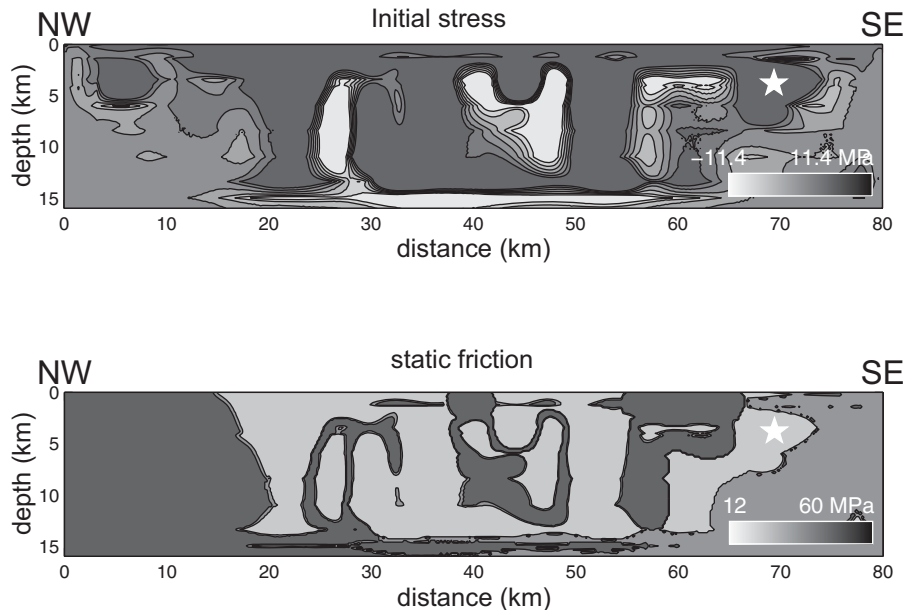


**Figure 12.8.** Initial stress field and peak static friction distribution of the Landers 1992 earthquake, used by Peyrat *et al.* (2001) in their best model. The slip-weakening distance for this model was constant:  $D_c = 1$  m.

of Fig. 12.8. The range of variation in the initial stress, computed from the kinematic slip, is roughly from  $-12$  MPa to  $12$  MPa. The figure shows darker regions, where the initial stress is very large and positive, close to  $11.4$  MPa, and lighter regions where the initial stress is negative; these are regions where rupture will not propagate during the earthquake. Together with this initial stress field it is necessary to provide a friction model (see (12.3)). This is shown in the lower panel of Fig. 12.8, where the lighter regions have peak friction  $\sigma_s - \sigma_k = 12.5$  MPa and the darker regions have very high values because in fact the friction law cannot be determined in the areas of the fault that did not slip during the earthquake. The slip-weakening distance for the dynamic model was assumed to be  $D_c = 0.8$  m, so that  $G_c = 5$  MJ/m<sup>2</sup>. This is a large value but is of the order expected for a magnitude 7.3 event. For significantly smaller values of  $G_c$  the rupture would break the fault at super-shear velocities, leaving a uniform final stress field and a slip distribution completely different from that of Wald and Heaton (1994). For higher values of  $G_c$ , however, rupture would simply not propagate at all along the fault.

A fully dynamic simulation of rupture was carried out, starting with the stress maps of Fig. 12.8. From the slip-rate model determined by the dynamic simulation, synthetic seismograms were computed using the discrete wave number integration method of Bouchon (1981) and Coutant (1990). These synthetic accelerograms were then compared with the observed ones. Inversion consisted in adjusting the initial stress field in order to improve the fit between the observed and computed accelerograms. Full details of the method are described in Peyrat *et al.* (2001). The result of the model is the slip distribution shown in Fig. 12.9, where the largest slip, close to 5 m, occurred near the northwestern end

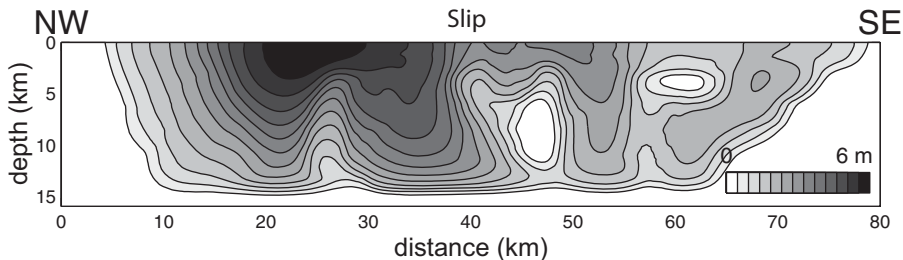


**Figure 12.9.** Slip distribution for the Landers 1992 earthquake obtained by Peyrat *et al.* (2001) using a trial-and-error method for dynamic inversion. The slip is concentrated in the NW part of the fault.

of the fault. The accelerograms computed by this model and the observed accelerograms are shown in Fig. 12.10. For each station we show the two horizontal components, the east (upper) and north (lower) components. There is very good agreement between the observed and computed records, especially northwest of the epicenter, where the amplitudes are larger and the signals shorter due to directivity. In the backward (southeast) direction, the amplitudes are relatively small and the fit is less good than in the forward direction of the fault. This is clearly observed in the station YER traces.

We can now make a quick calculation of the value of  $\kappa$  (12.7) for the model of Peyrat *et al.* (2001). For that purpose we need an average value for the stress drop  $\Delta\sigma$ , which can be computed from the initial and final stress fields. There are many ways to do this computation; the average dynamic stress drop was close to  $\Delta\sigma = 4$  MPa. For the length scale  $R$  we used a fault width  $W = 16$  km. Finally, we needed an estimate of the rigidity  $\mu$ . Although the structure near Landers is vertically heterogeneous we used the average value  $\mu = 33.7$  GPa.

With these values we found the value  $\kappa = 0.72$  for the Landers earthquake. This is very close to the critical value for rectangular faults,  $\kappa_c = 0.76$ , determined by Madariaga and Olsen (2002) for shallow rectangular strike-slip faults. Thus it appears that on average the rupture during the Landers earthquake was barely above the critical value  $\kappa_c$ ; this explains why the average rupture velocity was sub-shear. It must be pointed out, however, that the fault width is not the only length scale that controls rupture; the length scales that dominate the stress field shown in Fig. 12.8 are clearly smaller than 12 km. All this seems to indicate that the rupture in the Landers earthquake reproduces the general behavior of the kinematic model of Wald and Heaton (1994) only if  $\kappa$  were very close to critical. The fact that rupture must have been almost critical can be shown in another way. From a careful study of rupture propagation in the initial stress field shown at the upper panel in Fig. 12.8, Peyrat *et al.* (2001) found that rupture could only propagate in regions of high stress that are sufficiently wide. It takes only a very minor modification of the initial stress field to either stop rupture or guide it into a different area of the fault. This information was extensively used by Peyrat *et al.* (2001, 2004) to invert for the initial stress field from accelerograms recorded in the near field.

In conclusion the initial stress field controls rupture propagation very strongly. As long as the rupture conditions are very close to critical, the rupture extends following a relatively clear pattern of infiltration. It propagates into places where the stress is high over large patches and avoids completely zones where the stresses are low.

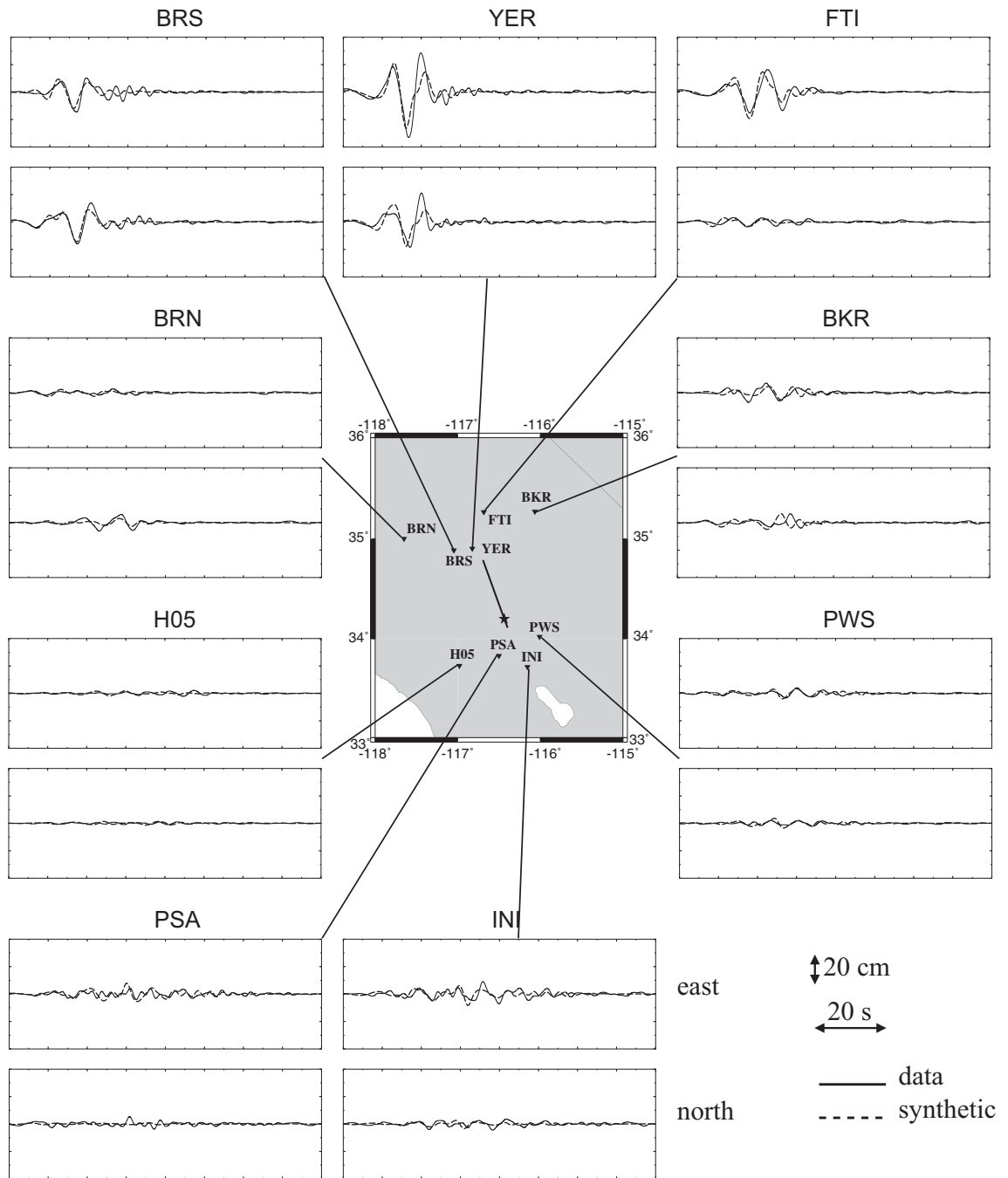


**Figure 12.10.** The observed (continuous-line) and synthetic (broken-line) displacements at the strong motion stations used in the inversion of the Landers 1992 earthquake (Peyrat *et al.*, 2001). The radiation is very strong in the forward direction of the fault (northwest).

## 12.7. Rupture of a geometrically complex earthquake: the Izmit event of August 1999

In the previous sections we studied flat models for simple earthquakes with a circular or rectangular shape and also an example of a heterogeneous stress distribution but a still flat earthquake. We have mentioned at several points in this book that the geometry, especially kinks, jogs, etc., must play a significant role in rupture propagation and consequently in seismic radiation. Many authors have studied the role of kinks in the stress field near a fault, but few have studied the radiation produced by the interaction between a rupture front moving at high speed and a kink. Andrews (1989) discussed the problem using concepts from dislocation mechanics and showed that there was a difficulty involving the interpenetration of matter. Polyakov *et al.* (2002) studied the stress field around the tip of a branching fault and Arias *et al.* (2011) showed that the stress field near the kink must satisfy certain mechanical constraints that solve the problem of interpenetration raised by Andrews (1989). Here we will illustrate these features for the well-studied Izmit, Turkey, earthquake. A careful mapping of the fault in the field was carried out by Barka *et al.* (2002); the result is shown at the top of Fig. 12.11. The fault trace was very complex at the surface, and we do not know how to extrapolate these surface observations to greater

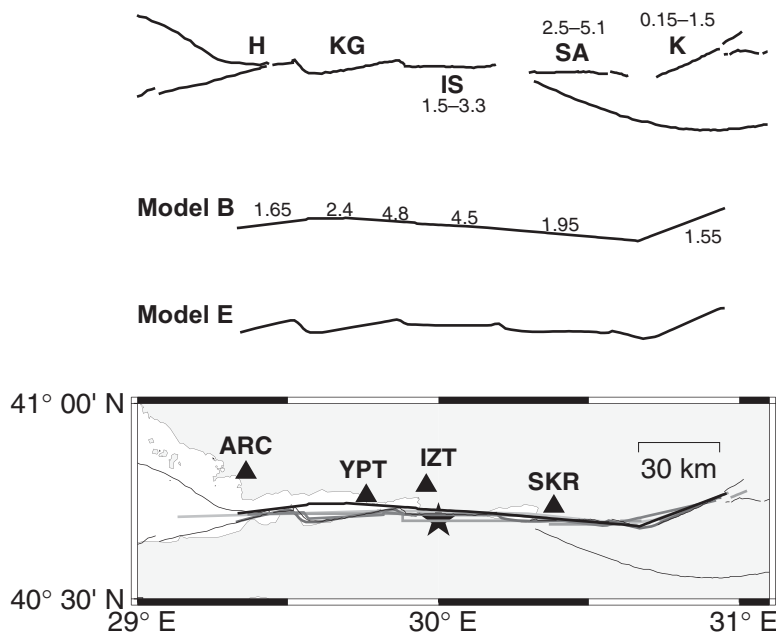


**Fig. 12.11.** Fault trace of the  $M_w = 7.4$  Izmit earthquake of 27 August 1999 in Turkey. At the top, the fault trace proposed by Barka *et al.* (2002) from a detailed field mapping of the fault. Model B and Model E are two extreme models derived from the observed fault trace for simulation purposes (Aochi and Madariaga, 2003). At the bottom the fault map and the strong motion sites that recorded this event are shown.

depths. Aochi and Madariaga (2003) studied several models that attempted to introduce the geometrical complexity of the Barka *et al.* map into rupture dynamics. They used a *boundary integral equation method* (BIEM) to solve the complex fault models shown in Fig. 12.11. The BIEM method they used had been developed by Fukuyama and Madariaga (1998) and Aochi *et al.* (2000). Once the slip distribution was found on the fault, the wave propagation around the fault was computed using a finite difference method. From the complete set of seven models studied by Aochi and Madariaga (2003) we chose models B and E, plotted in Fig. 12.11. Model B is a smoothed version of the Barka *et al.* (2002) map with variable slip along the strike direction, while model E is a segmented model with a set of regular kinks. These two models are extreme versions of smooth and complex fault geometries. In Fig. 12.12 we show the displacement field at different instants of time computed around the fault by the *finite difference method*. The difference between the fields produced by models B and E are striking. The EW components generated by these models are quite different: the smoother model produces a stronger displacement field around the fault because the slip is larger. The most impressive difference is in the transverse (NS) component, which is rarely plotted for flat source models because it is strongly concentrated near the crack tip. For the smooth model, B, the NS component shows a clear super-shear shock. The NS component of model E, however, propagates much more slowly and, although at several instants of time it tries to become super-shear, it remains sub-shear on the average. At the same time the high-frequency radiated waves are stronger for model B. Thus the fault trace geometry has a very large impact in seismic wave generation, which cannot be modeled with simple fault rupture models. Smooth faults favor propagation at fast velocities and eventual super-shear shocks, but generate less high-frequency radiation than complex ruptures. A similar idea was proposed on the base of seismic observations of the Kunlunshan earthquake of 2000 by Bouchon and Vallée (2003).

## 12.8. Dynamic inversion of the 2008 Iwate intermediate-depth earthquake

---

In section 12.6 we presented the trial and error method used by Peyrat *et al.* (2001, 2004) to develop a dynamic rupture model of the Landers earthquake. This is a tedious but enlightening method for understanding rupture propagation starting from a kinematic slip model. In the present section we introduce a dynamic non-linear inversion method where the best model is searched by exploration of the parameter field. This approach is non-linear because the seismic waves do not depend linearly on the parameters of the source model. However, if we can reduce the source model in such a way that it can be processed by a single node in a multicore machine, it is possible to run many different models in parallel. The first attempts at dynamic inversion were made by Peyrat and Olsen (2004), Corish *et al.* (2007) and Di Carli *et al.* (2010), who inverted the  $M_W = 6.7$  Tottori 2000 earthquake in Japan. From these earlier experiences it was clear that dynamic inversion was only feasible for relatively simple models. Di Carli *et al.* (2010) used an elliptical



**Fig. 12.12.** Elastodynamic displacement field simulated around two fault models of the  $M_W = 7.4$  Izmit 1999 earthquake (Aochi and Madariaga, 2003). The plots show the displacement distribution on the surface at 2 s intervals. The NS components show that these two models produce significantly different radiation. In the smoother model a super-shear shock is observed after 10 s.

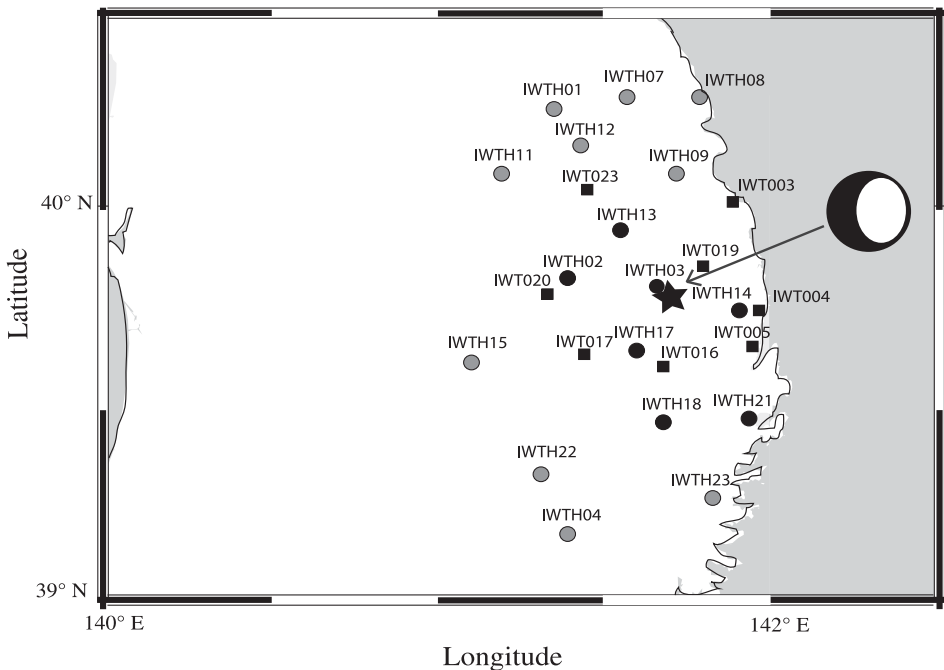


**Fig. 12.13.** Dynamic inversion of the  $M_W = 7.1$  Iwate intermediate-depth earthquake of 24 July 2008. The rectangles show the stations used for the inversion and the circles show the stations used by Ruiz and Madariaga (2013) for verification of the inversion results.

patch model proposed by Vallée and Bouchon (2004) to capture the long-wavelength features of an inverted event.

The 2008 Iwate  $M_W = 7.1$  intraplate earthquake at 115 km depth was well recorded by the Japanese strong motion networks KiKnet and K-NET, as shown in Fig. 12.13 where the star shows the epicenter and the rectangles show the locations of the strong motion instruments used in the inversion. The grey and black circles show the sites that were used by Ruiz and Madariaga (2013) to do a second inversion. The Iwate earthquake was studied in detail by Suzuki *et al.* (2009), who proposed a kinematic source model.

For dynamic inversion we used a single elliptically shaped fault model instead of the usual grid of rectangles in kinematic inversions. The stress and friction were uniform inside the elliptical fault patch. Rupture propagation was controlled by the slip-weakening friction law (12.3). For simplicity, in the following we will assume that the residual friction  $\sigma_k = 0$ . In the forward dynamic model rupture starts at the hypocenter, triggered by a small circular asperity as in the methodology of section 12.2. Once the rupture breaks the small asperity, it will grow or stop spontaneously depending on the values of the stress field  $\sigma_0$  and the friction law. For the dynamic inversion Ruiz and Madariaga (2013) used a total of 10 parameters, which included the parameters of the friction law and the geometry of the fault. In contrast with section 12.4 the initial asperity could be located anywhere inside the fault. Its location was part of the inversion. Since from the seismic data we cannot distinguish between the barrier and asperity models, the inversion was made using the

Table 12.1 Best dynamic model for the Iwate intermediate-depth earthquake				
$a$ (km)	$b$ (km)	$\sigma_0$ (MPa)	$\sigma_s$ (MPa)	$D_c$ (m)
4.02	8.06	34.25	55.96	1

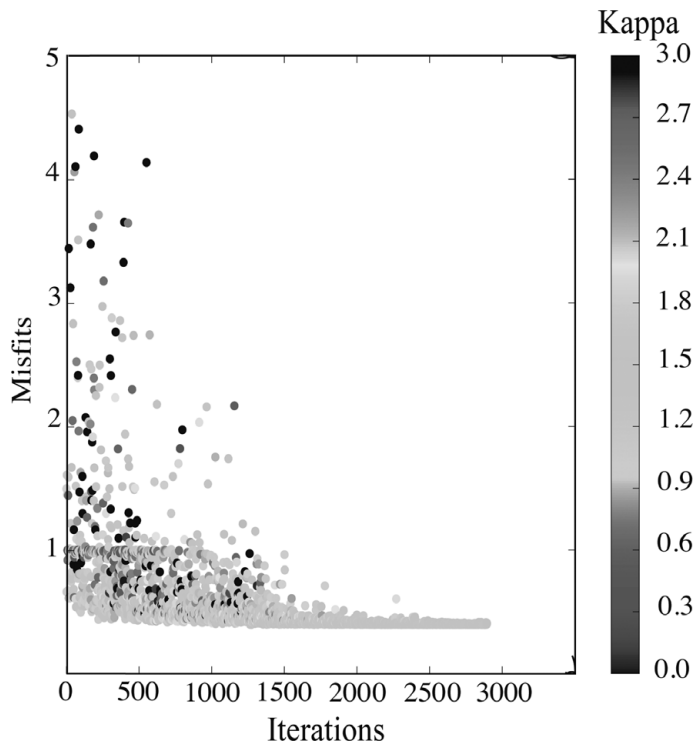
asperity model; the region outside the ellipse was considered to have a very large negative initial stress load that was enough to stop the rupture when it reached the edge of the ellipse. The synthetic and observed records were compared using a simple normalized L2 norm. The search for the best model was made using the neighborhood algorithm (NA) of Sambridge (1999, 2001) although other minimization techniques, such as a genetic algorithm, can be used.

A three-dimensional fourth-order staggered-grid finite difference method with absorbing boundaries and thin fault boundary conditions was used to solve the forward dynamic rupture simulation (Madariaga *et al.*, 1998; Dalguer and Day, 2006, 2007). The spatial and temporal steps were 200 m and 0.005 s respectively, so that the CFL constant (12.5) for this grid is everywhere less than 0.3 and the finite difference method is stable. The grid had  $160 \times 160 \times 160$  elements and was centered at the hypocenter on the fault plane. The fault zone was 32 km wide and 32 km deep but only a small part broke during the earthquake. The AXITRA spectral code was used to simulate wave propagation from the source to the receivers.

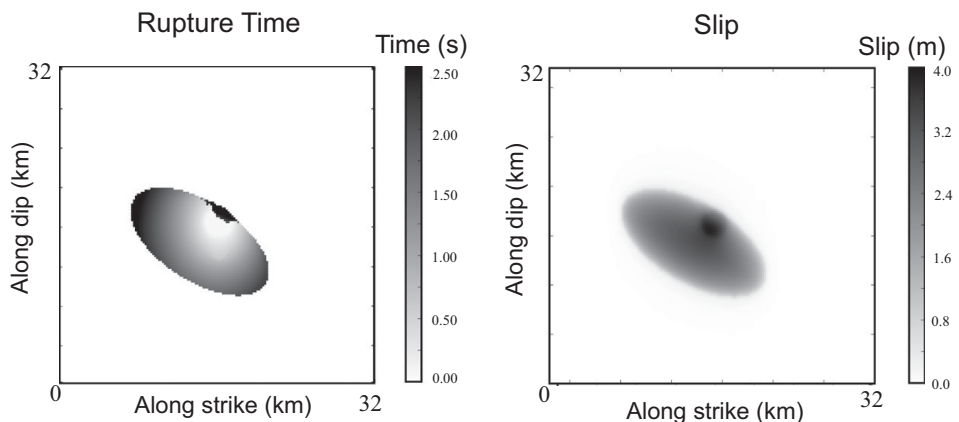
Non-linear dynamic inversion was carried out for the strong motion records located within a radius of 40 km around the hypocenter, in order to avoid wave conversion effects outside the so-called S-window. Beyond this distance conversion into local surface waves may affect the records significantly. Table 12.1 shows the optimal values for the most significant parameters obtained by dynamic inversion. In the table  $a$  and  $b$  are the semiaxes of the source ellipse and the stresses are referred to kinematic friction  $\sigma_k = 0$ . The best model obtained by the neighborhood algorithm had a misfit  $\chi^2 \approx 0.4$ , meaning that our model explains 60% of the observed data, which also converge to a seismic moment  $M_0 \approx 1.5 \cdot 10^{19}$  N m, similar to that obtained by Suzuki *et al.* (2009) from kinematic inversion. The misfits for each step in the inversion are shown in Fig. 12.14. In this figure we also show the values of  $\kappa$  computed from (12.7) for each model using an average radius of the source ellipse for  $R$ ;  $\kappa$  converges to the value 1.34. The convergence to a well-defined value of  $\kappa$  can be explained by a trade-off between the initial stress and the friction law parameters.

Figure 12.15 shows, on the left, the rupture time and, on the right, the slip distribution for the best dynamic models obtained by the neighborhood algorithm. The overall characteristics are a short rupture duration of less than 2.1 s, implying a very high sub-shear rupture velocity. Rupture starts in the small asperity and then propagates to the rest of the fault, mainly in a direction away from the surface. Figure 12.16 shows snapshots of the slip rate on the fault plotted every 0.4 s. The largest values of slip rate are attained near the boundaries of the ellipse where the large negative stress stopped the rupture.

The results listed in Table 12.1 and shown in the preceding figures indicate that the Iwate intermediate-depth earthquake had a relatively small size considering that the maximum



**Fig. 12.14.** Convergence of the neighborhood algorithm misfit with iteration for the dynamic inversion of the 2008 Iwate earthquake. A total of 3000 models were tested until convergence was obtained (Ruiz and Madariaga, 2013).



**Fig. 12.15.** Rupture time delay and slip distribution for the best model found by dynamic inversion of the 2008 Iwate earthquake (Ruiz and Madariaga, 2013).

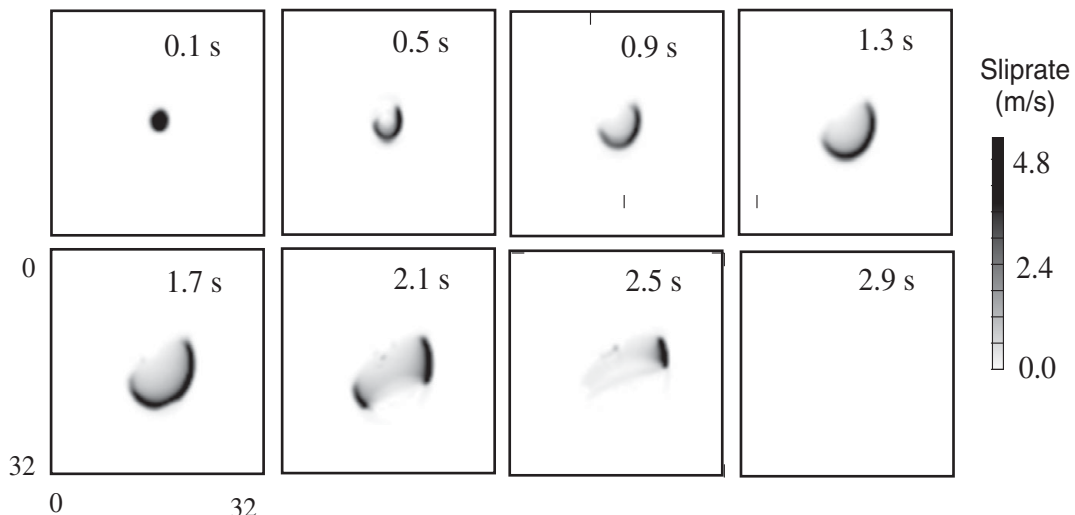


**Fig. 12.16.** Snapshots of the slip rate field for at 0.4 s intervals for the best model found by dynamic inversion for the 2008 Iwate earthquake (Ruiz and Madariaga, 2013). The sides of each square are 32 km in length.

slip was 4 m, as shown in Fig. 12.15. The moment of the event was  $1.5 \times 10^{19}$  Nm. As a consequence the stress drop was large, 34.65 MPa, which is about 10 times larger than the stress drops for similar events at shallower depths. The most important parameters from a dynamic point of view are the peak friction stress  $\sigma_s = 56$  MPa and the slip-weakening distance  $D_c = 1$  m, which together give an energy release rate 23 MJ/m<sup>2</sup>; this is also very large compared with those estimated for events of this magnitude at shallower depths. These results imply that intermediate-depth earthquakes have much smaller dimensions and higher stresses than shallow-depth events, something that is not surprising.

Synthetic and observed horizontal displacements are shown in Fig. 12.17 for various strong motion sites. The synthetic displacements reproduce the observed records very well with the exception of those for stations IWTH23, IWTH22 and IWTH04. The duration of the signals is of the order of 4–5 s, implying a very fast rupture and a massive stress drop. In Fig. 12.18 we show the Fourier spectra computed for the EW components of two records shown in Fig. 12.17. The dynamic models fit the spectra very well: they all resemble the Brune  $\omega^{-2}$  model beyond the low-frequency cut-off of the low-pass filter applied to the data.

## 12.9. Conclusion and perspectives

The increasing availability of good quality high-dynamic-range strong motion data makes dynamic modeling and inversion possible for many earthquakes. As computer resources increase, more earthquakes will be amenable to modeling and inversion but, for the moment, inversion can only be envisaged for events with relatively simple geometries that can be parameterized using a small number of parameters.

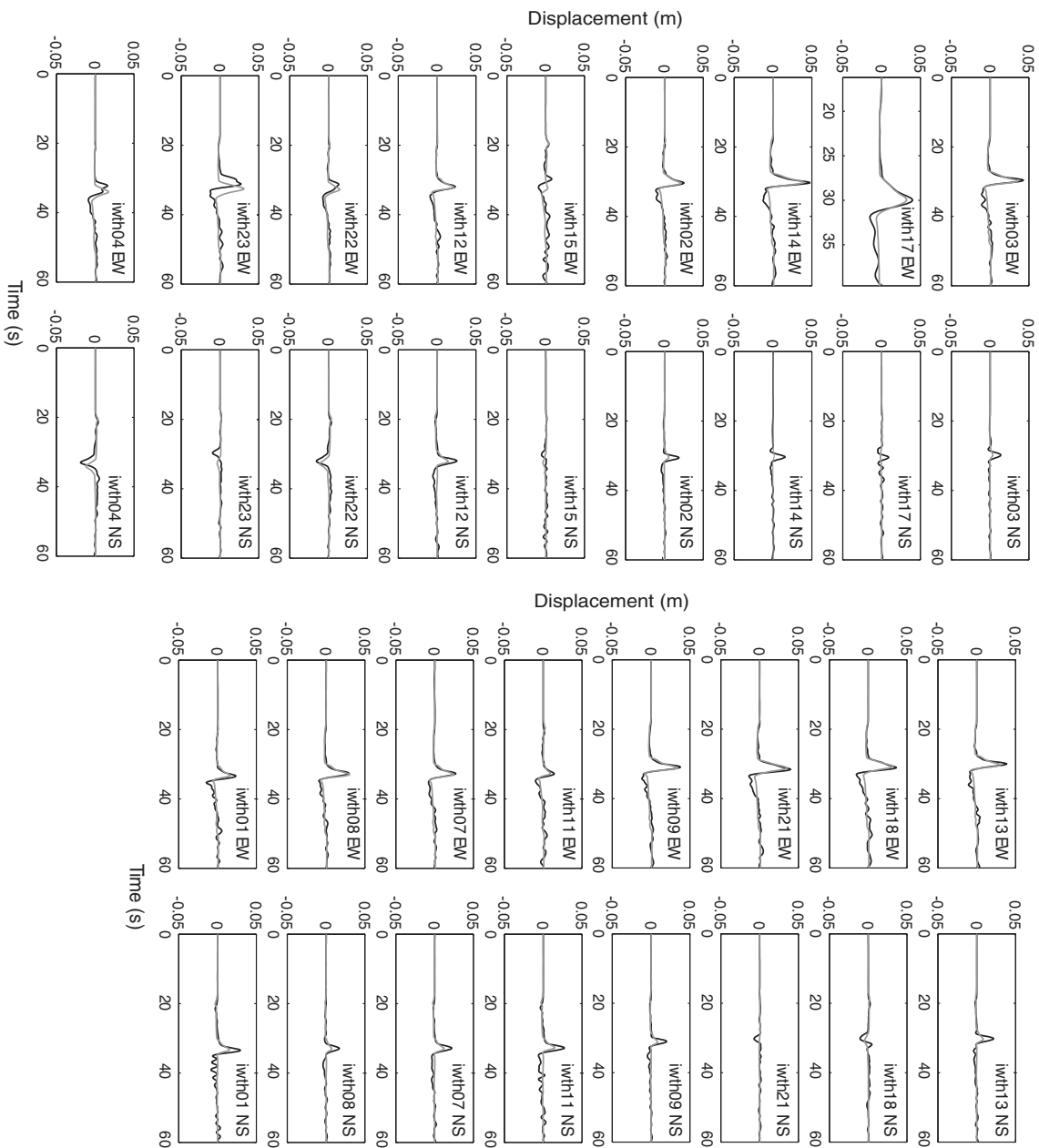


**Fig. 12.17.**

For comparison, the observed and synthetic strong motion records integrated to show the displacements for a chosen set of stations that recorded the 2008 Iwate earthquake.

It is possible to envisage different strategies for inversion using a non-linear approach for the determination of global parameters followed by a linearized inversion around these global values. This approach was partially implemented by Ruiz and Madariaga (2013) for the Iwate intermediate-depth earthquake and by Twardzic *et al.* (2012) for the Parkfield

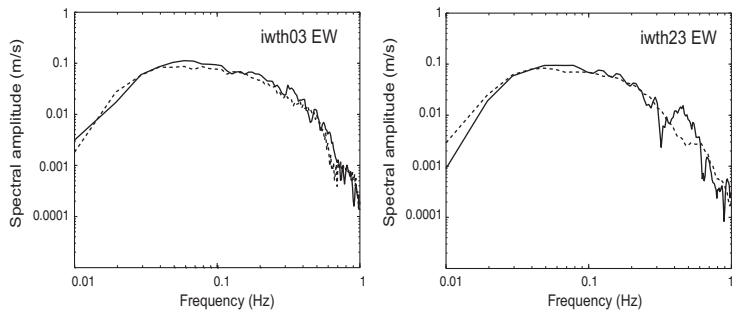


**Fig. 12.18.** The observed and synthetic spectra for two stations that recorded the 2008 Iwate earthquake. Station IWTH03 was located close to the epicenter and IWTH23 was some 50 km to the south.

earthquake. These authors used a Monte Carlo technique to explore the parameter space around the best solution obtained with the neighborhood algorithm. It turns out, as expected from theoretical considerations, that the parameters of the friction law cannot be inverted independently of the geometry of the source. The trade-off can be quantified, however. More difficult problems lie ahead, in particular how to parameterize the source beyond the simple elliptical-shaped models used so far. A very important step is to establish a connection between dynamic and kinematic inversion.

The other area that is making rapid progress is that of forward modeling with the goal of predicting strong motion for different earthquake scenarios with increasing accuracy. Here, the rupture velocity, high or low stress-drop events and the complexity of slip are determinant. As an example we cite the large-scale simulations by Olsen *et al.* (2009) or the significant efforts to take into account the spatial changes in stress and friction in the determination of source complexity (Mai and Beroza, 2002; Liu *et al.*, 2006; Schmedes *et al.*, 2012). Studies of the interaction of a rupture front with heterogeneities in the stress or friction and the role of geometry in controlling dynamic ruptures are still in their infancy. The description of the roughness and heterogeneity of fault surfaces in statistical terms is also a major subject of current research, which should have a strong influence in the modeling of seismic ruptures, especially at high frequencies (Brodsky *et al.*, 2011; Candela *et al.*, 2012).

## References

- Abercrombie, R. E. and J. R. Rice (2005). Can observations of earthquake scaling constrain slip weakening? *Geophys. J. Int.*, **162**, 406–424.
- Adda Bedia, M. and R. Madariaga (2008). Seismic radiation from a kink on an antiplane fault. *Bull. Seism. Soc. Am.*, **98**, 2291–2302.
- Aki, K. (1966). Generation and propagation of G waves from the Niigata earthquake of June 16, 1964. Estimation of earthquake movement, released energy and stress-strain drop from G wave spectrum. *Bull. Earthq. Res. Inst.*, **44**, 23–88.
- Aki, K. (1967). Scaling law of seismic spectrum. *J. Geophys. Res.*, **73**, 5359–5376.
- Aki, K. (1979). Characterization of barriers on an earthquake fault. *J. Geophys. Res.*, **84**, 6140–6148.
- Aki, K. (1984). Asperities, barriers, characteristic earthquakes and strong motion prediction. *J. Geophys. Res.*, **89**, 5867–5872.
- Aki, K. and P. G. Richards (1980). *Quantitative Seismology. Theory and Methods*, Two volumes. San Francisco: W. H. Freeman
- Ampuero, J. P. and A. M. Rubin (2008). Earthquake nucleation on rate and state faults – aging and slip laws. *J. Geophys. Res.*, **113**, B01302, doi:10.1029/2007JB005082.
- Andrews, D. J. (1976). Rupture velocity of plain stress shear cracks. *J. Geophys. Res.*, **81**, 5679–5687.
- Andrews, D. J. (1989). Mechanics of fault junctions. *J. Geophys. Res.*, **94**, 9389–9397
- Andrews, D. J. (1999). Test of two methods for faulting in finite-difference calculations. *Bull. Seism. Soc. Am.*, **89**, 931–937.
- Aochi, H., and R. Madariaga (2003). The 1999 Izmit, Turkey, earthquake: non-planar fault structure, dynamic rupture process, and strong ground motion. *Bull. Seismol. Soc. Am.*, **93**, 1249–1266.
- Aochi, H., E. Fukuyama, and M. Matsu’ura (2000). Spontaneous rupture propagation on a non-planar fault in 3-D elastic medium. *Pure Appl. Geophys.* **157**, 2003–2027.
- Archuleta, R. J. (1984). A faulting model for the 1979 Imperial Valley earthquake. *J. Geophys. Res.*, **89**, 4559–4585.
- Arias, R., R. Madariaga and M. Adda-Bedia (2011). Singular elasto-static field near a fault kink. *Pageoph.*, **168**, 2167–2179.
- Avallone, A., M. Marzario, A. Cirella, A. Piatanesi, A. Rovelli, C. Di Alessandro *et al.* (2011). Very high rate (10 Hz) GPS seismology for moderate-magnitude earthquakes: the case of the  $M_W$  6.3 L’Aquila (Central Italy) event. *J. Geophys. Res.*, **116**, B02305, doi:10.1029/2010JB007834, 2011.
- Backus, G. E. (1977). Interpreting the seismic glut moments of total degree two or less. *Geophys. J. Roy Astr. Soc.*, **51**, 1–25.

- Backus, G. E. and M. Mulcahy (1976a). Moment tensors and other phenomenological descriptions of seismic waves. I. Continuous displacements. *Geophys. J. Roy Astr. Soc.*, **46**, 341–361.
- Backus, G. E. and M. Mulcahy (1976b). Moment tensors and other phenomenological descriptions of seismic waves. II. Discontinuous displacements. *Geophys. J. Roy Astr. Soc.*, **47**, 301–330.
- Barbot, S., N. Lapusta and J. P. Avouac (2012). Under the hood of the earthquake machine: toward predictive modeling of the seismic cycle. *Science*, **336**, 707–710.
- Barenblatt, G. I. (1959a). The formation of equilibrium cracks during brittle fracture. General ideas and hypotheses. Axially-symmetric cracks. *J. Appl. Math. Mech.*, **23**, 622–636.
- Barenblatt, G. I. (1959b). On equilibrium cracks, formed in brittle fracture. *Doklady, USSR Academy of Sciences*, **127**, 47–50 (in Russian).
- Barenblatt, G. I. (1962). The mathematical theory of equilibrium cracks in brittle fracture. *Adv. Appl. Mech.*, **7**, 55–129.
- Barka, A., H. S. Akyüz, E. Altunel, G. Sunal, Z. Cakir, A. Dikbas et al. (2002). The surface rupture and slip distribution of the August 17, 1999 Izmit earthquake, M 7.4, North Anatolian Fault, *Bull. Seism. Soc. Am.*, **92**, 43–60.
- Båth, M. (1965). Lateral inhomogeneities of the upper mantle. *Tectonophys.*, **2**, 483–514.
- Beeler, N. M. and T. E. Tullis (1996). Self-healing slip pulses in dynamic rupture models due to velocity dependent strength. *Bull. Seism. Soc. Am.*, **86**, 1130–1148.
- Beeler, N. M., T. E. Tullis and J. D. Weeks (1994). The roles of time and displacement in the evolution effect in rock friction. *Geophys. Res. Lett.*, **21**, 1987–1990.
- Ben Menahem, A. (1961). Radiation of seismic surface waves from finite moving sources. *Bull. Seism. Soc. Am.*, **51**, 401–453.
- Ben Menahem, A. (1962). Radiation of seismic body waves from finite moving sources in the earth. *J. Geophys. Res.*, **67**, 396–474.
- Ben Menahem, A. and S. J. Singh (1981). *Seismic Waves and Sources*. Berlin: Springer.
- Berckhemer, H. (1962). Die Ausdehnung der Bruchfläche im Erdbebenherd und ihr Einfluss auf das seismische Wellenspektrum. *Gerland Beitr. Geophys.*, **71**, 5–26.
- Bernard, P. and R. Madariaga (1984). A new asymptotic method for the modeling of near-field accelerograms. *Bull. Seism. Soc. Am.*, **74**, 539–557.
- Bilich, A., J. F. Cassidy and K. Larson (2008). GPS seismology: application to the 2002  $M_W$  7.9 Denali fault earthquakes. *Bull. Seism. Soc. Am.*, **98**, 593–606.
- Bizzarri, A. and M. Cocco (2003). Slip-weakening behavior during the propagation of dynamic ruptures obeying rate- and state-dependent friction laws. *J. Geophys. Res.*, **108**, doi: 10.1029/2002JB002198. Issn: 0148-0227.
- Bizzarri, A. and S. Das (2012). Mechanics of 3-D shear cracks between Rayleigh and shear wave rupture speeds. *Earth Planet. Sci. Lett.*, **357–358**, 397–404.
- Boatwright, J. (1978). Detailed spectral analysis of two small New York state earthquakes, *Bull. Seism. Soc. Am.*, **68**, 1117–1131.
- Bodin, P. and J. N. Brune (1996). On the scaling of slip and rupture for shallow strike-slip earthquakes: quasi-static models and dynamic rupture propagation. *Bull. Seism. Soc. Am.*, **86**, 1292–1299.

- Boore, D. M., C. Stephens and W. B. Joyner (2002). Comments on baseline correction of digital strong-motion data: examples from the 1999 Hector Mine, California, earthquake. *Bull. Seism. Soc. Am.*, **92**, 1543–1560.
- Bouchon, M. (1981). A simple method to calculate Green's function for elastic layered media. *Bull. Seism. Soc. Am.*, **71**, 959–971.
- Bouchon, M. (1982). The complete synthesis of seismic crustal phases at regional distances. *J. Geophys. Res. B*, **87**, 2156–2202.
- Bouchon, M. (1997). The state of stress on some faults of the San Andreas system as inferred from near-field strong motion data. *J. Geophys. Res.*, **102**, 1731–1744.
- Bouchon, M., and M. Vallée (2003). Observation of long supershear rupture during the  $M_s = 8.1$  Kunlunshan (Tibet) earthquake, *Science*, **301**, 824–826.
- Bouchon, M., M. Bouin, H. Karabulut, M. N. Toksöz, M. Dietrich, and A. J. Rosakis (2001). How fast is rupture during an earthquake? New insights from the 1999 Turkey earthquakes. *Geophys. Res. Lett.*, **28**, 2723–2726.
- Bouchon M., V. Durand, D. Marsan, H. Karabulut and J. Schmittbuhl (2012). The long precursory phase of most large interplate earthquakes. *Nature Geosci.*, **6**, 299–302.
- Bouchon, M., N. Toksoz, H. Karabulut, M.-P. Bouin, M. Dieterich, M. Aktar *et al.* (2002). Space and time evolution of rupture and faulting during the 1999 I'zmit (Turkey) earthquake. *Bull. Seism. Soc. Am.* **92**, 256–266.
- Brace, W. F. and J. B. Walsh (1962). Some direct measurements of the surface energy of quartz and orthoclase. *Amer. Mineral.*, **47**, 111–112.
- Bracewell, R. (1965). *The Fourier Transform and its Applications*. New York: MacGraw-Hill.
- Brantut N. and J. R. Rice (2011). How pore fluid pressurization influences crack tip processes during dynamic rupture. *Geophys. Res. Lett.*, **38** L24314, doi:10.1029/2011GL050044
- Brillinger, D. R., A. Udías and B. A. Bolt (1980). A probability model for regional focal mechanism solutions. *Bull. Seism. Soc. Am.*, **70**, 149–170.
- Broberg, K. B. (1999). *Cracks and Fracture*. San Diego, CA: Academic Press.
- Brodsky, E. E., J. G. Gilchrist, A. Sagy and C. Colletini (2011). Faults smooth gradually as a function of slip. *Earth Planet. Sci. Lett.*, **302**, 185–193.
- Brune, J. (1970). Tectonic stress and the spectra of seismic shear waves from earthquakes. *J. Geophys. Res.*, **75**, 4997–5009.
- Brune, J. (1971). Correction. *J. Geophys. Res.* **76**, 5002.
- Burridge, R. (1969). The numerical solution of certain integral equations with non-integral kernel arising in the theory of cracks propagation and elastic wave diffraction. *Phil. Trans. Roy. Soc. A*, **265**, 353–381.
- Burridge, R. and G. S. Halliday (1977). Dynamic shear cracks with friction as models for shallow focus earthquakes. *Geophys. J. Roy. Astr. Soc.*, **25**, 261–283.
- Burridge, R. and L. Knopoff (1964). Body force equivalents for seismic dislocations. *Bull. Seism. Soc. Am.*, **54**, 1875–1888.
- Burridge, R. and L. Knopoff (1967). Model and theoretical seismicity. *Bull. Seism. Soc. Am.*, **57**, 341–371.
- Byerly, P. (1928). The nature of the first motion in the Chilean earthquake of November 11, 1922. *Am. J. Sci. (series 5)*, **16**, 232–236.

- Candela, T., F. Renard, Y. Klinger, K. Mair, J. Schmittbuhl, and E. E. Brodsky, (2012). Roughness of fault surfaces over nine decades of length scales. *J. Geophys. Res.*, **117**, doi: 10.1029/2011JB009041.
- Carlson, J. M. and J. S. Langer (1989). Properties of earthquakes generated by fault dynamics. *Phys Rev. Lett.* **32**, 2632–2635.
- Cesca, S., E. Buorn, and T. Dahm (2006). Moment tensor inversion of shallow earthquakes in Spain. *Geophys. J. Int.*, **166**, 839–854,
- Cesca, S., S. Heimann, K. Stammmer and T. Dahm (2010). Automated point and kinematic source inversion at regional distances. *J. Geophys. Res.*, **115**, B06304, doi:10.1029/2009JB006450.
- Chapman, C. H. (1978). A new method for computing synthetic seismograms. *Geophys. J. Roy. Astr. Soc.*, **54**, 481–518.
- Chen, Y. T. and L. S. Xu (2000). A time-domain inversion technique for the tempo-spatial distribution of slip on a finite fault with applications to recent large earthquakes in the Tibetan plateau. *Geophys. J. Int.* **143**, 407–416.
- Cocco, M. and A. Bizzari (2002). On the slip-weakening behavior of rate and state friction laws. *Geophys. Res. Lett.*, **29**, 1516.
- Cochard, A. and R. Madariaga (1994). Dynamic faulting under rate depending friction. *Pageoph.*, **142**, 419–445.
- Cochard, A. and R. Madariaga (1996). Complexity of seismicity due to high rate-dependent friction. *J. Geophys. Res.*, **101**, 25 321–25 336.
- Corish, S. C., R. Bradley and K. B. Olsen (2007). Assessment of a nonlinear dynamic rupture inversion technique. *Bull. Seismol. Soc. Am.*, **97**, 901–914.
- Cottrell, A. H. and B. Bilby (1949). Dislocation theory of yielding and strain ageing of iron. *Proc. Phys. Soc. A*, **62**, 49–62.
- Coutant, O. (1990). Programme de simulation numerique AXITRA, Rapport LGIT. University Joseph Fourier, Grenoble, France
- Cowie, P. A. and C. H. Scholz (1992). Displacement-length scaling relationship for faults: data synthesis and discussion. *J. Struct. Geol.*, **14**, 1149–1156.
- Cruz-Atienza, V. M., and J. Virieux (2004). Dynamic rupture simulation of non-planar faults with a finite-difference approach. *Geophys. J. Int.*, **158**, 939–954.
- Custodio, S., P. Liu and R. J. Archuleta (2005). The 2004  $M_W$  6.0 Parkfield, California, earthquake: inversion of near-source ground motion using multiple data sets. *Geophys. Res. Lett.*, **32**, L23312, doi:10.1029/2005GL024417.
- Dahlen, F. A. and J. Tromp (1998). *Theoretical Global Seismology*. Princeton: Princeton University Press.
- Dahm, T. (1996). Relative moment tensor inversion based on ray theory: theory and synthetic tests. *Geophys. J. Int.*, **124**, 245–257.
- Dahm, T. and F. Krüger (1999). Higher-degree moment tensor inversion using far-field broad-band recordings: theory and evaluation of the method with application to the 1994 Bolivia earthquake. *Geophys. J. Int.*, **137**, 35–50.
- Dahm, T., G. Manthei and J. Eisenblatter (1999). Automated moment tensor inversion to estimate source mechanisms of hydraulically induced micro-seismicity in salt rock. *Tectonophys.*, **306**, 1–17, DOI: 10.1016/S0040-1951(99)00041-4

- Dalguer, L. A. and S. M. Day (2006). Comparison of fault representation methods in finite difference simulations of dynamic rupture. *Bull. Seism. Soc. Am.*, **96**, 1764–1778.
- Dalguer, L. A. and S. M. Day (2007). Staggered-grid split-node method for spontaneous rupture simulation. *J. Geophys. Res.* **112**, B02302, doi:10.101029/2006JB004467.
- Das, S. (1980). A numerical method for determination of source time functions for general 3 dimensional rupture propagation. *Geophys. J. Roy. Astr. Soc.*, **62**, 591–604.
- Das, S. and K. Aki (1977a). Fault planes with barriers: a versatile earthquake model. *J. Geophys. Res.*, **82**, 5648–5670.
- Das, S. and K. Aki (1977b). A numerical study of two dimensional spontaneous rupture propagation. *Geophys. J. Roy. Astr. Soc.*, **50**, 643–668.
- Das, S. and B. V. Kostrov (1983). Breaking of a single asperity: rupture process and seismic radiation. *J. Geophys. Res.*, **88**, 4277–4288.
- Das, S. and B. V. Kostrov (1997). Determination of the polynomial moments of the seismic moment rate density distribution with positivity constraints. *Geophys. J. Int.*, **131**, 115–126.
- Day, S. M. (1982). Three dimensional simulation of spontaneous rupture, the effect of non uniform prestress. *Bull. Seism. Soc. Am.*, **72**, 1881–1902.
- Delouis, B., P. Lundgren, J. Salichon and D. Giardini (2000). Joint inversion of InSAR and teleseismic data for the slip history of the 1999 Izmit (Turkey) earthquake, *Geophys. Res. Lett.* **27**, 3389–3392.
- Deschamps, A., H. Lyon-Caen and R. Madariaga (1980). Mise au point sur les méthodes de calcul de séismogrammes synthétiques de long périod. *Ann. Géophys.* **36**, 167–178.
- Di Carli, S., C. Francois-Holden, S. Peyrat and R. Madariaga (2010). Dynamic inversion of the 2000 Tottori earthquake based on elliptical subfault approximations, *J. Geophys. Res.*, **115**, B12 328, doi: 10.1029/2009JB006358
- Di Toro, G., R. Han, T. Hirose, N. De Paola, S. N. K. Mizoguchi, F. Ferri *et al.* (2011). Fault lubrication during earthquakes, *Nature*, **471**, 494–498.
- Dieterich, J. H. (1979a). Modeling of rock friction: 1. Experimental results and constitutive equations, *J. Geophys. Res.*, **84**, 2161–2168.
- Dieterich, J. H. (1979b). Modeling of rock friction. 2. Simulation of preseismic slip. *J. Geophys. Res.* **84**, 2169–2175.
- Dieterich, J. H. (1992). Earthquake nucleation on faults with rate and state-dependent strength. *Tectonophysics*, **21**, 115–134.
- Dieterich, J. H. (2007) Application of rate-and-state-dependent friction to models of fault slip and earthquake occurrence. In: *Earthquake Seismology*, eds. G. Schubert, and H. Kanamori, *Treatise on Geophysics*, vol. 4, pp.107–129. Elsevier.
- Doornbos, D. J. (1982). Seismic moment tensors and kinematic source parameters. *Geophys. J. Roy. Astr. Soc.*, **69**, 235–251.
- Dreger, D. S. (1994). Empirical Green's function study of the January 17, 1994 Northridge, California earthquake. *Geophys. Res. Lett.*, **21**, 2633–2636,
- Dreger, D. S. and D. V. Helmberger (1993). Determination of source parameters at regional distances with three-component sparse network data. *J. Geophys. Res.*, **98**, 8107–8125.
- Duan, B. (2010). Role of initial stress rotations in rupture dynamics and ground motion: a case study with implications for the Wenchuan earthquake, *J. Geophys. Res.*, **115**, B05301, doi:10.1029/2009JB006750.

- Duan, B., and D. D. Oglesby (2006). Heterogeneous fault stresses from previous earthquakes and the effect on dynamics of parallel strike-slip faults, *J. Geophys. Res.*, **111**, doi:10.1029/2006JB004138.
- Dugdale, D. S. (1960). Yielding of steel sheets containing slits. *J. Mech. Phys. Solids*, **8**, 100–104.
- Dunham, E. M. and R. J. Archuleta (2004). Evidence of supershear transient during the 2002 Denali Fault earthquake. *Bull. Seism. Soc. Am.*, **94**, S256–S268.
- Dziewonski, A. M. and D. L. Anderson (1981). Preliminary reference Earth model. *Phys. Earth Planet. Int.*, **25**, 297–356.
- Dziewonski, A. M. and J. H. Woodhouse (1983). Studies of the seismic source using normal mode theory. In: *Earthquakes: Observation, Theory and Interpretation*, eds. H. Kanamori and E. Boschi. New York: North Holland, 45–137.
- Dziewonski, A. M., T. A. Chou and J. H. Woodhouse (1981). Determination of earthquake source parameters from waveform data for studies of global and regional seismicity. *J. Geophys. Res.*, **86**, 2825–2852.
- Ellsworth, W. L. and G. C. Beroza, (1995). Seismic evidence for an earthquake nucleation phase. *Science*, **268**, 851–865.
- Engdahl, E. R., and A. Villaseñor (2002). Global seismicity: 1900–1999. In: *International Handbook of Earthquake and Engineering Seismology*, eds. W. H. K. Lee, H. Kanamori, P. C. Jennings and C. Kisslinger, Part A, pp. 665–690. London: Academic Press.
- Eshelby, J. D. (1957). The determination of the elastic field of an ellipsoidal inclusion and related problems. *Proc. Roy. Soc. A*, **241**, 376–396.
- Eshelby, J. D. (1959). The elastic field outside an ellipsoidal inclusion. *Proc. Royal Soc. A*, **252**, 561–569.
- Fossum, A. F. and L. B. Freund (1975). Non uniformly moving shear crack model of a shallow focus earthquake mechanism. *J. Geophys. Res.*, **80**, 3343–3347.
- Freund, L. B. (1972a). Crack propagation in an elastic solid subjected to general loading. I. Constant rate of extension. *J. Mech. Phys. Solids*, **20**, 129–140.
- Freund, L. B. (1972b). Energy flux into the tip of an extending crack in an elastic solid. *J. Elasticity*, **2**, 341–349.
- Freund, L. B. (1972c). Flux into a tip of an extending crack in an elastic solid. *J. Elasticity*, **2**, 341–349.
- Freund, L. B. (1979). The mechanics of dynamic shear crack propagation. *J. Geophys. Res.*, **84**, 2199–2209.
- Fröhlich, C. (2006). *Deep Earthquakes*. Cambridge: Cambridge University Press.
- Fuchs, K and G. Müller (1971). Computation of synthetic seismograms with the reflectivity method and comparison with observations, *Geophys. J. Roy. Astr. Soc.*, **23**, 417–433.
- Fukuyama, E. and K. Irikura (1986). Rupture process of the 1983 Japan Sea (Akita-Oki) earthquake using a wave form inversion method. *Bull. Seism. Soc. Am.*, **76**, 1623–1649.
- Fukuyama, E. and R. Madariaga (1998). Rupture dynamics of a planar fault in a 3D elastic medium: rate and slip weakening friction. *Bull. Seism. Soc. Am.*, **88**, 1–17.
- Fukuyama, E. and T. Mikumo (1993). Dynamic rupture analysis: Inversion for the process of the 1990 Izu-Oshima, Japan, earthquake ( $M = 6.5$ ). *J. Geophys. Res.*, **98**, 6529–6542.

- Gel'fand, I. M. and G. E. Shilov (1964). *Generalized Functions*. New York: Academic Press.
- Gershanik, S. (1996). *Sismología*. La Plata: Universidad Nacional de la Plata.
- Gilbert, F. (1970). Excitation of the normal modes of the Earth by earthquakes sources. *Geophys. J. Roy. Astr. Soc.*, **22**, 223–226.
- Goldsby L. and T. E. Tullis (2011). Flash heating leads to low frictional strength of crustal rocks at earthquake slip rates, *Science*, **334**, 216–218.
- Griffith, A. (1921). The phenomenon of rupture and flow in solids. *Phil. Trans. Roy. Soc.*, **221**, 163–198.
- Guatteri, M., and P. Spudich (2000). What can strong-motion data tell us about slip-weakening fault-friction laws? *Bull. Seism. Soc. Am.*, **90**, 98–116.
- Gubbins, D. (1990). *Seismology and Plate Tectonics*. Cambridge: Cambridge University Press.
- Gutenberg, B. and C. F. Richter (1942). Earthquake magnitude, intensity, energy and acceleration. *Bull. Seism. Soc. Am.*, **32**, 163–191.
- Gutenberg, B. and C. F. Richter (1954). *Seismicity of the Earth and associated phenomena*. 2nd edn. Princeton: Princeton University Press.
- Gutenberg, B. and C. F. Richter (1956). Earthquake magnitude, intensity, energy and acceleration (second paper). *Bull. Seism. Soc. Am.*, **46**, 105–145.
- Han, R., T. Shimamoto, T. Hirose, J. H. Ree and J. Ando (2007). Ultralow friction of carbonate faults caused by thermal decomposition. *Science*, **316**, 878–881.
- Hanks, T. C. (1977). Earthquake stress-drops, ambient tectonics stresses and stresses that drive plates. *Pure Appl. Geophysics*, **115**, 441–458.
- Hanks, T. C. and M. Wyss (1972). The use of body-wave spectra in the determination of seismic source parameters. *Bull. Seism. Soc. Am.*, **62**, 561–589.
- Hanks, T. C. and H. Kanamori (1979). A moment magnitude scale. *J. Geophys. Res.*, **84**, 2348–2350.
- Harris, R., and Day, S. (1993). Dynamics of fault interaction: parallel strike-slip faults, *J. Geophys. Res.*, **98**, 4461–4472.
- Harris, R. A., M. Barall, R. Archuleta, E. Dunham, B. Aagaard, J. P. Ampuero *et al.* (2009). The SCEC/USGS dynamic earthquake rupture code verification exercise, *Seismol. Res. Lett.*, **80**, 119–126.
- Hartzell, S. H. (1978). Earthquake aftershocks as Green's functions. *Geophys. Res. Lett.*, **5**, 1–4.
- Hartzell, S. H. and T. H. Heaton (1983). Inversion of strong ground motion and teleseismic waveform data for the fault rupture history of the 1979 Imperial Valley, California, earthquake. *Bull. Seism. Soc. Am.*, **73**, 1553–1583.
- Haskell, N. A. (1964). Total energy and energy spectral density of elastic wave radiation from propagating faults. *Bull. Seism. Soc. Am.*, **54**, 1811–1841.
- Haskell, N. A. (1966). Total energy and energy spectral density of elastic wave radiation from propagating faults, Part II. *Bull. Seism. Soc. Am.*, **56**, 125–140.
- Harskov, J. and L. Ottemöller (2010). *Routine Data Processing in Earthquake Seismology*. Berlin: Springer.
- Heaton, T. H. (1990). Evidence for and implications of self-healing pulses of slip in earthquake rupture. *Phys. Earth Planet. Int.*, **64**, 1–20.

- Herrero, A. and P. Bernard (1994). A kinematic self-similar rupture process for earthquakes. *Bull. Seism. Soc. Am.*, **72**, 2037–2062.
- Helberger, D. V. (1974). Generalized ray theory for shear dislocations. *Bull. Seism. Soc. Am.*, **64**, 45–64.
- Hirasawa, T. and W. Stauder (1965). On the seismic body waves from a finite moving source. *Bull. Seism. Soc. Am.*, **55**, 237–262.
- Houston, H., H. Benz, and J. E. Vidale (1998). Time functions of deep earthquakes from broadband and short period stacks. *J. Geophys. Res.*, **103**, 29 895–29 913.
- Hudson, J. A. (1980). *The Excitation and Propagation of Elastic waves*. Cambridge: Cambridge University Press.
- Husseini, M. I. and M. J. Randall (1976). Rupture velocity and radiation efficiency. *Bull. Seism. Soc. Am.*, **66**, 1173–1187.
- Husseini, M. J., D. B. Jovanovich, M. J. Randall and L. B. Freund (1975). The fracture energy of earthquakes. *Geophys. J. Roy. Astr. Soc.*, **43**, 367–385.
- Ida, Y. (1972). Cohesive forces across the tip of a longitudinal shear crack and Griffith's specific surface energy. *J. Geophys. Res.*, **77**, 3796–3805.
- Ida, Y. (1973). Stress concentration and unsteady propagation of longitudinal shear cracks. *J. Geophys. Res.*, **78**, 3418–3429.
- Ide, S. (2002). Estimation of radiated energy of finite-source earthquake models. *Bull. Seism. Soc. Am.*, **92**, 2994–3005.
- Ide, S. and M. Takeo (1997). Determination of constitutive relations of fault slip based on seismic wave analysis. *J. Geophys. Res.*, **102**, 27 379–27 391.
- Ide, S., G. Beroza, S. Prejean and W. Ellsworth (2003). Apparent break in earthquake scaling due to path and site effects on deep borehole recordings. *J. Geophys. Res.*, **108**, doi:10.1029/2001JB001617.
- Irwin, G. R. (1957). Analysis of stresses and strains near the end of a crack transversing a plate. *J. Appl. Mech.*, **64**, 361–364.
- Jeffreys, H. (1931). On the cause of oscillatory movements in seismograms. *Mon. Not. Roy. Astr. Soc. Geophys. Suppl.*, **2**, 407–416.
- Johnson, L. R. and R. M. Nadeau (2002). Asperity model of an earthquake: static problem. *Bull. Seism. Soc. Am.*, **92**, 672–686.
- Johnson, L. R. and R. M. Nadeau (2005). Asperity model of an earthquake: dynamic problem. *Bull. Seism. Soc. Am.*, **95**, 75–108.
- Jost, M. L. and R. B. Herrmann (1989). A student's guide to and review of moment tensors. *Seism. Res. Lett.*, **60**, 37–57.
- Kame, N. and T. Yamashita (1997). Dynamic nucleation process of shallow earthquake faulting on a fault zone. *Geophys. J. Int.*, **128**, 204–216.
- Kame, N. and T. Yamashita (1999a). A new light on arresting mechanism of dynamic earthquake faulting. *Geophys. Res. Lett.*, **26**, 1997–2000.
- Kame, N. and T. Yamashita (1999b). Simulation of the spontaneous growth of a dynamic crack without constraints on the crack tip path. *Geophys. J. Int.*, **139**, 345–358.
- Kanamori, H. (2004). The diversity of the physics of earthquakes. *Proc. Japan Acad. B*, **80**, 297–316.

- Kanamori, H. and D. L. Anderson (1975). Theoretical basis of some empirical relations in seismology. *Bull. Seism. Soc. Am.*, **65**, 1073–1095.
- Kanamori, H. and E. E. Brodsky (2004). The physics of earthquakes. *Rep. Progr. Phys.* **67**, 1429–1496.
- Kanamori, H. and J. W. Given (1981). Use of long period surface waves for rapid determination of earthquake source parameters. *Phys. Earth Planet. Int.*, **27**, 8–31.
- Kanamori, H. and G. S. Steward (1978). Seismological aspects of the Guatemala earthquake of February 4, 1976. *J. Geophys. Res.*, **83**, 3427–3434.
- Kaneko, Y., J. P. Avouac and N. Lapusta (2010). Towards inferring earthquake patterns from geodetic observations of interseismic coupling. *Nature Geosci.*, **3**, 363–369.
- Kasahara, K. (1963). Computer program for a fault plane solution. *Bull. Seism. Soc. Am.*, **53**, 1–13.
- Kennet, B. L. N. (1981). Seismic waves in a stratified half space – II. Theoretical seismograms. *Geophys. J. Roy. Astr. Soc.*, **61**, 1–10.
- Kennet, B. L. N. (2001). *The Seismic Wavefield. Vol. I: Introduction and theoretical development*. Cambridge: Cambridge University Press.
- Kennet, B. L. N. and E. R. Engdahl (1991). Traveltime for global earthquake location and phase identification. *Geophys. J. Int.*, **105**, 429–465.
- Keylis-Borok, B. V. (1956). Methods and results of the investigation of earthquake mechanism. *Publ. Bureau Central Seism. Inter. Ser A. Trav. Scient.*, **19**, 205–14.
- Keylis-Borok, B. V. (1959). On the estimation of the displacement in an earthquake source and of source dimensions. *Ann. Geofisica*, **12**, 205–214.
- Keylis-Borok, V. I., I. I. Pistetskii-Shapiro, V. F. Pisarenko and T. S. Zhelankina (1972). Computer determination of earthquake mechanism. In: *Computational Seismology*, New York: Plenum Publishing.
- Kasahara, K. (1981). *Earthquake Mechanics*. Cambridge: Cambridge University Press.
- Kikuchi, M. and H. Kanamori (1982). Inversion of complex body waves. *Bull. Seism. Soc. Am.*, **72**, 491–506.
- Kikuchi, M. and H. Kanamori (1991). Inversion of complex body waves III. *Bull. Seism. Soc. Am.*, **81**, 2335–2350.
- Koch, K. (1991). Moment tensor inversion of local earthquake data. Investigation of the method and its numerical stability with model calculations. *Geophys. J. Int.*, **106**, 305–319.
- Knopoff, L. (1958). Energy release in earthquakes. *Geophys. J. Roy. Astr. Soc.*, **1**, 44–52.
- Knopoff, L. (1961). Analytical calculation of the fault-plane problem. *Publ. Dominion Observatory*, **24**, 309–315.
- Knopoff, L. (1967). The mathematics of the seismic source. Institute of Geophysics, University of Karlsruhe (unpublished lecture notes).
- Knopoff, L. and F. Gilbert (1960). First motions from seismic sources. *Bull. Seism. Soc. Am.*, **50**, 117–134.
- Knopoff, L. and M. Randall (1970). The compensated vector linear dipole: a possible mechanism for deep earthquakes. *J. Geophys. Res.*, **75**, 4957–4963.
- Kostrov, B. V. (1964). Self-similar problems of propagation of shear cracks. *J. Appl. Math. Mech.*, **28**, 1077–1087.

- Kostrov, B. V. (1966). Unsteady propagation of longitudinal cracks. *J. Appl. Math. Mech.*, **30**, 1241–1248.
- Kostrov, B. V. (1975). On the crack propagation with variable velocity. *Int. J. Fracture*, **11**, 47–56.
- Kostrov, B. V. and S. Das (1982). Idealized models of fault behavior prior to dynamic rupture. *Bull. Seism. Soc. Am.*, **72**, 679–703.
- Kostrov, B. V. and S. Das (1988). *Principles of Earthquake Source Mechanics*. Cambridge: Cambridge University Press.
- Kostrov, B. V. and L. V. Nikitin (1970). Some general problems of mechanics of brittle fracture. *Archiwum Mechaniki Stosowanej*, **22**, 749–776.
- Lamb, H. (1904). On the propagation of tremors over the surface of an elastic solid. *Phil. Trans. Roy. Soc. A*, **203**, 1–42.
- Lancieri, M., R. Madariaga and F. Bonilla (2012). Spectral scaling of the aftershocks of the Tocopilla 2007 earthquake in northern Chile. *Geophys. J. Int.*, **188**, 469–480.
- Lapwood, E. R. (1949). The disturbance to a line source in a semi-infinite elastic medium. *Phil. Trans. Roy. Soc. London. A*, **242**, 63–100.
- Larson, K. (2009). GPS seismology. *J. Geod.*, **83**, 227–233.
- Lay, T. and T. C. Wallace (1995). *Modern Global Seismology*. Academic Press.
- Liu, P., R. J. Archuleta and S. H. Hartzell (2006). Prediction of broadband ground-motion time histories: Hybrid low/high-frequency method with correlated random source parameters. *Bull. Seism. Soc. Am.*, **96**, 2118–2130.
- Love, A. E. H. (1927). *The Mathematical Theory of Elasticity*. 4th edn. Cambridge: Cambridge University Press.
- Luco, J. E. and Apsel, R. J. (1982). On the Green's functions for a layered half-space: Part I. *Bull. Seism. Soc. Am.*, **72**, 275–302.
- Luco, J. E. and R. J. Apsel (1983). On the Green function for a layered half-space: Part I. *Bull. Seism. Soc. Am.*, **73**, 909–929.
- Ma, S., S. Custodio, R. Archuleta and P. Liu (2008). Dynamic modeling of the 2004  $M_W$  6.0 Parkfield, California, earthquake. *J. Geophys. Res.*, **113**, B02 301, doi:10.1029/2007JB005216
- MacCraffrey, R., G. Abers and P. Zwick (1991). Inversion of teleseismic body waves. In: *Digital Seismogram Analysis and Wave Form Inversion*, ed. W. H. K. Lee. IASPEI Software Library, vol. 3, pp. 81–166.
- Madariaga, R. (1976). Dynamics of an expanding circular fault. *Bull. Seism. Soc. Am.*, **66**, 639–666.
- Madariaga, R. (1977). High frequency radiation from crack (stress drop) models of earthquake faulting. *Geophys. J. Roy. Astr. Soc.*, **51**, 525–551.
- Madariaga, R. (1979). On the relation between seismic moment and stress drop in the presence of stress and strength heterogeneity. *J. Geophys. Res.*, **84**, 2243–2250.
- Madariaga, R. (2009). Seismic source theory. In: *Earthquake Seismology* (Treatise on Geophysics, vol. 4) eds. H. Kanamori and G. Schubert, pp. 59–82. Amsterdam: Elsevier.
- Madariaga, R. and A. Cochard (1994). Seismic source dynamics, heterogeneity and friction. *Ann. Geofis.*, **37**, 1349–1375.

- Madariaga, R. and K. B. Olsen (2000). Criticality of rupture dynamics in three dimensions. *Pageoph.*, **157**, 1981–2001.
- Madariaga, R. and K. B. Olsen (2002). Earthquake dynamics. In: *Int. Handbook of Earthquake and Engineering Seismology*, vol. 81A, pp. 175–194.
- Madariaga, R., K. B. Olsen and R. Archuleta (1998). Modeling dynamic rupture in a 3D earthquake fault model. *Bull. Seism. Soc. Am.*, **88**, 1182–1197.
- Mai, P. M. and G. C. Beroza (2002). A spatial random field model to characterize complexity in earthquake slip. *J. Geophys. Res.*, **107**, doi:10.1029/2001JB000588.
- Marone, C. (1998). Laboratory-derived friction laws and their application to seismic faulting. *Ann. Rev. Earth Planet. Sci.*, **26**, 643–696.
- McGarr, A. and J. B. Fletcher (2003). Maximum slip in earthquake fault zones, apparent stress, and stick-slip friction. *Bull. Seism. Soc. Am.*, **93**, 2355–2362.
- McGuire, J. J. (2004). Estimating finite source properties of small earthquake ruptures. *Bull. Seism. Soc. Am.*, **94**, 377–393.
- McGuire, J. J., Li Zhao and H. Jordan (2001). Teleseismic inversion for the second-degree moment of earthquake space–time distributions. *Geophys. J. Int.*, **145**, 661–678.
- Mendiguren, J. (1977). Inversion of surface wave data in source mechanism studies. *J. Geophys. Res.*, **82**, 889–894.
- Menke, W. (2012). *Geophysical Data Analysis: Discrete Inverse Theory*. 3rd edn. Waltham, Massachusetts: Academic Press.
- Mikumo, T. (1992). Dynamic fault rupture and stress recovery processes in continental crust under depth dependent shear strength and frictional parameters. *Tectonophys.*, **211**, 201–222.
- Mikumo, T. (1994). Dynamic fault rupture of moderate size earthquakes inferred from the results of kinematic wave form inversion. *Ann. Geofis.*, **37**, 1377–1389.
- Mikumo, T. and T. Miyatake (1978). Dynamic rupture process on a three-dimensional fault with non-uniform friction and near field seismic waves. *Geophys. J. Roy. Astr. Soc.*, **54**, 417–438.
- Mikumo, T. and T. Miyatake (1995). Heterogenous distribution of dynamic stress drop and relative fault strength recovered from the results of wave form inversion: the 1984 Morgan Hill, California earthquake. *Bull. Seism. Soc. Am.*, **85**, 178–193.
- Mikumo, T., E. Fukuyama, K. B. Olsen and Y. Yagi (2003). Stress breakdown time and critical weakening slip inferred from the slip-velocity function on earthquakes faults. *Bull. Seism. Soc. Am.*, **93**, 264–282.
- Mizoguchi, K., T. Hirose, T. Shimamoto, and E. Fukuyama (2007). Reconstruction of seismic faulting by high-velocity friction experiments: an example of the 1995 Kobe earthquake. *Geophys. Res. Lett.*, **34**, L01 308, doi:10.1029/2006GL027931.
- Molnar, P., B. E. Tucker and J. N. Brune (1973). Corner frequency of P and S waves and models of earthquakes sources. *Bull. Seism. Soc. Am.*, **63**, 101–104.
- Morse, P. M. and H. Feshbach (1953). *Methods of Theoretical Physics*. New York: McGraw-Hill.
- Müller, G. (1985). The reflectivity method: a tutorial. *J. Geophys.*, **58**, 153–174.
- Muskhelishvili, N. I. (1973). *Singular Integral Equations*. Groningen, Netherlands: P. Noordho.

- Nabelek, J. L. (1984). Determination of earthquake source parameters from inversion of body waves. Ph.D. thesis, Massachusetts Institute of Technology, Cambridge, Massachusetts.
- Nakano, H. (1923). Notes on the nature of forces which give rise to the earthquakes motion. *Seism. Bull. Cent. Meteor. Obs. Japan*, **1**, 92–120.
- Nielsen, S. and R. Madariaga (2003). On the self-healing fracture mode. *Bull. Seism. Soc. Am.*, **93**, 2375–2388.
- Nishimura, G. (1937). On the elastic waves due to pressure variations on the inner surface of a spherical cavity in an elastic solid. *Bull. Earthq. Res. Inst. Tokyo*, **15**, 614–635.
- Noda, H., E. M. Dunham, and J. R. Rice (2009). Earthquake ruptures with thermal weakening and the operation of major faults at low overall stress levels, *J. Geophys. Res.*, **114**, B07 302, doi:10.1029/2008JB006143.
- Ogata, Y. (1988). Statistical models for earthquake occurrences and residual analysis for point processes, *J. Amer. Statist. Assoc.*, **83**, 401, 9–27.
- Ohnaka, M. (2000). Physical scaling relation between the size of an earthquake and its nucleation zone size. *Pageoph.*, **157**, 2259–2282.
- Ohnaka, M. (2013). *The Physics of Rock Failure and Earthquakes*. Cambridge: Cambridge University Press.
- Okada, Y. (1992). Internal deformation due to shear and tensile faults in a half-space. *Bull. Seism. Soc. Am.*, **82**, 1018–1040.
- Okubo, P. G. (1989). Dynamic rupture modeling with laboratory-derived constitutive relations. *J. Geophys. Res.*, **94**, 12 321–12 335.
- Olsen, K. B., R. Madariaga and R. J. Archuleta (1997). Three-dimensional dynamic simulation of the 1992 Landers earthquake. *Science*, **278**, 834–838.
- Olsen, K. B., S. M. Day, L. A. Dalguer, J. Mayhew, Y. Cui, J. Zhu *et al.* (2009). ShakeOut-D: ground motion estimates using an ensemble of large earthquakes on the southern San Andreas fault with spontaneous rupture propagation. *Geophys. Res. Lett.*, **36**, L04 303, doi:10.1029/2008GL036832.
- Olson, H., J. A. Orcutt and G. A. Frazier (1984). The discrete wavenumber/finite element method for synthetic seismograms, *Geophys. J. Roy. Astr. Soc.*, **77**, 421–460.
- Omori F. (1894). On the aftershocks of earthquakes. *J. Coll. Sci., Imperial University of Tokyo*, **7**, 111–200.
- Palmer, A. C. and J. R. Rice (1973). The growth of slip surfaces in the progressive failure of over-consolidated clay. *Proc. Roy. Soc. A*, **332**, 527–548.
- Panza, G. (1985). Synthetic seismograms: the Rayleigh waves modal summation. *J. Geophys.*, **58**, 125–145.
- Passelègue, F. X., A. Schubnel, S. Nielsen, H. S. Bhat, and R. Madariaga (2013). From sub-Rayleigh to supershear ruptures during stick-slip experiments on rocks. *Science*, **340**, 1208–1211.
- Peyrat, S. (2001). Modélisation des tremblements de terre: rupture, rayonnement et inversion. Thèse de Doctorat, Université Paris Sud.
- Peyrat, S., and K. B. Olsen (2004). Nonlinear dynamic rupture inversion of the 2000 Western Tottori, Japan, earthquake, doi: 10.1029/2003GL019058.
- Peyrat, S., K. B. Olsen and R. Madariaga (2001). Dynamic modeling of the 1992 Landers earthquake. *J. Geophys. Res.*, **106**, 26 467–26 482.

- Peyrat, S., K. B. Olsen. and R. Madariaga, (2004). Which dynamic parameters can be estimated from strong ground motion? *Pageoph.*, **161**, 2155–2169.
- Poliakov, A., R. Dmowska, and J. R. Rice (2002). Dynamic shear rupture interactions with fault bends and off-axis secondary faulting, *J. Geophys. Res.*, **107**, 2295, doi 10.1029/2001JB000572.
- Prawirodirjo, L. and Y. Bock (2004). Instantaneous global plate motion model from 12 years of continuous GPS observations. *J. Geophys. Res.*, **109**, doi 10.1029/2003JB002944
- Pro, C. (2002). Estudio del efecto de directividad en la forma de ondas. Tesis Doctoral, Universidad Complutense de Madrid.
- Pujol, J. and R. H. Herrmann (1990). Student's guide to point sources in homogeneous media. *Seism. Res. Lett.*, **61**, 209–224.
- Reasenberg, P. and D. Oppenheimer (1985). FPFIT, FPPLLOT and FPPAGE: Fortran computer programs for calculating and displaying earthquake fault-plane solutions. US Geological Survey, Open File Report, pp. 85–739.
- Reches, Z. and D. A. Lockner (1994). Nucleation and growth of faults in brittle rocks. *J. Geophys. Res.*, **99**, 18 159–18 173.
- Reid, H. F. (1911). The elastic rebound theory of earthquakes. *Bull. Dept. Geol., University of California*, **6**, 412–444.
- Rice, J. R. (1968). A path independent integral and the approximate analysis of strain concentration by notches and cracks. *J. Appl. Mech.*, **35**, 379–386.
- Rice, J. R. (1980). The mechanics of earthquake rupture. In: *Physics of Earth's interior*, eds. A. M. Dziewonski and E. Boschi pp. 555–649. North Holland, Amsterdam.
- Rice, J. R., and A. L. Ruina (1983). Stability of steady frictional slipping. *J. Appl. Mech.*, **50**, 343–349.
- Rice, J. R., N. Lapusta and K. Ranjith (2001). Rate and state dependent friction and the stability of sliding between elastically deformable solids. *J. Mech. Phys. Sol.*, **49**, 1865–1898.
- Romanowicz, B. (1982). Moment tensor inversion of long period Rayleigh waves. A new approach. *J. Geophys. Res.*, **87**, 5395–5407.
- Romanowicz, B. (1992). Strike-slip earthquakes on quasi-vertical transcurrent faults: inferences for general scaling relations. *Geophys. Res. Lett.*, **19**, 1944–1988.
- Rosakis, A., J. O. Samadrula and D. Coker (1999). Cracks faster than the shear wave speed. *Science*, **248**, 1337–1340.
- Rubin, A. M., and J.-P. Ampuero (2005). Earthquake nucleation on (aging) rate and state faults, *J. Geophys. Res.*, **110**, B11 312, doi: 10.1029/2005JB003686.
- Ruina, A. (1983). Slip instability and state variable friction law. *J. Geophys. Res.*, **88**, 10 359–10 370.
- Ruiz, S. and R. Madariaga (2013). Kinematic and dynamic inversion of the 2008 Northern Iwate earthquake. *Bull. Seism. Soc. Am.*, **103**, 694–708.
- Sambridge, M. (1999). Geophysical inversion with a Neighbourhood Algorithm – I. Searching a parameter space. *Geophys. J. Int.*, **138**, 479–494.
- Sambridge, M. (2001). Finding acceptable models in nonlinear inverse problems using a neighbourhood algorithm. *Inverse Problems*, **17**, 387–403.

- Sato, T. and T. Hirasawa (1973). Body wave spectra from propagating shear cracks. *J. Phys. Earth*, **21**, 415–431.
- Savage, J. C. (1966). Radiation from a realistic model of faulting. *Bull. Seism. Soc. Am.*, **56**, 577–592.
- Savage, J. C. (1972). Relation of corner frequency to fault dimensions. *J. Geophys. Res.*, **77**, 3788–3795.
- Savage, J. C. and R. O. Burford (1973). Geodetic determination of relative plate motion in central California. *J. Geophys. Res.*, **78**, 832–845.
- Savage, J. C. and M. D. Wood (1971). The relation between apparent stress and stress drop. *Bull. Seism. Soc. Am.*, **61**, 1381–1388.
- Scherbaum, F. (1996). *Of Poles and Zeros. Fundamentals of Digital Seismology*. Dordrecht: Kluwer Academic Publishers.
- Schmedes, J., R. J. Archuleta, and D. Lavallée (2013). A kinematic rupture model generator incorporating spatial interdependency of earthquake source parameters. *Geophys. J. Int.* **192**, 1116–1131.
- Schmedes, J., R. J. Archuleta and D. Lavallée (2010). Correlation of earthquake source parameters inferred from dynamic rupture simulations, *J. Geophys. Res.*, **115**, doi:10.1029/2009JB006689
- Scholz, C. H. (1990). *The mechanics of earthquakes and faulting*, Cambridge: Cambridge University Press.
- Scholz, C. H. (2007). Fault mechanics. In: ed. A. B. Watts, *Treatise on Geophysics*, vol. 6, pp. 441–483. Amsterdam: Elsevier.
- Schwab, F., K. Nakanishi, M. Cuscito, G. F. Panza, G. Liang and J. Frez (1984). Surface wave computations and the synthesis of theoretical seismograms at high frequencies. *Bull. Seism. Soc. Am.*, **74**, 1555–1578.
- Shimazaki, K. (1986). Small and large earthquakes: the effect of the thickness of the seismogenic layer and the free surface. *Earthquake Source Mechanics, AGU Geophys. Mon.* **37**. American Geophysical Union. 209–216.
- Silver, P.G. and T. H. Jordan (1983). Total moment spectra of fourteen large earthquakes. *J. Geophys. Res.*, **88**, 3273–3299.
- Silver, P. G. and T. H. Jordan (1982). Optimal estimation of scalar seismic moment. *Geophys. J. Roy. Astr. Soc.*, **70**, 755–787.
- Sin Vigny, C., A. Socquet, S. Peyrat, J.-C. Ruegg, M. Metois, R. Madariaga *et al.* (2011). The 2010  $M_W$  8.8 Maule mega-thrust earthquake of Central Chile, monitored by GPS. *Science*, **331**, 1417–1421.
- Sipkin, S. A. (1982). Estimation of earthquake source parameters by the inversion of wave form data: synthetic waveforms. *Phys. Earth Planet. Inter.*, **30**, 242–259.
- Sipkin, S. A. (1986). Estimation of earthquake source parameters by the inversion of waveform data. Global seismicity, 1981–1983. *Bull. Seism. Soc. Am.*, **76**, 1515–1541.
- Sipkin, S. A. (1994). Rapid determination of global moment-tensor solutions. *Geophys. Res. Letters*, **21**, 1667–1670.
- Somerville, P., K. Irikura, R. Graves, S. Sawada, D. Wald, Y. I. T. Kagawa, N. Smith and A. Kowada (1999). Characterizing crustal earthquake slip models for the prediction of strong ground motion. *Seism. Res. Letters*, **70**, 59–80.

- Spudich, P. and L. N. Frazer (1984). Use of ray theory to calculate high-frequency radiation from earthquake sources having spatially variable rupture velocity and stress drop *Bull. Seismol. Soc. Am.*, **74**, 2061–2082.
- Spudich, P. and Cranswick, E. (1984). Direct observation of rupture propagation during the 1979 Imperial Valley earthquake using a short baseline accelerometer array. *Bull. Seism. Soc. Am.*, **74**, 2083–2114.
- Steketee, J. A. (1958). Some geophysical applications of the theory of dislocations. *Can. J. Phys.* **36**, 1168–1198.
- Strelitz, R. A. (1978). Moment tensor inversion and source models. *Geophys. J. Roy. Astr. Soc.*, **52**, 359–364.
- Strelitz, R. A. (1989). Choosing the best double couple from a moment tensor inversion. *Geophys. J. Int.*, **99**, 811–815.
- Stump, B. W., and L. R. Johnson (1977). The determination of source properties by linear inversion of seismograms. *Bull. Seism. Soc. Am.*, **67**, 1489–1502.
- Suzuki, W., S. Aoi and H. Sekiguchi (2009). Rupture process of the 2008 northern Iwate intraslab earthquake derived from strong-motion records, *Bull. Seism. Soc. Am.*, **99**, 2825–2835.
- Tago, J., V. M. Cruz-Atienza, J. Virieux, V. Etienne and F. J. Sánchez-Sesma (2012). A 3D hp-adaptive discontinuous Galerkin method for modeling earthquake dynamics. *J. Geophys. Res.*, **117**, B09 312, doi:10.1029/2012JB009313.
- Tapley, W. C. and J. E. Tull (1992). Guide to the UNIX version of SAC. Lawrence Livermore National Laboratory, University of California.
- Tarantola, A. (1987). *Inverse Problem Theory: Methods for Data Fitting and Model Parameter Estimation*. Amsterdam: Elsevier.
- Tinti, E., Spudich, P. and Cocco, M. (2005a). Earthquake fracture energy inferred from kinematic rupture models on extended faults, *J. Geophys. Res.*, **110**, B12 303, doi:10.1029/2005JB003644.
- Tinti, E., M. Cocco, E. Fukuyama and A. Piatanesi (2009). Dependence of slip weakening distance ( $D_c$ ) on final slip during dynamic rupture of earthquakes. *Geophys. J. Int.*, **177**, 1205–1220.
- Tinti, E., E. Fukuyama, A. Piatanesi and M. Cocco (2005b). A kinematic source time function compatible with earthquake dynamics. *Bull. Seism. Soc. Am.*, **95**, 1211–1223.
- Thio, H. K. and H. Kanamori (1995). Moment-tensor inversions for local earthquakes using surface waves recorded at TERRAscope. *Bull. Seism. Soc. Am.*, **85**, 1021–1038.
- Toda, S., R. S. Stein, V. Sevilgen, and J. Lin, (2011). Coulomb 3.3 graphic-rich deformation and stress-change software for earthquake, tectonic, and volcano research and teaching – User guide. US Geological Survey Open File Report 2011-1060, 63 pp., available at <http://pubs.usgs.gov/of/2011/1060/>.
- Tsuboi, C. (1956). Earthquake energy, earthquake volume, aftershock area and strength of the earth's crust. *J. Phys. Earth*, **4**, 63–66.
- Tsutsumi, A. and T. Miyamoto (1997). High-velocity frictional properties of gabbro. *Geophys. Res. Lett.*, **24**, 699–702.

- Twardzik, C., R. Madariaga, S. Das and S. Custodio (2012). Robust features of the source process for the 2004 Parkfield, California, earthquake from strong-motion seismograms. *Geophys. J. Int.*, **191**, 1245–1254.
- Udías, A. (1971). Source parameters of earthquakes from spectra of Rayleigh waves. *Geophys. J. Roy. Astr. Soc.*, **22**, 353–376.
- Udías, A. (1989). Development of fault plane studies for the mechanism of earthquakes. In: *Observatory Seismology*, ed. J. J. Litehiser, pp. 243–256. Berkeley: University of California Press.
- Udías, A. (1999). *Principles of Seismology*. Cambridge: Cambridge University Press.
- Udías, A. and E. Buorn (1988). Single and joint fault-plane solutions from first data. In: *Seismological Algorithms*, ed. D. Doornbos, pp. 443–453. London: Academic Press.
- Vallée, M., and M. Bouchon (2004). Imaging coseismic rupture in far field by slip patches. *Geophys. J. Int.*, **156**, 615–630.
- Vallée, M., M. Landès, N. M. Shapiro and Y. Klinger (2008). The 2001/11/14 Kokoxili (Tibet) earthquake: high frequency seismic radiation originates from the transitions between subRayleigh and supershear rupture velocity regimes. *J. Geophys. Res.*, **113**, B07 305, doi:10.1029/2007JB005520, 2008.
- Virieux, J. and R. Madariaga (1982). Dynamic faulting studied by a finite difference method. *Bull. Seism. Soc. Am.*, **72**, 345–369.
- Vvedenskaya, A. V. (1956). Determination of displacement fields for earthquakes by means of the dislocation theory. *Izv. Akad. Nauka SSSR, Geofiz.*, **3**, 277–284 (in Russian).
- Wald, D. J. and T. H. Heaton (1994). Spatial and temporal distribution of slip for the 1992 Landers, California, earthquake. *Bull. Seismol. Soc. Am.*, **84**, 668–691.
- Weertman, J. (1967). Uniformly moving transonic and supersonic dislocations. *J. Appl. Phys.*, **38**, 5293–5302.
- Wesnouzky, S. G. (1998). The Gutenberg–Richter or characteristic earthquake distribution, which is it? *Bull. Seism. Soc. Am.*, **88**, 1940–1959.
- Wickens, A. J. and J. H. Hodgson (1967). Computer reevaluation of earthquake mechanism solutions. *Publ. Dominion Observatory*, **33**, 1–560.
- Wyss, M. and J. B. Brune (1967). The Alaska earthquake of March 28, 1964. A complex multiple event. *Bull. Seism. Soc. Am.*, **57**, 1017–1023.
- Wyss, M. and J. N. Brune (1968). Seismic moment, stress and source dimensions for earthquakes in the California-Nevada region. *J. Geophys. Res.*, **73**, 4681–4694.
- Xia, K., A. J. Rosakis, and H. Kanamori (2004). Laboratory earthquakes: the sub-Rayleigh-to-supershear transition. *Science*, **303**, 1859–861.
- Yagi, Y., and M. Kikuchi (2000). Source rupture process of the Kocaeli, Turkey, earthquake of August 17, 1999, obtained by joint inversion of near-field data and teleseismic data. *Geophys. Res. Lett.*, **27**, 1969–1972.
- Yamashita, T. and M. Ohnaka (1991). Nucleation process of unstable rupture in the brittle regime: theoretical approach based on experimentally inferred relations. *J. Geophys. Res.*, **96**, 8351–8367.
- Yoffe, E. (1951). The moving Griffith crack. *Phil. Mag.*, **42**, 739–750.
- Zheng, G. and J. R. Rice (1998). Conditions under which velocity-weakening friction allows a self healing versus a cracklike mode of rupture. *Bull. Seism. Soc. Am.*, **88**, 1466–1483.

# Index

- amplitude spectra, 32, 34, 86, 125, 132, 137, 145, 177, 230, 269  
analogue data, 25  
arrest, 141, 151, 189, 246, 250–1, 269  
asperity, 269, 271, 278–9  
barriers, 243, 250–2  
Bath, 21  
Betti's theorem, 46  
bilateral, 138, 141–2, 146, 161, 177  
body forces, 63, 68, 90–2, 190, 209–10, 216, 223, 260  
body waves  
    source inversion, 165  
boundary integral, 210, 213, 235, 259, 276  
Brune's model, 148, 161, 164, 167, 195, 199, 204, 230, 245  
circular fault, 5, 135, 163, 192–3, 195, 200–1, 227, 231, 263, 265  
    expanding, 223  
cohesive force, 232  
cohesive zone, 232–7, 244, 246, 251  
corner frequency, 197, 200, 204, 230–1, 269  
crack, 12, 153, 159, 189–90, 198, 203, 209, 216, 223, 233  
crack growth, 205  
crack opening displacement, 205  
crack tip, 207–8, 211–12, 214, 220  
critical slip, 238–9, 246, 251  
digital data, ix, 25, 162, 165  
directivity, 124, 132, 268, 273  
    apparent source time function, 172  
    anti-directivity, 171  
    of body waves, 170  
    of Rayleigh waves, 167  
directivity effects, 148–9  
directivity function, 148  
directivity, ratio, 107  
directivity station, 150, 171  
double couple, 63–4, 90, 111, 124, 127, 135, 197  
    major and minor, 103  
    propagating, 135  
driving force, 18, 221  
dynamic inversion, 244, 276  
dynamic range, 25, 249, 281  
dynamics of fractures, 232  
earthquake cycle, 7, 9  
elastic rebound, 2, 7, 9  
energy, 201, 205, 27  
    elastic potential, 11  
    fracture, 199  
    friction, 12  
    kinetic, 88  
    potential, 88  
    radiated, 83  
    radiation, 88  
    seismic, 9  
    specific surface, 205  
    strain, 157, 198  
    total, 9, 12  
    scaling, 203  
energy barrier, 250  
energy flux, 88  
energy focussing, 148  
energy integral, 89  
energy ratio, 262  
energy release, 119, 200  
energy release rate, 207–8, 214, 235, 261  
energy balance, 198, 226  
energy flow, 209  
equation of motion, 16, 23, 37, 42, 48, 90, 190, 210, 262  
equivalent forces, 61, 63  
far field, 55–6, 73, 99, 111, 135, 196  
    extended source, 170  
far-field pulse, 229  
far-field spectra, 160  
far-field dynamic fault, 227  
far-field inversion, 173  
fault  
    dynamic models of, 189  
    kinematic models of, 155, 189  
    numerical determinations, 114  
    point source, 109  
    rectangular, 138  
    shear, 88  
fault creep, 5  
fault geology, 2

- fault geometry, 5  
 fault motion, 2  
 fault plane, 3, 75, 97  
 fault plane geometry, 77  
 fault plane graphical methods, 111  
 fault plane solutions, 110  
 fault types, 4, 6  
 finite differences method, 183, 223  
 focal region, 59, 63, 92, 189  
 focal sphere, 75, 80, 109, 111, 115  
     geographical axes, 78  
     projections, 111  
 fracture propagation, 85, 192, 216, 251  
     modes of, 192  
 friction, 9, 193, 214, 251, 260  
     dynamic, 16, 220, 237  
     kinematic, 15, 220, 237  
 friction law, 219, 237–40, 260, 262  
 friction model, 220, 233, 238, 246  
     rate-and-state, 239–40, 242  
     slip-weakening, 219, 233, 255, 278  
     static, 220, 263
- GPS, 188, 249  
     observations using, 39
- Green function-tensor**
- Green's function or Green's tensor, 44, 46, 52, 62, 64, 91, 93, 117, 119–20, 127, 217, 259  
     definition, 45  
     derivatives, 69, 124  
     empirical, 123  
     for near and far fields, 55  
     in infinite medium, 54  
     in layered media, 57  
     methods using, 128  
     numerical methods using, 183
- Green–Volterra equation**, 46
- Griffith's fracture, 205, 207, 227
- ground motion, 13, 24–5, 28, 30, 164, 173  
     acceleration in, 38  
     instrumental deconvolution of, 32  
     displacement in, 32  
     GPS data for, 39  
     horizontal components of, 34  
     in time domain, 29  
     in velocity domain, 37  
     recorded by seismographs, 22
- Gutenberg and Richter
- energy relations, 14  
     law, 19
- Haskell's model, 138  
     bilateral, 146  
     statistical, 147  
     unilateral, 146
- healing, 253, 260, 265  
 healing front, 154, 254
- healing phases, 225, 269  
 Heaton pulse, 154, 253  
 heterogeneous models, 232  
 Hooke's law, 42, 223
- instrumental
- deconvolution, 30, 32  
     response, 22, 27, 39, 121
- Irwin, 189, 207
- Iwate earthquake, 276, 282
- Izmit earthquake, 186, 255, 259, 275
- kinematic
- inversion, 181, 244, 259, 269, 271, 278  
     models, 61, 138, 151, 155, 157, 185, 189, 231, 259, 267, 273, 278  
     slip model, 276  
     source, extended, 135, 141, 163, 167, 177, 253
- Landers earthquake, 244, 255, 259, 270, 276
- magnification in seismographs, 24
- magnitude, 13, 19, 63, 121, 176, 197, 200  
     body wave, 13  
     moment, 14, 108, 200  
     surface wave, 13
- modes of propagation, 191
- moment-rate tensor, 107
- moment tensor, 157, 177, 184–5, 260  
     body wave, 128  
     centroid of, 101  
     compensated linear vector dipole, 104  
     components of, 94, 126  
     definition, 90  
     density, 90–1  
     deviatoric, 94  
     eigenvalues of, 93  
     eigenvectors of, 93  
     explosive source, 96  
     first-order, 92, 109  
     frequency domain, 100  
     higher-order, 105  
     inversion of, 124, 132, 185  
     isotropic, 94  
     moments higher, 106  
     point source, 99  
     principal axes of, 98  
     referred to geographical axes, 98  
     separation of, 102, 128  
     shear fracture, 97  
     surface wave, 130  
     synchronous, 99, 126  
     temporal dependence of, 100  
     tension fracture, 96
- near field, 55, 70, 188, 196, 250, 255, 259, 271, 273  
     definition, 55

- near field (cont.)
   
     Green's tensor for, 55
   
     inversion of, 181
   
     radiation pattern of, 74
   
     records of, 38
   
     time dependence of, 72
   
     nucleation, 108, 177, 189, 232, 241, 262–3
   
         definition, 151
   
         models of, 249
   
         Savage's model, 153
   
     nucleation zone, 246
   
  
 Omori's law, 20–1
   
  
 particle motion, 30, 35
   
 point source, 57, 63, 75, 86, 101, 135, 140, 170, 228, 230
   
     best, 102, 132
   
     energy of, 88
   
     inversion to find, 116, 124
   
     isotropic, 63
   
     moment tensor for, 90
   
     orientation of, 108
   
     parameters for, 87
   
     shear fracture, 66, 69
   
     time function for, 85
   
 potentials, 43, 48, 57
   
 pressure, 68, 192
   
 pressure axes, 64, 98, 108, 111
   
 pressure forces, 66
   
 pulse, 82, 135, 146–7, 149, 153, 195, 223, 230, 267
   
 body wave, 170
   
 far-field, 160
   
 propagating, 154, 253
   
 rectangular, 153
   
  
 radiation pattern, 52, 55, 71, 74, 111, 135, 141, 148, 155, 164, 166, 197, 228
   
     and focal sphere, 80
   
     far-field energy in, 88
   
     near-field, 71
   
     P wave, 118
   
     **far-field**
  
 rectangular fault, 5, 135, 138, 164, 174, 269, 273
   
     oblique, 142
   
 Reid's model, 2, 7
   
 representation theorem, 45, 60, 64, 66, 214
   
 rupture arrest, 251, 269
   
 rupture nucleation, 151, 247, 262
   
 rupture propagation, 107, 141–2, 169, 177, 192, 222–3, 238, 241, 250–1, 254, 259–60, 263, 270, 273, 276
   
  
 Seismic Analysis Code, 22, 31–2
   
 Sato and Hirasawa, 157, 223, 267
   
  
 scaling laws, 200
   
 seismic moment, 9, 18–19, 63, 67, 81, 100, 106, 108, 140, 159, 163, 170, 194, 200, 203, 228
   
     energy of, 89
   
     time rate of, 70, 118, 175, 184
   
 seismometer equation, 24
   
 shear fracture, 2, 11, 64, 66, 97, 103, 108, 111, 124, 156, 176, 189, 192
   
     far-field, 74, 80
   
     geometry of, 77
   
     point source, 69
   
     propagation of, 216
   
     time function for, 72
   
 single couple, 64
   
 slip distribution, 138, 156, 158, 165, 188, 198, 213, 225, 241, 245, 271
   
     inversion of, 173
   
 slip rate, 6, 82, 106, 141, 153, 163, 174, 214, 232, 238, 242, 260, 266
   
 slip weakening, 233–4, 238, 243, 260, 263, 272
   
 slip-weakening distance, 246
   
 Somigliana's tensor, 44, 48, 52, 55–7
   
 source dimensions, 63, 135, 138, 145, 148, 163, 176, 189
   
 source inversion, 177, 181, 184–5
   
 source time function, 6, 72–4, 76–7, 80–1, 83, 85–6, 89, 106, 108–9, 117, 124, 140, 156, 171–2, 175, 184, 229
   
 spectra, 32, 163
   
     properties, 86, 160
   
 static problem, 190, 192
   
 stick-slip movement, 14, 220
   
 stress, 94
   
     apparent, 12
   
     average, 11
   
     cohesive, 232
   
     effective, 195
   
     initial, 246
   
     due to kinematic friction, 15, 220
   
     singularities in, 212
   
     due to static friction, 220
   
     velocity-stress method, 261
   
 stress glut, 62, 91, 262
   
 stress drop, 9, 11
   
     average, 165
   
     dynamic, 16
   
     static, 16, 158, 190
   
 stress intensity factor, 194, 207, 214, 218
   
     static, 215
   
 sub-shear velocity, 237
   
 super-shear velocity, 272
   
  
 velocity
   
     sub-shear, 389
   
     super-shear, 448
   
 velocity weakening, 238